DISSERTATION

A Precision Measurement of Fiducial and Differential Cross Sections of WW Production with the ATLAS Detector at $\sqrt{s} = 13$ TeV

José Antonio Fernández Pretel

ALBERT-LUDWIGS-UNIVERSITÄT FREIBURG

CERN-THESIS-2024-361
21/06/2024

DISSERTATION

ZUR ERLANGUNG DES DOKTORGRADES (DR. RER. NAT.)

A Precision Measurement of Fiducial and Differential Cross Sections of WW Production with the ATLAS Detector at $\sqrt{s} = 13$ TeV

VORGELEGT VON

José Antonio Fernández Pretel

AUS ALMUÑÉCAR (SPANIEN)

BETREUERIN

Prof. Dr. Beate Heinemann

FAKULTÄT FÜR MATHEMATIK UND PHYSIK

ALBERT-LUDWIGS-UNIVERSITÄT FREIBURG

Dekan:	Prof. Dr. Michael Růžička
Betreuerin:	Prof. Dr. Beate Heinemann
1. Gutachterin:	Prof. Dr. Beate Heinemann
2. Gutachter:	Prof. Dr. Marc Schumann
Datum der mündlichen Prüfung:	21. Juni 2024
1. Prüferin:	Prof. Dr. Beate Heinemann
2. Prüfer:	Prof. Dr. Stefan Dittmaier
3. Prüfer:	Prof. Dr. Markus Schumacher
Datum:	9. April 2024

Abstract

Measuring production cross sections of W-boson pairs (W^+W^-) at particle colliders provides an important test of the predictions of Standard Model of particle physics in both perturbative quantum chromodynamics and electroweak domains. In this thesis, fiducial and differential cross-section measurements of W^+W^- production are presented. A dataset recorded with the ATLAS detector between 2015 and 2018 in proton-proton collisions at a center-of-mass energy of $\sqrt{s} = 13$ TeV at the Large Hadron Collider is analyzed, corresponding to an integrated luminosity of $140\ \mathrm{fb}^{-1}$.

The event selection targets leptonic decays into an electron and a muon of opposite electric charge ($W^+W^- \to e^{\pm}\nu_e\mu^{\mp}\nu_\mu$). In contrast to many previous measurements that enhance the W^+W^- signal purity by vetoing hadronic jets in the final state, the first measurement of the W^+W^- production cross sections using a fully jet-inclusive selection is presented in this thesis. Contributions from top-quark and lepton misidentification backgrounds are estimated using data-driven techniques. The latter relies on the definition of lepton selection criteria targeting non-prompt lepton contributions. An accurate modeling of prompt leptons fulfilling these selection requirements is ensured by performing a dedicated calibration using the tag-and-probe method. The associated uncertainties are drastically reduced, no longer being a limiting factor in the precision of W^+W^- cross-section measurements.

The fiducial W^+W^- cross section is determined in a maximum-likelihood fit with an uncertainty of $3.1\,\%$. The measurement is extrapolated to the full phase space, resulting in a total W^+W^- cross section of

$$\sigma\left(pp \to W^+W^-\right) = 127 \pm 1\,(\mathrm{stat.}) \pm 4\,(\mathrm{syst.})\,\mathrm{pb}\,,$$

providing the most precise measurement of the W^+W^- production cross section achieved in hadron-hadron collisions to date. Differential cross sections are measured as a function of twelve observables describing the kinematics of leptons, jets, and the missing transverse energy of the W^+W^- system. State-of-the-art theory predictions are in excellent agreement with the reported measurements. Differential distributions at reconstruction level are used to constrain anomalous electroweak gauge boson self-couplings and interactions between the Higgs scalar field, leptons, and quarks in the framework of a dimension-six effective field theory.

To address the numerous challenges in environments of high instantaneous luminosity expected during the operation of the LHC Run 3 and High-Luminosity LHC, upgrades of the experimental detectors were carried out between 2019 and 2022. These involved the replacement of the innermost muon chambers in the ATLAS detector's endcaps with the New Small Wheels (NSWs). A new facility to test small-strip Thin Gap Chambers (sTGC), one of the main technologies of the NSW, has been commissioned in Freiburg. Design, installation, and validation of the gas and high-voltage systems necessary for operating a sTGC prototype under nominal conditions of LHC data-taking are reported in this thesis.

Zusammenfassung

Die Messung des Wirkungsquerschnitt der Produktion von W-Bosonpaaren (W^+W^-) an Teilchenbeschleunigern stellt einen wichtigen Test der Vorhersagen des Standardmodells der Teilchenphysik sowohl im Bereich der perturbativen Quantenchromodynamik als auch der elektroschwachen Wechselwirkung dar. In dieser Arbeit werden Messungen des fiduziale und differentielle Wirkungsquerschnitts des W^+W^- Prozesses vorgestellt. Es wird ein Datensatz von Proton-Proton-Kollisionen analysiert, welcher zwischen 2015 und 2018 mit dem ATLAS-Detektor bei einer Schwerpunktsenergie von $\sqrt{s} = 13$ TeV am Large Hadron Collider aufgenommen wurde. Dieser entspricht einer integrierten Luminosität von $140\ \mathrm{fb}^{-1}$.

Die Ereignisauswahl zielt auf leptonische Zerfälle in ein Elektron und ein Myon mit entgegengesetzter elektrischer Ladung ab ($W^+W^- \to e^\pm\nu_e\mu^\mp\nu_\mu$). Im Gegensatz zu vielen früheren Messungen, die die Reinheit des W^+W^--Signals erhöhen indem sie hadronische Jets im Endzustand ausschließen, wird in dieser Arbeit die erste Messung der W^+W^--Wirkungsquerschnitte unter Verwendung einer vollständig jet-inklusiven Auswahl präsentiert. Beiträge von Top-Quark- und Leptonenfälschungs-Untergründen werden unter Verwendung datengetriebener Techniken abgeschätzt. Letztere beruht auf der Definition von Leptonenauswahlkriterien, welche nicht-prompten Leptonbeiträge abschätzen, deren Modellierung durch eine dedizierte Kalibrierung mit der Tag-and-Probe Technik verbessert wird. Die damit verbundenen Unsicherheiten werden drastisch reduziert und sind nicht mehr der limitierende Faktor für die Präzision der W^+W^--Wirkungsquerschnittsmessungen.

Der fiduziale W^+W^--Wirkungsquerschnitt wird in einem Maximum-Likelihood-Fit mit einer Unsicherheit von $3.1\,\%$ bestimmt. Die Messung wird auf den gesamten Phasenraum extrapoliert, was zu einem Gesamt-W^+W^--Querschnitt von

$$\sigma\left(pp \to W^+W^-\right) = 127 \pm 1\,(\mathrm{stat.}) \pm 4\,(\mathrm{syst.})\,\mathrm{pb}$$

führt und die präziseste Messung der W^+W^--Wirkungsquerschnitte darstellt, die bisher in Proton-Proton-Kollisionen erreicht wurde. Differentielle WIrkungsquerschnitt werden als Funktion von zwölf Observablen gemessen, die die Kinematik von Leptonen, Jets und fehlender transversaler Energie des W^+W^--Systems beschreiben. Modernste theoretische Vorhersagen stimmen ausgezeichnet mit den berichteten Messungen überein. Differentielle Verteilungen auf rekonstruiertem Niveau werden verwendet, um anomale elektroschwache Eichboson-Selbstwechselwirkungen und Wechselwirkungen zwischen dem Higgs-Skalarfeld, Leptonen und Quarks im Rahmen einer effektiven Feldtheorie der Dimension sechs einzuschränken.

Um den zahlreichen Herausforderungen in Umgebungen hoher instantaner Luminosität zu begegnen, die während des Betriebs des LHC Run 3 und High-Luminosity-LHC zu erwarten sind, wurden zwischen 2019 und 2022 Aufrüstungen der experimentellen Detektoren durchgeführt. Dies umfasste den Austausch der innersten Myonkammern in den Endkappen des ATLAS-Detektors durch die New Small Wheels (NSWs). In Freiburg wurde eine neue Einrichtung zur Prüfung von Small-Strip Thin Gap Chambers (sTGC), einer der Haupttechnologien des NSW, in Betrieb genommen. Das Design, die Installation und die Validierung der Gas- und Hochspannungssysteme, die für den Betrieb eines sTGC-Prototyps unter den nominalen Bedingungen der LHC-Datennahme erforderlich sind, werden in dieser Arbeit beschrieben.

Contents

Introduction

"I do not insist," answered Don Quixote, "that this is a full adventure, but it is the beginning of one, for this is the way adventures begin."

— Miguel de Cervantes Saavedra (1547 – 1616).

In the quest to unravel the mysteries of the cosmos, humanity's innate curiosity about the nature of its surroundings has been an enduring force, propelling civilizations through epochs of scientific inquiry and technological progress. From the earliest days of Mesopotamia, or the later philosophical inquiries of ancient Greece, the pursuit of understanding the fundamental constituents of matter has been a recurrent thread through human history. This journey has led to insights into celestial motions, the formulation of gravitational laws, advancements in chemistry with classifications of elements, breakthroughs in electricity and magnetism encapsulated in Maxwell's Equations [1], and the quantum theory. Today, these questions resonate in the field of particle physics, where researchers seek to understand the fundamental building blocks of the universe and the forces that govern their interactions. This Ph.D. thesis serves as a modest contribution to the lineage of human fascination with the question: *What are things made of?* By delving into cutting-edge experiments and theoretical calculations, it aims to bridge the gap between the ancient inquiries of our predecessors and the forefront of contemporary particle physics research.

The postulation of the electron [2] in 1897 was crucial to describe the structure of the atom [3]. Since the beginning of the 20th century, the photon is known as the mediator of light. Postulated as a particle (or *light quantum*) to describe the photoelectric effect [4], it also allowed to explain the wave radiation quanta in Planck's work on the black body radiation problem [5]. The two approaches were conciliated by A. H. Compton [6, 7]. The positron [8] (after its postulation by P. Dirac's theory [9]) the muon, and the antimuon [10] and their corresponding neutrinos [11, 12, 13, 14] were known experimentally[1]. The efforts to understand the patterns proposed by the *Eightfold Way* [18], crucial to find the Ω^- baryon in 1964 [19], paved the way to the concept of quarks as presented by Gell-Mann [20], Zweig [21], and Petermann [22] to explain the flavor symmetry observed experimentally. Three distinct elementary fermions (up, down, and strange quarks) were necessary to account for the observed meson and baryon spins, with the *color* charge [23] and its confinement [24] to accommodate Fermi-Dirac statistics with the existence of fully symmetric baryon states such as the Δ^{++}. Additionally, further evidence of the theory

[1] Once suggested by Pauli in relation to beta decays, a first experimental verification was provided by C. L. Cowan and F. Reines [15, 16, 11] in 1953, while its differentiation with respect to the antineutrino was found experimentally later by R. Davis and D. S. Harmer [12] in relation to lepton-number conservation, which has been postulated by E. J. Konopinski and H. M. Mahmoud [17]. B. Pontecorvo suggested that several kinds of neutrinos should exist [13], and the first piece of evidence of the two-neutrino hypothesis was obtained in 1962 [14].

of Quantum Chromodynamics (QCD) as a meaningful description of nature came from the three-jet event measurement [25], first achieved by the four different collaborations at the PETRA e^-e^+ accelerator (1978–86), regarded as an experimental proof of the existence of the gluon. The theoretical formulation of asymptotic freedom was obtained in 1973 by D. Gross, F. Wilczek [26, 27] and D. Politzer [28, 29]. The running of α_S was also confirmed by various experiments[2]. Owing to the cooperative effort of many experimental and particle physicists around the world, the *Standard Model of particle physics* (SM) was then acknowledged to explain natural phenomena such as the radioactive beta decay (initially explained by Fermi in 1933 [31]) and the existence of atomic nuclei.

Simultaneously, the theory of electroweak (EW) interactions emerged. A decisive step was achieved in 1956 by C. S. Wu with her experiment establishing the parity-violating nature of weak interactions [32]. Weak interactions had to be described by a chiral theory. The unification of electromagnetic and weak interactions in the EW theory was described by S. Glashow [33], A. Salam [34] and S. Weinberg [35]. The renormalizability of the EW theory was proven in 1971 by G. 't Hooft and M. J. G. Veltman [36, 37]. Observations of the neutral currents by the Gargamelle experiment [38] and the discovery of $W^\pm$ [39, 40] and Z bosons [41, 42] in 1983 by the UA1 and UA2 experiments at the $Sp\bar{p}S$ proton-antiproton ($p\bar{p}$) collider at CERN [43, 44, 45] provided an outstanding confirmation of the formulation of the EW theory.

The so-called *November revolution* started when charm and bottom quarks were confirmed via the discovery of J/ψ mesons (by both the Brookhaven National Laboratory [46], and the SLAC SPEAR accelerator [47]) and bottonium states. Additionally, the discovery of CP violation in the kaon system, as documented in experiments like KTeV [48] and NA48 [49] in 1999, needed the introduction of a third-generation quark. This concept was elucidated in 1973 by M. Kobayashi and T. Maskawa, who demonstrated that it was the only viable way for the CKM matrix to incorporate a complex CP-violating phase [50]. This idea gained further support with the detection of the bottonium Υ (the ground state of the $b\bar{b}$ quark-antiquark pair) in 1977 at Fermilab [51], following the earlier discovery of the tau (τ) lepton in 1975 at SLAC [52]. The top quark's higher mass exceeded the energy capabilities of available e^-e^+ accelerators such as PETRA at DESY, TRISTAN in Japan, PEP and SLC at SLAC, and LEP at CERN, delaying its discovery until 1994 at the Tevatron proton-antiproton collider at Fermilab [53], while some indirect determinations of the top quark's mass were already underway in 1993 at LEP and SLC [54].

The Large Electron-Positron (LEP) collider [55, 56, 57] offered a clean and controlled environment for precise measurements of the EW parameters. These measurements include the confirmation of the number of light neutrinos [54] (supported later by the discovery of the τ neutrino in 2000 with the DONUT experiment at Fermilab [58]), the masses and decay widths of the $W^\pm$ and Z bosons [54, 59], the EW mixing angle represented by $\sin^2\theta_W$, and the characterization of gluon and vector boson self-couplings, among many others. However, the missing piece in the puzzle of the SM was the elusive Higgs boson[3]. These consequences strongly motivated the construction of the Large

[2] For a review, see Ref. [30].

[3] While some constraints on its mass of $m_H \lesssim 1$ TeV were derived from e^-e^+ collider analyses and theoretical considerations, none of these machines were capable of definitively discovering the Higgs boson with sufficient statistical significance [60, 61]. It was understood that vector-boson scattering processes would violate unitarity at high energies without the presence of a massive scalar field. This understanding led to the establishment of a bound on the Higgs mass, suggesting it to be less than or around 1 TeV.

Hadron Collider (LHC) at CERN [62, 63, 64]. The spontaneous breaking of the gauge symmetry [65, 66, 67] describing EW interactions causes three of the four mediators of this force, namely the $W^{\pm}$ and Z bosons, to acquire mass by means of interactions with the *Higgs field*. The photon γ, as the fourth mediator, remains massless. The discovery of the Higgs boson was announced by the ATLAS [68] and CMS [69] Collaborations in 2012. The first LHC run of proton-proton (pp) collisions, spanning from 2009 to 2012, primarily focused on probing the Higgs boson's interactions with gauge bosons at center-of-mass energies of 7 and 8 TeV. The subsequent run, operating at $\sqrt{s} = 13$ TeV of pp collisions from 2015 to 2018, enabled the study of the Higgs Yukawa couplings with the third generation of charged fermions, specifically the top and bottom quarks, as well as the τ lepton. Furthermore, the LHC has conducted a multitude of cross section and parameter measurements, with increasingly competitive precision compared to previous e^-e^+ collider experiments[4].

The production of W-boson pairs (W^+W^-) is sensitive to the properties of gauge vector boson self-interactions, and provides a test of the SM predictions in perturbative QCD and the EW theories. Two mechanisms are involved in W^+W^- production: (i) the radiation of two $W^{\pm}$ bosons from the proton constituents and (ii) their production via the exchange of a virtual photon or a Z boson. Both production mechanisms exhibit infinite growth with energy, but they interfere destructively. This ensures exact cancellation of effects from longitudinally polarized gauge bosons if the coupling strengths of $W^{\pm}$ bosons to quarks, the photon, and the Z boson agree with SM predictions. To date, hadron colliders provide the highest achievable center-of-mass energies allowing the study of these predictions. Additionally, W^+W^- production constitutes a large background in the measurement of, e.g., Higgs boson production and searches for physics beyond the SM. Apart from measuring the mass and width of the $W^{\pm}$ bosons, this process was exploited at LEP to also characterize the self-couplings among gauge vector bosons with high precision [59]. The W^+W^- production rates have been measured in pp collisions at $\sqrt{s} = 5$ TeV [72], 7 TeV [73, 74], 8 TeV [75, 76, 77] and 13 TeV [78, 79, 80, 81, 82], and in $p\bar{p}$ collisions [83, 84, 85] at the Tevatron collider [86].

Precise theoretical calculations, incorporating perturbative corrections in QCD and EW theories, are vital for the description of the W^+W^- process and the analysis of collision data at high precision. Strong interactions confine outgoing quarks and gluons into bound states from initial and final state real QCD radiation, observable as hadronic jets. Ongoing improvements in these calculations further motivate experimental measurements of W^+W^- production. Production rates of pairs of $W^{\pm}$ bosons are measured in this thesis, comparing them to state-of-the-art theoretical predictions. The first part of this thesis is devoted to the discussion of the theoretical foundations. Chapter 1 offers a brief overview of quantum field theories forming the Lagrangian density of the SM, which can be extended with extra operators to account for anomalous interactions that might be proven at the energy regime of the LHC in the context of *Effective Field Theories* (EFTs). Chapter 2 includes its application for physics at hadron colliders, offering also an overview of state-of-the-art Monte Carlo event generators. Chapter 3 supplements these two chapters, including a brief review on the simulation of W^+W^- production and more specific information on the state-of-the-art generators relevant to this process.

[4] Prominent examples are the experimental determinations of the W-boson mass, which has reached an accuracy of 16 MeV [70], or $\alpha_S(m_Z) = 0.1183 \pm 0.0009$ [71].

The ATLAS experiment, placed at one of the interaction points of the LHC, is designed for particle measurements in hadron-hadron collisions. This thesis focuses on the measurement of two $W^{\pm}$ bosons produced in pp collisions at a center-of-mass energy of $\sqrt{s} = 13\,\mathrm{TeV}$, using a dataset with an integrated luminosity of $140\ \mathrm{fb}^{-1}$ recorded between 2015 and 2018. The $W^{\pm}$ bosons are identified through their decay products into leptons (electrons or muons) accompanied by associated neutrinos, serving as clear signatures of an electroweak process. The expectedly larger instantaneous luminosity during the third run of data-taking at the LHC, and particularly in the High-Luminosity LHC (HL-LHC), pose multiple challenges that need to be addressed for a successful physics program. Doing so, upgrades were implemented from 2019 to 2022, involving the replacement of the innermost muon chambers in the ATLAS detector's endcaps with the *New Small Wheels* (NSWs). The second part of this thesis addresses the experimental setup and statistical methods used. In Chapter 4, the LHC accelerator complex is outlined before the description of the ATLAS detector and its subsystems. The methods to reconstruct and calibrate the relevant objects for this thesis such as leptons and jets are also presented. The NSW in the context of the HL-LHC program, focusing on the relevance of the small-strip Thin Gap Chamber (sTGC) technology, is presented in Chapter 5. The author has designed, installed, and validated gas and high-voltage systems required for running a sTGC prototype in nominal data-taking conditions in a new test laboratory in Freiburg. The results of this work are also discussed in this chapter. The statistical methods used for fiducial and total cross-section measurements in this thesis are outlined in Chapter 6.

The final part of this thesis focuses on fiducial and total cross-section measurements of W^+W^- production, including their interpretation in the context of EFTs. It begins with a review of prior W^+W^- measurements and defines the analysis strategy in Chapter 7. As the leptonic W^+W^- decay involves two neutrinos in the final state, the full reconstruction of the $W^{\pm}$ bosons is not possible. This leads to a significant contamination from other SM processes mimicking the W^+W^- signature. The experimental challenges are intensified by the high instantaneous luminosity provided by the LHC, necessitating the understanding of the detector effects and background processes visible in the data. The expected number of event candidates arising from top-quark pair production ($t\bar{t}$), the largest background for this measurement, is reduced by rejecting events containing jets with b-hadron decays (b-jets). This background contribution is precisely estimated with a data-driven method, allowing for the reduction of uncertainties arising in the theoretical modeling of top-quark pairs and the efficiency of identifying b-jets. Another large source of uncertainties in measurements of W^+W^- cross sections arise from $W + \mathrm{jets}$ events with a misidentified or non-prompt lepton. The author developed a data-driven method to estimate these contributions with high precision. Requirements targeting the selection of such leptons are defined for the extrapolation of the data-driven background into the signal region. The author also performs, for the first time in W^+W^- measurements, a dedicated calibration of prompt leptons fulfilling these selection criteria. These contributions were crucial in minimizing the primary systematic uncertainties in this analysis, facilitating the level of precision achieved in the reported cross-section measurements. The remaining backgrounds are estimated based on theoretical predictions. The dilepton invariant mass is required to be greater than $85\,\mathrm{GeV}$, to reduce the background due to Drell-Yan production of leptonically decaying τ-lepton pairs. The details of the background estimation techniques employed for the W^+W^- cross-section measurements performed in this thesis are studied in Chapter 8. The measurement presented in this thesis,

for the first time in hadron-hadron colliders, extends the event selection to include final states with no restrictions on the number of reconstructed hadronic jets other than b-jets, significantly reducing sensitivity to theoretical uncertainties subject to large logarithmic corrections and enhancing the precision of the measurement. It is also advantageous from an experimental perspective as jet-related uncertainties are reduced. Chapter 9 details the methodology followed in the experimental determination of the W^+W^- fiducial cross sections whose results, presented in Chapter 10, have been publicly released in Ref. [87]. The author contributed to the study of the state-of-the-art theoretical calculations aiming to describe the reported measurements and to extrapolate the results in the fiducial volume to the full phase-space. In Chapter 11, the results are interpreted to constrain anomalous couplings defined using the SM degrees of freedom in an EFT. Owing to the increased dataset and enhanced precision, the limits obtained by the author improve results in global fits of Higgs, electroweak and top-quark data at the $95\,\%$ CL [88, 89] for the operators most sensitive to W^+W^- production.

Part I

Theoretical Foundations of Particle Physics

Chapter 1
The Standard Model of Particle Physics

"The hidden harmony is better than the obvious."

— Pablo Picasso (1881 – 1973).

In physics, the behavior of natural phenomena can be predicted based on four fundamental forces acting on matter: the electromagnetic, strong, weak, and gravitational interactions. Contemporary understanding interprets matter as composed of fundamental particles. The Standard Model of particle physics (SM), a Quantum Field Theory (QFT), offers a framework for precise calculations in the description of matter and its interactions, detailed in Refs. [90, 91]. This chapter provides an overview of the SM, summarizing its particle content in Section 1.1. The strong interaction is incorporated into the SM as described in Section 1.2, while Section 1.3 introduces the electroweak (EW) unification, explaining the interplay between electromagnetic and weak interactions. The spontaneous symmetry breaking mechanism is presented in Section 1.4, and the resulting terms complete the SM Lagrangian. This Lagrangian enables the computation of fiducial and differential cross sections for various processes as outlined in Section 1.5. However, the SM Lagrangian falls short in explaining certain experimental observations, listed in Section 1.6. Deviations with respect to the SM can be parameterized in the context of Effective Field Theories (EFT) whose formalism, outlined in Section 1.7, is used in this dissertation to interpret fiducial differential cross-section measurements of W^+W^- production.

1.1 The Particle Content of the Standard Model

The SM characterizes the laws of nature at the most fundamental scale, where components of matter are assumed to be indivisible. Elementary particles and their interactions need to be addressed respecting the conservation laws of physics. The *Noether theorem* [92] plays a crucial role when connecting these requirements by proving a direct mathematical relation between continuous *gauge symmetries* in a theory with physical conservation laws. As a *gauge theory*, EW and strong interactions emerge in the SM by postulating renormalizability and local symmetry invariance under the non-abelian group $\mathrm{SU}(3)_C \otimes \mathrm{SU}(2)_L \otimes \mathrm{U}(1)_Y$[1]. Every symmetry has a corresponding charge, which allows charged quantum fields (associated to particles) to interact under the corresponding symmetry. Quantum fields are classified according to their *spin*, taking half-integer numbers[2] (1/2, 3/2, ...) for *fermionic* fields and integer values (0, 1, ...) for *bosonic* fields. *Fermions*, i.e. fundamental particles associated to quanta of a fermionic field, come in three *generations* and can be divided into six *quarks* and six *leptons*, whether they are

[1] To date, a unified description of gravitational, electromagnetic, strong and weak interactions as a quantum theory with satisfactory results has not been achieved.

[2] Natural units $\hbar = c = 1$ are used in this dissertation. Therefore, energy, momenta and masses are quoted in units of *electronvolts* (eV).

charged under the $\mathrm{SU}(3)_C$ symmetry or not, respectively. Leptons can be divided into three electrically-charged massive[3] leptons called *electron* (e), *muon* (μ), and *tauon* (τ), three neutral *neutrinos* ν_e, ν_μ, and ν_τ, and their corresponding *antiparticles*[4]. All generations share the same quantum numbers but differ in their particle masses.

The *strong interaction*, governed by the gauge group $\mathrm{SU}(3)_C$ whose invariance imposes the conservation of three charges denoted as *color* [23], is described in the SM by mediation of eight *gluons*. Only quarks and gluons carry color charge and therefore interact through the strong interaction. The color charge can take values of *red*, *green* and *blue*, and their corresponding antivalues. Only particles with vanishing net color, the so-called *hadrons*, have been experimentally observed. The *valence quarks* of a hadron define its quantum properties according to the quark model [20, 21, 22]. Following this evidence, only *mesons* (composed by two colored-opposed quarks) and *baryons* (superpositions of all three colors or anticolors) can be produced. This phenomenon is known as *color confinement* [24]. The QFT describing strong interactions within the SM, known as Quantum Chromodynamics, is described in Section 1.2.

As all stable matter in the universe is composed only by elementary particles of the first generation, the second and third generations contain unstable particles that decay into lighter ones. These particle decays are described in the SM by the *electroweak interaction*, whose formalism is outlined in Section 1.3. EW interactions arise from the gauge group $\mathrm{SU}(2)_L \otimes \mathrm{U}(1)_Y$, where $\mathrm{SU}(2)_L$ acts only on left-handed particles with associated *weak isospin* (T) while $\mathrm{U}(1)_Y$ acts on particles with *weak hypercharge* (Y). The third component of T (T_3), when added to Y, provides the *electric charge* $Q = T_3 + \frac{Y}{2}$. The *photon* γ, a massless gauge boson that conveys the interaction between electrically-charged particles, and three massive gauge bosons, $W^{\pm}$[5] and Z, mediate the EW interaction among particles. Under the $\mathrm{SU}(2)_L$ group, quantum fields forming doublets are referred to as *left-handed* fermion fields, while singlet fields are known as *right-handed* fermion fields. This structure introduces *maximal parity violation*[6], as proven experimentally in β^- decays [32]. Weak interactions also introduce the violation of charge and parity discrete symmetries (known as *CP violation*) in the quark sector, regulating mass and interaction eigenstates of up-down quarks parameterized by the *Cabibbo–Kobayashi–Maskawa (CKM) matrix* [93, 50], whose standard formulation can be found in Refs. [94, 95].

Since the EW gauge symmetry does not allow gauge bosons to be massive, it is necessary to break this symmetry to generate massive *electroweak gauge bosons* in the SM, $W^{\pm}$ and Z, according to experimental evidence [39, 40, 41, 42]. This is done by introducing a new complex scalar doublet with four new degrees of freedom in the theory [66, 67, 65]. Only one of them has physical meaning, the *Higgs field*, with the rest being removed by gauge transformations during the *Electroweak Symmetry Breaking* (EWSB), introduced in Section 1.4. The EW gauge bosons and fermions acquire mass once the symmetry is broken. The massive nature of $W^{\pm}$ and Z bosons restrict weak interactions to short ranges. In 2012, a Higgs boson candidate was discovered by the ATLAS [68] and the

[3] In contradiction with experimental evidence (see Section 1.6), neutrinos are considered to be massless in the traditional formulation of the SM.

[4] If not explicitly stated, the label ℓ will be used to denote a lepton ℓ^- and its corresponding antilepton ℓ^+ without distinction.

[5] If not explicitely stated, W^+ and W^- bosons are indistinguishably referred to as $W^{\pm}$ bosons.

[6] *Parity* refers to the discrete symmetry transformation that drives spatial coordinates to their opposite, $P(\vec{x}) = -\vec{x}$.

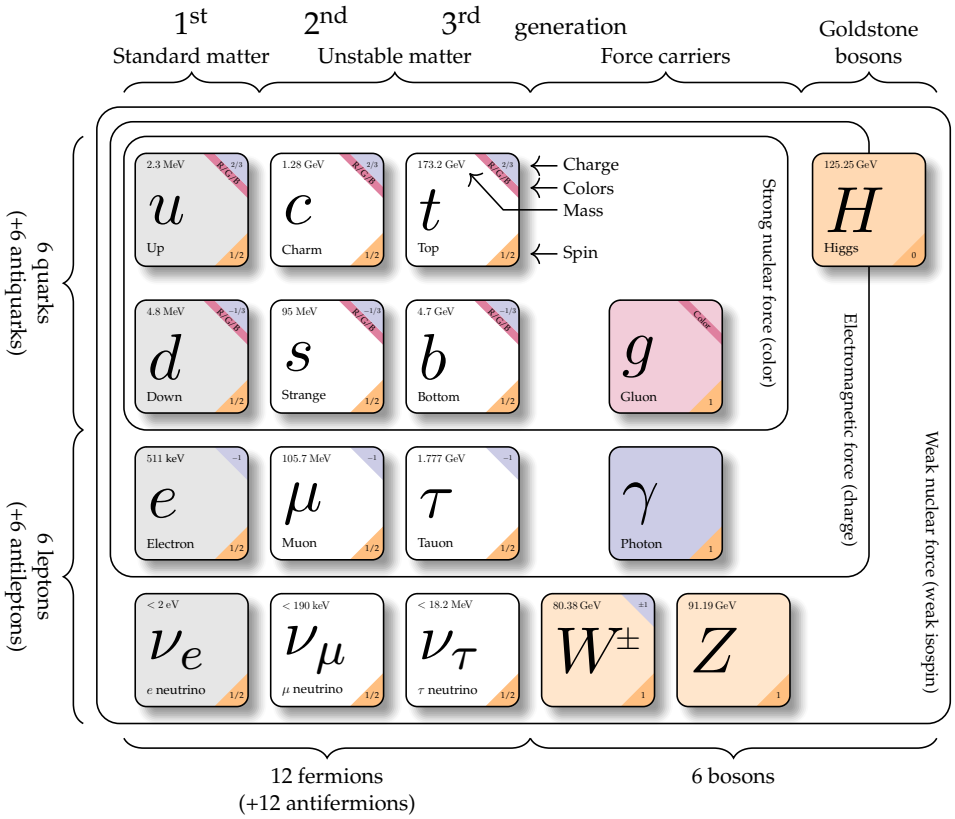

Figure 1.1: Elementary particles in the Standard Model. Adapted from [96].

CMS [69] collaborations at the Large Hadron Collider (LHC) [62, 63, 64]. To date, its mass ($m_H = 125.25 \pm 0.17\,\text{GeV}$[7]), decay width ($\Gamma_H = 3.2^{+2.4}_{-1.7}\,\text{MeV}$[8]), its couplings, and other quantum properties such as spin or electric charge are consistent with the SM predictions [101, 102, 95]. The aforementioned lepton, quark and boson content of the SM is summarized in Figure 1.1, where the fundamental particles are classified according to their quantum numbers and masses.

1.2 Quantum Chromodynamics

Strong interactions can be described by a QFT imposing Lorentz and local gauge invariance under trasformations of the quark color fields q under the group $\mathrm{SU}(3)$. Such a QFT is known as *Quantum Chromodynamics* (QCD). The *free Dirac Lagrangian density*[9] of free color spin-half fermion fields $\mathscr{L}_{\text{Dirac},C}$ can be written as

$$\mathscr{L}_{\text{Dirac}} = \sum_{j}^{3} \bar{q}_j \left(i\gamma^\mu \partial_\mu - m\right) q_j \,, \tag{1.1}$$

[7]The last tabulated value [95] is given, although the latest measurements have already achieved a precision of 0.01% [97, 98].

[8]This points to the tabulated value, corresponding to the measurement performed by the CMS Collaboration [99]. A measurement performed by ATLAS was recently released [100]. Both make use of the off-shell contributions to the $ZZ \to 4\ell$ decay channel.

[9]In the following, the Lagrangian density will be referred to as *Lagrangian*.

by summing over the three color charges. The contraction of the *Dirac matrices* γ^μ [9] is given by $\gamma^\mu\partial_\mu$, and m is the mass of the quark. *Local gauge invariance* is required in $\mathrm{SU}(3)_C$ by means of the transformation $q_j \to e^{i\alpha(x)\cdot\mathbf{T}}\, q_j$, where $\mathbf{T} = \{T_a\}$, with $a = 1, ..., 8$, is the set of eight generators of the $\mathrm{SU}(3)$ symmetry group. These generators are related to the *Gell-Mann matrices* λ (3×3 matrices) by $T_a = \frac{\lambda_a}{2}$ in the fundamental representation. Since the generators $\mathbf{T}$ do not commute[10], the group is *non-abelian*. Introducing vector fields with transformation properties given by the *covariant derivative*

$$\partial_\mu \to \partial_\mu + ig_s\frac{\lambda}{2}G^a_\mu\,, \tag{1.2}$$

$$G^a_\mu \to G'^a_\mu = G^a_\mu - \frac{1}{g_s}\partial_\mu\alpha_a(x) - f_{abc}\alpha_b(x)G^c_\mu\,, \tag{1.3}$$

coupling the eight massless[11] *gluon fields* G^a_μ with a *coupling strength* g_s, yields local gauge invariance under $\mathrm{SU}(3)_C$ in the Lagrangian of QCD,

$$\mathscr{L}_{\mathrm{QCD}} = \sum_j^3 \bar{q}_j\left(i\gamma^\mu\partial_\mu - m\right)q_j - g_s\left(\bar{q}_j\gamma^\mu\frac{\lambda_a}{2}q_j\right)G^a_\mu - \frac{1}{4}G^a_{\mu\nu}G^{\mu\nu}_a\,. \tag{1.4}$$

$G^a_{\mu\nu} = \partial_\mu G^a_\nu - \partial_\nu G^a_\mu - g_s f_{abc}G^b_\mu G^c_\nu$ denotes the field strength tensor. The *kinetic term* for the gauge fields is given by $-\frac{1}{4}G^a_{\mu\nu}G^{\mu\nu}_a$. As a peculiarity of $\mathrm{SU}(3)$ and its non-abelian structure, additional interaction terms arise in QCD from this strength tensor, allowing *self-interactions* between gluon fields.

An additional gauge-invariant renormalizable term $\theta_{\mathrm{QCD}}\frac{g_s^2}{32\pi^2}\tilde{G}^a_{\mu\nu}G^a_{\mu\nu}$, being $\tilde{G}^a_{\mu\nu} = \epsilon^{\mu\nu\rho\delta}G^a_{\rho\delta}$ the dual gluon field strength tensor and $\epsilon^{\mu\nu\rho\delta}$ the completely antisymmetric Levi-Civita tensor, introduces physical implications in Eq. (1.4) such as the violation of the discrete CP symmetry in strong interactions. The value of θ_{QCD}, which dictates the amount of this violation, is strongly constrained by experimental measurements ($\theta_{\mathrm{QCD}} < 10^{-10}$) and therefore omitted. This choice introduces a fine-tuning in the theory widely known as *strong CP problem*, discussed in e.g. Ref. [103].

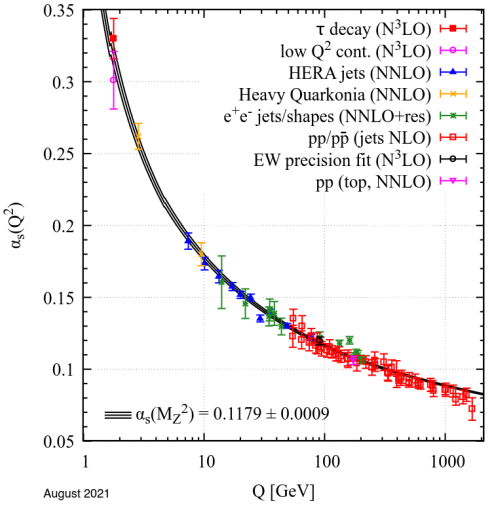

Figure 1.2: Summary of measurements of α_S as a function of the energy scale Q. Source: [95].

Experimental evidence heavily supports the existence of quarks. However, no free quark was experimentally found to date[12]. The hypothesis of *color confinement* [24], describing colored objects as confined to color-singlet states, explains the absence of any object with non-zero color charge propagating as a free particle. Color confinement is believed to originate from the gluon–gluon self-interactions that arise from the non-abelian structure of QCD. To date, no analytical proof

[10] Commutation relations are $[T_a, T_b] = if_{abc}T_c$, where f_{abc} are the *structure constants* of the group $\mathrm{SU}(3)$.
[11] Gluon mass terms break the gauge invariance of $\mathscr{L}_{\mathrm{QCD}}$.
[12] The manifestation of fractionally charged particles in nature could indicate the existence of free quarks.

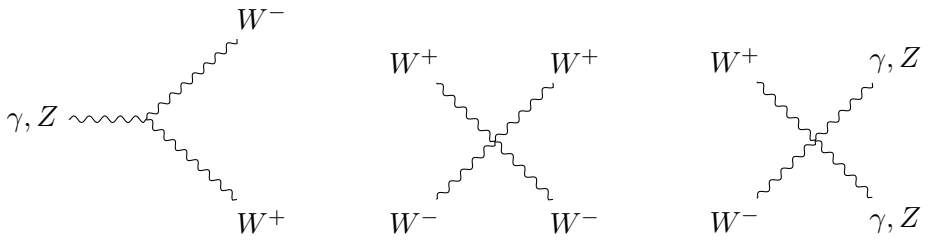

Figure 1.3: Feynman diagrams for electroweak gauge boson self-interaction terms.

of this concept has been found [104]. Another consequence of the color confinement hypothesis is that gluons, as colored particles, are also confined to colorless objects. Therefore, gluons do not propagate over macroscopic distances.

The value of the coupling constant of strong interactions $\alpha_S = g_s^2/4\pi$ depends on the energy scale Q of the interaction,

$$\alpha_S(Q^2) = \frac{12\pi}{(33 - 2n_f)\log\left(\frac{Q^2}{\Lambda^2_{\mathrm{QCD}}}\right)},$$

being n_f the number of quark flavors. In the low-energy regime, below the *confinement scale* Λ_{QCD}, values of α_S are large enough that perturbation theory is not convergent. Techniques in *lattice QCD* are employed in these circumstances[13]. Processes such as hadronization, described in Section 2.3, lie within this energy regime. At sufficiently high energies, the evolution of α_S with Q can be computed up to a certain order in perturbation theory. This dependence of α_S on the transferred energy is shown in Figure 1.2. The value of α_S becomes smaller with increasing Q. This phenomenon, known as *asymptotic freedom* [26, 28, 27, 29], is strongly supported by experimental results from multiple experiments across several orders of magnitude in Q.

1.3 The Electroweak Sector of the Standard Model

In the SM, electromagnetic and weak interactions are described in a unified framework named the *electroweak theory* that requires local gauge invariance under transformations of the $\mathrm{SU}(2)_L \otimes \mathrm{U}(1)_Y$ group. In this group, fermion fields are represented by left-handed (LH) doublets χ_L and right-handed (RH) singlets ψ_R. For first-generation leptons[14], they are expressed as a function of electron and neutrino fields, e and ν_e, as

$$\chi_L(x) = \begin{pmatrix} \nu_e \\ e \end{pmatrix}, \quad \psi_R = e_R\,. \tag{1.5}$$

Local gauge invariance under symmetry groups $\mathrm{SU}(2)_L$ and $\mathrm{U}(1)_Y$ is imposed by

$$\chi_L \to e^{i\beta(x)Y + i\alpha_a(x)\tau_a}\chi_L\,, \tag{1.6}$$

[13] An extensive review on Lattice QCD techniques can be found in Ref. [95].

[14] The derived expressions for the first-generation quarks as well as second and third quark and lepton generations are analogous.

$$\psi_R \to e^{i\beta(x)Y}\psi_R\,, \tag{1.7}$$

where the three *Pauli matrices* τ_a are the generators of $\mathrm{SU}(2)_L$ while the *weak hypercharge* Y appears as generator of the group $\mathrm{U}(1)$. Both $\beta(x)$ and $\alpha_a(x)$ are the local phase transformations. The value of the hypercharge for a LH fermion field takes $Y = -1$, being $Y = -2$ for RH fermion fields. By transforming the derivative ∂_μ to the covariant derivative, the Lagrangian describing interactions between massless gauge boson fields and massless fermion fields is obtained,

$$\begin{aligned}\mathscr{L}_{\mathrm{EW}} &= \mathscr{L}_{\mathrm{EW,\,int}} + \mathscr{L}_{\mathrm{EW,\,kin}} \\ &= \bar{\chi}_L\gamma^\mu\left[i\partial_\mu - g_w\frac{\tau_a}{2}W_\mu^a + \frac{g'_w}{2}B_\mu\right]\chi_L + \bar{\psi}_R\gamma^\mu\left[i\partial_\mu + g'_wB_\mu\right]\psi_R - \frac{1}{4}W^a_{\mu\nu}W_a^{\mu\nu} - \frac{1}{4}B_{\mu\nu}B^{\mu\nu}\,,\end{aligned} \tag{1.8}$$

where, the kinematic term $\mathscr{L}_{\mathrm{EW,\,kin}}$ for the *massless* gauge field strength tensors $B_{\mu\nu}$ and $W_{\mu\nu}$ was included to preserve gauge invariance in terms of the *weak coupling constants* g_w and g'_w. Interactions between massless gauge boson fields and massless fermion fields W_μ^a $(a = 1, 2, 3)$ described in this theory are in contradiction with experimental evidence [39, 40, 41, 42]. In order to address these, the *physical fields* $W_\mu^\pm$, Z_μ and A_μ of $W^\pm$ and Z bosons as well as the photon γ, respectively, are expressed as linear combinations of the original gauge fields B_μ and W_μ^a,

$$W_\mu^\pm = \frac{1}{\sqrt{2}}\left[W_\mu^1 \mp iW_\mu^2\right] \quad , \quad \begin{pmatrix} A_\mu \\ Z_\mu \end{pmatrix} = \begin{pmatrix} \cos\theta_W & \sin\theta_W \\ -\sin\theta_W & \cos\theta_W \end{pmatrix}\begin{pmatrix} B_\mu \\ W_\mu^3 \end{pmatrix}, \tag{1.9}$$

where the *weak mixing angle* θ_W needs to be $\sin\theta_W = g'_w/\sqrt{g_w^2 + g_w'^2}$ to obtain the A_μ current from electrodynamics. The expansion of $\mathscr{L}_{\mathrm{EW,\,kin}} = -\frac{1}{4}W^a_{\mu\nu}W_a^{\mu\nu} - \frac{1}{4}B_{\mu\nu}B^{\mu\nu}$, for EW gauge fields (1.8) introduces, in the same way as seen in Section 1.2 for QCD, *self-interaction terms* among the EW bosons. Figure 1.3 shows the corresponding Feynman diagrams.

The non-abelian structure of the EW theory is crucial to ensure its renormalizability. In absence of the gauge vector boson self-couplings (Figure 1.3), the predicted cross sections in the EW theory would not respect unitarity. The production of W-boson pairs in electron-positron (e^-e^+) interactions can be used as an example. If diagrams involving e.g. the triple-gauge coupling ZWW, the cross section would grow faster than the total cross section in e^-e^+ interaction. The confirmation of the non-abelian structure of the EW sector was provided by the Large Electron-Positron

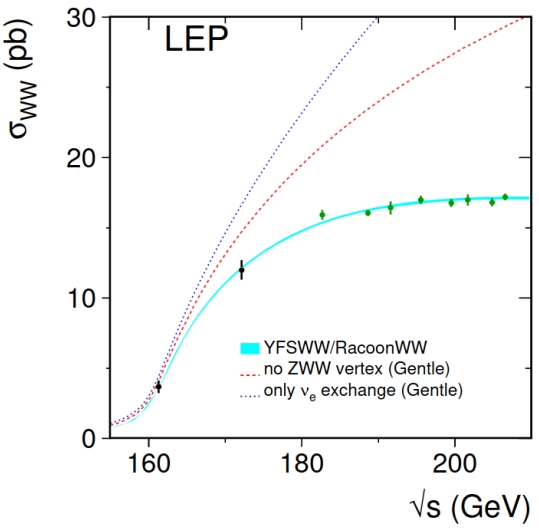

Figure 1.4: Total W^+W^- production cross-section (σ_{WW}) measurements from the LEP-II combination, compared to SM theory predictions at various center-of-mass energies ($\sqrt{s}$). Experimental uncertainties are shown, along with scenarios excluding the ZWW gauge coupling (dashed line) and $e^+e^- \to W^+W^-$ production via only t-channel neutrino exchange (dotted line). The shaded blue curve accounts for theoretical uncertainties on the SM prediction, below 2% [59].

(LEP) collider at CERN [55, 56, 57] measuring the total $e^+e^- \to W^+W^-$ production cross section at different center-of-mass energies [59], as shown in Figure 1.4.

Local gauge invariance under the symmetry group $\mathrm{SU}(2)_L \otimes \mathrm{U}(1)_Y$ forbids these gauge boson fields and the fermion fields to be massive[15]. Adding mass terms for these fields destroys *renormalization* and *unitarity*, which are crucial for the predictive power of the theory. To address the experimental observations tackling the aforementioned inconveniences, additional terms need to be added to $\mathscr{L}_{\mathrm{EW}}$. This necessity leads to the appearance of the *Higgs field* in the theory, that allows the EW gauge bosons to acquire mass, whose values have been observed experimentally with high accuracy. This mechanism is introduced in the following.

1.4 Spontaneous Symmetry Breaking, the Higgs Boson and the Standard Model Lagrangian

Addressing the inconsistencies between the SM predictions and the experimental measurements of EW interactions requires an extension of the theoretical framework outlined in Section 1.3 to incorporate mass terms for fermions and massive gauge vector bosons within a renormalizable formulation of $\mathscr{L}_{\mathrm{EW}}$. To achieve this, a new complex scalar boson field ϕ is introduced, characterized by a non-vanishing expectation value in the ground state. The interaction between the field ϕ and the gauge boson fields is established through the covariant derivative, inducing a phenomenon known as *spontaneous symmetry breaking* within the group $\mathrm{SU}(2)_L \otimes \mathrm{U}(1)_Y$,

$$\mathscr{L}_{\mathrm{EW}}^{\phi} = (D_\mu \phi)^\dagger D^\mu \phi - V(\phi) = (D_\mu \phi)^\dagger D^\mu \phi - \mu^2 \phi^\dagger \phi + \lambda \phi^\dagger \phi \,, \tag{1.10}$$

with $D_\mu = \left(i\partial_\mu - \frac{g_w}{2} \tau_a W_\mu^a - i\frac{g'}{2} B_\mu \right)$ being the covariant derivative for $\mathrm{SU}(2)_L \otimes \mathrm{U}(1)_Y$. The potential $V(\phi)$ is the most general way to keep both renormalizability of the theory (at most ϕ^4 terms) and gauge invariance with $\mu^2 < 0$ and $\lambda > 0$, having a local maximum and infinite-degenerated minima. Only multiplets in $\mathrm{SU}(2)_L \otimes \mathrm{U}(1)_Y$ can be considered for ϕ to ensure gauge invariance. The symmetry $\mathrm{U}(1)_Q$ needs to be unbroken, so that non-zero hypercharge and isospin are required for ϕ while the photon remains massless. This new complex scalar field has 4 degrees of freedom. Three of these, the so-called Goldstone modes [105, 106], can be absorbed by gauge transformation in the theory (as longitudinal polarization modes of the massive gauge bosons). The remaining degree of freedom $h(x)$, the scalar *Higgs field*, generates the Higgs boson mass. These features lead to a potential

$$\phi(x) = \frac{1}{\sqrt{2}} \begin{pmatrix} 0 \\ v + h(x) \end{pmatrix} , \tag{1.11}$$

with minimum at $|\phi_0| = \sqrt{\frac{-\mu}{2\lambda}} = \frac{v}{\sqrt{2}}$ also known as its *vacuum expectation value*. For the chosen vacuum expectation value to break the $\mathrm{SU}(2)_L \otimes \mathrm{U}(1)_Y$ symmetry, the physical Higgs field is electrically neutral since $Y = +1$, $T = \frac{1}{2}$ and $T_3 = -\frac{1}{2}$. The interactions of this field with the EW gauge bosons, arising from Eq. (1.10), provide the corresponding

[15] That is, terms of the kind $m_\psi \psi \bar{\psi}$, $m_W W_\mu W^\mu$ or $m_B B_\mu B^\mu$ break the required local gauge invariance when they are included *ad-hoc* in the Lagrangian.

mass terms in the Lagrangian. The EW gauge boson masses are related to the vacuum expectation value of the Higgs field,

$$m_W = \frac{g \cdot v}{2}\,, \quad m_H = \sqrt{2\mu^2}\,, \quad m_Z = \frac{m_W}{\cos\theta_W} = \frac{v^2\sqrt{g^2+g'^2}}{2}\,, \quad m_A = 0\,. \tag{1.12}$$

Along the same calculation, self-interactions of the Higgs field arise. The aforementioned couplings also resolve unitarity and renormalizability of the EW theory[16] mentioned in Section 1.3.

Even though the Brout-Englert-Higgs mechanism incorporated the mass terms for the EW gauge bosons into the Lagrangian (1.10), the mass terms for fermions are still missing. The same Higgs doublet (1.11) is sufficient to explain also the fermion mass terms by means of spontaneous symmetry breaking of the same group. Gauge invariant terms $\mathscr{L}_{\text{Yukawa}}$ under the $\mathrm{SU}(2)_L \otimes \mathrm{U}(1)_Y$ symmetry can be incorporated. As an example, the corresponding term for lepton fields χ_L and ψ_R is shown,

$$\mathscr{L}_{\text{Yukawa}} = -G_\ell \left[\bar{\chi}_L \phi \psi_R + \bar{\psi}_R \phi^* \chi_L\right]\,, \tag{1.13}$$

with arbitrary parameters G_ℓ, and $\ell = e, \mu, \tau$. Using the same parameterization (1.11) for the Higgs field, the mass terms for the different leptons and the interaction terms of the different leptons with the Higgs field h are

$$\mathscr{L}_{\text{Yukawa}} = \mathscr{L}_{\text{mass}} + \mathscr{L}_{h\ell\ell,int} = \frac{G_\ell v}{\sqrt{2}}\left(\bar{\ell}_L \ell_R + \bar{\ell}_R \ell_L\right) - \frac{G_\ell}{\sqrt{2}}\left(\bar{\ell}_L \ell_R + \bar{\ell}_R \ell_L\right) h\,. \tag{1.14}$$

Adding the Lagrangian terms from QCD given by Eq. (1.4), the EW sector (1.8) describing the kinematics for the vector gauge bosons, their self-interactions, lepton and quark kinematic energies and interactions with vector gauge bosons, the couplings of vector gauge boson fields to the Higgs (1.10), and the Lagrangian term describing lepton and quark masses and their couplings to the Higgs field (1.13) provides the full *SM Lagrangian* $\mathscr{L}_{\text{SM}}$. Most of the precision measurements carried out in particle collider experiments so far are in agreement with the SM predictions [95]. As an example, a summary of SM cross-section measurements performed with the ATLAS experiment at the LHC is shown in Figure 1.5.

1.5 Branching Ratios and Cross Sections in Particle Physics

Characterizing the decays of unstable particles is one of the main tasks in particle physics. Since an unstable particle can decay into different final states (so-called *decay modes*), determining the probability per unit of time to decay into a specific final state, the so-called *decay rate* Γ, is of great interest. The sum of all individual decay rates provides the *total decay rate* Γ_{tot}, with the *lifetime* of the particle being its inverse, Γ_{tot}^{-1}. Once the rates to

[16] As an example, the predicted cross section of vector boson scattering $W^+W^- \to W^+W^-$ in the absence of the Higgs boson would be proportional to the center-of-mass energy of the system $\sqrt{s}$ as, $\sigma \sim s/m_W$, where m_W is the mass of the W boson. The cross section σ would then grow faster than the total cross section of the pp interaction. Introducing diagrams involving the Higgs boson in the computation of the cross section solves this divergence, ensuring unitarity.

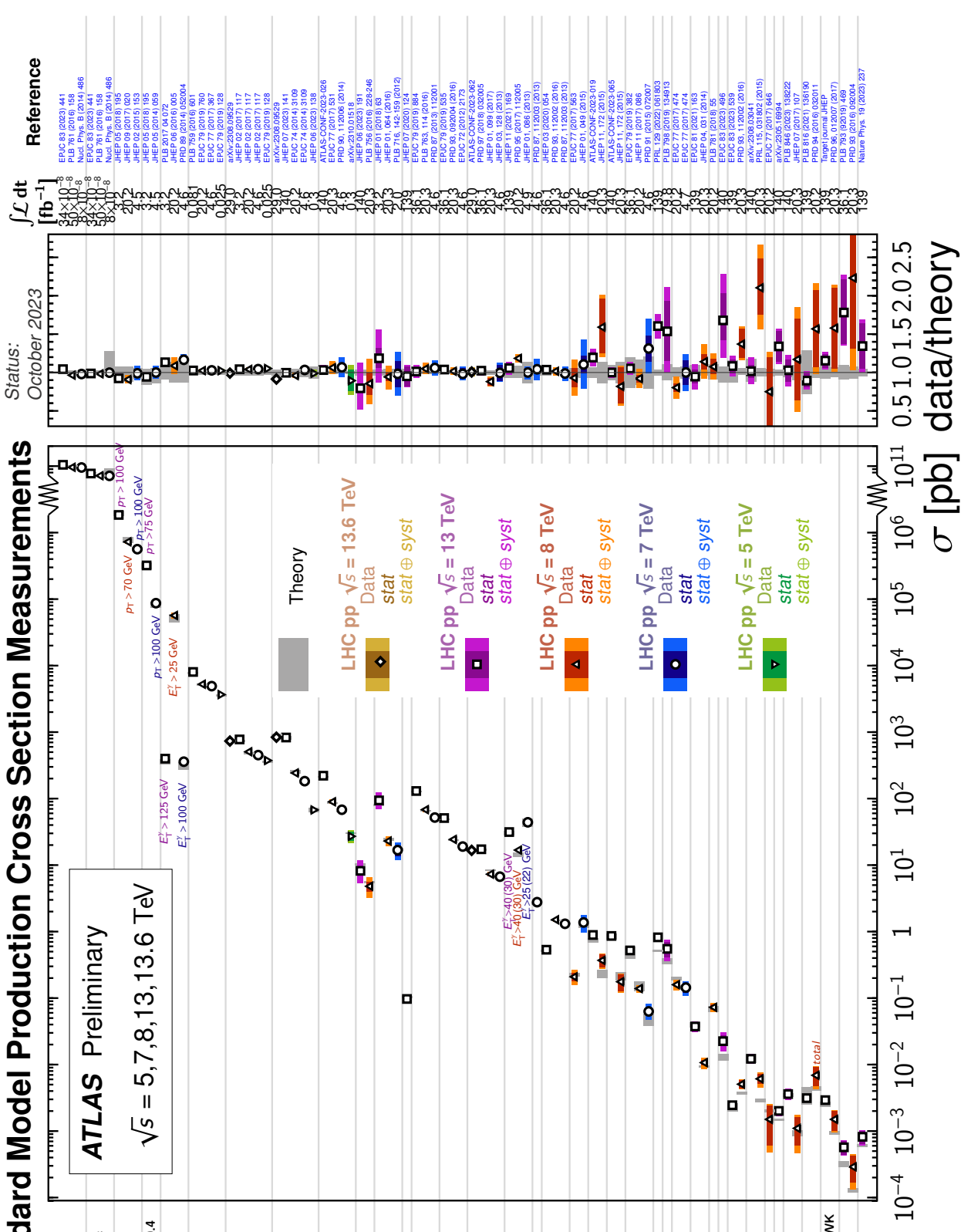

Figure 1.5: Overview of cross-section measurements for a wide variety of SM processes as reported by the ATLAS Collaboration at the LHC for pp collisions at center-of-mass energies of 7, 8, 13 and 13.6 TeV [107]. On the right-hand side, the data-to-theory ratio is presented. Uncertainties from the experimental value and the theoretical predictions are shown in colored bars.

individual decay modes have been computed, the fraction of given unstable particles in an initial set that decay into a certain final state, so-called *branching ratio*, can be inferred.

In collisions of two objects, one of the most interesting variables to measure is the cross-sectional area of a target for a given projectile. In particle physics, a scattering process can be classified as either *elastic*, i.e. the particles in the final state are the same as in the initial state ($a + b \to a + b$), or *inelastic*, when one or more of the initial-state particles can break down, yielding n particles[17] in the final state ($a + b \to \sum_{i=1}^{n} c_i$). Each of the possible scattering events has its own *exclusive cross section* σ_X for the final state X, with the *total cross section* being the sum of all of them. To determine a cross section σ, the experimentalist can scan only a certain region of the phase space Ω, referred to as *fiducial phase space*. The proportionality between an infinitesimal $\mathrm{d}\sigma$ given an infinitesimal variation of the phase space $\mathrm{d}\Omega$ is called *differential cross section* $\mathcal{D}$, so that $\mathrm{d}\sigma = \mathcal{D}(\theta)\mathrm{d}\Omega$, where θ specifies the variable in which the infinitesimal variation is taking place. Given an incoming beam of particles with uniform *luminosity* $\mathcal{L}$ (i.e. the number of particles per unit of time and area), the number of particles produced within an infinitesimal region of the phase space $\mathrm{d}\Omega$ after the scattering process is given by $\mathrm{d}N = \mathcal{L}\mathrm{d}\sigma = \mathcal{L}\mathcal{D}(\theta)\mathrm{d}\Omega$. This means that, using the number of particles per unit of time $\mathrm{d}N$ (event rate) covered within $\mathrm{d}\Omega$, where the luminosity is predetermined by the accelerator facility providing the beam, a differential cross section can be defined as $\mathrm{d}\sigma/\mathrm{d}\Omega = \mathrm{d}N/\mathcal{L}\mathrm{d}\Omega$.

Considering a general process $a + b \to c_1 + c_2 + \ldots c_n$, the computation of a cross section of a scattering process involving particles a and b into a final state of n particles $X = c_1 + c_2 + \ldots c_n$ is then given by the *(Fermi's) golden rule*,

$$\sigma_X = 2\pi \cdot |\mathscr{M}_X|^2 \cdot \mathrm{d}\Phi_n(k_a + k_b;\, k_1, \ldots, k_n) = \frac{(2\pi)^4}{4k_a \cdot k_b} \int |\mathscr{M}_X|^2 \prod_{m=1}^{n} \frac{\mathrm{d}^3 k_m}{(2\pi)^3 2k_m^0} \delta^4(k_a + k_b - \sum_{m=1}^{n} k_m), \tag{1.15}$$

where $\mathrm{d}\Phi_n$ denotes a Lorentz-invariant differential n-particle phase-space volume and k_i is the four-momentum of the particle c_i, $k_i = (k_i^0, \vec{k}_i)$. The computation of scattering cross sections can be decomposed in (i) the scattering amplitude $\mathscr{M}_X$, which contains the likelihood of a process involving fundamental particles to take place, and (ii) the density of accessible quantum states, which depends on the kinematics of the process being considered. The former is given by the QFT under consideration, fulfilling *unitarity* constraints such that total probabilities lead to conservation of total cross sections or total decay rates. The latter relies solely on the experimental conditions.

1.6 An Incomplete Theory

The history of the SM presents a long list of achievements in both experimental and theoretical domains. Theoretical physicists, on the one hand, provide the framework necessary to interpret experimental results. On the other hand, experimental physicists design and conduct experiments to test the theories, refining and validating the theoretical concepts. Despite its remarkable success, numerous aspects of the SM and the Higgs sector remain unexplored[18]. To unravel the mysteries that remain elusive, described in the fol-

[17] The incoming particles a and b might or might not be included in the final state particles c_i.

[18] These include, e.g., investigations into the Higgs boson's interactions with the first and second-generation fermions as well as the Higgs's self-couplings, characterizing the structure of the Higgs potential.

lowing, the collaboration of the experimental and theoretical domains is crucial.

The extensive volume of data collected at the LHC to date has corroborated the SM and has not revealed any significant deviations from its predictions, as Fig. 1.5 summarizes. Nevertheless, the evidence of physics not described by the SM persists. The SM in its current form is therefore acknowledged to be an incomplete theory. Several phenomena remain unaccounted for within the SM Lagrangian, with perhaps the most notorious being the *gravitational force*. Observations from cosmology indicate that visible matter constitutes just a mere 5% of the total energy content of our universe, supported by numerous gravitational observations began by Zwicky's work in 1933 [108]. A substantial portion, approximately 26%, is believed to be comprised of *dark matter* [109, 110, 111], yet the SM fails to describe this mysterious substance. The remaining 69% is attributed to *dark energy*, initially conceived with Einstein's cosmological constant and subsequently integrated into cosmological models with the advent of inflationary theories [112]. Additionally, the SM does not provide a comprehensive mechanism for the *matter-antimatter asymmetry* observed in the universe [113]. Although the SM satisfies all three of Sakharov's conditions for baryogenesis [114], it is quantitatively inadequate.

Despite the initial presumption of massless left-handed particles, the well-established evidence of *neutrino oscillations* [115] has proven, within the current theoretical knowledge, that neutrinos must be massive[19]. The precise mechanism through which neutrinos acquire mass is still to be found. Among many unresolved questions in neutrino physics, another important aspect is whether neutrinos should be described in terms of Dirac or Majorana fields, as an observation of neutrinoless double-beta decays would suggest.

The SM relies on a total of 19 free parameters, offering no insight into the origin of their specific values. The pronounced hierarchy observed among fermion masses and the tight constraints on θ_{QCD} driving to the strong CP problem remain enigmatic within the SM formalism. While anomaly cancellations, necessary to preserve gauge symmetries at the quantum level, lead to the quantization of electric charge, the SM fails to offer a profound explanation for why particle charges should exclusively manifest in fractions of the elementary electron charge.

Furthermore, despite the central role of the Higgs boson in the SM, the Higgs mass suffers instability due to radiative corrections, with m_H^2 being highly sensitive to scales associated with new physics. Given that the measured Higgs mass aligns with the electroweak scale, resolving this challenge within the SM requires substantial cancellations and unnatural fine-tuning of the Lagrangian parameters. This is referred to as the *hierarchy problem* [117].

Indications of new physics have also emerged from deviations of the data from the SM predictions. Findings from Fermilab regarding the anomalous magnetic dipole moment of the muon seemed to exhibit deviations from SM predictions, attaining a significance level of 4.2σ [118]. These results were recently updated with a precision of 0.2 parts-per-million (ppm) [119], to be contrasted with updated theoretical calculations. Additionally, an analysis based on Tevatron data from the CDF collaboration in 2022 reported a measurement of the W-boson mass that exceeded the SM prediction with a remarkably high significance of 7σ [120], to be corroborated by LHC experiments. If even a subset of these

[19] For a updated review on neutrino masses, mixing, and oscillations, including the experimental evidence, see Ref. [95]. See Ref. [116] for a more pedagogical overview of neutrino physics.

findings was confirmed, it could potentially unveil a pathway towards new physics.

This brief but yet inevitably incomplete set of evidences motivates to actively seek physics beyond the SM. Particle colliders represent invaluable instruments for investigating the fundamental constituents of our universe, with the LHC continuing to play an important role in this endeavor.

Precision Measurements as Path Towards New Discoveries

After a careful scrutiny of the data at the TeV scale, no new particles beyond the ones of the SM have been directly detected. While *direct searches* aim to detect new particles whose mass lie within the energy regime of a given collider ($E_{\text{th}} < E_{\text{coll}}$, Figure 1.6a), *indirect* approaches are sensitive to contributions from new physics at an energy scale beyond the experimentally reachable energies ($E_{\text{th}} > E_{\text{coll}}$, Figure 1.6b), quantifying deviations mainly at the high-energy tails of differential distributions. The triumphant history of the SM has proven that indirect hints of new particles are remarkably effective, paving the way to a better understanding of nature. One way to quantify such deviations is by further generalizing the SM Lagrangian with additional higher-dimensional operators, introducing new interactions between fundamental particles. The observed phenomenology beyond the SM (BSM) could then be parameterized in an effective field theory, constraining the free anomalous coupling strengths with experimental data of increasing precision. This approach is used in this dissertation, whose principles are presented in Section 1.7.

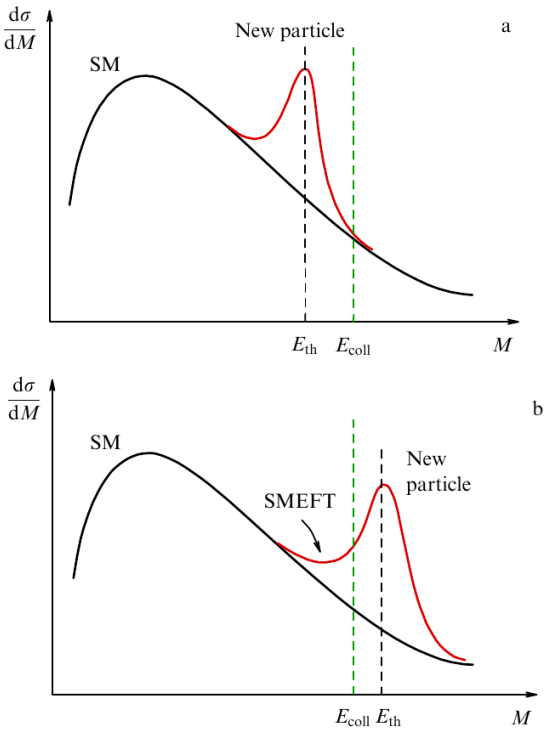

Figure 1.6: Two hypothetical cases in a differential cross section as a function of an observable with dimensions of mass M, when the characteristic collision energy E_{coll} is (a) greater or (b) lower than the threshold E_{th} where new physics is realized. The latter can be evaluated in the context of the SM Effective Field Theory (SMEFT). Source [121].

Both direct and indirect approaches are fully complementary. The quest for precision is also highly beneficial for direct searches, since they provide improved understanding of, e.g., detector and SM predictions that compose the background contributions. The steadily improved precision of LHC measurements, planned for further enhancement with the upcoming high-luminosity upgrade[20] [122] that is projected for completion by 2029 [123], is highly encouraging to pursue this approach. In parallel, a vigorous endeavor must be devoted in improving the accuracy of theoretical predictions, so that the

[20]The High-Luminosity LHC targets seven times greater instantaneous luminosity ($5 \cdot 10^{34}\ \text{cm}^{-2}\,\text{s}^{-1}$) than the LHC provided between 2015 and 2018, collecting a dataset of about 250 fb^{-1} per year [122].

associated uncertainties do not become the limiting factor in the convergence of precision. This is definitely not a straightforward task, given the intricate nature of theoretical simulations involving LHC events, as further discussed in Chapter 2.

1.7 The Standard Model as an Effective Field Theory

The quest for a *theory of everything* has been a primary effort in the past century. This pursuit has enabled physicists to envision a coherent framework that unifies quantum theories of matter and gravity into a single, comprehensive theory applicable across all regimes, ideally characterized by a reduced (potentially vanishing) number of free parameters. Such a theory, when extrapolated to low energies, would converge to the SM. However, a shift in perspective has happened in recent decades, focusing rather on the development of *theories of something* designed to be valid within specific, well-defined regimes. These approaches, commonly referred to as *Effective Field Theories* (EFTs), simplify the formal description of the theory at scales where the intricate details are not relevant. An introduction to EFTs, elucidating their underlying principles, is given in the following. The Standard Model Effective Field Theory (SMEFT), the theoretical framework for the understanding of fundamental interactions in the energy range characterized by the presence of non-SM particles that can be probed at the LHC, is emphasized. In this dissertation, the differential cross-section measurements of W^+W^- production are interpreted to constrain contributions from anomalous couplings within the context of the SMEFT. The outcomes of this analysis are presented in Chapter 11.

Introduction

Numerous scientific breakthroughs have been achieved across an extensive range in the energy scale over the past two centuries. These range from explorations of the fundamental particles of nature at the smallest distances up to the astronomical scales, as vast as the observable universe itself. In QFTs, it is convenient to use the energy of the process of interest as the referred scale Λ. As we move towards lower energies that can be formalized after integrating out the UV degrees of freedom, the defined *effective Lagrangian* $\mathscr{L}_{\mathrm{EFT}}$ can still describe the physics phenomenology under study, providing all low-energy observables without referring to the full UV-complete Lagrangian. A powerful simplification of $\mathscr{L}_{\mathrm{EFT}}$ can be achieved in the presence of *scale separation* [124], i.e. when the mass of the fundamental objects whose kinematic properties are described by the full Lagrangian is much larger that the energy scale of the process, $E \ll M$. In such a case, $\mathscr{L}_{\mathrm{EFT}}$ can be expressed as a *local Lagrangian*, i.e. in terms of polynomials of the field and its derivatives. In a local $\mathscr{L}_{\mathrm{EFT}}$, a power counting scheme can be implemented, where a specific order with respect to the expansion parameter is specified in each term. Contributions from terms beyond a certain order in Λ become highly suppressed within the relevant regime and can be neglected, since $E \ll \Lambda$. This systematic approach ensures that calculations can be performed with the desired level of precision, and the Lagrangian comprises a finite number of terms once the order in the expansion is specified. This facilitates a step-by-step process of renormalization.

A classical example of how an EFT can enhance the comprehension of a specific theory is found in Fermi's theory of weak interactions [31]. When examining the low-energy

regime, the muon decay $\mu \to e\bar{\nu}_e\nu_\mu$ can be approximated by a 4-fermion interaction. Fermi ingeniously introduced this effective contact interaction to describe muon decay accurately without relying on the at-the-time unknown and experimentally inaccessible W propagator fields. This contact interaction is characterized by the effective Fermi coupling strength constant G_F which since then has been precisely measured [95]. With the development of experimental technologies and the full higher-energy EW theory, the process was elucidated through the mediation of a W boson. This underscores the significance of employing an EFT in the absence of a comprehensive understanding of the complete theory, as it not only yields accurate predictions but also serves as a catalyst for exploration and advancements within the existing theory.

While the SM offers highly precise predictions within specific energy ranges, it might fail to comprehend significant effects at higher (or lower) energy scales. Nevertheless, these limitations are widely acknowledged and efforts have already been made to address them within its working energy scales. These efforts include the development of various EFTs such as the soft Collinear Effective Field Theory (SCET) [125], the Chiral Perturbation Theory (ChPT) [126, 127], the Heavy Quark Effective Theory (HQET) [128] or the Standard Model Effective Field Theory (SMEFT) [129, 130, 131, 132]. The latter is further discussed in the next section, following [133] as the main reference.

The Standard Model as an Effective Field Theory

If an EFT using the SM degrees of freedom is considered to describe general fundamental interactions in the energy range $\Lambda \ll \mathcal{O}(\mathrm{TeV})$, motivated by the lack of discovery of new physics at the LHC, the SMEFT is a commonly used approach. This EFT is constructed as the local Poincaré-invariant QFT describing physics within the energy regime of the LHC above the EW scale ($\Lambda \gg m_W$) with the SM degrees of freedom and invariant under the local SM gauge symmetry, $\mathrm{SU}(3)_C \times \mathrm{SU}(2)_L \times \mathrm{U}(1)_Y$[21]. To cancel the UV divergencies in the non-renormalizable theory of SMEFT, an infinite number of terms need to be considered in the effective Lagrangian $\mathscr{L}_{\mathrm{SMEFT}}$. The assumption of scale separation allows the SMEFT to be local, allowing to use *power counting* on the canonical dimension of an gauge-invariant interaction to organize these infinite terms in the Lagrangian as powers of the energy scale Λ,

$$\mathscr{L}_{\mathrm{SMEFT}} = \sum_{d=2}^{\infty} \mathscr{L}_d = \sum_{d=2}^{\infty} \sum_i C_{i,d}\mathcal{O}_{i,d} = \sum_{d=2}^{\infty} \sum_i \frac{c_{i,d}}{\Lambda^{d-4}}\mathcal{O}_{i,d}, \tag{1.16}$$

where i runs over all independent gauge-invariant operators constructed out of the SM fields at a given dimension, and $C_{i,d}$ are field-independent coupling constants denoted to as *dimension-d Wilson coefficients* (or *dim-d* for brevity). The Wilson coefficients can be written in terms of dimensionless couplings strengths $c_{i,d}$ such that a Lagrangian of dimension four, $[\mathscr{L}_{\mathrm{SMEFT}}] = 4$, can be built with Wilson coefficients of dimension $[C_{i,d}] = 4 - d$. The dimensionless coefficients $c_{i,d}$ are functions of the couplings and mass ratios in the

[21] An alternative approach can be followed by imposing the EW gauge symmetry $\mathrm{SU}(3)_C \times \mathrm{U}(1)_{\mathrm{em}}$, referred to as the Higgs EFT (HEFT). In the HEFT, the generators of the larger $\mathrm{SU}(3)_C \times \mathrm{SU}(2)_W \times \mathrm{U}(1)_Y$ gauge symmetry that do not belong to $\mathrm{SU}(3)_C \times \mathrm{U}(1)_{\mathrm{em}}$ are described as a non-linear transformation of the scalar Goldstone bosons absorbed by the W and Z bosons. The differences between HEFT and SMEFT in the description of anomalous interactions are discussed in Refs. [134, 135].

UV completion of SMEFT, as well as of the SM couplings. The construction of the $\mathscr{L}_{\text{SMEFT}}$ by power counting relies on the assumption that $c_{i,d} \sim 1$. Therefore, (dimensionless) tree-level scattering amplitudes in SMEFT will be proportional to $\mathscr{M} \sim C_{i,d}E^{d-4} \sim (E/\Lambda)^{d-4}$. This means that, the higher the dimension of the SMEFT operator, the smaller its contribution on the phenomenology of $\mathscr{L}_{\text{SMEFT}}$ is (since $\Lambda \gg E$), and therefore the larger its suppression becomes. This allows to truncate the SMEFT Lagrangian at some particular $d_{\max}$, ignoring the rest of contributions for the remaining high-dimensional terms and constraining $\mathscr{L}_{\text{SMEFT}}$ to a finite set of operators[22]. SMEFT with the standard power counting and truncated at a finite $d_{\max}$ is as renormalizable as the renormalizable theories in the standard sense (e.g. in the SM when $d_{\max} = 4$). In the SMEFT, all new physics is assumed to be above the high energy scale $\Lambda \sim 1$ TeV. However, scattering amplitudes still grow with increasing energy approaching Λ, reaching a regime where unitarity is violated.

Up to $d = 4$, all possible gauge-invariant operators constitute the SM Lagrangian, showing one of the main goals of the SMEFT: reproducing the SM as the leading terms of the EFT expansion. Beyond $d = 4$, the following gauge-invariant interactions at $d = 5$ of the form $\mathscr{L}_5 = -(\bar{l}^J H^\dagger)C_{5,JK}(\bar{l}^K H^\dagger) + \text{h.c.}$ can be considered [136], with C_5 being a 3×3 matrix in the generator space, giving rise to *Majorana neutrino masses* after EWSB. It also generates a mass term for left-handed neutrinos[23] like $m_\nu \sim (c/\Lambda)v^2$. A great fraction of the SMEFT research focuses on dim-6 operators, first introduced in Ref. [129]. These 3045 independent operators bring a broad phenomenology in Higgs physics, electroweak precision, flavor and nuclear physics, etc. The so-called *Warsaw basis* [137] is widely used to parameterize the SMEFT interactions described by dim-6 operators. $\mathscr{L}_6$ can be decomposed in bosonic operators (constructed out of the SM gauge and Higgs fields without involving any fermionic fields), Yukawa-like interactions, current-like and dipole operators. Four-fermion interactions constitute the remaining category and account for most of the dim-6 operators, split into four-lepton, two-lepton and two-quark, one-lepton and three-quark, and four-quark interactions. The number of operators keeps growing when increasing $d_{\max}$: 1542 independent operators arise at dim-7, 44807 at dim-8, and so on [138], complicating their analysis enormously. However, the lack of experimental evidence for non-SM physics described by contributions of dim-6 SMEFT operators motivates to neglect higher-dimension operators in $\mathscr{L}_{\text{SMEFT}}$, which are considerably more suppressed. Explorations beyond dim-6 operators are usually not necessary and justified only in rare circumstances when the anomalous interactions cannot be probed at dimension 6[24].

Upon the assumption of baryon number conservation, the SMEFT landscape reduces up to 59 independent dim-6 gauge-invariant operators [137]. To establish experimental constraints on these operators, the association between each Wilson coefficient and the dedicated observable of interest must be derived. This task is performed in the context of *global EFT fits* [89, 88], conducted within the parameter space spanned by the base of Wilson coefficients. After the components of the Wilson coefficient base are fitted to the

[22] This truncation would not be valid anymore if $E \sim \Lambda$, in which case all the infinite number of terms of the expansion would be needed. The SMEFT would be unusable in such a regime.

[23] Given the current neutrino mass bounds, the required energy scale is very large: taking $c \sim 1$ and $m_\nu \sim 1$ eV implies that conservation $\Lambda \sim (v^2/m_\nu) \sim 10^{13}$ GeV.

[24] This is the case, for instance, for photon-induced processes or vector boson scattering, where dimension-8 operators are necessary.

data across the observable X, any deviations observed in the coefficients from their null values during this fitting process serve as an indicator of new physics phenomena manifesting at the corresponding effective interaction vertices. If no deviations are observed, the SMEFT can be used to impose bounds on the scale and parameters of various UV theories or scenarios.

To evaluate the influence of each individual operator on X, the SMEFT provides a systematic framework, expressed as a perturbative expansion based on powers of $1/\Lambda^2$,

$$X = X_{\mathrm{SM}} + \frac{1}{\Lambda^2}\sum_i C_i X_i^{(1)} + \frac{1}{\Lambda^4}\sum_{ij} C_i C_j X_{ij}^{(2)} + \mathcal{O}(\Lambda^{-4}). \tag{1.17}$$

This expansion encompasses the SM description of the observable X, X_{SM}, alongside the interactions arising from the effective dim-6 operators scaling proportionally with C_i/Λ^2, commonly referred to as *linear terms*, and *quadratic terms* proportional to C_iC_j/Λ^4. The *interference terms* associated with dim-8 operators between SM diagrams and effective coupling terms, which occur at the order of Λ^{-4}, are not included in Eq. (1.17). Non-SM operators arising at $d > 6$ are also neglected. The effect of anomalous interactions on SM observables such as gauge massive boson decay widths must be taken into account, which can be used to further constrain the Wilson coefficients [139].

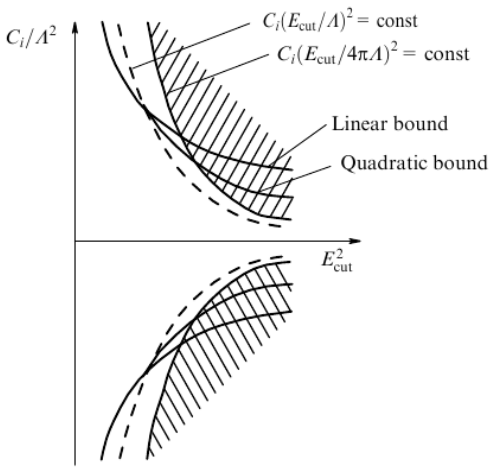

Figure 1.7: Schematic representation of the reporting procedure for extracting Wilson coefficient bounds in SMEFT. Source [121].

When quadratic terms $\mathcal{O}(\Lambda^{-4})$ are included in the fit but dim-8 operators are excluded, only a subset of the dim-8 parameter space is considered. Nowadays, it is common practice to use the difference between fitting results obtained via the *linear-only* and *linear + quadratic* models as a function of a certain energy upper cutoff[25], E_{cut}, to qualitatively estimate an uncertainty due to the missing $\mathcal{O}(\Lambda^{-4})$ contributions [140], as illustrated in Figure 1.7. The regions above the curves labeled as $C_i(E_{\mathrm{cut}}/\Lambda)^2 = \mathrm{const.}$ and $C_i(E_{\mathrm{cut}}/4\pi\Lambda)^2 = \mathrm{const.}$ correspond to the ranges where either the calculation of the higher corrections fails or the perturbative unitarity condition is violated. The optimal value of the cutoff E_{cut} is found where these two methods of analysis yield close constraints on the Wilson coefficient C_i. The inclusion of quadratic terms proportional to Λ^{-4} is recommended for several reasons. Firstly, if only terms of the order of Λ^{-2} are kept, the effects from Λ^{-4} are not accounted for. Secondly, the interference of dim-6 operators with the SM contributions might have an important influence. If these terms are neglected, the calculation of the SMEFT cross section might be ill-defined[26]. Lastly, comparing the limits of both linear-only and linear + quadratic approaches clarifies the applicability range of the SMEFT approach, helping to obtain more reasonable constraints. This strategy is described in detail in Ref. [141].

[25] Kinematical variables such as the total energy of the parton process or the total transverse energy H_T can be used.

[26] This is especially the case if the linear term in an important Wilson coefficient is negative while the SM contribution is very small.

Chapter 2

Phenomenology of Proton-Proton Collisions

"Whatever is most abstract may perhaps be the summit of reality."

— Pablo Picasso (1881 – 1973).

To test theoretical predictions against any experimental observable obtained in collider environments, the formal results from the Lagrangian formalism studied in Chapter 1 turn out to be insufficient. In order to compare experimental data to theory predictions, so-called *General Purpose Monte Carlo* (GPMC) generators such as HERWIG [143, 144, 145], PYTHIA [146, 147, 142], SHERPA [148], POWHEG [149, 150], or MADGRAPH [151] (among others[1]) are used, reproducing high-energy hadron-hadron (hh) or lepton-lepton ($\ell\ell$) collisions event by event[2]. In experimental particle physics, this provides a paramount tool to understand not only phenomenological aspects of the theory under consideration, but also the behavior of the experimental setup by adding detector effects to the simulation. The latter can also be exploited in the planning and optimization of future experiments. GPMC simulations provide a list of particles with their corresponding kinematic properties at different *levels* of the production and the decay chain. Firstly, the *parton level* provides information on the quarks and gluons involved in the simulation (i.e. before hadronization[3]), where unstable particles such as top-quarks or $W^{\pm}$ bosons may also be accessible. At the *particle level*, only information about objects in the final state, such as hadrons or jets[4], is accessible. Finally, the *detector* or *reconstruction level* includes effects from the finite detector response and resolution on the kinematics of the event. Details on general-purpose event generators for LHC physics can be found in Refs. [95, 152].

GPMC generators are built in several steps, from the high-energy interaction up to the non-perturbative effects. Figure 2.1 illustrates the full process. Due to the running of α_S, the short-scale interactions can be characterized in perturbation theory by computing cross sections at a given order. Section 2.1 presents the computation of the so-called *matrix element*, as given by the SM once the hadron structure has been taken into account. Unfortunately, fixed-order predictions present limitations in reproducing collision events, especially if a large activity from gluon radiation is expected. An approximation to all orders via *parton shower* algorithms, summarized in Section 2.2, is necessary in these cases. At larger distances, the soft phenomena are described by QCD-inspired models matched to experimental data. These include hadronization models, outlined in Section 2.3, that produce the colorless particles in the final state comparable to experimental results. The

[1] A full list of event generators can be found in Refs. [95, 152].

[2] In this dissertation, data recorded in pp collisions are analyzed. In the following, the description will be devoted to pp collisions only, although the presented formalism can be used in $\ell\ell$ collisions as well as generalized to any other hh interaction.

[3] Hadronization models are discussed in Section 2.3.

[4] Particles are considered stable if their decay length $c\tilde{t}$, being $\tilde{t}$ the mean lifetime of the particle, is greater than $1\,\mathrm{cm}$. The definition and modeling of *jets*, and the reconstruction techniques with the ATLAS detector, are introduced in Section 4.3.4.

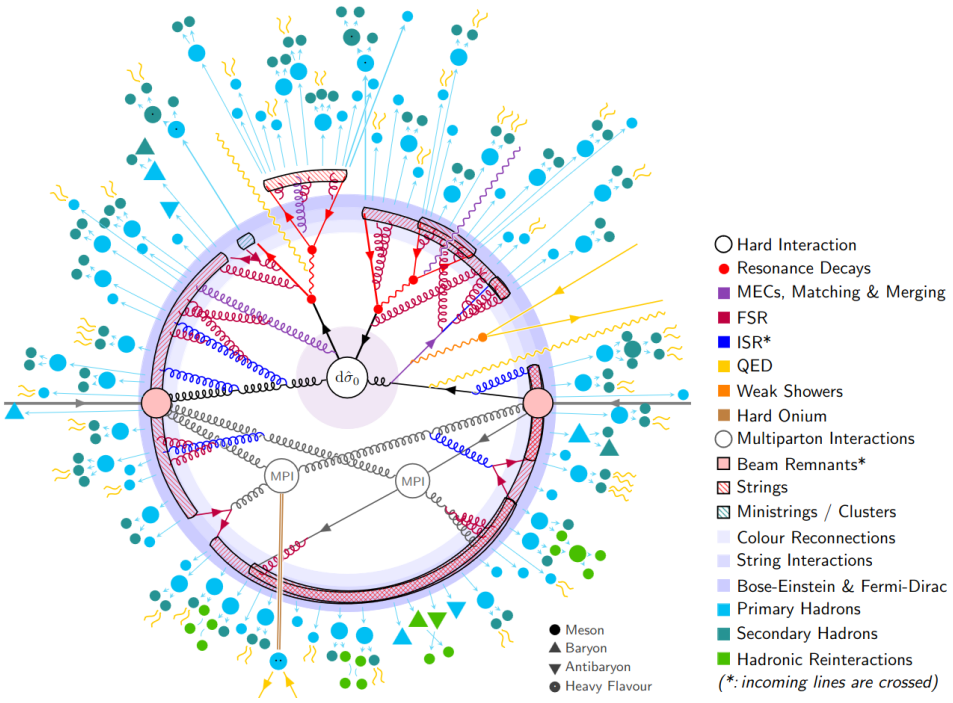

Figure 2.1: Pictorial representation of a $t\bar{t}$ event produced in a simulated pp collision with PYTHIA 8.3 [142]. First, the initial state of the process (taking in consideration the structure of both protons in the collision) is simulated. Initial state radiation of gluons and photons is taken into account at this stage. The hard scattering comes next, incorporating the partonic cross section $\mathrm{d}\hat{\sigma}_0$. In the same collisions, *multiple parton interaction* (MPI) can take place. Photons are radiated off the leptons (yellow curly lines). The underlying event is also simulated. Gluons undergo *fragmentation* and hadronize into baryons which decay into lighter particles. The beam remnants are also taken into account in MC simulations. Source: [142].

remaining collision activity composes the so-called *underlying event*, including hadrons originating from the beam remnant.

2.1 Fixed-Order Perturbation Theory and Parton Distribution Functions

Only interactions between fundamental particles are described in the SM. Therefore, predictions of a process of interest need to take into account the proton structure and all possible initial states in a pp collision. In the *parton model* [153], a pp collision is described as the collision of two fundamental proton constituents (known as *partons*) carrying a certain momentum fraction of their corresponding proton. To date, there is no way to determine experimentally the energy fraction carried by a parton. Therefore, the probability functions $f_a(x_a)$ of a certain parton a to carry a momemtum fraction x_a of the proton momentum needs to be defined. The probability density functions are known as *Parton Distribution Fractions* (PDF). The *factorization theorem* [154, 155, 156] allows for a separation of cross-section calculation into the two following parts. First, a short-distance (or high-energy) component that can be computed by means of the perturbative approximation in QCD or EW theories, or both. And lastly, a long-distance (or low-energy) part extrapolated from phenomenological models. The theorem allows to separate the com-

putation parton by parton. In QCD, the cross section for a process X in a pp collision, $p_1p_2 \to X$, can be written by generalizing Eq. (1.15) as a sum of partonic cross sections[5] $\mathrm{d}\hat{\sigma}_{ab\to X}(x_a, x_b, \mu_F, \mu_R, Q^2)$,

$$\frac{\mathrm{d}\sigma_{p_1p_2\to X}}{\mathrm{d}\mathscr{O}} = \sum_{a,b}\int_0^1 \mathrm{d}x_a\mathrm{d}x_b \sum_{X'}^{X'\in X} \int \mathrm{d}\Phi_{X'} f_a(x_a,\mu_F,Q^2)\cdot f_b(x_b,\mu_F,Q^2)\cdot \\ \cdot\frac{\mathrm{d}\hat{\sigma}_{ab\to X}(x_a,x_b,\mu_F,\mu_R,Q^2)}{\mathrm{d}\mathscr{O}} D_{X'}(\hat{\mathscr{O}}\to\mathscr{O},\mu_F)\,, \tag{2.1}$$

where two massless partons a and b in the initial state with momentum fractions x_a and x_b from the first and second proton in the collision, respectively, produce the final state X at the partonic center-of-mass energy Q^2. The partonic cross section depends on the *renormalization scale* μ_R at which α_S is evaluated in the computation of the matrix element. The sum over X' includes all orthogonal final states composing X included in the process $a+b\to X$ under study. The phase space spanned by the final state X' is denoted by $\mathrm{d}\Phi_{X'}$. The parton distribution functions f_{q_i}, with $i = a, b$, rely on non-perturbative calculations. So does the *fragmentation function* $D_{X'}$, which parameterizes the dependence of the transition from the free quarks to the bound states in the hadronization process (described in Section 2.3) across a given observable[6] $\mathscr{O}$. These components are described in more detail in the following.

Using Eq. (1.15), the computation of the partonic cross section can be inferred as

$$\hat{\sigma}_{ab\to X}(x_a,x_b,\mu_F,\mu_R,Q^2) = \sum_{k=0}^{\infty}\int d\Phi_{X+k}\left|\sum_{l=0}^{\infty}\mathscr{M}^{(l)}_{ab\to X+k}(x_a,x_b,\mu_F,\mu_R,Q^2)\right|^2, \tag{2.2}$$

being $\mathscr{M}_{ab\to X+k}$ refers to the transition *matrix element* (ME) of the process $a+b\to X$, with k additional quarks and/or gluons. In this way, the phase space for inclusive production of X can be divided in processes with k additional particles in the final state. These account for corrections from *real emissions*. The sum over l introduces additional diagrams involving *virtual corrections* (also referred to as *loops*). The number of real and virtual corrections fixes the order in perturbation theory considered in the computation. The case $k = l = 0$ corresponds to the leading order (LO) prediction for inclusive X production. Real emissions $k = n$ with $l = 0$ provide the cross section of X production in association with n additional partons (denoted to as $X + n\,\mathrm{jets}$ for QCD corrections[7]) at LO, while varying both k and l such that $k + l \leq n$ provides the X production cross section at next-to-leading order (NLO) for $n = 1$, next-to-next-to-leading order ($n = 2$, referred to as NNLO), or any n up to N^{n}LO. The N^{n}LO prediction includes the N^{n-1}LO computation for $X + 1\,\mathrm{jet}$, N^{n-2}LO computation for $X + 2\,\mathrm{jets}$, and so on. In practice, no ME of a hard-scattering can be computed to all orders in the perturbative expansion[8]. Predictions for most SM and BSM processes at LO and NLO in QCD have been automated in GPMC

[5] Variables computed at partonic level are denoted by a hat.

[6] Inclusive observables such as total cross sections can be computed without measurable objects (e.g. hadrons) because a sum over all possible final states $a + b \to X$ is involved.

[7] See Section 4.3.4 for a definition of jets.

[8] Techniques such as *parton showers* or *resummation*, presented in upcoming sections, can be used to approximate contributions from higher-orders.

generators. NNLO predictions (or even N^{3}LO in cases such as Higgs or Drell-Yan production) are currently the state-of-the-art. Predictions of W^+W^- production, the process of interest in this dissertation, are further discussed in Chapter 3.

The matrix element $|\mathscr{M}_{ab\to X'}|^2$ in Eqs. (2.1) and (2.2) is computed at a certain order in the perturbative expansion in, e.g., QCD. It implies summing over color and spin indices, a procedure performed in QFT via the Wick's theorem [157] and the Lehnman-Symanzik-Zimmermann (LSZ) reduction formula [158]. Then, $|\mathscr{M}_{ab\to X'}|^2$ can be computed taking into account all Feynman diagrams contributing to the scattering process at hand, where each interaction vertex is proportional to the product of some coupling constants characteristic of the theory. The ME relies on the arbitrary energy scales μ_F and μ_R, whose meaningful values are given by the characteristic scale of the process. The higher the order in perturbation theory at which the ME is computed, the weaker the dependence of the cross-section calculation on μ_F and μ_R becomes. For this reason, precise predictions require the highest available order in perturbation theory. The choice of the given μ_F and μ_R is arbitrary and, to date, no mathematical formalism to propagate uncertainties arising from the dependence on μ_F and μ_R is available. It has become customary to vary μ_F and μ_R individually by a certain factor (usually a factor of two[9]), accounting for all possible combinations in the so-called *7-point configuration*.

The introduction of virtual corrections usually leads to *divergences* that need to be either suppressed or subtracted. In general, only partons with momenta much lower than the energy scale of the process $a + b \to X$ are allowed in the ME corrections, to avoid the presence of so-called *ultraviolet* (UV) and *infrared* (IR) *divergences*. IR divergences can be avoided by redefinition of the *bare* particles in the ME. *Dressed* particles are conventionally used, i.e. the momenta of the collinear radiation within a given proximity are attributed to the given particle. Since experimentally-observable quantities of dressed particles such as charge or mass are renormalized, their definition is *IR-safe*.

Given a production cross section of a given final state X, the ratio of a higher-order result over the LO prediction is usually denoted as K-factor, $K_X^{\text{(N)NLO}} = \sigma_{\text{tot},X}^{\text{(N)NLO}}/\sigma_{\text{tot},X}^{\text{LO}}$. In hadron collisions, new partonic channels arise in higher-order corrections when calculating the cross section, leading to a significant increase of the higher-order corrections in some processes, far outside the respective scale uncertainty variations at LO[10]. Giant K-factors are particularly relevant for processes such as diboson production, especially in association with additional partons [159].

The PDFs $f_a(x_a, \mu_F, Q^2)$ in Eq. (2.1) provide the probability density functions parameterizing the likelihood of parton a to carry a momentum fraction equal to x_a inside the hadron given an energy scale of μ_F. Due to the factorization theorem, it is possible to measure the PDFs at a certain energy scale Q^2 and extrapolate results to different energy scales by means of the *Dokshitzer, Gribov, Lipatov, Altarelli and Parisi* (DGLAP) evolution equations [161, 162, 163], relying on the *Altarelli-Parisi splitting func-*

[9] There is some dispute on whether a factor of 2 is sufficiently large to account for all uncertainties and on which permutations of μ_F and μ_R should be considered.

[10] These discrepancies can become more prominent when considering certain fiducial regions in, e.g., calculations of differential cross sections. Either due to computational difficulties or the constraints defining the fiducial region, some kinematic regions (especially in the LO prediction) might be constrained. The extra radiation at higher orders also extends constrained regions of the phase space. This problem is partially alleviated by the implementation of parton showers or resummation, described in the following sections.

tions[11] encoding the probability for the parton i to emit a parton j carrying a fraction of the original parton momentum. The energy threshold at which perturbative and non-perturbative calculations are performed is controlled by the *factorization scale* μ_F, introduced as an input in the calculation. The PDFs cannot be obtained from theoretical considerations, requiring *fits* to experimental results from *Deep Inelastic Scattering* (DIS) experiments such as the H1 [165] and ZEUS [166] experiments at the HERA ep collider, but also from experiments at the Tevatron and the LHC. These fits are usually stored in grids available for the community [167]. PDF fits are performed by several independent collaborations such as NNPDF [168], MMHT14 [169], CT18 [170], MSHT20 [171], or MSTW2008 [172], but also by the experimental collaborations such as HERA [173], ATLAS [174], CMS [175, 176], or the PDF4LHC Working Group [177]. The unpolarized proton PDFs are shown in Figure 2.2 as derived by the NNPDF Collaboration. The valence quarks of the proton (uud) are visibly enhanced at high x, likely to carry a high fraction of the proton momentum. The low x regime is dominated by the sea quarks and gluons, especially at high transferred energy. An exhaustive review of splitting functions and PDFs can be found in Refs. [178, 179, 180].

The use of NNLO PDF fits, mandatory to match the level of precision of the LHC data, is standardized nowadays[12]. However, a simple counting of powers of α_S indicates that the contributions from NLO EW and NNLO QCD corrections have a similar impact on the prediction. Photon PDFs need to be taken into account when initial-state EW radiation takes place [184, 185]. These have been implemented in NNPDF3.1LUXQED [186], while progress from the MMHT Collaboration has also been reported [187]. Chapter 3 presents the impact of photon PDFs in the production of W-boson pairs.

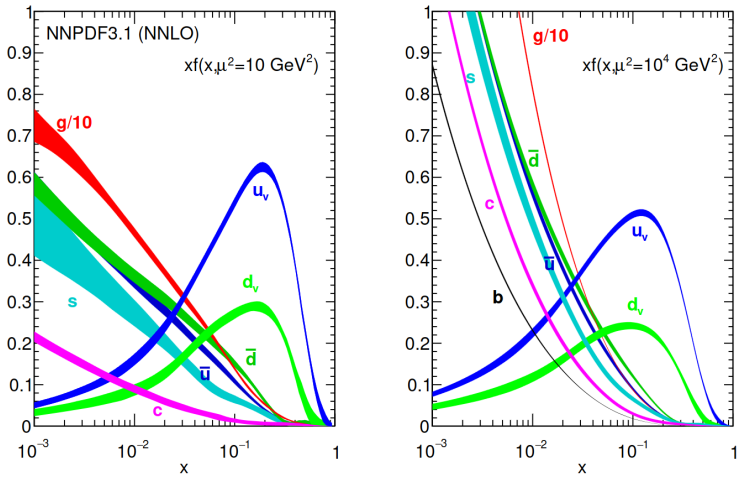

Figure 2.2: NNPDF3.1 parton distribution functions of gluons, valence and sea quarks composing a proton at NNLO along two different energy scales of (left) 10 GeV^2 and (right) 10^4 GeV^2. Source: [160].

Resummation

The reliability of a perturbative expansion for the computation of the ME $|\mathscr{M}_X|^2$ in Eq. (2.2) builds upon (i) small coupling parameters and (ii) well-behaved coefficients. While the former can be confidently applied in high-energy pp collisions, the latter needs careful consideration. Terms may lead to large numerical corrections to the cross section after the subtraction of the formal divergencies. In such a case, powers in α_S may increase and the truncation in the perturbative expansion becomes meaningless. *Resummation* solves

[11] The exact form of the DGLAP and Altarelli-Parisi functions can be found in, e.g., Ref. [164].
[12] Progress towards splitting functions [181, 182] and PDFs [183] at N^{3}LO is currently being pursued.

this issue by isolating and summing up the ill-defined terms to all orders in α_S. Contributions of the form

$$\frac{\mathrm{d}\sigma}{\mathrm{d}p_{T,WW}} \sim \sum_{n=0}^{\infty} \alpha_S^n \sum_{m=0}^{2n-1} \left[\log^m \left(\frac{m_{WW}^2}{p_{T,WW}^2} \right) + \dots \right] \tag{2.3}$$

arise in the production cross section of W-boson pairs. The logarithmic terms become singular for low transverse momentum of the diboson system, $p_{T,WW} \to 0$. This behavior is enhanced in regimes where, for instance, $p_{T,WW}$ is much smaller than the diboson mass, $p_{T,WW} \ll m_{WW}$, e.g., when parton radiation recoiling against the W^+W^- pair is suppressed. These singularities cancel out once real and virtual corrections are combined at all orders. At any order n in perturbation theory, the highest power of the logarithm is $m = 2n - 1$ (*leading logarithm*, LL), as they are usually the ones that are the most numerically significant, followed by $m = 2n - 2$ (*next-to-leading logarithm*, NLL), and so on up to a given order N^{p}LL. Resummation affects the central value of the computed cross section, but it also reduces its theoretical uncertainty[13]. To date, resummation up to N^{3}LL matched to NNLO fixed order predictions in QCD are publicly available [188, 189].

Electroweak Corrections

Although the EW coupling constants α_W (~ 0.01) are much smaller than α_S (~ 0.1), EW corrections become increasingly important at the precision frontier. Real EW corrections rely on an energy scale set to the mass of the radiated gauge boson, providing a cut-off for integrals to avoid divergence during the emission. These results in *EW Sudakov factors*

$$\hat{\sigma}_{\mathrm{EW,real}} \sim \frac{\alpha_W}{4\pi} \log^2 \left(\frac{s}{m_W^2} \right) \hat{\sigma}_0 \,, \tag{2.4}$$

where s is the hard scale at which the process is being evaluated, equivalent to the QCD scale in QCD corrections, and $\hat{\sigma}_0$ is the LO partonic cross section. Analogous but *negative* Sudakov factors arise for virtual corrections exchanging $W^\pm$ or Z bosons. The net effect of real corrections is usually small, being virtual corrections the subject of most theoretical studies [190, 191, 192]. The size of the leading relative EW corrections can be estimated using Eq. (2.4) as $\delta^{\mathrm{EW}} = \hat{\sigma}_{\mathrm{EW,virtual}}/\hat{\sigma}_0$. Electroweak corrections are typically of the order of a few percent, but these can be enhanced in certain kinematic regions[14]. The implementation of automated NLO EW corrections in GPMC generators such as MadGraph [193] and Sherpa [194] is completed at fixed order.

2.2 Parton Showers and Matching

The radiation of a large number of soft objects such as partons or photons must be included in fixed-order predictions, limited by the chosen order in perturbation theory and the energy scales. This is crucial to be able to compare these predictions to experimental conditions. The computational demand of exact calculations of such radiation would be

[13] Resummation includes additional terms that depend on the renormalization and factorization scales μ_R and μ_F, such that the effect of the scale variations on the prediction is reduced.

[14] Using Eq. (2.4), EW corrections of $\delta^{\mathrm{EW}}(\sqrt{s} = 1\,\mathrm{TeV}) \sim 10\%$ are expected in regions of high invariant mass or transverse momentum.

	Parton shower	Matrix elements
Number of partons	No limitation (resummed to all orders)	Small, limited by computing power
Separated particles	Approximation	Exact calculation
Collinear particles	Exact computation	Computation fails (collinear divergencies)
Interference, spin, color	Approximation	Exact

Table 2.1: Pros and cons of matrix element and parton shower calculations of extra radiation.

unpractical. In contrast, algorithmic approximations are implemented via *parton showers* (PS). These were first developed in the 1980s [195, 196, 197] and are becoming more sophisticated over the years [152, 198]. A parton shower models the emissions from all initial- and final-state partons before and after the hard scattering, complementing the ME computation by incorporating the partons missed beyond the factorization scale.

The general workflow of a parton shower includes recursively generating sequences of soft and/or collinear emissions, ordered in decreasing momentum or angle, based on the probability that each involved parton splits into two lower-energy ones. The most common approach, known as *collinear factorization* followed by the HERWIG [199] and PYTHIA [200] PS models, is then applied iteratively to all outgoing partons in both the initial- or final-states, performing the splitting until the shower reaches a *hadronization scale* of about 1 GeV. Instead of focusing on collinear emission, an alternative formulation can be achieved by instead considering soft emission as the basic splitting mechanism, where a parton pair (called dipole) leads the branching process [201]. This approach is the foundation of the *Catani-Saymour dipole factorization* [202], used by default in SHERPA showers. In the PS algorithms, the necessary MEs are typically computed with LL precision, constituting one of the leading uncertainties of theoretical predictions.

Extra radiation can therefore be accounted for by either (i) higher orders in the ME calculation or (ii) by the PS. From the advantages and disadvantages of both approaches, summarized in Table 2.1, one can observe that both are rather complementary. The best of both prescriptions can be achieved by combining them using the so-called *matching schemes*, where the PS is initiated out of the diagrams produced by the fixed-order ME. As illustrated in Figure 2.3, careful consideration with Feynman diagrams beyond LO must be taken to ensure that contributions from different configurations of the ME-PS matching of the same radiation (diagrams on the same diagonal) are accounted only once. Several matching algorithms up to NNLO in QCD [204] are followed by different MC generators. First approaches were implemented by the CKKM scheme [205], leading to variants such as CKKW-L [206]. Multipurpose MC generators at LO such as MADGRAPH [151] include these algorithms. At NLO, the matching to the PS exploits the increased accuracy of the ME, but must consider the extra radiation. This is done by, e.g., the MC@NLO [207] and the POWHEG BOX [149, 150] matching schemes, evolving to the also widely used AMC@NLO [208]. HERWIG 7 implements variants of POWHEG and MC@NLO ap-

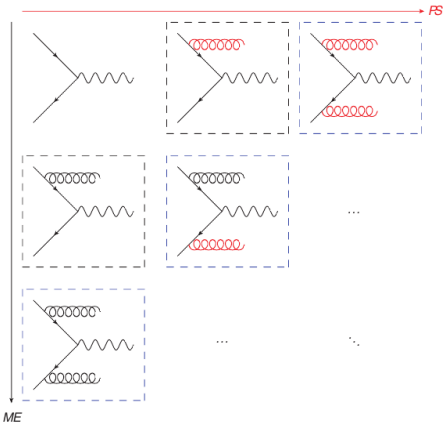

Figure 2.3: Illustration of initial state radiation arising from the matrix element (vertical axis) and/or the parton shower (horizontal axis). Source [203].

proaches, while SHERPA [148] developed a variant of the MC@NLO method. A comparative study of these algorithms is presented in Ref. [209].

For applications requiring high accuracy in the kinematics of more than one hard, large-angle parton radiation from the ME, the MEPS@NLO [210] or MINLO [211] methods have been proposed. Solutions beyond NLO have been found via NNLO+PS generators, i.e. generators that, besides being NLO accurate for the production of an associated jet, are also NNLO accurate for fully inclusive observables. The MINNLO$_{PS}$ method [212], used in this dissertation, extends the MINLO approach based on the POWHEG matching via reweighting [213]. Event generation of W^+W^- production, relevant for this thesis, is available in both MINLO [214] and MINNLO$_{PS}$ [215, 216]. A complete list of the available matching algorithms at different orders in perturbation theory and their formal approaches is presented in Refs. [95, 152, 217] and citations therein.

2.3 Hadronization, Underlying Event, and Pile-up

After the PS model is processed, colored partons are grouped into a set of color-neutral hadrons. These hadrons may then subsequently decay further into secondary particles, either leptons, photons or additional hadrons. This non-perturbative transition, known as *hadronization*, takes place at the so-called hadronization scale, $Q_{\text{had}} \sim 1\,\text{GeV}$. In the absence of first-principles solutions to the relevant dynamics, event simulation programs use QCD-inspired phenomenological models such as the *string* or *Lund model* [218, 219] (implemented in PYTHIA [146, 147]) or the *cluster model* [220, 221, 222] (based on the concept of *preconfinement* [223, 224] and available in HERWIG [143, 145] and SHERPA [225]) to describe this transition.

After the aforementioned algorithms have been applied in the GPMC simulations, there are still some experimental signatures to be described, known as the *underlying event*. Additionally, *multiple parton interactions* (MPI) [226] can take place within the same protons in the hard collision, although the fraction of such events is typically small. The additional activity caused by non-interacting partons of the proton is known as *beam remnant*. The beam remnants must be included when applying hadronization models to the entire final state, as it is only upon this inclusion that color is conserved. It is necessary to keep track of the color flows between the MPI and the beam remnant with so-called *color-reconnection schemes* [227, 228]. Color reconnection plays an important role in W^+W^- production, especially in hadronic decay modes [229]. More details on the soft-QCD component of pp event simulations can be found in Refs. [95, 152].

If multiple pp interactions among the colliding bunches take place, the process is usually referred to as *pile-up*. Pileup increases with higher luminosity, becoming hard to handle in busy environments in pp colliders with high instantaneous luminosity such as the LHC. Further details are given in Chapter 4.

Chapter 3

W-boson Pair Production in the Standard Model

Scientific knowledge is a body of statements of varying degrees of certainty. Some most unsure, some nearly sure, none absolutely certain.

— Richard Feynman (1918 – 1988).

The SM provides a mathematical formalism describing the production, interaction, and subsequent decays of gauge vector bosons, which can be used to derive predictions as discussed in Chapter 2. The non-abelian symmetry and local gauge invariance of the electroweak sector of the SM, presented in Chapter 1, also allows self-interactions between gauge vector bosons. Experimental testing of these predictions is crucial for validating the theory. This dissertation focuses on diboson processes, particularly W^+W^-, the most abundant diboson process for testing SM predictions (see Fig. 1.5). The chapter outlines the main phenomenological features of W^+W^- production, serving as benchmarks for theory predictions. Additionally, diboson processes, with W^+W^- as a key example, are essential for disentangling potential signals with lower cross sections, such as those from Higgs boson production[1], from other background contributions. The properties of W^+W^- production relevant to these tests are summarized in Section 3.1. Finally, diboson processes, specifically W^+W^-, play a crucial role in constraining BSM contributions which introduce anomalous Triple Gauge Couplings (aTGCs), as discussed in Section 3.2.

3.1 Phenomenology of W^+W^- Production at the LHC

W-boson pair production can be realized in hadron collisions mainly via $q\bar{q}$ scattering and gluon-gluon fusion (gg). Illustrative Feynman diagrams are depicted in Figure 3.1. In pp collisions, the production of W-boson pairs is dominated by $q\bar{q}$ annihilation, containing t-channel (Fig. 3.1a) and s-channel. The exchange of a $Z/\gamma^\star$ decaying into W^+W^- via the triple gauge coupling vertex is involved in the latter.

The total production cross section of W-boson pairs was first calculated in 1979 [230] for the lowest-order diagrams in Figs. 3.1a and 3.1b. The analytic expression of the partonic cross section is proportional to the partonic center-of-mass energy as $\sim \ln \hat{s}/\hat{s}$, whose scaling behavior highly depends on the gauge boson self-couplings described in the theory. Moreover, longitudinally polarized $W^\pm$ bosons introduce additional linear and constant terms in $\hat{s}$, diverging with infinitely large center-of-mass energies. In a renormalizable theory such as the SM, the divergent terms among the diagrams shown in Figure 3.1 cancel out exactly at all values of $\sqrt{s}$. In the SM, the issue is addressed

[1] The total production cross section of a single Higgs boson is about $55\,\mathrm{pb}$ in pp collisions at $\sqrt{s} = 13\,\mathrm{TeV}$, roughly a factor of 2 smaller than the production of W^+W^-. The background-to-signal ratio becomes more challenging when considering W^+W^- final states, with a branching ratio of $20\,\%$ [95].

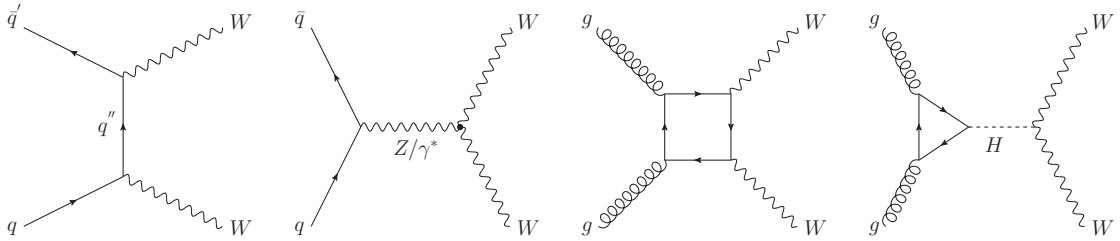

(a) t-channel $q\bar{q}$ (b) s-channel $q\bar{q}$ (c) $gg \to WW$ (d) $gg \to H \to WW$

Figure 3.1: Illustrative Feynman diagrams for W^+W^- production via (a) the t-channel and (b) s-channel in $q\bar{q}$ scattering, (c) gluon-gluon fusion, and (d) off-shell Higgs production.

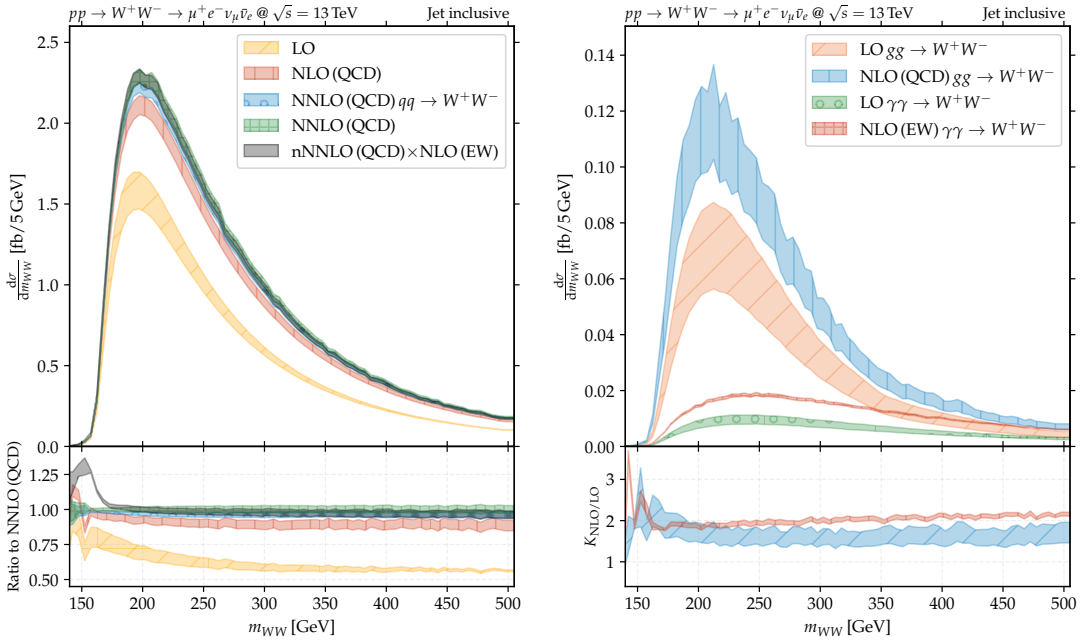

(a) (b)

Figure 3.2: Differential cross sections of $pp \to W^+W^- \to \mu^+e^-\nu_\mu\bar{\nu}_e$ production at a center-of-mass energy of $\sqrt{s} = 13$ TeV as a function of the invariant mass of the W^+W^- system (m_{WW}) computed with MATRIX [231]. Fixed-order predictions are displayed for (a) W^+W^- production at LO, NLO, NNLO (both full and only via $q\bar{q} \to WW$ production), and nNNLO accuracy in QCD, including also EW corrections at NLO; and (b) $gg \to WW$ and $\gamma\gamma \to WW$ production at LO and NLO. Uncertainties include effects from the 7-point scale variations of μ_F and μ_R, the dependence on the α_S value, and the PDF choice (NNPDF3.1-LUXQED [186]). The predictions are derived in a fiducial jet-inclusive phase space defined in Section 9.1.1.

via the inclusion of triple gauge couplings such as ZWW and γWW predicted by the non-abelian structure of the EW sector, allowing the production of W-boson pairs by s-channel decays of Z bosons (Fig. 3.1b). Measurements of W^+W^- production cross sections therefore allow testing the non-abelian structure of the EW theory. As shown in Section 1.3, the total cross-section measurements of $e^+e^- \to W^+W^-$ production at the LEP collider serve as empirical confirmation of the non-abelian structure of the SM (Fig. 1.4).

At NLO in QCD, W^+W^- production via quark-gluon (qg and $\bar{q}g$) scattering can also

take place implying additional partons in the final state according to the SM predictions. K-factors arise at NLO, increasing the LO prediction by about $40\,\%$, lying far outside the scale uncertainties at LO [232]. This feature of W^+W^- predictions is shown in Figure 3.2 as a function of m_{WW} in a jet-inclusive fiducial phase space (defined in Section 9.1.1). The large increase in the NLO calculation (Fig. 3.2a) can be explained by the sizable contributions of the new diagrams introduced by the qg and $\bar{q}g$ initial states[2] in the calculation at $O(\alpha_S)$ for pp collisions at the LHC center-of-mass energies, which are not contemplated at LO. The differences also depend on the differential distribution of interest. Therefore, caution has to be taken when relying on the modeling of W^+W^- production at LO, both in normalization and differentially. At NLO, the production cross sections are also underestimated. Additionally, W-boson pairs can be produced via non-resonant gg production, referred to as *gluon-gluon fusion* ($gg \to WW$), via a quark loop (Fig. 3.1c) in absence of additional final-state parton radiation. This production mode contributes at $O(\alpha_S^2)$ in perturbative QCD and increases the total W^+W^- production cross section by about $10\,\%$ [232] with respect to NLO. The NLO correction of this production mode added to the NNLO QCD prediction of $q\bar{q} \to WW$ constitutes part of the N^{3}LO correction to W^+W^- production and the combined prediction is therefore labeled as nNNLO. In high-energy pp collisions, $gg \to WW$ production has a sizable contribution due to the enhanced gluon luminosities at high momentum transfer to the partons in the proton structure (see Fig. 2.2). As observed in Figure 3.2a, the NNLO/NLO K-factor is dominated by pure perturbative corrections of $q\bar{q} \to WW$ production [233], although $gg \to WW$ has a sizable contribution to the enhancement of the NNLO prediction with respect to NLO. Resonant production of a Higgs boson via gluon-gluon fusion which further decays into a W-boson pair is also involved, as depicted in Fig. 3.1d, and its interference with the W^+W^- diagrams must also be considered [234, 235, 236].

After the first LO predictions [230], approximate NLO corrections were published [237, 238] considering stable W bosons. After the one-loop helicity amplitudes became available [239], full NLO calculations were possible [240, 159] considering the decay products of the W bosons, allowing predictions in fiducial regions closer to experimental environments. Full NNLO calculations for $q\bar{q} \to WW$ production have been available for almost a decade [232, 233], where scale uncertainties reach the level of a few percent. At this level in perturbation theory, diagrams resulting in single-top and $t\bar{t}$ production can arise in the calculation. While single-top and Wt production is realized at NLO in W^+W^- production, $t\bar{t}$ enters the computation at NNLO. These contributions can be handled by assessing the number of quark flavors considered in the PDF set [232, 233], distinguishing mainly between four-flavor and five-flavor schemes (i.e. including b-quark PDFs in the set and considering it to be massless in perturbative corrections). If five-flavor schemes are chosen, single-top and Wt diagrams must be subtracted. The contributions from $t\bar{t}$ production at NNLO should be subtracted in both flavor schemes. The $gg \to WW$ production was computed for the first time in Refs. [241, 242], also including leptonic final states [243, 244], spin correlations, and off-shell effects [245]. This process is currently available up to NLO including both resonant and non-resonant diagrams combined with $q\bar{q} \to WW$ production up to $O(\alpha_S^3)$ [246, 247]. As presented in Figure 3.2b, an increase of $70\,\%$ in the $gg \to WW$ production mode arises after considering NLO QCD corrections. EW corrections, necessary to reach the percent level

[2] Unless specified, W^+W^- production via $q\bar{q}$, qg, and $\bar{q}g$ will be inclusively referred to as $q\bar{q} \to WW$.

of accuracy in both inclusive and differential observables, were first available considering on-shell W bosons [248, 249, 250] and now also including off-shell effects [251, 252]. Figure 3.2a shows the effect of NLO EW corrections on the predicted fiducial cross section of the fully-leptonic $W^+W^- \to e^+\mu^-\bar{\nu}_e\nu_\mu$ production as a function of m_{WW} in a jet-inclusive phase space defined in Section 9.1.1. A reduction of about $4\,\%$ of the fiducial cross-section is predicted after EW corrections at NLO accuracy have been accounted for, which becomes more prominent at high m_{WW} where the Sudakov factors illustrated in Eq. (2.4) are larger. Fixed-order predictions of W^+W^- production including the aforementioned processes and corrections are publicly available in programs such as MATRIX [232, 233, 253, 247, 231] (including transverse momentum resummation with RADISH [254, 189]) or MCFM [255, 256] (including jet-veto resummation). Detailed simulation of W^+W^- events is available in generators such as POWHEG BOX [257], HERWIG [258], or SHERPA [259] up to one jet. Nowadays, unified descriptions of fixed-order predictions of W^+W^- production up to NNLO in QCD matched to parton showers are available, allowing both high accuracy and a fully differential description of experimental data [215, 216, 260, 261]. Efforts towards including EW corrections in such schemes are also ongoing [262, 263]. Predictions of polarized W^+W^- final states are available up to NNLO in QCD using the double-pole approximation [264] and NLO QCD in semileptonic decays [265], and analysis techniques to extract production cross sections of polarized W bosons and polarization fractions relying on template fits to theoretical predictions [266] but also longitudinal massive gauge boson tagging to increase experimental sensitivity in fully leptonic [267, 268] and semileptonic final states [269].

When both QCD and EW corrections are sizable, effects at NNLO from mixed QCD-EW contributions $O(\alpha_S\alpha_W)$ become important. Different schemes on the combination of NNLO QCD and NLO EW corrections can be consider to account for these effects [231].

- A purely *additive* combination,

$$\mathrm{d}\sigma_{\mathrm{NNLO\,QCD\oplus NLO\,EW}} = \mathrm{d}\sigma_{\mathrm{LO}}(1+\delta_{\mathrm{QCD}}+\delta_{\mathrm{EW}}) + \mathrm{d}\sigma^{gg}_{\mathrm{LO}}\,, \tag{3.1}$$

- and a factorized *multiplicative* scheme that applies the EW correction to the entire NNLO QCD cross section

$$\mathrm{d}\sigma_{\mathrm{NNLO\,QCD\otimes NLO\,EW}} = \mathrm{d}\sigma_{\mathrm{LO}}(1+\delta_{\mathrm{QCD}})(1+\delta_{\mathrm{EW}}) + \mathrm{d}\sigma^{gg}_{\mathrm{LO}}\,. \tag{3.2}$$

  The multiplicative prescription generates extra $O(\alpha_S\alpha_W)$ and $O(\alpha_S^2\alpha_W)$, approximating the higher-order mixed QCD-EW corrections[3].

Experimental collaborations[4] usually veto additional hadronic activity surpassing a certain threshold in transverse momentum p_T^{veto} to enhance the purity of W^+W^- signal events over background processes. In such cases, the measured fiducial cross section in this *jet-vetoed* selection is extrapolated to the inclusive selection using a *jet-veto efficiency* $\varepsilon_{\mathrm{veto}} = \sigma_{\mathrm{veto}}/\sigma_{\mathrm{incl.}}$, where the fiducial jet-vetoed and inclusive cross sections (σ_{veto} and $\sigma_{\mathrm{incl.}}$, respectively) are determined from SM predictions. However, these type of vetoes

[3] This factorization assumption is justified, e.g., in scattering energy regimes $Q \gg m_W$ dominated by Sudakov logarithms while the QCD effects arise at energies below Q. The multiplicative approach is not justified in regions affected by giant EW K factors [231].

[4] An overview of the experimental measurements of W^+W^- production is presented in Section 7.2.

can lead to more unreliable fixed-order calculations since large logarithms of the form $\log(p_T^{\text{veto}}/m_{WW})$ arise when the energy scale introduced by p_T^{veto} is much smaller than the scale of the process m_{WW}, as shown in Eq. (2.3). In such a case, the predictions must be recovered via resummation [270, 271, 255, 272, 256]. Transverse momentum [273, 274, 271, 260], jet-veto [270, 275], and threshold [276] resummation approaches are available.

Photon-induced W^+W^- production ($\gamma\gamma \to WW$) also contributes at leading order when EW radiative corrections in the proton are accounted for. As shown in Figure 3.2b, this production mode contributes especially at high m_{WW} [248, 252]. At the current level of precision in W^+W^- production at the LHC, photon PDFs and $\gamma\gamma \to WW$ production must be included for an accurate assessment of the cross-section prediction since photon-induced contributions are larger than the corresponding PDF uncertainties [186]. The contribution of $\gamma\gamma \to WW$ to the W^+W^- differential production cross section increases from 1 % at $m_{WW} = 300$ GeV up to 35 % at $m_{WW} = 3$ TeV, although contributions to the W-boson transverse momentum distributions are of the order of 1 % [186]. In this work, the NNPDF3.1LUXQED PDF set [186], containing photon contributions, is used. In W^+W^- production at the LHC, lepton PDFs can be neglected [277].

3.2 Sensitivity to Anomalous Couplings in W^+W^- Production

The access of W-boson pair production to the self-couplings among massive gauge vector bosons in the SM gives sensitivity to test anomalous interactions that are not contemplated in the SM prescription. In the past, W^+W^- production has been exploited in colliders such as LEP and the Tevatron to set limits on aTGCs using the *anomalous coupling formalism* [278], which assigns arbitrarily constant values to the coupling strengths of the anomalous couplings among gauge vector bosons [279, 280], limited by unitarity constraints [281]. In this formalism, the W bosons are required to decay on-shell and the longitudinal components of the neutral gauge bosons are neglected. Moreover, the contributions of the coupling terms at higher orders are not suppressed at energies $E > m_W$, so they cannot be neglected. EFTs, discussed in Section 1.7, offer several advantages when compared to the anomalous coupling formalism [131, 282]. The assumptions introduced in the anomalous coupling formalism are not required, and it is possible to constrain anomalous couplings without loss of generality. In the SMEFT Lagrangian expansion (Eq. 11.1), operators at higher-orders are suppressed by powers of energy scale Λ^{-1}. As discussed in Chapter 11, even though dim-6 operators would violate unitarity at large s/Λ^2, the EFT is known to be inapplicable at this regime by definition. In addition, constraints in the anomalous coupling formalism can be reinterpreted as dim-6 Wilson coefficients by well-defined expressions given in Ref. [131], which also reduces the number of free parameters. EFT interpretations have been used in the past [283, 284, 285, 286, 287] in the production of massive gauge vector bosons, although this approach was not much pursued by the community. It was not until the analyses of the full dataset of pp collisions at $\sqrt{s} = 13$ TeV that the SMEFT formalism was widely adopted in studies of LHC results.

An illustration of the effects from an anomalous triple gauge coupling among three W bosons on the SM prediction is depicted in Figure 3.3. The cross section including the contributions from anomalous couplings is computed by squaring the sum of the SM amplitudes with the ones introduced by a WWW coupling with its corresponding strength given by the Wilson coefficient c_{WWW}. While the contributions from the interference do

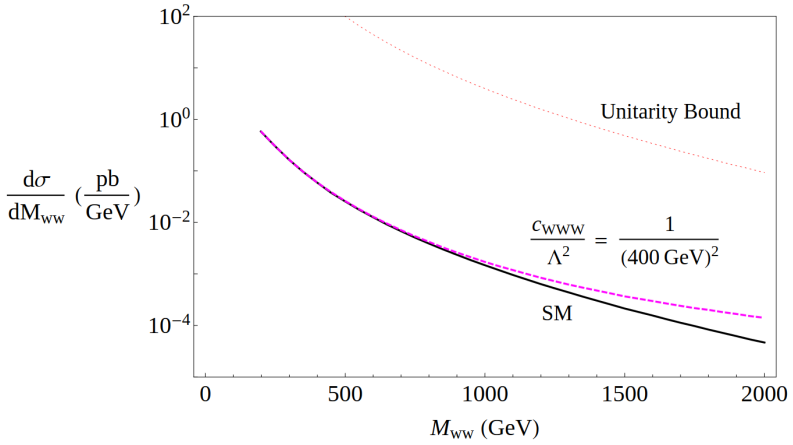

Figure 3.3: Differential W^+W^- cross section as a function of the invariant mass of the diboson system m_{WW} at the LHC in pp collisions at $\sqrt{s} = 14$ TeV. The SM prediction (solid line), the effects of the dimension-6 operator $\mathcal{O}_{WWW}$ (dashed line) in a SMEFT of energy scale $\Lambda = 400$ GeV and the unitarity bound on the cross section (dotted line) are shown. Source: [131].

not grow with energy, the effect from the squared anomalous amplitude leads to a growth with s^2/Λ^4 that is observed at the high-energy tails of the distribution. Based on experimental data, bounds on the c_i/Λ^2 terms can be set. If data were found to match the curve with c_{WWW} contributions at all values of m_{WW} with sufficient significance, one could conclude that (i) the energy scale of new physics Λ is greater than the measured value at the highest reachable energy in the experimental result and (ii) the value of Λ chosen for the predicted contributions of the anomalous coupling is lower than the energy scale leading to unitarity violation [133].

The characteristic features of the W^+W^- production signature along with its clean reconstruction and high production rate can be exploited to also constrain specific BSM models. An example is the production of *axion-like particles* (ALPs), which are candidates to describe Dark Matter in extensions of the SM that could also solve the strong CP problem [288, 289]. These ALPs could couple to diboson final states such as W^+W^-, ZZ or $Z\gamma$ [290, 291]. Constraints on the mass and couplings to gauge vector bosons of such particles can be set using LHC data [290, 292]. Extensions including vector boson scattering processes have also been investigated [293], including sensitivity in global SMEFT interpretations [294].

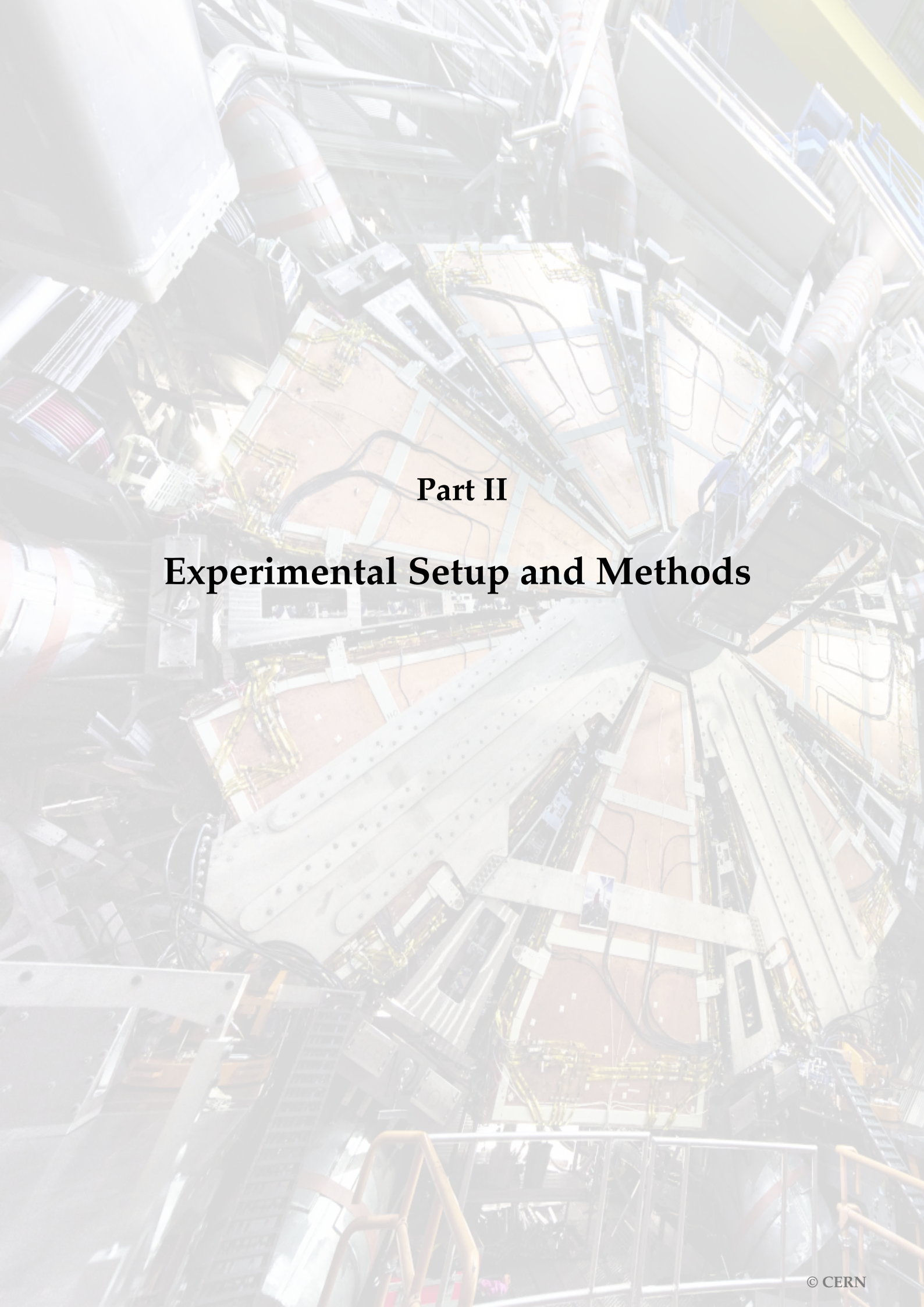

Part II

Experimental Setup and Methods

Chapter 4
The LHC and the ATLAS detector

"Measure what can be measured, and make measurable what cannot be measured."

— Galileo Galilei (1564 – 1642).

The ATLAS Collaboration conducts fundamental research in particle physics through experimental measurements in proton-proton (pp) collisions[1] at the Large Hadron Collider, located at the European Organization for Nuclear Research (CERN) in Geneva, Switzerland. Over 5900 members (about 2900 scientific authors) from 182 institutions, representing 42 countries all around the world, constitute this collaboration [295]. In this chapter, the facilities of the Large Hadron Collider accelerator and their specifications are outlined in Section 4.1. The ATLAS detector is described in more detail in Section 4.2. To identify and reconstruct different kinds of particles and the process of interest in this thesis, multiple algorithms and selection criteria are applied on the signals recorded in the different components of the ATLAS detector. The corresponding methodology followed by ATLAS is presented in Section 4.3.

4.1 The Large Hadron Collider at CERN

Despite the consolidation of the SM with increasing experimental evidence, the Higgs boson was still to be found after strong exclusions from theoretical and phenomenological considerations [61] and experimental searches from the Large Electron Positron (LEP) collider [55, 56, 57] at CERN and the Tevatron at Fermilab (USA) [86] in the 1990s. Additionally, various models of BSM physics include new heavy gauge bosons (Z',W'), supersymmetric particles, or new models proposing the existence of extra dimensions leading to a characteristic energy scale of quantum gravity in the TeV region. The center-of-mass energy of the collisions under study has to be maximized to be sensitive to such physics processes. Due to the small production cross sections involved in the aforementioned processes, especially in their final states of cleanest signatures, large instantaneous luminosities are required to generate a significant statistical dataset sufficient for observation. The increased luminosity and enhanced cross sections make possible to conduct even more precise tests of QCD, electroweak interactions, and flavour physics. I this way, a pp collider fulfilling these requirements would also act as a top-quark factory with a production rate of several tens of Hz, offering a chance to explore its couplings and spin with unprecedented precision.

At CERN, the European Organization for Nuclear Research founded in 1954 in Geneva (Switzerland), a particle collider with unprecedented values of center-of-mass energies and rate of particle collisions[2] was installed — the Large Hadron Collider (LHC) [62, 63,

[1] Also, heavy ions such as lead or xenon are accelerated at the LHC for specific studies and their products are also measured with the ATLAS experiment. Nevertheless, only pp collisions are relevant for this thesis. The discussion, unless specified, will focus on pp collisions.

[2] The highest instantaneous luminosity was surpassed by the SuperKEKB e^+e^- collider in 2020 [298, 299].

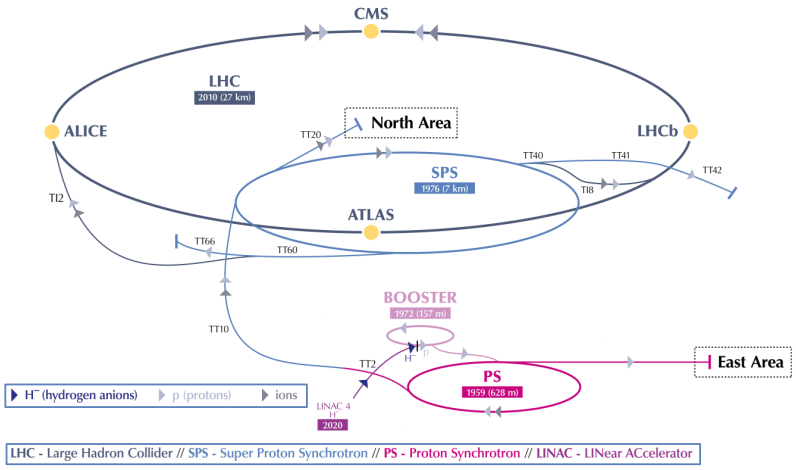

Figure 4.1: Particle acceleration facilities at CERN from the LINear ACcelerator (LINAC2, replaced by LINAC4 in 2020 [296], shown in purple), passing through the BOOSTER (in pink), the Proton Synchrotron (PS, shown in lilac) and the Super Proton Synchrotron (SPS, in light blue) up to the Large Hadron Collider (LHC, in dark blue). The particle types accelerated are shown as arrows in different colors. In colored rectangles, the length if the given accelerator (in curly brackets) and the starting date of operation are given. Adapted from [297].

64]. To cover the complete unexplored Higgs mass spectrum up to the upper threshold of 1 TeV required by unitarity constraints and the aforementioned physics searches, the design parameters of the LHC were carefully selected. Hadrons (either protons or heavy ions) are accelerated approximately 100 m underground in a collider of a circumference of 26.7 km. The LHC is composed of eight arcs and eight straight sections installed in the tunnel that previously hosted the LEP collider.

In collider experiments, the event production rate of a certain process X with production cross section σ_X is inferred as described in Section 1.5,

$$\dot{N}_X = \frac{dN_X}{dt} = L \cdot \sigma_X \,, \tag{4.1}$$

where L corresponds to the *instantaneous luminosity*, representing the flux of colliding particles. The instantaneous luminosity L is defined by the experimental setup (e.g. the beam conditions during the collision run) and it has the dimension of number of particles per area per time. The cross section of the process in place is computed following a specific physical model evaluated using Eq. (2.1). To explore processes with small cross sections, the instantaneous luminosity needs to be maximized in order to achieve a considerable statistical set to carry out a precision measurement, or claim either an evidence or a discovery. The total number of interactions depends on the *integrated luminosity* $\mathcal{L}$

$$N_X = \sigma_X \cdot \int L(t)dt \equiv \mathcal{L} \cdot \sigma_X \,, \tag{4.2}$$

whose value is measured in units of inverse barn. At the LHC, units of inverse femtobarn (fb^{-1}) are commonly used.

Bunches composed of $\mathcal{O}(10^{11})$ protons are obtained at the LHC by ionizing hydrogen using electric fields. The extracted protons are then injected into the pre-acceleration chain. The pre-acceleration facilities of the LHC employed between 2015 and 2018 [64]

are presented in Figure 4.1, involving the linear accelerator LINAC2 that accelerates the protons up to $50\,\mathrm{MeV}$. Further, the particles proceed to the *Booster*, where the incoming beam is split and accelerated simultaneously to $1.4\,\mathrm{GeV}$ in four superimposed synchrotron rings, then recombined and injected into the *Proton Synchrotron*. The Proton Synchrotron, speeding up the particles up to $15\,\mathrm{GeV}$. Finally, the *Super Proton Synchrotron* (SPS) accelerates the protons up to $450\,\mathrm{GeV}$. These constitute the pre-acceleration facilities, which were historically very important in milestones of the SM validation such as the discovery of the $W^{\pm}$ [39, 40] and Z [41, 42] bosons, and underwent major upgrades in order to meet the demanding requirements of the LHC. Only about 0.1% of the initial protons are injected into the LHC, the rest being used by lower-energy experiments along the chain.

Protons at $450\,\mathrm{GeV}$ are then injected into the LHC and accelerated with a separation of $25\,\mathrm{ns}$ (approximately $7.5\,\mathrm{m}$ for maximum proton speed) by 16 radio-frequency cavities. Opposite magnetic dipole fields are needed to bend two counter-rotating proton beams on a circular path. A total of 1232 superconducting niobium-titanium (NbTi) dipole magnets, that produce a magnetic field of $8.3\,\mathrm{T}$ below critical temperature with superfluid helium at $1.9\,\mathrm{K}$, are used to drive, steer, and focus the particle beams. Up to 12 poles installed within corrector magnets are used to stabilize the beam against disturbances or field irregularities of the dipole and quadrupole magnets (used to squeeze the beam at the interaction point) across the acceleration line. The nominal filling scheme of the LHC allows the accelerator to introduce 2808 bunches per injection period per beam, colliding at a rate of $40\,\mathrm{MHz}$ with a specific *crossing angle* to prevent parasitic collisions on both sides of the desired interaction point. After certain assumptions[3], the resulting instantaneous luminosity is given by

$$L = \frac{f\, n_b\, N_1\, N_2}{2\pi\sqrt{(\sigma_{x,1}^2 + \sigma_{x,2}^2)}\sqrt{(\sigma_{y,1}^2 + \sigma_{y,2}^2)}} \times S\,, \tag{4.3}$$

where f is the revolution frequency, n_b is the number of bunches, N_i is the number of protons in bunch $i = 1, 2$, and $\sigma_{x,i}$ and $\sigma_{y,i}$ denote the beam width of bunch i along x and y axes in the transverse plane, respectively. As a good approximation, beam sizes can be assumed to be gaussian-distributed with equal widths. The factor S depends on the operating conditions (such as the crossing angle of the two beams) [301] and it usually takes values around 0.8 [302]. The instantaneous luminosity is determined using dedicated detectors and experimental techniques such as *Van der Meer calibration scans* [303]. The ATLAS luminosity-sensitive detectors and the luminosity measurement for the data collected between 2015 and 2018 are outlined in Section 4.2.6. During this period, the peak instantaneous luminosity recorded in the ATLAS detector was $21 \cdot 10^{34}\,\mathrm{cm}^{-2}\mathrm{s}^{-1}$, measured in 2018.

Designed to operate at center-of-mass energies up to $\sqrt{s} = 14$ TeV and an instantaneous luminosity of $L = 10^{34}\,\mathrm{cm}^{-2}\mathrm{s}^{-1}$, the LHC faced technical constraints such as the maximum dipole field and magnet quench limits, forcing the center-of-mass energy of the LHC (tied to the magnetic rigidity of the ring) to steadily increase over time [62]. The

[3] To obtain the given expression, certain assumptions on the beam configuration need to be made. Uncorrelated bunches with gaussian profiles along the three spatial axes (x, y, s) with the same bunch length are considered, colliding colinearly head-on with equal and opposite velocities. The revolution frequency of the two beams is also considered to be synchronized [300].

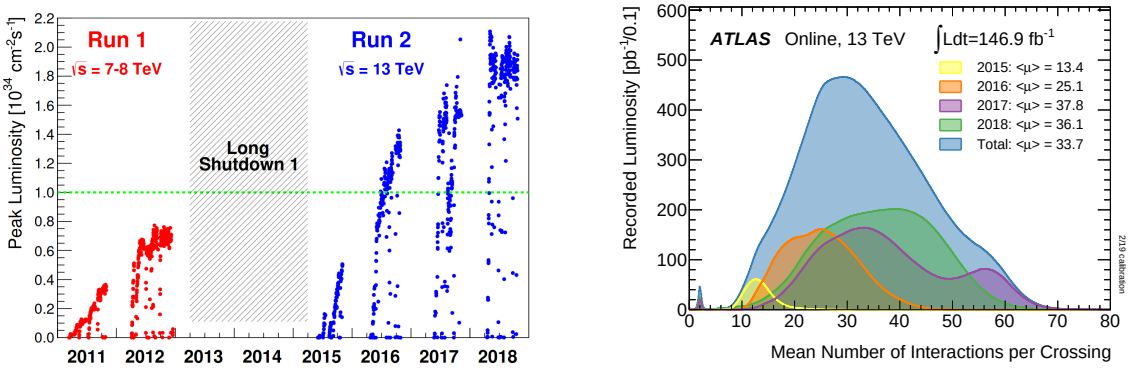

(a) LHC peak luminosity.

(b) Average number of pile-up interactions.

Figure 4.2: (a) Peak luminosity for pp collisions at the LHC for Run 1 (red) and Run 2 (blue). The dashed green line shows the design instantaneous luminosity of the LHC. Source [302]; and (b) Number of interactions per bunch-crossing $\langle\mu\rangle$ per year for data recorded by the ATLAS detector in Run 2. Source [304].

periods between accelerator and detector upgrades, known as *Runs*, correspond to the timeframes when data is collected. The LHC exhibited exceptional performance surpassing the design luminosity by a factor of two from 2016 to 2018 during Run 2, owing to reductions in beam emittances and β^* parameters [302]. Details of LHC collision parameters across different years of Run 2 are summarized in Table 4.1. However, collisions are halted during winter months to reduce energy costs. The augmented instantaneous luminosity resulted in a higher number of collisions per bunch crossing, known as *pile-up*. Figure 4.2b illustrates the mean number of interactions per bunch crossing $\langle\mu\rangle$ for datasets recorded at $\sqrt{s} = 13$ TeV for various years, showing a maximum around $\langle\mu\rangle$ = 30 for the integrated results of full Run 2. The majority of high pile-up events, with values between 30 and 70, occurred in 2017 and 2018 when the instantaneous luminosity reached its peak.

The collisions take place in four different *interaction points*, with their products recorded by nine different experiments. The four largest experiments that are set along the interaction points are ATLAS [305] and CMS [306], general-purpose detectors[4] of complementary design; the ALICE detector focuses on heavy-ion collisions and studies of confinement in QCD and properties of the quark-gluon plasma [307]; and LHCb, which is designed to carry out optimized measurement on b-hadron decays [308]. TOTEM (measuring elastic scattering phenomena and total cross sections) is installed at the same interaction point as CMS [309]. LHCf (that studies the origin of ultra-high-energy cosmic rays) [310], SND@LHC [311] (neutrino measurements produced at the LHC), and FASER [312] (for searches of new light and weakly coupled elementary particles) are installed along with ATLAS; and MoEDAL [313] (for direct searches of magnetic monopoles) sits with LHCb. This work is based on data recorded using the ATLAS experiment in pp collisions for the Run 2 period. The different components of the ATLAS detector are described in the following.

[4]General-purpose experiments are designed to study a wide range of physics phenomena, including the Higgs boson and the electroweak sector of the SM, the study of the properties of the top quark, flavor physics, and searches for physics BSM.

Parameter	Design [62]	2015	2016	2017	2018
Proton energy [TeV]	7	6.5	6.5	6.5	6.5
Peak L [$10^{34}\,\mathrm{cm}^{-2}\mathrm{s}^{-1}$]	1.0	0.5	1.4	2.1	2.1
Average pile-up $\langle\mu\rangle$	34	13	25	38	37
Maximum n_b	2808	2244	2220	2556/1868	2556
Bunch N_i at start of stable beams [10^{11}]	1.15	1.0-1.25	1.0-1.25	1.0-1.25	1.0-1.25
Emittance at injection [µm]	3.75	∼3.0	∼1.6	∼1.6	∼1.4
β^* [cm]	55	80	40	40-30	30-25
Half crossing angle [cm]	142.5	145	185/140	150-120	10-130
Delivered $\mathcal{L}$ [fb^{-1}]	—	4.2	39.7	50.6	66

Table 4.1: LHC parameters during pp collisions for physics analyses during Run 2 delivered to the ATLAS and CMS experiments. Adapted from [302].

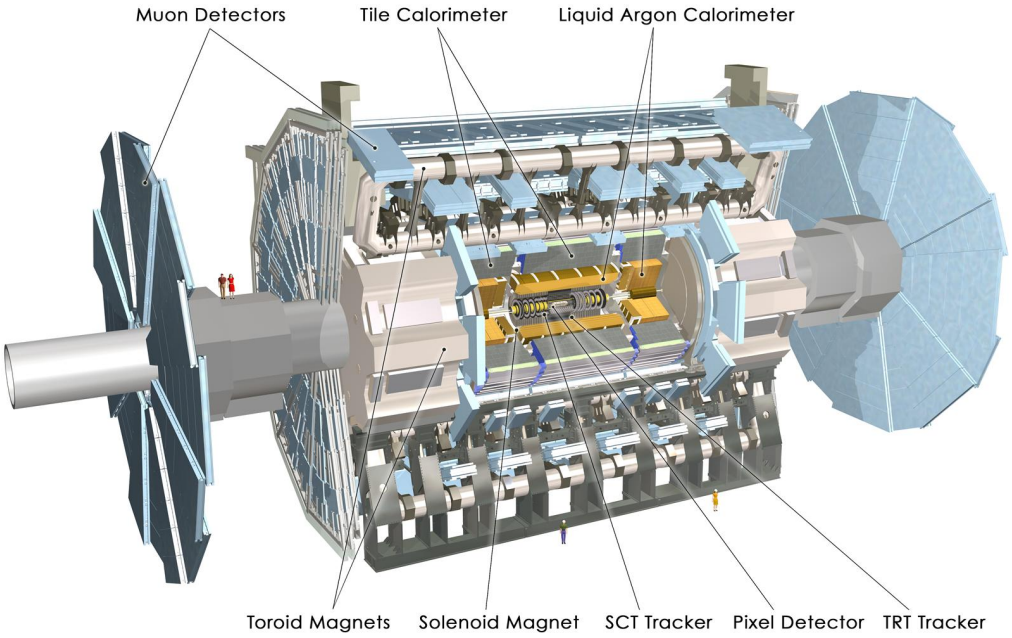

Figure 4.3: Schematic view of the ATLAS detector and its components. Taken from [314].

4.2 The ATLAS Experiment

The ATLAS[5] experiment [305] is a general-purpose particle detector at the LHC designed for precision measurements and searches for new phenomena in high-luminosity environments. These are set by the demanding LHC program. Exploring the physics behind the QCD and electroweak theories of the SM, especially the electroweak symmetry breaking mechanism, as well as either discovering or excluding the SM Higgs boson and other extended Higgs sectors, supersymmetry, new dynamics at the electroweak scale via, e.g., new massive electroweak gauge bosons at the TeV regime, new quarks or leptons, lepton flavor and CP symmetry violation, and many more, are among the fundamental goals of the physics program of the ATLAS experiment.

[5]The acronym ATLAS stands for *"A Toroidal LHC ApparatuS"*.

Due to the small cross sections expected for most of the processes under investigation, the LHC requires very high collision rates. However, due to an inelastic pp cross section of $80\,\mathrm{mb}$ (see Fig. 1.5), the LHC will still produce 10^9 inelastic events per second at design luminosity. This brings a significant experimental challenge, as each candidate event for new physics will be accompanied by an average of 38 inelastic events per bunch-crossing (Fig. 4.2b). Moreover, QCD jet production cross sections dominate over the rare processes being studied in pp collisions. As a result, experimental signatures that are unique to the physics processes in question, such as *missing transverse energy* (E_T^{miss}) or secondary vertices, need to be unambiguously identified. This, in turn, places additional demands on the particle identification capabilities of the detector.

The ATLAS detector is designed to overcome these challenges and exploit the full discovery potential of the LHC. These challenging purposes require

1. a large coverage in both azimuthal and polar angles,
2. very fast and reliable detector response composed of radiation-hard electronics and sensors, including vertex detector close to the interaction point to resolve secondary vertices crucial for b-jet and τ identification,
3. a fine detector granularity to disentangle signal particles from overlapping events,
4. a highly efficient tracker system to characterize charged particles with high momentum resolution and reconstruction efficiency,
5. electromagnetic calorimeters with excellent energy resolution to reconstruct four-momenta of high-energy particles, identify electrons and photons, and isolate prompt production from other secondary decays. This must be complemented by a full-coverage hadronic calorimeter for accurate hadron and jet energy reconstruction, crucial to perform measurements of E_T^{miss},
6. an accurate identification of muons and precise measurement of their momentum across a broad spectrum with unequivocal determination of the charge of high-momentum muons, and
7. an effective triggering system on low-energy objects with efficient rejection over background to only select interesting physics events over the large inelastic pp cross section and QCD jet production.

In the *barrel* region, the detector subsystems are installed in concentric layers around the beam pipe in the central region. Additional detector layers are placed as transverse discs along the beam pipe in the *forward region*. Regions at both halves of the detector cylinder containing these transverse disks are referred to as *endcaps*. The detector subsystems complement each other for an accurate lepton reconstruction and identification. The required energy resolution and performance of each of these, assessed by detailed detector simulations of the full ATLAS detector [315], are presented in Table 4.2. The overall layout is presented in Figure 4.3. A coordinate system suiting its shape is presented in Section 4.2.1. The layers can be divided into four main groups according to their roles. Following the trajectory of the collision products at the interaction point towards the outside of the detector, the *inner detector* measures tracks of charged particles with very high

Detector component	Location	Required resolution	$\lvert\eta\rvert$ coverage	
			Measurement	Trigger
Tracking		$\sigma_{p_T}/p_T = 0.05\% p_T \oplus 1\%$	2.5	—
Electromagnetic calorimeter		$\sigma_E/E = 10\%/\sqrt{E} \oplus 0.7\%$	3.2	2.5
Hadronic calorimeter	Barrel and Endcap	$\sigma_E/E = 50\%/\sqrt{E} \oplus 3\%$	3.2	
	Forward	$\sigma_E/E = 100\%/\sqrt{E} \oplus 10\%$	[3.1 , 4.9]	
Muon spectrometer		$\sigma_{p_T}/p_T = 10\% p_T$ at $p_T = 1$ TeV	2.7	2.4

Table 4.2: General performance goals of the ATLAS detector. Units for energy (E) and transverse momentum (p_T) are in GeV. Adapted from [305].

precision and it is covered in Section 4.2.2. The magnet system, composed by a solenoid surrounding the inner detector and the toroid magnets, is outlined in Section 4.2.4. Measurements on the particle energies for photons and electrons, and separately for most of the hadrons, are carried out by the electromagnetic and hadronic *calorimeters*, respectively, as described in Section 4.2.3. Precise measurements of the muon four-momenta are performed using the *muon spectrometer*, covered in Section 4.2.5. Dedicated detectors are used to perform accurate measurements of the recorded luminosity. These are presented in Section 4.2.6. The trigger and data acquisition systems of ATLAS in Run 2 are outlined in Section 4.2.7. Section 4.2.8 introduces the detector simulation infrastructure. Further technical details on any of these components of the ATLAS detector can be found in Ref. [305].

4.2.1 Coordinate System

At the ATLAS detector, the x-axis of the right-handed coordinate system points towards the center of the LHC, the y-axis is defined upwards and the z-axis is parallel to the beam pipe. For convenience, spherical coordinates are normally used. The origin of the coordinate system is determined *per event* at the nominal interaction point (whose definition and reconstruction are described in Section 4.3.1). The angular coordinates are the *polar angle* θ, defined as the angle from the beam axis, and the *azimuthal angle* ϕ, which is measured around the beam axis in the transverse plane (given by the $x-y$ plane). The *rapidity* y is defined with respect to the beam axis as

$$y = \frac{1}{2} \ln \left(\frac{E + p_z}{E - p_z} \right) . \tag{4.4}$$

where E denotes the energy of the particle and p_z the z-component of its momentum vector $\vec{p}$. Contrarily to other space coordinates, the difference of rapidity between two objects is invariant under Lorentz boosts along the z-axis. Therefore, the rapidity is more convenient to describe kinematics in hadron collider experiments than the polar angle θ. Nevertheless, the *pseudorapidity* η is used instead since it tends to the rapidity in the limit of massless particles (i.e the high-energy limit), directly related to the polar angle θ. It is defined as

$$\eta = -\ln \tan \left(\frac{\theta}{2} \right) , \tag{4.5}$$

taking values from 0 in the transverse plane ($\theta = 90°$) to $+\infty$ or $-\infty$ (when $\theta \to 0°$ or $\theta \to 180°$, respectively) along the beam axis. Based on these definitions, transverse

variables such as the *transverse momentum* $p_T = |\vec{p}| \sin\theta$ are well-defined in the $x-y$ plane in terms of η and ϕ as[6]

$$p \equiv |\vec{p}| = p_T \cdot \cosh\eta \,. \tag{4.6}$$

The angular separation in the pseudorapidity-azimuthal angle space between two objects can also be defined as

$$\Delta R = \sqrt{\Delta\eta^2 + \Delta\phi^2} \,. \tag{4.7}$$

4.2.2 Inner Detector

At the rates and radiation levels of the LHC, semiconductor detectors are the most suitable technology for efficient particle tracking [316]. These technologies have revolutionized high-energy physics experiments allowing electronic readout of particle tracks and an increase of two orders of magnitude in spatial resolution with respect to the previously used wire chambers. A charged particle traversing a material loses energy via ionization or photon absorption by the material. Semiconductor detectors make use of this energy generating electron-hole pairs in pn junctions. Tracking detectors must provide exceptional spatial resolution in high-energy physics to resolve the enormous particle multiplicity produced in hh collisions at the LHC. Spatially sensitive semiconductor technologies such as pixel and microstrip detectors are used in the inner tracker of the ATLAS detector. Due to the small size of the pads (of the order of several μm) and the high drift velocities, the maximum time needed by the charge carriers to pass the space-charge region is of the order of a few ns, perfectly suited to cope the collision rate of the LHC (25 ns).

The momentum resolution of a tracking detector can be inferred from the measurement of the curvature $\kappa = -q/|q|R$ of a circular particle trajectory of radius R, and therefore the measurement of the momentum component perpendicular to the magnetic field of strength B, $p_T = 0.3|q/e|BR$. The determination of the *sagitta*[7] for small curvature angles or equivalently high particle momenta is proportional to the curvature radius. The resolution on the sagitta can be improved by increasing the number of position measurements of the track, which is therefore proportional to the curvature resolution. Propagating the uncertainty due to the curvature resolution for many position measurements ($N \geq 10$), the momentum resolution of a tracking detector can be determined as [316]

$$\left(\frac{\sigma_{p_T}}{p_T}\right)_{\text{meas}} = \frac{p_T|q|}{0.3q} \frac{\sigma_{\text{meas}}}{L_p^2 B} \sqrt{\frac{720}{N+4}} \,, \tag{4.8}$$

with L_p being the distance between the first and last track measurement in the bending plane. This relation, called the *Gluckstern formula*, is applicable at high momenta when multiple scattering can be neglected [317]. At lower momenta, multiple scattering affects the deflection angle and an additional term must be added, which is inversely proportional to B, L_p, and the velocity of the particle. Since these are defined by the detector design, one can parameterize the detector resolution as

$$\left(\frac{\sigma_{p_T}}{p_T}\right)_{\text{meas}} := \sqrt{(ap_T)^2 + b^2} \equiv ap_T \oplus b \,,$$

[6] The properties $\cot\theta = \sinh\eta$ and $\cosh\eta = \sin^{-1}\theta$ are useful to derive these relations.

[7] The sagitta represents the maximum distance of the particle trajectory perpendicular to the line connecting its entrance and exit points within the magnetic field volume.

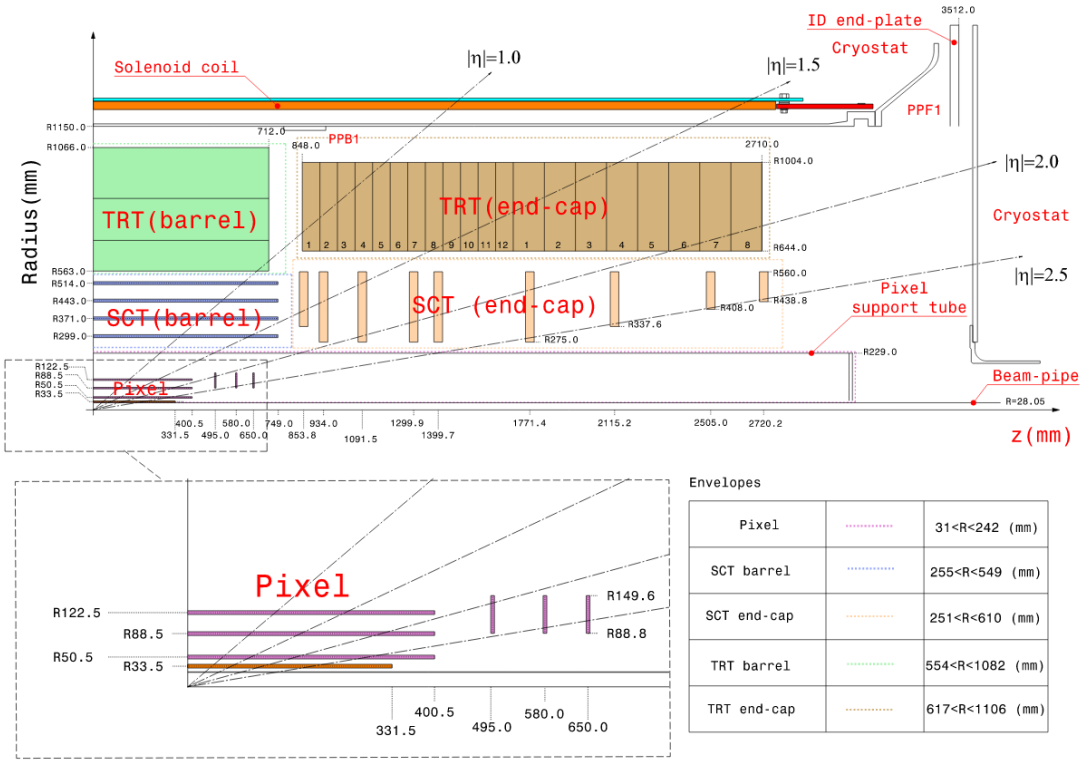

Figure 4.4: The $r - z$ cross-section view of the layout of the ATLAS Inner Detector for Run 2. The top panel shows the entire Inner Detector, whereas the bottom panel shows a magnified view of the Pixel detector region, where the Insertable B-layer introduced for Run 2 is shown in orange. Source [320].

where a and b measure the contributions from the position measurement (Eq. (4.8)) and multiple scattering, respectively. Therefore, the momentum resolution of a tracking detector is improved by (i) increasing the precision of the position measurement, (ii) the size of the detector, (iii) a strong magnetic field, (iv) greater number of position measurements, and (v) particles with high perpendicular momenta to the magnetic field.

To achieve the momentum resolution of $\sigma_{p_T}/p_T = 0.05\% \cdot p_T \oplus 1\%$ required by its ambitious physics program (see Table 4.2), the ATLAS inner tracker combines several layers of pixel and strip semiconductor detectors along with a *transition radiation detector* that allows for improved particle identification. The ATLAS inner detector [318, 319] provides a precise pattern recognition, high momentum resolution, and accurate measurements of tracks for electrically-charged particles above $0.5\,\mathrm{GeV}$ within a pseudorapidity of $|\eta| < 2.5$ and full coverage in ϕ. This allows a confident reconstruction of primary and secondary vertices. It is immersed in a $2\,\mathrm{T}$ magnetic field generated by a *thin superconducting solenoid* that surrounds the inner detector. Momenta of charged particles are then inferred with high precision from the trajectory curvature, reconstructed from the track assigned to charged particles built using the hits on the different detectors of the inner tracker (see Section 4.3.1).

Three independent and complementary subsystems compose the inner detector, presented in Figure 4.4. Four barrel layers of *silicon pixel detectors* allow for high resolution at pattern recognition from 33 up to $155\,\mathrm{mm}$ of the detector radii. Each layer provides a

spatial resolution of $10\,\mu\mathrm{m}$ along the azimuthal direction and $115\,\mu\mathrm{m}$ along the axial (radial) direction of the barrel layers (disc layers). The high granularity of the pixel detector and its proximity to the interaction point is crucial for the reconstruction of primary and secondary vertices with high resolution, essential for flavor tagging and τ reconstruction. The pixel detector was upgraded in 2014 by inserting the newest, innermost barrel layer called the *Insertable B-Layer* (IBL) [321] at $33.5\,\mathrm{mm}$ from the beam pipe. The IBL improved the track reconstruction performance by more than 40% [322], providing a better precision at vertex reconstruction and significant rejection of photon conversion.

Four and two more layers of stereo pairs of *silicon microstrip* detectors composing the so-called *SemiConductor Tracker* (SCT) span the detector radius from 299 up to $560\,\mathrm{mm}$ in the barrel and endcap regions, respectively. In order to reconstruct 2D position information using strips, each module is made of two layers of silicon micro-strip detector sensors glued back to back with a relative stereo angle of $40\,\mathrm{mrad}$[8] [323] to improve the measurement of the z coordinate and the radial coordinate for tracks of charged particles in the barrel and disc layers, respectively. A clear disadvantage is that the amount of material doubles, increasing secondary interactions in the tracker and also multiple scattering. The SCT layers provide around eight hits per track with an intrinsic resolution of $17\,\mu\mathrm{m} \times 500\,\mu\mathrm{m}$ per layer with a data-quality efficiency of $99.85\,\%$ in Run 2 [324].

Charged particles crossing the interface of two media with differing dielectric properties emit *transition radiation* in the form of photons. These photons can be absorbed by gas tubes, generating an ionization signal that can be used for tracking and particle identification. In the ATLAS detector, the *Transition Radiation Tracker* (TRT) consists of multiple layers of gaseous straw drift tubes situated at the outermost part. This tracker detects transition-radiation photons, covering a track momentum range from 1 to $200\,\mathrm{GeV}$. The gas tubes are arranged cylindrically and radially in the barrel and endcap regions, respectively. They are constructed with $4\text{-}\mathrm{mm}$ diameter wires surrounded by $19\,\mu\mathrm{m}$ thick polypropylene fibers (in the barrel) and foils (in the endcaps), serving as transition radiators. The TRT spans the radial region from 563 up to $1066\,\mathrm{mm}$ and exhibits substantial particle identification capabilities, particularly for distinguishing between electrons and hadrons (especially pions). It also enhances momentum resolution for $|\eta| < 2.0$ and $p_T > 0.5\,\mathrm{GeV}$. In high pile-up events, approximately 35 hits are recorded in the TRT for a *prompt lepton*[9], with straw efficiencies exceeding $96\,\%$ [325].

4.2.3 Calorimeter System

Calorimeters are employed for the experimental determination of energy of highly energetic particles. These particles deposit energy in the detector through a series of inelastic interactions, ultimately being absorbed after reaching a critical absorption energy in the material. Particle showers are categorized as either *electromagnetic* (comprising purely $e^{\pm}$ and γ) or *hadronic* (involving hadronic activity). While the momentum resolution of trackers degrades proportionally with p_T (Eq. (4.8)), calorimetry improves energy resolu-

[8] Arranging the strip layers at small crossing angles, so-called *stereo angles*, is beneficial in multiple ways. First, the detector can be oriented in such a way that the worsened spatial resolution in the direction of the magnetic field is minimized. Secondly, smaller stereo angles reduce the density of wrong hit assignments, which simplify the patter recognition. The readout chips for the entire strip module can also be placed in one side of the detector.

[9] A prompt lepton denotes any lepton produced in the hard scattering process.

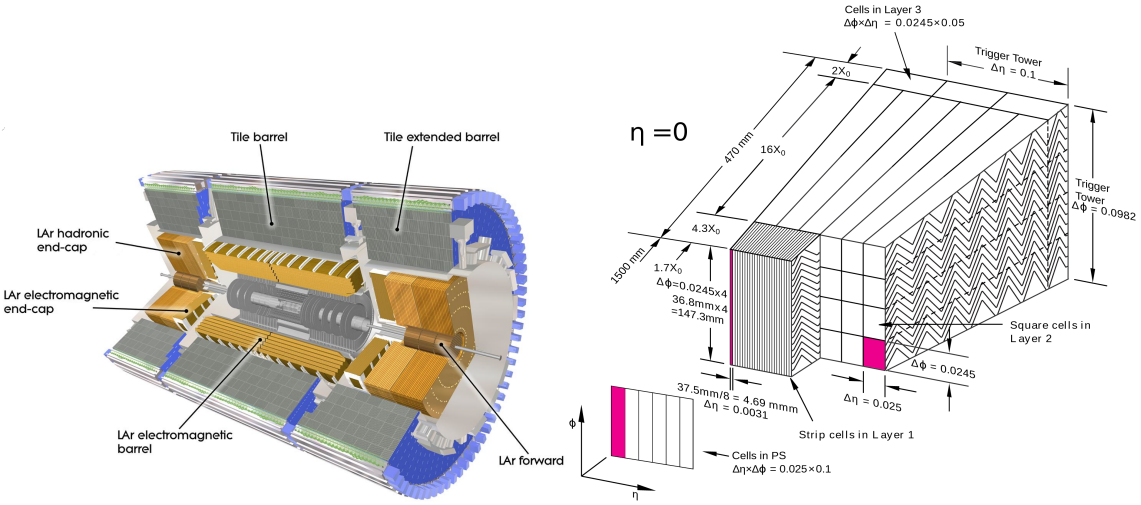

(a) Overview of the ATLAS calorimetry system. (b) Barrel module of the EMCAL.

Figure 4.5: (a) The overall calorimetry system of the ATLAS detector, and (b) an sketch of a barrel module of the electromagnetic calorimeter (EMCAL) showing the different cell granularity arranged along the three calorimeter layers and trigger towers across the η and ϕ detector coordinates. Adapted from [305].

tion at higher energies ($2 - 15\%/\sqrt{E/\text{GeV}}$ for electromagnetic and $35 - 120\%/\sqrt{E/\text{GeV}}$ for hadronic calorimeters). Calorimetry is therefore crucial for achieving accurate energy resolution at high particle energies, being also sensitive to neutral particles interacting electromagnetically or via the strong force. The shape of electromagnetic showers is the result of characteristic constributions from both bremsstrahlung and pair production processes, terminated when the energy loss through bremsstrahlung equals ionization at a critical energy E_c. Hadronic showers result from highly energetic hadrons interacting with nucleons in a dense medium, with the main identifier being the *nuclear absorption length*, dependent on the inelastic cross section and material density. Hadronic calorimeters, typically denser and larger, are designed with a greater nuclear absorption length compared to electromagnetic showers.

The most significant quality factor of a calorimeter is its energy resolution. It is typically influenced by the stochastic fluctuations in the number of charged particles that contribute to the signal. The resolution can be calculated as[10]

$$\frac{\sigma_E}{E} = \frac{a}{\sqrt{E}} \oplus \frac{b}{E} \oplus c, \tag{4.9}$$

where a parameterizes the stochastic fluctuations of the shower development, b accounts for the electronic noise, and c includes effects from mechanical and electronic imperfections. The resolution is therefore enhanced with higher energies, until the constant term given by c is reached. To determine the shape of the shower, a calorimeter must have good energy and position resolution, being also complete and hermetic to capture the full shower. In *sampling calorimeters*, passive and active media are alternated in layers to further develop and record the shower decays, respectively [316].

After passing through the inner detector and the solenoid, particles produced in hh collisions at the LHC reach the calorimetry system of the ATLAS detector [305], designed

[10] Assuming that the square root of the number of charged particles that contribute to the signal is proportional to the primary energy and whose standard deviation follows Poisson statistics.

to efficiently perform at measuring energy and position of different kinds of particles. The calorimetry system of the ATLAS detector is depicted in Figure 4.5a. The *electromagnetic calorimeter* (EMCAL) is divided in two main components: the *presampler* and a high granularity liquid-argon (LAr) detector further divided in *front*, *middle*, and *back* layers with granularities of 0.0031×0.1, 0.025×0.0245, and 0.05×0.025 in the $\eta \times \phi$ coordinates, respectively. These are sketched in Fig. 4.5b. The finest granularity, offered by the front layer up to $|\eta| < 2.5$, allows for particle discrimination against charged-pion decays and multiple photon showers such as the ones produced in π^0 decays. Further, it offers a precise estimation of the pseudorapidity of the impact point. In combination with the middle layer, an estimation of the photon pointing direction can be achieved. At high energies, most of the EM shower energy is deposited in the middle layer. The two outer-most layers are only available for $|\eta| > 2.4$. In the transition region from the barrel to the endcap calorimeter at $1.37 < |\eta| < 1.52$, energy measurements are considerably affected due to the large amount of upstream material in the inner detector. This region is referred as *crack region* and it is normally excluded in physics analyses. The endcap EM calorimeters are divided into two wheels, the outer and the inner wheel covering the ranges $1.375 < |\eta| < 2.5$ and $2.5 < |\eta| < 3.2$, respectively. Outside the acceptance of the inner detector the granularity is reduced up to 0.1×0.1 in the $\eta \times \phi$ space. The energy resolution of the EMCAL is $10\,\%/\sqrt{\mathrm{GeV}} \oplus 0.17\,\%$.

Hadronic activity is absorbed in the *scintillator-tile hadronic calorimeter* (HCAL) surrounding the EMCAL. The HCAL is divided in three longitudinal segments with a coarser segmentation than the EMCAL (0.1×0.1 for the barrel region in $\eta \times \phi$ and coarser at higher η). A scintillator-tile calorimeter carries out the hadronic calorimetry in the ATLAS detector, separated into a large barrel tile up to $|\eta| < 1.7$ and two smaller extended barrel cylinders, sitting on both sides A and C of the central barrel. The endcaps, in the range $1.5 < |\eta| < 3.2$ are based on liquid argon. The spatial segmentation in the HCAL is much lower than for the EMCAL (0.1×0.1 for barrel region in the $\eta \times \phi$ space) and it gets coarser for increasing $|\eta|$. An energy resolution of $50\%/\sqrt{\mathrm{GeV}} \oplus 3\%$ is available for the HCAL in the barrel and endcap layers, worse than the resolution of the EMCAL.

4.2.4 Magnets

The ATLAS magnet system is a crucial element in particle detection. By bending the trajectory of charged particles, it enables the determination of their momenta. This is achieved through the use of four large superconducting magnets that cover a diameter of $22\,\mathrm{m}$ and a length of $26\,\mathrm{m}$.

Positioned in front of the calorimeter system, the central solenoid generates a $2\,\mathrm{T}$ central field within the inner detector. The large size of the ATLAS experiment is primarily caused by an air-core *toroid magnet system*, which generates a magnetic field to curve muon tracks in the $r - z$ plane (in contrast to the $r - \phi$ plane in the inner detector) for enhanced momentum resolution. Comprising a barrel toroid with a $0.5\,\mathrm{T}$ central field and two flanking endcap toroids aligned with the central solenoid, all three toroids feature eight coils arranged symmetrically and radially around the beam axis. The endcap toroids, resembling a racetrack shape and housed in aluminum alloy, create a $1.0\,\mathrm{T}$ central field. Figure 4.7 illustrates a schematic of the magnet system.

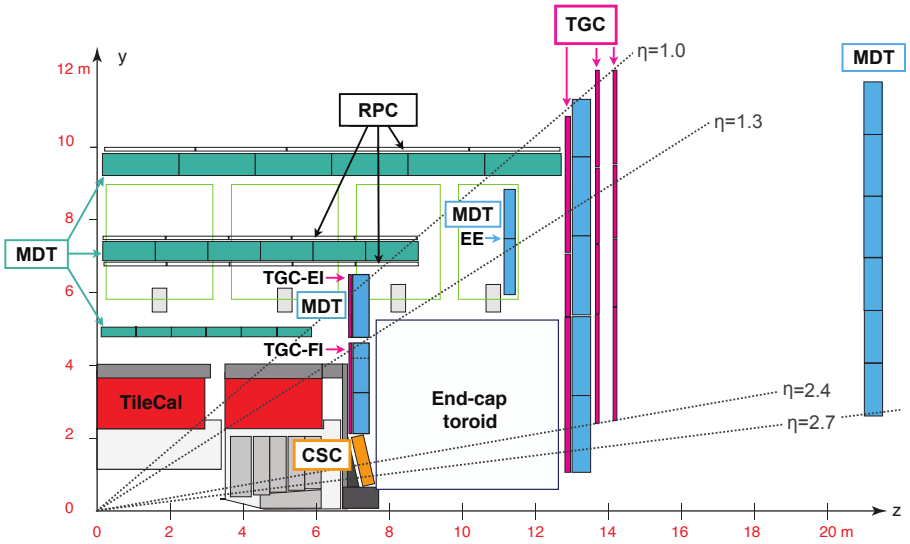

Figure 4.6: Arrangement of different technologies of the Muon Spectrometer of the ATLAS detector across the $y-z$ plane during Run 2 of the LHC. Green and blue sectors illustrate the position of the MDTs installed in barrel and endcaps, respectively. In the barrel, the middle (outer) station is covered by two (one) layers of RPCs (white boxes with black edges). Similarly, one layer of TGCs for the small wheel and three in the middle wheel (pink) are installed in the endcaps. Source [326].

The bending power is assessed through the field integral $\int Bdl$, calculated along a straight trajectory from the innermost to the outermost planes of the muon chamber. Here, B represents the field component perpendicular to the muon trajectory. Within $0 < |\eta| < 1.4$, the barrel toroid yields a bending power in the range of 1.5 to $5.5\,\mathrm{Tm}$, while the endcap toroids offer approximately 1 to $7.5\,\mathrm{Tm}$ for $1.6 < |\eta| < 2.7$. The bending power is reduced in the overlap region of the two magnets ($1.4 < |\eta| < 1.6$).

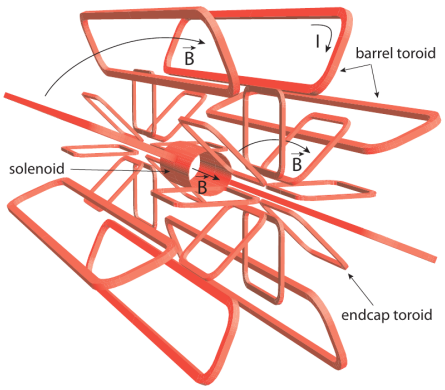

Figure 4.7: The eight barrel and endcap toroid coils of the ATLAS detector are shown in red. The solenoid winding is placed inside the calorimeter volume, depicted as a red cylinder. The pointing direction of the generated magnetic field ($\vec{B}$) and electric current (I) are depicted as black arrows. The forward shielding disk is omitted for clarity. Taken from [316].

4.2.5 Muon Spectrometer

At the most outer part of the ATLAS detector, tracking gaseous detectors compose the Muon Spectrometer (MS) with about 5500 individual chambers. The MS is designed to trigger events with charged particles exiting the barrel and endcap calorimeters with $|\eta| < 2.4$, where particle momenta can be measured in the pseudorapidity range of $|\eta| < 2.7$. These charged particles are mostly muons, highly-penetrating particles that can traverse the full inner detector and calorimetry systems.

The location of the different detector technologies across the $r-z$ plane of the ATLAS detector is illustrated in Figure 4.6. In the barrel region, precision tracking chambers are located both between and on the superconducting barrel toroid magnets, arranged in three concentric layers (*inner*, *middle*, and *outer*) around the beam axis at radii of approx-

Function	Detector	Chamber resolution (RMS)			Measurements per track	
		z/r [mm]	ϕ [mm]	Time resolution [ns]	Barrel	Endcaps
Tracking	MDT	0.035 (z)	—	—	20	20
	CSC	0.04 (r)	5	7	—	4
Trigger	RPC	10 (z)	10	1.5	6	—
	TGC	2–6 (r)	3–7	4	—	9

Table 4.3: Values for space and time resolutions, and number of measurements per track of the four subsystems of the MS. The values for the spatial resolution do not include alignment uncertainties. Values of time resolution do not include delays due to read-out electronics.

imately 5, 7.5, and $10\,\mathrm{m}$. In the two endcap regions, muon chambers form large *wheels* perpendicular to the z axis and located at $|z|$ distances of approximately 7.4, 10.8, 14, and $21.5\,\mathrm{m}$ from the interaction point. In the center of the detector, a coverage gap is open for services to the solenoid magnet, calorimeters, and inner detector. Considering a straight track, this gap is about $|\eta| \leq 0.08\,(0.04)$ in the outer and middle (inner) layers. Additional gaps in the acceptance occur in sectors installed on the supporting structure of ATLAS.

According to the performance goals of the ATLAS physics program, the p_T resolution is required to be about $10\,\%$ for $1\,\mathrm{TeV}$ tracks (Table 4.2), which translates into a sagitta along the z axis of about $500\,\mu\mathrm{m}$ to be measured with a resolution of $50\,\mu\mathrm{m}$ or better. With the MS alone, a muon p_T of up to a few GeV can be measured. Although track reconstruction combines inner detector with MS standalone measurements (see Section 4.3.1), the MS standalone track p_T reconstruction still provides sufficient momentum resolution and excellent charge identification.

The spatial and temporal resolution of the four different detector technologies of the MS are summarized in Table 4.3. The momentum measurement is performed with high precision by the *Monitored Drift Tube* (MDT) chambers. These cover the acceptance range of $|\eta| < 2.7$, and only up to $|\eta| < 2.0$ in the inner-most endcap layer. These chambers consist of three to eight layers of drift tubes, operated at an absolute pressure of $3\,\mathrm{bar}$, which achieve an average resolution of $80\,\mu\mathrm{m}$ per tube, or about $35\,\mu\mathrm{m}$ per chamber. To cope with the higher muon rates, *Cathode-Strip Chambers* (CSC) are installed in the forward region ($2.0 < |\eta| < 2.7$). These multiwire proportional chambers with cathode planes segmented into strips in orthogonal directions allow both coordinates to be measured from the induced-charge distribution. The resolution of one of these chambers is $40\,\mu\mathrm{m}$ and $5\,\mathrm{mm}$ in the bending and transverse planes, respectively. To achieve the sagitta resolution quoted above, the locations of MDT wires and CSC strips along a muon trajectory must be known up to less than $30\,\mu\mathrm{m}$. To this end, a high-precision optical *alignment system* monitors the positions and internal deformations of the MDT chambers. The presence of charged particles produced in hadron collisions after the calorimetry systems is a crucial signature for interesting physics. Therefore, it is essential to introduce efficient triggering capabilities in the MS. The tracking chambers are complemented by fast-triggering technologies of charged particles, which are capable of constructing track information and position (in both η and ϕ coordinates) within $10 - 25\,\mathrm{ns}$ after the particle has passed. In the barrel region ($|\eta| < 1.05$), *Resistive Plate Chambers* (RPC) are used for this purpose, while *Thin Gap Chambers* (TGC) have been chosen for the endcap region ($1.05 < |\eta| < 2.4$). The design goal targets identification of bunch-crossing with $\geq 99\,\%$ probability. The timing resolution of these detectors allows a successful tagging of bunch-

crossings, which takes place every 25 ns. After determining the coordinates of the track hits for both tracking and triggering detectors, hits from both systems are matched for a standalone MS track measurement. More details on muon reconstruction are given in Section 4.3.3.

4.2.6 Forward Detectors for Luminosity Measurement

Due to the high peak luminosities in LHC collisions, the fraction of non-interacting crossing bunches is minimal. Elevated radiation levels in the very forward region of the ATLAS detector forbid the use of traditional scintillation counters for luminosity monitoring. Dedicated detector technologies are essential for direct measurements of pile-up vertices. ATLAS employs two detectors for luminosity monitoring in the very forward region: LUCID [327] (LUminosity measurement using Cherenkov Integrating Detector) located at $\pm 17\,\mathrm{m}$ from the interaction point and primarily dedicated to online luminosity monitoring, and ALFA [328] (Absolute Luminosity For ATLAS), consisting of scintillating-fiber trackers inside Roman pots at $\pm 240\,\mathrm{m}$ from the interaction point. LUCID-2, commissioned in 2016 [329], detects inelastic pp scattering to measure integrated luminosity and provides online monitoring of instantaneous luminosity and beam conditions. The assumption is that the number of interactions in a bunch crossing is proportional to the number of detected particles, even when most of them originate from secondary interactions. Further details on the design and installation of these detectors can be found in Ref. [305]. A historical review of the experimental methods used for luminosity calibration and measurement in hh colliders is available in Ref. [330].

4.2.7 Trigger and Data Acquisition Systems

In the ATLAS experiment, data are collected from collisions of hadrons accelerated by the LHC. The detector is a complex machine with approximately 100 million read-out channels. The detector produces about $1.6\,\mathrm{MB}$ of data per event every $25\,\mathrm{ns}$ of bunch spacing. This results in a rapid memory filling of $64\,\mathrm{TB/min}$, posing challenges for resource and disk usage. To address these issues, ATLAS employs a sophisticated trigger system [331]. A schematic overview of the TDAQ system is shown in Figure 4.8. The *Level-1 trigger system* (L1) [332] processes collisions at $40\,\mathrm{MHz}$ using fast decisions with *Field Programmable Gate Array* (FPGA) components and based on less detailed detector information. The L1 trigger comprises the *Level-1 Calorimeter* (L1Calo) [333] and *Level-1 Muon* (L1Muon) [326] triggers, which identify *Regions of Interest* (RoIs) and generate *trigger objects* (TOBs) based on calorimeter and muon chamber data. Trigger decisions depend on the number of TOBs surpassing an energy threshold. The L1Calo system also computes missing transverse energy or total energy in the event, with a latency of about $2.1\,\mu\mathrm{s}$. The L1Muon estimates muon transverse momenta with a latency of approximately $2\,\mu\mathrm{s}$. The *Muon-to-CTP-Interface* (MUCTPI) [334] connects the results from the L1Muon to the *Level-1 Topological* (L1Topo) trigger, which processes these objects and makes decisions based on more complex topological criteria. The Central Trigger Processor (CTP) [335] collects information from these components and issues an *L1-Accept* (L1A) signal, reducing the event rate from $40\,\mathrm{MHz}$ to $100\,\mathrm{kHz}$ and directing accepted events to the *High-Level*

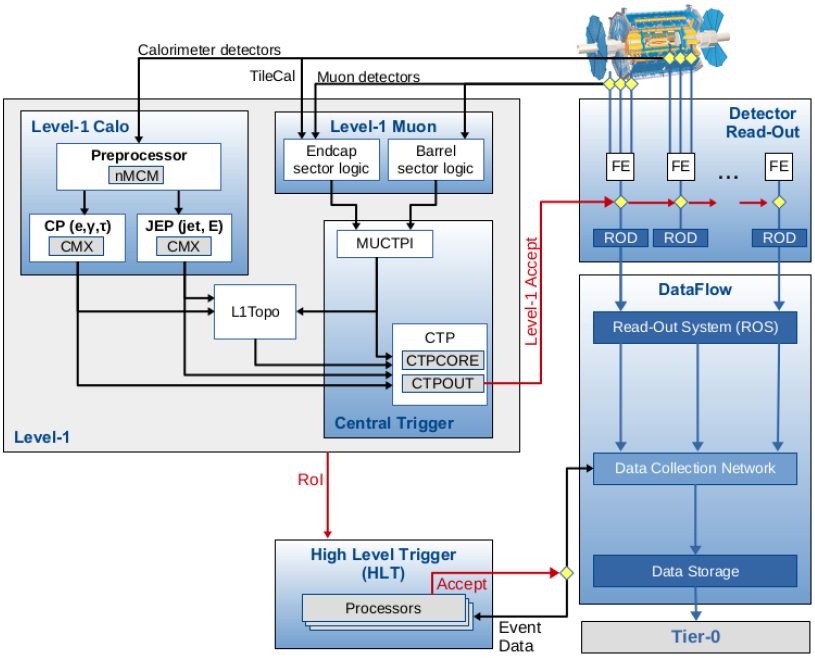

Figure 4.8: Schematic of the ATLAS trigger and data acquisition system in Run 2. Adapted from [331].

Trigger (HLT) [336]. The HLT, a software-based system using ATHENA[11], performs the final event selection before storage and runs on a computing farm at LHC Point-1 with approximately 40 000 processing units. It reduces the event rate from 100 kHz at the L1 trigger to an average of 1 kHz[12], storing data at an average rate of 1.2 GB/s for subsequent analysis. The entire process involves the coordination of *Front-End* (FE) electronics, *Timing, Trigger, and Control* (TTC) network, buffers, *Read-Out Drivers* (ROD), and *Read-Out System* (ROS). Once the HLT requests detector information from the ROS for final trigger decision processing, it sends a signal to the *Sub-Farm Output* (SFO) to transmit the data to CERN's Tier-0 facilities for offline processing and permanent storage if the event is accepted. The trigger system applies predefined selection criteria in *trigger chains*[13], configuring each with a *prescale* value of $n \geq 1$, which means that one for each n events is accepted. This is done in order to control the trigger rate and define the accessible phase space for offline analysis. Prescales enable the recording of events with high trigger rates without introducing a bias in relevant kinematic distributions. The *trigger menu* consists of all the trigger chains in a run of data taking and is of vital importance as it defines the regions of the phase space available for offline analysis. Thorough validation and constant monitoring ensure its exceptional performance, and during LHC data-taking periods, diverse selections [337, 338, 339] are implemented to broadly accept compelling physics scenarios, optimized by physics groups via the study of MC simulation for targeted physics processes.

Requiring events to pass the lowest unprescaled single-lepton triggers in Table 4.4 is

[11] ATHENA is the ATLAS offline software infrastructure.

[12] A maximum rate of 1.2 kHz could be handled during data taking in 2018.

[13] Trigger chains can be associated with object types, such as single leptons or missing transverse momentum triggers, or even more complex combinations that involve more than one object type. For instance, simultaneous selections on two leptons (*dilepton*), or *b*-jet multiplicity and missing transverse energy.

Lepton	Year	Trigger label	E_T/p_T cut [GeV]	Identification WP	Isolation WP
Electron	2015	HLT_e24_lhmedium_L1EM20VH	24	LHMedium	—
		HLT_e60_lhmedium	60	LHMedium	—
		HLT_e120_lhloose	120	LHLoose	—
	2016–2018	HLT_e26_lhtight_nod0_ivarloose	26	LHTight	ivarloose
		HLT_e60_lhmedium_nod0	60	LHMedium	—
		HLT_e140_lhloose_nod0	140	LHLoose	—
Muon	2015	HLT_mu20_iloose_L1MU15	20	—	iloose
	2016–2018	HLT_mu26_ivarmedium	26	—	ivarmedium
	2015–2018	HLT_mu50	50	—	—

Table 4.4: Triggers included in the combined single-electron (single-muon) trigger definition, commonly used in ATLAS physics analyses, with their corresponding E_T (p_T) thresholds, identification and isolation working point (WP). If the reconstructed objects in an event fulfill *at least one* of the tabulated triggers, the event is recorded and considered for physics analysis. This trigger configuration is also used for the physics analysis presented in Chapter 9. Definitions of identification and isolation criteria are given in Sections 4.3.2 and 4.3.3 for electron and muon WPs, respectively. The label nod0 indicates that no requirements on the d_0/σ_{d_0} of the electron are considered.

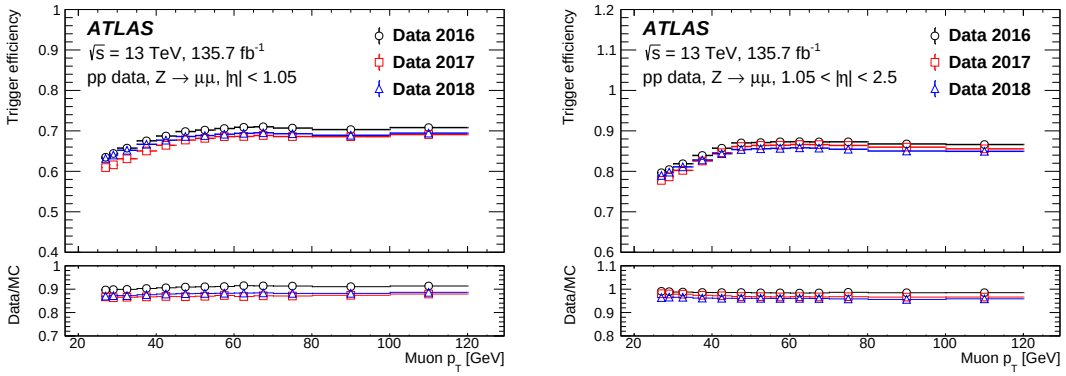

(a) $|\eta| < 1.05$ (b) $1.05 < |\eta| < 2.5$

Figure 4.9: Efficiency of passing either the HLT_mu26_ivarmedium or the HLT_mu50 trigger in (a) the barrel and (b) endcaps as a function of the muon p_T, computed using data taken in 2016–2018. The data-to-MC ratios are shown on the bottom plots. The error bars show the statistical uncertainties only. Source [326].

a common strategy in physics analyses, offering a fairly inclusive strategy at the cost of approximately 20 % of the total L1 and HLT trigger rate. The trigger rate is reduced by two orders of magnitude when compared to L1 only. The demand for a low threshold and HLT rate imposes stringent constraints on the lepton identification criteria employed by these HLT. The efficiencies of primary single-lepton trigger chains are determined using the *tag-and-probe method*, detailed in Section 8.4.5, requiring prompt leptons in a phase space dominated by on-shell $Z \to \ell\ell$ production. Figure 4.9 illustrates the efficiency of the combined single-muon triggers from Table 4.4 between 2016 and 2018 in the barrel and endcap regions as a function of the probe muon p_T. Inefficiency in the turn-on region arises from the absence of isolation criteria for the offline selected muon. A similar efficiency rise at $p_T \sim 50$ GeV is due to the lack of an isolation criterion in the HLT_mu50 trigger. Discrepancies between simulation and data efficiencies, particularly in the barrel, are addressed by employing data-to-MC ratios as *scale factors* (SF) to adjust the simulation. A small p_T dependence of the SFs is observed, with the difference in the ratio attributed to a constant L1 efficiency (about 90 %) used in simulation [326].

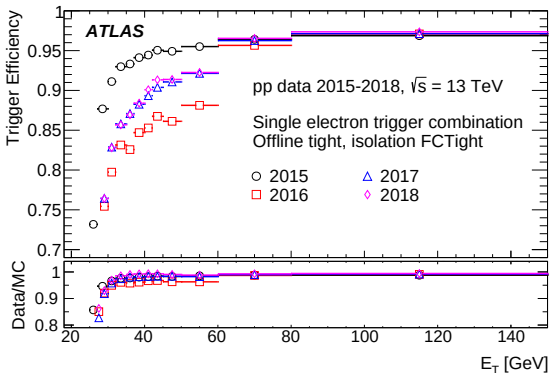

(a) Trigger efficiency as a function of E_T.

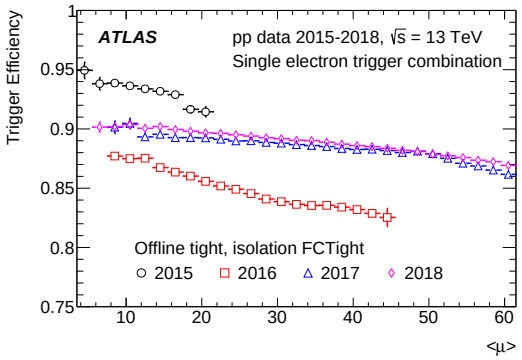

(b) Trigger efficiency as a function of the pile-up $\langle\mu\rangle$.

Figure 4.10: Evolution of the combined single-electron trigger efficiency as a function of the (a) offline electron E_T and (b) pile-up $\langle\mu\rangle$ during Run 2. The efficiencies are given with respect to the tight version of the offline lepton identification criteria and the `FCTight` isolation working point, described in Section 4.3.2. The data-to-MC efficiency ratio is also shown. The error bars indicate statistical and systematic uncertainties combined in quadrature. Source [340].

	LHC Runs					
	Run 1 [341]		Run 2 [342]			Run 3 [123]
	2010-2011	2012	2015–2016	2017	2018	2022-2025
$\sqrt{s}$ [TeV]	7.0	8.0	13.0			13.6
ATLAS $\mathcal{L}$ good for physics [fb^{-1}]	4.6 ± 0.1	20.3 ± 0.4	36.6 ± 1.4	44.6 ± 1.1	58.8 ± 0.6	250*
Integrated $\mathcal{L}$ per Run [fb^{-1}]	24.9 ± 0.5		140.1 ± 1.2			

* Run 3 is ongoing while this document is being written. The given value shows the target integrated luminosity.

Table 4.5: Center-of-mass energy and recorded integrated luminosities by the ATLAS detector along different LHC Runs after passing good-for-physics quality requirements.

Three single-electron triggers are used simultaneously in a typical analysis selection, constituting the *combined single-electron triggers*. Figure 4.10 presents the trigger efficiencies for this combination, listed in Table 4.4 across different years in Run 2. At low E_T, triggers with identification and isolation requirements are used to manage the data bandwidth, while higher values of E_T allow the introduction of additional triggers with looser identification and no isolation requirements. The efficiency turn-on as a function of E_T in 2015, as shown in Figure 4.10a, is influenced by a looser identification requirement (`LHMedium` versus `LHTight` from 2016), a lower E_T threshold (24 GeV versus 26 GeV from 2016), and no isolation requirement. The evolution of the combined single-electron trigger efficiency from 2015 to 2018 as a function of the average number of collisions per bunch crossing

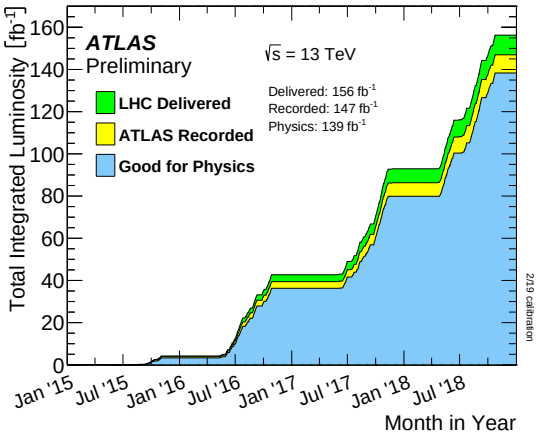

Figure 4.11: Cumulative values of the integrated luminosity as delivered by the LHC, recorded by ATLAS, and deemed of good-quality for physics analyses as a function of time during stable beams in pp collisions of the LHC Run 2. The luminosity ready for physics differs with respect to the newest luminosity measurement given in Table 4.5. Source [304].

is also depicted in Figure 4.10b. Despite similar identification, isolation, and E_T requirements in 2016–2018, inefficiencies at $E_T < 60\,\text{GeV}$ in 2016 is attributed to the different electron trigger configuration used in that year. Inefficiencies of the single electron triggers in the pseudorapidity regions $1.37 < |\eta| < 1.52$ and $|\eta| > 2.37$ is caused by a significant amount of material budget of the detector [340].

Due to non-ideal data acquisition systems of ATLAS, the luminosity recorded is lower (but close) to the luminosity delivered by the LHC. If at least one of the ATLAS subsystems experiences problems, data recorded in that collision is not considered of *good-quality* for physics analyses. In total, $95.6\,\%$ of the data recorded by the ATLAS detector during Run 2 passed the good-quality criteria [343]. The cumulative distribution of the integrated luminosity delivered by the LHC along years of Run 2 is given in Figure 4.11. The values of integrated luminosity as collected by the ATLAS experiment in different LHC runs of pp collisions used in physics analyses are classified in Table 4.5.

4.2.8 Detector Simulation

To obtain accurate information on the position and energy of the particles reconstructed by the ATLAS detector, it is essential to consider the impact of its material budget and response. This requires a meticulous simulation of the energy deposition of particles in different detector components, as well as their responses to matter interactions, detector signals, and processing. To enable direct comparisons between data and simulated events, physics events from MC generators are utilized to feed the detailed detector simulation. The GEANT4 simulation toolkit [344] is employed to model the geometry of the ATLAS detector and the response of each of the components of its systems. Details about the simulation software for particle collisions, detector response, and triggers used in the ATLAS simulation infrastructure can be found in Ref. [345].

4.3 Object Reconstruction and Particle Identification

The signals provided by the readout electronics of the different subsystems of the ATLAS detector, presented in Section 4.2, are used to build physical objects relevant for physics analyses such as lepton or jet candidates. This involves complex algorithms and selection criteria to reliably identify and reconstruct particles, interaction vertices, and tracks, minimizing interference from background processes. This section outlines the methodology employed in the ATLAS experiment during Run 2. Section 4.3.1 discusses how the interaction vertices and associated particle tracks are inferred. Essential to the data analysis presented in this dissertation are electrons, muons, and jets, whose reconstruction techniques are outlined in Sections 4.3.2, 4.3.3, and 4.3.4, respectively. Given the short lifetime of tauons, they are reconstructed through their decay products into electrons, muons, or hadrons. Accurately determining the flavor of reconstructed jets is vital for event selection, and the associated algorithms employed in Run 2 are detailed in Section 4.3.5. The reconstructed objects are then utilized to calculate the missing transverse energy as outlined in Section 4.3.6. Managing overlaps between the object reconstruction of different objects is crucial, and the approach taken in this dissertation is introduced in Section 4.3.7.

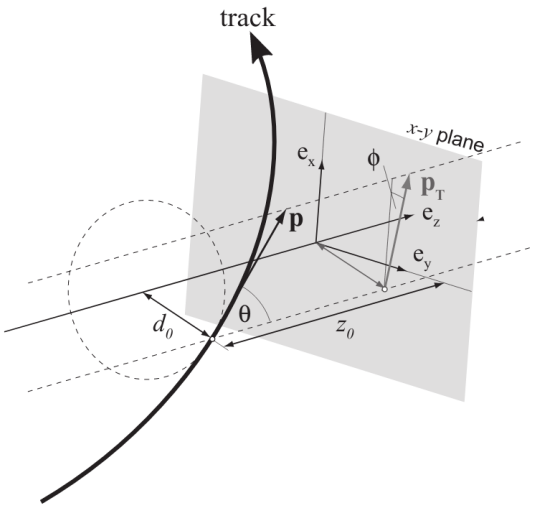

Parameter	Description
q/p	Ratio of the reconstructed charge from the curvature of the track over the magnitude of the momentum vector
ϕ_0	Azimuthal angle of the momentum vector of the track in the transverse plane
θ	Polar angle of the momentum vector of the track in the longitudinal plane
d_0	*Transverse impact parameter*: point of closest approach of the track to the reference axis in the transverse plane
z_0	*Longitudinal impact parameter*: analogous to d_0 in the longitudinal axis

Figure 4.12: Sketch on the global track parameters defining the helix topology of a particle track. The parameters d_0 and ϕ_0 are defined in the $x-y$ plane, while z_0 and $\cot\theta$ are defined in the $x-z$ plane. The magnetic field B points to the positive direction of the z-axis. Source: [346].

4.3.1 Track and Vertex Reconstruction

The tracks of charged particles can be reconstructed along the full ϕ range and $|\eta| < 2.5$ using the hits recorded within the inner detector. The MS also comes into play for the case of muons. These tracks are fitted to return a helix trajectory defined by a set of five parameters, denoted by d_0, z_0, ϕ_0, $\cot\theta$, and q/p. These parameters, along a sketch on their definitions are shown in Figure 4.12. The transverse and longitudinal *impact parameters*, d_0 and z_0, are defined as the distance of closest approach to the interaction vertex and its z coordinate, respectively. The parameter ϕ_0 (defined within the range $[-\pi, \pi]$) is the azimuth at the point of closest approach, and $\cot\theta$ (where θ takes values within $[0, 2\pi]$) gives the inverse slope of the track in the $r-z$ plane. The *inverse transverse momentum* q/p_T, with q being the charge assigned to the reconstructed track, can be deduced from the measured radius of curvature. The corresponding uncertainties of these parameters are denoted by σ_{param} (e.g. σ_{d_0} and σ_{z_0} for transverse and longitudinal impact parameters, respectively). The ratios of the impact parameters over their uncertainties are referred to as *significances* (i.e., d_0/σ_{d_0} or z_0/σ_{z_0}, for transverse and longitudinal impact parameters, respectively) and they are commonly used in physics analyses. Once the values of these parameters are known, the analytical path of the track trajectory is unambiguously defined.

A particle track can be reconstructed in ATLAS following different approaches [347]. For this dissertation, the most relevant one is the *inside-out* algorithm which starts by being seeded with three hits from silicon detectors in the inner detector. Additional hits

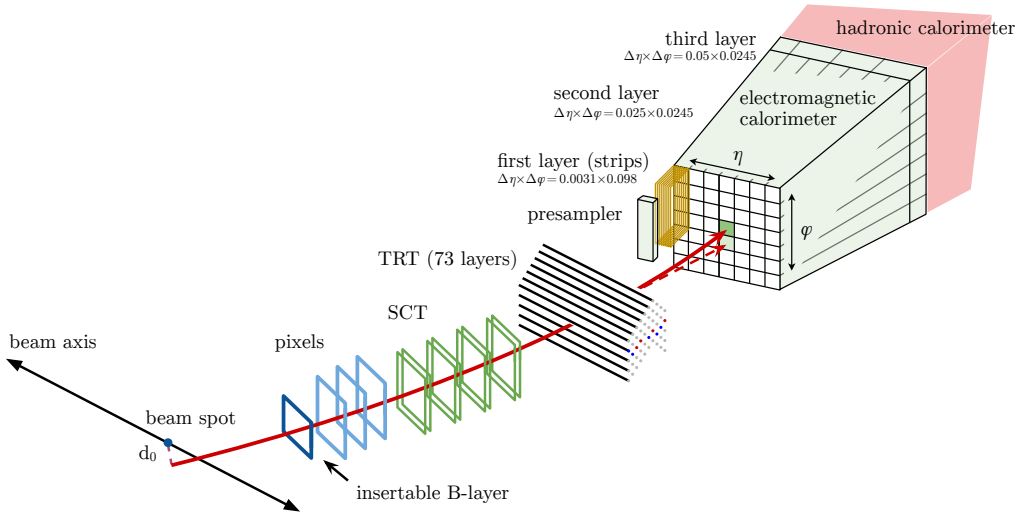

Figure 4.13: Illustration of the electron reconstruction and identification through its path along the different layers within the ATLAS inner detector. The hypothetical path of an electron (red) traverses the tracking system (pixel detectors, SCT, and lastly the TRT) and then enters the electromagnetic calorimeter. The interaction of this electron with the detector material along its path through the tracking system can produce photons by means of bremsstrahlung. The dashed red arrow shows the path for one of these photons. Both particles would be finally absorbed by the electromagnetic calorimeter, with their energy being measured in different towers of the EMCAL that compose the cluster. Source: [353].

are continuously added to the track by elongation from the interaction point. This elongation is tackled with specific techniques such as global χ^2 fits, *Kalman filters* [348], and *non-Gaussian noise* [349], along with *dynamic noise adjustments* from energy recovery due to bremsstrahlung processes. It takes advantage of the knowledge about the magnetic field configuration and material budget in the ID. With the inside-out algorithm, transverse momenta of $p_T > 0.4\,\text{GeV}$ are required for reconstructed tracks. Details on the different approaches for particle track reconstruction can be found in Ref. [347].

Primary vertex reconstruction is essential when inferring the full kinematic properties of the event. It is identified by matching reconstructed tracks pointing to an original common vertex. Details on the vertex reconstruction and pile-up determination can be found in Ref. [350]. Firstly, a vertex seed is considered as maximum of the distribution of the z coordinate of reconstructed tracks. Then a vertex is fitted using χ^2 minimization. Incompatible tracks by more than $7\,\sigma$ are discarded. A resolution of the longitudinal vertex position of about $30\,\mu\text{m}$ is achieved for events with high multiplicity of reconstructed tracks, while a resolution of the transverse position is better than $20\,\mu\text{m}$ [351, 352]. Estimated values of the tracking efficiency can be found in Ref. [352] as a function of η and the number of interactions per bunch crossing $\langle\mu\rangle$. The reconstruction algorithms have proven to perform well in very dense environments. The track reconstruction efficiency decreases with greater values of $|\eta|$, being close to $90\,\%$ for low μ and decreasing to about $70\,\%$ for denser pile-up environments.

4.3.2 Electrons and Photons

In the central region ($|\eta| < 2.5$), electron reconstruction in ATLAS involves three key components: clusters of energy deposits recorded in the EMCAL, reconstructed tracks

in the inner detector, and the matching between them. Photons undergo a similar process, with their presence in the inner detector inferred from conversion vertices[14]. Figure 4.13 illustrates the relevant components of the ATLAS detector for electron reconstruction. The process starts with energy deposits forming clusters in the EMCAL, using *dynamically-sized clustering algorithms* [354]. These clusters, known as *superclusters*, are then used in conjunction with tracks to reconstruct electrons. The selection involves identifying *topoclusters* and matching them to inner detector tracks, considering specific criteria in η and ϕ. The momentum of these tracks is adjusted for bremsstrahlung losses. Conversion vertices are constructed and matched to corresponding topoclusters. Supercluster building is performed separately, and after corrections for initial positions and energy calibrations, electrons are matched with tracks and conversion vertices. The resulting electron and photon objects undergo an energy calibration, and discriminating variables are added for background separation. The algorithm, described in detail in Ref. [354], achieves about $35\,\%$ improvement in energy resolution compared to the older sliding-window approach [355]. Dilepton invariant mass measurements also see a $10\,\%$ improvement in resolution, maintained in high pile-up environments [356].

Electron reconstruction involves matching at least one track to the supercluster. Preference is given to tracks with hits in the pixel detector, followed by those with hits in the SCT. Tracks with a better ΔR match to the cluster in the second layer of the EMCAL are prioritized. Following these preferences, a best-matching track is chosen to retrieve the electron kinematics, combining information from the supercluster and the highest-ranked track. The four-momentum of the electron is determined using the energy of the cluster (E_T), with ϕ and η coordinates retrieved from the best-matching track at the vertex. The electric charge is derived from the curvature of the best-matched track. Charge misreconstruction may occur in approximately $0.3\,\%$ of the electrons due to track assignment errors or poor curvature measurement. Energy calibration follows a procedure closely based on Ref. [357], updated with a supercluster-based energy reconstruction algorithm. The new energy measurement via the clustering algorithm exhibits scale variations below $0.1\,\%$ with an average number of collisions per bunch crossing $\langle\mu\rangle$. Electron reconstruction efficiencies range from $96.5\,\%$ to $99.5\,\%$ ($p_T > 20\,\text{GeV}$) depending on pseudorapidity, with deviations of around $5\,\%$ for increasing inelastic interactions per bunch crossing [354]. Reconstruction algorithms do not discriminate against background processes such as hadronic jets that can mimic electron signatures. In order to remove these contributions *electron identification* working points are defined. The identification of prompt electrons relies on a likelihood discriminant constructed from various quantities related to the primary electron track, lateral and longitudinal development of the electromagnetic shower development, and spatial compatibility between the track and the cluster. Detailed descriptions of the variables involved are available in Ref. [353]. Three reference working points (*Loose*, *Medium*, and *Tight*) are defined for increasing background rejection efficiencies. For the *Tight* working point (referred to as `LHTight`), the electron identification efficiency during the 2015–2016 data-taking period ranges from $75\,\%$ to $90\,\%$ within the considered electron E_T regime. Tighter working points with lower efficiency values result in increased background rejection. Electrons misidentified from multijet production are rejected by a factor of 5 using the `LHTight` working point compared to `LHLoose`, in the E_T range of 4 to $50\,\text{GeV}$. The identification efficiency at

[14]Since photon candidates are not relevant for the physics analyses performed in this dissertation, the description focuses on the reconstruction, identification, and isolation of electrons.

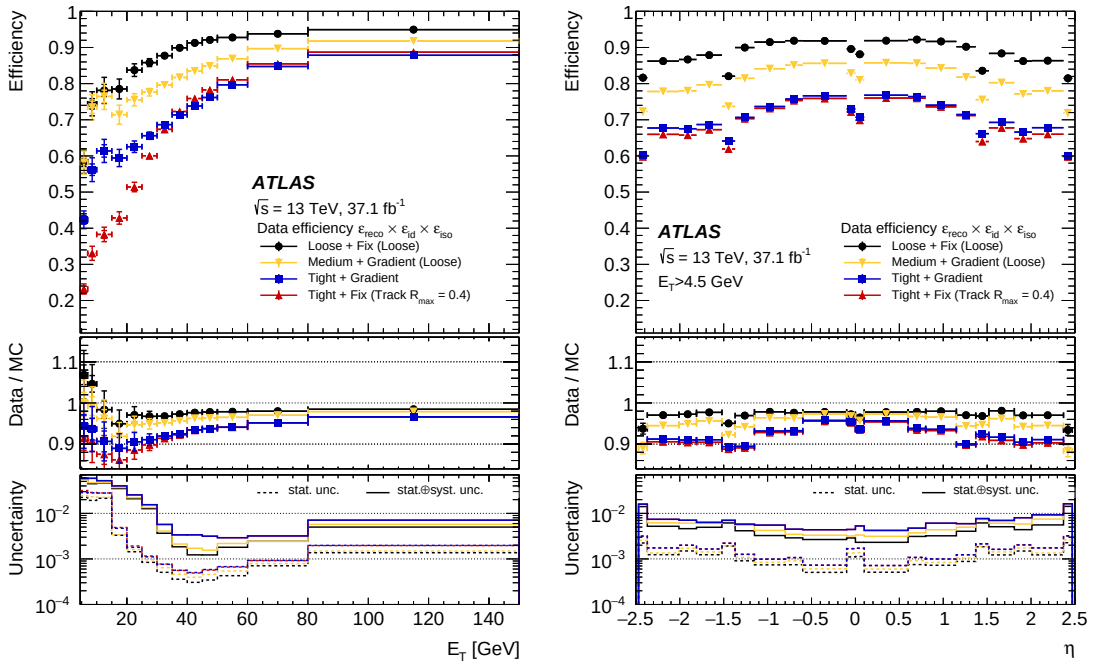

(a) Efficiency as a funcion of p_T.

(b) Efficiency as a funcion of η.

Figure 4.14: The product of electron reconstruction, identification, and isolation efficiencies $\varepsilon_{\text{reco}} \times \varepsilon_{\text{id}} \times \varepsilon_{\text{iso}}$, derived from $Z \to ee$ events, is shown as a function of (a) electron E_T and (b) electron η for $E_T > 4.5\,\text{GeV}$ for various identification and isolation working points. The inner uncertainties are statistical while the total uncertainties include both the statistical and systematic components. The lower panels show data-to-simulation ratios as well as the relative statistical and total uncertainties (statistical and systematic added in quadrature) applicable to both the data efficiencies and correction factors. Source [353].

around $E_T = 40\,\text{GeV}$ has a total uncertainty of $0.3\,\%$ for this working point [353]. Furthermore, *isolation criteria* are needed when balancing between a highly-efficient identification of prompt electrons and good background rejection from heavy-flavour decays or light hadrons misidentified as electrons. Different working points are also defined for electron isolation [354]. The `Gradient` isolation working point will be used throughout this thesis, designed to give an η-uniform isolation efficiency of $90\,\%$ at $p_T = 25\,\text{GeV}$ and $99\,\%$ $p_T = 60\,\text{GeV}$. The dependency on E_T and η for the product of reconstruction, identification, and isolation efficiencies $\varepsilon_{\text{reco}} \times \varepsilon_{\text{id}} \times \varepsilon_{\text{iso}}$ for data 2015–2016 is shown in Figure 4.14. Electrons in simulation are calibrated using the shown data-to-simulation ratios. As seen from the second ratio plot, systematic sources of error dominate, increasing the total uncertainty by roughly one order of magnitude across for $E_T > 20\,\text{GeV}$.

4.3.3 Muons

To identify muons, the first step consists of performing separate reconstructions in the inner detector and muon chambers, since hits of a muon candidate are expected in both of these detectors. The muon chambers are searched for track patterns using the read-out hits, and track segments are formed for each chamber in the MS. Muon candidate tracks are then constructed by fitting the track segments together, starting from the middle layers of the MS and searching for compatible segments in the inner and outer layers.

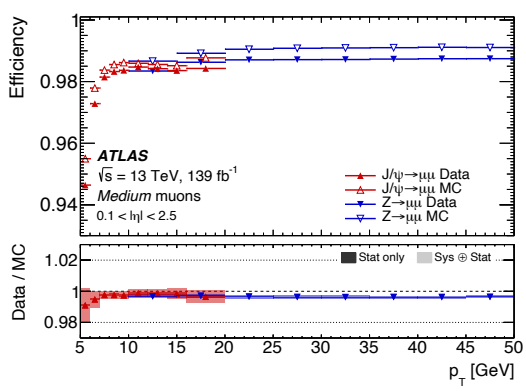

(a) Efficiency as a function of p_T.

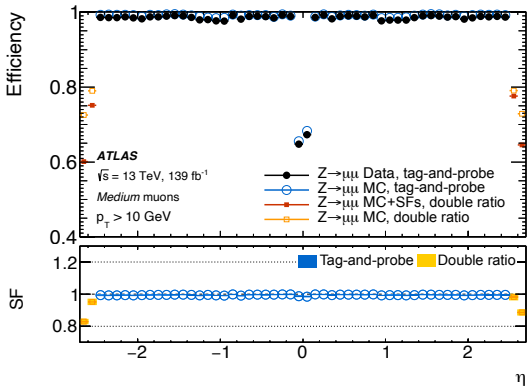

(b) Efficiency as a funcion of η.

Figure 4.15: Muon reconstruction and identification efficiencies for the `Medium` working point derived from $J/\psi \to \mu\mu$ and $Z \to \mu\mu$ events as a function of (a) the muon p_T and (b) the muon pseudorapidity η. The lower panels show data-to-simulation ratios, where statistical and total uncertainties (sum in quadrature of statistical and systematic components) are shown. Source [358].

In most of the detector geometry, two matching segments are required to build a muon track, except in the transition region between the barrel and the endcap, where a single high-quality segment suffices. Further quality criteria are then applied to reject fake muons[15], based on a χ^2 test after fitting all hits in a candidate track. Although different types of muon candidates are defined by the ATLAS muon reconstruction strategy, only *combined muons* are used in this thesis. To reconstruct a combined muon, tracks are formed by combining hits from both the tracker and muon chambers using a global fit. Usually, an outside-in pattern recognition approach is adopted, where tracks in the MS are identified first and extrapolated to the inner detector to look for matching tracks.

To select prompt over fake muons, quality requirements are imposed on candidate tracks. Hadronic decays in the inner detector typically result in muon tracks with a distinctive *kink*, leading to lower track fit quality when segments from the MS are combined with hits in the tracker. Simulated $t\bar{t}$ events are used to investigate various discriminants between prompt and fake muons. The final discrimination is based on the quality of the track fit, the number of holes in the candidate muon trajectory, and momentum compatibility between inner detector and MS measurements. Four identification working points, namely `Loose`, `Medium`, `Tight`, and `High-pT`, defined inclusively with tighter requirements with respect to the previous (looser) point, are constructed and provided centrally for physics analyses. The prompt muon efficiency, as estimated from MC, lies between $78.1\,\%$ for the tightest working point, `High-pT`, up to $96.7\,\%$ for `Loose`, at low muon p_T. At high muon p_T, the efficiencies range between $80.4\,\%$ to $98.1\,\%$. Reconstruction and identification efficiencies, as well as data-to-simulation calibration factors, can be found in Figure 4.15. The muon reconstruction efficiency is close to $99\,\%$ within $|\eta| < 2.5$ and $p_T > 25\,\text{GeV}$ for the `Medium` working point used in this thesis, which relies solely on measurements in $Z \to \mu\mu$ events. Muon reconstruction and isolation is severely deteriorated for $|\eta| < 0.1$, where the service gap is not covered by middle and outer layers

[15] In contrast to muons originated in the hard scattering, *fake muons* originate from secondary sources such as hadron decays.

of the MS (see Section 4.2.5). The identification efficiencies in the range $2.5 < |\eta| < 2.7$, evaluated using a different (so-called *double ratio*) method, are significantly lower due to different strategies of reconstruction. For instance, more stringent track selections are applied where the coverage of the inner detector is minimal. MC simulation hardly reproduces the data in this forward region, leading to large correction factors [358]. Muons within $2.5 < |\eta| < 2.7$ are therefore not considered in this dissertation. In general, prompt muons from hard scattering events can be clearly identified with respect to other objects in the event. However, muons arising from hadronic showers in jets tend to be aligned with the jet itself. To ensure that only prompt muons are selected, *isolation criteria* are applied to eliminate muons originating from hadron decays. ATLAS provides different isolation working points centrally, targeting different performance requirements for physics analyses. The working points are defined by applying a selection criterion based on the ratio of the p_T sum of tracks within a cone centered on the reconstructed muon to the measured p_T of the muon (denoted to as $p_{T,\,\mathrm{cone}}$). The isolation efficiency varies between 93 and 100 %. Isolation efficiencies of muons passing the `Tight` working point are greater than 85 % for $p_T > 20\,\mathrm{GeV}$ increasing up to 100 % at $p_T > 60\,\mathrm{GeV}$. These efficiencies are well modeled by simulation within uncertainties. Calibration factors are provided to physics analyses, being computed as a function of the muon p_T and the angular separation between the muon and the closest jet[16] [358].

The momentum resolution is measured to be 2.9 % in $Z \to \mu\mu$ decays [358], owing to the clean muon signals obtained from the MS. This allows for an excellent background rejection for muon identification and isolation.

4.3.4 Jets

In pp collisions, color-charged particles produced in the hard-scattering undergo hadronization before reaching the detector, resulting in complex collimated showers of energy depositions and tracks due to QCD confinement. Identifying individual particles is challenging as the original partons cannot be directly detected. However, these collimated hadron sprays retain some kinematic properties from the hard scattering, allowing further understanding of the physics process in the hadron collision. To simplify reconstruction, these cascades are grouped into single objects known as *jets*, ideally corresponding to the complete hadronic shower of a parton from the hard scattering or the radiation from either initial- or final-state particles. The most common approach to reconstruct jets in high-energy physics involves the k_T *algorithms* [359], conceptualizing a jet as a cone extending from the production vertex to the calorimetry system. These algorithms aggregate input objects into jets based on their relative distances, allowing a single jet to contain multiple objects. The k_T algorithms proceed iteratively, calculating first the distance

$$d_{ij} = \min(k_{T,i}^{2n}, k_{T,j}^{2n}) \frac{\Delta R_{ij}^2}{\Delta R^2}$$

between an input object i and all other objects j, using their transverse momenta k_T, angular separations (ΔR_{ij}), and a parameter ΔR related to the size of the final reconstructed jet. The choice of parameter n labels the algorithm used, corresponding to (i) the

[16] The definition of jets and the reconstruction techniques in ATLAS are covered in Section 4.3.4.

Cambridge-Aachen algorithm for $n = 0$, (ii) the k_T *algorithm* for $n = 1$, or (iii) the widely-used *anti-k_T algorithm* [359] employing $n = -1$.

The anti-k_T algorithm, used to build jets in this thesis, starts the reconstruction with the highest-energy inputs. The jet obtained in this way exhibits a cone-shaped structure that better approximates the expected geometry of hadronic showers in the detector. The jet radius ΔR is crucial for effectively capturing signals left by cascades and obtaining accurate energy measurements. For studying low-energy products of the hard-scattering event, *small-R jets* of radius $\Delta R = 0.4$ are typically used. The second step in the anti-k_T algorithm determines the distance of the object i to the jet-candidate axis as $d_{i,B} = k_{T,i}^{-2}$ so that any object j closer to i than the axis can be merged into the same object. Once no more objects are closer to the jet-candidate axis than i, a jet is defined and the particles clustered during its construction are removed from the set of inputs. The previous steps are repeated iteratively until all available inputs are clustered into jets.

The ATLAS tracking system combines the inner detector and calorimeters to achieve enhanced momentum resolution. Jets, concentrated in small areas, produce large signals in groups of *topoclusters*. Dedicated algorithms [360] identify clusters by starting with a seed of calorimeter cells with signals four times greater than electronic noise, adding adjacent cells with a signal-to-noise ratio of 2 or more. *Clusters* are completed by adding a ring of guard cells around the candidate, regardless of their measured signal. Constructing *Particle-Flow* (PFlow) jets involves a combination of topoclusters with compatible reconstructed tracks from charged particles in the hadronic cascade. The inner detector facilitates track measurement for low-energy particles, extending the acceptance to lower kinematic regimes. Once the jet objects are constructed, the *Jet Energy Scale* (JES) undergoes a series of adjustments made to the jet energy and position [361, 362]. The topocluster coordinates are recalculated with respect to the main primary vertex for improved η resolution. The topocluster energy is calibrated relying on the measurement in the EMCAL[17], and for PFlow jets, the track-measured momentum is replaced for energies above $100\,\mathrm{GeV}$. Addressing pile-up effects involves a two-step correction process, estimating and subtracting the average energy from pile-up collisions, followed by a residual correction using bunch crossing information. The total systematic uncertainties for PFlow jets are given in Figure 4.16 as a function of p_T. Systematic uncertainties of the JES for central jets ($|\eta| < 1.2$) vary from $1\,\%$ for high-p_T jets to $5\,\%$ at low p_T ($20\,\mathrm{GeV}$).

Precision SM measurements and BSM searches involving jet production require excellent *Jet Energy Resolution* (JER)[18]. The JER is evaluated in a dijet-balanced system for precise momentum determination, and is parameterized as in Eq. (4.9). For PFlow jets, used in this thesis, the relative JER ranges from 0.25 to 0.04 depending on jet p_T as shown in Figure 4.17. The resolution is primarily influenced by the JES and theory modeling uncertainties.

Absolute calibrations are subsequently applied to correct the jet η and energy scale. These corrections are derived from MC simulation, where the jet energy and direction at particle level are known. Truth jets are reconstructed using the simulated particles as inputs, being later matched to the reconstructed jets based on an angular separation requirement ($\Delta R < 0.3$). The *Global Sequential Calibration* (GSC) [363] procedure fur-

[17] This is the baseline energy scale at which electromagnetic showers absorbed by the calorimeter are measured robustly.

[18] The JER also affects the E_T^{miss} resolution (see Section 4.3.6).

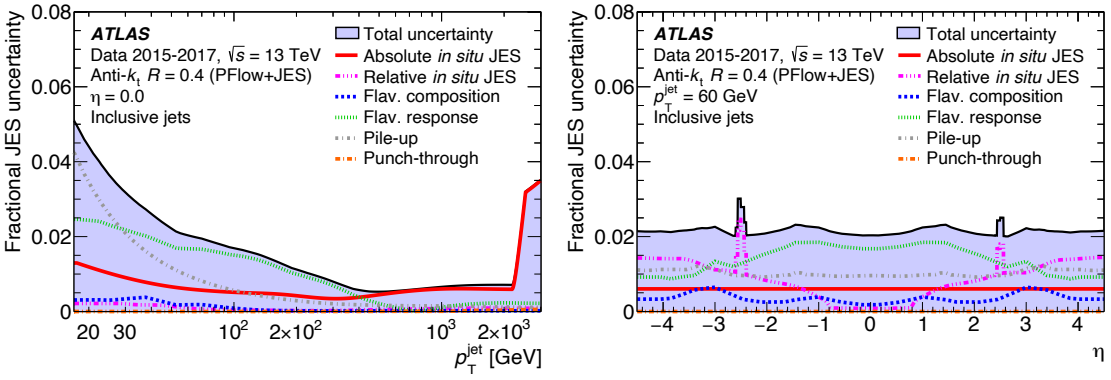

(a) Dependence on p_T^{jet}.

(b) Dependence on η.

Figure 4.16: Systematic uncertainties of the jet energy scale (JES) for PFlow jets reconstructed using the anti-k_T algorithm with $\Delta R = 0.4$ evaluated using the 2015–2017 dataset recorded with the ATLAS detector as a function of (a) the jet transverse momentum p_T^{jet} and (b) the jet pseudorapidity η. Source [361].

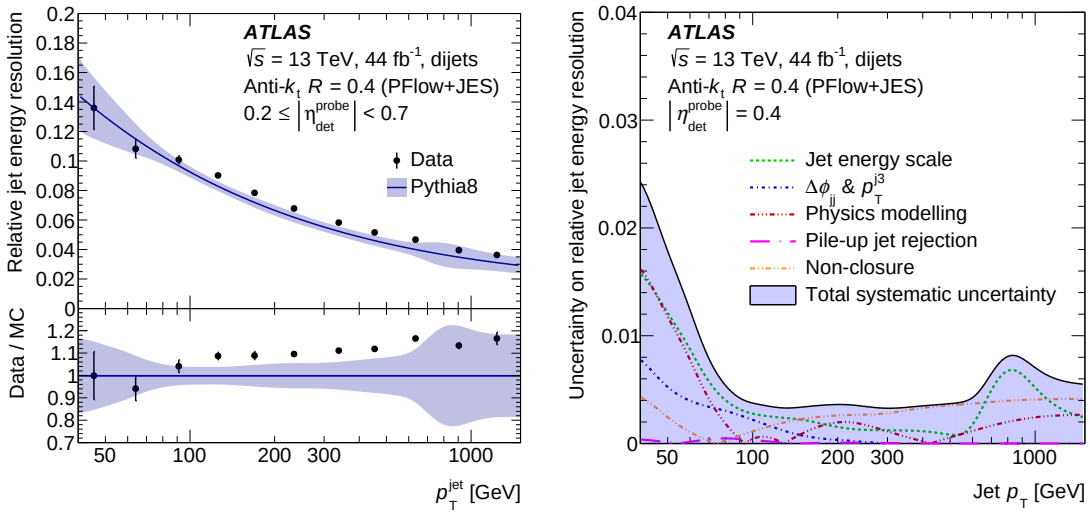

(a) Jet energy resolution.

(b) Relative uncertainty.

Figure 4.17: (a) Jet energy resolution and (b) corresponding uncertainties applying the jet energy scale (JES) as a function of the jet transverse momentum p_T^{jet}. Jets are reconstructed using the anti-k_T algorithm with $\Delta R = 0.4$, evaluated using the 2015–2017 dataset recorded with the ATLAS detector. Source [361].

ther refines the jet energy response using global properties of the jet in MC-simulated dijet events. Leveraging information from associated tracks, the GSC minimizes differences in calorimeter response observed in jets of various flavors, improving the JER by incorporating details of the calorimeter energy deposits. Additionally, for very energetic jets extending beyond the calorimeter, information from the muon chambers is also included. The GSC does not alter the average JES in the dijet sample. Finally, an in-situ calibration is derived from data to address differences between MC simulation and actual detector readout. Selection efficiencies exceed $95\,\%$ for $p_T > 20\,\text{GeV}$, rising to $99.5\,\%$ for $p_T > 100\,\text{GeV}$ [364].

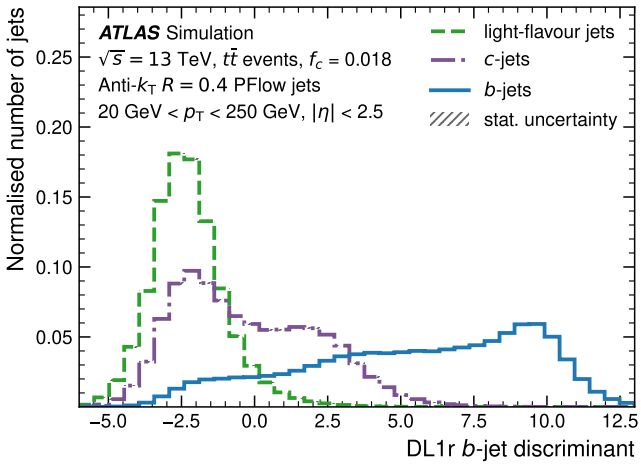

Figure 4.18: Distributions of the b-tagging discriminant of the DL1r b-tagging algorithm for b-jets (solid blue), c-jets (dashed purple), and light-flavour (dashed green) jets in $t\bar{t}$ simulated events. Source: [369].

The activity generated in a large number of interaction vertices per bunch-crossing in LHC collisions reduces the accuracy of the jet energy reconstruction, also leading to the misassignment of numerous jets from pile-up to the primary interaction. The ATLAS system employs the so-called *Jet Vertex Tagger* (JVT) algorithm [365, 366] to identify jets originating from the hard scattering. Via a track-based approach, the JVT combines multivariate analysis techniques to assess the probability that a given jet originated from the hard scattering process. The algorithm utilizes jet-based quantities following the identification of the primary vertex and calculates the *jet vertex fraction* (JVF) for each jet, defined as the ratio of the sum of transverse momenta of tracks compatible with the main primary vertex to the sum of transverse momenta of all tracks associated with other primary vertex candidates in the event. JVT algorithms are optimized separately for central and forward jets using the nominal JVT algorithm and a *forward-JVT* (fJVT) algorithm, respectively [366, 367].

In addition to pile-up effects, other detected signals can result in false reconstructed jets. Examples include non-collision background signals from cosmic rays or beam-induced effects like muons generated from beam losses. Noise in the calorimeter readout can also contribute. To mitigate the presence of fake jets that were not produced in LHC collisions, a *jet cleaning* process [368] is carried out for physics analyses. This process implements various criteria based on the energy ratio across different calorimeter layers, along with tracking information. These requirements are combined into working points with 95 % (99.5 %) efficiency for jet transverse momentum $p_T > 20\,\text{GeV}$ ($p_T > 100\,\text{GeV}$).

4.3.5 Jet Flavor Tagging

The discrimination between jets containing b- and c-hadrons (referred to as b-jets and c-jets, respectively) against jets containing only lighter hadrons (i.e., bound states of u, d, and s quarks, referred to as *light-flavor jets*) is essential in physics analyses whose final states are sensitive to different quark flavors. The techniques implemented to identify b, c, and light jets based on its kinematic features are know as *flavor tagging*.

The identification of b-jets (so-called *b-tagging*) has been explored in-depth in the ATLAS Collaboration. These algorithms exploit the characteristic high mass, high charge-particle multiplicity and long lifetime of around $t_\tau \sim 1.5\,\mathrm{ps}$ [95] of b-hadrons, allowing them to travel a distance inside the detector of about $ct_\tau \sim 4.5\,\mathrm{mm}$ before their consecutive decay. The tracks assigned to the product of the secondary hadron decay result in larger impact parameter d_0 than the expected results from light-jets, allowing to experimentally resolve a secondary vertex in addition to the primary vertex. The addition of the IBL to the ATLAS pixel detector enhances the impact parameter resolution, resulting in an improved performance of the b-tagging algorithms during Run 2 [321]. The DL1 algorithm [369, 370] is an artificial deep neural network trained on a hybrid sample constructed with balanced MC simulation of light, c- and b-quark flavor production. The output is a multidimensional array that provides the probability for each jet to contain either a b, c, or light hadrons, which are combined into a tagging discriminant. A newer version of this tagger, DL1r, is used in this thesis. It includes a new algorithm, known as RNNIP, based on recurrent neural networks as an additional input that learns the impact parameter correlations among the tracks assigned to the given jet [371]. The working points of DL1r combine the selection criteria over the DL1r outputs, shown in Figure 4.18, to provide specific b-jet acceptance efficiency in simulated $t\bar{t}$ samples. Several working points are provided centrally to be used in physics analyses, with their corresponding calibrations that translate into b-tagging efficiencies of $60\,\%$, $70\,\%$, $77\,\%$, $80\,\%$, and $85\,\%$. The larger the acceptance to select jets originated from b-decays, the larger the probability of accepting mistagged jets becomes.

The b-tagging algorithms require knowledge of the truth information about the hadron-flavor content of the jets used in the training, obtained from MC simulation. Scale factors are then applied to MC samples in the physics analyses for a good description of the data. The uncertainties on the scale factors include statistical errors, systematic uncertainties from jet reconstruction, and MC modeling of systematic uncertainties. The corresponding scale factors are estimated in well-identified processes comparing data to MC, and are parameterized as a function of the jet flavor and its p_T. The b-tagging efficiency is extracted from $t\bar{t}$ dilepton events with exactly two jets, where a combinatorial likelihood approach is adopted to extract the jet flavor composition and b-tagging efficiency simultaneously [372]. The b-tagging probability is determined for a jet momentum range between $20\,\mathrm{GeV}$ and $400\,\mathrm{GeV}$. For jets with $p_T > 400\,\mathrm{GeV}$, a high-p_T extrapolation is used to determine the probability of being tagged. The calibration factors correcting for the b-tagging efficiency are measured to be very close to 1 with uncertainties ranging between $1\,\%$ and $8\,\%$. The rate for wrongly tagged jets containing c-hadrons is estimated from semileptonic $t\bar{t}$ events, where the c-jet mistagging rate is extracted from those associated with the hadronic W decay [373]. For the DL1r tagger, the scale factors are close to 1, with efficiencies ranging between $3\,\%$ and $17\,\%$ [374]. The rate of mistagged light-jets is studied with methods targeting $Z + \mathrm{jets}$ topologies [375].

4.3.6 Missing Transverse Momentum

Neutrinos, and other hypothetical particles interacting purely via the weak force, do not produce any signal on the different detector layers. Consequently, these particles introduce imbalances in the sum of total momenta of the measurable particles. An inference of their momenta can be done in the transverse plane using the *missing transverse momentum*

E_T^{miss}. The components of E_T^{miss} and its azimuthal angle ϕ^{miss} can be obtained from

$$\left.\begin{array}{l} E_x^{\text{miss}} = -\sum_i E_i \sin\theta_i \cos\phi_i \\ E_y^{\text{miss}} = -\sum_i E_i \sin\theta_i \sin\phi_i \end{array}\right\} \quad \begin{array}{c} E_T^{\text{miss}} = \sqrt{(E_x^{\text{miss}})^2 + (E_y^{\text{miss}})^2}\,, \\ \phi^{\text{miss}} = \arctan\left(\frac{E_y^{\text{miss}}}{E_x^{\text{miss}}}\right)\,. \end{array} \tag{4.10}$$

Misreconstruction of object energies directly affects the amount of E_T^{miss} in an event, which can result from either detector resolution effects or decays of particles invisible to the detector. Both real and "fake" sources of E_T^{miss} lead to contributions to the missing transverse momentum vector that cannot be distinguished from each other. The resolution and performance of E_T^{miss} are highly dependent on the reconstruction efficiencies of every object i entering into the sum given by Eq. (4.10). Fully calibrated electrons, muons, photons, hadronically decaying τ-leptons, and jets reconstructed from calorimeter energy deposits and charged-particle tracks are used for the computation of Eq. (4.10), as well as soft-hadronic activity measured by reconstructed charge-particles tracks that were not associated with hard objects. The influence of pile-up is notorious [376]. Performance of missing transverse momentum reconstruction with the ATLAS detector using proton-proton collisions at $\sqrt{s} = 13$ TeV and further details about its reconstruction can be found in Ref. [377].

4.3.7 Ambiguities between Reconstructed Objects

The considered selection criteria for particle identification do not impose any requirement on the presence of other kinds of particles, even though the efficiency of exclusion is high. When high statistics come into play, particle misidentification can play an important role involving background contributions in concrete regions of the phase space of a measurement. For instance, leptons can be produced inside a jet and they might be able to pass the selection criteria for electron identification. However, they can be efficiently removed by requiring additional conditions on their reconstruction, especially on energy depositions and associated tracks. These conditions are usually known as *isolation requirements*. Calorimeter isolation is carried out by defining the variable $E_T^{\text{cone},X}$ as the sum of transverse energies of topological clusters with positive energy in a cone of predefined aperture ΔR [355]. This clustering is different for electrons and muons. Considering transverse momenta from the reconstructed tracks, a similar definition can be done for $p_T^{\text{cone},X}$ defined as the sum of transverse momenta from all the assigned tracks to an object, excluding the best-matching track. The value of X refers to the chosen ΔR (e.g. a value of X = 30 will involve a choice of ΔR = 0.3).

The same produced element might be selected by the reconstruction algorithms of different types of objects, causing a double counting of the element of interest in the reconstruction of the event. This happens especially among electrons, muons, and jets. In such cases, one of the superposing objects must be discarded by applying *overlap removal* requirements. The standard approach used in ATLAS can be found in Ref. [378].

Chapter 5

Gas and high voltage systems for small Thin Gap Chambers of the ATLAS New Small Wheel

"Every step we take on earth brings us to a new world."

— Federico García Lorca (1898 – 1936).

The high instantaneous luminosity and pile-up conditions expected for LHC Run 3 and most prominently for the High-Luminosity Large Hadron Collider (HL-LHC) challenges the rates of the single-lepton trigger. These are of paramount importance for the accomplishment of the LHC physics program. During the upgrades taking place from 2019 until 2022, the innermost muon chambers in the endcaps of the ATLAS detector were substituted by the so-called *New Small Wheels* (NSWs), incorporating the Micromegas and small-strip Thin Gap Chamber detector technologies for improved tracking and trigger capabilities. The upgraded setup is able to successfully operate in the harsher environments anticipated for the ATLAS experiment at the HL-LHC. This chapter presents the design, installation, and validation of a gas and high-voltage systems necessary to run a small-strip Thin Gap Chamber prototype in nominal data-taking conditions in a test laboratory in Freiburg. For a safe and efficient operation of the experimental setup, even from a distance, a monitoring system and remote control system have been implemented.

5.1 Introduction

The ATLAS and CMS experiments collected about 140 fb^{-1} of pp collisions at a center-of-mass energy of $\sqrt{s} = 13$ TeV by the end of Run 2, far beyond the expectations of the physics program. Such an accomplishment also allowed the implementation of innovative calibration and analysis techniques that substantially improved the precision of the physics results. However, the data collected at the LHC has not revealed any signs of physics beyond the SM, which is expected given its incomplete description of nature as outlined in Section 1.6. This motivates the collection of more data, increasing the chance to observe unexpected signals arising over the SM contributions. The LHC plays a leading role in both direct and indirect searches of BSM phenomena, and its foreseen upgrade by 2029 [123] into the HL-LHC [122] is favorable in both approaches. On the one hand, the increase of the center-of-mass energy up to $\sqrt{s} = 14$ TeV and seven times greater instantaneous luminosity (targeting $5 \cdot 10^{34} \mathrm{cm}^{-2}\,\mathrm{s}^{-1}$ and about 250 fb^{-1} per year) enable the optimization of triggering schemes that enable the quest for rare processes and phenomena. On the other hand, the large amounts of data expected for the HL-LHC will allow the scrutiny of systematic uncertainties leading to an even better understanding of our experimental techniques, pushing further the precision frontier at the LHC. With a target of integrated luminosity of 3000 fb^{-1} delivered approximately 12 years after the

upgrade [122], an extensive physics program involving experimental tests of SM predictions in Higgs, flavor physics, as well as direct and indirect searches for BSM phenomena becomes accessible at the HL-LHC, also including the study of high-density QCD using heavy-ion beams [379]. Carrying out the physics program at the HL-LHC successfully is a top priority of the European Strategy for Particle Physics [380] and the Particle Physics community in the USA [381]. In order to keep up with the drawn plan, important efforts from the theoretical (see Chapter 2), experimental, and accelerator communities are necessary, including optimization of the computing resources, software, infrastructure, and greenhouse gas emissions.

At the HL-LHC, the increase in instantaneous luminosity results in an environment expected with a higher pile-up of ~ 55 (at $2\times10^{34}\,\mathrm{cm}^{-2}\,\mathrm{s}^{-1}$) to ~ 140 (at $5\times10^{34}\,\mathrm{cm}^{-2}\,\mathrm{s}^{-1}$) mean number of interactions per bunch-crossing, assuming a collision rate of $25\,\mathrm{ns}$. Therefore, it is mandatory to ensure that the detector is able to operate minimizing radiation damage at high particle occupancy while coping with the vertex and track reconstruction efficiencies enforced by the physics program of ATLAS (discussed in Section 4.2).

The upgrade is divided into two steps. The *Phase-I* upgrade [382] (between 2019 and 2022), brings the technologies of MS [383], TDAQ [384], and calorimeter electronics [385] closer to HL-LHC requirements. This first stage focuses on sharpening the trigger turn-on threshold values while rejecting background events, keeping the trigger rates at an acceptable level for physics without either prescaling or increasing the p_T thresholds[1]. The *Phase-II* upgrade [386] (from 2026 until the end of 2029) incorporates a new full-silicon inner tracker [387, 388] and high-granularity timing detector [389] into the ATLAS experiment, as well as further improvements of the Muon detectors [390], LAr [391] and Tile [392] calorimeters, along with the TDAQ system [393].

This chapter focuses on the NSWs [383], which fully replaced the innermost layer of muon detectors in the endcap region of the ATLAS detector during the Phase-I upgrades for the LHC Run 3 [394]. The NSWs are essential to cope with the physics performance of the muon trigger rates and momentum resolution at high luminosity environments of the HL-LHC. An overview of the motivation for their installation, its layout and main detector technologies is given in Section 5.2. This thesis presents the commissioning of a dedicated laboratory in Freiburg to perform tests of the small-strip Thin Gap Chambers (sTGCs). In particular, Section 5.3 describes the gas and monitoring systems necessary to run a sTGC prototype in nominal data-taking conditions, which has been designed, installed, and validated for this new laboratory. The conclusions in Section 5.4 close the chapter.

5.2 The ATLAS New Small Wheel

Most of the Phase-I upgrade effort was allocated to installing the two NSWs that are necessary to be able to cope with the single-muon trigger rates during Run 3 and the

[1]The expected rise in L1MU trigger p_T thresholds from $p_T > 20\,\mathrm{GeV}$ to $p_T > 40\,\mathrm{GeV}$ without the installation of the NSW would result in a loss of acceptance in $H \to b\bar{b}$ ($H \to WW^{\star}$) events for physics analyses. The signal acceptance is expected to drop from roughly $93\,\%$ to $61\,\%$ ($75\,\%$). The acceptance is reduced even further to $43\,\%$ ($72\,\%$) if muons with $p_T > 20\,\mathrm{GeV}$ are only triggered in the barrel region. The installation of the NSW allows to keep the trigger rates at similar values as in Run 2 data-taking without increasing the p_T thresholds of the L1MU triggers [383].

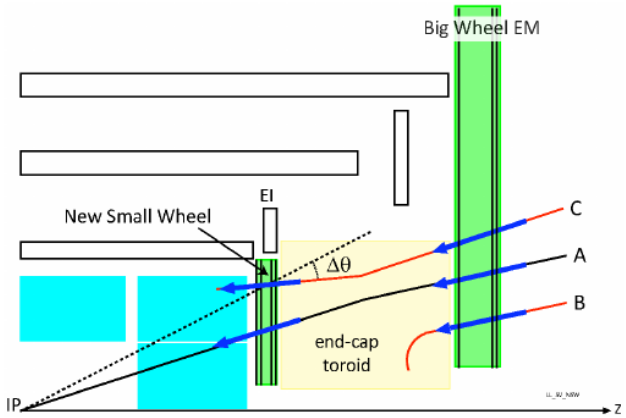

(a) Sketched layout of the muon spectrometer during the LHC Run 3.

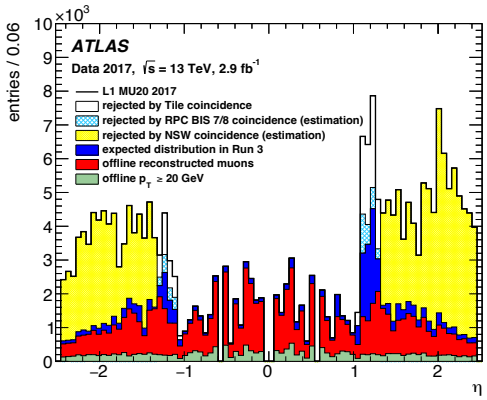

(b) Expected muon trigger rate reduction as a function of the muon pseudorapidity.

Figure 5.1: Illustration of the single-muon trigger rate increased by fake muons in the end-cap region. On the left, (a) shows the sketched layout of the muon spectrometer in the LHC Run 3 with prompt muons originating at the primary vertex (A, shown as a blue line), and fake muons from charged particles from the forward shielding of the detector (B and C, shown as red lines). The outermost endcap wheel is not displayed. On the right, (b) presents the expected muon trigger rate reduction from the NSW and Level-1 Muon endcap upgrades. Source: [394, 383].

HL-LHC. ATLAS reserves no more than $25\,\mathrm{kHz}$ of the total $100\,\mathrm{kHz}$ L1 bandwidth for the lowest p_T single-muon triggers. Without the NSW technology, these trigger rates are anticipated to rise up to $50\,\mathrm{kHz}$, for a p_T threshold of $20\,\mathrm{GeV}$.

In the forward-most region of the detector, a significant background component proportional to the instantaneous luminosity arises. This background emerges from low-energy charged particles produced in the hadronic showers within the forward shielding, which enters the cryostats of the endcap toroid without traversing the innermost muon wheel. As they travel through the toroids, their trajectories are bent by the magnetic field, and a portion of them follow paths mimicking those of muons originating from the IP. Figure 5.1a illustrates this phenomenon. On the one hand, these events lead to a notable increase in the false positive rate [383] when the middle wheels were solely used for triggering. The original TGC doublets in the inner wheels lacked sufficient resolution in the bending direction and an adequate number of detector layers to form track segments pointing to the IP. The number of RoIs identified by the L1 single-muon trigger experiences a sharp rise for values of $|\eta| > 1$, as shown in Figure 5.1b. In Run 1, most RoIs for $|\eta| > 1$ were primarily caused by the background originated in the forward shielding. Since the background rate in the endcap region increases with luminosity, it will eventually exceed the allocated L1Muon trigger rate, and this background can only be suppressed by increasing the p_T threshold of the lowest unprescaled muon trigger to alleviate the risen rates. The background rates in the region of the inner wheel stations are much higher than in the middle wheels, so the relatively coarse granularity of the legacy TGCs implied that at high luminosity nearly all triggers from the middle wheels would have had corresponding background hits in the original small wheels, leading to a coincidence requirement that is less effective. On the other hand, the 30 mm-diameter MDTs used in the old small wheels are limited by space charge build-up effects [395] at high background rates, expecting a degradation of their precision tracking capabilities at the

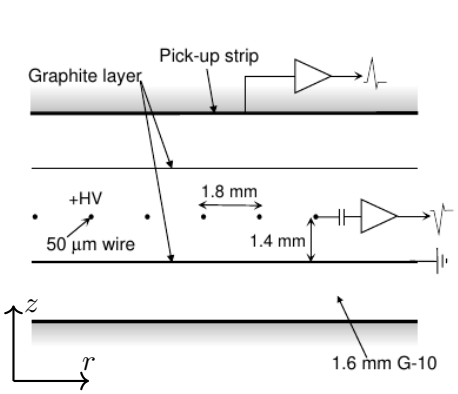

(a) (Legacy) Thin Gap Chamber [305].

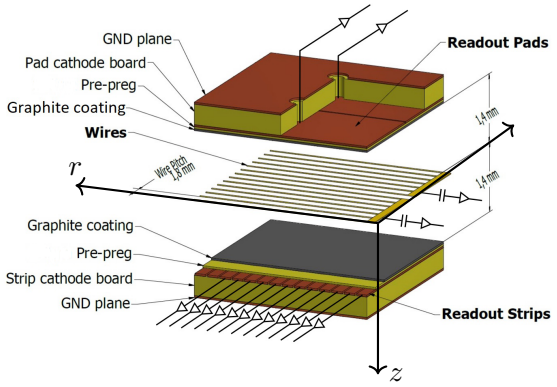

(b) Small-strip Thin Gap Chambers [394].

Figure 5.2: Illustrative sketches of the two technologies implemented in the New Small Wheels: (a) Micromegas, and (b) the small-strip Thin Gap Chambers.

HL-LHC. The successful replacement of the small wheels by the NSWs accomplish both (i) the suppression of the high trigger rates in the forward-most region, keeping them at a manageable level flat across the $|\eta|$ distribution[2], and (ii) the very fast and precise track-segment matching capabilities while maintaining the offline tracking performance of the old small wheels from Runs 1 and 2 over the same polar angle range ($1.3 < |\eta| < 2.7$). The remaining detectors within the MS are kept in Run 3 and continue to play the same essential roles in both the muon trigger and offline tracking, just as they did in previous runs (see Section 4.2.5). The Run 3 setup meets the performance goal (discussed in Section 4.2) of a standalone transverse momentum resolution better than $15\,\%$ for $1\,\mathrm{TeV}$ tracks, which requires the sagitta of about $500\,\mu\mathrm{m}$ of the roughly $15\,\mathrm{m}$ long tracks through the endcap MS to be measured with a resolution of about $75\,\mu\mathrm{m}$.

Two technologies are incorporated in the NSWs: the small-strip Thin Gap Chambers (sTGCs) and the micromesh gaseous structure (Micromegas, or MM for short) detectors.

- The MM detectors, introduced in 1995 [396], employ a slim planar design, replacing traditional high-voltage wire planes with a metallic micromesh structures. The NSW MM detector features two parallel electrodes for drift and readout, creating a $128\,\mu\mathrm{m}$ drift gap and a $5\,\mathrm{mm}$ amplification gap [397]. Electric fields of $100\,\mathrm{V/cm}$ and $40\,\mathrm{kV/cm}$ in the drift and amplification regions, respectively, achieve a gas gain of 10^4 in a mixture of 93% argon, 5% CO_2, and 2% isobutane. A positive high voltage of $+500\,\mathrm{V}$ is applied to resistive strips for amplification, with a drift cathode at $-240\,\mathrm{V}$. Gas ionization triggers electron drift ($100\,\mathrm{ns}$) and rapid amplification, generating a quick pulse on the readout strip. MM detectors excel in high flux due to efficient positive ion evacuation [383]. Mitigating electrical discharge risks, a protective system incorporates resistive strips above readout strips, spaced $425\,\mu\mathrm{m}$ apart. The detector's orientation aligns with the toroidal magnetic field, achieving spatial resolutions of $300\,\mu\mathrm{m}$ and $12\,\mathrm{mm}$ in the bending and second coordinates, respectively.

[2]The observed asymmetry in the trigger performance between the two ends of the detector is attributed to the opposite bending directions of positively charged protons originating from interactions within the shielding.

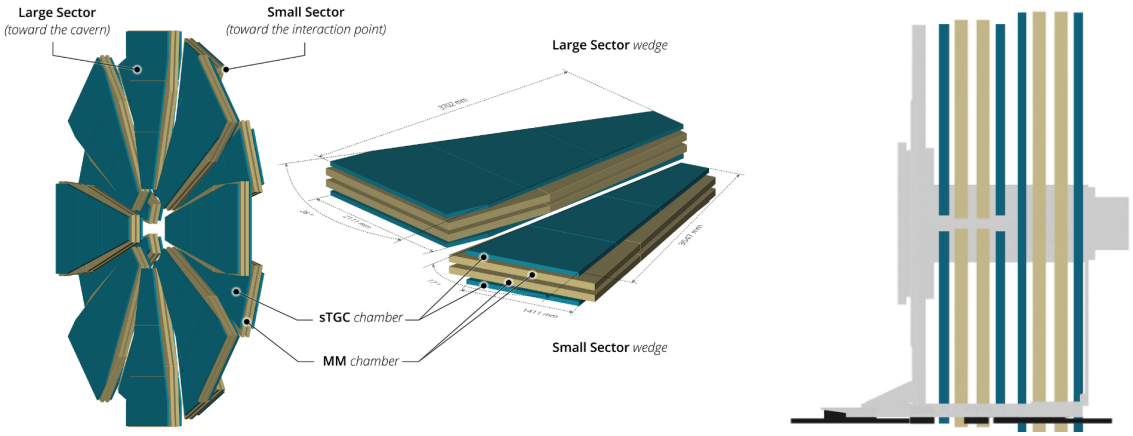

(a) (b)

Figure 5.3: Illustration of (a) the layout of the New Small Wheel and (b) the arrangement of small-strip Thin Gap Chambers (blue) and Micromegas (orange) in the layout. The shielding and mechanical system holding both technologies onto the wheel is shown in gray. Adapted from [394].

- The sTGC, a multi-wire proportional chamber technology [398, 399] optimized for high-rate environments, serves as the primary trigger detector for the NSWs, retaining much of the legacy TGC configuration [400] (Figure 5.2a). The chamber features two graphite-resin-coated cathodes spanning a $2.8\,\mathrm{mm}$ gap, filled with a 55:45 CO_2:n-pentane mixture, where n-pentane acts as a quencher to minimize photon avalanches. Gold-plated tungsten wires ($50\,\mu\mathrm{m}$ diameter) are aligned parallel to the radial axis at a pitch of $1.8\,\mathrm{mm}$, applying a nominal potential of $+2.8\,\mathrm{kV}$. Unlike the azimuthal orientation in previous TGC detectors, the wire direction in sTGCs is radial (see Figure 5.2b). Anodes are grouped in sets of $\sim$ 20 wires sharing a common HV capacitor, ensuring efficiency at high rates ($20\,\mathrm{kHz/cm^2}$). Signals are capacitively induced on fine copper readout strips and pads on either side of the gap, with a finer pitch and readout layer than TGCs. The readout layer is under a thin insulating layer, supported by a $1.3 - 1.4\,\mathrm{mm}$ thick PCB with a copper grounding skin. The sTGC's high electric field and narrow anode spacing result in a time resolution of less than $25\,\mathrm{ns}$, enabling differentiation of muons from consecutive bunch-crossings. This technology allows fast online tracking for L1 trigger, with a position resolution of $45\,\mu\mathrm{m}$ for perpendicular incidents, increasing to $\sim 150\,\mu\mathrm{m}$ at angles of $20 - 30°$ [401].

  Six sizes of sTGC quadruplets are available: three sizes for small- and large-sector wedges, respectively. The HV wires of innermost quadruplets in each wedge (those closest to the beam pipe) are split in two, creating two HV regions within a common gas volume: a high and low background region for $2.4 < |\eta| < 2.7$ and $|\eta| < 2.4$, respectively. Each sTGC wedge is enclosed around its periphery by a gas-tight envelope that is continuously flushed with CO_2. This maintains a dry atmosphere around HV elements and dilutes possible leaks of operating gas. If n-pentane traces are detected, both HV and low voltage (LV) are switched off and an alarm is fired.

The general configuration of each NSW, illustrated in Figure 5.3a, consists of eight small sectors, which are aligned with the barrel toroid coils and placed against the shield-

ing disc, as well as eight large sectors forming a second plane slightly farther from the IP. To ensure full instrumented coverage, there is a mechanical overlap between the large and small sectors. The MMs regions overlap between adjacent large and small sectors, in contrast to the sTGC regions. These instrumented areas are organized into trapezoidal modules, each incorporating four layers of MMs and sTGC detector planes, collectively referred to as *quadruplets*. These quadruplets, available in various sizes, are radially assembled into sTGC *wedges* and MMs double wedges, which are then combined to form large and small *sectors*. A sector is composed of eight sTGCs and eight MMs active detector layers, which are constructed on a central spacer frame. This frame is attached to the wheel spokes in a manner that maximizes the separation between the sTGC wedges, as depicted in Figure 5.3b, which serve as the primary trigger components. To ensure precise alignment between the MMs and sTGC quadruplet modules, an optical alignment monitoring system is installed [402]. This system periodically collects data approximately every two hours to assess the displacements, rotations, and specific deformation modes of each individual quadruplet. Furthermore, the shielding disc and central hub of the NSW have a crucial role in protecting the detector layers from the elevated radiation levels anticipated in HL-LHC collisions.

5.3 Gas and High-Voltage Systems for Small-strip Thin Gap Chambers of the ATLAS NSW

The efficient operation of a gaseous detector depends on factors influencing gas amplification, drift velocity, signal quality, operational safety, and detector material preservation. Achieving high gas ionization at a sufficiently low electric field is crucial, often favoring noble gases like argon. However, their high photon production rate and short radiation length bring challenges for signal quality and precision. CO_2 serves as a suitable ionization gas, finding a balance at typical electric potentials. Polyatomic gases, known as *quenching gases*, offer a broad absorption spectrum of photon energies to control photon avalanches. Hydrocarbons like methane or isobutane are common choices, but they can cause undesired electrode polymerization under high radiation load, leading to ageing effects that compromise detector performance. The choice of a nominal gas must take into account these ageing effects. Technical aspects for safe and stable gas mixture production under normal laboratory conditions are also vital. Mixtures of CO_2 and n-pentane, operated in saturated proportional mode, meet the stringent gaseous detector requirements in particle colliders, delivering reduced Landau tails and a high signal-to-noise ratio. This mixture has extensively been used in both sampling calorimetry [403, 404] and muon triggering [405, 305, 383], as it features excellent ageing properties [406, 407] and provides amplifications of over 10^5 at approximately $3\,\mathrm{kV}$, which makes it also accessible in any physics laboratory.

At the University of Freiburg, a testing facility has been commissioned to evaluate effects of the gas mixture configuration and readout parameters using cosmic radiation. Since no thin gap chambers were run at these facilities before, the laboratory had to be adapted to fulfill stringent safety requirements and performance. For this dissertation, the necessary system to prepare the nominal CO_2:n-pentane gas mixture has been designed, built, and commissioned, including the applied high and low voltages for the sTGC chambers and their readout cards.

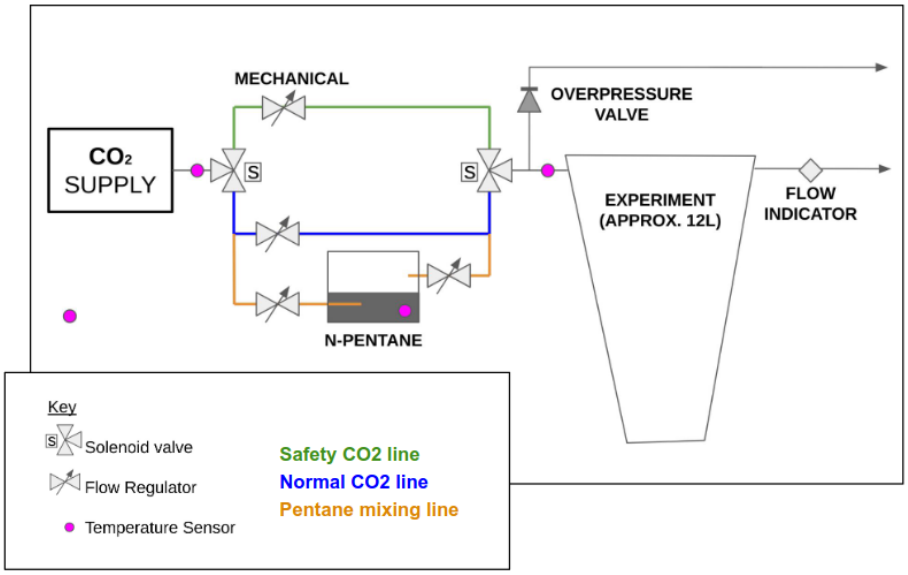

Figure 5.4: Schematic diagram of the gas system commissioned to operate sTGC detectors at the University of Freiburg.

Design

sTGCs have been constructed and tested in laboratories based in Chile, China, Israel, Canada, and CERN [407, 408], with gas systems fulfilling tight safety and operation requirements. Gas systems aiming to run sTGCs must provide continuous operation in a safe and stable manner with fluctuations of a few percent of n-pentane concentration to ensure optimal performance of the signal collection after ionization by the traversing charged particle. Additionally, mixtures of n-pentane with oxygen become flammable. A steady flow of pure CO_2 is therefore needed to keep the detector free of oxygen and other pollutants that might contaminate the gaseous mixture and the detector in case of intervention. A negative-pressure exhaust system with the appropriate sniffers are compulsory for triggering undesired leakages and freeing the experimental environment before human intervention. Similarly, the n-pentane available in the system has to be carefully refilled so that no air or other contaminants are introduced in the gas mixture. Since n-pentane is known to attack rubber, plastics, and other coatings, every material in contact with the gas mixture must be compatible with this substance to keep all chemicals from contaminating the inner detector volume. Moreover, sTGCs are sensitive to small pressure differences, leading to deformation in the inner geometrical symmetries crucial for uniform electric fields and recording of the signal. Remote control and monitoring are also compulsory for a safe operation of the facility, even when there are no personnel in the lab. A reliable and safe operation must be ensured in adverse conditions such as power cuts or fire alarms. The system should offer flexibility to modify flow rates and gas mixture provided to the sTGC chambers.

Inspired by the gas system in the Canadian test facility [408], Figure 5.4 shows the system designed in this dissertation for the commissioned laboratory at the University of Freiburg. The gas starts flowing from a bottle of pressurized and pure[3] CO_2 whose flow

[3] CO_2 is purchased commercially from *Linder* with a purity of 99.995%.

is divided into three different paths. The first path delivers pure CO_2 (labelled as *CO_2 line* and shown in blue) with a flow rate of 16.6 up to $100\,\mathrm{ml/min}$ while a second streamline drives up to $50\,\mathrm{ml/min}$ of CO_2 to a *mixing system*, where the inlet gets in contact with liquid n-pentane[4]. The gas flow of these two forks can be monitored and adjusted remotely using unidirectional *flow regulators*. A second flow regulator is installed after the mixing system to know the mass flow of the mixture at the outlet. Temperature *PT100 sensors* (shown as pink dots) are used to monitor the temperatures of the room[5], inlet and outlet of the mixing system, and the liquid pentane with a precision of $\pm 0.1\,^{\circ}\mathrm{C}$. Additionally, the n-pentane in the mixing vessel is cooled, whose temperature is remotely configured and monitored. Both pure CO_2 and n-pentane mixing paths are then merged back in a *three-way solenoid valve*. In the case of a power cut (when the flow regulators close automatically) or a ventilation failure, the three-way valves switch the gas flow through a third *safety line* (shown in green) that incorporates a mechanical flow regulator fixed to about $100\,\mathrm{ml/min}$. This safety line ensures a fast and safe flow of pure CO_2 to evacuate any n-pentane left in the system in adverse circumstances. The three-way valves can be controlled to use the safety line by switching off the applied LV. The pressure difference in the system with respect to the atmosphere is monitored at the sTGC inlet using a *pressure sensor* with a sensitivity of $\pm 0.3\,\mathrm{mbar}$. If the desired pressure is exceeded, a glass bubbler filled with industrial oil[6] used as *overpressure valve* vents the gas mixture to a dedicated exhaust system[7]. The maximum pressure drop, configured by the height of the oil column in the overpressure valve, is set to $5\,\mathrm{mbar}$. The gas mixture with appropriate working conditions is then introduced in the sTGC chamber which, after passing through another glass bubbler used as flow indicator, is vented to the dedicated exhaust. Careful insertion of the industrial oil into the flow indicator bubbler has to be considered, minimizing the column height to avoid an increase in the pressure drop that might damage the detector. The mixture is safely vented to the exhaust system[8]. Stainless-steel pipes with $6\,\mathrm{mm}$ diameter are used to connect the components of the gas system, while a $10\,\mathrm{mm}$-diameter pipe made of copper is used for the exhaust system. Both materials are proven to be compatible with n-pentane.

The mixing system is depicted in Figure 5.5. It consists of a total volume of $7\,\mathrm{L}$ able to contain up to $5\,\mathrm{L}$ of liquid pentane. The contact surface of the CO_2 gas, introduced via a pipe pierced with four $0.15\,\mathrm{mm}$-diameter holes, is increased by bubbling the gas through the liquid n-pentane to improve the mixing of the gas. The temperature of the liquid

[4]Purchased with a purity greater than 99% at *Carlroth*.

[5]The boiling point of n-pentane at atmospheric pressure is $36.1\,^{\circ}\mathrm{C}$, while it liquefies at about $16\,^{\circ}\mathrm{C}$ [409]. Tracking the ambient temperature in the laboratory is therefore mandatory to ensure that a gaseous mixture with the expected conditions is introduced in the detector volume.

[6]The vacuum pump oil *Ravenol ISO VG 100* is used. It has low vapor pressure, which is important to avoid this substance to contaminating the detector volume.

[7]To avoid fire and smoke traveling among rooms and laboratories, the common exhaust system of the institute is blocked in case of a fire alarm. The high flammability of n-pentane requires the depletion of any fraction of CO_2:n-pentane mixture in the gas system as fast as possible in case of a fire emergency. Therefore, a dedicated exhaust system is needed, flushing a high flow rate of CO_2 into the system to remove any n-pentane left.

[8]The available exhaust capacity is $40\,\mathrm{m^3/min}$. Due to the high degree of dilution, the released substances cannot create a hazardous explosive atmosphere in the exhaust air system, which happens at a threshold density of $33\,\mathrm{g/m^3}$. Under these conditions, the safe discharge of n-pentane into the building exhaust air has been proven to be possible without any concerns. The fractions of n-pentane exposed to the atmosphere have negligible environmental impact [410].

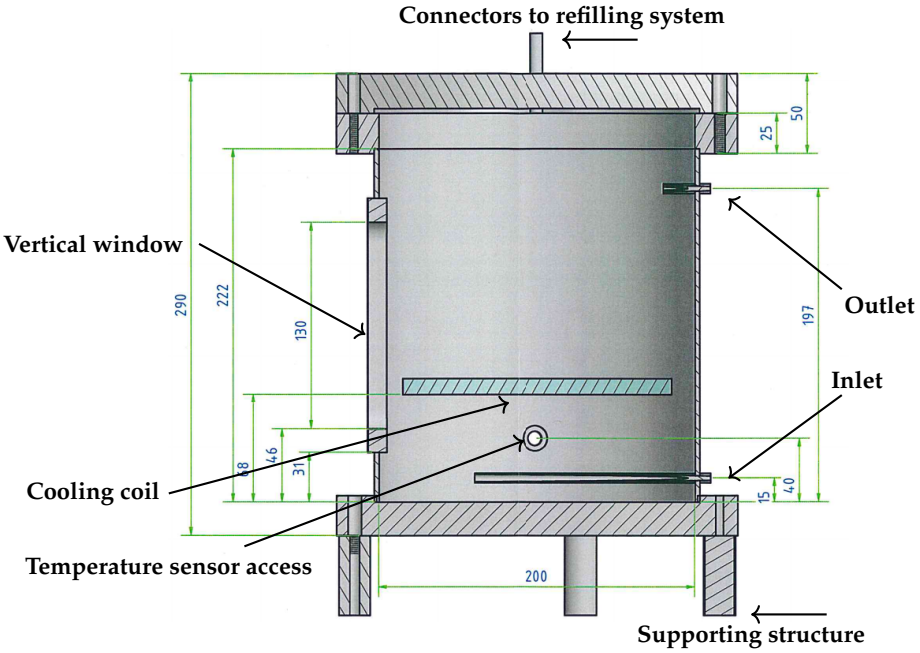

Figure 5.5: Lateral view of the mixing vessel. Dimensions are shown in millimeters. Three-dimensional images by Benhard Pfeifer.

n-pentane is set by pumping water at a given temperature[9] through a spiral-shaped coil installed at $68\,\mathrm{mm}$ above the bottom of pentane volume in order to maximize the heat transfer between the water and the n-pentane. The cooling temperature can be set remotely, and it is monitored by a temperature sensor at the bottom of the bubbler volume, with a temperature stability of roughly $0.5\,^{\circ}\mathrm{C}$. A vertical window spanning the height from the cooling coil up to the outlet is installed to control the n-pentane volume difference consumed by a run. Two fast connectors with fully-hermetic opening valves are installed at the top of the vessel for refilling. Temperature fluctuations in the mixing system are reduced by covering the vessel with a thermal insulator. The mixing system, the flow regulators, and the solenoid valves presented in Figure 5.5 are installed in a $2\,\mathrm{m}$-high *gas rack*, while the sTGC detector rests on a custom-designed horizontal structure close to the pressure sensor, the overpressure valve and the flow indicator. An additional pressure sensor is installed at the exhaust system to track possible blockages of the venting system.

Gaseous n-pentane is denser than air, and therefore it drops onto the floor when mixed with air in the laboratory in case of a leakage. Two sniffing flammable gas sensors[10] are installed inside funnels covering any dropped volume of n-pentane escaping the gas system in both the gas rack and the detector holding structure. These flammable gas sensors provide analog readings for monitoring, and they activate the solenoid valves and alarms via a relay interlock box. The interlock box has been provided by the institute's staff at the workshop of electronics, after discussing the specifications of the gas sensors and the safety needs of the gas system.

Due to the high volatility and flammability of n-pentane, its storage, transportation,

[9]The cooling liquid (distilled water) pumped with a *Lauda RE 630 S*.
[10]Two single explosive gas detectors *Oldham iTrans2* are used, provided by *Teledyne*.

and refilling of the mixing vessel must avoid any leakage of oxygen into the system. Large quantities of n-pentane required for this experiment are stored in the chemical storage area located in the basement of the physics institute. There is no access to this area for employees working on the experiment, except during the opening times. The n-pentane can only be provided to the personnel of the laboratory in dedicated $2\,\mathrm{L}$ bottles with ignition sensors by those authorized to access the chemistry storage. The bottles are carried to a chemical storage cupboard near the laboratory. Refilling equipment should only be handled in a fume hood, able to close in case of spillage. A refilling recipient made of stainless steel is designed to transport the liquid n-pentane from the fume hood to the mixing system with no oxygen intrusion. Its layout is presented in Figure 5.6. With a volume of about $3\,\mathrm{L}$, it also incorporates two fast connectors that attach to the mixing bubbler. A protocol is designed to fill the vessel with n-pentane, extracting any fraction of air in the process and minimizing extra pressure drop in the gas system. A summary of the refilling protocol stands as follows:

1. Once placed into the fume hood, the n-pentane is poured into the refilling vessel. Once filled, the lid of the filling container is loosely closed and CO_2 is flushed into the volume through one of the two fast connectors at the bottom, whose pipe reaches the upper part of the vessel. After a few minutes of CO_2 influx, the container is fully closed after removing the CO_2 inlet. Since the pipe of this inlet almost reaches the top of the vessel, no n-pentane can escape when disconnecting the CO_2 input. The filling container is placed onto the transport wagon and wheeled to the lab. Once the wagon is hold onto the floor, the vessel is pulled up and placed on top of the bubbler lining up the corresponding connectors. The valves are then screwed together using appropriate o-rings.

2. The valves are then opened in a specific order: first, the two valves of the refilling vessel are opened. Then, the bubbler valve at the shortest pipe follow. Lastly, the remaining valves of the bubbler are opened. The valves are left open until the n-pentane in the filling vessel is depleted.

3. Unscrew the valve connectors and lift the container back using the transport wagon.

After discussing the requirements of the gas system, both the mixing and refilling vessels were built by technicians at the physics institute using stainless steel. The mixing and refilling vessels were tested to be leakage-free by flushing gaseous $_2$He around their surface while holding a vacuum of up to $10^{-6}\,\mathrm{bar}$, which is mainly limited by the glass windows. The gas system, including both vessels and the mountings for the PT100 sensors, is also hermetic when compressing gaseous $_2$He up to $3\,\mathrm{bar}$. The proposed gas system and the given protocols have been certified by a third-party contractor, providing the legal approval to run the experiment.

The electric field necessary for optimal amplification in the chamber is built with four HV channels[11] that are fully configurable and monitored from remote, providing up to $8\,\mathrm{kV}$ ($3\,\mathrm{mA}$) with a resolution of $200\,\mathrm{mV}$ ($50\,\mathrm{nA}$) of voltage (current). The HV module is connected to a PC in the lab via Ethernet, which hosts the monitoring and remote control services. The calibration from the manufacturer is verified using a voltmeter of refer-

[11] A single *CAEN N1470ET* module is utilized.

ence[12]. The HV system passed successfully different stress tests, ensuring that no voltage peaks or trips appear after sudden variations of voltage and current during various days. Before any HV is supplied, five complete gas volume exchanges of nominal mixture in the chamber are recommended for a safe operation.

The data from the temperature and pressure sensors is recorded with data acquisition units[13]. Data requests for each sensor are submitted every minute using Standard Commands for Programmable Instruments (SCPI) [411] and stored in a SQL database. The database is displayed online using *Grafana*[15], hosted in a *Raspberry-Pi* running in a computing room to allow monitoring in case of a power cut. The system notifies the lab users via telegram and email in case of warning, error, or failure alarms. A warning includes events that require human intervention before reaching a state where the run must be interrupted. An error in the system requires switching to the safe CO_2 running mode of the chamber, flushing $16.6\,\mathrm{ml/min}$ via the pure CO_2 line. A failure indicates that the system must be switched to the safety CO_2 line immediately.

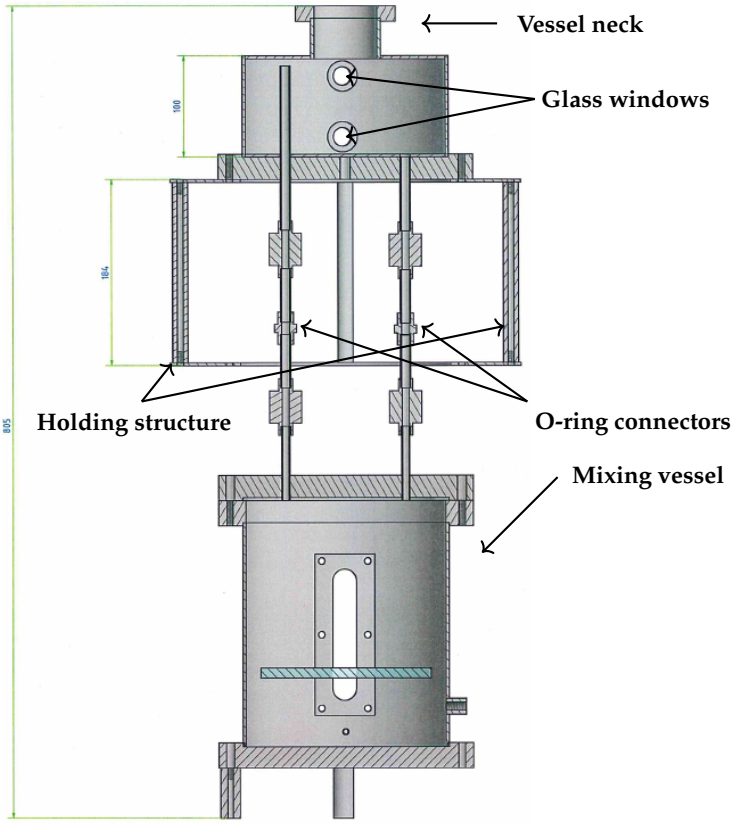

Figure 5.6: Frontal view of the refilling system connected to the mixing bubbler. Dimensions are given in millimeters. Image by Benhard Pfeifer.

Temperature and Pressure Sensors Calibration

Four-wire measurements halve the noise in temperature determination, which eliminate fluctuations of the wire conductivity. Increasing the Power Line Cycles (PLCs) of voltage measurements to 100 in the data acquisition reduces noise in temperature and pressure measurements, yielding averaged results within a $2\,\mathrm{ms}$ integration time.

Calibrating PT100 sensors involves determining the temperature offset, as the manufacturer provides the linear fit slope. Offset temperature is determined by comparing extended temperature measurements to a reference value. However, both the slope and offset of the pressure sensor have to be determined. To assess calibration across pressure differences, both the pressure sensor and a $6\,\mathrm{mm}$-diameter U-shaped tube filled with col-

[12]The voltages provided by CAEN agree with the reference voltmeter *Heizinger DVM 65*.

[13]Two measurement units are used. An *Agilent 34980A* is employed for temperature and pressure sensors, while a *Agilent 34970A* is used to control the LV supplies[14] needed for the three-way valves that switch to the safety CO_2 line.

[15]See the documentation for further details: `https://grafana.com/docs/grafana/latest/`.

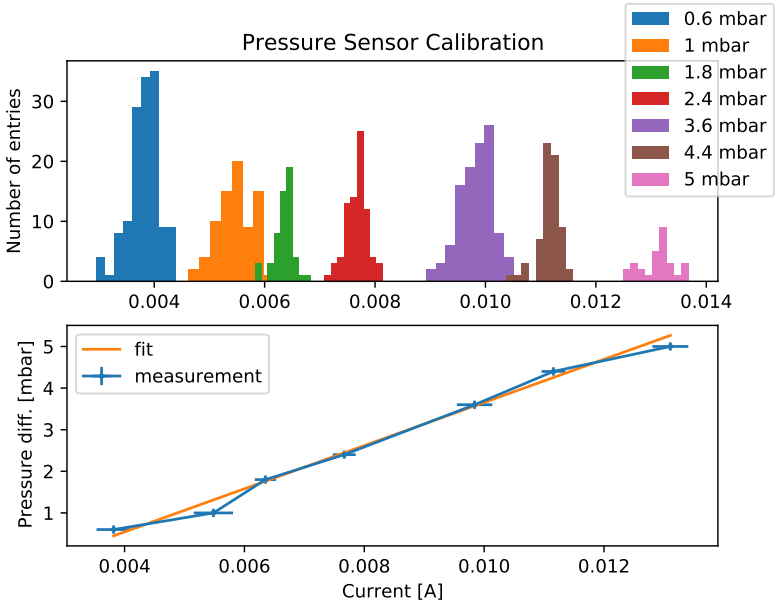

Figure 5.7: Measurements of pressure difference and current obtained with a U-shaped water tube and the pressure sensor, respectively, both connected in parallel to a water vessel. On top, histograms of the measurements of current attributed to the a given pressure difference are shown. At the bottom figure, the measurements of pressure difference are plotted as a function of the mean value of current within its standard deviation. The fit using orthogonal distance regression is shown by the solid orange line, with slope of $518 \pm 24\,\mathrm{mbar/A}$ and an offset of $-1.53 \pm 0.20\,\mathrm{mbar}$.

ored water are attached to the bottom of a vessel. Water added to the vessel allows pressure difference determination by measuring the height disparity in the U-shaped tube. Collected current measurements from the pressure sensor are matched with corresponding U-shaped tube readings. Central current values and their 1σ uncertainty are computed using mean and standard deviation, respectively, within a given time frame and pressure difference. Uncertainty in pressure difference is derived from height measurements of the water columns. The calibration involves seven pressure differences, detailed in Figure 5.7. Orthogonal Distance Regression (ODR) [412], implemented in the *Scipy* library, is employed for a linear fit, which considers uncertainties in both current and pressure difference measurements. The resulting calibration coefficients are stored in the database for the monitoring infrastructure to display calibrated values.

Gas Characterization

The amount of n-pentane provided to the gas mixture is controlled with the cooling temperature of the mixing vessel, since the vapor pressure of n-pentane varies strongly with temperature. This dependence can be derived assuming the vapor behaves as an ideal gas via Amagat's and Dalton's laws, leading to the *Antoine equation*

$$\log_{10} p = A - \frac{B}{C + T}\,, \tag{5.1}$$

where p is the vapor pressure, T is temperature, and A, B, and C are constants defined by the compound of interest. Additionally, the pressure decreases by about $12\,\mathrm{mbar}$ every

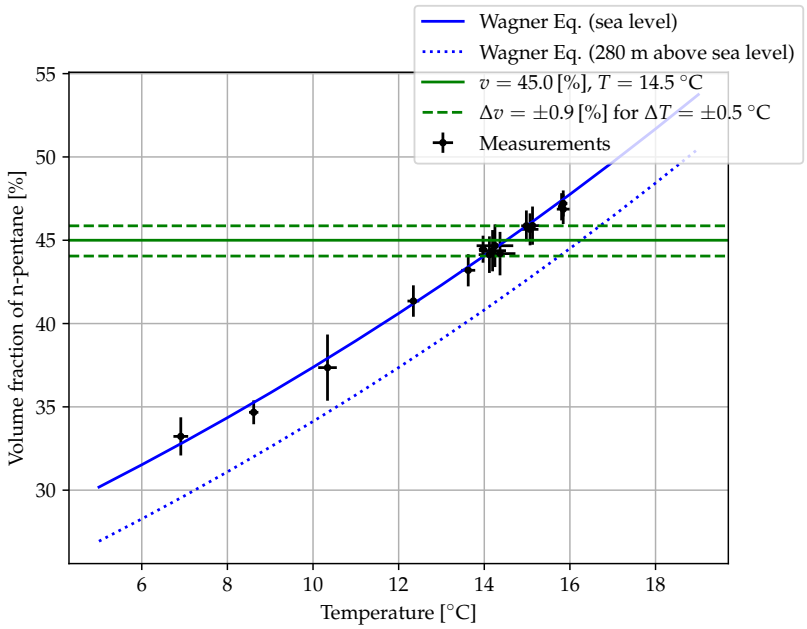

Figure 5.8: Predicted dependence of the n-pentane volume fraction in the gas mixture as a function of the temperature (solid line) as derived using the Wagner Eq. (5.2). The pressure drop due to the altitude difference of the laboratory (located in Freiburg at 280 m above the sea level) is presented as a dotted line. The green horizontal line displays the desired working point of the sTGC gas mixture along with a temperature variation of half a degree Celsius (dashed line), corresponding to the fluctuation of cooling temperature.

100 m at low altitudes above the sea level. In Freiburg, an atmospheric pressure drop of about 32.5 mbar is expected at 280 m of altitude. The *Wagner equation* [413] is known to improve the description given by Eq. (5.1), performing well in a wider range of temperatures,

$$\ln p_{\text{red}} = \frac{a(1-T_{\text{red}}) + b(1-T_{\text{red}})^{1.5} + c(1-T_{\text{red}})^{2.5} + d(1-T_{\text{red}})^{5}}{T_{\text{red}}}\,, \tag{5.2}$$

where T_{red} and p_{red} are the fractions of temperature and pressure with respect to the critical values (the so-called *reduced* temperature and pressure), respectively. The parameters a, b, c, and d are tabulated and they are characteristic of the chemical compound [409].

Figure 5.8 displays the dependence of n-pentane volume fraction on temperature, considering the parameters of Eq. (5.2) from Ref. [414]. The vapor pressure of n-pentane correlates directly with temperature, yielding a desired working point of $45.0 \pm 0.9\,\%$ at approximately $14.5 \pm 0.5\,^{\circ}\text{C}$. The uncertainty in temperature accounts for fluctuations of the cooling equipment, larger than the temperature measurement. The corresponding fluctuation of n-pentane concentration meets the sTGC requirements (lower than $\pm 3\,\%$). Assuming no losses of CO_2 gas flow throughout the mixing procedure, the volume of n-pentane in the gas can be inferred from the ratio of mass flow rates after and before the mixing system by imposing mass flow conservation. The mean measured values performed along time with the gas system presented in Figure 5.4 are displayed as black dots, whose uncertainties are computed as the standard deviation of all measured values. The experimental results align with the Wagner equation trend within uncertainties, validating the gas mixture characterization method. The data supports the Wagner equation without altitude-related pressure drop. This means that the overall pressure difference

from the setup altitude and the exhaust system matches the pressure increase from the mixing mechanism, the sTGC chamber, and the overpressure valve. The verification of Eq. 5.2 confirms that the implemented gas system is ready for safe operation in sTGC chambers with flexible n-pentane concentrations for muon measurements.

5.4 Conclusions

The small-strip Thin Gap Chambers in the ATLAS New Small Wheel play a crucial role in meeting tracking and triggering requirements in the anticipated high-luminosity conditions of the Large Hadron Collider. To ensure optimal gas amplification and signal readout, a continuous supply of a saturated gas mixture (55% CO_2 and 45% n-pentane) under stable and safe conditions is essential, with the detector performing optimally under high voltages ($2.8\,\mathrm{kV}$). This dissertation details the design, installation, and validation of the gas and high voltage systems required for operating these detectors in a new laboratory in Freiburg. The four high-voltage channels pass all stress and stability tests, and the gas system can supply both pure CO_2 and the nominal mixture while meeting safety requirements during adverse events. Protocols for handling, transportation, and storage of n-pentane are included, and the gas system is third-party certified for safe operation. Remote monitoring and operation are implemented for both gas and high voltage systems. The system meets gas concentration requirements, and the gas is characterized by accurately reproducing the temperature dependence of n-pentane vapor pressure with sufficient stability.

Chapter 6

Statistical Methods for Cross-Section Measurements and Their Interpretations

"Between living and dreaming there is a third thing. Guess it."

— Antonio Machado (1875 – 1939).

In high-energy particle physics, complex processes are experimentally detected by sophisticated instruments. The quantum properties of the interactions produced and their record with particle detectors bring inherent randomness, requiring advanced statistical methods for modeling and interpretation. Chapter 2 has highlighted the dependence on MC techniques in simulating Standard Model processes. The simulation of SM processes, from the calculation of the hard-scattering process up to the modeling of the detector response, relies heavily on MC techniques to address the aforementioned intrinsic randomness. Any conclusions made from such datasets must be drawn based on probabilistic prescriptions. Discrepancies between predicted and measured distributions may arise from fluctuations in stringently-constrained datasets, limited accuracy in model predictions, and finite knowledge of detector response and reconstruction methods. These limitations must be carefully categorized and quantified in statistical analyses, included as *uncertainties* associated with the measured properties of the reconstructed objects in the event. These analyses facilitate the extraction of pertinent information, allowing the derivation of quantitative conclusions from observations. Moreover, they provide means to test various signal hypotheses that might be involved in the production of the recorded dataset with sufficient confidence.

Following Ref. [415], this chapter summarizes the main concepts of such statistical methods. Sections 6.1 and 6.2 introduce the relevant methods for the estimation of parameters and hypothesis testing, respectively, using experimental data. The impact of detector inefficiencies on reconstructed observables can be quantified and corrected using MC simulation. Section 6.3 details unfolding techniques employed for these corrections, enabling the publication of detector-independent experimental results. Unfolding allows direct comparisons not only between experiments but also with theoretical predictions from the community.

In this thesis, production cross sections of W-boson pairs in pp collisions at $\sqrt{s} = 13$ TeV are extracted using data recorded at the LHC with the ATLAS detector. The methodology used to perform those measurements, based on the techniques outlined in this chapter, are discussed in Chapter 9. Chapter 10 presents the measurements of both fiducial differential (Section 10.2) and integrated cross sections (Section 10.3) of W^+W^- production. Within the framework of EFTs (discussed in Section 1.7), the analysis explores anomalous couplings between SM fields, constraining their presence in agreement with the data. Statistical inference in Chapter 11 evaluates intervals for each coupling at a given confidence level.

6.1 Parameter Estimation

In statistical interpretations of data produced in particle collisions, events recorded in two consecutive bunch-crossings are considered as completely independent. In this sense, the observables extracted from collision data can be treated as *random variables* within the formalism of probability theory. These random variables follow a given *probability distribution function* (pdf) that connects the measurements with the theoretical models. In this context, if all the information regarding the physics process is encoded in a set of n random variables, $\boldsymbol{x} = \{x_1, \ldots, x_n\}$, each event is considered as a *measurement* where each of those variables take a specific value, $\bar{\boldsymbol{x}} = \{\bar{x}_1, \ldots, \bar{x}_n\}$. An *event sample* $\bar{\boldsymbol{X}} = \{\bar{\boldsymbol{x}}_1, \ldots, \bar{\boldsymbol{x}}_M\}$ is constructed with a set of M measurements of the variables $\bar{\boldsymbol{x}}_i$ of such a process in each event. If the physics model that describes the recorded data depends on a series of parameters $\boldsymbol{\theta} = (\theta_1, \ldots, \theta_m)$, so does the pdf $f(\boldsymbol{x}|\boldsymbol{\theta})$ that characterizes the behaviour of the random variables $\boldsymbol{x}$. Experimentally, the pdf not only needs to describe the different particle physics processes involved, but also the detector response, which typically results in complex forms of the pdf with large number of unknown parameters to be determined. A *statistical inference*, commonly referred to as *fit*, starts with the determination of the *parameters of interest* (POIs), $\boldsymbol{\theta}$, to be extracted from the experimental data. The POIs are later used for *hypothesis testing* of different physics models. Due to the intrinsic randomness of the observables extracted from measurements, the true values of these parameters always remain unknown and *estimations* of their values within an uncertainty have to be pursued with a given *confidence level*[1] α.

Assuming a certain hypothesis for $f(\bar{\boldsymbol{x}}|\boldsymbol{\theta})$ (including the value of $\boldsymbol{\theta}$) describing the distribution of $\boldsymbol{x}$, given all x_i, $i = 1, \ldots, n$ being statistically independent, the probability for a particular dataset $\bar{\boldsymbol{X}}$ is the product of the individual probabilities for each measurement $\bar{\boldsymbol{x}}$, i.e.,

$$\mathrm{L}(\bar{\boldsymbol{x}}|\boldsymbol{\theta}) = \prod_{i=1}^{M} f(\bar{\boldsymbol{x}}_i|\boldsymbol{\theta})\,. \tag{6.1}$$

This product of probabilities represents the *likelihood function* $\mathrm{L}(\bar{\boldsymbol{x}}|\boldsymbol{\theta})$[2], providing the compatibility of the measured values of the random variables, $\bar{\boldsymbol{x}}$, via the pdf $f(\bar{\boldsymbol{x}}_i|\boldsymbol{\theta})$ given values of the parameters $\boldsymbol{\theta}$. The closer the measurement $\bar{\boldsymbol{x}}$ and the parameters $\boldsymbol{\theta}$ are to their true values, the greater the likelihood[3] $\mathrm{L}(\bar{\boldsymbol{x}}|\boldsymbol{\theta})$ becomes. The parameters $\boldsymbol{\theta}$ can then

[1] This confidence, a probability, can be interpreted following mainly two schools of thought: On the one hand, the *frequentist approach* computes such probabilities, or *confidence level* α, by counting the fraction of favorable outcomes over the total number of repetitions of the experiment. The true value of θ is therefore expected to fall inside the uncertainty interval a fraction α of the repeated experiments. On the other hand, the probability in the *Bayesian approach* is a measure of the degree of belief about a certain outcome to be true, modified after each repetition of the experiment. In this context, the uncertainty or credible interval is believed to contain the true value of θ with a probability of α. Both approaches treat the data in different ways and therefore lead to different results. Unless stated different, the frequentist approach is adopted in the following and in the rest of this thesis. The uncertainty interval might also not be symmetric with respect to the central value in some cases, being denoted as $\theta = \hat{\theta}^{+\delta\theta_{\mathrm{up}}}_{-\delta\theta_{\mathrm{down}}}$.

[2] Note the abusive use of notation of conditional probability, although in the frequentist approach, a hypothesis H is only used as a random variable if it refers to the outcome of a repeatable experiment.

[3] This definition of the likelihood function cannot be interpreted as a probability distribution, even though each point represents the probability of measuring the values $\hat{\boldsymbol{x}}$, since the hypothesis under which $\boldsymbol{x}$ is sampled does not remain constant. Also, the integral of the likelihood function over the full parameter space does not necessarily add up to one.

be freely adjusted as arguments of the function $\mathrm{L}(\bar{\boldsymbol{x}}|\boldsymbol{\theta})$. The likelihood function can then be used as an *estimator* to find the set of parameters $\boldsymbol{\theta}$ that leads to the highest likelihood value for the measured variables $\bar{\boldsymbol{x}}$. This is known as *maximum likelihood estimator* (MLE)[4]. Depending on the complexity of the problem, the likelihood function may not have an expression that can be maximized analytically and numerical methods need to be employed. Since the available packages offer minimization algorithms, the negative logarithm of the likelihood function, $-2\log \mathrm{L}(\bar{\boldsymbol{x}}|\boldsymbol{\theta})$, is usually used for a better numerical performance

In particle physics experiments, it is convenient to fit the expected number of events of the process of interest sorted in n_{bins} bins of a histogram within a certain region of the phase space. In such cases, the number of events $\boldsymbol{N} = \{N_1, \ldots, N_{n_{\text{bins}}}\}$ expected to be measured in each bin b from a sample of independent events follow the Poisson distribution with mean value υ for a sufficiently-large sample. The parameters $\boldsymbol{\theta}$ can then be estimated by maximizing the so-called *profile likelihood* using the corresponding pdf $\mathrm{Poisson}(\boldsymbol{N}|\boldsymbol{\theta})$ as

$$\mathrm{L}\left(\boldsymbol{N}|\boldsymbol{\theta}\right) = \prod_{b}^{n_{\text{bins}}} \mathrm{Poisson}\left(N_b \middle| N_b^{\text{pred}}\left(\boldsymbol{\theta}\right)\right) \times \prod_{k}^{n_{\text{syst}}} f_k\left(\theta_k\right) = \prod_{b}^{n_{\text{bins}}} \frac{N_b^{\text{pred}}(\boldsymbol{\theta})^{N_b} e^{-N_b^{\text{pred}}(\boldsymbol{\theta})}}{N_b!} \times \prod_{k}^{n_{\text{syst}}} f_k\left(\theta_k\right) , \tag{6.2}$$

where n_{bins} is the total number of bins, N_b the number of observed events in the bin b, and $\upsilon \equiv N_b^{\text{pred}}$ is the expected number of events in the bin b of the process of interest, which depends on the parameters $\boldsymbol{\theta}$. The observed number of events is also subject to background contributions, their modeling, the detector response, its acceptance, and other effects. The corresponding uncertainties k, $k = 1, \ldots, n_{\text{syst}}$, can be modeled in the likelihood via *nuisance parameters* distributed as a given pdf f_k. Gaussian *profiles* are generally well justified by the central limit theorem to parameterize f_k. The nuisance parameters can also be constrained using auxiliary measurements[5].

After the nuisance parameters have been constrained, the deviations with respect to the pre-fit setup can be quantified by using the parameter *pulls*

$$\mathrm{pull}(\theta) = \frac{\hat{\theta} - \theta_0}{\Delta\theta} , \tag{6.3}$$

with $\hat{\theta}$ being the value of the parameter after the fit has been performed, and θ_0 its pre-fit value with uncertainty $\Delta\theta$. The pull of the parameter θ indicates the number of standard deviations that the parameter has been dragged by the fit with respect to its pre-fit value. For Gaussian-profiled uncertainties, the pull will be distributed as a standard Gaussian with mean zero and unit width [416], i.e., $\theta_0 = 0$ and $\Delta\theta = 1$. A pull of zero shows that the pre-fit expectation is good to describe the data. If large pulls are observed, the expected distributions fed into the fit are not suitable to describe the data within the expected uncertainties and further investigations are needed. If the uncertainty on a

[4] In the limit of a large number of experiments, the MLE is consistent, i.e., its bias (if present) tends to zero, and its efficiency tends to 1. MLEs are also invariant under reparameterizations of the likelihood function: if $\hat{\boldsymbol{\theta}}$ are the estimated values of the parameters after maximizing the likelihood function, then, for any transformation g over $L(\bar{\boldsymbol{x}}|\boldsymbol{\theta})$, the values that maximize the transformed likelihood function are $g(\hat{\boldsymbol{\theta}})$.

[5] Ideally, the likelihood of these auxiliary measurements in which their central values are determined should be included in the likelihood function of the problem under study. In practice, however, this is usually not feasible and they enter the likelihood function through constraining terms.

nuisance parameter is highly reduced compared to the pre-fit uncertainty of $\pm 1\sigma$, the nuisance parameter is said to be *overconstrained* by the data. The pre-fit (post-fit) *impact* of a nuisance parameter θ on the POI maximizing the likelihood $\hat{\mu}$ is defined as

$$\text{impact}(\theta) = \hat{\hat{\mu}}(\hat{\theta} \pm \Delta\theta) - \hat{\mu}\,,$$

i.e., the value of the POI obtained by fixing θ to its post-fit value varied by the pre-fit (post-fit) uncertainties. Assessing the impacts allows gauging which nuisance parameters contribute more strongly to the results of the fit.

Once the values of the parameters have been estimated, an uncertainty needs to be associated to their estimated value. In the approximation $N \to \infty$, the MLE for a given parameter is expected to follow a Gaussian distribution, and the statistical uncertainty can be obtained from its variance. The variance can be accessed in two ways. On the one hand, the experimental result can be simulated multiple times using MC methods, which allows getting a different estimate of the parameter in each iteration. The variance of the distribution of the MLE after combining the measurement from all pseudo-experiments is already the statistical uncertainty on the estimated value of the parameter. On the other hand, the likelihood function of the problem is expected to tend to a Gaussian when the size of the used sample is large. The $-\log L$ then results in a parabola, and the uncertainty on the parameter can be obtained as the values for which $-\log L$ increases by 2 with respect to its minimum.

The agreement between a data distribution and its description by a hypothesis providing a certain functional form f can be quantified using *goodness-of-fit* tests. In these, a test statistic sensitive to the level of agreement between the two distributions must be constructed. The *Pearson's χ^2 test* is one of the most common goodness-of-fit tests applied in particle physics. For binned distributions of the values $\bar{\boldsymbol{y}}$ across n_{bins} bins centered at x_i, the number of entries N_i in bin i can be compared with the expected histogram of entries ν_i within the uncertainty[6] of the prediction σ_i

$$\chi^2 = \sum_i^{n_{\text{bins}}} \frac{(\bar{y}_i - \nu_i)^2}{\sigma_i^2}\,, \tag{6.4}$$

If the function describes the data well, the differences between the measurement and the prediction should be ideally of the order or smaller that the uncertainty for all bins. The sum χ^2 is therefore expected to be close to n_{bins} in ideal cases. If the χ^2 value is significantly larger, the prediction is not ideal to describe the observation. Using the χ^2 test, the given prediction can also be optimized to describe the data distribution by fitting m of its parameters. In such a case, the *reduced* χ^2 is used, where the χ^2 sum is divided by the number of *degrees of freedom*, i.e. $n_{\text{bins}} - m$ for binned distributions.

6.2 Hypothesis Testing

The goal of a statistical test is to quantify the agreement of the data with respect to a given prediction by means of a *hypothesis test*. The hypothesis under evaluation is often the so-called *null* or *background-only hypothesis* H_0, constructed by postulating the experimental

[6] The values of x_i are considered to be exact, and measured and predicted histograms must be constructed with the same binning.

dataset to be produced only by SM processes. The *alternative* or *signal-plus-background hypothesis* H_1 assumes that also the process of interest has contributed to the recorded collisions, being contrasted against the null hypothesis based on the observations. The process of interest could be, e.g., a rare prediction of the SM that is to be observed, or new-physics effects. Hypothesis testing leads to the quantification of the probability of discarding one of them within a certain confidence level. If a pdf or likelihood function, $\mathrm{L}(\boldsymbol{x}|H_i)$, uniquely describes a hypothesis H_i, the hypothesis is said to be *simple*. If at least one of the parameters θ of the pdf is free, the hypothesis is *composite*. To quantify the level of agreement between the data and the given hypothesis, a *test statistic* t is constructed as a function of the measured variables $\boldsymbol{x}$. The compatibility between the hypotheses and the data is established in terms of a decision to accept or reject a given H_0 according to the defined *critical region* for t, or its complementary *acceptance region* separated by a given *decision boundary* t_{cut}. If the observed t lies in the critical region, H_0 is rejected. The critical region is chosen such that the probability for $t \leq t_{\mathrm{cut}}$ to be observed there, under assumption of the hypothesis H_0, is some value α called the *level of significance* of the test. If H_0 is accepted (i.e. $t \leq t_{\mathrm{cut}}$) but the true hypothesis was not H_0 but rather an alternative hypothesis H_1 one refers to the *power* of the test to discriminate against H_1.

The acceptance region giving the highest power (and hence the highest signal purity) for a given α (or selection efficiency $\varepsilon = 1 - \alpha$) between H_0 and H_1 is the region of the t-space such that

$$\lambda(\bar{\boldsymbol{x}}) = \frac{\mathrm{L}(\bar{\boldsymbol{x}}|H_1)}{\mathrm{L}(\bar{\boldsymbol{x}}|H_0)} > c\,,$$

where the constant c is determined by the desired α. As stated by the Neyman-Pearson lemma [417], this holds when the *likelihood ratio* $\lambda(\bar{\boldsymbol{x}})$ describing both hypotheses is uniquely defined, i.e., when both H_0 and H_1 are simple. As given in Eq. (6.1), the likelihood functions can be factorized as the product of the pdf of each of the variables x_i when the random variables $\boldsymbol{x}$ are independent from each other. If the two hypotheses under study are *nested* (i.e., the null hypothesis can be considered as a particular case of the alternative hypothesis), the following discriminant can be constructed,

$$q(\mu) = -2\ln\frac{\mathrm{L}(\boldsymbol{x}|\mu,\hat{\hat{\boldsymbol{\theta}}})}{\mathrm{L}(\boldsymbol{x}|\hat{\mu},\hat{\boldsymbol{\theta}})}\,. \tag{6.5}$$

where $\hat{\mu}$ and $\hat{\boldsymbol{\theta}}$ are the values estimated from data, and therefore the ones that maximize the likelihood function in the case of the alternative hypothesis, while $\hat{\hat{\boldsymbol{\theta}}}$ are the values that maximize the likelihood function under the assumption that $\mu = \mu_0 = 0$. These are obtained by performing two separate fits to data, where the values in the numerator are estimated fitting the pdf of the background-only hypothesis, while the values in the denominator are obtained by fitting the pdf of the background plus signal hypothesis. The test statistic built in this way is known as *profile likelihood ratio* and is frequently used in data analyses at the LHC to observe rare SM processes or to derive exclusion limits in case of no new phenomena is discovered in BSM searches. Confidence intervals of the POI μ can then be derived using Wilks' theorem [418] with the discriminant in Eq. (6.5) assuming that $q(\mu)$ follows the χ^2 distribution. In case the observation matches, to a certain level, the predictions from the background-only hypothesis, H_1 is examined to understand the compatibility of the measurement with an underfluctuation of the signal process, with the main objective of rejecting it in favor of the null hypothesis. In this

sense, the two hypotheses are inverted with respect to the computation of the *p-value*, which is now computed for the pdf of the test statistic under H_1. Differently to the case of discovery of new physics, the p-value required to reject the signal hypothesis is usually set to $p < 0.05$, which corresponds to confidence level of $95\,\%$.

6.3 Unfolding

According to the considerations made in Section 1.5, the expected event candidates in pp collisions for a given process depend on the product of the predicted production cross section and integrated luminosity. However, corrections have to be considered to account for the non-ideal detection efficiencies. The efficiency is subject to factors like detector acceptance, resolution, and reconstruction efficiencies, varying across the phase space. This complexity increases in differential cross-section measurements. In the context of binned-distributions from multiple particle collisions, detector effects may cause events to deviate from the theoretical expectation across bins. Addressing these effects through unfolding techniques involves correcting the distributions, enabling the estimation of the theoretical predictions. The understanding of experimental effects guides the design of the unfolding procedure, resulting in several *unfolding inputs* derived from simulated collisions.

The number of events observed in data $N_{\mathrm{data,\,i}}$ in the bin i can be parameterized as the sum of detector-corrected signal distribution μ predicted by a given model (e.g., the SM) plus the corresponding number of event candidates expected to arise from background contributions $N_{\mathrm{bkg,\,i}}$,

$$N_{\mathrm{data,\,i}} = \sum_{j}^{n_{\mathrm{bins}}} R_{ij}\mu_j + N_{\mathrm{bkg,\,i}}\,,$$

where the *response matrix* R accounts for the response of the detector that relocates events from the bin j of the theoretical distribution to the bin i of the reconstructed distribution. In this case, the theoretical distribution of the given signal can be *folded* from either the parton or the particle level to the reconstructed level by multiplying by the corresponding response matrix. The response matrix is usually constructed with (i) *fiducial corrections* f accounting for events outside the fiducial phase space that were reconstructed due to smearing effects in the detector, (ii) *efficiency corrections* ϵ due to detector reconstruction, and (iii) a *migration matrix* M obtained by contrasting the predicted distribution of interest versus its results after reconstruction. The matrix M provides the migration of signal events between bins caused by the reconstruction, and can be characterized by its *purity* and *stability*. The purity of M is quantified by the fraction of predicted events that where correctly reconstructed in the same bin, while the stability refers to the number of reconstructed events that originated from the same bin at truth level[7]. The response matrix can therefore be parameterized as

$$R_{ij} = \frac{1}{f_i} M_{ij}\epsilon_j\,.$$

The chosen binning for the predicted and reconstructed distributions can be optimized to target a specific signal significance in each bin.

[7] Although the definitions of purity and stability appear to be analogous, they are defined at particle and reconstructed level, respectively.

Since both detector effects and kinematic properties of the event are fully non-deterministic, the migration of a particular event to a certain bin of the reconstruction level should be addressed in a probabilistic manner. Various algorithms such as *bin-by-bin*, *migration matrix inversion*, or the *iterative Bayesian* methods allow unfolding reconstructed distributions, which are publicly available in libraries such as `RooUnfold` [419]. The later is used in this work and presented in the following.

The iterative Bayesian unfolding [420, 421] addresses the probabilistic behavior of the unfolding procedure by recursively solving the Bayes theorem using the output of the previous iteration as a prior probability. The unfolded events of an observable $\mathcal{O}$ in a given bin j at particle level can be computed as

$$N_{\mathcal{O},j} = \frac{1}{\epsilon_j} \sum_{i}^{n_{\text{bins}}} f_i N_{\mathcal{O},i} P(N_{\mathcal{O},j}|N_{\mathcal{O},i}) \,.$$

The unfolding matrix, denoted as $P(N_{\mathcal{O},j}|N_{\mathcal{O},i})$, represents the conditional probability of an observable $\mathcal{O}$ at particle level, given its value at detector level, being reconstructed in a given data bin. This probability is obtained making use of the Bayes theorem:

$$P(N_{\mathcal{O},j}|N_{\mathcal{O},i}) = \frac{P(N_{\mathcal{O},i}|N_{\mathcal{O},j})P(N_{\mathcal{O},j})}{\sum_j P(N_{\mathcal{O},i}|N_{\mathcal{O},j})P(N_{\mathcal{O},j})} \,,$$

with $P(N_{\mathcal{O},i}|N_{\mathcal{O},j})$ being the conditional probability of reconstructing values $N_{\mathcal{O},i}$ given the prediction $N_{\mathcal{O},j}$. The probability of observing the reconstructed distribution given the predicted distribution is therefore providing the migration matrix. The first prediction $P(N_{\mathcal{O},j})$ acts as the prior.

The unfolded distribution is influenced by the prior distribution, which relies on the given signal prediction on the first iteration. The arbitrary choice of the prediction used to parameterize the unfolding procedure introduces a bias in the unfolded measurement, becoming model-dependent. The increase of the number of iterations reduces the bias from the choice of the prior. An important parameter that optimizes the Bayesian unfolding method is the number of iterations. The closer the initial prediction is to the underlying true distribution, the faster the convergence of the iterative method becomes. However, increasing the number of iterations inevitably magnifies statistical uncertainties of the unfolding method, computed from the covariance matrix of the unfolded distribution, due to the feedback loop inherent in the algorithm. An optimized number of iterations can be found using pseudodata, balancing the reduction of the bias with still moderate statistical uncertainties [419].

Part III

W^+W^- Cross-Section Measurements and Interpretations

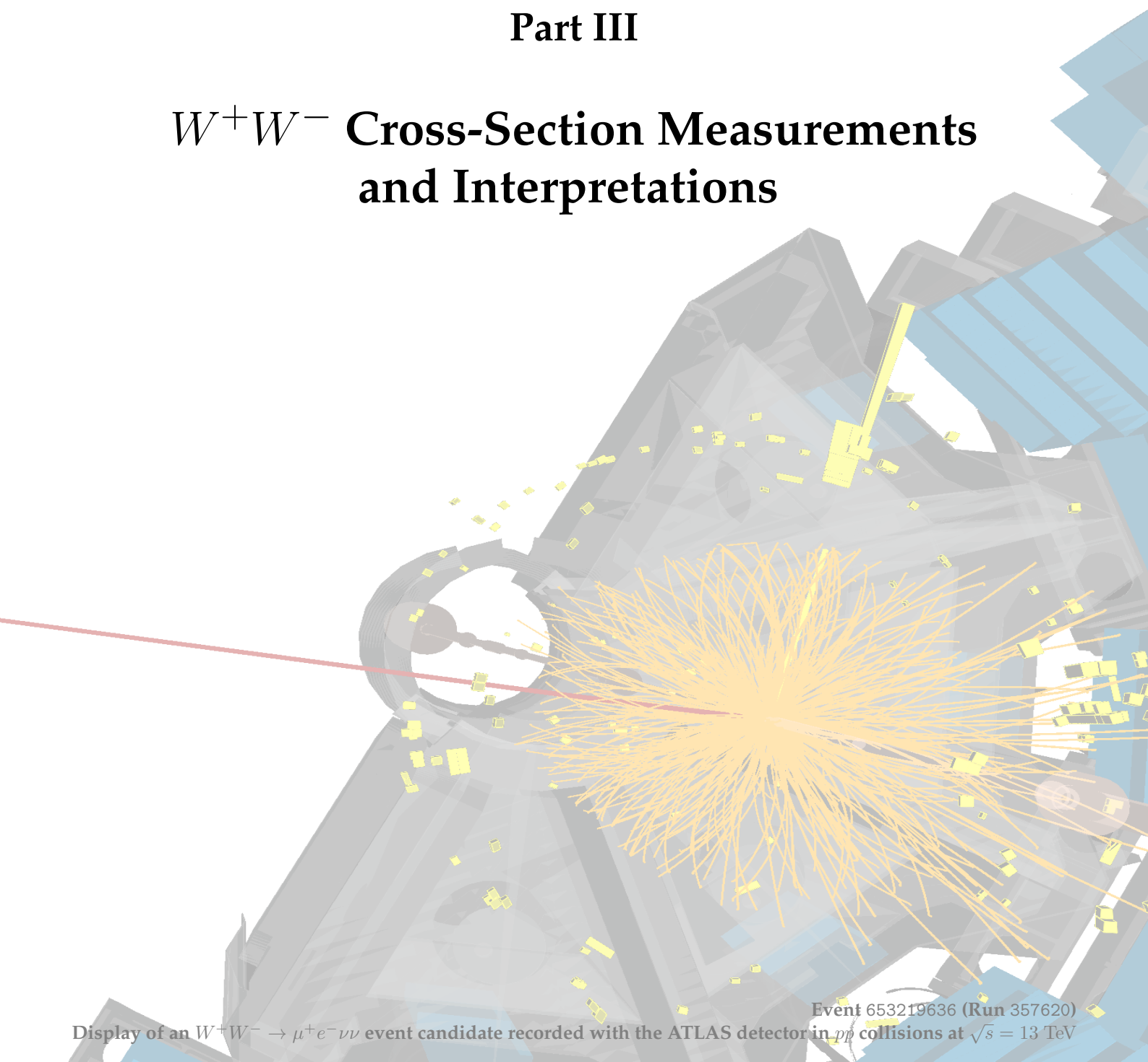

Event 653219636 (Run 357620)
Display of an $W^+W^- \to \mu^+e^-\nu\nu$ event candidate recorded with the ATLAS detector in pp collisions at $\sqrt{s} = 13$ TeV

Chapter 7
Analysis Strategy

"By three methods we may learn wisdom: First by reflection, which is noblest; second, by imitation, which is easiest; and third by experience which is bitterest."

— Confucius (551 – 479 B.C.).

In this thesis, an empirical determination of W^+W^- fiducial integrated and differential cross sections is conducted using data recorded with the ATLAS experiment. In this chapter, the analysis strategy is motivated and outlined. An overview of the decay modes in W-boson pair production exploited in experimental measurements along with their expected background contributions is outlined in Section 7.1. Section 7.2 provides an overview of previously reported W^+W^- measurements, and the results therein will inform the formulation of analysis strategy goals discussed in Section 7.3. The datasets which were scrutinized for the measurements presented in this work, comprising events from experimental data and simulated events using the MC techniques described in Chapter 2, are detailed in Section 7.4. Selection criteria of physical objects such as electrons, muons, jets, and missing transverse energy optimal for the analysis are defined. The selection criteria applied for this work, as well as the definition of the signal region (SR) for W^+W^- measurements, are described in Section 7.5.

7.1 Decay Modes and Backgrounds in W^+W^- Production

The production of W-boson pairs can result in several possible final states according to the decay modes of each of the produced massive gauge bosons:

- *Fully leptonic* decays ($W^+W^- \to \ell^-\bar{\nu}_\ell\ell'^+\nu_{\ell'}$) take place when each W boson of the pair decays leptonically into a lepton and a neutrino. The expected signature contains two well-reconstructed leptons within the detector acceptance whose transverse momenta are unbalanced due to the two untraceable neutrinos. In high-energy hadron colliders such as the Tevatron or the LHC, multiple SM processes with analogous signature are expected to contribute as *irreducible backgrounds*. Firstly, large contributions from leptonic Drell-Yan $Z + \text{jets}$ production are expected, especially in *same-flavor* decay channels (i.e., with $\ell = \ell'$) that can be suppressed by considering the resonant production of the Z boson and the momentum balance in the event selection. If the event sample is sufficiently large, the selection may be restricted to *different-flavor* decays ($W^+W^- \to e\nu_e\mu\nu_\mu$) to suppress this background, where only $Z \to \tau\tau$ decays can pass the selection. Secondly, top-quark production (mainly from $t\bar{t}$) will dominate in regions with additional hadron activity, especially from heavy-flavor hadron radiation. Such contributions can be reduced by suppressing hadron activity over a certain p_T threshold or implementing *flavor-tagging techniques* (Sec. 4.3.5). Additional irreducible backgrounds arise from diboson production VZ, with $V = W^\pm, Z$, where the additional leptons are not reconstructed due to limited detector acceptance or efficiency.

- If a hadronic and a leptonic decay happen simultaneously for each of the W bosons in the pair, a *semileptonic* decay takes place. In this case, the production cross section of both $W + \text{jets}$ and $Z + \text{jets}$, two and one orders of magnitude greater than that of W^+W^- production, respectively, overwhelms any reconstruction of the signal in hadron colliders.

- An even more challenging scenario is the reconstruction of *fully hadronic* W^+W^- decays into four quarks, which are then reconstructed as jets in the detector. In this decay mode, even more copious background contributions from QCD multijet (with a production cross section of the order of 10^6 pb, see Fig. 1.5) and hadronic decays in W and Z boson production are expected.

Additionally, *reducible backgrounds* can arise from the limited detector resolution and performance of object reconstruction. In W^+W^- measurements in hadron colliders, this is the case when a lepton is misreconstructed from hadronic activity or from a secondary hadronic decay. These sources are usually known as *fake* or *non-prompt* leptons, respectively, and arise from multijet production or, in fully leptonic decay modes, typically from $W + \text{jets}$ and semihadronic $t\bar{t}$ production.

7.2 Previous Measurements of W^+W^- Production

Measurements of W^+W^- production were accomplished in e^-e^+ collisions as one of the main goals of the scientific program of the LEP-II collider. The production of W-boson pairs was also measured in proton-antiproton ($p\bar{p}$) collisions at the Tevatron experiments CDF and D0 and in pp collisions at the LHC by ATLAS and CMS. In the following, a summary of the released measurements is presented in chronological order.

7.2.1 Tevatron

The first measurements of W^+W^- production were carried out at the Tevatron $p\bar{p}$ collider [86]. A first observation was reported by the CDF Collaboration at a center-of-mass energy of $\sqrt{s} = 1.8$ TeV [83], using fully-leptonic decays with an integrated luminosity of $108\ \text{pb}^{-1}$. This observation was followed by precision measurements achieved at the second run of LEP (next section) and the Tevatron with the D0 [422] and later with the CDF [423] experiments at $\sqrt{s} = 1.96$ TeV. The first reported total cross section at $\sqrt{s} = 1.96$ TeV by the D0 Collaboration is $11.5 \pm 2.1\,(\text{stat} + \text{syst}) \pm 0.7\,(\text{lumi.})\,\text{pb}$, using fully-leptonic decays $W^+W^- \to \ell\ell'\nu\nu'$ ($\ell = e, \mu$) and a recorded dataset of $1\ \text{fb}^{-1}$ with a precision of $19\,\%$ dominated by systematic uncertainties arising from the background estimates [424]. The CDF Collaboration reported later another measurement of the total W^+W^- production cross section of $12.1 \pm 0.9\,(\text{stat.}) \pm 1.5\,(\text{syst.})\,\text{pb}$ [425], using an integrated luminosity of $3.6\ \text{fb}^{-1}$ and reducing the uncertainty of the total cross section to $15\,\%$ of signal and background events.

These first measurements on W-boson pair production at the Tevatron were later updated, increasing the integrated luminosity to $9.7\ \text{fb}^{-1}$ of $p\bar{p}$ collisions at a center-of-mass energy of $\sqrt{s} = 1.96$ TeV, reconsidering also the selection criteria. In the context of their Higgs boson search, the D0 Collaboration performed a measurement of the non-resonant

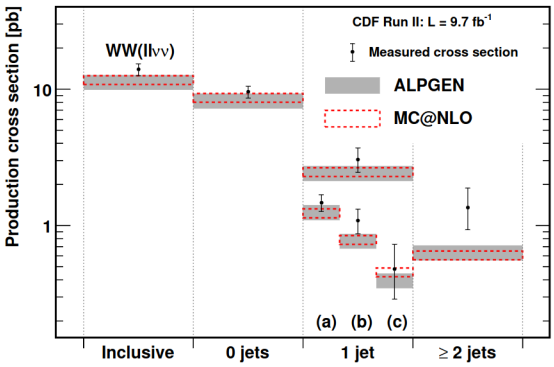

Figure 7.1: Measurement and predictions of the total production cross section of W-boson pairs measured by the CDF experiment in $p\bar{p}$ collisions at $\sqrt{s} = 1.96$ TeV at the Tevatron collider. Values are given inclusively and differentially as functions of jet multiplicity and jet transverse energy. Cross sections of $WW + 1\,\text{jet}$ production are given differentially in jet transverse energy for (a) $15 < p_T^{\text{jet}} < 25\,\text{GeV}$, (b) $25 < p_T^{\text{jet}} < 45\,\text{GeV}$, and (c) $p_T^{\text{jet}} > 45\,\text{GeV}$. Source: [85].

W^+W^- production cross section [84]. A set of boosted decision trees were developed to isolate signal events from background contributions. The measurement was achieved in regions with none and one jets in the final state, defined with $p_T^{\text{jet}} > 20\,\text{GeV}$ and $|\eta^{\text{jet}}| < 2.4$ for a cone of $\Delta R = 0.5$,

$$\sigma_{\text{D0-II}}(p\bar{p} \to W^+W^-) = 11.6 \pm 0.4\,(\text{stat.}) \pm 0.6\,(\text{syst.})\,\text{pb},$$

decreasing the uncertainty of the cross-section measurement to $6.2\,\%$, which is dominated by multijet, $W + \text{jets}$ and $Z + \text{jets}$ background estimates. The result is in agreement with the SM prediction of $11.3 \pm 0.7\,\text{pb}$ at NLO in QCD.

CDF also reported a total cross-section measurement of W^+W^- in a jet-inclusive phase space [85],

$$\sigma_{\text{CDF-II}}(p\bar{p} \to W^+W^-) = 14.0 \pm 0.6\,(\text{stat.}) \pm 1.1\,(\text{syst.}) \pm 0.8\,(\text{lumi.})\,\text{pb},$$

with a precision of $10\,\%$ and consistent with the SM prediction at both fixed-order and including parton shower effects. A neural network was trained to discriminate between signal and backgrounds, with no requirements on the jet multiplicity. The publication reported, for the first time, differential distributions in bins of jet-multiplicity and p_T^{jet} shown in Figure 7.1, with jets selected with $p_T^{\text{jet}} > 15\,\text{GeV}$ and $|\eta^{\text{jet}}| < 2.5$ reconstructed in a cone of $\Delta R = 0.4$.

7.2.2 LEP-II

In e^-e^+ collisions, W-boson pairs were experimentally accessible for the first time during the second run of the LEP collider, referred to as LEP-II. From 1996 until 2000, these collisions were recorded by the ALEPH [426], L3 [427], OPAL [428], and DELPHI [429] experiments at progressively increasing center-of-mass energies ranging from $\sqrt{s} = 161$ GeV up to $\sqrt{s} = 206$ GeV. Each of the four detectors recorded an integrated luminosity of about $0.7\ \text{fb}^{-1}$, corresponding to more than 40 000 expected W-boson pair candidates.

Due to the clean environments of e^-e^+ collisions, all decay channels of the W^+W^- system can be experimentally exploited for cross-section measurements: fully-leptonic decays ($\ell\ell'\nu\nu'$, with $\ell = e, \mu, \tau$), semihadronic decays ($qq\ell\nu$), and fully hadronic decays ($qqqq$). In fully leptonic events, the main backgrounds arise from $ee \to Z/\gamma* \to \ell\ell$ where the final state manages to fake the missing momentum balance characteristic of the W^+W^- decay. This happened specially in $\tau\tau$ final states. Four-fermion final states (for instance ZZ where one of the Z decays into neutrinos) act as an irreducible background of this measurement. Production of $\gamma\gamma \to \ell\ell$ events can also fake W^+W^- final states. Among the fully-leptonic channels, the background contamination varies between $8\,\%$ and roughly $25\,\%$ in channels where one τ lepton is involved[1], according to the selection efficiencies. Background contaminations in semihadronic events vary between $4.5\,\%$ and $9\,\%$. Backgrounds in the fully hadronic decay mode constitute less than $1\,\%$ of the selected events.

The LEP-II combination of the ALEPH [431], L3 [432], DELPHI [433], and OPAL [430] results up to the highest center-of-mass energies are in agreement with the theoretical predictions [59]. In Figure 1.4, the data are also compared with hypothetical predictions where W-pair production happens in absence of the ZWW triple gauge coupling predicted by the SM, or where WW can only be produced via neutrino mediation. Theoretical calculations above $170\,\mathrm{GeV}$ have uncertainties of $0.7\,\%$, being lower at higher center-of-mass energies. Data favors the necessity for diagrams with a ZWW vertex, an astonishing confirmation of the non-abelian nature of the electroweak SM up to the $1\,\%$ precision level.

7.2.3 LHC

Measurements of W-boson pair production have been reported by both ATLAS [305] and CMS [306] experiments at different center-of-mass energies at the LHC (see Table 4.5).

At $\sqrt{s} = 7$ TeV, the reported total cross sections from ATLAS [73] and CMS [74] are

$$\sigma^{7\,\mathrm{TeV}}_{\mathrm{ATLAS}}\,(pp \to W^+W^-) = 51.9 \;\pm\; 2.0\,(\mathrm{stat.}) \;\pm\; 3.9\,(\mathrm{syst.}) \;\pm\; 2.0\,(\mathrm{lumi.})\,\mathrm{pb}\,,$$

$$\sigma^{7\,\mathrm{TeV}}_{\mathrm{CMS}}\,(pp \to W^+W^-) = 52.4 \;\pm\; 2.0\,(\mathrm{stat.}) \;\pm\; 4.5\,(\mathrm{syst.}) \;\pm\; 1.2\,(\mathrm{lumi.})\,\mathrm{pb}\,,$$

using $4.6\ \mathrm{fb}^{-1}$ and $4.9\ \mathrm{fb}^{-1}$, respectively. Both of them are consistent with the SM prediction of $44.7 \pm 2.0\,(\mathrm{stat.}) \pm 4.5\,(\mathrm{scale}) \pm 3.0\,(\mathrm{PDF})\,\mathrm{pb}$ at NLO in QCD. Both results followed earlier ATLAS [434, 435] and CMS [436] measurements at the LHC Run 1. These measurements exploited the fully leptonic decay modes of the W^+W^- system, using both same-flavor (e^-e^+ and $\mu^-\mu^+$) and different-flavor decays ($\mu^\pm e^\mp$) to collect sufficient statistics.

New measurements were released at the LHC Run 1 at an increased center-of-mass energy of $\sqrt{s} = 8$ TeV and integrated luminosity, yielding W^+W^- total cross-section measurements of

$$\sigma^{8\,\mathrm{TeV}}_{\mathrm{ATLAS}}\,(pp \to W^+W^-) = 71.1 \;\pm\; 1.1\,(\mathrm{stat.}) \;\pm\; 5.4\,(\mathrm{syst.}) \;\pm\; 1.4\,(\mathrm{lumi.})\,\mathrm{pb}\,,$$

$$\sigma^{8\,\mathrm{TeV}}_{\mathrm{CMS}}\,(pp \to W^+W^-) = 60.1 \;\pm\; 0.9\,(\mathrm{stat.}) \;\pm\; 3.2\,(\mathrm{exp}) \;\pm\; 3.1\,(\mathrm{theo}) \;\pm\; 1.6\,(\mathrm{lumi.})\,\mathrm{pb}\,,$$

[1] Percentages given in this paragraph are taken from the OPAL measurement of W-boson pairs [430].

from ATLAS [75] and CMS [76], with an integrated luminosity of $20.3\ \text{fb}^{-1}$ and $19.4\ \text{fb}^{-1}$, respectively. Fully leptonic decays into e^-e^+, $\mu^\pm e^\mp$, and $\mu^-\mu^+$ were selected by both experiments, using also a third-lepton veto to suppress other multiboson contributions. While ATLAS used a jet veto (where jets with $p_T^{\text{jet}} > 25\,\text{GeV}$ and $|\eta^{\text{jet}}| < 4.5$ were reconstructed with the anti-k_t algorithm with $R = 0.4$) to suppress contributions from top-quark background sources, CMS selected final states with either 0 or 1 jet (within $p_T^{\text{jet}} > 30\,\text{GeV}$ and $|\eta^{\text{jet}}| < 4.7$). CMS also rejected events with two or more b-tagged jets (i.e., requires $N_{b-\text{jets}} < 2$) for this measurement. Both experiments implement data-driven estimations of the background contributions from top-quark and lepton misidentification with a precision of $10\,\%$ ($10-20\,\%$) and $55\,\%$ ($35\,\%$ for e fakes and $50\,\%$ for μ fakes) of the background yield in the signal region of the ATLAS (CMS) result. Both measurements have a precision of $8\,\%$. The ATLAS total cross-section measurement is dominated by systematic uncertainties from the jet energy scale, the background modeling of misidentified leptons, and the luminosity measurement. Theory modeling uncertainties due to the jet veto and lepton efficiency uncertainties dominate the CMS result. While the theoretical prediction of $63.2 \pm 1.5\,(\text{scale}) \pm 1.2\,(\text{PDF})\,\text{pb}$ at NNLO in QCD is in excellent agreement with the CMS measurement, this prediction underestimates the ATLAS measurement by about 1.3 standard deviations.

The disagreement of the ATLAS measurement in the jet-vetoed region was alleviated with a second measurement requiring opposite-flavor leptonic decays with one additional jet in the final state [77]. The fiducial cross section for $\leq 1\,\text{jets}$ is determined simultaneously by combining 0-jet (from Ref. [75]) and 1-jet fiducial cross sections using a log-likelihood fit to the data. The result in the fiducial phase space is extrapolated to the full phase space, giving a total production cross section of

$$\sigma^{8\,\text{TeV}}_{\text{ATLAS}}\,(pp \to W^+W^-) = 68.2\ \pm\ 1.2\,(\text{stat.})\ \pm\ 3.4\,(\text{syst.})\ \pm\ 2.8\,(\text{lumi.})\,\text{pb}\,,$$

which agrees slightly better with the theoretical prediction. The precision of the total cross-section measurement is improved to $6.9\,\%$.

After analyzing the first $3.16\ \text{fb}^{-1}$ of LHC Run 2 data [78], ATLAS published a fiducial cross-section measurement of W-boson pairs at $\sqrt{s} = 13$ TeV using an increased dataset of $36.1\ \text{fb}^{-1}$ recorded in 2015 and 2016 [79]. The event selection involves criteria on $p_T^{\text{miss}} > 30\,\text{GeV}$, $p_T^{e\mu} > 30\,\text{GeV}$, and $m_{e\mu} > 55\,\text{GeV}$ to suppress Drell-Yan and lepton misidentification backgrounds, as well as a b-jet veto for $p_T^{\text{jet}} > 20\,\text{GeV}$ and $|\eta^{\text{jet}}| < 2.5$ and a jet veto for $p_T^{\text{jet}} > 35\,\text{GeV}$ and $|\eta^{\text{jet}}| < 4.5$. The measured total cross section is

$$\sigma^{13\,\text{TeV}}_{\text{ATLAS},\,36\ \text{fb}^{-1}}\,(pp \to W^+W^-) = 137\ \pm\ 2\,(\text{stat.})\ \pm\ 10\,(\text{syst.})\,\text{pb}\,,$$

with a total uncertainty of $7.4\,\%$ dominated by systematic uncertainties from b-tagging ($3.4\,\%$), the modeling of the lepton misidentification background ($3.1\,\%$), the jet energy scale uncertainty ($3.0\,\%$), and the modeling of the top-quark background ($2.6\,\%$). Top-quark and lepton misidentification backgrounds are estimated using data-driven techniques.

The ATLAS measurement at $\sqrt{s} = 13$ TeV using the partial LHC Run 2 dataset was followed by CMS using $35.9\ \text{fb}^{-1}$ [80]. A novel strategy was pursued in this publication. First, a total production cross section is reported by carrying out a (traditional) sequential cut-based analysis by selecting W^+W^- events in four regions of the phase space with

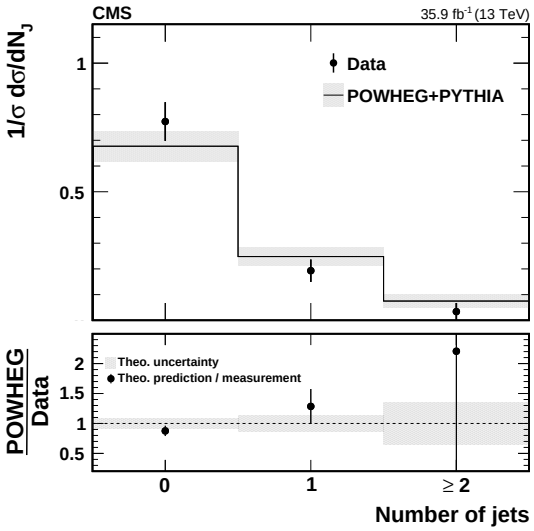

Figure 7.2: W-boson pair production cross section in pp collisions at $\sqrt{s} = 13$ TeV recorded with the CMS detector as a function of the jet multiplicity in bins of 0, 1 and 2 or more jets. After background subtraction, Data is shown as black points. Solid lines represent the SM prediction obtained with POWHEG+PYTHIA. The lower panel shows the ratio of the theoretical prediction to the measurement. The error bars on the data points represent the total uncertainty of the measurement, and the shaded band shows the uncertainty of the MC prediction. Source: [80].

same- and different-flavor dilepton decays where none or exactly one additional jet in the final state is reconstructed. With this approach, top-quark contributions are suppressed by discarding events containing b-tagged jets. The Drell-Yan background is reduced using a BDT discriminant. The total cross section is extracted from a simultaneous fit of the four regions of the phase space, yielding the result

$$\sigma_{\mathrm{CMS}}^{13\,\mathrm{TeV}}\,(pp \to W^+W^-) = 117.6 \;\pm\; 1.4\,(\mathrm{stat.}) \;\pm\; 5.5\,(\mathrm{syst.}) \;\pm\; 3.2\,(\mathrm{lumi.})\,\mathrm{pb}\,,$$

consistent with the SM prediction of $118.8 \pm 3.6\,\mathrm{pb}$ at NNLO. The uncertainty of the total cross-section measurement is $5.7\,\%$, dominated by systematic uncertainties on the luminosity measurement, jet energy scale and resolution, as well as uncertainties from lepton selection efficiencies. In addition, an independent measurement relies on two *random forest discriminants*, trained to classify signal versus Drell-Yan and top-quark backgrounds, using the cut-based analysis preselection as a baseline. This approach yields a purer signal compared to the sequential-cut analysis, although with a strong bias of the signal sensitivity towards low values of p_T^{WW}. In this region, the production cross section of total W^+W^- is independently measured with an accuracy of $6.6\,\%$. The degraded precision observed in cross-section measurements using the random-forest approach is caused by a significant reliance on signal modeling, particularly enhanced in the extrapolation of the fiducial cross section to the full phase space. Since the random forest does not apply explicit requirements on the jet multiplicity, a measurement of event fractions was published, as shown in Figure 7.2, where jets with $p_T^{\mathrm{jet}} > 30\,\mathrm{GeV}$ and $|\eta^{\mathrm{jet}}| < 2.4$ are binned into $N_{\mathrm{jets}} = 0, 1, \geq 2$. After unfolding the distribution to the particle level, measured fractions exhibit total uncertainties of $7.9\,\%$, $22.6\,\%$, and $100\,\%$ in the 0, 1, and $\geq 2\,\mathrm{jets}$ bins, respectively, driven by systematic uncertainties. This is the first unfolded distribution of the jet-multiplicity in W-boson pair production measured at the LHC, although

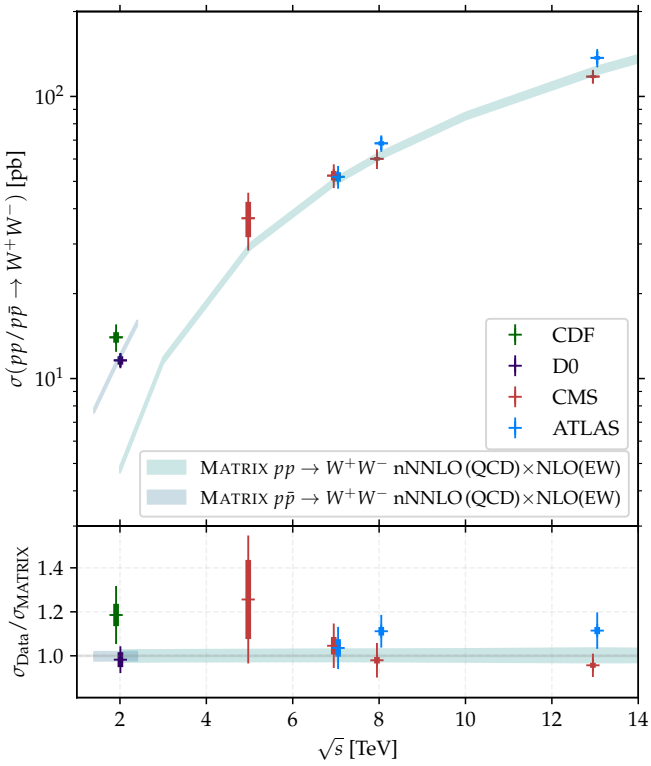

Figure 7.3: Comparison of W^+W^- measurements in $p\bar{p}$ collisions obtained by D0 [84] and CDF [85] Collaborations at $\sqrt{s} = 1.96$ TeV as well as in pp collisions by ATLAS [73, 77, 79] and CMS [72, 74, 76, 80] at $\sqrt{s} = 5.02$, 7, 8 and 13 TeV. The measurements are compared to the state-of-the-art theory prediction computed with MATRIX [231] at NNLO accuracy in QCD including EW corrections up to NLO. Contributions from gluon-gluon and photon-induced WW production are included up to NLO (nNNLO). The uncertainties on the theory prediction include effects from the 7-point scale variations of μ_F and μ_R and the choice of the PDF (NNPDF31-LUXQED [186]). The sum in quadrature of statistical, systematic, and luminosity uncertainties on the experimental values are shown in the error band, with the statistical component being displayed in a wider inner error.

influenced by substantial model dependence.

Furthermore, the CMS collaboration has conducted a measurement at the LHC, determining the W^+W^- production cross section at a center-of-mass energy of $\sqrt{s} = 5.02$ TeV,

$$\sigma_{\text{CMS}}^{5.02\,\text{TeV}}\,(pp \to W^+W^-) = 37.0 \;\pm\; 5.4\,(\text{stat.}) \;\pm\; 2.7\,(\text{syst.})\;\text{pb}\,.$$

The result, based on an integrated luminosity of 302 pb^{-1} [72], aligns with the SM prediction, albeit with a considerable relative uncertainty of 16 % dominated by the limited statistical dataset.

The aforementioned measurements both in $p\bar{p}$ and pp collisions are all summarized in Figure 7.3 for the reported center-of-mass energies of $\sqrt{s} = 1.96$ TeV in $p\bar{p}$ collisions at the Tevatron collider as well as $\sqrt{s} = 5.02$, 7, 8, and 13 TeV in pp collisions at the LHC. The measurements are compared with respect to the state-of-the-art theory prediction computed with MATRIX at NNLO accuracy in QCD, including EW corrections up to NLO. Contributions from gluon-gluon and photon-induced WW production, computed up to NLO, are included. The experimental results from various experiments and colli-

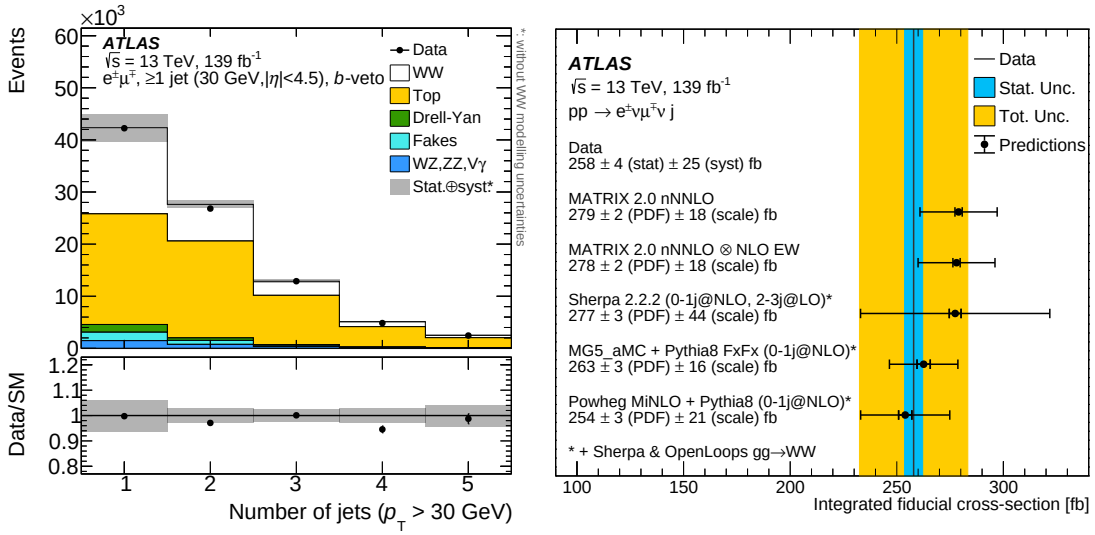

(a) (b)

Figure 7.4: (a) Pre-fit data and SM expectation as a function of the jet-multiplicity in the SR reported in the $WW+\geq 1\,\text{jets}$ production cross-section measurement by the ATLAS Collaboration at $\sqrt{s} = 13$ TeV. Data are shown as black markers, together with the predictions for the signal and background processes. The last bin contains also events with $N_{\text{jets}} > 5$. The lower panel displays the ratio of the data over the total prediction. The uncertainty bands show the sum of statistical and systematic uncertainties, excluding theory uncertainties on the signal. (b) Comparison of the measured fiducial $WW+\geq 1\,\text{jets}$ cross section with various theoretical predictions at parton level. Theoretical predictions are indicated as points with inner (outer) error bars denoting PDF (PDF + scale) uncertainties. The central value of the measured cross section is indicated by a vertical line with the narrow band representing the statistical uncertainty and the wider band the total uncertainty including statistical and systematic uncertainties. Source: [81].

sion energies are still in agreement with the predictions of the SM, whose precision has improved by approximately a factor of 2 over the last decade.

The first and only measurement at the LHC reporting differential measurements in a one-jet-inclusive phase space to date was performed by ATLAS using the full Run 2 dataset [81]. This complements the previous results arising from combinations in different bins of jet multiplicity. Fiducial and differential cross sections across twelve observables related to lepton, jet, and missing transverse energy kinematics were conducted. W-boson pairs were measured in association with jets (i.e. at least one jet must be reconstructed in the final state) with $p_T^{\text{jet}} > 30\,\text{GeV}$ and $|\eta^{\text{jet}}| < 4.5$. The event was discarded if any jet of $p_T^{\text{jet}} > 20\,\text{GeV}$ and $|\eta^{\text{jet}}| < 2.5$ contained b-hadron activity. Using different-flavor decays, Drell-Yan contributions were heavily suppressed by an additional requirement on the dilepton mass of $m_{e\mu} > 85\,\text{GeV}$. The jet-multiplicity distribution in the signal region is presented in Figure 7.4a once this selection has been applied. The signal region was heavily dominated by background contributions, mainly from the production of top-quark pairs. The fiducial cross-section measurement in this new phase space was determined with a precision of $10\,\%$, dominated by jet-related systematic uncertainties ($6.3\,\%$), followed by background modeling uncertainties of the top-quark ($4.5\,\%$), and non-prompt lepton ($4.3\,\%$) contributions. The fiducial cross section was found to be in good agreement with the state-of-the-art theory predictions at the date of the publication, which provided a precision of about $7\,\%$ on the predicted value, as shown in Figure 7.4b. This highlights the value reported by ATLAS, enabled by an innovative data-driven top-

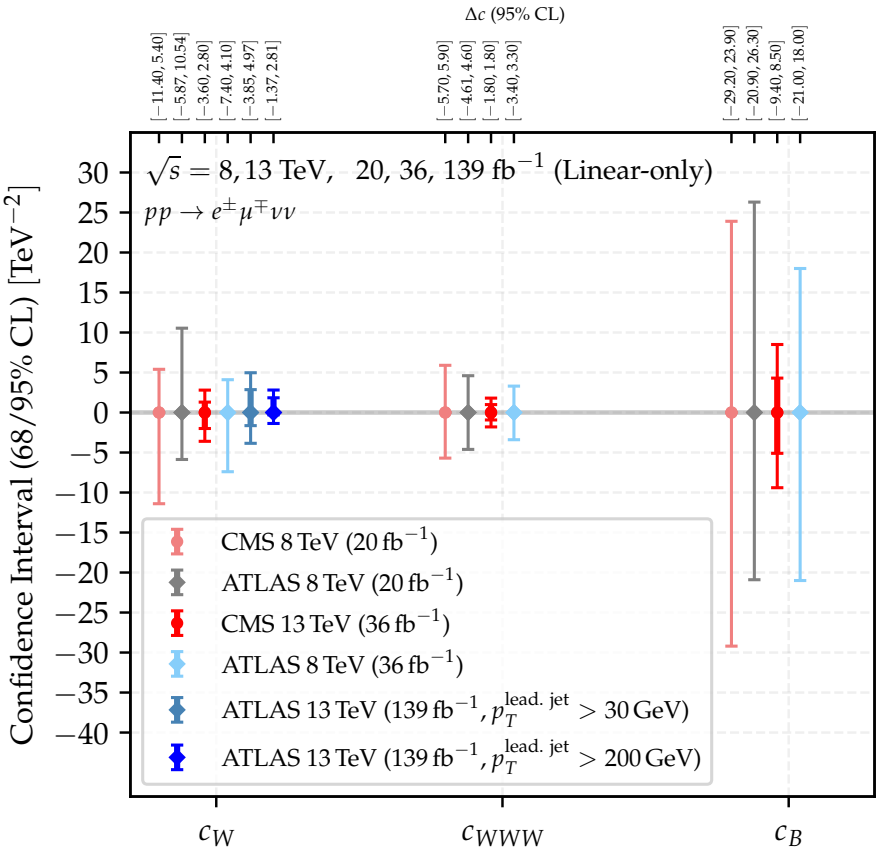

Figure 7.5: Observed 68 % (inner wider band) and 95 % (outer thinner band) confidence intervals on SMEFT Wilson coefficients reported in W^+W^- production cross-section measurements from data recorded in pp collisions at center-of-mass energies of $\sqrt{s} = 8$ TeV by ATLAS [75] and CMS [76], at $\sqrt{s} = 13$ TeV using a partial Run 2 dataset by ATLAS [79] and CMS [80], and with the full Run 2 dataset by the ATLAS Collaboration [81] in one-jet-inclusive final states. The latter reports constraints on SMEFT coefficients when the leading jet is reconstructed either with $p_T^{\text{lead. jet}} > 30$ GeV or $p_T^{\text{lead. jet}} > 200$ GeV to assess the suppression of the interference between SMEFT contributions from the c_W Wilson coefficient and the SM.

quark background estimate derived from the simultaneous determination of the effective $t\bar{t}$ differential cross section and the b-jet reconstruction efficiency. This method, described in Section 8.1, is improved for the analysis presented in this thesis.

Some of the referenced publications report limits on the $WW\gamma$ and WWZ aTGCs, whose contributions would enhance the production rate for diboson processes at high boson p_T and high invariant mass. These constraints are based on the HISZ [285] and the SMEFT parameterizations discussed in Section 1.7. Both ATLAS and CMS have reported limits on the dimension-six SMEFT operators $\mathcal{O}_{WWW}$, $\mathcal{O}_W$, and $\mathcal{O}B$, corresponding to the three CP-invariant couplings between electroweak vector bosons in the SMEFT parameterization [131]. The corresponding Wilson coefficients c_{WWW}, c_W, and c_B are regarded as free parameters. Anomalous effects in all reported results are restricted using templates in bins of either $p_T^{\text{lead. lep.}}$ or the $m_{\ell\ell}$ distribution, assumed to originate predominantly from diagrams in the dominant $q\bar{q} \to WW$ production. More stringent constraints are observed in physics analyses of pp collision data at higher center-of-mass

energies, which enhance the sensitivity to anomalous effects. Results from pp collisions at $\sqrt{s} = 13$ TeV by both ATLAS and CMS are also derived from larger datasets, corresponding to integrated luminosities of $36\,\text{fb}^{-1}$ and $139\,\text{fb}^{-1}$.

In diboson production studies, the SMEFT operator $\mathcal{O}_W$ is of special interest due to its enhanced sensitivity to gauge-boson self-couplings. Strong constraints on this operator can be achieved at the LHC energy regime as effects from anomalous gauge-boson self-couplings are more prominent at greater center-of-mass energies. However, the suppressed interference between the SM and amplitudes from anomalous couplings at higher energies, attributed to different helicities of the dominant contributions to the two amplitudes, limits the sensitivity to $\mathcal{O}_W$ [437, 438]. Consequently, the square of the anomalous dimension-six amplitude (proportional to the quadratic term c_W^2/Λ^4) dominates. This interference suppression not only weakens limits on c_W in measurements of diboson production but also challenges the validity of the dimension-six SMEFT model, as discussed in Section 1.7. Introducing a high-energetic jet alongside the diboson pair modifies the helicity configurations and reduces the interference suppression [439], as proven by the constraints reported in the $WW+\geq 1\,\text{jets}$ measurement by ATLAS [81].

7.3 Motivation of the Analysis Strategy

As discussed in Section 3.1, backgrounds from top-quark, Drell-Yan, lepton misidentification, and other sources such as diboson and triboson can fulfill the selection criteria and mimic the W^+W^- production decaying in fully leptonic final states. Different methods to estimate these background contributions have been followed in measurements at hadron collider experiments outlined in Section 7.2. The choice of the method depends on the composition of such a background in the phase space where the cross-section measurement should be conducted with a competitive level of precision. Figure 7.6 shows the composition of the SM prediction in the signal regions defined by the last two ATLAS measurements of W^+W^- cross sections with no reconstructed jets (Fig. 7.6a) [79] and with at least one jet (Fig. 7.6b) [81] in the final state. In both measurements, event candidates arising from top-quark production sources dominate the background composition despite being suppressed by a b-jet veto. The production of $t\bar{t}$ constitutes more than $90\,\%$ of the top-quark contributions, decaying almost exclusively[2] into $W^+W^- + b\bar{b}$. These contributions are therefore expected to dominate in regions of the phase space with high jet-multiplicity, even after vetoing events with b-tagged jets. In $W^+W^- \to \ell\ell'\nu\nu'$ production at leading order, no jets are expected in the final state. Additional hadron activity in this process arises via initial or final state radiation due to higher-order corrections in the perturbative expansion. W^+W^- production is therefore enhanced in regions with no jets. The composition of background sources from multiboson production and lepton misidentification varies mildly in events with and without additional jets in the W^+W^- signal regions, since their production is highly suppressed and it is mostly independent on the jet multiplicity of the event. Since Drell-Yan and multiboson production take place without additional parton radiation at leading order, an enhancement of these backgrounds with respect to top-quark contributions is expected when events without jets are selected.

[2] In the SM, the top-quark decays into a W-boson and a b-quark with a probability of $99.8\,\%$ as dictated by the W_{tb} coupling of the CKM matrix [95].

Source	Event yields $\pm$ (stat $\oplus$ syst)	
	(a)	(b)
Top	3120 ± 380	55800 ± 1500
Drell-Yan	431 ± 50	2200 ± 700
Fakes	310 ± 300	2700 ± 1100
Multiboson	380 ± 40	2800 ± 500
W^+W^-	7690 ± 230	28100 ± 1200
Total background	4240 ± 480	63500 ± 1800
Total SM	11930 ± 530	91600 ± 2500

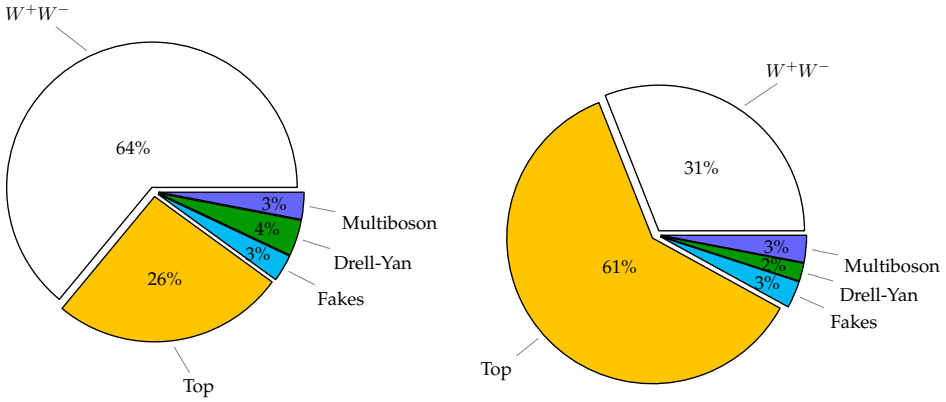

(a) $W^+W^- + 0$ jets 36 fb^{-1}. (b) $WW+\geq 1$ jets 139 fb^{-1}.

Figure 7.6: Composition of signal (W^+W^-), top-quark (Top), misidentified leptons (Fakes), and other diboson and triboson (Multiboson) background contributions of the SM prediction. Results are presented for signal regions defined in previous cross-section measurements of W^+W^- production of the ATLAS Collaboration at $\sqrt{s} = 13$ TeV, using (a) the partial (2015-2016) Run 2 dataset with no additional hadron activity in the final state [79], and (b) the full Run 2 dataset with at least one jet in the final state [81]. The table displays the total yield for each signal and background source, with errors representing the sum in quadrature of statistical and systematic uncertainties. The percentages on the charts indicate the relative contribution to the total SM prediction.

The expected W^+W^- signal as well as Drell-Yan and multiboson background contributions are usually estimated using MC simulations. The assigned uncertainties rely on the theoretical precision involved in the matrix element calculation (variations on factorization and renormalization scales in α_S), PDF, and parton shower modeling. Theoretical calculations of α_S up to NLO are incorporated for the two measurements shown in Figure 7.6, leading to uncertainties between $4\,\%$ and $30\,\%$, depending on the process and the region of interest.

The estimation of background contributions arising from fake and non-prompt leptons is of great importance in W^+W^- measurements at hadron colliders. In SM processes with production cross sections orders of magnitude greater than W^+W^- producing one prompt lepton, a dilepton final state can arise when another object (e.g, a jet) fulfills the lepton selection criteria of a prompt lepton or a secondary lepton is simply misassigned to the primary vertex[3]. Since MC simulations poorly model the detector effects that influence lepton reconstruction, data-driven techniques are indispensable to fulfill this task.

[3]This is the case of W + jets or semihadronic $t\bar{t}$ production, discussed in Section 8.4.3.

Although the event yields from fakes in the signal region are small, the modeling of this background is of great complexity, translating into large systematic uncertainties. This can be seen, e.g., in the W^+W^- results listed in Section 7.2.3. In the ATLAS results for $WW+\geq 1\,\text{jets}$ production at $\sqrt{s} = 8$ TeV, non-prompt lepton contributions are modeled with $40\,\%$ ($60\,\%$) accuracy in the signal region with 1 jet (0 jets) in the final state [75, 77]. Although fakes only constitute $7\,\%$ of the total background, its modeling is the main limiting factor in the precision of the cross-section determination [77]. Similar conclusions can be drawn from ATLAS analyses at a center-of-mass energy of $\sqrt{s} = 13$ TeV. In the $W^+W^- + 0\,\text{jets}$ measurement using a dataset of 36 fb^{-1}, fakes are estimated with a total relative error of $90\,\%$ using data-driven methods (see Fig. 7.6a). After uncertainties from flavor tagging, the modeling of this background constitutes the second largest uncertainty of the measured cross section [79]. These two results implemented the so-called *matrix method*, a widely used data-driven technique discussed in Section 8.4.1. Using the full Run 2 dataset, estimated event yields in the $WW+\geq 1\,\text{jets}$ signal region originating from fakes are estimated with a total uncertainty of $40\,\%$ (Fig. 7.6b), which is the third leading uncertainty of the cross-section measurement after jet calibration and top background modeling uncertainties. Fake background modeling uncertainties are dominant at the lowest $p_T^{\text{lead. lep.}}$ bin up to 40 GeV [81].

Systematic uncertainties related to the estimation of the top-quark background, the reconstruction of jets, and the b-jet tagging usually dominate W^+W^- cross-section measurements. A precise estimation of the top-quark background is therefore one of the cornerstones to achieve high precision in W^+W^- production. At the LHC in jet-vetoed W^+W^- signal regions such as the one presented in Figure 7.6a, the event yields arising from this background have been estimated with a precision of roughly $20\,\%$ at 7 TeV [73], converging to $10\,\%$ at 8 [75, 77] and 13 TeV [79] for the ATLAS measurements. These rely mainly on a data-driven method known as the *Jet Veto Survival Probability* (JVSP) [440], corresponding to a variant of the *transfer factor* (TF) presented in Section 8.1.2. In measurements where no jets are reconstructed in the signal region, the JVSP method can be used by extracting the probability of surviving the jet veto requirement in a control region dominated by the targeted background. The strong dependence on the data in this method reduces the modeling and detector-level uncertainties from the top-quark simulation compared to a fully MC-based background estimation. However, MC input is still required for the computation of the extrapolation factors to the signal region. The latest CMS measurement at $\sqrt{s} = 13$ TeV reports a precision of $5\,\%$[4] in jet-vetoed regions for the top-quark background estimate, as well as $3\,\%$ in 1-jet signal regions defined by the sequential-cut approach [80]. By including the normalization of the MC-based top-quark background yields in a simultaneous fit with the signal strength of the W^+W^- measurement, uncertainties related to the top-quark background are strongly constrained. The latest $WW+\geq 1\,\text{jets}$ measurement at $\sqrt{s} = 13$ TeV from ATLAS reports a precision of $2.7\,\%$ of the top-quark background yields in the signal region [81], achieved by using a data-driven method referred to as *b-tag counting*, which is based on an in-situ determination of the differental effective cross section of the $t\bar{t}$ background in the signal region. The level of precision of this background allows for the first time a competitive W^+W^- measurement in bins of high jet multiplicity in a model-independent approach, where the top-quark background constitutes $61\,\%$ of the total SM prediction and $88\,\%$ if the total

[4] These are post-fit uncertainties.

Process	Generator	Parton shower	PDF	Matrix element $\mathcal{O}(\alpha_S)$	Normalization
$q\bar{q} \to WW$	MiNNLO	Pythia 8	NNPDF3.0nnlo	NNLO	Generator
$gg \to WW$	Sherpa 2.2.2	Sherpa	NNPDF3.0nnlo	LO (0-1 jet)	NLO
$t\bar{t}$	Powheg Box 2	Pythia 8	NNPDF3.0nlo	NLO	NNLO+NNLL
Wt	Powheg Box 2	Pythia 8	NNPDF3.0nlo	NLO	NLO+NNLL
$Z+$jets	Sherpa 2.2.1	Sherpa	NNPDF3.0nnlo	NLO (0-2 jets), LO (3-4 jets)	NNLO
WZ, ZZ	Sherpa 2.2.2	Sherpa	NNPDF3.0nnlo	NLO (0-1 jet), LO (2-3 jets)	Generator†
$W\gamma, Z\gamma$	Sherpa 2.2.8	Sherpa	NNPDF3.0nnlo	NLO (0-1 jet), LO (2-3 jets)	Generator†

†: The cross section calculated by Sherpa is found to be in good agreement with the NNLO result [441, 442, 443, 444, 233].

Table 7.1: Summary of the nominal Monte Carlo simulated samples used in the analysis. The $gg \to WW$ simulation includes Higgs boson contributions. The last two columns give the order in α_S of the matrix element calculation and the overall cross-section normalization. The samples generated with Sherpa relies on its default set of tuned parton-shower parameters, while for the Powheg Box samples the A14 set of tuned parameters and the NNPDF2.3lo PDF set are employed for the parton shower.

background. This dissertation relies on an improved implementation of this approach, which is described in Section 8.1.

A way to maximize the signal acceptance in W^+W^- measurements would be to merge both strategies from the last two ATLAS measurements. On the one hand, the $WW+\geq 1\,\text{jets}$ measurement provides accurate background estimates with sensitivity to W^+W^- production at high jet multiplicities. On the other hand, the jet-vetoed region offers the best sensitivity to W^+W^- final states into fully leptonic channels, followed by larger theory and jet-related uncertainties arising from the jet-veto requirement (see Section 3.1). In this way, the sensitivity to W^+W^- production can be strongly increased in a fully jet-inclusive phase space. This can be achieved by exploiting the most precise theory predictions to date as well as an optimized estimation of the backgrounds.

The techniques implemented to estimate the top-quark, Drell-Yan and diboson backgrounds are outlined in Sections 8.1, 8.2 and 8.3, respectively. Special effort has been devoted to reduce systematic uncertainties of the fake lepton background, which constitutes one of the focuses of this dissertation. The sources of this background, the different methods implemented, and the corresponding systematic uncertainties are studied in detail in Section 8.4. Finally, a discussion of the W^+W^- event candidates in the studied signal regions as well as their background composition is presented in Section 10.1.

7.4 Dataset and Simulated Events

The analysis presented in this thesis makes use of data collected in pp collisions at a center-of-mass energy of $13\,\text{TeV}$ from 2015 to 2018 with the ATLAS detector at the LHC (see Table 4.5). After applying data quality criteria [343], the dataset corresponds to $140\ \text{fb}^{-1}$ of integrated luminosity, with an uncertainty of $0.83\,\%$ [342], which has been obtained using the LUCID-2 detector [329] for the primary luminosity measurements.

The modeling of signal $q\bar{q} \to WW$ events is performed with Powheg MiNNLO [216, 212], which is next-to-next-to-leading order (NNLO) accurate in QCD for inclusive observables. The simulation of the signal sample and all other W^+W^- production processes described in the following is produced making use of the PDF set NNPDF3.0nnlo [445]. The events were interfaced to Pythia 8.245 [147] for the modeling of the parton shower, hadronization, and underlying event, with parameters set according to the A14 tune [446] relying on the NNPDF2.3lo PDF set [447]. The matrix element calculation of $gg \to WW$

production, which includes off-shell effects and Higgs boson contributions, incorporates up to one additional parton emission at LO. This contribution was simulated with the SHERPA2.2.2 [148, 259] generator, which was matched and merged with the SHERPA parton shower based on the Catani-Seymour dipole [448, 202] with the MEPS@NLO prescription [449, 210, 205, 450]. The virtual QCD corrections were provided by the OPENLOOPS library [451, 452]. The electroweak production of a diboson in association with two jets ($VVjj$) was simulated with the SHERPA2.2.2 [148] generator. The LO-accurate matrix elements were also matched to a parton shower based on the Catani-Seymour dipole factorization scheme [448, 202] using the MEPS@LO prescription [449, 210, 205, 450]. A dedicated set of tuned parton-shower parameters developed by the SHERPA authors was employed for all SHERPA samples.

The generator POWHEG BOX 2 [453, 149, 454, 150] is used to model the production of $t\bar{t}$ and single-top Wt events at NLO accuracy, relying on the NNPDF3.0NLO [445] PDF. The events were interfaced to PYTHIA 8.230 [147] to model the parton shower, hadronization, and underlying event, with the A14 set of tuned parameters [446] and accessing the NNPDF2.3LO set of PDFs [447]. For $t\bar{t}$ event generation, the h_{damp} parameter[5] was set to $1.5\,m_{\mathrm{top}}$ [455]. The diagram-removal scheme [456] was employed to handle the interference between the Wt and $t\bar{t}$ production processes [455]. Alternative samples were generated to assess the uncertainties in the top-background modeling. The uncertainty due to initial-state radiation and higher-order QCD effects was estimated by simultaneous variations of the h_{damp} parameter and the renormalization and factorization scales, and by choosing the VAR3C up/down variants of the A14 set of tuned parameters, corresponding to the varying of α_{S} in the parton shower, as described in Ref. [457]. The impact of final-state radiation was evaluated with weights that account for the effect of varying the renormalization scale for final-state parton-shower emissions up or down by a factor of two. To assess the dependence on the $t\bar{t}$-Wt overlap removal scheme, the diagram-subtraction scheme [456] was employed as an alternative. The uncertainty due to the parton shower and hadronization model was evaluated by comparing the nominal sample of events with an event sample generated by POWHEG BOX 2 and interfaced to HERWIG 7.04 [144, 145], with the H7UE set of tuned parameters [145] and the MMHT2014LO PDF set [169]. To estimate the uncertainty in the matching of NLO matrix elements to the parton shower, the nominal sample was compared to a sample generated by MADGRAPH5_AMC@NLO 2.6.2 [208] at NLO in QCD using the five-flavour scheme and the NNPDF2.3NLO PDF set. The events were interfaced with PYTHIA 8, as for the nominal sample. The $t\bar{t}$ sample was normalized to the cross-section prediction at NNLO in QCD including the resummation of next-to-next-to-leading logarithmic (NNLL) soft-gluon terms calculated with TOP++2.0 [458, 459, 460, 461, 462, 463, 464]. The inclusive cross section for single-top Wt was corrected to the theory prediction calculated at NLO in QCD with NNLL soft-gluon corrections [465, 466].

The background due to $Z/\gamma^* + \mathrm{jets}$ production was simulated with the SHERPA 2.2.1 generator with NLO-accurate matrix elements for up to two jets, and LO-accurate matrix elements for three and four jets calculated with the COMIX [448] and OPENLOOPS libraries. They were matched with the SHERPA parton shower [202] using the MEPS@NLO prescription [449, 210, 205, 450] and the set of tuned parameters developed by the SHERPA

[5]The h_{damp} parameter is a resummation damping factor and one of the parameters that control the matching of POWHEG matrix elements to the parton shower and thus effectively regulates the high-p_T radiation against which the $t\bar{t}$ system recoils.

authors. The NNPDF3.0NNLO set of PDFs was employed, and the samples were normalized to a NNLO prediction [467].

The production of diboson final states was simulated with the SHERPA 2.2.2 (WZ, ZZ) and SHERPA 2.2.8 ($V\gamma$, with $V = W, Z$) generators running OPENLOOPS at NLO QCD accuracy for up to one additional parton and LO accuracy for two to three additional parton emissions, matched and merged with the SHERPA parton shower. The VZ simulation includes $V\gamma^*$ contributions for $m(\ell\ell) > 4\,\text{GeV}$. The NNPDF3.0NNLO PDF set was used. The samples are normalized to the cross section calculated by the generator.

Samples generated with POWHEG BOX or MADGRAPH5_AMC@NLO rely on the EVTGEN program [468] to model the decay of bottom and charm hadrons. The effect of multiple interactions in the same and neighboring bunch crossings (pile-up) was modeled by overlaying the hard-scattering event with simulated inelastic pp events generated with PYTHIA 8.186 using the NNPDF2.3LO set of PDFs and the A3 set of tuned parameters [469]. Table 7.1 summarizes the nominal MC samples used in the analysis.

For the interpretation of the measurement in the SMEFT (presented in Chapter 11), the MADGRAPH5_AMC@NLO 2.9.5 generator based on the SMEFTSIM 3.0 [470, 471] model was used to simulate events of fully-leptonic W^+W^- production at leading order [151]. The $\{m_W, m_Z, G_\text{F}\}$ electroweak input parameter scheme is used. A flavor symmetry in the first two quark generations and in all three lepton generations, $U(2)_q \times U(2)_u \times U(2)_d \times U(3)_\ell \times U(3)_e$, is assumed. The MADGRAPH5_AMC@NLO reweight module is used to model the effect of the eleven Wilson coefficients affecting the signal process. Events were interfaced to PYTHIA 8.245 [147] to simulate parton shower and hadronization.

To account for detector effects, all samples were passed through a full simulation of the ATLAS detector [345], based on GEANT 4 [344]. The physics objects are reconstructed and calibrated to the data following the methods described in Section 4.3. Based on these, a selection criteria of W^+W^- candidates is defined.

7.5 Selection Criteria

Candidate W^+W^- events are selected by requiring exactly one high-p_T electron and one muon with opposite electric charges. These leptons are required to be isolated, i.e., there should be little hadronic activity in the vicinity of the lepton, to suppress backgrounds due to misidentified leptons or leptons from hadron decays. Events with two isolated leptons of the same flavor are not considered in the analysis due to the higher background from Drell-Yan events.

Events were recorded by either single-electron or single-muon triggers listed in Table 4.4. The minimum p_T threshold varied during data-taking between 24 GeV and 26 GeV for electrons, and between 20 GeV and 26 GeV for muons, both requiring `loose` to `medium` isolation criteria [340, 326]. Triggers with higher p_T thresholds and looser isolation requirements are also used to increase the efficiency. The trigger selection efficiency is more than 99 % for signal events fulfilling all other selection requirements detailed in the following. Figure 7.7 shows the fraction of trigger-matched leptons[6] for each of the offline

[6]Only well-identified and well-isolated electrons and muons are considered, fulfilling the selection criteria listed in Table 7.2 besides the p_T requirement.

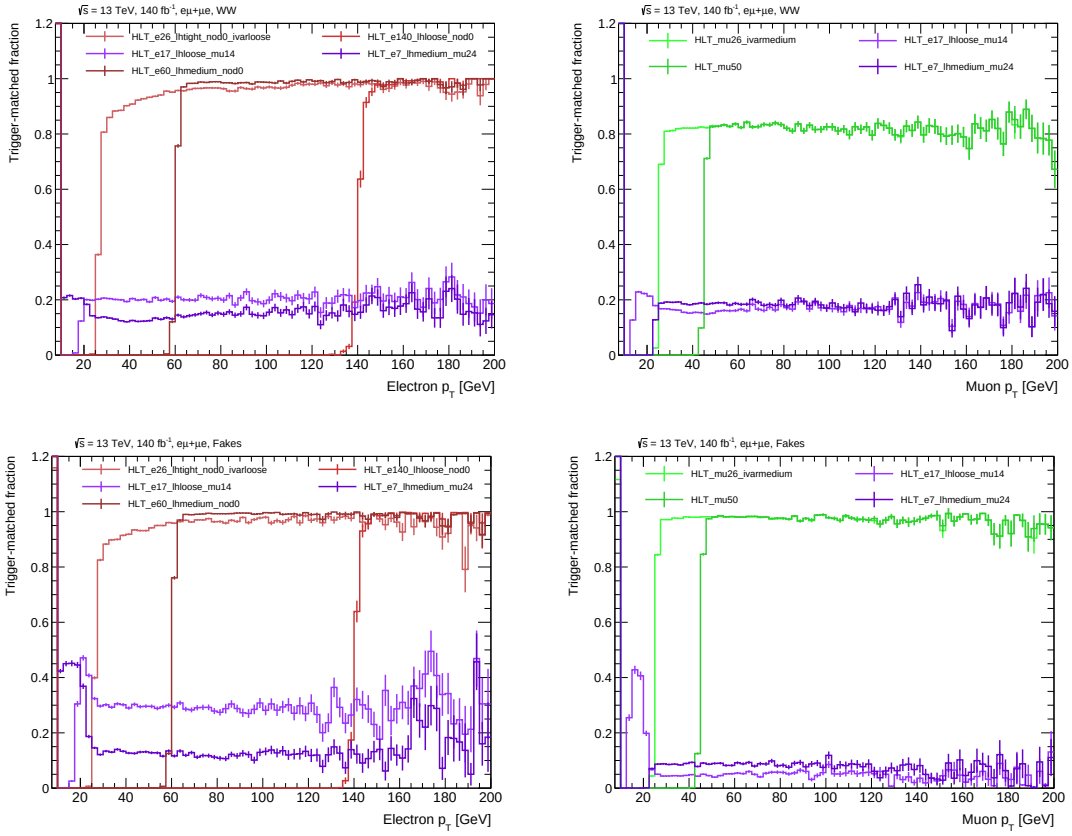

Figure 7.7: Fraction of trigger-matched electrons (left) and muons (right) by offline single-lepton and $e\mu$ dilepton triggers during ATLAS data-taking between 2016 and 2018 in MC simulation of W^+W^- (top) and events involving lepton misidentification (bottom). The fractions are computed in dilepton events, where electron and muon selection requirements fulfill the criteria listed in Table 7.2 besides the p_T requirement. Error bars show statistical uncertainties.

single-lepton (listed in Table 4.4) and $e\mu$ unprescaled dilepton triggers available in ATLAS data-taking between 2016 and 2018 for both W^+W^- events and contributions from lepton misidentification[7]. The passing rate of single-lepton triggers increases rapidly following the expected turn-on shape once the lepton p_T surpasses the threshold of the trigger. Single lepton triggers with higher p_T thresholds are more efficient than the ones with lower p_T due to looser identification and isolation requirements. Only roughly $20\,\%$ of leptons in W^+W^- events are matched using dilepton triggers while their efficiency to trigger events involving lepton misidentification is a factor 2 higher at lepton $p_T < 26\,\text{GeV}$, where dilepton triggers are effective. Dilepton triggers are therefore rather inefficient for W^+W^- events in comparison to single-lepton triggers. Including dilepton triggers in the trigger menu is also inconvenient for data-driven estimations of the lepton misidentification background (described in Section 8.4). Therefore, only single-lepton triggers are considered for this analysis.

Trajectories of charged particles are reconstructed as tracks in the inner detector, whose common vertices are considered to extract interaction vertex candidates, as described in

[7]Events involving lepton misidentification in dilepton final states are simulated as the sum of W + jets, semi-hadronic $t\bar{t}$, and single-top production.

Object	Requirement	Criteria
Lepton	p_T	$> 27\,\text{GeV}$
	η	$\lvert\eta\rvert \in [0\,,\,1.37) \cup (1.52\,,\,2.47)$ (electron); $\lvert\eta\rvert < 2.5$ (muon)
	Identification	`TightLH` (electron), `Medium` (muon)
	Isolation	`Gradient` (electron), `Tight_FixedRad` (muon)
	Impact parameters	$\lvert d_0/\sigma_{d_0}\rvert < 5, 3$ (electron, muon); $\lvert z_0 \cdot \sin\theta\rvert < 0.5\,\text{mm}$
Jet	b-tagging	$p_T > 20\,\text{GeV}$, $\lvert\eta\rvert < 2.5$, DL1r (85 % eff. WP)
	Selection	$p_T > 30\,\text{GeV}$, $\lvert\eta\rvert < 4.5$
Event	Leptons	1 electron and 1 muon of opposite electric charge, no additional lepton with $p_T > 10\,\text{GeV}$, `Loose` isolation, and `LooseLH` (electron) / `Loose` (muon) identification
	Number of b-jets	0
	$m_{e\mu}$	$> 85\,\text{GeV}$

Table 7.2: Summary of the object and event selection criteria.

Section 4.3.1. Candidate events are required to have at least one vertex having at least two associated tracks with $p_T > 500\,\text{MeV}$. The vertex with the highest $\sum p_T^2$ of the associated tracks is taken as the primary vertex.

Object Selection

In this section, the selection criteria for the objects used in the measurement of W-boson pair production along with any number of hadronic jets in the final state are presented.

Electrons are reconstructed from energy deposits in the calorimeter that are matched to tracks [353], as described in Section 4.3.2. Electron candidates are required to fulfill the `TightLH` likelihood-based identification criteria as defined in Ref. [472]. Furthermore, they are required to have $E_\text{T} > 27\,\text{GeV}$ and $|\eta| < 2.47$, excluding the transition region between barrel and endcap, $1.37 < |\eta| < 1.52$.

Muons are required to fulfill a set of quality requirements recommended by the Muon CP group and outlined in Section 4.3.3. Muon candidates are reconstructed by combining a track in the inner detector with a track in the muon spectrometer [358]. Muons are required to have $p_T > 27\,\text{GeV}$ and $|\eta| < 2.5$ and to satisfy the `Medium` identification selection, as defined in Ref. [358].

Leptons are required to be compatible with the primary vertex by imposing requirements on the impact parameters of associated tracks. The transverse impact parameter significance is required to satisfy $|d_0/\sigma_{d_0}| < 5\,(3)$ for electrons (muons). The longitudinal impact parameter must satisfy $|z_0 \cdot \sin\theta| < 0.5\,\text{mm}$, where θ is the polar angle of the track. Additionally, leptons are required to be isolated using information from the inner-detector tracks and energy clusters in the calorimeters in a cone around the lepton. The `Gradient` (`Tight_FixedRad`[8]) working point is used for electron (muon) isolation [472, 473]. The electron or muon trigger object is required to match the respective reconstructed lepton.

Jet reconstruction relies on the anti-k_t algorithm [359] with a radius parameter of $R = 0.4$ building particle-flow objects [474], preselected by requiring $p_T > 20\,\text{GeV}$ and $|\eta| <$

[8]This isolation working point is similar to the `Tight` selection defined in Ref. [473] but with altered criteria at muon $p_T > 50\,\text{GeV}$ in order to increase the background rejection.

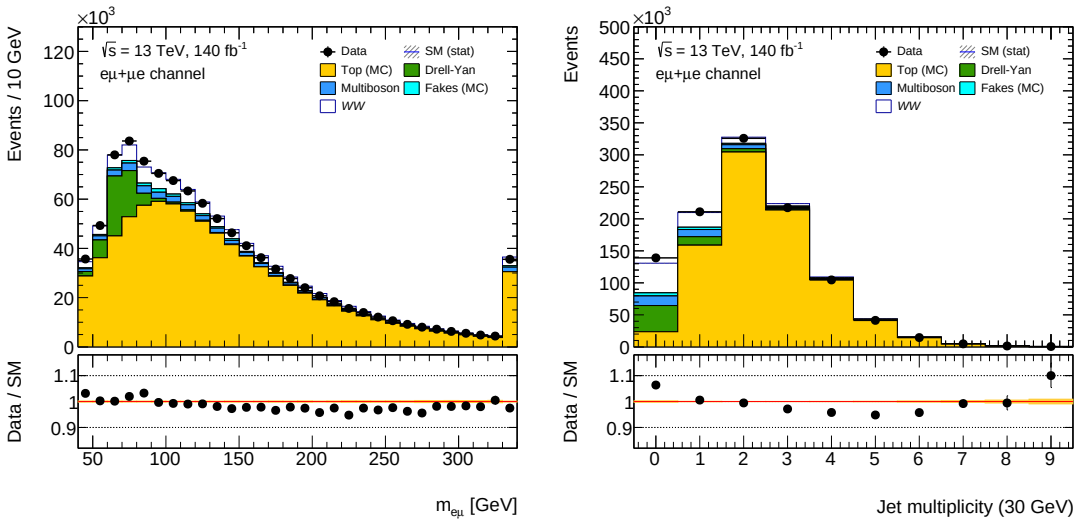

(a) Dilepton invariant mass. (b) Jet multiplicity.

Figure 7.8: Kinematic distributions of (a) the dilepton invariant mass $m_{e\mu}$ and (b) the jet multiplicity after requiring two leptons of $p_T > 27\,\text{GeV}$ at the preselection stage. Signal and backgrounds are estimated using MC simulation. Only statistical uncertainties of the MC samples are displayed. Overflow events are included in the last bin.

4.5. To suppress jets that originate from pile-up, a jet-vertex tagger [475] is applied to jets with $p_T < 60\,\text{GeV}$ and $|\eta| < 2.4$. The jet energy scale is recalibrated with a correction that is dependent on η and p_T [361]. The selected calibrated jets are required to have $p_T^{\text{jet}} > 30\,\text{GeV}$ and $|\eta^{\text{jet}}| < 4.5$. Jets with $p_T^{\text{jet}} > 20\,\text{GeV}$ and $|\eta^{\text{jet}}| < 2.5$ containing decay products of a b-hadron are identified employing the DL1r b-tagging algorithm [476, 372] (see Section 4.3.5) at the $85\,\%$ efficiency working point. This is the highest efficiency working point provided centrally by the flavor tagging group of ATLAS and it is chosen to maximize the rejection of top-quark contributions. Choosing b-jets with a lower p_T threshold[9] results in a higher rejection of the $t\bar{t}$ background.

In order to resolve the overlap between particles reconstructed as multiple physics objects in the detector, non-b-tagged jets are removed if they overlap, within $\Delta R < 0.2$, with an electron, or with a muon if the jet has less than three associated tracks with $p_T > 500\,\text{MeV}$ and satisfies $p_T^{\mu}/p_T^{\text{jet}} > 0.5$, and the ratio of the muon p_T to the sum of the track p_T associated with the jet is greater than 0.7. After the aforementioned overlap requirements have been addressed, electrons or muons overlapping within $\Delta R < 0.4$ with any jet, including b-tagged jets, are removed. The standard approach of *overlap removal* used in ATLAS is introduced in Section 4.3.7 and details can be found in Ref. [378].

The missing transverse momentum, with magnitude E_T^{miss}, is computed as the negative vectorial sum of the transverse momenta of tracks associated with jets and muons, as well as tracks in the ID that are not associated with any other component, as described in Section 4.3.6. The p_T of the electron track is replaced by the calibrated transverse momentum of the reconstructed electron [377].

After selecting events with two well-identified and well-isolated leptons of different-flavor as defined in Section 7.5, Figure 7.8 illustrates the signal and background compo-

[9] Calibrations for the DL1r flavor tagging algorithm are provided for $p_T^{\text{jet}} > 20\,\text{GeV}$, see Section 4.3.5.

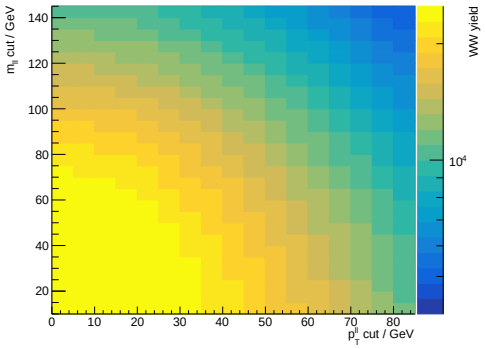

(a) Signal W^+W^-.

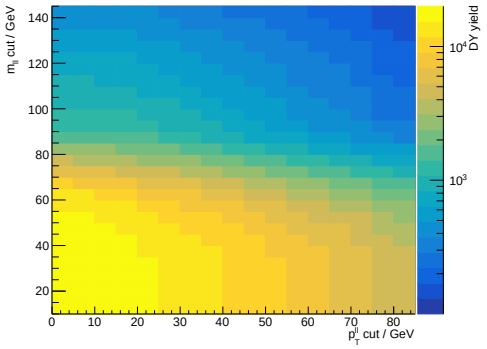

(b) Drell-Yan $Z + \text{jets}$.

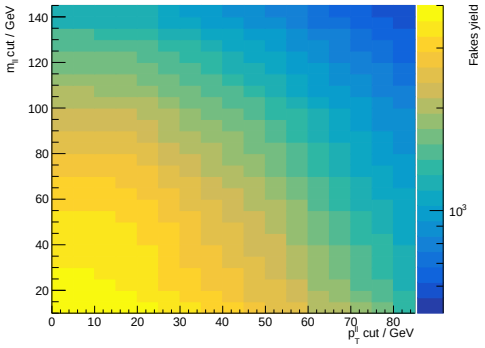

(c) Fake and non-prompt lepton contributions.

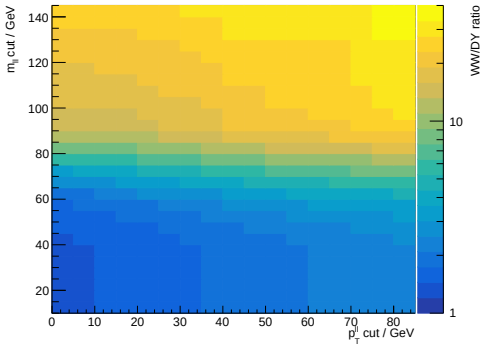

(d) Ratio of event yields W^+W^- over $Z + \text{jets}$.

Figure 7.9: Number of simulated events corresponding to an integrated luminosity of 139 fb^{-1} as a function of cut thresholds applied simultaneously on $m_{e\mu}$ and $p_T^{\ell\ell}$ at the preselection stage for (a) W^+W^-, (b) Drell-Yan Z+jets and (c) fake-lepton contributions, together with (d) the ratio of W^+W^- event yields over Z+jets. Final states into one electron and one muon are used over the full Run 2 dataset.

sition across the distributions of both the dilepton invariant mass and the jet multiplicity. This is selection stage is referred to as *preselection*. While diboson and fake-lepton events are subdominant, Drell-Yan is enhanced at values of $m_{\ell\ell}$ around 70 GeV, as expected from a resonant $Z \to \tau\tau$ decay. Top-quark contributions, composed by mostly $t\bar{t}$ production, dominate at higher values of the $m_{\ell\ell}$ spectrum and high jet multiplicities as they decay into two W bosons plus b-jets. After calibrating the objects reconstructed in the event, the data can be described well by MC simulation of the SM processes listed in Table 7.1.

Event Selection

The event selection is designed to enhance W^+W^- signal over background contributions from top-quark, Drell-Yan, lepton misidentification and other multiboson processes such as VZ, $V\gamma$, or VVV ($V = W^\pm, Z$). Events with additional isolated leptons with $p_T > 10$ GeV satisfying the `Loose` isolation and `LooseLH` (`Loose`) identification requirements for electrons (muons) are vetoed to reduce backgrounds due to $W^\pm Z$ and ZZ production. This requirement is referred to as *third lepton veto*. Drell-Yan contributions, dominated by $Z + \text{jets}$ decaying into τ-lepton pairs, are suppressed by requiring the invariant mass

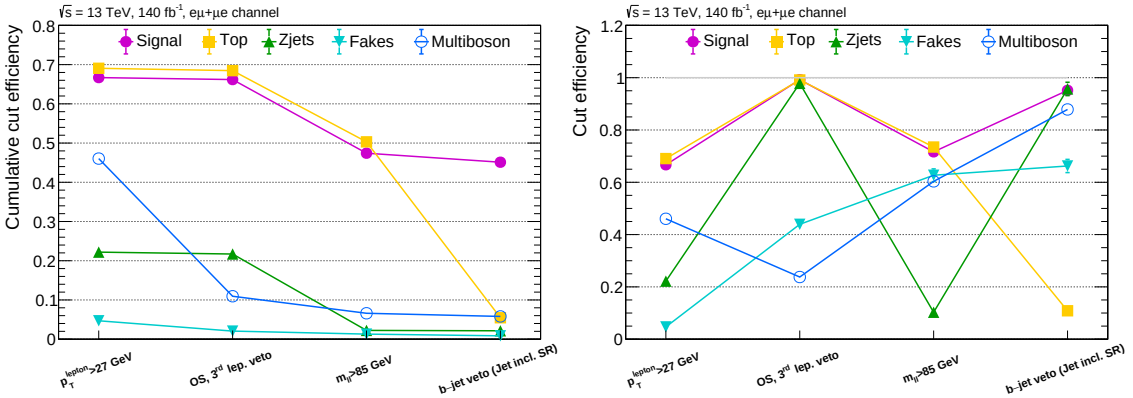

(a) Cumulative selection efficiencies.

(b) Cut selection efficiencies.

Figure 7.10: (a) Cumulative and (b) cut selection efficiencies (with respect to previous cut) per cut stage defined in the event selection. Signal and backgrounds are estimated using MC simulation. The first efficiencies are computed with respect to the selection of a well-identified and well-isolated $e\mu$ lepton pair. Only statistical uncertainties of the MC samples are displayed.

of the dilepton system to be $m_{e\mu} > 85\,\text{GeV}$, imposing the two leptons to have opposite electric charge. As observed from Figure 7.8a, this requirement is effective at rejecting $Z + \text{jets}$ events, but also suppressing the contribution of resonant $gg \to H \to WW$ production to proportions below $1\,\%$ of the W^+W^- yield. Studies for the $WW + \geq 1\,\text{jets}$ analysis showed the choice of this value significantly improves the signal-to-background ratio, tested in combination with additional selection criteria on variables such as $p_T^{\ell\ell}$ and E_T^{miss}. Figure 7.9 shows the event yields for the W^+W^- signal together with Drell-Yan and lepton misidentification backgrounds as a function of the cut thresholds applied on $m_{e\mu}$ and $p_T^{\ell\ell}$. An enhancement of W^+W^- contributions is observed on the ratio of W^+W^- yields over Drell-Yan after imposing $m_{e\mu} > 85\,\text{GeV}$ (Fig. 7.9d), while the ratio is roughly constant across $p_T^{\ell\ell}$. Criteria on $p_T^{\ell\ell}$ and E_T^{miss} were not considered to avoid an increase on systematic uncertainties. To reduce the dominant background from top-quark sources, events with at least one b-tagged jet are vetoed. The above requirements define the *jet-inclusive signal region*. A summary of the lepton, jet, and event selection requirements is presented in Table 7.2.

The selection efficiencies for each of the requirements defining the event selection are displayed in Figure 7.10, both cumulative (Fig. 7.10a) and with respect to the previous criterion (Fig. 7.10b). The requirement on the lepton p_T discards $33\,\%$ of the signal and $95\,\%$ of misidentified leptons. While contributions from lepton misidentification decrease slowly, mainly after rejecting events with two leptons of same electric charge and low $m_{e\mu}$ events, the third lepton veto removes roughly $80\,\%$ of the diboson contributions with the effect on the signal, top-quark and Drell-Yan backgrounds being lower than $1\,\%$. Similarly, the high $m_{e\mu}$ requirement is very powerful in suppressing $90\,\%$ Drell-Yan contributions, at the cost of $30\,\%$ of the signal. The signal is finally enhanced by the b-jet veto, which discards $90\,\%$ of the dominant top-quark contributions and only $5\,\%$ of the signal.

Chapter 8
Background Estimates

"Perfect is the enemy of good."

— M. de Voltaire (1694 – 1778).

The signature of a fully-leptonic W^+W^- candidate event is expected to contain two well-reconstructed leptons within the detector acceptance whose transverse momenta are unbalanced due to the two untraceable neutrinos. As outlined in Section 7.1, multiple SM processes with analogous signature such as Drell-Yan $Z + \text{jets}$, top-quark production, and multiboson processes are expected to contribute as backgrounds in measurements of W^+W^- production at the LHC. Accurate estimations of the contributions from background processes enhance the precision of the measurement. The background contributions are dominated by top-quark production processes, especially $t\bar{t}$. These contributions are estimated with high accuracy using data-driven techniques as described in Section 8.1. Background sources from Drell-Yan $Z + \text{jets}$, diboson (WZ, $W\gamma$, ZZ, and $Z\gamma$) and triboson production are described in Sections 8.2 and 8.3, respectively. Non-prompt or misidentified leptons produced mainly in $W + \text{jets}$ and semileptonic $t\bar{t}$ events can also fulfill the lepton selection criteria, becoming backgrounds of W^+W^- final states. Section 8.4 describes the data-driven techniques used to estimate this reducible background contributions.

8.1 Top-Quark Background

The production of top-quarks in pp collisions is associated to the production of b-jets, i.e., the hadronized collimated signature of the b-quarks produced. Decays into $W^+W^- + b\bar{b}$ characteristic of $t\bar{t}$ production can fulfill the W^+W^- selection criteria if the b-jets in the final state are not reconstructed, e.g., after either inefficiencies in the b-jet identification, or if the jet falls outside the acceptance of the inner detector.

The measurement presented in this dissertation estimates top-quark background events using various techniques. The dominant $t\bar{t}$ component of this background relies on the data-driven *b-tag counting method*, described in Section 8.1.1. The remaining contributions can be attributed to single-top production, estimated using MC simulation. The b-tag counting method is augmented using a *transfer factor method* in certain regions of the phase space where the b-tag counting method suffers from large statistical uncertainties. The transfer factor method, and a comparison with respect to the b-tag counting method, is presented in Section 8.1.2. A region where top-quark contributions are enhanced is used to validate the background estimation. The validation as well as systematic uncertainties of the background estimation propagated to the final measurement in the signal region is presented in Section 8.1.3.

8.1.1 The b-tag Counting Method

The b-tag counting method is a data-driven technique implemented to estimate the $t\bar{t}$ background contributions. Following the procedure considered in measurements of the $t\bar{t}$ production cross section by the ATLAS Collaboration [477] and as a background estimate in the measurement of $WW+\geq 1\,\text{jets}$ production [81], two regions requiring exactly one and two b-tagged jets are defined, based on the signal region definition (see Table 7.2). An estimation of the observed $t\bar{t}$ events in data in a b-vetoed phase space can be performed by evaluating

$$N_{0b} = N_{\geq 0b}^{t\bar{t}} \cdot \left(1 - 2\varepsilon_b + C_b\varepsilon_b^2\right) + N_{0b}^{\text{bkg}}\,, \tag{8.1}$$

$$N_{1b} = N_{\geq 0b}^{t\bar{t}} \cdot 2\varepsilon_b\left(1 - C_b\varepsilon_b\right) + N_{1b}^{\text{bkg}}\,, \tag{8.2}$$

$$N_{2b} = N_{\geq 0b}^{t\bar{t}} \cdot C_b\varepsilon_b^2 + N_{2b}^{\text{bkg}}\,. \tag{8.3}$$

By measuring the number of events in the regions with exactly one (N_{1b}) and two b-jets (N_{2b}) in data, the effective b-tagging efficiency ε_b as well as the effective $t\bar{t}$ cross section ($N_{\geq 0b}^{t\bar{t}}$) can be calculated. This also applies in regions of phase space requiring events with less than two jets, since b-tagged jets are tagged for a lower p_T threshold (20 GeV) than regular jets (30 GeV), as defined in the object selection of the analysis (Section 7.5). When tagging two b-jets in an event, the efficiency of tagging the first b-jet can be affected by the kinematics of the second b-jet, and vice versa. The *b-tagging correlation factor* C_b, defined as the ratio of the efficiency to tag two jets in the event (ε_{bb}) over the efficiencies of both independent b-jets (ε_b^2) is estimated from $t\bar{t}$ MC simulation. This constitutes the only input that is susceptible to $t\bar{t}$ modeling uncertainties in the b-tag counting method. The correlation factor C_b is derived as follows,

$$C_b = \frac{4 \cdot N_{\text{MC}}^{t\bar{t}} N_{2b,\text{MC}}^{t\bar{t}}}{\left(N_{1b,\text{MC}}^{t\bar{t}} + 2 \cdot N_{2b,\text{MC}}^{t\bar{t}}\right)^2}\,, \tag{8.4}$$

with $N_{\text{MC}}^{t\bar{t}} = N_{0b,\text{MC}}^{t\bar{t}} + N_{1b,\text{MC}}^{t\bar{t}} + N_{2b,\text{MC}}^{t\bar{t}}$ and $N_{kb,\text{MC}}^{t\bar{t}}$ being the number of $t\bar{t}$ events estimated from MC with $k = 0, 1, 2$ selected b-jets. The correction factor C_b is typically close to unity, between 0.99 and 1.01 across jet-inclusive distributions, like $m_{\ell\ell}$ (Figure 8.1a). In certain configurations, for example in events with exactly one jet with $p_T > 30\,\text{GeV}$, C_b can be as low as 0.8 (Figure 8.1b). The identification of two b-jets is possible for some of these events, as the b-jet p_T requirement is 20 GeV. However, the probability of identifying both b-jets is significantly smaller than ε_b^2 since the second jet is often outside the acceptance, and because the b-tagging efficiency is lower for jets with $p_T^{\text{jet}} \in [20, 30]\,\text{GeV}$. The disparity in jet kinematics therefore leads to smaller values of C_b while the reduced correlation of the uncertainties of finding the first and the second jet increases the uncertainty in C_b. The uncertainty in C_b is less than 1 % in most analysis bins.

The number of $t\bar{t}$ events with no reconstructed b-jet activity in the final state can therefore[1] be inferred as

$$N_{0b}^{t\bar{t}} = \frac{C_b}{4}\frac{\left(N_{1b}^{t\bar{t}} + 2N_{2b}^{t\bar{t}}\right)^2}{N_{2b}^{t\bar{t}}} + N_{0b}^{\text{bkg}}\,, \tag{8.5}$$

[1] Details of its derivation can be followed in Appendix A.1.

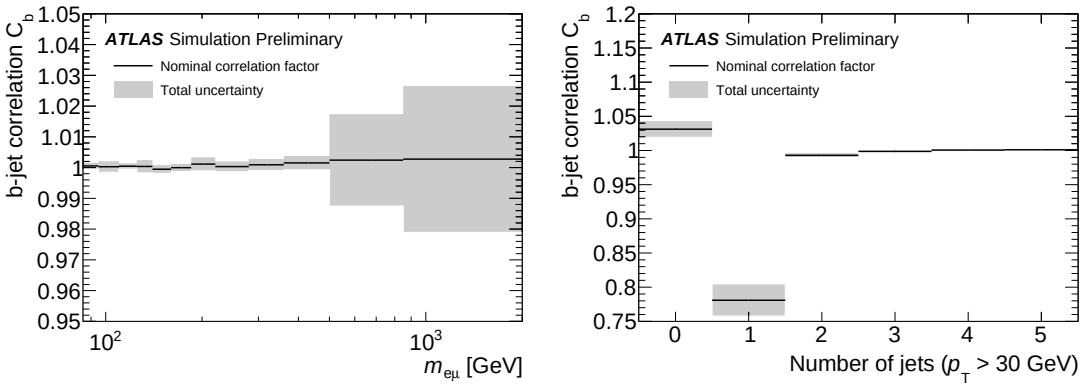

(a) Dilepton invariant mass $m_{e\mu}$.

(b) Jet multiplicity.

Figure 8.1: The b-jet correlation correction factor C_b derived from $t\bar{t}$ MC simulation in the jet-inclusive signal region as a function of (a) $m_{\ell\ell}$ and (b) the number of jets in the event. The displayed uncertainties account for statistical uncertainties from the regions with 0, 1, and 2 b-jets in the MC simulation ($N^{t\bar{t}}_{\mathrm{MC}}$ and $N^{t\bar{t}}_{kb,\mathrm{MC}}$) and experimental and theory modeling systematic errors from $t\bar{t}$ simulation. Published in Ref. [87].

where $N^{t\bar{t}}_{kb} = N_{kb} - N^{\mathrm{bkg}}_{kb}$ for $k = 0, 1, 2$. The b-tag counting method can also be applied in each individual bin for differential measurements.

The dominant background to $t\bar{t}$ events in the b-tagged regions arise from single-top Wt production. Table 8.1 lists the event yields in the 1 and 2 b-jet regions. In the jet-inclusive signal region, the contribution of non-$t\bar{t}$ events in the regions with 1 and 2 b-jets is 13 % and 4 % of the expected events, respectively, of which 90 % can be attributed to single-top Wt production.

	CR 1b-jet	CR 2b-jet
Data	260 971± 510	257 777± 507
Total SM	269 270±17 313	267 645±20 792
$t\bar{t}$ (MC)	232 779±15 741	256 644±20 698
Single-top	31 347± 7 102	9 954± 1 691
W^+W^-	1 961± 178	124± 15
Fakes	1 783± 812	806± 397
Z + jets	203± 42	17± 5
WZ	433± 56	37± 6
ZZ	34± 4	3± 0
$V\gamma$	77± 15	3± 2

Table 8.1: Event yields in the 1 and 2 b-jet regions for the b-tag counting method estimate in the jet inclusive SR.

Figure 8.2 shows the agreement between the data and SM simulation in the $t\bar{t}$ regions with one b-jet and two b-jets as a function of $m_{\ell\ell}$. At high dilepton invariant mass, the $t\bar{t}$ simulation underpredicts the data, as expected in MC simulations of $t\bar{t}$. This feature can also be seen in the high-$m_{\ell\ell}$ tails after the preselection is imposed (where $t\bar{t}$ contributions dominate, c.f. Figure 7.8a), and is corrected by the data-driven estimate. Despite this trend, excellent agreement of data and simulation is observed within uncertainties. To avoid any double counting between semileptonic top-quark events where a fake lepton is reconstructed when using the two data-driven methods, the data-driven fake background estimate presented in Section 8.4 is used in the $t\bar{t}$ control regions. Contributions from $t\bar{t}$ and single-top account only for fully-leptonic decay modes.

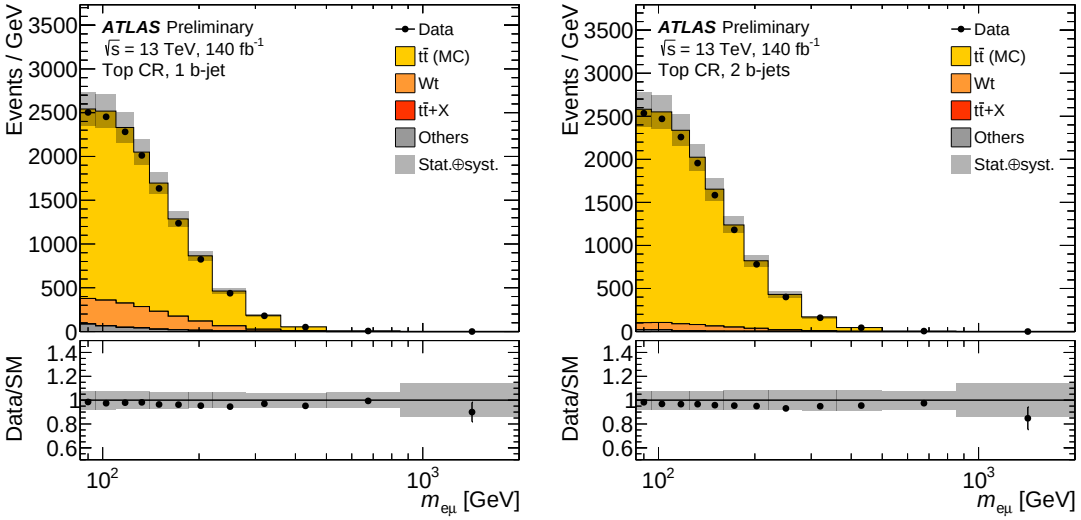

(a) 1 b-jet region. (b) 2 b-jet region.

Figure 8.2: Comparison of data and SM simulation in bins of $m_{\ell\ell}$ in the $t\bar{t}$ control regions with (a) 1 b-jet and (b) 2 b-jets selection requirements. Overflow events are contained in the last bin. Data are shown as black markers, together with the stacked histogram accounting for simulated SM processes listed in Table 7.1. The lower panels show the ratio of the data to the total SM prediction. The shown uncertainty bands include statistical and systematic uncertainties. Theory uncertainties on the W^+W^- signal are negligible and not shown. Published in Ref. [87].

8.1.2 The Transfer Factor Method

In a few analysis bins, the two-b-jet region defined in the b-counting method contains relatively few events, which would result in a large statistical uncertainty of the $t\bar{t}$ background estimate. To mitigate this problem, the top-quark background (i.e. including both $t\bar{t}$ and single-top Wt contributions) is instead estimated by extrapolating from a control region enriched in the production of top quarks. This control region is constructed by requiring at least one b-jet, with the other selection criteria being the same as for the SR. For each bin of the measured distribution of interest, the number of expected top-quark background events from both $t\bar{t}$ and Wt contributions, $N_{\mathrm{SR}}^{\mathrm{top}}$, is estimated from the corresponding bin in the region as

$$N_{\mathrm{SR}}^{\mathrm{top}} = \frac{N_{\mathrm{SR}}^{\mathrm{top,MC}}}{N_{\mathrm{CR}}^{\mathrm{top,MC}}} \times \left(N_{\mathrm{CR}}^{\mathrm{data}} - N_{\mathrm{CR}}^{\mathrm{MC,others}} \right) . \tag{8.6}$$

Here $N_{\mathrm{CR}}^{\mathrm{MC,others}}$ is the contribution from non-top background in the region, which is of the order of 10% of the total and estimated from MC simulation. The *transfer factor*, defined as the ratio of events expected in the signal and control regions and also estimated from MC simulation ($N_{\mathrm{SR}}^{\mathrm{top,MC}}/N_{\mathrm{CR}}^{\mathrm{top,MC}}$), gives name to this data-driven method. With an uncertainty of about 10%, the transfer factor method is only employed in a few bins at the high-mass tails ($m_{\ell\ell} \gtrsim 0.5\,\mathrm{TeV}$) of the distributions where there are 100 events or less in the 2 b-jet region, as its uncertainty is smaller than the uncertainty of the b-tag counting method in these bins. This approach is found to be optimal, as shown in Appendix A (Fig. A.1). The predictions from both transfer factor and b-tag counting methods are also

in very good agreement within uncertainties. In the transfer factor method, the effect of experimental and theory uncertainties is reduced compared to a background estimate purely based on simulation. The dominant uncertainties arise in the theoretical modeling of the top-quark background.

8.1.3 Systematic Uncertainties and Validation

The b-tag counting method is affected by systematic uncertainties in the $t\bar{t}$ modeling, through the input of the b-tagging correlation factor C_b, as well as by uncertainties in the non-$t\bar{t}$ estimate in the 1 and 2 b-jet regions. Similarly, the transfer factor approach is affected by uncertainties in the transfer factor and the non-top subtraction in the control region. As the $t\bar{t}$ background estimate is largely based on observed yields in data regions and the only input from $t\bar{t}$ simulation is the correlation factor C_b, the b-jet counting method strongly reduces experimental and theoretical uncertainties in the $t\bar{t}$ background estimate, and thus lowers its total uncertainty by a factor of approximately 5 in the inclusive phase space, corresponding to an uncertainty of about $3\,\%$. The single-top Wt background is estimated using simulation, with an attributed uncertainty on the predicted cross section of $30\,\%$. The subtraction of Wt backgrounds in the $t\bar{t}$ regions introduces an anticorrelation in the estimated Wt and $t\bar{t}$ event yields in the signal region so that the modeling uncertainties in Wt have a reduced impact on the measurement[2]. A detailed breakdown of the systematic uncertainties of b-tag counting, transfer factor, and MC estimation approaches for the top-quark background is given in Appendix A.2.

The nominal $t\bar{t}$ and single-top events are generated with POWHEG, using PYTHIA8 for the parton shower. As the generator setup is identical for both $t\bar{t}$ and single-top MC samples, modeling uncertainties are considered as correlated. The modeling uncertainties include[3]

- the dependence on the matrix element calculation, assessing the difference between nominal and MADGRAPH5_AMC@NLO+PYTHIA 8 samples as an uncertainty,
- the influence of the parton shower model, comparing the nominal sample with the predictions of POWHEG+HERWIG 7,
- the modeling of ISR, FSR, and QCD scale uncertainties via alternative generator weights (for QCD scales μ_R and μ_F, and ISR) and h_{damp} variation for $t\bar{t}$, and
- the modeling of the interference between $t\bar{t}$ and Wt events, estimated by comparing the nominal diagram-removal sample for single-top with an alternative sample generated according to the diagram-subtraction scheme [455].

[2]For instance, uncertainties in the single-top Wt production rate that are independent of the b-jet multiplicity, such as the cross-section uncertainty, partially cancel out because single-top Wt is the dominant background to $t\bar{t}$ in the $t\bar{t}$ regions. Additionally, a variation leading to a larger Wt prediction in the regions reduces the $t\bar{t}$ estimate, so if the same variation also leads to a larger Wt prediction in the signal region, the overall effect on the combined top background is reduced.

[3]The listed theory uncertainties follow the recommendations of the ATLAS top modeling working group [478]. Uncertainties from the choice of the PDF were found to be negligible in jet-inclusive phase spaces.

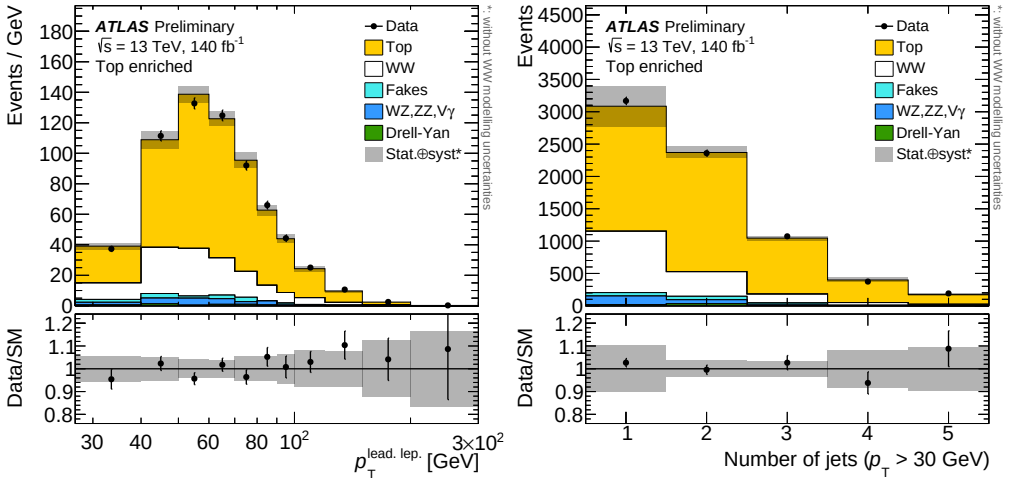

(a) Leading lepton p_T. (b) Jet multiplicity.

Figure 8.3: Detector-level distributions of (a) $p_T^{\text{lead. lep.}}$ and (b) the jet multiplicity in the top-enriched jet-inclusive region. Overflow events are included in the last bin. Data are shown as black markers, together with histograms for the predictions of signal and background processes. The top-quark background is estimated using the data-driven methods described in Section 8.1. The lower panels show the ratio of the data to the total prediction. The displayed uncertainty bands include statistical and systematic uncertainties. Theory uncertainties on the signal are negligible and, therefore, not shown. Published in Ref. [87].

In comparison to a pure MC estimate, the uncertainty in the matrix element calculation, the final state radiation, and the $t\bar{t}$ cross section, which dominate the modeling uncertainties, are strongly reduced by the b-tag counting method. As Wt events dominate the backgrounds in the 1 and 2 b-jet regions, any uncertainties affecting the Wt independently of b-jet multiplicity (e.g. the cross-section uncertainty) mostly cancel out.

The top-quark background estimate is validated in a top-enriched region that overlaps with the signal regions, by requiring at least one jet and $m_{\ell j} < 140\,\text{GeV}$ as well as $\Delta\phi_{e\mu} < \pi/2$ in addition to the normal event selection. Here $m_{\ell j}$ is the invariant mass of the leading jet and the closest lepton. This region is approximately $70\,\%$ pure in top events and shows good agreement between the data and the combined signal and background prediction, which uses the data-driven top-quark background estimate. Figure 8.3 show the distributions of the $p_T^{\text{lead. lep.}}$ (Fig. 8.3a) and the jet multiplicity (Fig. 8.3b), confirming the accurate modeling of lepton and jet-related properties in events without b-jets.

8.2 Drell-Yan Background

Despite the strong suppression of Drell-Yan $Z + \text{jets}$ contributions by the requirements of opposite-flavor dilepton system as well as dilepton invariant mass of $m_{e\mu} > 85\,\text{GeV}$ of the signal region definition listed in Table 7.2, decays into τ-lepton pairs ($Z/\gamma^* \to \tau^-\tau^+$, when the two τ-leptons decay leptonically into one electron, one muon and neutrinos) can still fulfill the selection criteria. The $Z + \text{jets}$ background is estimated using MC simulation computed with SHERPA 2.2.1. The relative contribution of this background to the selected W^+W^- event candidates in the jet-inclusive signal region is about $5\,\%$. In addition to the theoretical uncertainty in the $Z + \text{jets}$ cross section of $5\,\%$ [479], uncertainties

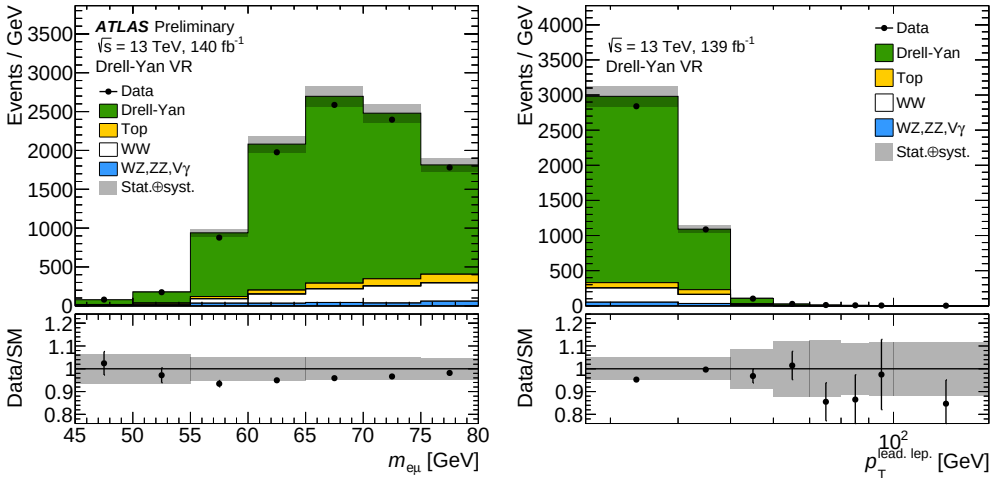

(a) Dilepton invariant mass $m_{e\mu}$. (b) Leading lepton p_T.

Figure 8.4: Detector-level distributions of (a) the dilepton invariant mass ($m_{e\mu}$) and (b) the leading lepton p_T ($p_T^{\text{lead. lep.}}$) in the Drell-Yan validation region. Overflow events are contained in the last bin. Data are shown as black markers, together with the stacked histogram accounting for signal and background processes. The top-quark and fake backgrounds are estimated using the data-driven methods described in Sections 8.1 and 8.4, respectively. Contributions from the non-prompt lepton background are negligible in this region. The lower panels show the ratio of the data to the total SM prediction. The shown uncertainty bands include statistical and systematic uncertainties. Theory uncertainties on the signal are negligible and, therefore, not shown. Published in Ref. [87].

in the $Z + \text{jets}$ background are estimated by assessing the 7-point scale variations of the renormalization and factorization scales used in the matrix element calculation.

The modeling of the $Z + \text{jets}$ estimation is evaluated in a validation region by modifying the dilepton invariant mass requirement of the W^+W^- selection to be between $45\,\text{GeV}$ and $80\,\text{GeV}$, imposing also that either $p_T^{\ell\ell} < 30\,\text{GeV}$ or $E_T^{\text{miss}} < 20\,\text{GeV}$, in addition to the remaining signal region conditions. The $Z + \text{jets}$ purity of this region is about $85\,\%$ and good modeling of the data is observed. Figure 8.4 shows the distribution of the dilepton invariant mass $m_{e\mu}$ (Fig. 8.4a) and the leading lepton p_T (Fig. 8.4b) in the Drell-Yan validation region, featuring the resonant $Z \to \tau^-\tau^+$ production over a rising background of top events. The background estimate is successfully validated by an excellent agreement with the data in this region.

8.3 Multiboson Contributions

Events arising from (i) WZ production (i.e., a W-boson in association with an off-shell $Z/\gamma^\star$ or an on-shell Z-boson) when one of the leptons is either not identified or lies outside the acceptance of the selected jet inclusive region, (ii) ZZ events where one lepton from each Z-boson escapes the W^+W^- selection acceptance, and (iii) $V\gamma$ (with $V = W, Z$) events when the photon is reconstructed and selected as an electron candidate, can mimic the expected signature of W^+W^- production.

Backgrounds from VZ and $V\gamma$ contributions are estimated from simulation using SHERPA MC generators (listed in Table 7.1), and are found to contribute about $3\,\%$ of the

total selected events in the jet-inclusive signal region. The SHERPA cross sections for these processes are found to be in good agreement with the NNLO predictions [441, 442, 443, 444]. The dominant contributions from diboson processes arise from WZ, and its modeling is observed to be well-described by the nominal SHERPA simulation in other WZ measurements by the ATLAS Collaboration [480]. Similarly to the $Z + \text{jets}$ background, uncertainties from the simulation of diboson processes due to missing higher-order QCD corrections are derived as the envelope of the 7-point scale variations of μ_R and μ_F used in the matrix element calculations. An additional uncertainty in the diboson cross section of $10\,\%$ [481, 482] is considered. Triboson production (VVV) has a relative contribution lower than $0.1\,\%$ in the signal region[4] and it is therefore neglected.

The VZ (WZ and ZZ) prediction is validated in events containing a third lepton having $p_T \geq 10\,\text{GeV}$ that must satisfy loosened identification criteria. The invariant mass of the resulting same-flavor opposite-charge pair of leptons is required to be between $80\,\text{GeV}$ and $100\,\text{GeV}$ (close to the Z-boson mass), while the remaining selection criteria are identical to the signal region. A purity greater than $90\,\%$ for diboson events is found in this region, and the prediction is in good agreement with the data. The E_T^{miss} distribution in this region shows strong separation power between ZZ and WZ events, as seen in Figure 8.5a.

$V\gamma$ ($W\gamma$ and $Z\gamma$) events enter the signal region as backgrounds when the photon is reconstructed and selected as an electron candidate. Double-counted events due to final-state photon radiation between Drell-Yan $Z + \text{jets}$ and $V\gamma$ MC simulation are discarded from the Drell-Yan MC samples using information at the event-generation level. Photons produced after initial- or final-state radiation are accounted for in this background contribution. To validate estimates of these backgrounds, the electron identification requirements are changed such that contributions from photon conversions increase[5]. As the electron candidates reconstructed from photon conversion are charge symmetric, both opposite-charge and same-charge candidates are selected with respect to the selected muon. For the $V\gamma$ validation region the p_T distribution of the electron candidates is shown in Figure 8.5b. It is dominated by electrons from photon conversion. Good agreement with the observed data in the validation regions is found.

8.4 Contributions from Fake and Non-Prompt Leptons

Reducible backgrounds due to lepton misidentification originate from events where the lepton selection criteria are fulfilled by a different object, making the event be accepted by the W^+W^- dilepton selection requirements. This happens mostly in the production of collimated jets and secondary decays that are misidentified as prompt leptons, and are referred to as *fake* and *non-prompt* leptons, respectively, or *fakes* for brevity). As discussed in Section 7.3, the estimation of the fake-lepton background is of great importance in W^+W^- measurements at hadron colliders. Due to the limitations of the MC simulation of these processes and the limited dataset of misidentified leptons, the modeling of the fake background requires complex data-driven techniques. In this section,

[4] For a dataset of $140\ \text{fb}^{-1}$, the predictions of WWW, WWZ, WZZ, and ZZZ production using SHERPA 2.2.2 MC simulation yield a sum of $81 \pm 1\,(\text{stat.}) \pm 10\,(\text{syst.})$ expected events in the jet inclusive SR.

[5] Photon conversions are enhanced by selecting electron candidates using the `LooseLH` identification working point, discarded if a hit in the IBL pixel detector is recorded.

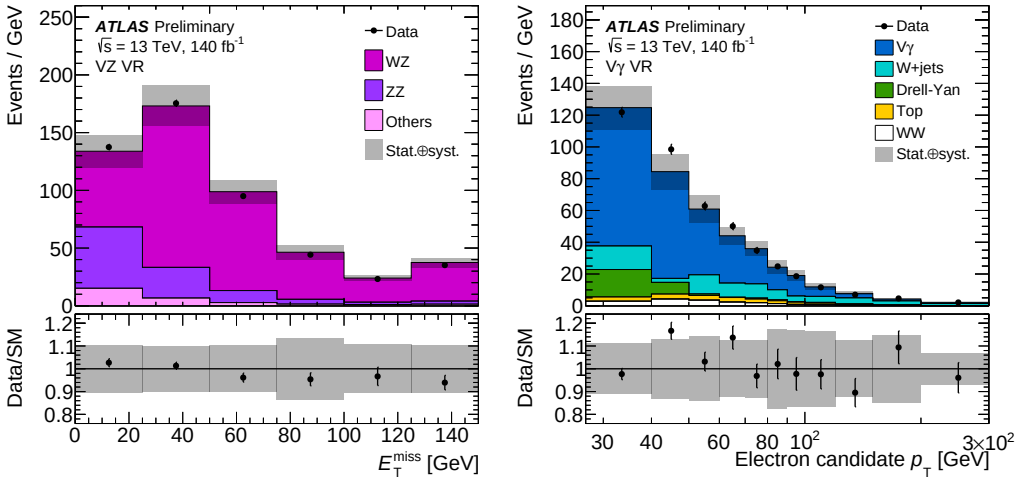

(a) Missing transverse energy in the VZ VR. (b) Electron candidate p_T in the $V\gamma$ VR.

Figure 8.5: Detector-level distributions of (a) E_T^{miss} in the VZ validation region and (b) the electron candidate p_T in the $V\gamma$ validation region. Overflow events are included. Data are shown as black markers, together with histograms for the predictions of signal and background processes. The top-quark background is estimated using the data-driven methods described in Section 8.1. The lower panels show the ratio of the data to the total prediction. The displayed uncertainty bands include statistical and systematic uncertainties. Theory uncertainties on the signal are negligible and, therefore, not shown. Published in Ref. [87].

the background contributions due to lepton misidentification are discussed. The *matrix method*, and a variant, the *fake-factor method*, are studied in Section 8.4.1 being the data-driven techniques used for the estimation of this background in W^+W^- analyses. These methods require additional lepton selection criteria, which are looser compared to the nominal selection (Table 7.2), defined in Section 8.4.2. Section 8.4.3 presents studies of the fake lepton composition in the measurements performed in this dissertation. The determination of the fake factors used for this analysis is presented in Section 8.4.4. A dedicated calibration of prompt leptons passing the loose selection requirements, presented in Section 8.4.5, has been performed to reduce systematic uncertainties, which are finally discussed in Section 8.4.7 after the validation of the background estimate.

8.4.1 Foundations of Matrix and Fake-Factor Methods

The backgrounds arising after the production of fake and non-prompt leptons are difficult to model accurately from simulation. These depend strongly on the details of the physics simulation, either on non-perturbative regions where the simulation is not expected to be reliable or the limited modeling of the material composition and response of the detector. The simulation of these processes with a sufficient statistical dataset requires enormous computing resources. Even though the event yields from fakes in the signal region are small, the modeling of the lepton misreconstruction background is highly complex, which translates into large systematic uncertainties propagated to the cross-section measurement. Data-driven techniques are therefore indispensable to estimate these background contributions with sufficient accuracy. The data-driven techniques considered in this analysis, denoted as *matrix* and *fake-factor methods*, are outlined in this section. The relationship between the two is studied in Ref. [483]. These and other methods used by

the ATLAS Collaboration for the fake and non-prompt lepton background estimation are also discussed in Ref. [484].

After a given baseline selection C is required, a certain number of events of the process a are selected by C_b, designed to enhance contributions of the process b, with efficiency $\varepsilon_a(C_b)$. A number of events $N(C_a)$ can therefore contribute to a given dataset where a total number of events N is selected. Background contributions are not fully rejected in real scenarios by the signal-region selection C_S, with $\varepsilon_{B_i}(C_S)$ being efficiency of the corresponding selection criteria of the background source B_i ($i = 1, \ldots, n$ number of background sources). The contributions to the events selected by C_S, $N(C_S)$, can be *estimated* by considering the corresponding selection efficiencies for each process as

$$N(C_S) = \varepsilon_S(C_S)N_S + \sum_{i=1}^{n} \varepsilon_{B_i}(C_S)N_{B_i}\,, \tag{8.7}$$

with the contributions N_S and N_{B_i} being defined with respect to a common baseline selection. A given selection efficiency $\varepsilon_a(C_X)$ is therefore defined as the ratio of a-selected events by a given selection C_X over all the events of a in the given baseline selection. The estimation of the contributions N_S and all N_{B_i} can be inferred by including additional selection criteria C_{B_i}, extending Eq. (8.7) to a system of equations that, in matrix notation, can be written as

$$\mathbf{N}_{\text{sel}} \equiv \begin{pmatrix} N(C_S) \\ N(C_{B_1}) \\ N(C_{B_2}) \\ \vdots \\ N(C_{B_n}) \end{pmatrix} = \begin{pmatrix} \varepsilon_S(C_S) & \varepsilon_{B_1}(C_S) & \varepsilon_{B_1}(C_S) & \cdots & \varepsilon_{B_n}(C_S) \\ \varepsilon_S(B_1) & \varepsilon_{B_1}(B_1) & \varepsilon_{B_1}(B_1) & \cdots & \varepsilon_{B_n}(B_1) \\ \varepsilon_S(B_2) & \varepsilon_{B_1}(B_2) & \varepsilon_{B_1}(B_2) & \cdots & \varepsilon_{B_n}(B_2) \\ \vdots & \vdots & \vdots & \ddots & \vdots \\ \varepsilon_S(B_n) & \varepsilon_{B_1}(B_n) & \varepsilon_{B_2}(B_n) & \cdots & \varepsilon_{B_n}(B_n) \end{pmatrix} \cdot \begin{pmatrix} N_S \\ N_{B_1} \\ N_{B_2} \\ \vdots \\ N_{B_n} \end{pmatrix} \equiv \hat{\varepsilon} \cdot \mathbf{N}\,. \tag{8.8}$$

Here, $\mathbf{N}_{\text{sel}}$ is the vector of events selected using the different selection criteria while $\mathbf{N}$ is the vector of *expected* baseline number of events contributing from each process. Note that, since the signal event yields observed in the data $N(C_S)$ are present in the equation, the signal region is not blinded when performing the estimation of the background contributions. The matrix $\hat{\varepsilon}$ is the so-called *efficiency matrix*, diagonal if all selection criteria C_a ($a = S, B_1, \ldots, B_n$) isolated the targeted process a perfectly. Therefore, the estimation of the vector $\mathbf{N}$ can be performed by inverting the efficiency matrix

$$\mathbf{N} = \hat{\varepsilon}^{-1} \cdot \mathbf{N}_{\text{sel}}\,. \tag{8.9}$$

The presented formalism, known as the *matrix method*, is in principle fully data-driven. However, the efficiency matrix ε needs to be determined beforehand. Depending on the processes to be estimated, control regions in data can be defined to extract the selection efficiencies using, e.g., the *tag-and-probe* method presented in Section 8.4.5. Nevertheless, this is sometimes not possible due to, for instance, limited statistics or challenging isolation of the process of interest. In such cases, MC simulations are required.

The matrix method has been extensively used in hadron collider measurements and traditionally in ATLAS W^+W^- measurements such as Refs. [75, 79] to estimate fake and non-prompt lepton background contributions. For fake-background estimations, the enrichment of signal and lepton misidentification is performed by using different lepton selection criteria. The former is enriched by using tight requirements (referred to as *ID*

selection, I) such as the ones listed in Table 7.2. The latter are usually enhanced by loosening the identification and isolation working points. Contributions from lepton misidentification can be further enriched by requiring the working point to fail the tight definition, being both completely orthogonal. This selection strategy is denoted to as *AntiID selection* (A). For dilepton final states under these conditions, Equation (8.8) reduces to

$$\begin{pmatrix} N(\mathrm{I}+\mathrm{I}) \\ N(\mathrm{I}+\mathrm{A}) \\ N(\mathrm{A}+\mathrm{I}) \\ N(\mathrm{A}+\mathrm{A}) \end{pmatrix} = \begin{pmatrix} \varepsilon_p^{\ell_0}\varepsilon_p^{\ell_1} & \varepsilon_p^{\ell_0}\varepsilon_f^{\ell_1} & \varepsilon_f^{\ell_0}\varepsilon_p^{\ell_1} & \varepsilon_f^{\ell_0}\varepsilon_f^{\ell_1} \\ \varepsilon_p^{\ell_0}(1-\varepsilon_p^{\ell_1}) & \varepsilon_p^{\ell_0}(1-\varepsilon_f^{\ell_1}) & \varepsilon_f^{\ell_0}(1-\varepsilon_p^{\ell_1}) & \varepsilon_f^{\ell_0}(1-\varepsilon_f^{\ell_1}) \\ (1-\varepsilon_p^{\ell_0})\varepsilon_p^{\ell_1} & (1-\varepsilon_p^{\ell_0})\varepsilon_f^{\ell_1} & (1-\varepsilon_f^{\ell_0})\varepsilon_p^{\ell_1} & (1-\varepsilon_f^{\ell_0})\varepsilon_f^{\ell_1} \\ (1-\varepsilon_p^{\ell_0})(1-\varepsilon_p^{\ell_1}) & (1-\varepsilon_p^{\ell_0})(1-\varepsilon_f^{\ell_1}) & (1-\varepsilon_f^{\ell_0})(1-\varepsilon_p^{\ell_1}) & (1-\varepsilon_f^{\ell_0})(1-\varepsilon_f^{\ell_1}) \end{pmatrix} \cdot \begin{pmatrix} N_{pp} \\ N_{pf} \\ N_{fp} \\ N_{ff} \end{pmatrix}, \tag{8.10}$$

with $\varepsilon_k^{\ell_0}$ and $\varepsilon_k^{\ell_1}$ being the efficiencies of the leading and subleading k lepton, respectively, fulfilling the baseline lepton selection criteria to also pass the tight criteria. The efficiencies ε_k^{ℓ}, where $k = p, f$ labels either a prompt or a fake lepton, depend on features of the lepton kinematics such as its transverse momentum p_T, $|\eta|$, or proximity in ΔR to other objects. After the inversion of Eq. (8.10), two components of the fake-lepton background can contribute to the background estimation, namely when only one of the fake leptons is misreconstructed as a prompt ($N_{pf} + N_{fp}$, mostly arising from $W + \mathrm{jets}$ and semileptonic $t\bar{t}$) or from cases where the two fake leptons are reconstructed as prompt (N_{ff}, originating from QCD multijet production). The background estimation is computed by accounting for these two terms in the ID+ID selection, which corresponds to the signal region,

$$N^{\mathrm{I+I}}_{\text{lepton misID}} = \varepsilon_p^{\ell_0}\varepsilon_f^{\ell_1} N_{pf} + \varepsilon_f^{\ell_0}\varepsilon_p^{\ell_1} N_{fp} + \varepsilon_f^{\ell_0}\varepsilon_f^{\ell_1} N_{ff}\,.$$

The aforementioned equations give an estimation of the normalization factor to be applied on the measured total number of data events. However, the method can also be used to estimate differential distributions by calculating a weight for each data event. The expression of the weight depends on the selection criteria fulfilled by the two leptons in the final state.

In usual definitions of the two lepton selection criteria, ε_p are close to 1, while ε_f are low to reject fake leptons. The ideal prompt and fake lepton selection criteria will make the efficiencies $\varepsilon_p \to 1$ and $\varepsilon_f \to 0$, which is the case when the efficiency matrix in Eq. (8.10) is diagonal. The lepton selection criteria used in this work are presented in Section 8.4.2. Using the one-lepton final state case of Eq. (8.10) for simplicity, the matrix inversion results in

$$N_f = \frac{1}{\varepsilon_p - \varepsilon_f}\left[(\varepsilon_p - 1)N(\mathrm{ID}) + \varepsilon_p N(\mathrm{AntiID})\right]\,. \tag{8.11}$$

Since MC simulation provides an accurate modeling and calibration of prompt leptons, a simplification of the matrix method can be performed by assuming $\varepsilon_p \to 1$. The contributions lost after this assumption can be accounted for by subtracting prompt contributions in the region with AntiID leptons using MC simulation. After these considerations, the estimated number of events in the ID region originating from lepton misreconstruction then is

$$N_{\text{lepton misID}} = \varepsilon_f N_f = \frac{\varepsilon_f}{1-\varepsilon_f} \cdot N(\mathrm{AntiID}) = F\left[N_{\mathrm{Data}}(\mathrm{AntiID}) - N_{p,\mathrm{MC}}(\mathrm{AntiID})\right]\,, \tag{8.12}$$

where the extrapolation factor F from the AntiID region to the signal region is the known as *fake factor*. In this approach, known as *fake-factor method*, the estimated background yield does not depend on the yield $N(\mathrm{ID})$, and the method can be used while blinding the data in the signal region. It should be noted that Eq. (8.12) also establishes a relation between the fake-lepton selection efficiencies ε_f and the fake factor F. Similarly as for ε_f, F depends on the fake-lepton kinematics. The fake factors are computed as the ratio of fake leptons fulfilling the ID requirements over the number of AntiID fake leptons, being normally derived from the number of events in data (after subtracting events from prompt lepton contamination) in a region enriched in fake-lepton production as

$$F = \frac{N_f(\mathrm{ID})}{N_f(\mathrm{AntiID})} = \frac{N(\mathrm{ID}) - N_{\mathrm{MC},p}(\mathrm{ID})}{N(\mathrm{AntiID}) - N_{\mathrm{MC},p}(\mathrm{AntiID})}\,. \tag{8.13}$$

Since differential distributions are available for N and $N_{\mathrm{MC},p}$ in Eq. (8.12), the fake background estimation can be performed by applying the method bin by bin across the differential observable of interest.

8.4.2 Definition of the AntiID Lepton Selection Criteria

In the matrix method, the challenge to be tackled when defining the loose lepton selection criteria is twofold. On the one hand, the difference $\varepsilon_p - \varepsilon_f$ is to be maximized to reduce the number of fake-lepton contributions in the signal region. On the other hand, one has to keep a sufficiently large dataset to derive the fake-lepton selection efficiencies with significant statistics. Additionally, the AntiID selection criteria imposes the ID conditions to be failed, constraining the lepton selection even further.

The electron and muon AntiID selection requirements used in this analysis are listed in Table 8.2, defined by loose conditions while failing the ID selection criteria (Table 7.2). AntiID electrons are required to satisfy the `MediumLH` identification, and the track- and calorimeter-based isolation requirements are relaxed imposing the `FixedCutPflowLoose` working point for electrons with $p_T < 55\,\mathrm{GeV}$. No isolation requirements are imposed for AntiID electrons of greater transverse momentum. AntiID electrons must fail either the identification requirements of the ID electron (`TightLH`) or the ID isolation working point (`Gradient`). The AntiID muon $|d_0/\sigma_{d_0}|$ is extended to the region $|d_0/\sigma_{d_0}| < 10$ to target production in secondary decays, as well as isolation conditions imposed to fulfill the looser `FixedCutPflowLoose` definition, based on track isolation only. AntiID muons must therefore fail the `Tight_FixedRad` muon isolation working point for muon $|d_0/\sigma_{d_0}| < 3$, allowed to be fulfilled if the muon impact parameter lies within the range $3 < |d_0/\sigma_{d_0}| < 10$. In terms of selection efficiency, the AntiID electron (muon) selection criteria are tighter than the ID definition by a factor of 8 (16). Table 8.3 shows the number of W^+W^- event candidates selected with both ID+ID and ID+AntiID selection requirements at the preselection stage.

As discussed in Section 4.2.7, the definition of the single lepton trigger chains makes use of lepton identification and track isolation criteria to improve the prompt lepton purity. This causes biases in the AntiID lepton sample, since the selection requirements in the trigger algorithm are implicitly tighter than the AntiID lepton selection. Using the full Run 2 dataset in the ID+AntiID control regions used to determine the data-driven background estimate, Table 8.4 shows the fractions of data events triggered by either the

	AntiID electron	**AntiID muon**
Pseudorapidity	$\|\eta\| < 1.37$ or $1.52 < \|\eta\| < 2.47$	$\|\eta\| < 2.5$
p_T [GeV]	$p_T > 15$	
$\|z_0 \sin\theta\|$ [mm]	$\|z_0 \sin\theta\| < 0.5$	
$\|d_0/\sigma_{d_0}\|$	$\|d_0/\sigma_{d_0}\| < 5$	$\|d_0/\sigma_{d_0}\| < 10$
Identification	`MediumLH`	`Medium`
Isolation	`FixedCutPflowLoose`	`FixedCutPflowLoose` ($p_T < 55\,\text{GeV}$)
Fail ID selection	Fail either `TightLH` ID or `Gradient` isolation	Fail either $\|d_0/\sigma_{d_0}\| < 3$ or `Tight_FixedRad` isolation

Table 8.2: AntiID lepton selection requirements for electrons and muons.

Channel	$e\mu$		μe	
AntiID lepton	muon	electron	muon	electron
ID+AntiID	3442 ± 25	3730 ± 30	1338 ± 15	5350 ± 30
ID+ID	41650 ± 90		38380 ± 80	

Table 8.3: Number of signal $qq \to W^+W^-$ event candidates for the full Run 2 dataset at the preselection stage using both ID+ID and ID+AntiID dilepton selection. Only statistical uncertainties are shown.

Lepton matched	**AntiID muon**		**AntiID electron**		Fraction [%]
	$e\mu$	μe	$e\mu$	μe	
ID only	4167	914	3160	6358	41.7
ID and AntiID	6382	2331	3578	4690	48.4
AntiID only	391	391	1257	1413	9.9

Table 8.4: Fractions of data events recorded in full Run 2 trigger-matched by either the ID lepton only, the AntiID lepton only, or both ID and AntiID leptons in the jet-inclusive region defined in Table 7.2 using ID+AntiID dilepton selection.

ID lepton, both ID and AntiID leptons, or the AntiID lepton only. The effects on these fractions introduced by the selection requirements defining the signal region are minor. The ID lepton drives the triggering of the event, either alone or together with the AntiID lepton, especially when being the lepton of highest-p_T in the event. Events triggered by the AntiID lepton only constitute $9.9\,\%$ of the total number of events, which would introduce a bias in the AntiID lepton definition. To account for this bias, the selected events are categorized according to the leptons that triggered the readout system, deriving fake factors individually for the categories where at least one ID lepton or only AntiID leptons fire the single lepton triggers.

Additionally, the fake-factor method assumes a good modeling of prompt leptons passing the looser selection. In this dissertation, an accurate modeling of prompt AntiID leptons is ensured for the first time deriving a dedicated calibration using tag-and-probe techniques. This endeavor, which improves the precision of the measurement considerably, is discussed in Section 8.4.5.

8.4.3 Sources and Composition of Misidentified Leptons. Definition of the Fake-enriched Region

The aforementioned fake leptons can be divided in two main categories. On the one hand, leptons produced in secondary hadron decays that fulfill the primary vertex assignment and lepton selection requirements of the analysis are referred to as *non-prompt*

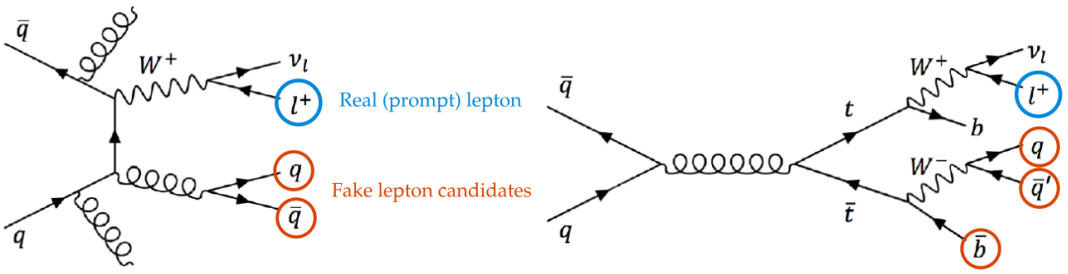

(a) W + jets production. (b) Semileptonic $t\bar{t}$ production.

Figure 8.6: Illustrative Feynman diagrams for the sources of fake and non-prompt leptons in the signal region defined in Table 7.2 for the W^+W^- analysis.

leptons. On the other hand, if a non-leptonic object such as a hadronic jet fulfills the lepton selection requirements, being finally misreconstructed as a lepton, it is denoted as *fake lepton*. These sources do not include leptons originated from photon conversions, accounted for in background contributions arising from $V\gamma$ production, described in Section 8.3. In contrast, prompt leptons are defined as electrons or muons directly produced either in the hard-scattering process or in the decay of a short-lived non-hadronic resonance (such as a $W^{\pm}$ and Z bosons). Non-prompt electrons are produced via secondary decays within the hadronic activity of a jet, while fake electrons are mainly highly-collimated jets[6] that leave little activity in the hadronic calorimeter and fulfill the reconstruction, identification and isolation criteria of prompt electrons. Most of misidentified muons arise from secondary decays within the hadronic activity of a jet, which further traverse the electromagnetic and hadronic calorimeters. Fake muons can also be produced via so-called *punch-through jets* that penetrate through the hadronic calorimeter, leaving signatures also in the first layers of the muon spectrometer. When referring to the *fake background* (or *fakes* for simplicity), contributions from both fake and non-prompt leptons are considered.

Due to the large electron (Section 4.3.2) and muon (Section 4.3.3) reconstruction efficiencies of the ATLAS detector, these background contributions stem from SM processes with much higher production cross sections with respect to the process of interest. In measurements of W^+W^- production, W+jets production dominates the source of lepton misreconstruction. In the jet-inclusive signal region (whose selection criteria are summarized in Table 7.2), these arise especially when charmed- (42 %) and light-hadron (40 %) decays are associated to the produced jets misreconstructed as leptons[7], according to flavor-filtered W + jets MC simulation. Only 3.5 % of the non-prompt and fake lepton sources in the signal region arise from top-quark production sources such as semileptonic $t\bar{t}$ or single-top. Illustrative Feynman diagrams are presented in Figure 8.6. Two-lepton misreconstruction in multijet QCD production, having a production cross section roughly four orders of magnitude greater than diboson W^+W^- (Fig. 1.5), contributes about 5 % of the total fake background at the lowest p_T regime of the analysis.

Lepton misidentification is enhanced in a region enriched in multiple jet production, ensuring that one lepton is reconstructed with at least one jet. The same requirements

[6] In measurements of processes with small cross sections, it is likely that photons are reconstructed as electrons. Due to the large W^+W^- production cross section with respect to processes producing a lepton and a photon in the final state (e.g. $W\gamma$, see Fig. 1.5) and the small fake probability, electron fakes from photons are neglected in this analysis.

[7] Note that a b-jet veto is involved in the jet inclusive signal region (see Table 7.2).

Dijet event selection
Exactly one electron or muon with $p_T > 15\,\text{GeV}$
$N_{\text{jet}} > 0$
b-tagging requirement on leading jet (either b-tagged or b-veto)
$p_T^{\text{tagging jet}} > 25\,(30)\,\text{GeV}$ with $\lvert\eta\rvert < 2.5\,(2.5 < \lvert\eta\rvert < 4.5)$
$\lvert\Delta\phi_{\ell,j0}\rvert > 2.8$
$m_T + E_T^{\text{miss}} < 50\,\text{GeV}$
Lepton is ID or AntiID

Table 8.5: Dijet event selection used in the W^+W^- analysis.

as the selection criteria in the signal region, described in Section 7.5, are used for object selection and flavor tagging. The lepton and the leading jet are required to be produced back-to-back, i.e., with a large difference in azimuthal angle of $|\Delta\phi_{\ell,j0}| > 2.8$. In this configuration, the lepton is very likely to arise from the production of a jet. This is a so-called *dijet region*. The selection criteria used in this analysis are summarized in Table 8.5. To vary the flavor composition of the jet leading to the misreconstructed lepton, different b-tagging requirements can be applied on the recoiling jet. The production of $W + \text{jets}$ events dominates the prompt lepton contamination, i.e., SM processes involving a prompt lepton in addition to hadronic activity in the final state. These can be suppressed by selecting events with low $E_{T,\,\text{Track}}^{\text{miss}} + m_T$.

The information of fake electrons and muons at particle level in the dijet MC samples is insufficient to infer the origin of the lepton[8]. An alternative approach to infer the jet-flavor composition of the fake leptons in the signal region is followed by comparing the MC predictions of lepton misidentification sources from $W + \text{jets}$, where the flavor of the hadronic activity in the final state is filtered, and semileptonic $t\bar{t}$ production. Three filters are used: (i) events where at least one of the partons in the final state is a b-quark (categorized as b-flavor), (ii) events where at least one of the partons in the final state is a c-quark while events containing b-quarks are vetoed (c-flavor), and (iii) the remaining events where no b- or c-flavored quarks are produced (light-flavor). Jet filters are applied at particle level (i.e. before any detector simulation) to a large unfiltered sample, with each MC sample being rescaled by a corresponding filter efficiency. Semileptonic $t\bar{t}$ and single-top production is included in the b-flavor category. Jet-flavor fractions for each category are computed with respect to the sum of the three flavor categories. By assumption of lepton universality in the MC production, the flavor composition of these samples is independent of the lepton flavor.

The dominant contributions from W^+W^-, $t\bar{t}$, and Drell-Yan production can be heavily suppressed by imposing a same-sign dilepton selection. This feature is exploited to enhance contributions from lepton misidentification, used to define validation regions for the estimation of this background. Figure 8.7 presents the flavor composition of $W + \text{jets}$, semileptonic $t\bar{t}$, and single-top production along the sequential stages that define the signal region of this analysis. The MC samples used as a source of lepton misidentification are enriched in $58\,\%$ b-flavor at the preselection stage, before same-sign and opposite-sign selections are imposed. These fractions drop by a factor of 3 after the b-jet veto is applied. The flavor composition between same- and opposite-sign selection criteria agrees

[8]Studies on fake lepton composition using the ATLAS `MCTruthClassifier` are presented in Appendix B.

reasonably well along the different cut stages. This shows that the same-sign validation region is appropriate in terms of jet-flavor composition. However, the signal region shows significantly high b-flavor fraction ($20\,\%$) despite being exposed to a b-jet veto requirement. Fake factors derived in either a b-vetoed or a b-tagged dijet region might not be appropriate for the estimation of the fake-lepton background in the signal region. Contrarily to the approach followed by the $WW+\geq 1\,\text{jets}$ analysis [81] where the b-vetoed fake factors were considered as nominal, the results presented following this approach motivate the redefinition of the nominal fake factors as an average of b-tagged and b-vetoed distributions, being the envelope of distributions from these two requirements an assessment of the uncertainty due to jet-flavor composition bias. The use of the average reduces the corresponding uncertainties by a factor of two with respect to the $WW+\geq 1\,\text{jets}$ analysis.

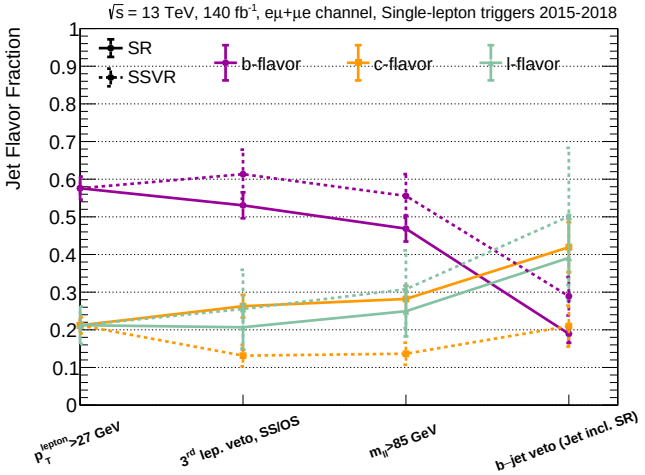

Figure 8.7: Flavor-composition fractions of the fake-lepton sources as derived from flavor-filtered MC samples of $W+\text{jets}$, semileptonic $t\bar{t}$, and single-top production in the same-sign and opposite-sign signal regions. Only statistical uncertainties in the simulated MC samples are displayed.

8.4.4 Fake-Factor Measurement

Since no further requirements on the jet multiplicity enter the definition of the dijet region, the fake factors computed for the $WW+\geq 1\text{jets}$ analysis [81] are also implemented in this measurement. In the dijet region defined in Table 8.5, where each event contains at least one lepton candidate balanced by a jet, a control sample of data events enhancing the reconstruction of non-prompt leptons is selected for the determination of the fake factors using Eq. (8.13). Contributions from prompt leptons, as predicted from MC simulation, are subtracted from the data beforehand. An unprescaling weight is applied to data events recorded with prescaled single-lepton triggers[9]. Similarly, the bias by the trigger selection on AntiID leptons is evaluated by computing fake factors using the nominal unprescaled triggers of the analysis, listed in Table 4.4. Fake factors using unprescaled single-lepton triggers are applied to events triggered by the AntiID lepton only (a total of $9.9\,\%$ of the events, as given in Table 8.4). The electron and muon fake factors are shown in Figure 8.8, together with their aforementioned systematic variations. Systematic variations to these, discussed in Section 8.4.6, are determined by deriving additional sets of fake factors. Prompt AntiID lepton mismodeling, studied in detail in the following section, can affect the calculation of the fake factors. The observed effects are negligible with

[9]The prescaled single-electron trigger `HLT_e12_lhvloose_nod0_L1EM10VH` and single-muon trigger `HLT_mu14` are implemented, with thresholds of $E_T > 12\,\text{GeV}$ and $p_T > 14\,\text{GeV}$, respectively. The values of the prescales vary according to the demands of the data acquisition system throughout data-taking.

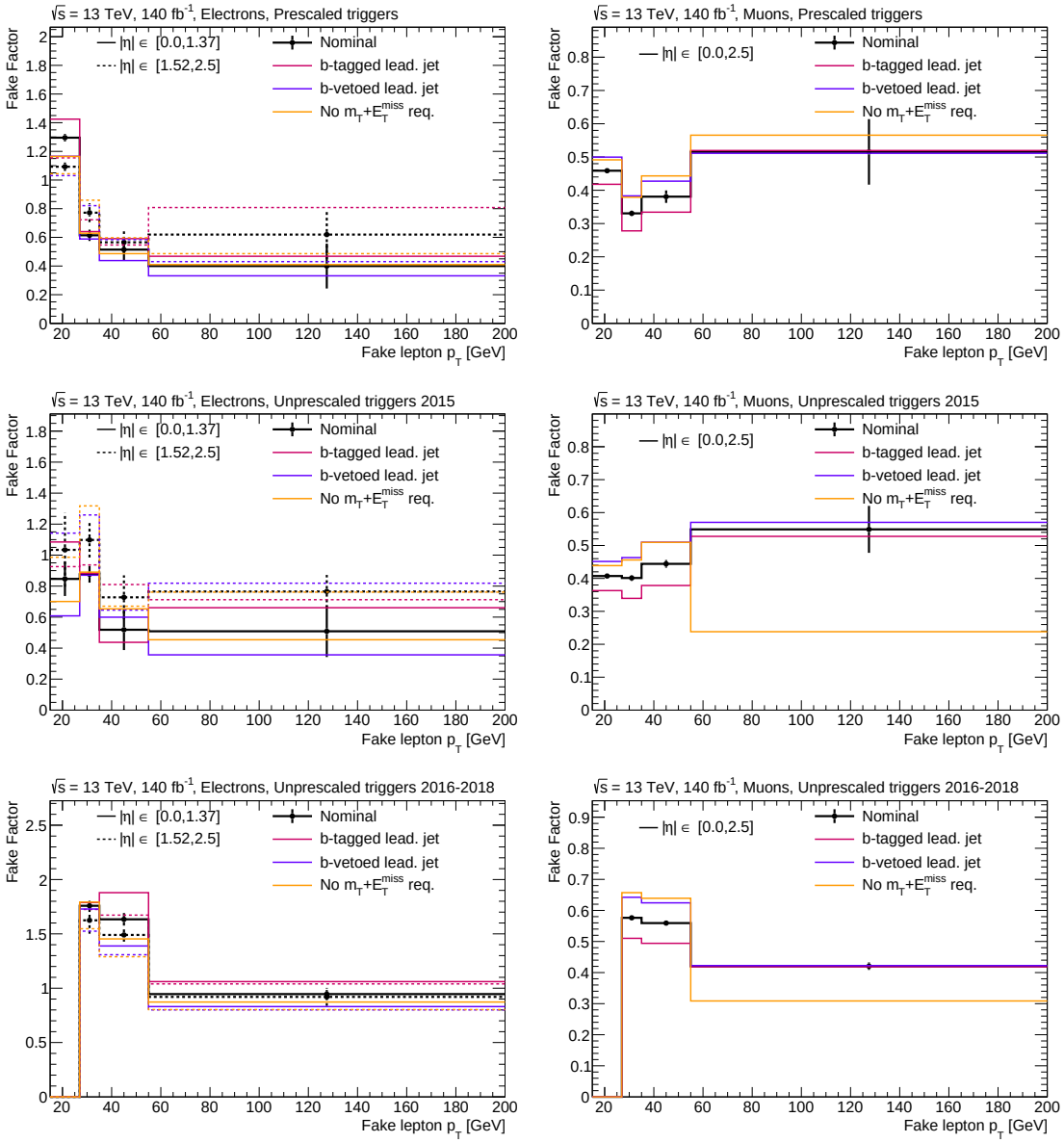

Figure 8.8: Fake factors derived in the dijet region defined in Table 8.5 for electrons (left) and muons (right) using prescaled (top), unprescaled analysis triggers in 2015 (centre) and 2016–2018 (bottom). Statistical uncertainties are displayed on the nominal distribution.

respect to the statistical uncertainties and are therefore not considered[10].

8.4.5 AntiID Prompt Lepton Calibration

The fake-factor method, introduced in Section 8.4.1, relies on the definition of both ID and AntiID lepton selection criteria. While the modeling of ID leptons in MC simulation is expected to be good after an exhaustive calibration performed by dedicated Combined Performance groups within the ATLAS Collaboration, an accurate modeling of AntiID leptons needs to be ensured for a reliable background estimate. This is particularly important if prompt contributions are large in AntiID regions, such as the dijet control region used in Eq. (8.13), or the ID+AntiID control region where the extrapolation to the ID+ID region is performed by applying the fake factors via Eq. (8.12). This is crucial for W^+W^- measurements, whose ID+AntiID control regions suffer from a large prompt contamination[11]. In this section, studies of this mismodeling and dedicated calibrations for the W^+W^- measurement are presented.

After systematic uncertainties from the parton shower modeling of the top-quark background and pile-up jets, uncertainties related to the mismodeling of prompt AntiID leptons were the largest in the $WW+\geq 1\,\mathrm{jets}$ analysis [81]. This was observed by comparing the lepton modeling in data and MC simulation in a region enriched in fully-leptonic decays of $t\bar{t}$. The agreement between ID and AntiID modeling of electrons and muons can be quantified using a *double ratio* (DR) by comparing the data-to-MC agreement in ID+AntiID and ID+ID selection criteria as

$$\mathrm{DR} = \frac{\left[\frac{N^{\mathrm{Data}} - N^{\mathrm{non-prompt,MC}}}{N^{\mathrm{prompt,MC}}}\right]_{\mathrm{ID+AntiID}}}{\left[\frac{N^{\mathrm{Data}} - N^{\mathrm{non-prompt,MC}}}{N^{\mathrm{MC}}}\right]_{\mathrm{ID+ID}}} \,. \tag{8.14}$$

Due to the given ratio, this method is particularly effective canceling out most of the systematic uncertainties affecting both event selections in a similar manner. In the $WW+\geq 1\,\mathrm{jets}$ analysis, the DR where found to be equal to 1.144 ± 0.007 for muons and 1.055 ± 0.006 electrons, showing a clear mismodeling of the simulated leptons passing AntiID selection requirements with respect to the leptons selected using the ID definition. This evidences a poor model of the prompt AntiID lepton selection efficiencies, which also differs between muons and electrons. In this analysis, a Z-peak ID+AntiID region is designed to study the modeling of prompt AntiID leptons in detail, whose definition and results are presented in the following.

The Z-peak and $t\bar{t}$ ID+AntiID Regions

In contrast to the $t\bar{t}$ region exploited during the $WW+\geq 1\,\mathrm{jets}$ analysis, an ID+AntiID region at the Z-boson resonance is used to study a richer dataset of prompt AntiID electrons

[10] The modeling of prompt AntiID lepton contamination in the dijet region can affect the subtraction of the background contamination in the denominator of the fake factor calculation given in Eq. (8.13). These are found to be about one and two orders of magnitude lower than the data for AntiID electrons and muons, respectively. The effects of such mismodeling where found to be at the percent level in each bin.

[11] A prompt contamination of about $75\,\%$ is found in the ID+AntiID region used in the W^+W^- measurement presented in this work (Fig. 8.17).

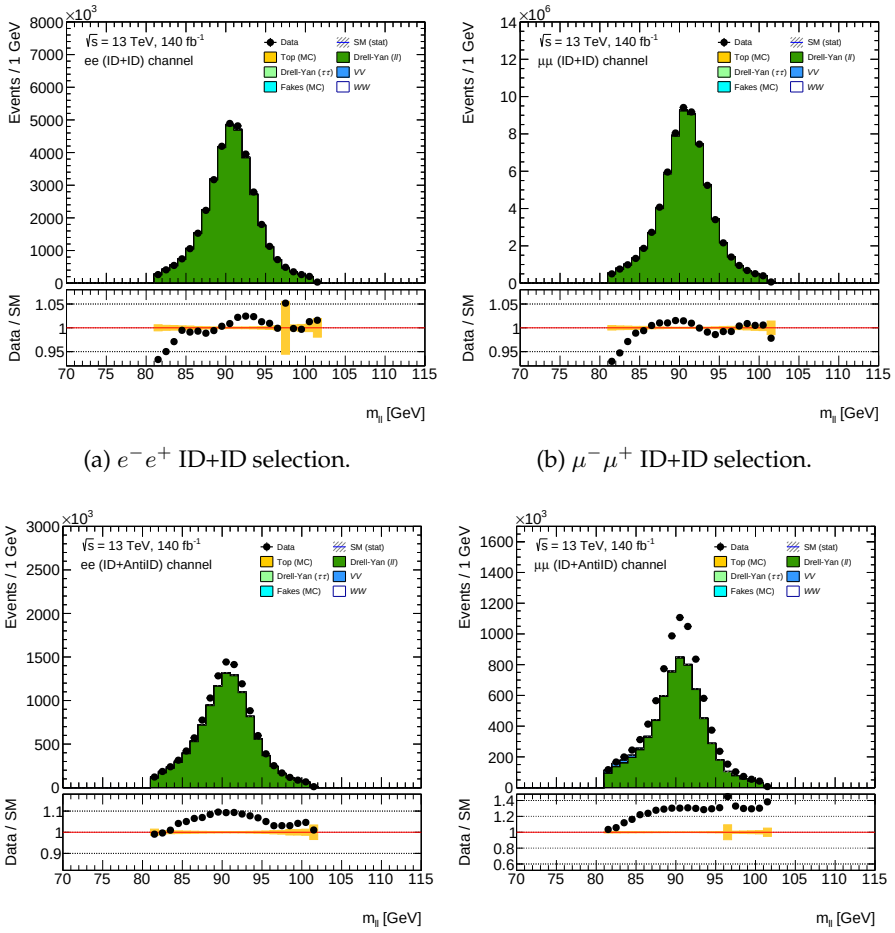

(a) e^-e^+ ID+ID selection.

(b) $\mu^-\mu^+$ ID+ID selection.

(c) e^-e^+ ID+AntiID selection.

(d) $\mu^-\mu^+$ ID+AntiID selection.

Figure 8.9: Data-to-MC agreement in the Z-peak region defined in Section 8.4.5 using a ID+ID dilepton requirement in (a) the e^-e^+ channel, and (b) $\mu^-\mu^+$ channel, and a ID+AntiID dilepton requirement in both (c) the e^-e^+ channel and (d) the $\mu^-\mu^+$ channel. Data is shown as black dots. The stacked histogram shows SM contributions from MC simulation. Only statistical uncertainties are shown.

and muons. The same selection criteria of ID (Table 7.2) and AntiID leptons (Table 8.2) is used. Same-flavor decays are considered, i.e., final states of muon-antimuon ($\mu^-\mu^+$ channel) and electron-positron (e^-e^+ channel) pairs. The same quality and trigger requirements as in the signal region are used. As done in the signal region, a third lepton veto is applied. The two leptons are required to have opposite-sign electric charge. At least one of the two leptons in the final state must fulfill ID lepton selection criteria, while the other one must satisfy the AntiID selection. To narrow prompt lepton production from Z-boson decays, a *Z window* of 10 GeV is imposed on the dilepton invariant mass $m_{\ell\ell}$, i.e. $|m_{\ell\ell} - m_Z^{\mathrm{PDG}}| < 10\,\mathrm{GeV}$, where $m_Z^{\mathrm{PDG}} = 91.1876 \pm 0.0021\,\mathrm{GeV}$ denotes the global average of the Z-boson mass [95].

Figure 8.9 shows the differences between ID+ID and ID+AntiID selection criteria in data-to-MC agreement for events at the Z-peak region in both e^-e^+ and $\mu^-\mu^+$ channels as a function of $m_{\ell\ell}$. Using the SHERPA 2.2.1 Z + jets MC simulated events, the data and expected SM contributions from MC simulation are in good agreement in ID+ID events

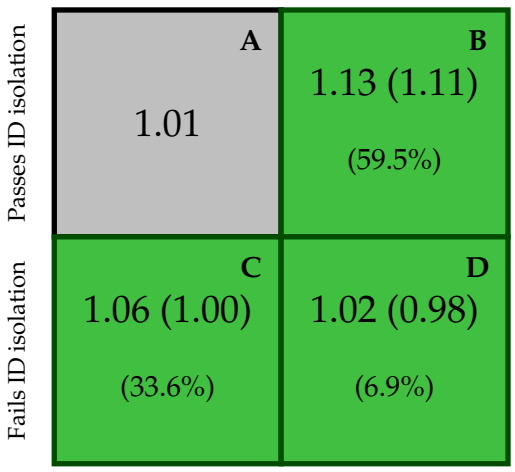

(a) e^-e^+ channel.

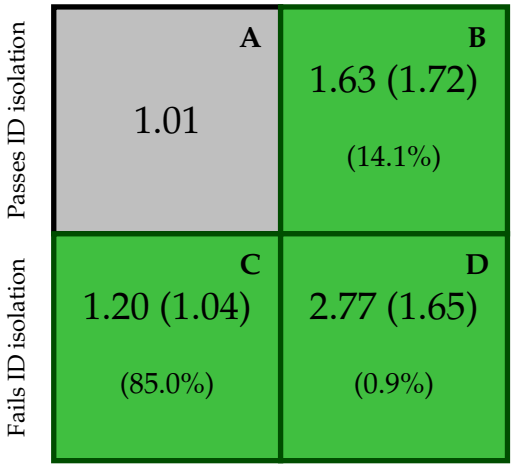

(b) $\mu^-\mu^+$ channel.

Figure 8.10: Data-to-MC ratios for the A (ID+ID selection, shown in grey), B, C, and D ID+AntiID Z-peak regions (in green) according to the fulfilled conditions of the AntiID lepton using SHERPA 2.2.1 $Z+$jets MC simulation. No prompt AntiID lepton calibration is applied. Results in both the (a) e^-e^+ channel and (b) $\mu^-\mu^+$ channel are shown. Ratios within parentheses are computed using a POWHEG+PYTHIA 8 $Z+$jets MC sample. Percentages give the portion of the corresponding region contributed to the total ID+AntiID region. Statistical errors are below 1 %.

at the Z-peak region, yielding data-to-MC ratios of 1.01 in both e^-e^+ and $\mu^-\mu^+$ channels[12]. However, these ratios increase up to 1.28 ($\mu^-\mu^+$) and 1.09 (e^-e^+) when selecting ID+AntiID events in the same region. When using an alternative $Z+$ jets MC sample produced with the POWHEG+PYTHIA 8 generator, data-to-MC ratios in the ID+AntiID Z-peak region drop to 1.10 and 1.06 in the $\mu^-\mu^+$ and e^-e^+ channels, respectively, showing a dependency of the AntiID prompt lepton mismodeling with the used MC generator.

To better understand the source of this disagreement, the Z-peak ID+AntiID region is further divided according to the selection requirement of the ID lepton that is failed in the definition of the AntiID selection. The four possible combinations are labeled as *A, B, C, and D regions*. For muons, these are either failing the $|d_0/\sigma_{d_0}| < 3$ condition of the ID muon, or its isolation working point (`Tight_FixedRad`), or both. Similarly for electron decays, the conditions to be failed are either the `LHTight` identification, or the `Gradient` isolation working points of the ID electron, or both. Since the four regions are orthogonal, the non-ID lepton populates only one of the A, B, C, or D regions. The definitions of these regions are therefore:

- Region A is populated by electrons and muons that do not fail any of the conditions of the ID selection. Therefore, region A corresponds to an ID+ID selection.
- Region B hosts electrons (muons) that fulfill the isolation of the ID lepton, but fail its identification ($|d_0/\sigma_{d_0}|$) criterion.
- Region C includes electrons (muons) that satisfy the identification ($|d_0/\sigma_{d_0}| < 3$) requirements of the ID lepton, failing the ID isolation working point.

[12]Errors in the given data-to-MC ratios are lower than 1 %, considering statistical fluctuations only.

ID+AntiID regions selection criteria	
Z-peak	$t\bar{t}$
Unprescaled single lepton triggers	
$p_{T,\ell} > 27\,\text{GeV}$, $\lvert\eta_\ell\rvert < 2.5$	
3rd lepton veto + opposite-sign leptons	
At least one ID lepton	
$\lvert m_{\ell\ell} - m_Z^{\text{PDG}}\rvert < 10\,\text{GeV}$	$m_{\ell\ell} > 20\,\text{GeV}$, $\lvert m_{\ell\ell} - m_Z^{\text{PDG}}\rvert > 15\,\text{GeV}$
	Two b-tagged jets
Non-ID lepton: **A** | **B** | **C** | **D**	

Table 8.6: Selection criteria for the Z-peak and $t\bar{t}$ ID+AntiID regions used for prompt AntiID lepton calibration.

- Electrons (muons) that fail *both* conditions, i.e. isolation *and* identification ($|d_0/\sigma_{d_0}| < 3$) of the ID lepton, are classified in Region D.

Figure 8.10 displays the data-to-MC ratios in the four regions as discussed, both in e^-e^+ and $\mu^-\mu^+$ decays. As anticipated in Section 8.4.5, region A (the ID+ID event selection) shows a good data-to-MC agreement in both e^-e^+ and $\mu^-\mu^+$ channels. The largest mismodeling in prompt AntiID muons arises in region B (data-to-MC equal to 1.63 when using the SHERPA2.2.1 Z + jets sample), corresponding to $14.1\,\%$ of the events in the ID+AntiID selection. More importantly, region C also shows a large data-to-MC disagreement (ratio of 1.2) while containing the majority of ID+AntiID events at the Z-peak ID+AntiID validation region ($85\,\%$). The largest mismodeling of prompt AntiID muons comes from region D, a small portion ($0.9\,\%$) of the set of AntiID muons. The prompt AntiID electron mismodeling is found to be smaller in all these three regions, with a different distribution of the populations among AntiID regions. Region B is the one with both largest population ($59.5\,\%$ of ID+AntiID events in e^-e^+ channel) and largest data-to-MC disagreement (ratio of 1.13 when using SHERPA2.2.1) in the e^-e^+ channel.

Additionally, the composition of AntiID leptons among B, C, and D regions is compared to the Z-peak using prompt leptons produced in events enriched in $t\bar{t}$ production decaying into two leptons of same flavor. The selection requirements defining the *same-flavor $t\bar{t}$ ID+AntiID region* are similar to the ones defined in studies for the $WW+\geq 1\,\text{jets}$ analysis. With respect to the Z-peak ID+AntiID region, a switch from the $10\,\text{GeV}$ Z-window to a requirement of exactly two b-jets in the event is implemented to enrich $t\bar{t}$ contributions. A Z-window of $15\,\text{GeV}$ is vetoed to suppress contributions from Z + jets, where heavy-flavor jets dominate[13]. The cross sections for these processes are usually underestimated in MC simulation [485]. This requirement also ensures the orthogonality between Z-peak and $t\bar{t}$ regions. Once these requirements have been fulfilled, the events are classified among regions A, B, C, and D according to the conditions of the ID selection failed by the non-ID lepton, as done for the Z-peak region. The selection criteria for both $t\bar{t}$ and Z-peak ID+AntiID regions are summarized in Table 8.6.

The ratios data-to-MC in the $t\bar{t}$ A, B, C, and D regions are shown in Figure 8.11. In contrast to Figure 8.10, only one ratio is shown using the POWHEG+PYTHIA 8 $t\bar{t}$ MC sample. Due to the different kinematic features of the enhanced $t\bar{t}$ decays, the data-to-

[13]Heavy-flavor jets refer to the additional jets in the final state arising from b- and c-hadron decays.

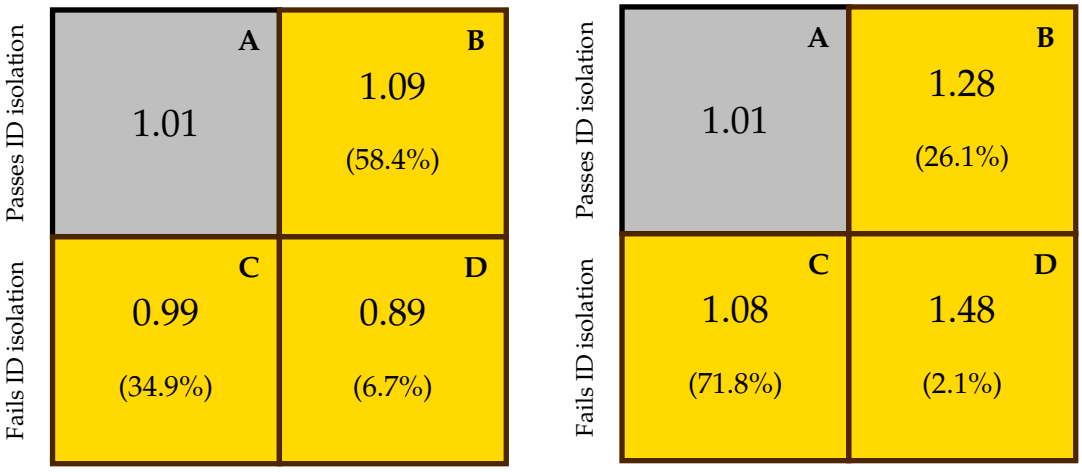

(a) e^-e^+ channel. (b) $\mu^-\mu^+$ channel.

Figure 8.11: Data-to-MC ratios for the A (ID+ID, shown in grey), B, C, and D ID+AntiID same-flavor $t\bar{t}$ regions (in yellow) according to the fulfilled conditions of the AntiID lepton using POWHEG+PYTHIA 8 $t\bar{t}$ MC simulation. On the left-hand side, results in the e^-e^+ channel are given. Ratios for the $\mu^-\mu^+$ channel are shown on the right-hand side. Percentages give the portion of the corresponding region contributed to the total ID+AntiID region. Statistical errors are below 1 %.

MC ratios and the composition of ID+AntiID events among B, C, and D regions slightly differ with respect to the ratios of the Z-peak region using POWHEG+PYTHIA 8 simulated events. For instance, the AntiID region B of the muon channel contributes $26.1\,\%$ of the ID+AntiID events in the $t\bar{t}$ region while only contribution $14.1\,\%$ at the Z peak. This can be caused by the higher jet activity in top-quark events, with larger contributions from b-flavor decays producing more muons within the hadron activity of the b-jets which are characterized by greater values of $|d_0/\sigma_{d_0}|$. The composition among AntiID regions does not vary considerably in the electron channel. Investigations are discussed later on.

In order to effectively address the differences of the three AntiID regions, calibration factors are computed independently per lepton flavor in the AntiID regions B, C, and D. Since different MC generators provide different modeling schemes of prompt AntiID electrons and muons, SHERPA and POWHEG+PYTHIA 8 samples are also calibrated separately with dedicated sets of scale factors. The applied calibration factors are then validated using *different-flavor* decays (i.e. the $e\mu + \mu e$ channel) enhancing $t\bar{t}$ production, closer to the ID+AntiID region used for the extrapolation of the fake-lepton background in the fake-factor method[14].

Determination of Correction Factors. The Tag-and-Probe Method

To ensure a good modeling of the data using simulated events, well-known processes can be exploited to provide reliable production mechanisms for the calibration of physics objects in experiments. Additionally, resonant decays provide large statistical datasets,

[14] A validation region enriched in W^+W^- decays becomes challenging due to the sizable contributions arising from non-prompt leptons.

where background contributions are usually very low. This is a common case in the calibration of lepton reconstruction, identification and isolation working points. The decays of the Z boson and the J/ψ meson are extensively used in collider experiments, decaying into pairs of leptons and hadrons. The *tag-and-probe method* is based on events selected in processes decaying into two objects of the same type, namely e^-e^+, $\mu^-\mu^+$, or $q\bar{q}$ final states. In the dilepton decay, one of the two leptons (the so-called *tag lepton*) is required to pass the selection triggers[15] and fulfill stringent reconstruction, identification, and isolation criteria. The remaining *probe lepton* is then very likely to be produced from the same source as the tag lepton, and it is therefore used to perform the calibration of the working point of interest. *Selection efficiencies* are computed as the ratio of the number of selected probe leptons over the total number of probe leptons, which are usually performed differentially as a function of, e.g., the probe-lepton p_T, η, its angular separation ΔR with respect to the closest jet, or combinations of these. To match the simulated events to the data distribution, the ratio of data and MC efficiencies can be applied as a correction factor to the simulation. Calibration procedures using the tag-and-probe method face limitations imposed by the kinematic features of the physics objects, product of the decay of the targeted process, as well as the size of the selected dataset. These result in restricted coverage of the phase space subjected to calibration. However, these limitations diminish as the integrated luminosity increases. The tag-and-probe method is extensively used in hadron collider physics. For instance, ATLAS muon reconstruction, identification and isolation efficiencies [358], as well as electron trigger [486], and identification efficiencies [472] used in this thesis have been derived using this approach.

In this analysis, the tag-and-probe technique is implemented in the ID+AntiID regions B, C, and D. The ID lepton acts as the *tag lepton* and it is required to match at least one of the nominal single-lepton triggers of the menu (c.f. Table 4.4). The *probe lepton* corresponds to the non-ID lepton, fulfilling the selection requirements of the AntiID regions B, C, or D. Selection efficiencies are derived in bins of p_T and $|\eta|$, $\varepsilon(p_T, |\eta|)$, in both the data and MC in each of these three regions. Only *signal probes* are used, i.e., AntiID selection efficiencies are computed in data after the expected contributions from background sources[16], as predicted by MC simulation, have been subtracted. Similarly, the selection efficiencies derived in simulation are derived using the MC sample of the process of interest. Taking selection efficiencies from data and signal MC, the prompt AntiID correction factors, also referred to as *Scale Factors* (SF), are computed in the i-th p_T bin and j-th $|\eta|$ bin as

$$\mathrm{SF}_{i,j} = \frac{\varepsilon_{i,j}^{\mathrm{Data}}}{\varepsilon_{i,j}^{\mathrm{Signal,\,MC}}} \,. \tag{8.15}$$

If kinematic constraints defining the AntiID regions B and C were orthogonal, prompt AntiID scale factors in region D could be computed as a product of the scale factors derived from these two regions. This is indeed the case for prompt AntiID muons, since the criteria on $|d_0/\sigma_{d_0}|$ and muon isolation are completely independent. Prompt AntiID muon scale factors in region D are therefore computed as the product $\mathrm{SF_B} \cdot \mathrm{SF_C}$, reducing

[15] This is particularly important if the working points under calibration are loose. In this way, the event is ensured to be selected while the working point under calibration is not biased by the p_T thresholds and isolation criteria involved in the definition of the trigger selection.

[16] These background sources are defined as the event candidates that do not correspond to prompt lepton production from the targeted process, namely prompt lepton decays arising in, e.g., Z boson or $t\bar{t}$ production at the Z-peak or $t\bar{t}$ ID+AntiID regions, respectively.

the statistical fluctuations of $\mathrm{SF_D}$ drastically. However, the fulfillment of electron identification and isolation requirements are correlated. For prompt AntiID electrons, dedicated scale factors are computed using the AntiID electron population in region D, with a portion considerably larger than in the muon case (see Figure 8.10). More details are given in Appendix B.

Studies on the τ Composition of Prompt AntiID Muons

In same-flavor final states, events arising from secondary leptonic decays of τ leptons ($\tau \to \ell\nu_\tau\bar{\nu}_\ell$, with $\ell = e, \mu$) could be accepted by the event selection. The reconstructed electrons and muons from such decays are expected to have a greater transverse impact parameter $|d_0/\sigma_{d_0}|$ of the lepton primary track than prompt electrons and muons, as well as large values of E_T^{miss} in the event due to the momentum unbalance caused by the unobserved neutrinos. The missing momentum balance in the event degrades the reconstruction of the dilepton invariant mass $m_{e\mu}$ in leptonic $Z \to \tau^-\tau^+$ decays, shifted to values lower than the mass of the Z boson. Additionally, the vector $\vec{E}_T^{\mathrm{miss}}$ is likely to fall within the azimuthal range spanned by the two secondary leptons in a $Z \to \tau^-\tau^+$ decay into two leptons. As discussed in Chapter 7, $Z \to \tau^-\tau^+$ production constitutes an important background source in the signal region targeting the selection of W^+W^- event candidates, enhanced by the requirement of a dilepton system of opposite-flavor. In the ID+AntiID region, $Z \to \tau^-\tau^+$ contributions play an important role in the subtraction of prompt contributions (see e.g. Figure 8.17). The Z-window requirement defining the Z-peak ID+AntiID region, employed to derive correction factors for AntiID prompt leptons, results in a pronounced suppression of $Z \to \tau^-\tau^+$ decays which are reconstructed with lower $m_{e\mu}$. To ensure the validity of such corrections in the ID+AntiID control region, the composition of muons originating from τ decays must be investigated. AntiID muons are especially susceptible to this mismodeling due to the higher $|d_0/\sigma_{d_0}|$ selection that defines the AntiID muon selection criteria.

To study the reliability of the prompt AntiID calibration in regions with high $|d_0/\sigma_{d_0}|$, signal probes[17] selected in data and MC are compared using three different selection requirements: (i) the Z-peak region, (ii) the $t\bar{t}$ region, and (iii) an additional region targeting larger contributions from $Z \to \tau^-\tau^+$ decays. This last selection is referred to as *$\tau\tau$-enhanced region*, defined as the Z-peak region but shifting the Z-window range to $m_{\ell\ell} \in [25, 65]\,\mathrm{GeV}$. Figure 8.12 shows the transverse impact parameter d_0 of probe signal muons and its significance in absolute value $|d_0/\sigma_{d_0}|$. Distributions of the signal processes simulated using POWHEG+PYTHIA 8 are used in the three regions to allow for a direct comparison to the simulated $t\bar{t}$ events. Events from the remaining processes as predicted by MC simulation are considered as background and they are subtracted from the data. The distribution of the muon d_0 impact parameter in the $\tau\tau$-enhanced region tends to mimic the trends observed in the $t\bar{t}$ region, where τ decays are not suppressed, showing a significant disagreement with the distributions extracted at the Z-peak region. On average, the primary track of non-ID muons in the Z-peak region is closer to the interaction point than those in $\tau\tau$-enhanced and $t\bar{t}$ regions, as expected from a decay of the

[17] For this study, $Z \to \ell^-\ell^+$ ($\ell = e\,,\mu\,,\tau$) contributions are considered as signal in the $Z + \mathrm{jets}$ regions, at both the Z-peak and the $\tau\tau$-enhanced region. Events from $t\bar{t}$ as expected from MC simulation account for the signal probes in the $t\bar{t}$ region.

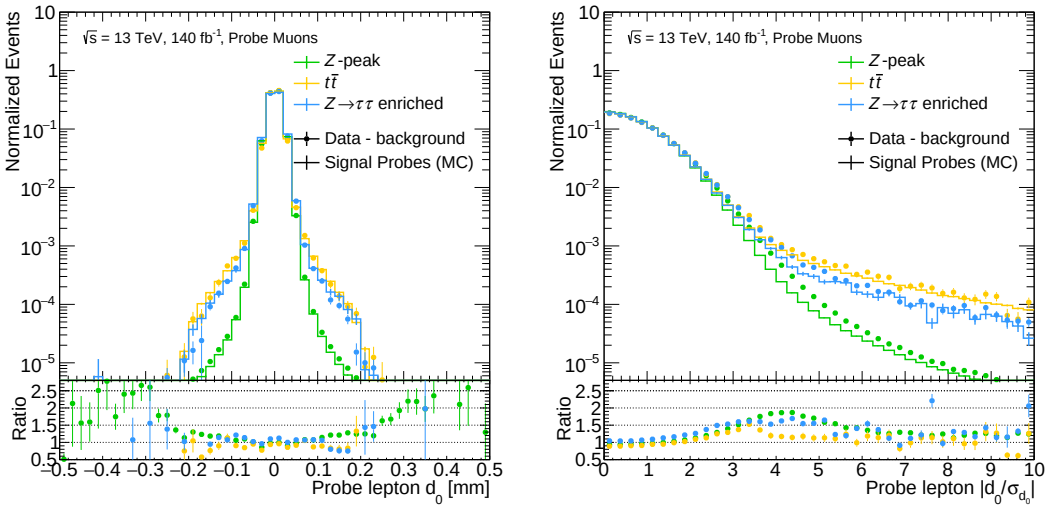

(a) Probe lepton d_0.

(b) Probe lepton $|d_0/\sigma_{d_0}|$.

Figure 8.12: Impact parameter distributions of (a) d_0 and (b) $|d_0/\sigma_{d_0}|$ of the probe leptons in data after the subtraction of background processes as estimated in MC (shown as markers) and signal process estimated using POWHEG+PYTHIA 8 MC samples (solid lines) in three different validation regions: the Z peak (green, Table 8.6), $t\bar{t}$ (orange, Table 8.6) and a $Z+\text{jets}$ region targeting a selection richer in $\tau\tau$ decays (blue) with the requirement $m_{\ell\ell} \in [25,\ 65]$ GeV. The bottom plot shows the ratio between background-subtracted data over signal probes estimated in MC simulation. No AntiID prompt lepton calibration is applied to the displayed distributions. Only statistical uncertainties are shown.

Z boson into two prompt muons. Clear differences between the three regions can be observed from the $|d_0/\sigma_{d_0}|$ distribution, directly correlated to the features of d_0. The rate of reconstructed muons with $|d_0/\sigma_{d_0}| > 3$ increases in $Z \to \tau^-\tau^+$ decays by about an order of magnitude compared to events at the Z-peak. This feature confirms the suppression of τ decays within the acceptance of the Z-peak region. Additionally, ratios between the distributions of background-subtracted data over signal-predicted probes are calculated independently in each of the regions and shown at the bottom plots bin by bin. A worse description of the data by the MC simulation is observed at the Z peak with $|d_0/\sigma_{d_0}| > 3$ with respect to both $\tau\tau$-enriched and $t\bar{t}$ regions. The calibration factors derived at the Z-peak region for high-$|d_0/\sigma_{d_0}|$ muons are therefore not applicable in regions where τ decays are not suppressed, e.g., the $t\bar{t}$ regions or the ID+AntiID control region, which is also closer to the signal region. In order to derive the correction factors for prompt AntiID muons in regions of high $|d_0/\sigma_{d_0}|$ susceptible to this mismodeling, the same-flavor $t\bar{t}$ region is used. Moreover, a reliable modeling of $Z \to \tau^-\tau^+$ simulated events is ensured by performing a standalone calibration of $Z \to \tau^-\tau^+$ contributions in a dedicated region, presented in the following.

Calibration of $Z \to \tau^-\tau^+$ Contributions

A region pure in $Z \to \tau^-\tau^+$ decays, inspired by the selection strategy of the $Z \to \tau^-\tau^+$ cross-section measurement of ATLAS at 7 TeV [487], is designed to derive scale factors for prompt AntiID τ leptons. The selection criteria of this region are summarized in Table 8.7. Considering different-flavor decays, the lepton and event preselection follow

$Z \to \tau^-\tau^+$ region
Preselection (see Section 7.5)
$25 < m_{\ell\ell} < 80\,\text{GeV}$
Third-lepton veto and $q_e \times q_\mu = -1$
$\sum_{i=0}^{1} \cos(\phi(\ell_i) - \phi(E_T^{\text{miss}})) > -0.15$
$H_T < 150\,\text{GeV}$
One ID lepton (matching single-lepton triggers)
Non-ID lepton in AntiID B, C, or D region

Table 8.7: Selection requirements defining the $Z \to \tau^-\tau^+$ region, used to derive the dedicated set of scale factors to calibrate prompt AntiID τ leptons.

140 fb^{-1} ($e\mu + \mu e$ channel)	Number of events in the $Z \to \tau^-\tau^+$ region		
	ID+ID	AntiID e	AntiID μ
$Z \to \tau^-\tau^+$	16760 ± 70	5850 ± 40	9790 ± 60
$Z \to \ell\ell$ ($\ell = e,\ \mu$)	240 ± 50	770 ± 90	112 ± 33
Expected SM	18490 ± 90	7380 ± 120	10440 ± 70
Data	17365	7209	11518
Purity $Z \to \tau\tau$ [%]	90.6 ± 0.6	79.3 ± 1.5	93.8 ± 0.8
Data/SM	0.939 ± 0.008	0.98 ± 0.20	1.103 ± 0.012

Table 8.8: Number of events recorded in data using the full Run 2 dataset in different flavor decays in the $Z \to \tau^-\tau^+$ region, as well as the expected SM contributions. The contributions from $Z \to \tau^-\tau^+$ and $Z \to \ell\ell$ ($\ell = e,\ \mu$) predicted by the SHERPA 2.2.1 MC simulation are also shown. The uncertainties correspond to statistical fluctuations in the simulated number of events. No AntiID lepton calibration is applied on simulation.

the same requirements as the Z-peak region. Constraints on the lepton p_T and $|\eta|$, electric charge and the third-lepton veto are implemented as in the signal region (Section 7.5). To enhance $Z \to \tau^-\tau^+$ decays, the direction of $\vec{E}_T^{\text{miss}}$ is constrained to lie within the direction of the $\vec{p}_T$ of both leptons by imposing $\sum_{i=0}^{1} \cos(\phi(\ell_i) - \phi(E_T^{\text{miss}})) > -0.15$, which is positive if $\vec{E}_T^{\text{miss}}$ is spanned within the trajectories of flight in the transverse plane of the two leptons in the event. Contributions from $t\bar{t}$ production are suppressed by restricting the phase space to low values of the total transverse momentum of the event (H_T),

$$H_T \equiv E_T^{\text{miss}} + \sum_{i=0}^{N_{\text{jets}}} p_{T,i}^{\text{jet}} + \sum_{j=0}^{N_{\text{lep}}} p_{T,j}^{\ell} < 150\,\text{GeV}.$$

For the events satisfying these requirements, at least one of the two leptons in the final state must fulfill the ID lepton selection criteria and match one of the unprescaled single-lepton triggers of the analysis. The second lepton in the event must pass the AntiID selection (either in region B, C, or D). Table 8.8 displays the selected $Z \to \tau^-\tau^+$ events and purities in this region, either when the electron or the muon correspond to the AntiID lepton in the event. Purities of at least $80\,\%$ are achieved in $Z \to \tau^-\tau^+$ production for the events satisfying these selection criteria, as predicted by $Z + \text{jets}$ MC simulation with SHERPA 2.2.1 (described in Section 7.4). The p_T distributions of the signal probe leptons are shown in Figure 8.13 for both the ID+ID region and the regions with either an AntiID electron or muon. An overprediction of the data by $6\,\%$ is observed in the ID+ID selec-

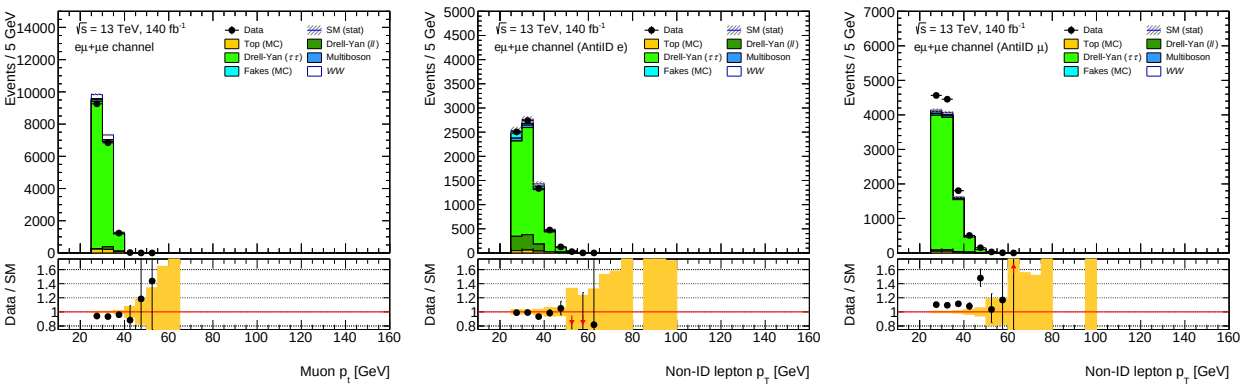

(a) ID+ID region. (b) ID muon + AntiID electron. (c) ID electron + AntiID muon.

Figure 8.13: Comparison of the data distribution and the SM expected events in the $Z \to \tau^-\tau^+$ region fulfilling (a) an ID+ID selection, and an ID+AntiID selection where the (b) electron and (c) muon does not fulfill the ID selection requirements. The expected contributions of SM processes are simulated using MC events. While the muon p_T is displayed in the ID+ID region, the non-ID lepton transverse momentum is shown for the ID+AntiID regions. The AntiID leptons are not calibrated for the presented events. Only statistical uncertainties are displayed.

tion. A good data-to-SM ratio is observed when the electron fulfills the AntiID selection requirements, a trade-off between both the overcorrection of ID muons and underestimation of AntiID electrons. A fraction of $10\,\%$ of the predicted events arises from $Z \to \mu^-\mu^+$ production, where one of the muons escapes the detector acceptance (introducing momentum imbalance in the event) while an AntiID electron is misreconstructed from the additional hadronic radiation in the event. The underestimation of the data increases up to $10\,\%$ when an AntiID muon is selected.

The prompt AntiID τ scale factors are computed using the data and MC probe selection efficiencies at the $Z \to \tau^-\tau^+$ region, analogously to the strategy followed at the Z-peak and $t\bar{t}$ regions. Signal-probe leptons from data and MC simulation are selected considering $Z \to \tau^-\tau^+$ contributions only.

Systematic Uncertainties in the Calibration of Prompt AntiID Leptons

To account for possible biases on the computation of the prompt AntiID lepton correction factors, different effects in the selection criteria are considered as systematic variations.

- The background subtraction performed to the data in Eq. (8.15) could be affected by possible MC mismodeling in regions of the phase space away from the Z-peak. Effects from this variation are found to be at the per mille level and therefore neglected. For this reason, additional scale factors are calculated after increasing the Z-window requirement from $|m_{\ell\ell} - m_Z^{\mathrm{PDG}}| < 10$ to $|m_{\ell\ell} - m_Z^{\mathrm{PDG}}| < 20$ GeV.

- The production of additional jets in the final state can carry an important portion of the activity in the detector. Jets could therefore bias the identification and isolation requirements imposed on non-ID leptons, having also an effect on the MC modeling of these. Additional sets of correction factors are derived after applying jet-veto

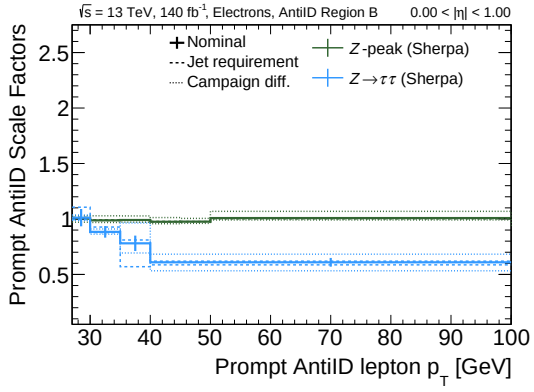

(a) AntiID $e^{\pm}$ with $0.0 < |\eta| < 1.0$ in Region B.

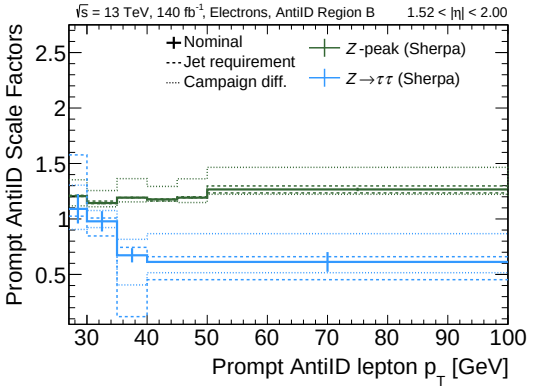

(b) AntiID $e^{\pm}$ with $1.52 < |\eta| < 2.0$ in Region B.

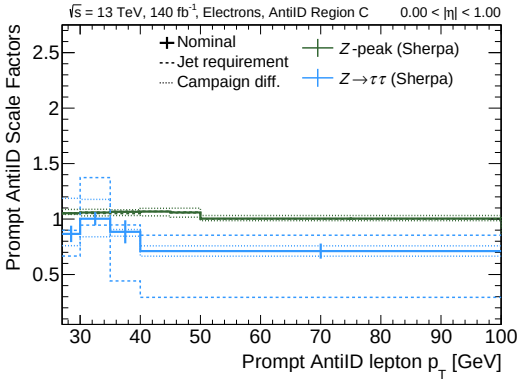

(c) AntiID $e^{\pm}$ with $0.0 < |\eta| < 1.0$ in Region C.

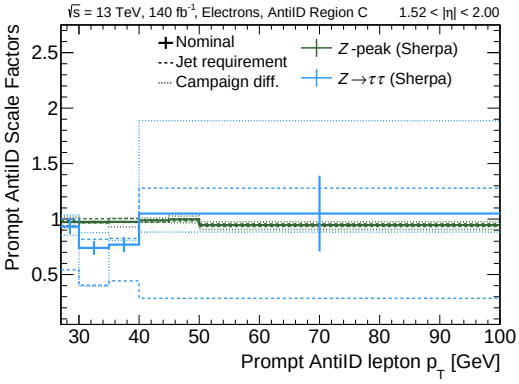

(d) AntiID $e^{\pm}$ with $1.52 < |\eta| < 2.0$ in Region C.

Figure 8.14: Illustrative prompt AntiID electron calibration factors in the AntiID region B at the Z-peak (Table 8.6, shown in green), and $Z \to \tau^{-}\tau^{+}$ regions (Table 8.7, shown in blue) for $|\eta|$ bins in (a) the central region ($0.0 < |\eta| < 1.0$), and (b) the forward region of the inner detector ($1.52 < |\eta| < 2.0$), as well as the AntiID region C for the same $|\eta|$ bins in (c) the central region, and (d) the forward region. Statistical uncertainties are displayed on the nominal scale factors. Systematic variations due to the jet-activity requirement (either jet-veto or one-jet-inclusive selection, displayed as dashed lines) and the envelope of differences across data-taking campaigns (dotted lines) are also compared to the nominal calibration factors (solid lines).

($N_{\text{jets}} = 0$) and one-jet-inclusive ($N_{\text{jets}} \geq 1$) requirements on the event selection criteria in both the Z-peak and $Z \to \tau^{-}\tau^{+}$ regions. Since the definition of the $t\bar{t}$ region imposes two tagged b-jets in the final state, this systematic uncertainty is not assessed for scale factors derived in $t\bar{t}$ events, ensuring a sufficiently large dataset in their calculation.

- Differences in pile-up, definitions of the trigger, or lepton identification and isolation working points exist for different data-taking campaigns of the ATLAS Run 2 dataset. Their impact on the prompt AntiID modeling is conservatively accounted for by quantifying the absolute deviations of the scale factors derived in independent data-taking campaigns (2015+2016, 2017, and 2018), while the nominal values of the correction factors are derived with full Run 2 dataset.

Distributions of the calibration factors for prompt AntiID electrons and muons, along

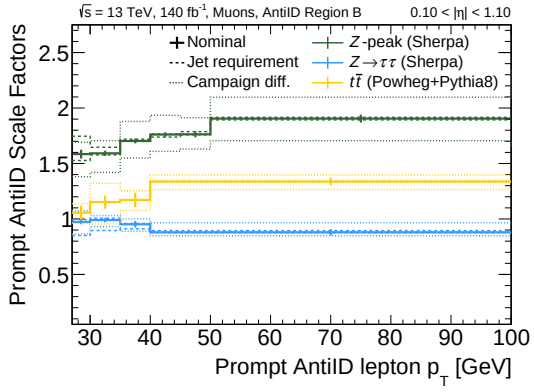

(a) AntiID $\mu^{\pm}$ with $0.1 < |\eta| < 1.1$ in Region B.

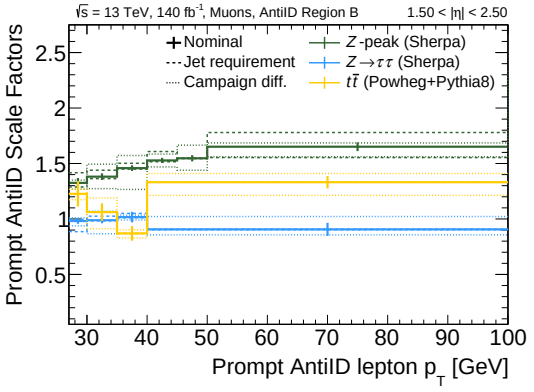

(b) AntiID $\mu^{\pm}$ with $1.5 < |\eta| < 2.5$ in Region B.

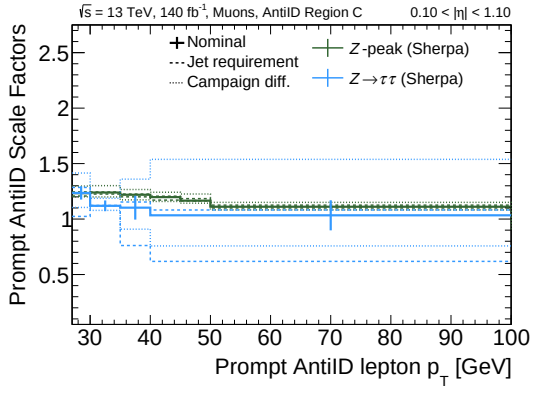

(c) AntiID $\mu^{\pm}$ with $0.1 < |\eta| < 1.1$ in Region C.

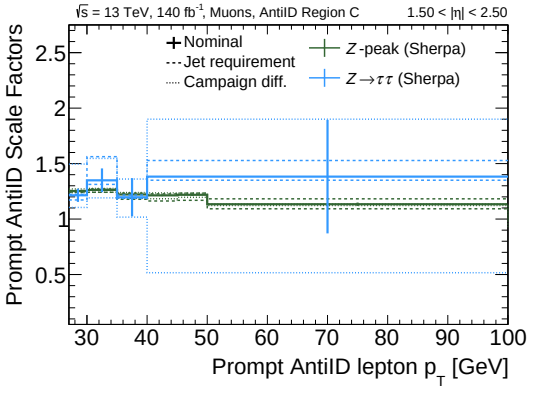

(d) AntiID $\mu^{\pm}$ with $1.5 < |\eta| < 2.5$ in Region C.

Figure 8.15: Illustrative prompt AntiID muon calibration factors in the AntiID region B at the Z-peak (Table 8.6, shown in green), same-flavor $t\bar{t}$ (Table 8.6, shown in orange), and $Z \rightarrow \tau^{-}\tau^{+}$ regions (Table 8.7, shown in blue) for $|\eta|$ bins in (a) the central region ($0.1 < |\eta| < 1.1$), and (b) the forward region of the inner detector ($1.5 < |\eta| < 2.5$), as well as the AntiID region C for the same $|\eta|$ bins in (c) the central region, and (d) the forward region. Statistical uncertainties are displayed on the nominal scale factors. Systematic variations due to the jet-activity requirement (either jet-veto or one-jet-inclusive selection, displayed as dashed lines) and the envelope of differences across data-taking campaigns (dotted lines) are also compared to the nominal calibration factors (solid lines). Scale factors in the $t\bar{t}$ region are derived only for muons with $|d_0/\sigma_{d_0}| > 3$ (region B) and are no subject to systematic variations due to the jet activity.

with the associated systematic uncertainties, are depicted in Figures 8.14 and 8.15, respectively, across illustrative central and forward bins of $|\eta|$ within the inner detector acceptance. The full set of scale factors can be found in Appendix B.2. The dominant source of uncertainty in the calibration stems from variations observed across different data-taking campaigns for both prompt AntiID electrons and muons. Significant differences exist between the calibration factors for prompt AntiID leptons obtained from Z-peak (defined in Table 8.6) and $Z \rightarrow \tau^{-}\tau^{+}$ (Table 8.7) regions, surpassing the bounds of both statistical and systematic uncertainties. Similar discrepancies are observed for scale factors derived in a same-flavor $t\bar{t}$ region (summarized in Table 8.6), used to correct the mismodeling of prompt AntiID muons in region B. The displayed uncertainties are propagated into the signal region by performing the estimation of the lepton misidentification background using alternative sets of scale factors in dedicated variations. The

total uncertainty is computed as the quadratic sum of the considered variations.

Additional systematic variations due to non-closure in a $t\bar{t}$ validation region using different-flavor dilepton final states, introduced in the following, are also computed using two-dimensional double ratios derived bin by bin for each ID+AntiID region and lepton flavor using Eq. (8.14). The deviations of the double ratios with respect to unity are then used to vary the nominal scale factors up and down in a symmetrized manner.

Validation of the Prompt AntiID Calibration. The Different-Flavor $t\bar{t}$ ID+AntiID Validation Regions

After the corrections on simulated prompt AntiID leptons have been applied, the closure of the prompt SM contributions to the data is evaluated in a $t\bar{t}$ validation region (Table 8.6) using fully leptonic decays of different flavor, which is closer to the selection of W^+W^- event candidates in the ID+AntiID control region used for the estimation of the lepton misidentification background. The non-ID electron and muon p_T distributions are presented in Figure 8.16 in AntiID regions B and C. Correction factors derived at the Z peak are applied to prompt AntiID electrons in regions B, C, and D, as well as AntiID muons in Region C. Prompt AntiID muons in region B are scaled using the correction factors derived at the $t\bar{t}$ same-flavor region. The corrections of prompt AntiID muons in region D are computed as the product of the correction factors of region B and C for the given muon p_T and $|\eta|$. The MC simulation of prompt contributions from Drell-Yan $Z \to \tau^-\tau^+$ production is calibrated using dedicated corrections derived in the $Z \to \tau^-\tau^+$ region. The sum in quadrature of statistical and AntiID lepton calibration uncertainties is displayed. A good closure is found in both electron and muon channels within $5\,\%$ across the differential distributions, covered by the systematic uncertainties of the method. The largest uncertainties in the $t\bar{t}$ validation region are observed at low AntiID lepton p_T, driven by the small non-closure with respect to the data. These are subject to MC fluctuations, resulting in non-smooth distributions of the error band. For prompt AntiID muons with $|d_0/\sigma_{d_0}| < 3$ failing the ID isolation requirement (region C), uncertainties at low p_T are dominated by the differences in prompt muon mismodeling across data-taking campaigns.

To assess the modeling of AntiID leptons with respect to the ID selection after the calibration has been performed, double ratios are computed in the different-flavor $t\bar{t}$ ID+AntiID region with respect to the corresponding ID+ID selection. The values are given in Table 8.9 for regions B, C, and D separately, as well as for the full ID+AntiID region corresponding to the sum of the three. AntiID leptons are found to be well described up to $3\,\%$, observing an important improvement with respect to the previous W^+W^- measurements of ATLAS. Data-to-MC disagreements with respect to the ID selection criteria are covered by the systematic uncertainties of the method, driven by the non-closure uncertainties in region C.

8.4.6 Systematic Uncertainties

To account for differences in the jet-flavor composition originating fake and non-prompt leptons between the dijet and signal regions, fake factors with two b-tag requirements are evaluated in dijet regions where the leading jet is either b-tagged or b-vetoed. As the

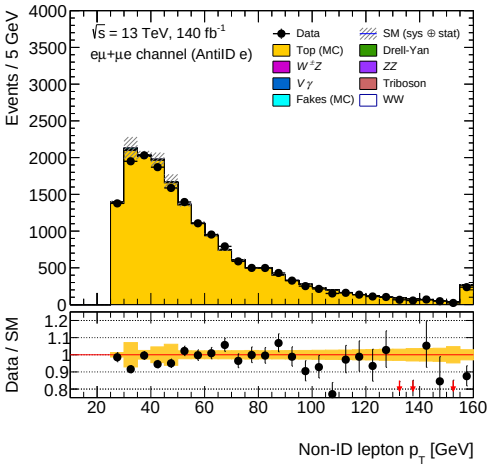

(a) ID $\mu^{\pm}$ + AntiID $e^{\mp}$ events in Region B.

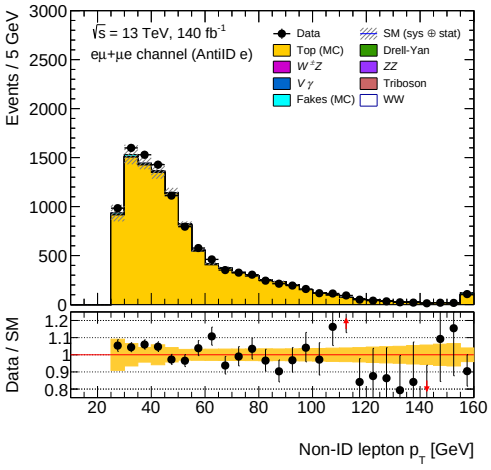

(b) ID $\mu^{\pm}$ + AntiID $e^{\mp}$ events in Region C.

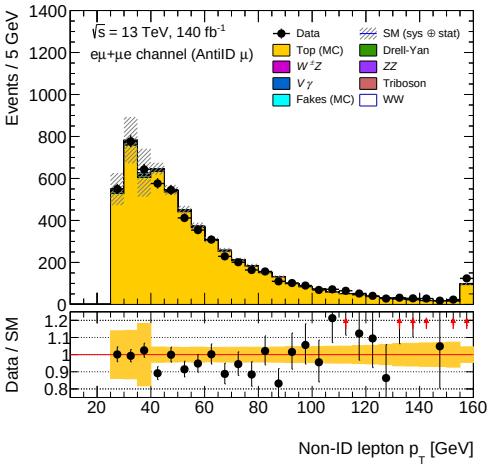

(c) ID $e^{\pm}$ + AntiID $\mu^{\mp}$ events in Region B.

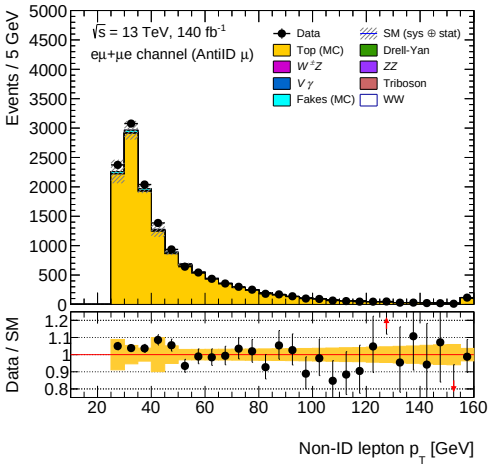

(d) ID $e^{\pm}$ + AntiID $\mu^{\mp}$ events in Region C.

Figure 8.16: Comparison of data and MC-simulated distributions across the non-ID electron (top) and non-ID muon (bottom) transverse momentum in different-flavor decays selected in the ID+AntiID $t\bar{t}$ validation regions (defined as in Table 8.6). The expected contributions of SM processes are simulated using MC events. Corrections factors for prompt AntiID leptons computed in the Z-peak, same-flavor $t\bar{t}$, and $Z \to \tau^{-}\tau^{+}$ regions are applied to the MC simulation. On the left, electrons and muons in the AntiID region B are presented. AntiID leptons in region C are shown on the right-hand side. The sum in quadrature of statistical and prompt AntiID calibration uncertainties is displayed in each bin.

signal region has a higher fraction of b-flavor fakes than the dijet region despite the b-veto, the nominal fake factors are taken as the average of these two extremes cases, taking the envelope as a systematic uncertainty.

The dominant source of prompt leptons in the dijet region arises from W + jets and it is suppressed by the $m_T + E_T^{\text{miss}} < 50\,\text{GeV}$ requirement, which still dominates the prompt subtraction for the computation of the fake factors. The modeling of the W + jets contribution is tested in a dedicated control region, designed to isolate this background. The ratio between data and total SM events yields 1.044 ± 0.007 and 1.050 ± 0.004 in the

AntiID lepton	AntiID region	(Data - non-prompt bkg.)/SM		Double ratio
		ID+ID	ID+AntiID	
Electron	B	0.9699 ± 0.0006	0.9705 ± 0.0017	1.0006 ± 0.0018
	C		1.0203 ± 0.0021	1.0519 ± 0.0022
	D		0.974 ± 0.006	1.004 ± 0.006
	ID+AntiID		0.9884 ± 0.006	1.0190 ± 0.0015
Muon	B	0.9796 ± 0.0005	0.9824 ± 0.0031	1.003 ± 0.003
	C		1.0294 ± 0.0020	1.0508 ± 0.0021
	D		0.929 ± 0.021	0.948 ± 0.021
	ID+AntiID		1.0130 ± 0.021	1.0341 ± 0.0018

Table 8.9: Double ratios calculated as given in Eq. (8.14) in the $t\bar{t}$ different-flavor validation regions B, C, and D, together with the full ID+AntiID region (B+C+D) once after prompt AntiID lepton calibration for electrons, muons and taus has been applied. The full Run 2 dataset in $e\mu$ decays is used. The breakdown when the AntiID lepton is either electron or a muon is shown. Only statistical uncertainties are considered in the error propagation.

electron and muon channels, respectively. Data and the MC model agree well within $10\,\%$ across the $m_T + E_T^{\text{miss}}$ distribution, as observed also in studies for the $WW+\geq 1\,\text{jets}$ measurement [81]. To assess the systematic bias on the measured fake factors from modeling uncertainties introduced in the prompt lepton subtraction, the total subtracted prompt background is increased and decreased by $10\,\%$, taking the difference between the nominal and varied fake factors as a systematic uncertainty.

The underlying jets around the fake leptons might affect the E_T^{miss} determination as well as the p_T measurement of the fake leptons, biasing the fake-factor measurement. Fake factors are therefore reevaluated without the $m_T + E_T^{\text{miss}}$ condition, and the difference between these and the nominal distributions is taken as the systematic uncertainty.

In the ID+AntiID control region defined in the fake-factor method, prompt dilepton contributions are subtracted based on MC simulation. The same systematic uncertainties as for the signal region affect these backgrounds. The systematic variations of the expected SM yields in ID+AntiID regions are therefore considered as fully correlated to the systematic variations performed in the signal region. This reduces the total background uncertainty slightly, while having a small impact on the estimated yield of the fake-lepton background[18]. Additional systematic uncertainties from the calibration of AntiID leptons, presented in Section 8.4.5, are considered.

The prompt contamination in the ID+AntiID control region arising from signal W^+W^- production is subtracted using MC simulation, constituting $37\,\%$ of the total prompt composition, shown in Figure 8.17. Due to the considerable fraction of W^+W^- events to be subtracted, the used W^+W^- simulation is corrected using the differential measurement in data in the signal region. The ratio of background-subtracted data and W^+W^- simulation in the signal region is applied bin by bin to the simulation in the ID+AntiID control region. The uncertainty on the correction factor is taken to be $5\,\%$, which covers uncertainties in the signal subtraction in all bins in which the uncertainty on the fake estimate constitutes a relevant contribution to the total uncertainty.

[18] A systematic variation leading to an increase of some background in the signal region also leads to an increased amount of prompt dilepton events subtracted in the ID+AntiID control region and therefore to a

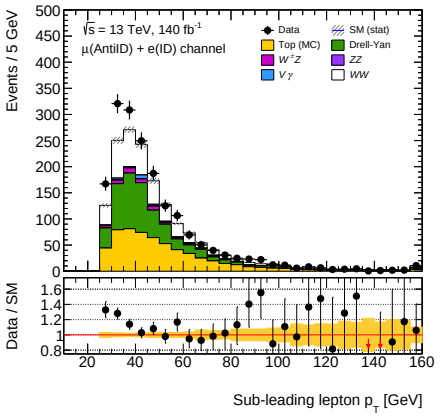

(a) Leading AntiID $\mu^{\mp}$ + subleading ID $e^{\pm}$.

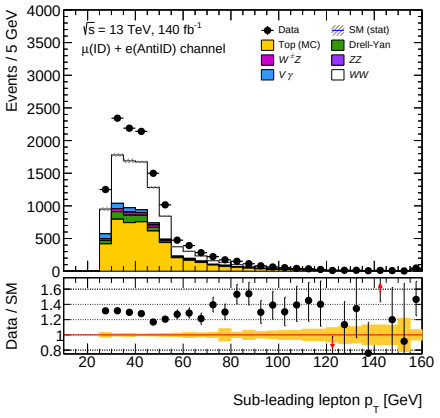

(b) Leading ID $\mu^{\mp}$ + subleading AntiID $e^{\pm}$.

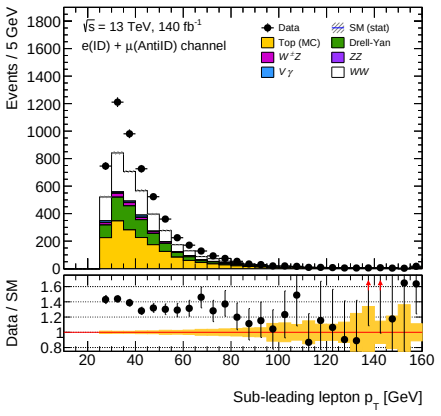

(c) Leading ID $e^{\pm}$ + subleading AntiID $\mu^{\mp}$.

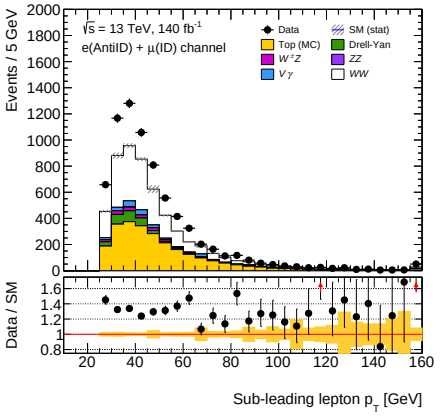

(d) Leading AntiID $e^{\pm}$ + subleading ID $\mu^{\mp}$.

Figure 8.17: Data and MC prompt distributions in the ID+AntiID jet-inclusive signal region of the subleading lepton p_T in events where the muon (top) and electron (bottom) have the highest lepton p_T in the event. Events where the muon fulfills the AntiID selection are presented on the left-hand side, while events with AntiID electrons are shown on the right column. Both data and MC distributions are presented already after applying the fake factors and the prompt AntiID mismodeling calibration. Therefore, the difference between data and prompt MC corresponds to the estimate of the non-prompt background in the signal (ID+ID) regions. Only statistical uncertainties are displayed.

The uncertainty breakdown of the fake-lepton background estimation in the signal region is shown in Table 8.10. The total relative uncertainty in the fake-lepton background is about 26 %, dominated by the discrepancies over data-taking campaigns in the prompt lepton mismodeling, the subtraction of prompt EW contributions to the data in the dijet region for the computation of the fake factors, and the jet-flavor composition uncertainties of the electron fake-factors. The former also leads the relative uncertainty of the background estimation due to the prompt AntiID lepton calibration, of 12.5 % of the lepton misidentification background yield in the signal region. Compared to the prompt AntiID lepton mismodeling uncertainty from the $WW+\geq 1\,\text{jets}$ measurement [81], this constitutes a reduction of a factor of 2. The presented fake-lepton background is the

lower fake estimate, thus having a slightly lower impact on the total background estimate.

Systematic variation			Fakes event yield			
Nominal			5383	±	129	(stat.)
Fake Factors	Electron	EW subtraction		±	539	(±10.0 %)
		No $E_T^{\text{miss}} + m_T$ cut		±	155	(±2.8 %)
		Jet Flavor Comp.		±	443	(±8.2 %)
	Muon	EW subtraction		±	266	(±4.9 %)
		No $E_T^{\text{miss}} + m_T$ cut		±	184	(±3.4 %)
		Jet Flavor Comp.		±	149	(±2.8 %)
Prompt AntiID Calib.	Electron	Non-closure up		+	33	(+0.6 %)
		Non-closure down		−	34	(−0.6 %)
	Muon	Non-closure up		−	15	(−0.3 %)
		Non-closure down		−	64	(−1.2 %)
	Jet-vetoed calibration			+	67	(+1.2 %)
	One-jet inclusive calibration			−	130	(−2.4 %)
	Campaign discrepancies up			+	522	(+9.7 %)
	Campaign discrepancies down			−	814	(−15.1 %)
Total statistical uncertainty				+	153	(±2.8 %)
Total uncertainty				±	1418	(26.3 %)

Table 8.10: Breakdown of systematic uncertainties on the non-prompt background estimate in the signal region.

most precise estimation among W^+W^- measurements carried out in hadron colliders, reviewed in Chapter 7. The achieved precision is also competitive with the most precise fake-lepton background estimates in other measurements of diboson production in ATLAS, of accuracies close to 20 % [488, 489].

8.4.7 Validation of the Non-Prompt Lepton Background

The validity of the estimation of background contributions arising from fake and non-prompt lepton misidentification is assessed by inverting the opposite-charge selection requirement in the signal region, requiring events with an electron-muon pair having the same electric charge. After suppressing prompt-lepton processes strongly, this selection increases the contribution of W + jets events to about 25 %. Despite the relatively low purity, the modeling of the fake-lepton background can be assessed since the dominant diboson background in this region, mostly from $W^{\pm}Z$ production, is known with a precision of about 10 % and validated in a dedicated region (Section 8.3). The distribution of the subleading lepton p_T in the same-sign validation region is shown in Figure 8.18. An excellent agreement of the prediction with the data is observed.

8.4.8 Outlook

Despite the competitive precision of the presented lepton misidentification background estimation, the presented method can be improved in multiple ways. Firstly, the cross-section normalization of the prompt lepton contamination in the fake-factor calculation could be controlled in dedicated regions to ensure a good description of the data, reducing the associated uncertainties considerably in a data-driven approach. Secondly, the discrepancies of this mismodeling among data-taking campaigns arising from different definitions of the lepton selection, the pile-up contamination, and other sources must be further understood. Lastly, differences in jet-flavor composition between the dijet region,

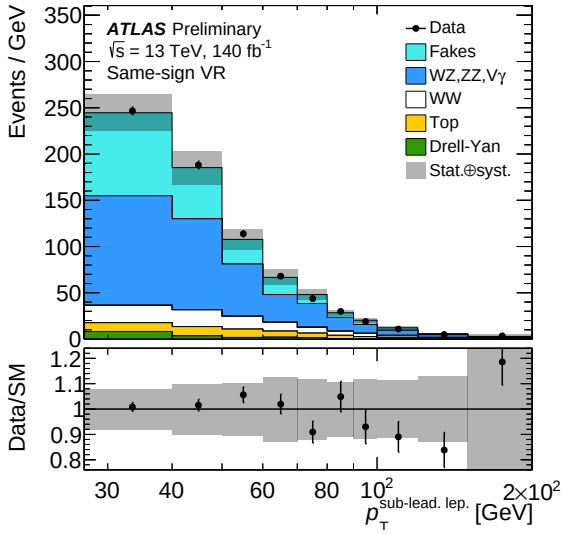

Figure 8.18: Detector-level distribution of the subleading lepton p_T in the same-sign validation region. Overflow events are included. Data are shown as black markers, together with histograms for the predictions of signal and background processes. The top-quark background is estimated using the data-driven methods described in Section 8.1. The lower panels show the ratio of the data to the total prediction. The displayed uncertainty bands include statistical and systematic uncertainties. Theory uncertainties on the signal are negligible and, therefore, not shown. Published in Ref. [87].

ID+AntiID control region, and the signal region could be addressed by the computation of the jet-flavor fractions from b-, c-, and light-jet production of lepton misidentification background following the method implemented in this thesis (Section 8.4.3). The simulation of flavor-filtered MC samples of multijet production can be beneficial for the optimization of the jet-flavor fractions in the dijet region. Further studies to increase the liability of these processes in MC simulation are needed for an optimization of this approach. Then, the selection criteria of dijet, control, and signal regions could be optimized based on the light-, c-, and b-flavored fake-lepton composition to reduce the bias in the background estimation caused by differences in jet-flavor composition.

Chapter 9

Measurements of Fiducial and Differential W^+W^- Production Cross Sections

The event candidates reconstructed with the ATLAS detector need to be translated into measurements that are independent of the detector configuration. The methodology used to calculate experimental results of differential fiducial and integrated cross sections is presented in Section 9.1. Furthermore, the sources of uncertainties affecting the measurements are discussed in Section 9.2. These measurements are compared to state-of-the-art theory predictions, studied in Section 9.3. The results are unveiled in Chapter 10, interpreted in the context of Standard Model Effective Field Theories to constrain anomalous couplings in Chapter 11.

9.1 Methodology

Various measurements are presented in this thesis. Cross sections are determined in a fiducial phase space defined at particle level close to the selection targeting the production of W^+W^- events in the detector (Table 7.2). Differential measurements are performed as a function of observables related to lepton, jet, and E_T^{miss} kinematics as discussed in Section 9.1.1. These allow the testing of different aspects of the theoretical calculations in perturbative QCD and electroweak theories, as well as an enhanced sensitivity to effects beyond the predictions of the SM. Additionally, Section 9.1.2 describes the calculation of the integrated cross section, which is performed in two steps. Cross sections are first obtained in the fiducial volume, which are then extrapolated to the full phase space.

9.1.1 Differential Cross Section Measurements

The differential cross sections of W^+W^- production are evaluated using an iterative Bayesian unfolding method [420, 421], introduced in Section 6.3, in a fiducial phase space defined at particle level close to the geometric and kinematic acceptance of the experimental analysis (Table 7.2). Exactly one prompt electron and one prompt muon of opposite electric charge are required, i.e., which do not originate from τ-lepton or hadron decays. The momenta of photons emitted within a cone of size $\Delta R = 0.1$ around the lepton direction that do not originate from hadron decays are added to the lepton momentum to form infrared-safe dressed leptons. Kinematic cuts on leptons in the fiducial phase space reproduce the constraints imposed at reconstruction level. Events with ad-

Fiducial phase space		
Object	Requirement	Criteria
Prompt Lepton	p_T	$> 27\,\text{GeV}$
	$\lvert\eta\rvert$	< 2.5
Loose Lepton	p_T	$> 10\,\text{GeV}$
	$\lvert\eta\rvert$	< 2.5
Jets	b-jets [490]	$p_T > 20\,\text{GeV}$, $\lvert\eta\rvert < 2.5$
	Other jets	$p_T > 30\,\text{GeV}$, $\lvert\eta\rvert < 4.5$
Event	Leptons	1 prompt electron and 1 prompt muon of opposite electric charge. No additional loose leptons
	Number of b-jets	0
	$m_{e\mu}$	$> 85\,\text{GeV}$

Table 9.1: Definition of the truth-level objects and the jet-inclusive fiducial phase space.

ditional prompt electrons or muons fulfilling a looser p_T requirement are vetoed. The invariant mass of the dilepton system, $m_{e\mu}$, is required to be greater than $85\,\text{GeV}$ at particle level. Stable final-state particles[1], excluding prompt neutrinos as well as prompt charged leptons and the associated photons, are clustered into particle-level jets using the anti-k_t algorithm with radius parameter $R = 0.4$. The nominal definition of the fiducial phase space includes a veto on particle-level b-jets with $p_T > 20\,\text{GeV}$ [490]. The missing transverse momentum is defined at particle level as the negative vectorial sum of the transverse momenta of visible particles. The selection criteria of the fiducial region are summarized in Table 9.1.

Cross sections are measured differentially as a function of the transverse momentum of the leading lepton ($p_T^{\text{lead. lep.}}$), the transverse momentum of the subleading lepton ($p_T^{\text{sublead. lep.}}$), the transverse momentum of the dilepton system ($p_T^{\ell\ell}$), the rapidity of the dilepton system ($y_{e\mu}$), the invariant mass of the lepton pair ($m_{e\mu}$), the azimuthal separation of the two leptons ($\Delta\phi_{e\mu}$), $\cos\theta^* = |\tanh(\Delta\eta_{e\mu}/2)|$, the magnitude E_T^{miss} of the missing transverse momentum vector $\vec{E}_T^{\text{miss}}$, defined as the negative vectorial sum of the transverse momenta of all visible particles, the scalar sum of E_T^{miss} and the lepton transverse momenta ($H_T^{\text{lep.+MET}}$), the transverse mass of the dilepton system and the missing transverse momentum, defined as

$$m_{T,e\mu} = \sqrt{(E_{\text{T},e\mu} + E_T^{\text{miss}})^2 - (\vec{p}_{\text{T},e\mu} + \vec{E}_T^{\text{miss}})^2}\,, \quad \text{where } E_{\text{T},e\mu} = \sqrt{|\vec{p}_{\text{T},e\mu}|^2 + m_{e\mu}^2}\,,$$

the scalar sum of all jet and lepton transverse momenta (S_T), and the jet multiplicity (N_{jets}). Distributions as a function of $p_T^{\text{lead. lep.}}$, $p_T^{\ell\ell}$, $m_{e\mu}$, $H_T^{\text{lep.+MET}}$, and $m_{T,e\mu}$ are correlated with the center-of-mass energy of the hard interaction and are sensitive to BSM contributions at high values of the partonic center-of-mass energy $\sqrt{\hat{s}}$. Variables such as $p_T^{\text{lead. lep.}}$, $p_T^{\ell\ell}$ are also highly correlated to the transverse momentum of the diboson system $p_{T,WW}$, and therefore very sensitive to higher-order QCD corrections. The azimuthal separation $\Delta\phi_{e\mu}$ gives access to the spin correlation between the two W bosons in the fi-

[1]Particles are considered stable if their decay length $c\tau$ is greater than $1\,\text{cm}$.

nal state and plays a special role in studies of the interference term in EFT interpretations (introduced in Section 1.7). The spin structure of the W-boson pair can also be studied via the $\cos\theta^*$ distribution [491]. The rapidity $|y_{e\mu}|$ is sensitive to the Lorentz boost of the W^+W^- system along the collision axis but also to the production mode of the W-boson pair ($q\bar{q}$, gq, or gg). Variables sensitive to neutrino production such as E_T^{miss} have typically low resolution. The jet-multiplicity distribution is particularly interesting to evaluate the accuracy in parton radiation of fixed-order QCD corrections and parton showers.

The binning of the distributions has been chosen for all observables to ensure the stability of the unfolding procedure (defined in Sec. 9.1.1): at least $70\,\%$ of the events are contained in the same bin on both particle and reconstruction level. Additionally, the optimized binning must keep statistical uncertainties below $10\,\%$ in each bin, except in the high-energy tails of the distributions where statistical uncertainties cannot surpass $20\,\%$ (keeping a stability at $70\,\%$). This allows the increase of the bin granularity at the high-energy tails, enhancing the sensitivity to effects beyond the SM prediction that can be exploited in interpretations such as the one presented in Chapter 11. The bin optimization, the evaluation of the unfolding inputs, as well as the validation and additional studies of the unfolding procedure are performed using the MC events of $q\bar{q} \to WW$ production simulated with POWHEG MINNLO+PYTHIA8, combined with $gg \to WW$ contributions as predicted with SHERPA 2.2.2. Background events, estimated following the methods discussed in Chapter 8, are subtracted from the data.

Migrations between bins in the distributions during the reconstruction of the events are handled by the migration matrix. This matrix illustrates the percentage of events at particle level reconstructed with the ATLAS detector within a bin of a given observable. Figure 9.1 shows the matrices for the percentage of event migrations between particle and reconstruction level across bins of the $p_T^{\text{lead. lep.}}$, $m_{e\mu}$, E_T^{miss}, and jet-multiplicity distributions. Most of the observables used for differential cross-section measurements are highly diagonal. The migrations happen mostly to adjacent bins. The migration matrices contain $80\,\%$ or more of the events in most of the diagonal bins. These are higher than $95\,\%$ in angular distributions such as $y_{e\mu}$, $\Delta\phi_{e\mu}$, or $\cos\theta^*$. Effects on the unfolded distributions arising from the dependencies of the migration matrices on the chosen signal model are therefore expected to be minor for these distributions. Larger migrations are also observed in regions of the distributions with high statistics, exposed to a finer resolution of the binning. The E_T^{miss} and N_{jets} distributions present some exceptions. The former, with over $25\,\%$ of events off the diagonal, is anticipated due to the challenging reconstruction of this observable (described in Section 4.3.6) compared to a well-defined construction of E_T^{miss} at the particle level. The latter shows greater migrations with increasing jet multiplicity, especially towards a greater number of jets at particle level. This feature can be explained due to contributions from pile-up jets misassigned to the primary vertex.

Events reconstructed in the signal region whose production happened outside the fiducial phase space are considered via fiducial corrections. These are calculated as the fraction of events reconstructed in the signal region that also originate from inside the fiducial region at truth level (see Sec. 6.3). Figure 9.2 shows the fiducial corrections across bins of $p_T^{\text{lead. lep.}}$ and jet-multiplicity distributions. The number of W^+W^- event candidates not matched to the fiducial volume is of about $13\,\%$, mostly flat across distributions and increasing up to $33\,\%$ in events with low-p_T leptons. These arise predominantly from W^+W^- decays into τ-leptons, which are not considered in the fiducial phase space.

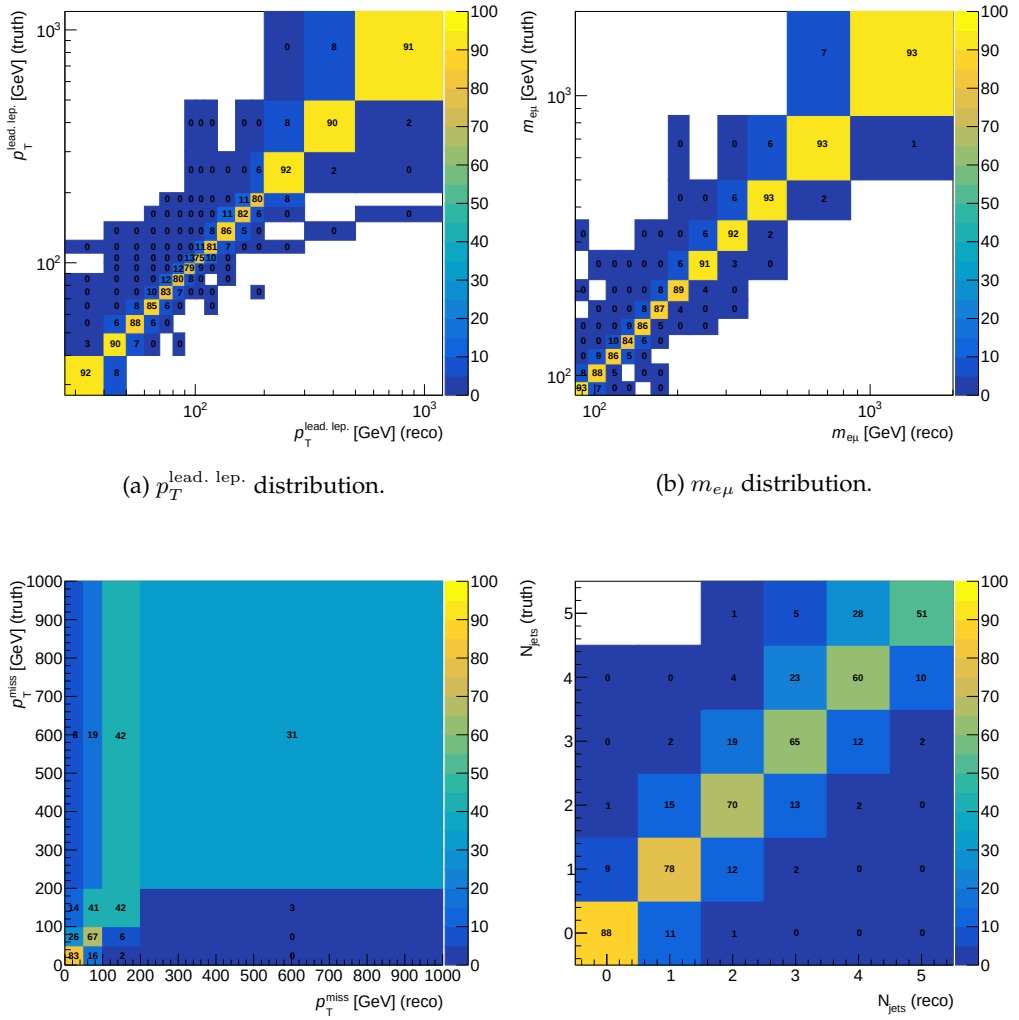

(a) $p_T^{\text{lead. lep.}}$ distribution.

(b) $m_{e\mu}$ distribution.

(c) E_T^{miss} distribution.

(d) Jet-multiplicity distribution.

Figure 9.1: Percentage of event migrations between the fiducial phase space at particle level, summarized in Table 9.1, and the reconstruction level (Table 7.2) in bins of the (a) $p_T^{\text{lead. lep.}}$ (b) $m_{e\mu}$, (c) E_T^{miss}, (d) jet-multiplicity distributions. The presented migration matrices were derived using MC simulation of $q\bar{q} \to WW$ events with POWHEG MINNLO+PYTHIA8 including $gg \to WW$ contributions predicted with SHERPA 2.2.2. Areas with no selected events are shown in white. Statistical uncertainties of the selected events are lower than 1%.

After subtraction of the background contributions, the data are finally multiplied by the fiducial correction before the unfolding. The unfolded result is then divided by the efficiency correction, where non-reconstructed events inside the fiducial signal region due to detector inefficiencies (about $44\,\%$ of events) are taken into account. The efficiency corrections are calculated as the fraction of events from the truth level fiducial region that are reconstructed in the signal region (see Sec. 6.3). Figure 9.3 presents the efficiency correction across bins of $p_T^{\text{lead. lep.}}$ and jet-multiplicity distributions. The efficiencies are usually low (about $38\,\%$) for leptons of $p_T < 40\,\text{GeV}$, increasing up to $65\,\%$ with greater p_T. The efficiency also deteriorates at higher jet-multiplicities. The efficiency reduction is pre-

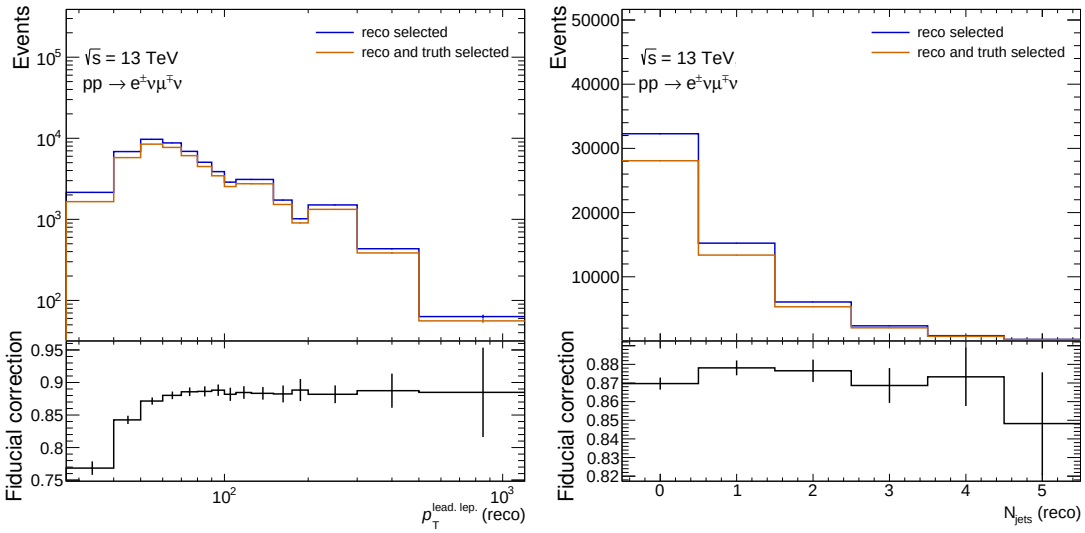

(a) $p_T^{\text{lead. lep.}}$ distribution. (b) Jet-multiplicity distribution.

Figure 9.2: Comparison of selected W^+W^- signal events at reconstruction level (blue) versus reconstructed events also selected within the (truth) fiducial phase space at particle level summarized in Table 9.1 (red) for the (a) $p_T^{\text{lead. lep.}}$ and (b) jet-multiplicity distributions. Their ratio is shown in the bottom plots, corresponding to the fiducial corrections used for the unfolding procedure. The distributions are derived using MC simulation of $q\bar{q} \to WW$ events with POWHEG MINNLO+PYTHIA8 including $gg \to WW$ contributions predicted with SHERPA 2.2.2. Vertical lines show statistical uncertainties in each bin.

dominantly caused by a combination of the lepton trigger efficiency (shown in Figs. 4.9 and 4.10), which are lower at high pile-up, as well as reconstruction, identification, and isolation efficiencies (Figs. 4.14 and 4.15).

Due to the good modeling of the data by simulation and relatively small migration effects, the unfolding converges quickly and only two iterations are required for most observables. Only the jet-multiplicity distribution, which is subject to larger modeling uncertainties, is unfolded using three iterations. Unfolded distributions for 1 up to 4 iterations of the unfolding procedure are shown in Figure 9.4. The bias arising due to the use of simulated distributions as a prior in the unfolding is estimated by reweighting the simulation with a smooth function such that it closely resembles the background-subtracted data. This reweighted detector-level prediction is unfolded using the nominal unfolding setup. The unfolding procedure is able to recover the generator-level distribution within $1\,\%$, indicating a negligible bias in the unfolding procedure.

In contrast to the integrated cross-section measurement, whose methodology is presented in Section 9.1.2, these results only weakly depend on the signal model since it is only used to estimate detector resolution and efficiency and remains approximately valid also in the presence of physics beyond the SM. This is confirmed by performing signal-injection tests using MC events including anomalous effects introduced by SMEFT operators modeled with MADGRAPH, described in Section 7.4, for various Wilson coefficients defined in Section 11.1. As the SM prediction of the MADGRAPH sample (only at LO) differs quite significantly from the default POWHEG MINNLO+PYTHIA8 SM prediction, all SMEFT predictions of the various distributions are rescaled bin-by-bin by the ratio of the POWHEG MINNLO+PYTHIA8 and the MADGRAPH SM prediction to improve the mod-

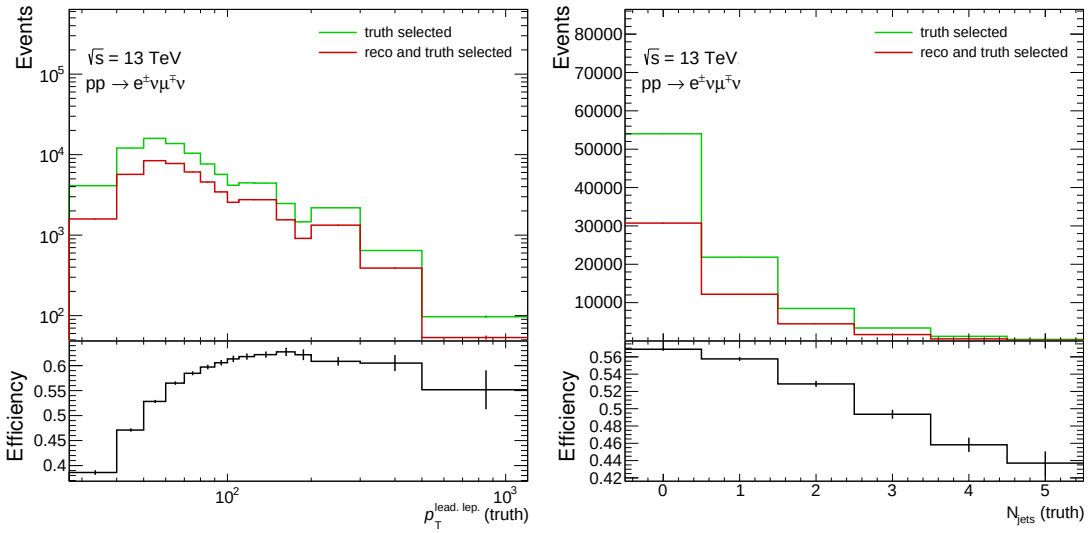

(a) $p_T^{\text{lead. lep.}}$ distribution. (b) Jet-multiplicity distribution.

Figure 9.3: Predicted distributions of number of events at particle level for signal production in the (truth) fiducial phase space summarized in Table 9.1 versus generated events also selected at reconstruction level (Table 7.2) as a function of (a) $p_T^{\text{lead. lep.}}$ and (b) jet-multiplicity. The ratio between selected events at (truth) particle level over events selected at both reconstruction and (truth) particle level is shown below, representing the detector efficiency. The distributions were derived using MC simulation of $q\bar{q} \to WW$ events with POWHEG MINNLO+PYTHIA8 including $gg \to WW$ contributions predicted with SHERPA 2.2.2. Vertical lines show statistical uncertainties in each bin.

eling. This reconstruction-level SMEFT prediction is unfolded using the aforementioned unfolding procedure. Figure 9.5 shows the SMEFT prediction at particle level divided by the SM prediction (solid lines), compared to the ratio of the unfolded SMEFT prediction over the SM prediction at reconstruction level (dashed lines) across bins of the $H_T^{\text{lep.+MET}}$ distribution. The true distribution is recovered almost perfectly for most Wilson coefficients, indicating that the unfolding procedure also recovers non-resonant BSM signals correctly.

9.1.2 Fiducial Integrated and Total Cross Sections

The integrated fiducial cross section is determined, as described in Section 6.1, using a profile-likelihood fit. In contrast to a cut-and-count result, where each event would contribute in the same way, the profile-likelihood approach allows regions where the SM contributions are predicted more precisely to have a greater impact on the determination of the signal normalization. Additionally, the fit allows to constrain nuisance parameters and to exploit the correlation between systematic uncertainties across bins of the chosen distribution.

The number of events in each bin is modeled as the predicted number of signal events scaled by a signal-strength modifier μ_{WW}, plus the number of background events. The likelihood for an observation of $\boldsymbol{N}^{\text{Obs}} = (N_1^{\text{Obs}}, \ldots, N_{n_{\text{bins}}}^{\text{Obs}})$ events is modeled following Eq. (6.2) using ROOFIT [492] as a product of Poisson distributions, multiplied by Gaussian profiles of nuisance parameters $\boldsymbol{\theta} = (\theta_1, \ldots, \theta_{n_{\text{syst}}})$ constraining the uncertainties on

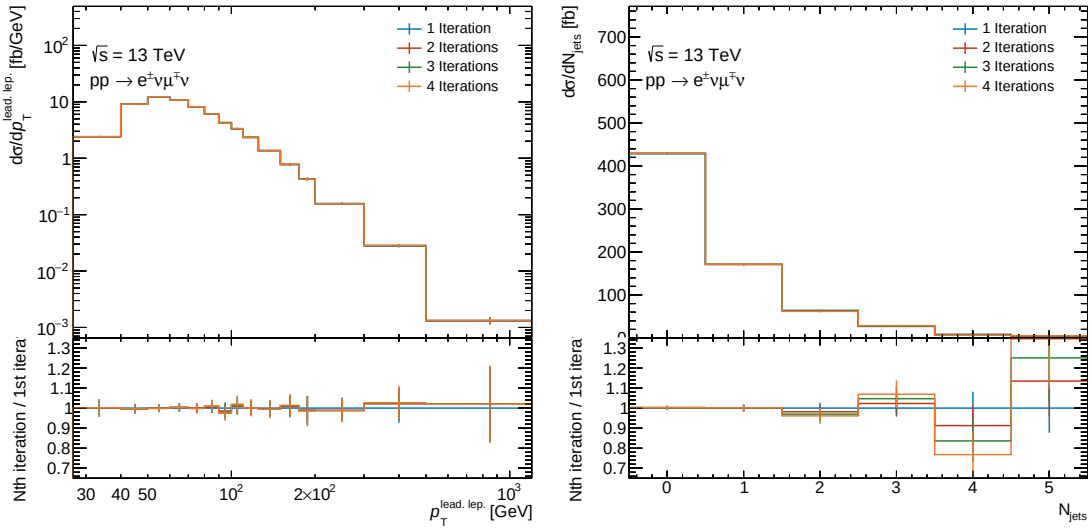

(a) $p_T^{\text{lead. lep.}}$ distribution. (b) Jet-multiplicity distribution.

Figure 9.4: Unfolded results after various iterations of the iterative Bayesian unfolding method (described in Section 6.3) between bins in the fiducial phase space at particle level summarized in Table 9.1 and the reconstruction level for (a) the $p_T^{\text{lead. lep.}}$, and (b) the jet-multiplicity distributions. The ratio between the unfolded result after the n-th iteration over the result at the first iteration is shown below. The presented distributions were derived using MC simulation of $q\bar{q} \to WW$ events with POWHEG MINNLO+PYTHIA8 including $gg \to WW$ contributions predicted with SHERPA 2.2.2. Statistical uncertainties are shown as vertical bars on each bin.

the number of events in bin b from signal (N_b^{S}) and background (N_b^{B}) predictions as

$$\text{L}\left(\boldsymbol{N}^{\text{Obs}}\middle|\mu,\boldsymbol{\theta}\right) = \prod_{b}^{n_{\text{bins}}} \text{Poisson}\left(N_b^{\text{Obs}}\middle|\mu_{WW}N_b^{\text{S}}\left(\boldsymbol{\theta}\right) + N_b^{\text{B}}\left(\boldsymbol{\theta}\right)\right) \times \prod_{i}^{n_{\text{syst}}} f\left(\theta_i\right) . \tag{9.1}$$

Signal contributions are predicted including the $q\bar{q} \to WW$ production mode using POWHEG MINNLO+PYTHIA8 MC simulation, as well as $gg \to WW$ and electroweak $WWjj$ production modes simulated with SHERPA 2.2.2. As the fit relies on the correct prediction of the signal shape from MC simulation, it is subject to signal modeling uncertainties and the result is only valid in a hypothesis where the data are described only by SM contributions.

Observable	Unct. on expected μ_{WW}
$p_T^{\text{lead. lep.}}$	± 0.038
$p_T^{\text{sublead. lep.}}$	± 0.044
$p_T^{\ell\ell}$	± 0.040
$H_T^{\text{lep.+MET}}$	± 0.039
$m_{\ell\ell}$	± 0.046
$\Delta\phi_{e\mu}$	± 0.042
S_T	± 0.034
N_{jets}	± 0.046

Table 9.2: Uncertainties on the signal strength μ_{WW} evaluated using Asimov data (i.e., $\mu_{WW} = 1.0$) for the profile-likelihood fit of the function given in Eq. 9.1.

First, the fitting procedure is repeated using Asimov data across various observables defined in Section 9.1.1 used for measurements of differential cross sections. All statistical, theoretical, and experimental uncertainties listed in Section 9.2 are considered. The results are compared to evaluate the distribution that best constrains the nuisance parameters. The resulting total uncertainties for the signal strength μ_{WW} after the fit are given in Table 9.2. Such effects may be important in

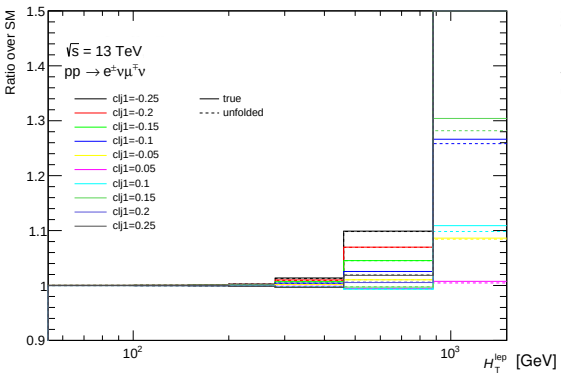

(a) $c_{\ell q}^{(1)}$ Wilson coefficient.

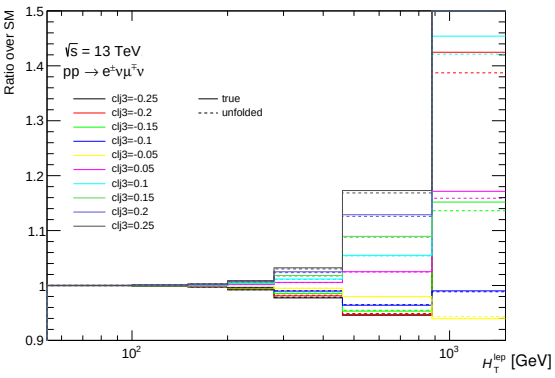

(b) $c_{\ell q}^{(3)}$ Wilson coefficient.

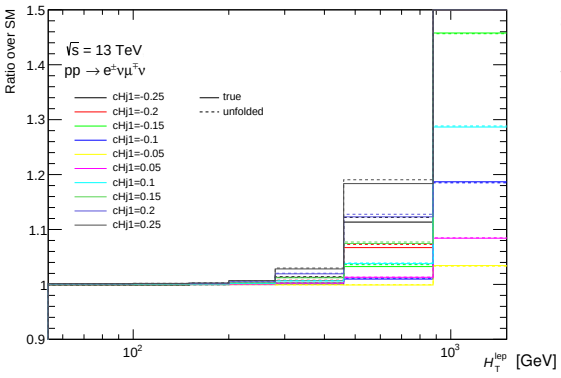

(c) $c_{Hq}^{(1)}$ Wilson coefficient.

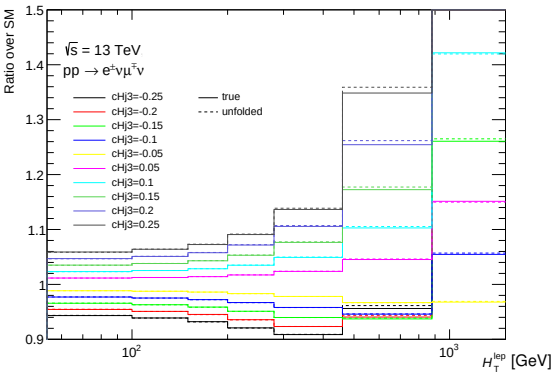

(d) $c_{Hq}^{(3)}$ Wilson coefficient.

Figure 9.5: EFT signal-injection tests in bins of the $H_T^{\text{lep.}+\text{MET}}$ distribution for different values of the (a) $c_{\ell q}^{(1)}$, (b) $c_{\ell q}^{(3)}$, (c) $c_{Hq}^{(1)}$, and (d) $c_{Hq}^{(3)}$ Wilson coefficients introduced in Chapter 11. The ratio of an EFT prediction with a non-zero EFT coefficient with respect to the SM prediction is plotted. Different lines show different Wilson coefficient values. Solid lines correspond to particle level SMEFT predictions. Dashed lines are SMEFT predictions at reconstruction level, unfolded using the nominal unfolding model presented in Section 9.1.1. No uncertainties are displayed.

the tails, where limited statistics may lead to artificial constraints on nuisance parameters. The observable S_T is chosen as the variable to be fitted since it has distribution that provides the smallest expected uncertainty.

The measured fiducial cross section is then obtained by multiplying the unconditional maximum-likelihood estimate of μ_{WW} with the predicted fiducial cross section of the signal model at particle level $\sigma_{\text{fid.}}^{\text{pred.}}$ as

$$\sigma_{\text{fid}}^{\text{Data}} = \mu_{WW} \cdot \sigma_{\text{fid, WW}}^{\text{pred}} \cdot \tag{9.2}$$

9.2 Uncertainties

Systematic uncertainties in the W^+W^- cross-section measurements arise from theoretical and experimental sources, including the background determination, and the procedures used to correct for detector effects. In the likelihood function given in Eq. (9.1) used to determine the integrated fiducial cross section, the same sources of uncertainty are instead modeled by nuisance parameters that are profiled in the fit.

Theoretical Uncertainties

Uncertainties due to missing higher-order QCD corrections in the simulation of signal and background processes are evaluated by varying the renormalization and factorization scales up and down by factors of two, avoiding opposite variations. The envelope of the 7-point variations is considered as the scale uncertainty. The scale variations are performed in both matrix element and parton shower.

The dependence on the arbitrary choice of the PDF sets has to be assessed. This is particularly important in precision measurements having enough experimental sensitivity to this choice. The assessment of the associated uncertainties follows the recommendations from the PDF4LHC Working Group [177], adopted also by other PDF collaborations. The $68\,\%$ uncertainty interval due to a given PDF set on the cross-section prediction can be evaluated in two different ways, depending on how the variations of the given PDF set are released. On the one hand, PDF sets from collaborations such as NNPDF [445, 493, 168] report a certain set of replicas, with the uncertainty evaluated as the standard deviation of the predicted values of the observable under consideration for each replica. On the other hand, collaborations such as PDF4LHC21 [177], MSHT20 [171], or MSTW2008 [172] release a certain number of PDF variations along the direction of eigenvectors as a result of a Principal Component Analysis. In such cases, the uncertainty is evaluated as the sum in quadrature of the fluctuations of the observable of interest along each of the available eigenvectors.

The effect of α_{S} must also be evaluated. The value of α_{S} is considered at the mass of the Z boson, $\alpha_{\text{S}}(m_Z^2) = 0.1180 \pm 0.0009$, consistent with the PDG global average [95]. The impact of this choice is assessed by evaluating the predicted cross section within the 1σ variations of $\alpha_{\text{S}} \pm 0.001$, including the effect on PDFs. The arising effect on the predicted cross section is then symmetrized. The theoretical uncertainty on a given prediction is finally calculated as the sum in quadrature of the scale (which dominates), α_{S}, and PDF uncertainties.

In the simulation of W^+W^- events, additional uncertainties on the parton shower are evaluated by varying the parameters of the A14 tune within their uncertainties, with the largest uncertainty resulting from the VAR3C variation [446] affecting the modeling of initial-state radiation. For this process, an additional uncertainty accounting for the modeling of heavy-flavor jets is introduced by varying the fraction of events containing at least one jet originating from a b-quark or a c-quark by $30\,\%$, which covers the difference between predictions from PYTHIA 8.230 and SHERPA 2.2.2. For the $gg \to WW$ process and electroweak $WWjj$ production, which make up only $5\,\%$ and $1\,\%$ of the signal in the targeted region of the measurement, respectively, no theoretical uncertainties are considered.

Experimental Uncertainties

The dominant experimental systematic uncertainties arise in the determination of the b-tagging efficiency and mistagged rates [372], the correction of the jet-energy scale and resolution [361], and the luminosity measurement [342]. Experimental sources also encompass uncertainties in the calibration of lepton trigger [486, 326], reconstruction, identification and isolation efficiencies [472, 358], the calibration of the lepton momentum or energy scale and resolution [472, 494], and the modeling of pile-up. The experimental methods and their evaluation are summarized in Section 4.3. All experimental uncertainties are evaluated by varying the respective calibrations, and propagating their effects through the analysis, affecting both the background estimates and the unfolding of detector effects. Both the effect of the total rate and the effect on the shape of distributions are taken into account for all sources of systematic uncertainties.

Uncertainties from Background Estimates

The estimate of the top-quark background, described in Section 8.1, is affected by the statistical uncertainty of the number of events in the control region, and by uncertainties in the modeling of $t\bar{t}$ and single-top Wt events, such as the uncertainty in the matrix element calculation, the parton shower modeling, the QCD scale choices, the initial- and final-state radiation and the interference between $t\bar{t}$ and single-top Wt events [495]. These are evaluated by using the alternative simulations as described in Section 8.1.3, and propagating the results through the top-quark background estimate. The effect of the PDF uncertainty on the top-quark background was evaluated, but found to be negligible.

Systematic uncertainties in the estimate of the contributions arising from fake-lepton production are derived by changing the selection used to estimate the extrapolation weights, in order to change the composition of the sources of fake leptons. Additionally, the subtraction of the prompt-lepton sources in the control region is varied, and the statistical uncertainties of the weights are propagated. More details on the uncertainties affecting the fake-lepton estimate can be found in Section 8.4.6.

The uncertainty in additional backgrounds, estimated using MC simulation, is evaluated by varying each of their cross sections within their respective uncertainties. An uncertainty of $5\,\%$ is considered for the predicted cross-sections of Drell-Yan $Z + \text{jets}$ production [496], while cross sections of diboson production are known with a precision of $10\,\%$ [482, 481]. Effects due to missing higher-order QCD corrections and the par-

ton shower model are accounted for using 7-point scale variations. The impact of these uncertainties on the cross-section measurements is small compared to the uncertainties associated with the fake lepton and top-quark background.

Uncertainties from the Unfolding Procedure

Systematic uncertainties on the differential cross sections are evaluated by repeating the unfolding procedure described in Section 9.1.1 with simulations based on varied assumptions on signal, background, and detector models. The resulting uncertainties are symmetrized and added in quadrature. Statistical uncertainties in the unfolded distributions are evaluated by creating pseudodata samples that are obtained by varying the data within their Poisson uncertainties in each bin, then propagating these varied samples through the unfolding algorithm. The statistical uncertainties of the background estimates, which include statistical fluctuations in both MC predictions and the control regions used in estimating the top and fake-lepton backgrounds, are evaluated using the same method.

9.3 Theoretical Predictions

Fiducial differential and integrated cross-section measurements are compared to three different theoretical predictions.

The first is a fixed-order prediction calculated using MATRIX 2.0.1 [231, 247, 233, 232, 253, 497, 498, 452, 451, 499, 500, 501, 502], which corresponds to the NNLO accuracy in QCD for the $q\bar{q} \to WW$ production, and to NLO QCD accuracy for the correction to $gg \to WW$ production. The latter constitutes part of the N^{3}LO correction to W^+W^- production and the combined prediction is labeled as nNNLO. The prediction also includes NLO electroweak corrections and contributions from photon-induced production. The PDF set NNPDF3.1@NNLO [493] is used, which accounts for the photon in the parton content with the LUXQED method [186]. The coupling constants, masses, and widths used as inputs were set as reported in Ref. [231]. The EW couplings are derived from the gauge-boson masses in the G_μ-scheme. The CKM matrix is assumed to be diagonal. Dynamic QCD scales are set to half the sum of W-boson transverse masses are used to assess uncertainties of missing higher-order QCD corrections as 7-point variations of the factorization and renormalization scales[2].

Comparisons between the nNNLO QCD prediction versus the combined EW-QCD prescriptions using both multiplicative and additive schemes [231] across bins of the $p_T^{\text{lead. lep.}}$, $p_T^{\ell\ell}$, $H_T^{\text{lep.+MET}}$, $m_{e\mu}$, N_{jets}, and E_T^{miss} distributions are shown in Figure 9.6. The large differences between the two schemes in the inclusive phase space indicate a large uncertainty due to mixed QCD-EW corrections. In the high-energy regime, not only electroweak but also QCD corrections are large as topologies with a high-p_T W boson recoiling against a high-p_T jet and a soft W boson are important. This causes large differences between additive and multiplicative schemes of combined QCD-EW corrections at the high-energy tails of the distributions. The EW corrections are combined with the QCD

[2]The setup was validated by reproducing the predictions of fiducial cross-section measurements reported in Ref. [231].

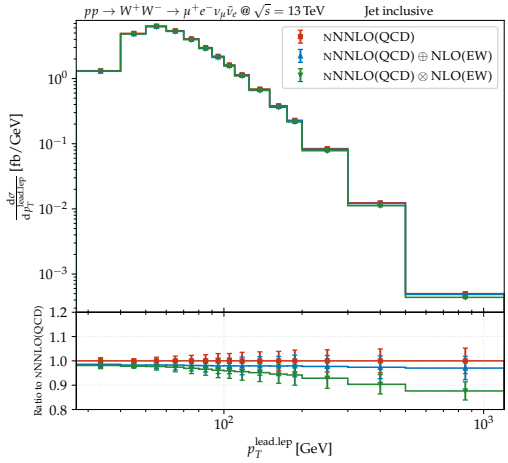

(a) $p_T^{\text{lead. lep.}}$ distribution.

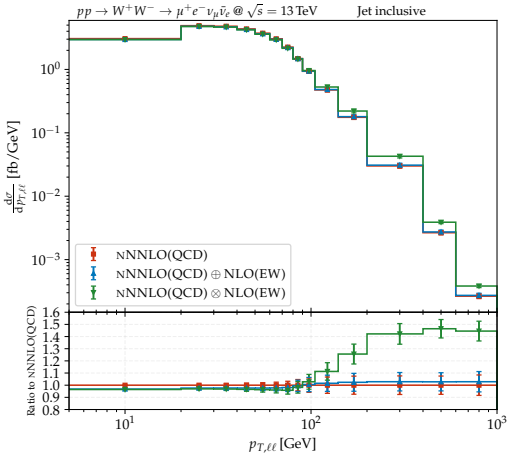

(b) $p_T^{\ell\ell}$ distribution.

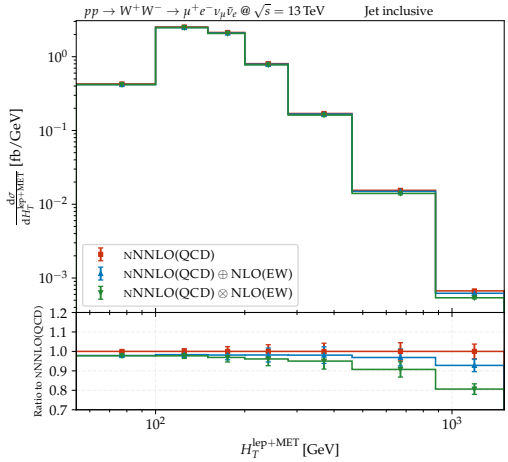

(c) $H_T^{\text{lep.+MET}}$ distribution.

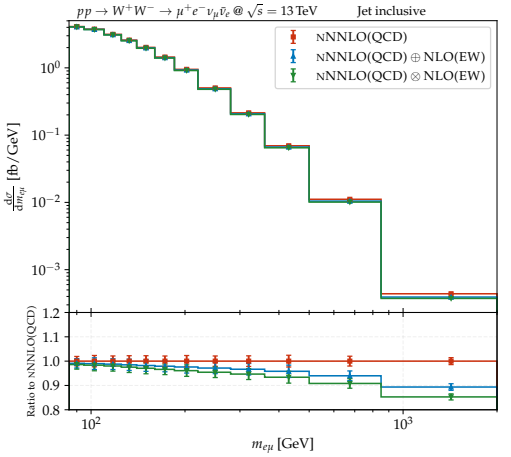

(d) $m_{e\mu}$ distribution.

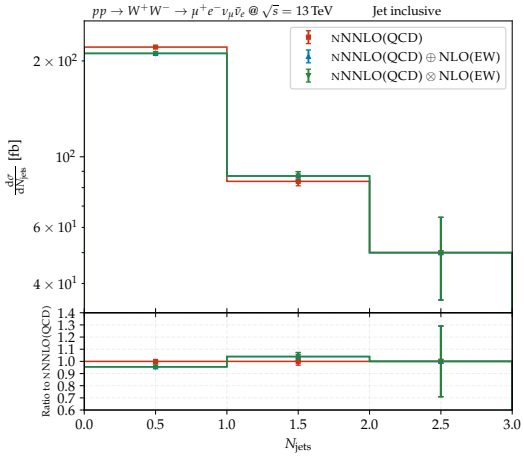

(e) Jet-multiplicity distribution.

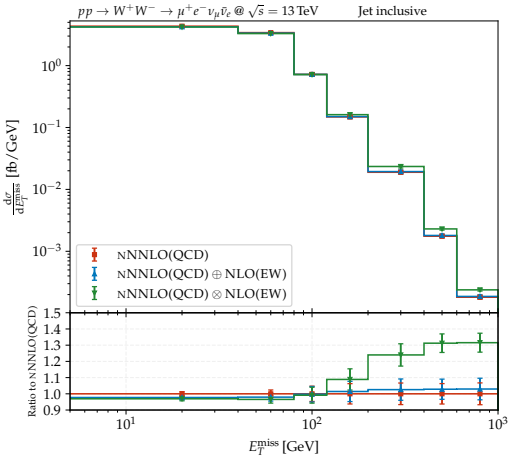

(f) E_T^{miss} distribution.

Figure 9.6: Predictions of differential fiducial cross sections of $W^+W^- \to \mu^+e^-\nu_\mu\bar{\nu}_e$ production in bins of (a) $p_T^{\text{lead. lep.}}$, (b) $p_T^{\ell\ell}$, (c) $H_T^{\text{lep.+MET}}$, (d) $m_{e\mu}$, (e) jet-multiplicity, and (f) E_T^{miss} generated with MATRIX 2.0.1 based on the NNPDF3.1@NNLO+LUXQED set of PDFs using various higher-order corrections. The prediction of W^+W^- production including nNNLO QCD corrections to the fully-leptonic W^+W^- production (red squares) is compared with those including NLO EW corrections via additive (blue up triangles) and multiplicative (green down triangles) schemes in the jet-inclusive fiducial phase space. Error bars show the sum in quadrature of scale, α_S, and PDF uncertainties. The same binning as the measurement, optimized as described in Section 9.1.1, is chosen.

correction to $q\bar{q} \to WW$ using the multiplicative scheme by default. The multiplicative scheme provides an increase in differential production cross section with respect to the nNNLO QCD distribution for the tails of the $p_T^{\ell\ell}$, E_T^{miss}, and jet-multiplicity distributions, while electroweak corrections are expected to reduce the production cross section as described in Section 3.1. The tails of these distributions are dominated by $W^+W^- + \text{jets}$ events, for which a multiplicative application of the EW corrections is not appropriate [231]. Therefore, the additive scheme is used for the $p_T^{\ell\ell}$, E_T^{miss}, and jet-multiplicity distributions instead. Photon-induced contributions are independently added to the cross-section prediction in both approaches.

As discussed in Section 3.1, photon-induced W^+W^- production must be included in theoretical predictions for an accurate description of differential observables correlated with the diboson invariant mass m_{WW}. Figure 9.7 displays the predicted differential cross section as a function of $p_T^{\text{lead. lep.}}$ in both nNNLO QCD and NLO EW correction components using different sets of PDFs. Predictions are computed using the NNPDF3.0 [445], NNPDF3.1 [493], NNPDF4.0 [168], CT18 [170], PDF4LHC21 [177], MSHT20 [171], and MSTW2008 [172]. All PDFs are considered at NNLO accuracy using the four-flavor scheme. Only the NNPDF3.1 predictions include photon PDFs using the LUXQED method [186]. In QCD corrections, affecting predominantly the $q\bar{q} \to WW$ and $gg \to WW$ production modes, the discrepancies among predictions are mostly flat. However, the use of photon PDFs with NNPDF3.1 enhances the high-energy tails of the $p_T^{\text{lead. lep.}}$ distribution by up to 30 %. Differences in normalization arise from the NNLO QCD corrections to the $q\bar{q} \to WW$ production mode, which dominates in the jet-inclusive fiducial phase space, as seen in Figure 9.8. For an accurate description of both fiducial integrated and differential cross sections, the NNPDF3.1@NNLO [493] set of PDFs was therefore chosen as default.

The second prediction is derived from the POWHEG MINNLO+PYTHIA8 $q\bar{q} \to WW$ sample [216, 212], a prediction of NNLO accuracy in QCD for inclusive observables introduced in Section 7.4. The POWHEG MINNLO+PYTHIA8 prediction is combined with the SHERPA 2.2.2 [148] $gg \to WW$ sample (Section 7.4). These samples were also used to estimate fiducial and efficiency corrections, as well as for the model of the W^+W^- signal in the maximum likelihood fit. The NNPDF3.0@NNLO [445] set of PDFs was used in the generation of these samples. Compared to the results from MATRIX, this prediction lacks photon-induced contributions as well as NLO EW corrections (beyond the contributions of photon radiation included in the PYTHIA parton shower), as well as the NLO corrections to the gluon-initiated production mode. Nevertheless, the inclusion of the parton shower effects improves the modeling of jets and distributions correlated to the transverse momentum of the W^+W^- system.

The third prediction was generated using SHERPA 2.2.12 [148]. The prediction is of NLO accuracy in QCD for up to one additional parton, and leading-order accuracy for two to three additional parton emissions for $q\bar{q}$ initial states. The matrix element calculations were matched and merged with the SHERPA parton shower based on Catani-Seymour dipole factorization [448, 202] using the MEPS@NLO prescription [449, 210, 205, 450]. The virtual QCD corrections were provided by the OPENLOOPS library [499, 451, 452]. The NNPDF3.0@NNLO set of PDFs was used [445], along with the dedicated set of tuned parton-shower parameters developed by the SHERPA authors. This prediction lacks the full NNLO QCD corrections but does include an extra parton emission at

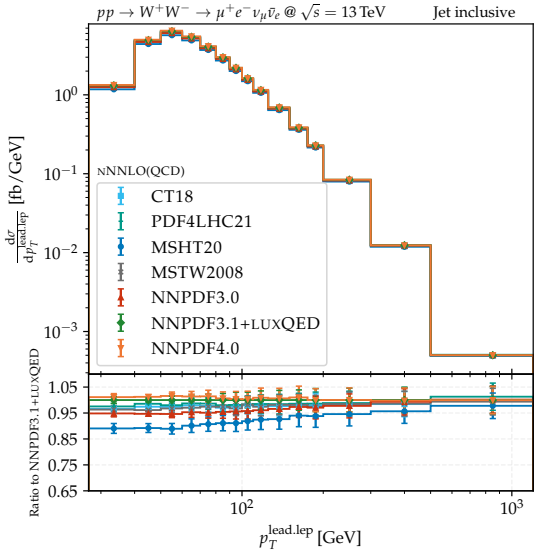

(a) NNNLO (QCD), $p_T^{\text{lead. lep.}}$ distribution.

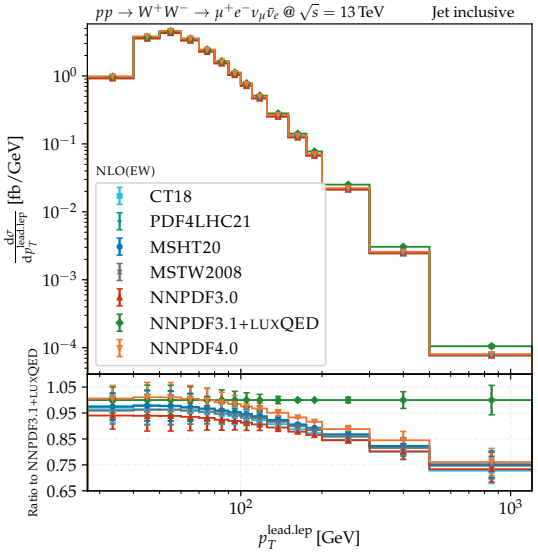

(b) $q\bar{q} \to WW$ NLO (EW), $p_T^{\text{lead. lep.}}$ distribution.

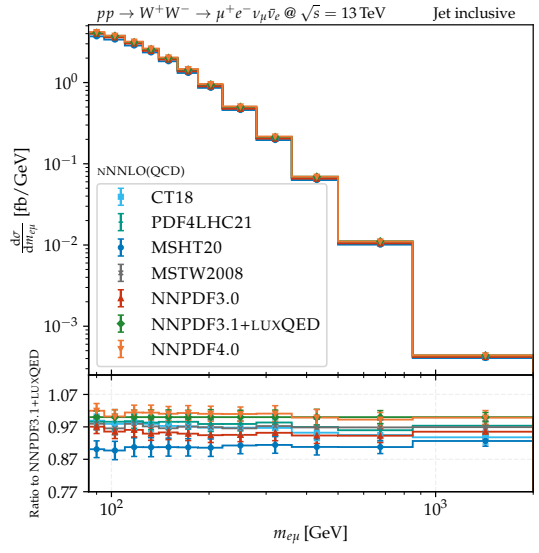

(c) NNNLO (QCD), $m_{e\mu}$ distribution.

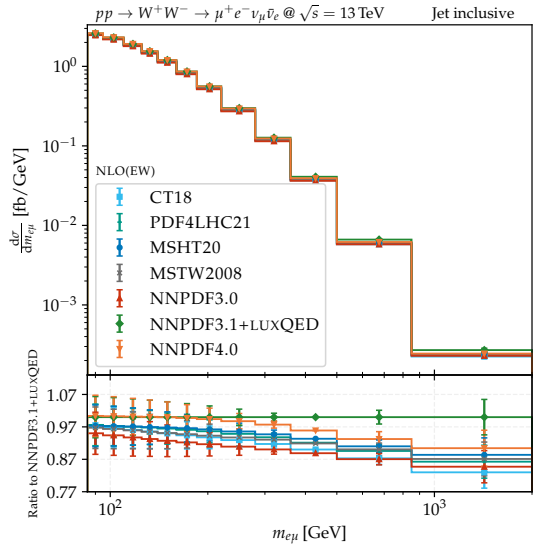

(d) $q\bar{q} \to WW$ NLO (EW), $m_{e\mu}$ distribution.

Figure 9.7: Predictions of differential fiducial cross sections of $W^+W^- \to \mu^+e^-\nu_\mu\bar{\nu}_e$ production generated with MATRIX 2.0.1 using the NNPDF3.0 [445] (red up triangle), NNPDF3.1 [493] (green diamonds), NNPDF4.0 [168] (orange down triangles), CT18 [170] (cyan squares), PDF4LHC21 [177] (green ticks), MSTW2008 [172] (grey crosses), and MSHT20 [171] (blue dots). The contributions from (a) nNNLO QCD and (b) NLO EW correction to the $q\bar{q} \to WW$ production mode are shown in the jet-inclusive fiducial phase space in bins of $p_T^{\text{lead. lep.}}$. Similarly, the contributions from (c) nNNLO QCD and (d) NLO EW correction to the $q\bar{q} \to WW$ in bins of $m_{e\mu}$ are displayed. Logarithmic scale is used on both horizontal and vertical axes. Error bars show the sum in quadrature of scale, α_S, and PDF uncertainties. The same binning as the measurement, optimized as described in Section 9.1.1, is chosen.

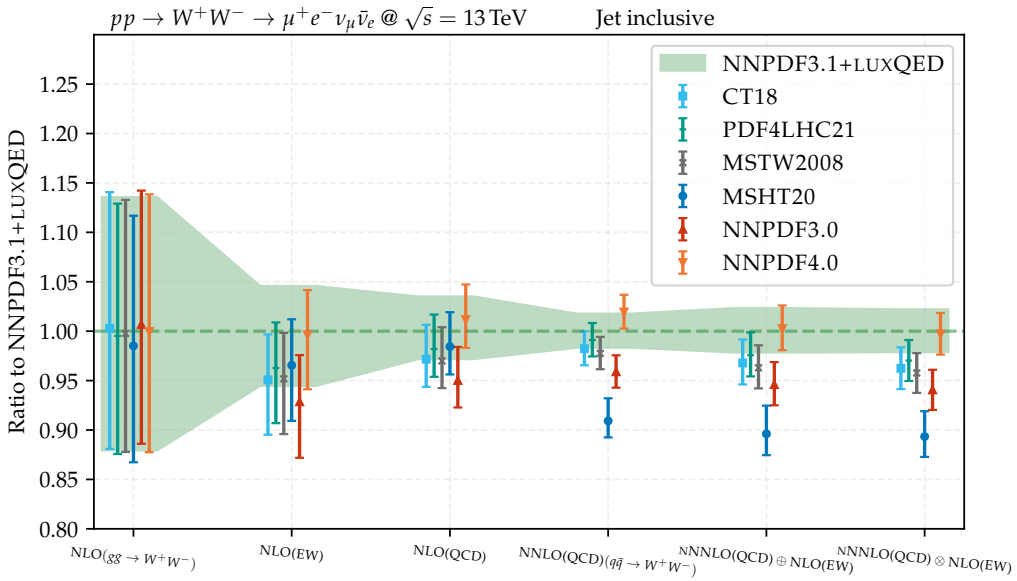

Figure 9.8: Ratios between MATRIX predictions of fiducial integrated cross sections of W^+W^- production in fully-leptonic final states in the jet-inclusive fiducial phase space using the NNPDF3.0 [445] (red up triangle), NNPDF4.0 [168] (orange down triangles), CT18 [170] (cyan squares), PDF4LHC21 [177] (green ticks), MSHT20 [171] (blue dots), and MSTW2008 [172] (violet cross) sets of PDFs with respect to the nominal prediction using NNPDF3.1 [493] (green band). The reference prediction using NNPDF3.1 includes photon PDFs using the LUXQED method [186]. Error bars show the sum in quadrature of scale, α_S, and PDF uncertainties.

LO, which does improve the modeling of high-multiplicity events.

The last two predictions are augmented by a simulation of electroweak production of a diboson pair in association with two jets ($VVjj$), which was generated with the SHERPA 2.2.12 [148] generator. Inclusively, the contribution of this production mode is negligible, but $WWjj$ production with a vector-boson scattering topology constitutes a correction of several percent in analysis bins dominated by events with at least two jets.

A comparison of fiducial cross-section predictions for $W^+W^- \to e^\pm\mu^\mp\nu_e\nu_\mu$ final states is given in Table 9.3. The $q\bar{q} \to WW$ cross sections predicted using NNPDF3.1 are $4\,\%$ larger than those using NNPDF3.0, as can be seen from the first two MATRIX predictions and Figures 9.7 and 9.8, which only differ in the PDF set used. The POWHEG MINNNLO prediction for $q\bar{q} \to WW$ is $3\,\%$ smaller than the fixed-order NNLO prediction using the same PDF, mainly due to parton shower effects, in particular final-state photon radiation which reduces the lepton momenta and thus the signal acceptance. The resummation scheme and the description of extra parton radiation at all orders implemented in the parton shower model also reduces the associated scale uncertainties with respect to fixed-order predictions. SHERPA 2.2.12 predicts a fiducial cross section that is similar to the one from POWHEG MINNLO, although with a larger scale uncertainty. The SHERPA 2.2.2 $gg \to WW$ prediction is significantly smaller than the MATRIX NLO prediction, which is partially compensated by the application of an inclusive K-factor of 1.7 to the former prediction. The NLO electroweak correction to $q\bar{q} \to WW$, given by the ratio of the NLO EW to the LO prediction, decreases the $q\bar{q} \to WW$ cross section by

Process	Code	PDF	Perturbative order	$\sigma_{\text{fid}} \pm (\text{scale})$ [fb]	
$q\bar{q} \to WW$	MATRIX	NNPDF3.1	NNLO QCD	674	$\pm 1.8\,\%$
	MATRIX	NNPDF3.0	NNLO QCD	646	$\pm 1.8\,\%$
	MINNLO+PYTHIA8	NNPDF3.0	NNLO QCD + PS	624	$\pm 1.1\,\%$
	SHERPA 2.2.12	NNPDF3.0	NLO QCD + PS †	630	$\pm 7.2\,\%$
$gg \to WW$	MATRIX	NNPDF3.1	NLO QCD	32	$\pm 13\,\%$
	SHERPA 2.2.2	NNPDF3.0	LO QCD + PS †	15	$\pm 30\,\%$
$\gamma\gamma \to WW$	MATRIX	NNPDF3.1	LO	5	$\pm 2.3\,\%$
	MATRIX	NNPDF3.1	NLO EW	11	$\pm 2.3\,\%$
$q\bar{q} \to WWjj$ (EW)	SHERPA 2.2.12	NNPDF3.0	LO + PS	4	$\pm 7.0\,\%$
	For calculation of NLO EW correction:				
$q\bar{q} \to WW$	MATRIX	NNPDF3.1	LO	436	$\pm 5.1\,\%$
	MATRIX	NNPDF3.1	NLO EW	418	$\pm 5.1\,\%$

†: Includes matrix elements with additional parton emissions, matched and merged with the parton shower, which increase the accuracy of the simulation of high jet multiplicity events but also increase the nominal scale uncertainty.

Table 9.3: Comparison of theoretical predictions for fiducial cross sections of various modes contributing to W^+W^- production. The names of the POWHEG MINNLO+PYTHIA8 prediction, the NNPDF3.0@NNLO, and NNPDF3.1@NNLO LUXQED PDF sets are shortened for simplicity. Cross-section predictions are given together with μ_R and μ_F scale uncertainties.

$4\,\%$ while doubling the photon-induced contribution up to $1.5\,\%$ of the predicted fiducial W^+W^- production cross section. In the calculation of δ_{EW}, scale variations are correlated between the numerator and denominator. While the former is absent in EW corrections, uncertainties on the latter cancel out in the ratio. As a consequence, higher-order EW corrections as well as multiplicative combinations of QCD and EW corrections have similar QCD scale uncertainties as for the underlying QCD cross sections at the same accuracy in perturbation theory.

Chapter 10

Results of W^+W^- Production Cross-Sections Measurements

Results of fiducial differential and total production cross sections of W-boson pairs are presented in the following. With the methodology established in Chapter 9, the cross sections are measured. The observed data events are compared to the SM expectation in Section 10.1, based on the estimation of background events discussed in Chapter 8. Section 10.2 contains the measurements of differential cross sections, unfolded to the fiducial phase space at particle level as a function of twelve different observables. The results are compared to the theoretical predictions described in Section 9.3. A measurement of the fiducial integrated cross section is given in Section 10.3. The impact of the PDF sets in the theoretical predictions is also evaluated. The measurement is extrapolated to the full phase space to report the total W^+W^- production cross section. Section 10.4 closes the chapter with a summary and an outlook. The interpretation of these measurements in the context of the Standard Model Effective Field Theory is discussed in Chapter 11, where constraints on anomalous couplings between gauge vector bosons, leptons, quarks, and the Higgs field are presented.

10.1 Selected W^+W^- Events

The total number of W^+W^- candidate events selected in the jet-inclusive signal region is presented in Table 10.1. Expected contributions from signal and background predictions and their respective uncertainties, as estimated using the techniques considered in Chapter 8, are also listed. Section 9.2 provides details on the calculation of the reported uncertainties. Approximately $60\,\%$ of events meeting requirements of the signal region selection are background events, with the top-quark background (either from $t\bar{t}$ or single-top Wt production) being the largest, constituting about $80\,\%$ of the total background in the signal region. The total number of events observed in data slightly exceeds the sum of estimated background and signal yields based on the SM predictions. Figure 10.1 presents a comparison of the observed number of events in data

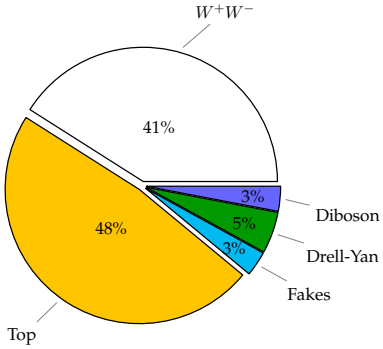

Source	Event yields
Top	66500 ± 1900
Drell-Yan	6500 ± 400
Fakes	5000 ± 1300
Diboson	4500 ± 600
W^+W^-	56900 ± 1100
Total background	82600 ± 2100
Total SM	139700 ± 2400
Data	144221

Table 10.1: Selected W^+W^- event candidates in data, along with the prediction of signal and background contributions described in Chapter 8. The uncertainties include statistical and systematic contributions. The percentages on the charts are given with respect to the total SM prediction. The individual uncertainties are correlated, and do not add up in quadrature to the total uncertainty.

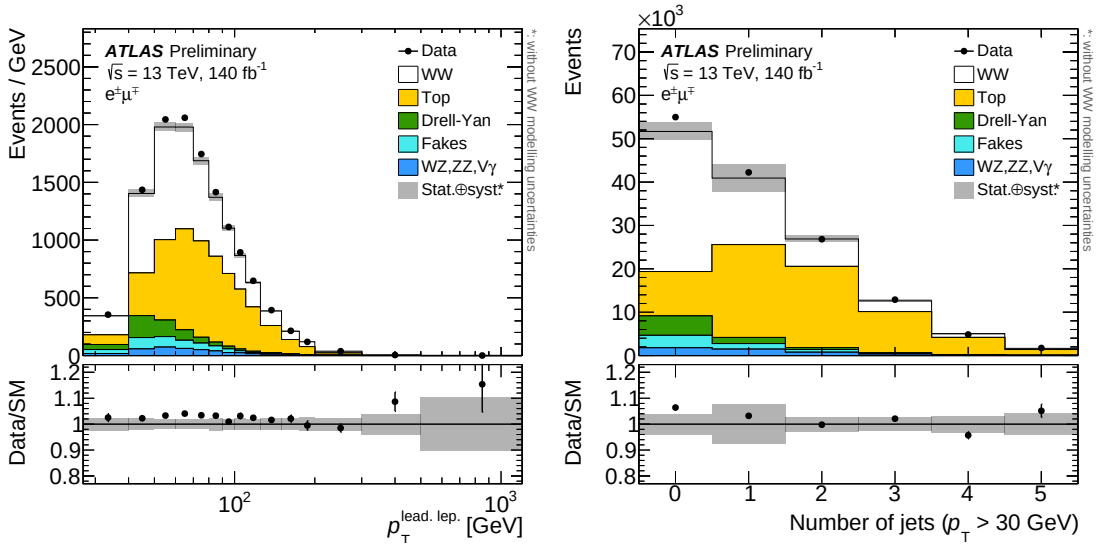

(a) Leading lepton transverse momentum, $p_T^{\text{lead. lep.}}$.

(b) Jet multiplicity.

Figure 10.1: Detector-level distributions of (a) $p_T^{\text{lead. lep.}}$ and (b) the jet multiplicity in the jet-inclusive signal region. Data are shown as black markers together with histograms for the predictions of signal and background processes. The rightmost bin contains overflow events. The lower panels show the ratio of the data to the total prediction. Top and fake backgrounds are determined using data-driven methods. The displayed uncertainty bands include statistical and systematic uncertainties, excluding theory uncertainties on the signal, which largely cancel in the measurement of W^+W^- cross sections. Published in Ref. [87].

against the expected signal prediction, and the background estimate in bins of leading lepton p_T (Fig. 10.1a) and jet-multiplicity (Fig. 10.1b). A slight underprediction of data occurs at intermediate values of p_T (between 50 and 90 GeV) and low jet activity, attributed to the choice of the PDF set for the W^+W^- prediction as discussed in Section 9.3. Overall, good agreement between the SM prediction and data is observed. Distributions for other observables listed in Section 9.1.1 for measuring differential cross sections are shown in Appendix C.

The relative uncertainties as a function of the unfolded $p_T^{\text{lead. lep.}}$ and S_T distributions are displayed in Figures 10.2a and 10.2b, respectively. Uncertainties on the number of reconstructed W^+W^- event candidates in low-$p_T^{\text{lead. lep.}}$ bins are dominated by modeling uncertainties of the simulation of top-quark production, necessary to compute the correlation coefficients C_b in the data-driven b-counting method as described in Section 8.1. Other systematic uncertainties follow, mainly from the luminosity measurement. Bins of $p_T^{\text{lead. lep.}} > 300\,\text{GeV}$ are dominated by statistical uncertainties. Fake-lepton and jet-calibration uncertainties are about 2 % or lower in most of the $p_T^{\text{lead. lep.}}$ bins. However, jet calibration uncertainties dominate the bins of $S_T < 250\,\text{GeV}$. At greater values of S_T, uncertainties from statistical fluctuations and the modeling of the top-quark background drive the total uncertainty band per bin. The precision on the measured number of events in this S_T regime is in general worse, since topologies with two or more jets dominate the event selection, which are effectively computed at leading order by the simulation of the parton shower.

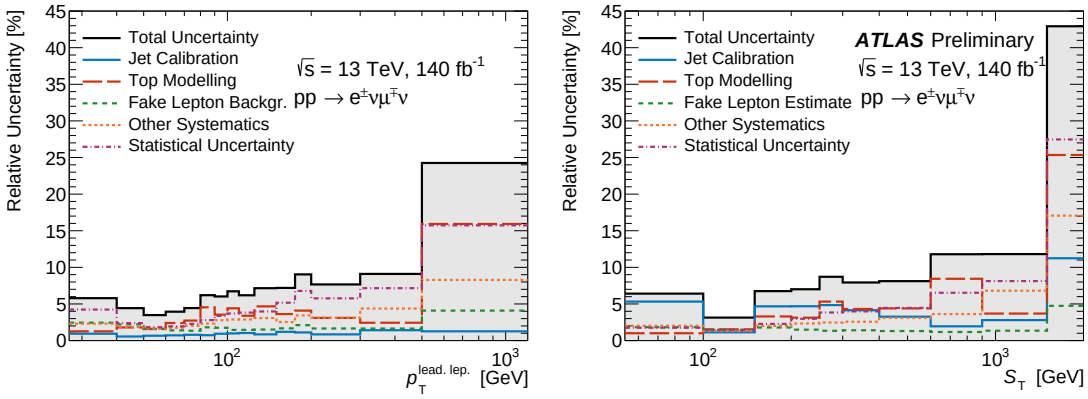

(a) $p_T^{\text{lead. lep.}}$ distribution. (b) S_T distribution.

Figure 10.2: Decomposition of uncertainties on the unfolded (a) $p_T^{\text{lead. lep.}}$ and (b) S_T distributions. *Jet calibration* uncertainties encompass jet-energy scale and resolution uncertainties, *Top modeling* are uncertainties in the theoretical modeling of the top-quark background, and *Fake Lepton Estimate* corresponds to the uncertainty in the estimate of the fake-lepton background. All systematic uncertainties related to minor prompt-lepton backgrounds, flavor tagging efficiencies and mistag rates, the luminosity, lepton calibration, pile-up reweighting, and signal modeling, are included in *Other systematics*. *Statistical Uncertainty* combines statistical uncertainties that arise in both the signal region and control regions used for the data-driven Top and fake-lepton estimates and also from backgrounds that are estimated using MC simulations. Published in Ref. [87].

10.2 Differential Cross-Section Measurements

Measurements of fiducial cross sections, derived following the methods discussed in Section 9.1.1, are presented in Figures 10.3 to 10.5. Excellent agreement with the fixed-order MATRIX prediction is observed. The multiplicative scheme for mixed QCD-EW corrections improves the modeling of high-mass events for some distributions (e.g., $m_{\ell\ell}$ or E_T^{miss}) but overcorrects for other distributions such as $p_T^{\text{lead. lep.}}$. The overcorrection is expected as the multiplicative combination scheme does not always yield an appropriate estimate of mixed QCD-EW effects, in particular in regions of phase space that are dominated by events with hard QCD radiation, as is the case for high $p_T^{\text{lead. lep.}}$ [231]. The POWHEG MINNLO+PYTHIA8 and SHERPA 2.2.12 predictions matched to parton showers model the data well except for an underprediction of the cross section in most regions of phase space, which can largely be explained by the different choice of the PDF set. The parton shower improves the modeling at low diboson transverse momentum (see, e.g., Fig. 10.3c) and allows for the simulation of events with more than two jets.

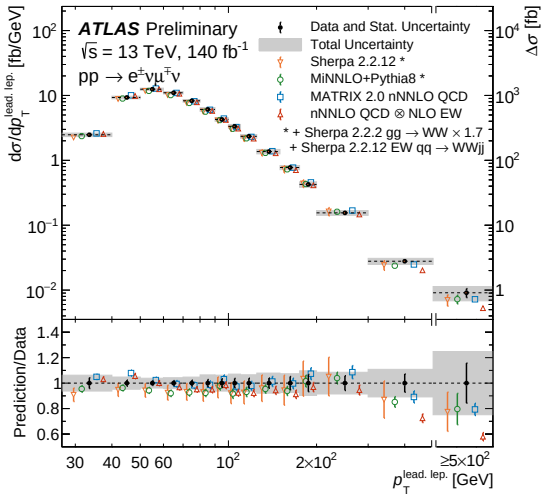

(a) $p_T^{\text{lead. lep.}}$ distribution.

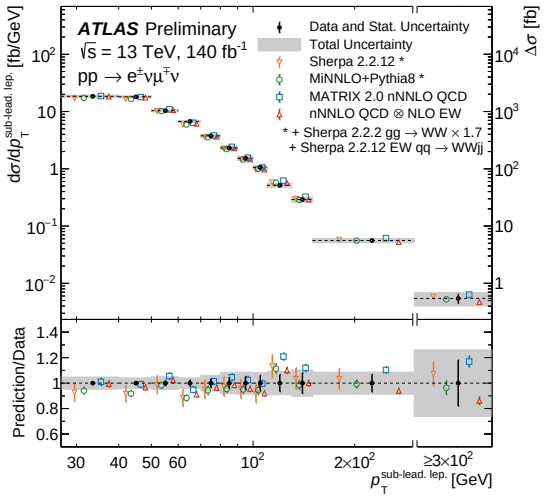

(b) $p_T^{\text{sublead. lep.}}$ distribution.

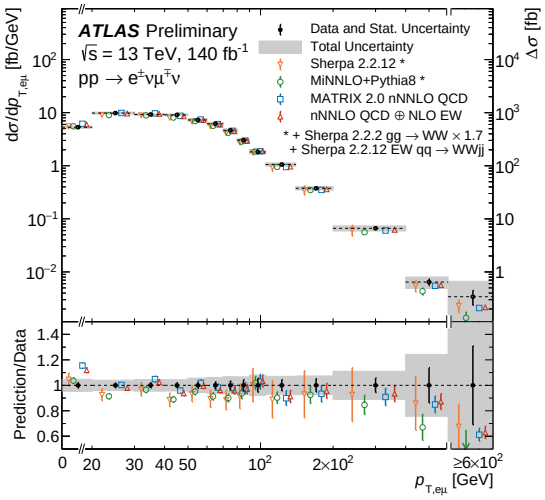

(c) $p_T^{\ell\ell}$ distribution.

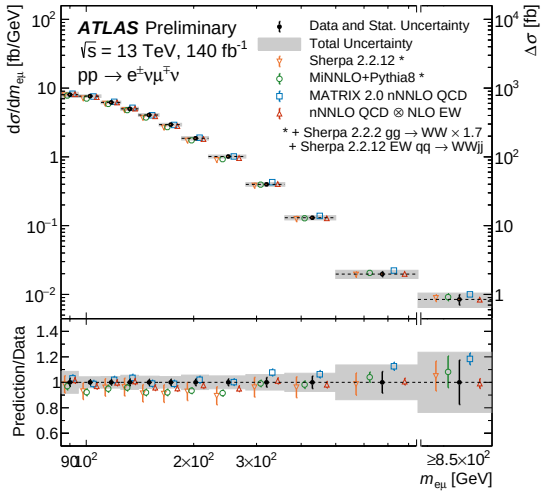

(d) $m_{e\mu}$ distribution.

Figure 10.3: Measurements of fiducial differential cross sections as a function of (a) $p_T^{\text{lead. lep.}}$, (b) $p_T^{\text{sublead. lep.}}$, (c) $p_T^{\ell\ell}$, and (d) $m_{e\mu}$. The measured cross-section values are shown as points with error bars giving the statistical uncertainty and solid bands indicating the size of the total uncertainty. The right-most bin shows the integrated fiducial cross section in the overflow bin, indicated by the right-hand-side axis. The results are compared to fixed-order nNNLO QCD + NLO EW predictions of MATRIX 2.0.1, as well as the NNLO predictions from POWHEG MINNLO+PYTHIA8 parton shower, and SHERPA 2.2.12 at NLO in QCD, also including parton shower effects. The last two predictions are combined with SHERPA 2.2.2 for the gg-induced W^+W^- production and SHERPA2.2.12 for the electroweak $WWjj$ production. The $gg \to WW$ contributions, predicted at LO, are corrected to NLO QCD by applying a K-factor of 1.7. Theoretical predictions are indicated as markers with vertical lines denoting PDF, scale and parton shower uncertainties. Markers are staggered for a better visibility. Published in Ref. [87].

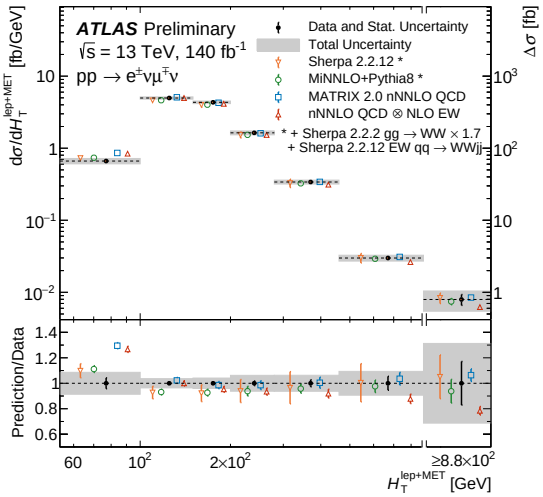

(a) $H_T^{\mathrm{lep.+MET}}$ distribution.

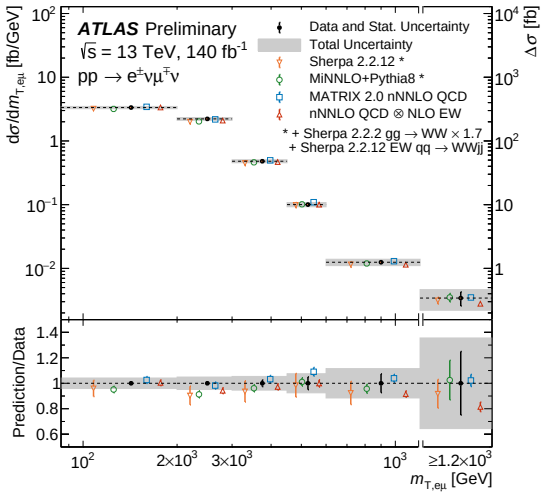

(b) $m_{T,e\mu}$ distribution.

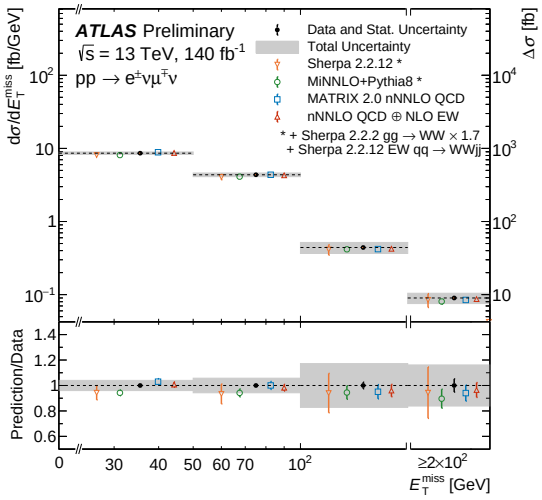

(c) E_T^{miss} distribution.

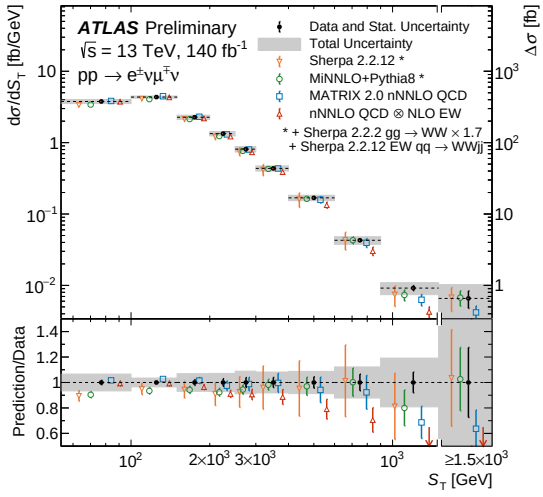

(d) S_T distribution.

Figure 10.4: Fiducial differential cross sections as a function of (a) $H_T^{\mathrm{lep.+MET}}$, (b) $m_{T,e\mu}$, (c) E_T^{miss}, and (d) S_T. The measured cross-section values are shown as points with error bars giving the statistical uncertainty and solid bands indicating the size of the total uncertainty. The right-most bin shows the integrated fiducial cross section in the overflow bin, indicated by the right-hand-side axis. The results are compared to fixed-order nNNLO QCD + NLO EW predictions of MATRIX 2.0.1, as well as the NNLO predictions from POWHEG MINNLO+PYTHIA8 parton shower, and SHERPA 2.2.12 at NLO in QCD, also including parton shower effects. The last two predictions are combined with SHERPA 2.2.2 for the gg-induced W^+W^- production and SHERPA2.2.12 for the electroweak $WWjj$ production. The $gg \to WW$ contributions, predicted at LO, are corrected to NLO QCD by applying a K-factor of 1.7. Theoretical predictions are indicated as markers with vertical lines denoting PDF, scale and parton shower uncertainties. Markers are staggered for a better visibility. Published in Ref. [87].

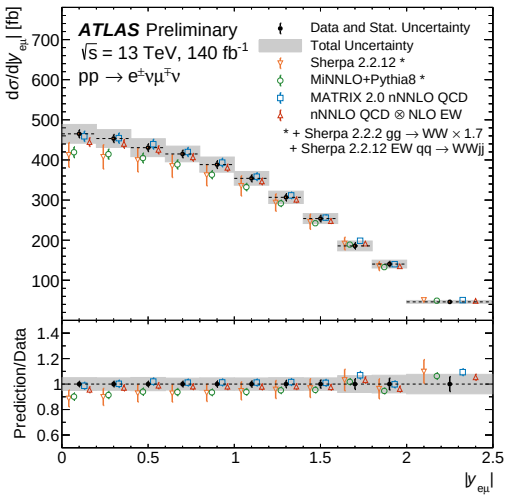

(a) $y_{e\mu}$ distribution.

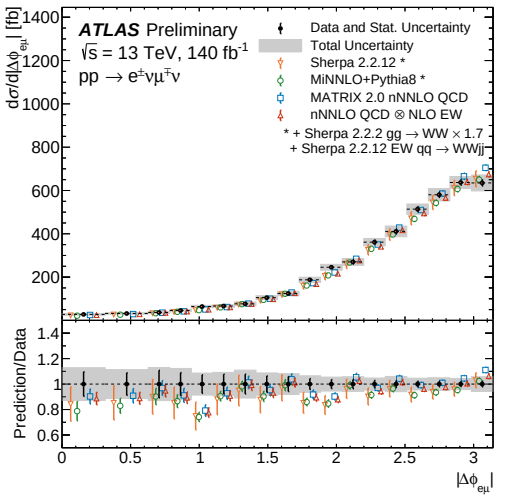

(b) $|\Delta\phi_{e\mu}|$ distribution.

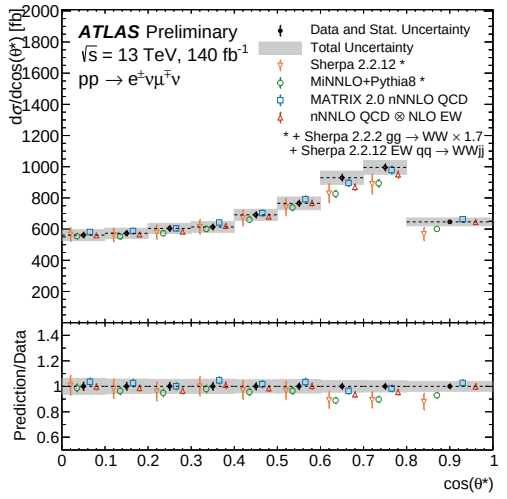

(c) $\cos\theta^*$ distribution.

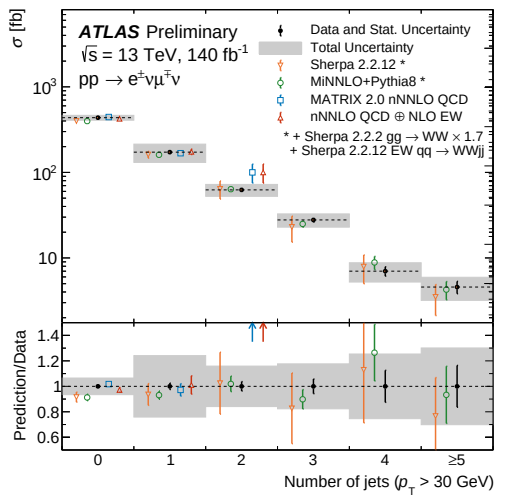

(d) Jet-multiplicity distribution.

Figure 10.5: Fiducial differential cross sections as a function of (a) $y_{e\mu}$, (b) $|\Delta\phi_{e\mu}|$, (c) $\cos\theta^*$, and (d) the jet-multiplicity of the event. The measured cross-section values are shown as points with error bars giving the statistical uncertainty and solid bands indicating the size of the total uncertainty. The results are compared to fixed-order nNNLO QCD + NLO EW predictions of MATRIX 2.0.1, as well as the NNLO predictions from POWHEG MiNNLO+PYTHIA8 parton shower, and SHERPA 2.2.12 at NLO in QCD, also including parton shower effects. The last two predictions are combined with SHERPA 2.2.2 for the gg-induced W^+W^- production and SHERPA2.2.12 for the electroweak $WWjj$ production. The $gg \to WW$ contributions, predicted at LO, are corrected to NLO QCD by applying a K-factor of 1.7. Theoretical predictions are indicated as markers with vertical lines denoting PDF, scale and parton shower uncertainties. Markers are staggered for a better visibility. Published in Ref. [87].

Uncertainty source	Effect [%]
Top modeling	1.6
Fake lepton background	1.5
Flavor tagging	0.7
Other background	0.9
Signal modeling	1.0
Jet calibration	0.6
Luminosity	0.8
Other systematic uncertainties	0.9
Stat. uncertainty	1.1
Total uncertainty	3.1

Table 10.2: Impacts of uncertainties on the integrated fiducial cross-section measurement after performing the profile-likelihood fit described in Section 9.1.2. The categories *Top modeling* and *Signal modeling* encompass uncertainties in the theoretical modeling of the respective processes, *Fake lepton background* contains the total uncertainty in the estimation of the non-prompt lepton background (Section 8.4), while the category *Other background* encompasses the uncertainty due to minor prompt-lepton backgrounds. *Flavor tagging* refers to all uncertainties related to flavor-tagging efficiency and mistagged rates, and *Jet calibration* uncertainties include jet-energy scale and resolution uncertainties. The category *Luminosity* adds the uncertainty arising from the luminosity measurement [342]. All the systematic uncertainties belonging to none of the above categories are included in *Other systematic uncertainties*. Statistical uncertainties arise in both the signal and control regions used for the data-driven top and fake-lepton estimates, and also from backgrounds that are estimated using MC simulations. Published in Ref. [87].

10.3 Fiducial and Total Cross-Section Measurements

Following Section 9.1.2, a model based on the sum of signal and background estimates determined using the methods presented in Chapter 8 is fit to the data. The signal strength parameter is found to be

$$\mu_{WW} = 1.077 \pm 0.033,$$

corresponding to a reduction from $4.1\,\%$ using the pre-fit cut-and-count approach to an uncertainty of $3.1\,\%$. Table 10.2 gives a breakdown of the uncertainties in the fiducial cross section measured in the profile-likelihood fit. The cross-section measurement is dominated by the uncertainties of the top and fake-lepton background estimates, which have been improved with respect to previous measurements of W^+W^- cross sections.

Figures 10.6a and 10.6b present the pre-fit and post-fit distributions of S_T, respectively. The fit of the S_T distribution successfully reduces uncertainties associated with the top-quark background, which dominates in bins of high S_T and, to a lesser extent, of Drell-Yan and fake-lepton uncertainties, which contribute more at low S_T. Uncertainties of the post-fit yields (the uncertainty bands in Figure 10.6b) are therefore strongly reduced due to the correlations taken into account in the fit. Variations that are incompatible with the observed yields are more strongly constrained. The impact of the systematic uncertainties in the fit to the data and the pulls of the corresponding nuisance parameters are shown in Figure 10.7. Nuisance parameters remain very close to their initial values. No individual nuisance parameter is constrained to more than $80\,\%$ of its pre-fit uncertainty. The background normalizations are changed by less than $2\,\%$ with respect to their nominal pre-fit estimates. No pulls beyond 0.5σ are observed, showing a

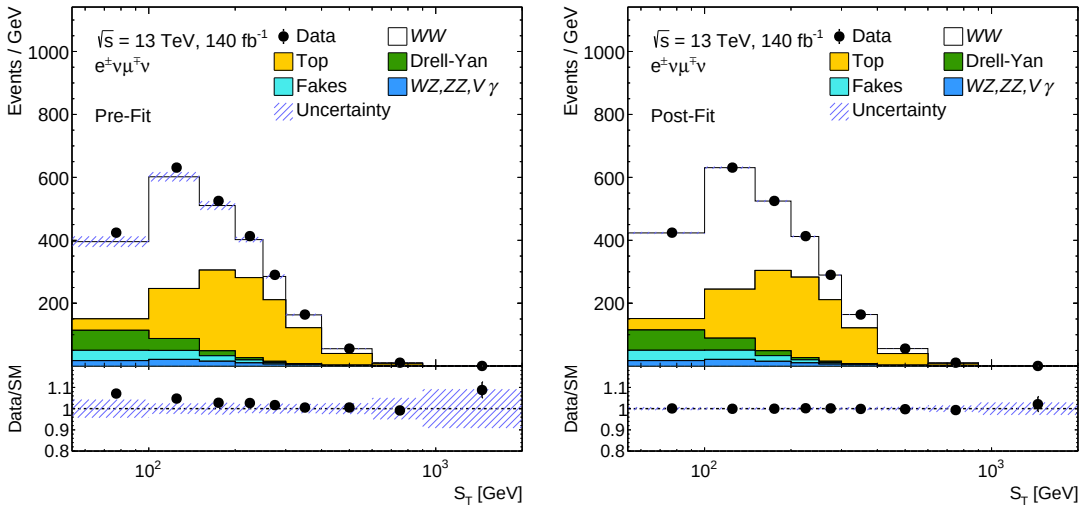

(a) Pre-fit distribution.

(b) Post-fit distribution.

Figure 10.6: (a) Pre-fit and (b) post-fit model for the profile-likelihood fit in the S_T distribution. Data are shown as black markers together with the predictions for the signal and background production processes. The rightmost bin contains overflow events. The lower panels show the ratio of the data to the total prediction. Top and fake backgrounds are determined using the data-driven methods described in Chapter 8. The uncertainty bands shown include statistical and systematic uncertainties from both experimental and theoretical sources listed in Section 9.2.

reliable estimation of the systematic uncertainties of the various SM contributions. The impact of modeling uncertainties for W^+W^- and top-quark production is successfully reduced by the fit.

The measured fiducial cross section for W^+W^- production in pp collisions at $\sqrt{s} = 13$ TeV decaying into $W^+W^- \to e^\pm\mu^\mp\nu_e\nu_\mu$ final states within the fiducial volume defined in Table 9.1 is determined from the profile-likelihood fit to be

$$\sigma^{13\,\text{TeV}}_{\text{ATLAS, 140 fb}^{-1}}(pp \to e^\pm\mu^\mp\nu_e\nu_\mu) = 707 \pm 7\,(\text{stat.}) \pm 20\,(\text{syst.})\,\text{fb}\,, \tag{10.1}$$

with a total uncertainty of 3.1 %.

The fiducial cross-section measurement is compared in Figure 10.8 to fixed-order predictions computed with MATRIX 2.0.1 using PDF sets released by different collaborations. Three different versions of NNPDF (3.0 [445], 3.1 [493] and 4.0 [168]), CT18 [170], PDF4LHC21 [177], MSHT20 [171], and the MSTW2008 [172] PDFs are evaluated. All PDFs are considered at NNLO accuracy using the four-flavor scheme. Photon PDFs using the LUXQED method [186] are accounted for only in NNPDF3.1 predictions. Predictions of $W^+W^- \to e^\pm\mu^\mp\nu_e\nu_\mu$ at NLO accuracy in QCD[1] are, as discussed in Section 3.1, insufficient to describe the data without the application of K-factors to NNLO. As seen in Figure 9.8, a consistent increase of 2 % (3 %) is obtained using NNPDF3.1+LUXQED (NNPDF4.0), in excellent agreement with the data, with respect to the other predictions from CT18, PDF4LHC21, and MSTW2008 at all orders. The predictions from CT18, PDF4LHC21, and MSTW2008 agree within uncertainties at all orders. Predictions re-

[1]The presented predictions at NLO in QCD also rely on the PDF sets at NNLO accuracy.

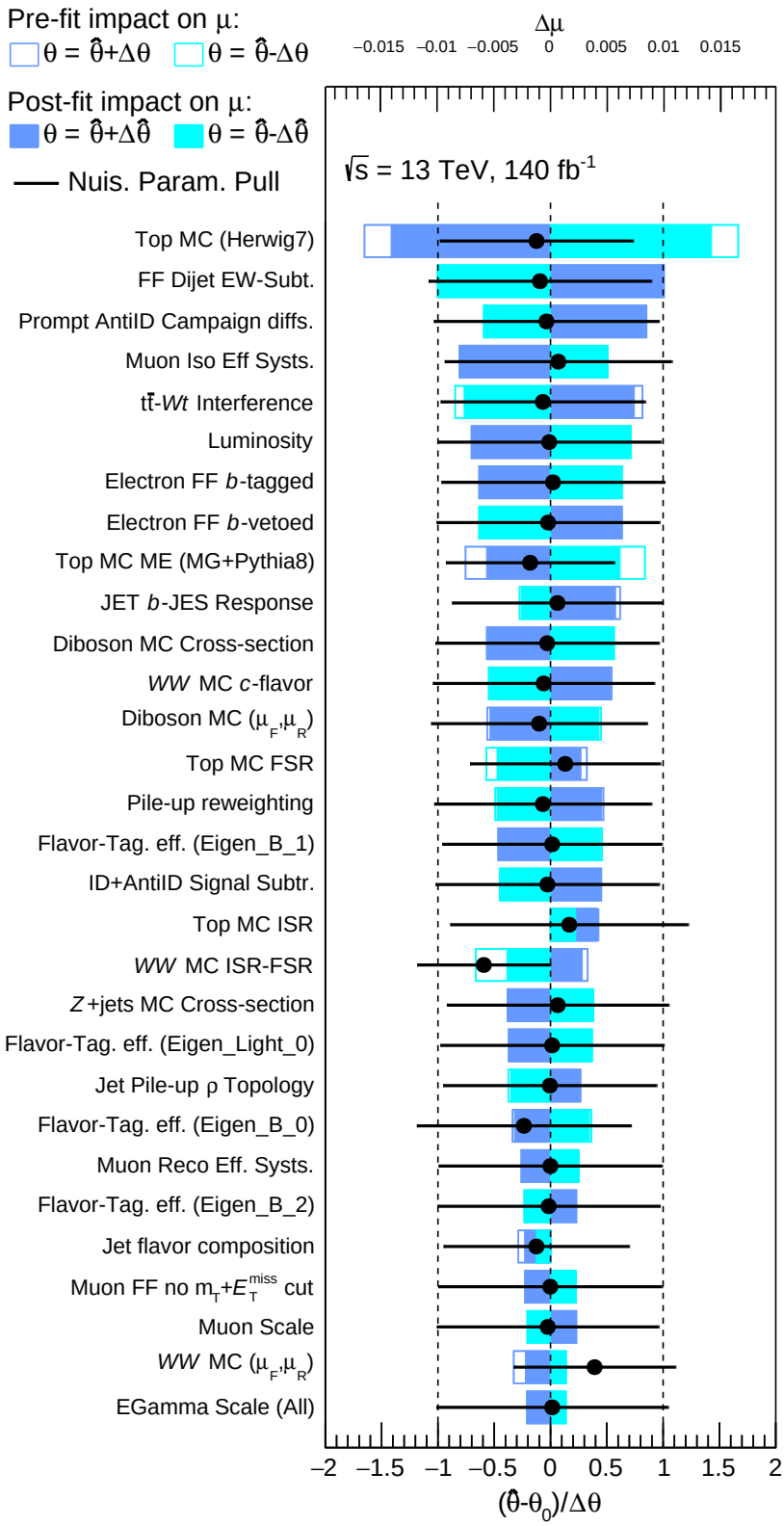

Figure 10.7: Pulls (shown as black dots) and impacts (horizontal bands) for the nuisance parameters corresponding to 30 systematic uncertainties of highest impact in the fit to data using the S_T distribution. The vertical dashed lines indicate the 1-sigma thresholds of the pulls at the bottom horizontal axis. The upper axis displays the impact on μ_{WW} of each nuisance parameter for both pre-fit (white horizontal bands) and post-fit (filled blue bands).

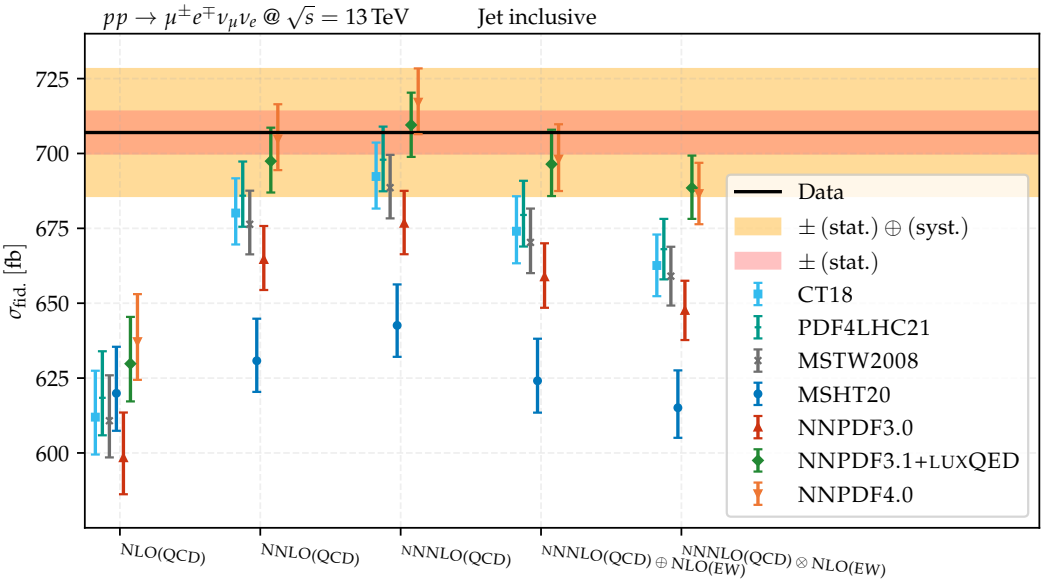

Figure 10.8: Fiducial integrated cross sections predicted with MATRIX 2.0.1 using various configurations of higher-order QCD and EW corrections up to nNNLO and NLO accuracy in QCD and EW theories, respectively. Predictions relying on NNPDF3.0 (red up triangles), NNPDF3.1 (green diamonds), NNPDF4.0 (orange down triangles), CT18 (cyan squares), PDF4LHC21 (light green markers), MSHT20 (dark blue dots), and the MSTW2008 (purple crosses) PDF sets are compared. Vertical bars on the predictions show the sum in quadrature of scale and PDF uncertainties. The predictions are computed for $W^+W^- \to \mu^{\pm}e^{\mp}\nu_\mu\nu_e$ production in the jet-inclusive fiducial phase space. The cross-section measurement performed in this thesis is displayed as a horizontal line, where statistical and systematic components are depicted as horizontal orange bands.

lying on NNPDF3.0 underestimate the ones from NNPDF3.1 and NNPDF4.0 by $4\,\%$ and $5\,\%$, respectively. Including contributions of gluon-induced production at NLO in QCD into the NNLO QCD prediction results in the best agreement with the data for the largest number of predictions. The results using NNPDF3.1+LUXQED provide $4\,\%$ greater fiducial cross sections than the NNPDF3.0 predictions, which are not able to describe the measurement within the 1σ error bands. Combinations of the nNNLO QCD predictions with electroweak corrections at NLO via either additive or multiplicative schemes are also shown. The introduction of electroweak corrections using the additive (multiplicative) combination scheme decreases the predicted cross sections by $3\,\%$ ($6\,\%$) in the jet-inclusive phase space. Once electroweak corrections are taken into account, only the cross-section calculations using NNPDF3.1+LUXQED and NNPDF4.0 succeed in describing the measurement. Although the predicted fiducial cross sections using MSHT20 are in agreement with other predictions at NLO, predictions relying on this PDF set are not able to describe the measured cross section of W^+W^- production at NNLO. Further investigations to understand the origin of this disagreement are needed. The experimental result at the achieved precision proves to be sensitive to the choice of the PDFs considered in the theoretical predictions, providing useful information to validate and constrain fits of parton distribution functions for LHC results in future iterations of these efforts.

The predicted fiducial cross section of W^+W^- production is sensitive to the mass

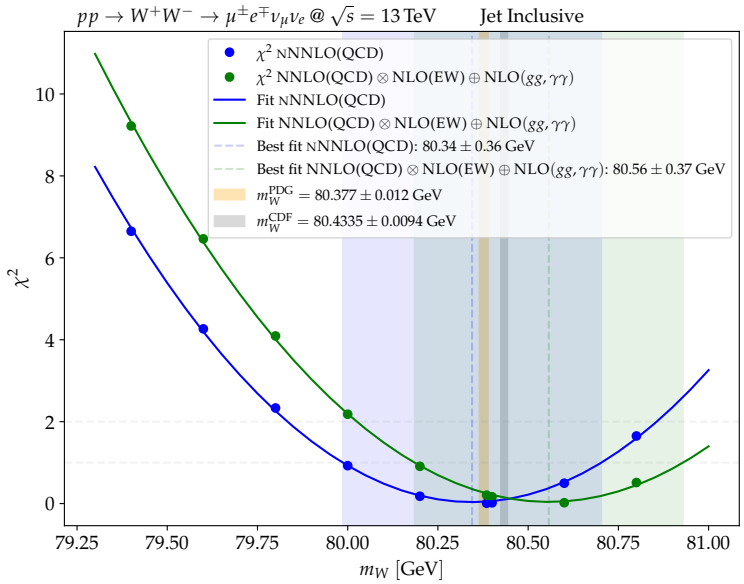

Figure 10.9: Assessment of the sensitivity to the mass of the W boson via χ^2 minimization of the fiducial cross-section measurement (Eq. 10.1) versus predictions generated with MATRIX 2.0.1 using the NNPDF3.1@NNLO+LUXQED PDF set and different m_W masses as input to the prediction. The predictions are computed at nNNLO order in QCD (blue), and including NLO EW corrections as well as contributions from gluon- and photon-induced production at NLO (green) to the fully leptonic W^+W^- production in the jet-inclusive fiducial phase space.

of the $W^\pm$ bosons. By evaluating the MATRIX predictions described in Section 9.3 with the NNPDF3.1+LUXQED PDF sets at NNLO accuracy using different values of m_W, a χ^2-minimization is performed to find the best-fit value of m_W and the associated uncertainty at 68 % confidence level. The latter acts as an assessment of the expected sensitivity to the mass of the $W^\pm$ bosons from fiducial W^+W^- production cross-section measurements. The results are shown in Figure 10.9. The fit is performed to predictions at two different perturbative orders considering the fully leptonic W^+W^- production in the jet-inclusive fiducial phase space: at nNNLO order in QCD (blue), and also including NLO EW corrections via the multiplicative scheme, both including contributions from gluon- and photon-induced production at NLO (green). A sensitivity of 370 MeV is found by fitting the integrated fiducial cross-section measurement. The best-fit value of m_W is increased by 220 MeV when considering electroweak corrections in the theoretical prediction. Although better sensitivity is expected by performing a minimization of differential distributions, the found sensitivity is more than an order of magnitude coarser that the necessary resolution to discern between the CDF measurement [120] and the global fit [95] values of the W-boson mass.

The experimental result reported in Eq. (10.1) is also compared to the other theoretical models including parton shower simulation in Figure 10.10. The comparison includes (i) the nominal POWHEG MINNLO+PYTHIA8 model used in the analysis for $q\bar{q} \to WW$ production, (ii) $q\bar{q} \to WW$ production using SHERPA 2.2.12, (iii) the nNNLO-QCD predictions of MATRIX 2.0.1 as well as (iv) the same nNNLO predictions combined with NLO electroweak corrections. The POWHEG MINNLO+PYTHIA8 and the SHERPA predictions are augmented with simulations of gluon-induced and electroweak produc-

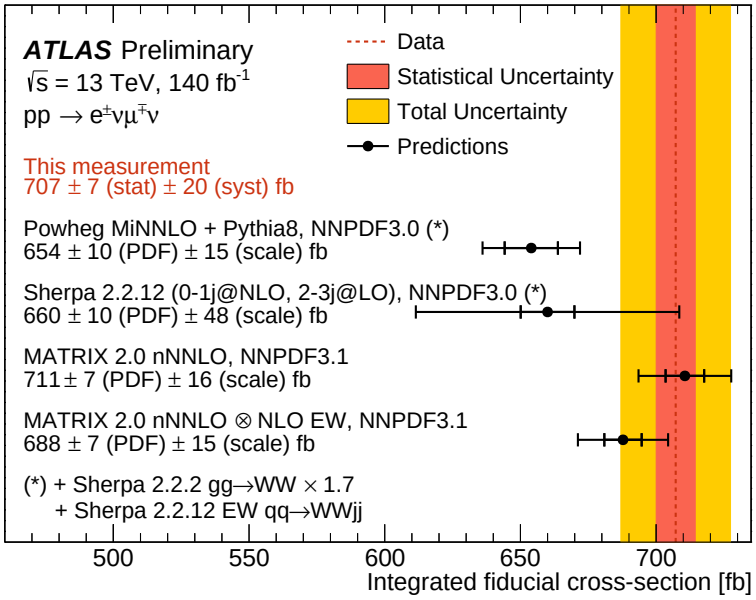

Figure 10.10: Measured fiducial cross sections, compared to theoretical predictions from POWHEG MINNLO+PYTHIA8, SHERPA 2.2.12, and MATRIX 2.0.1. The nNNLO prediction includes photon-induced contributions and NLO-QCD corrections to the gluon-induced initial state. The POWHEG MINNLO+PYTHIA8 and SHERPA 2.2.12 predictions are combined with SHERPA 2.2.2 and SHERPA 2.2.12 to model gluon-induced W^+W^- production and the electroweak production of $WWjj$, respectively. An inclusive NLO K-factor of 1.7 is applied to the SHERPA 2.2.2 prediction. Inner (outer) error bars on theory prediction correspond to PDF (the combination of scale and PDF) uncertainties. Published in Ref. [87].

tion modes using SHERPA 2.2.12 introduced in Section 9.3. While the measured value is about two standard deviations larger than the cross section predicted by POWHEG MINNLO+PYTHIA8, it agrees well with the MATRIX predictions. As discussed in Section 9.3 (see Table 9.3), the main reasons for the larger cross section predicted by MATRIX are the updated NNPDF PDF version, which results in an increase of 28 fb, as well as an additional 11 fb increase due to photon-induced contributions. The fiducial cross section predicted by SHERPA 2.2.12 is in good agreement with the POWHEG MINNLO+PYTHIA8 prediction (NNLO) owing to the inclusion of real QCD corrections up to one jet at NLO in QCD and up to three jets at LO.

The measurement is extrapolated to the full phase space of W^+W^- production based on the acceptance of $23.7 \pm 0.3\,\%$ for $W^+W^- \to e^\pm\mu^\mp\nu_e\nu_\mu$ events, calculated at nNNLO with MATRIX including NLO electroweak corrections and by accounting for a leptonic $W^\pm$ branching ratio of $10.86\,\%$ [95]. The uncertainty on the acceptance is $1.1\,\%$, estimated by varying the renormalization and factorization scales by factors of two, avoiding variations in opposite directions, by evaluating the PDF uncertainty, and by comparing the multiplicative with the additive scheme for electroweak corrections, with the last being the dominant uncertainty. After this extrapolation, the measured total production cross section of W-boson pairs is found to be

$$\sigma^{13\,\mathrm{TeV}}_{\mathrm{ATLAS},\,140\ \mathrm{fb}^{-1}}\,(pp \to W^+W^-) = 127 \pm 1\,(\mathrm{stat.}) \pm 4\,(\mathrm{syst.})\,\mathrm{pb}\,.$$

In Figure 10.11, the total cross section is compared to measurements of ATLAS [79] and CMS [80] in pp collisions at $\sqrt{s} = 13$ TeV based on datasets of 36 fb^{-1}. The improved

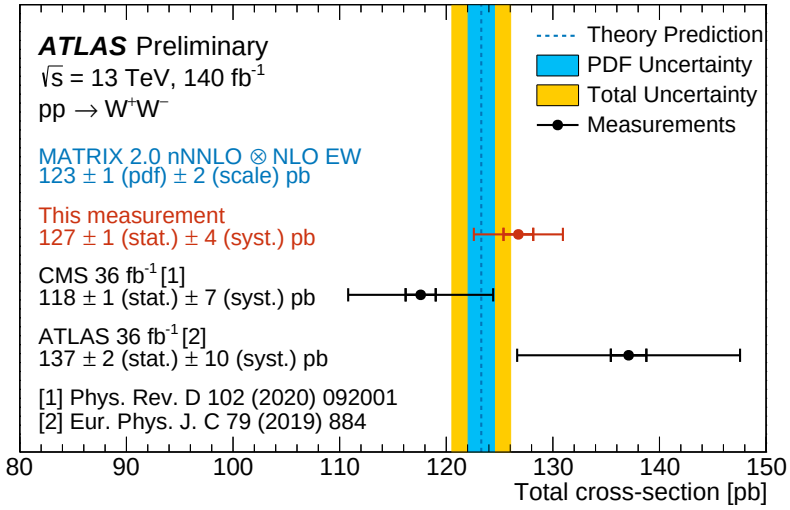

Figure 10.11: Measured total W^+W^- cross sections, compared to a theoretical prediction from MATRIX +OPENLOOPS [231] and previous measurements of ATLAS [79] and CMS [80]. The theoretical prediction uses the NNPDF3.1@NNLO LUXQED set of parton distribution functions, is of NNLO accuracy in QCD for $q\bar{q} \to WW$ production and includes NLO-QCD corrections to $gg \to WW$ production, which constitute part of the N^{3}LO correction. It includes photon-induced contributions and is combined multiplicatively with NLO-EW corrections to $q\bar{q} \to WW$. Inner (outer) error bars on experimental measurements correspond to statistical (total) uncertainty. The inner (outer) error band includes PDF uncertainties (PDF and scale uncertainties added in quadrature). Published in Ref. [87].

precision of this measurement with respect to its predecessor [81] is due to more precise data-driven top quark and fake lepton estimates, the improved luminosity determination [342], and the measurement in a jet-inclusive phase space, which reduces jet-related uncertainties as well as theoretical uncertainties on the extrapolation to the full phase space. The reported value constitutes the most precise W^+W^- production cross-section measurement performed at a hadron collider to date. The level of experimental precision reported in this measurement matches also the accuracy of the state-of-the-art predictions, reaching the limit in which the theory of the SM can be tested in W^+W^- production.

10.4 Discussion and Outlook

The measurement of W-boson pairs at hadron colliders is an important test of the SM, sensitive to the self-couplings of vector bosons, which also provides a probe for perturbative QCD and electroweak theories. In this chapter, fiducial cross-section measurements of W-boson pair production have been presented using a dataset corresponding to an integrated luminosity of $140\ \text{fb}^{-1}$ recorded between 2015 and 2018 with the ATLAS detector at the LHC in pp collisions at $\sqrt{s} = 13\ \text{TeV}$. A jet-inclusive event selection, along with improved data-driven estimates of the top-quark and fake-lepton background, allowed reducing the uncertainty in the fiducial cross-section to $3.1\,\%$. This uncertainty is dominated by experimental systematic uncertainties arising from the modeling of top-quark and non-prompt lepton backgrounds. The impact of the experimental and theoretical uncertainties propagated into the measurement, introduced in a profile likelihood fit as

Gaussian-profiled nuisance parameters, is shown in Figure 10.7. The measurement is extrapolated to the full phase space, resulting in a total W^+W^- cross section of 127 ± 4 pb. The reported value is the most precise W^+W^- production cross-section measurement performed in a hadron collider to date. The cross sections are also measured differentially as a function of twelve observables related to the lepton, jet, and E_T^{miss} kinematics of the event. The reported level of precision, limited by theoretical and experimental systematic uncertainties, allows to include double-differential cross-section measurements in the near future. Combinations of the rapidity $|y_{e\mu}|$ of the dilepton system with observables such as $p_T^{\ell\ell}$ or $m_{e\mu}$ would act as proxies for the longitudinal and transverse boost of the W^+W^- system, which could be used to constrain parton distribution functions. These could be complemented with observables sensitive to charge and CP asymmetries in the production of W-boson pairs [503, 504]. Additionally, double-differential measurements of the azimuthal difference $|\Delta\phi_{e\mu}|$ with observables correlated to the invariant mass of the diboson system such as $m_{e\mu}$, $p_T^{\ell\ell}$, $H_T^{\text{lep.+MET}}$, or $p_T^{\text{lead. lep.}}$ can be beneficial to constrain anomalous interactions in the context of the SMEFT.

A state-of-the-art fixed-order prediction at nNNLO QCD [247] using the NNPDF3.1 PDF [493], including the photon in the parton content using the LUXQED method [186], gives a good description of differential cross sections. The multiplicative combination with EW corrections improves the description of some observables while it does not represent an adequate description in other cases, as the combination cannot take into account non-factorizing EW-QCD effects [231]. Predictions matched to parton showers, generated with POWHEG MINNLO+PYTHIA8 [216, 147] and SHERPA 2.2.12 [148], provide a better description of the data in bins dominated by events with small W^+W^- p_T or high jet activity. Considering experimental and theoretical uncertainties, the predictions are found to be in excellent agreement with the measurement.

Dominant uncertainties from the top-quark background arise from the theoretical modeling of $t\bar{t}$ production in MC, concretely in the simulation of the parton shower with an alternative model. Additionally, the prescription of the interference subtraction between $t\bar{t}$ and single-top Wt matrix element diagrams and their computation with an alternative model (MADGRAPH5_AMC@NLO+PYTHIA 8) are among the leading uncertainties of the cross-section measurement. Significant efforts focus on improving the modeling in the simulation of this process based on experimental results [495], while also ensuring consistency in their descriptions across experimental collaborations [505]. These studies will benefit from the enhanced precision achieved in the latest differential cross-section measurements of $t\bar{t}$ production using an increased dataset recorded in the LHC Run 2 by both ATLAS and CMS Collaborations [506, 507, 508]. The endeavor to compute $t\bar{t}$ production at higher orders in perturbation theory[2] has been prioritized by the community [217, 509]. Fully-differential NNLO calculations of $t\bar{t}$ production were recently released within the MATRIX framework [510, 511], also matched to parton showers via the POWHEG MINNLO+PYTHIA8 prescription [512, 513] for on-shell production of the top-quark pair. Improving the accuracy of matrix element calculations to NNLO in QCD will lessen uncertainties in the modeling of $t\bar{t}$ production. This involves reducing uncertainties from missing higher-order corrections, which can be further improved with

[2]The reduction of PDF uncertainties in precision calculations of $t\bar{t}$ production deserves attention. However, these were found to be negligible for the reported W^+W^- production cross-section measurements and will not be discussed in this thesis.

resummation schemes, as well as minimizing reliance on the parton shower modeling. The simulation of $t\bar{t}$ production using these techniques will strongly benefit future measurements of W^+W^- production. Effects from electroweak corrections at NLO [514, 515] and NNLL threshold resummation [516] have also been studied, which allows the prediction of differential distributions with an even higher accuracy.

The modeling of the background contributions arising from the misreconstruction of non-prompt leptons has important effects in the final precision of the W^+W^- cross-section measurements. Due to the choice of the AntiID lepton selection criteria (defined in Section 8.4.2), ensuring a good modeling of prompt leptons passing these requirements becomes a crucial task. The data-driven estimation method used in this thesis, presented in Section 8.4.1, relies on a dijet region to compute the scaling factors needed to extrapolate the estimation from a control ID+AntiID dilepton region to the signal region. The description of prompt contributions relies heavily on MC simulation of the various production sources. For a suitable subtraction of these contamination sources, their predicted production cross sections should be accurate enough. The uncertainties on the production cross sections of the processes involved constitutes the dominant source of error arising from the estimation of this background into the W^+W^- cross-section measurement. Using dijet events, the different prompt contamination sources could be isolated in dedicated control regions to rescale their production cross sections to the data, reducing the associated uncertainties in a data-driven approach[3]. Additionally, this measurement reports, for the first time, a dedicated calibration of such leptons in Section 8.4.5 in ID+AntiID dilepton control regions defined for the extrapolation of the data-driven background into the signal region, reducing these modeling uncertainties by more than a factor of 2. Nevertheless, discrepancies of this mismodeling among data-taking campaigns arising from different definitions of the lepton selection, the pile-up contamination, and other sources must be further understood. An improved understanding of these sources will have a sizable impact in the precision of future measurements of W^+W^- production. Furthermore, improvements of a factor of two are achieved with respect to the previous measurement of $WW+\geq 1\,\text{jets}$ [81] by assessing the jet-flavor fractions from b-, c-, and light-jet production of lepton misidentification background in the signal region. The quantification of the jet-flavor fractions relies on flavor filters of the additional QCD radiation in MC events. A quantitative comparison of the jet-flavor fractions between signal and dijet regions will help to better control this source of uncertainty. In order to proceed, MC simulation of multijet production making use of b-, c-, and light-flavor filters is necessary to address the jet-flavor composition in lepton misidentification in the dijet region, which requires the reconstruction of one lepton in the final state. Additionally, a good modeling needs to be ensured in the MC simulation of events producing c- and b-jets in the final state for processes leading to lepton misidentification (mainly $W+\text{jets}$ and semileptonic $t\bar{t}$). Once these processes are reliable at the required level of precision, dijet, control, and signal regions could be optimized based on the light-, c- and b-flavored fake-lepton composition to reduce the bias in the background estimation caused by differences in jet-flavor composition.

[3]The latest measurement of electroweak production of same-sign $W^\pm W^\pm jj$, where the lepton misidentification background is the second largest contributor to the total number of selected event candidates, an analogous background estimation method is implemented [489]. For this measurement, the production cross section of $W+\text{jets}$ events only is corrected to data in the dijet region, reducing the associated prompt subtraction uncertainty into the measurement from $10\,\%$ to $5\,\%$.

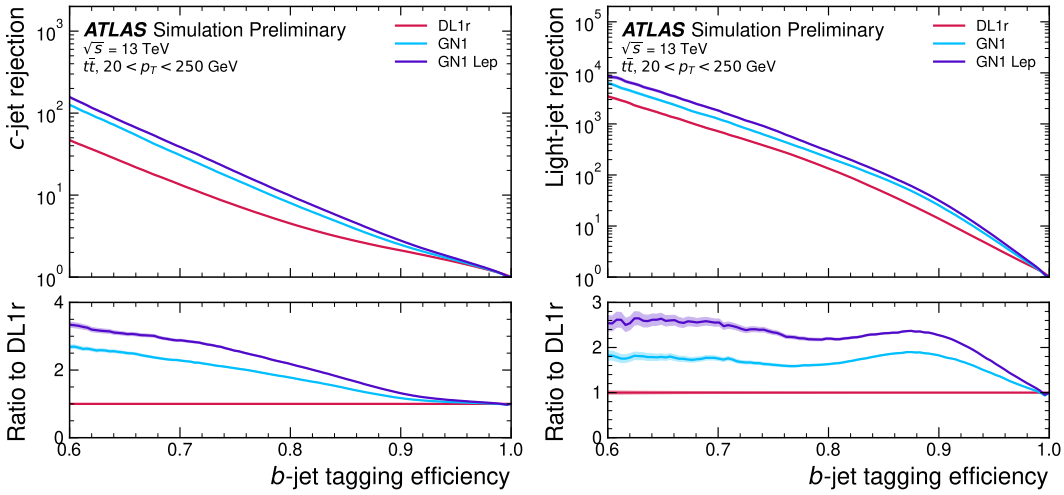

Figure 10.12: Improvements in c (left) and light-jet (right) rejection in b-tagging by different jet-flavor taggers developed by the ATLAS Collaboration for analyses of Run 2 (DL1r) and Run 3 (GN1) data. Source: [517].

State-of-the-art predictions of W^+W^- production at NNLO matched to parton showers are used in an experimental measurement for the first time in this thesis. These reduce the associated theoretical uncertainties, which benefit the measurement via the profile likelihood fit of the signal strength μ_{WW} (presented in Section 9.1.2). Nevertheless, the different fractions of the additional radiation arising from b- and c-quarks provided by different MC generators must be understood. The effects of electroweak corrections are also contrasted with the experimental measurements, testing the validity of different combination schemes between QCD and electroweak corrections. The difference between additive and multiplicative schemes has to be addressed as an additional source of theoretical errors. Selection requirements can be introduced to suppress regions of the phase space where one high-p_T vector boson recoils against a high-p_T jet, reducing associated uncertainties due to mixed QCD-EW corrections. The use of so-called *dynamic jet vetoes* is a promising approach to both reducing uncertainties due to mixed QCD-EW corrections and increasing the W^+W^- signal significance over background contributions, enhancing also the sensitivity of searches for anomalous gauge couplings at large energies when compared to traditional jet vetoes [231]. When using the b-counting method for the estimation of top-quark background contributions, the drastic decrease in statistics in 1 and 2-b-jet regions must be taken into account. Dynamic jet vetoes are also susceptible to increased experimental uncertainties related to the energy reconstruction of jets, as well as theoretical uncertainties from the jet-veto requirement.

The measurement is also affected by experimental uncertainties from jet-flavor tagging [369], arising from the assessment of the b-tagging and mistagging efficiencies necessary for the b-jet classification. These efficiency uncertainties are significantly larger for low-p_T tagged-jets[4]. The lowest p_T thresholds for b-tagged jets ($p_T > 20\,\text{GeV}$) were used to maximize the statistics in the 1 and 2 b-jet regions defined within the b-tag counting method used for the data-driven estimation of the top-quark background (discussed in Section 8.1). The statistical limitations of this method are critical in regions with no additional jets in the final state, which are reconstructed for $p_T > 30\,\text{GeV}$. Additionally, the jet

[4]See Table 5 in Ref. [372] and the corresponding section for further details.

energy scale (Fig. 4.16) and resolution (Fig. 4.17) deteriorate at low jet p_T. Addressing the associated b-tagging uncertainties in this specific region, providing the highest sensitivity to W^+W^- event candidates, is crucial. Future analyses could benefit from incorporating the jet and b-tagged jet p_T thresholds into optimizations of the event selection (Table 7.2) to further reduce these uncertainties. Moreover, improved b-tagging algorithms are being deployed by the ATLAS Collaboration for the analysis of Run 3 data [517, 518]. As illustrated in Figure 10.12, the background rejection of c and light jets using the ATLAS jet-flavor taggers for Run 3 (GN1) improve by a factor of 2 or higher with respect to the Run 2 tagger (DL1r) for b-tagging efficiencies about $85\,\%$ or higher. Innovative methods were also necessary for the derivation of the mistagged efficiencies after this increase of background rejection [375]. The benefits for W^+W^- production cross-section measurements from these improvements are expected in several ways. Firstly, a richer and more reliable event sample from $t\bar{t}$ production in the 1 and 2 b-jet regions defined within the b-tag counting method is expected, enhancing the precision of the derived differential distributions of $t\bar{t}$ production in the signal region. And lastly, this enables the definition of b-tag working points with efficiencies greater than $85\,\%$, which would lead to a stronger suppression of the top-quark background by the b-veto requirement of the signal region.

The installation of an improved full silicon Inner Tracker after the LHC LS3 with acceptance of $|\eta| < 4$ in the ATLAS detector opens new possibilities of exploring physics with flavor tagging in the forward region with $2.5 < |\eta| < 4$, inaccessible with the current ATLAS detector [387, 388]. Despite the reduced resolution in the measurement of impact parameters in high pileup environments, the available flavor-tagging algorithms have been tested using simulations of the new technologies, finding improvements with minor modification of the current tagger architectures [519, 520]. The smaller pixel pitch for the new inner tracker[5] and the reduced radius of the first pixel layers with respect to the beam pipe improve the classification capabilities of the taggers.

Prospects for the HL-LHC

The results obtained using Run 2 data can be extrapolated to assess the level of precision with the full dataset to be collected during the HL-LHC. Expected to yield a dataset corresponding to $3000\ \text{fb}^{-1}$ and following the planned improvements [379], an scenario where relevant systematic uncertainties are scaled down can be outlined[6]. In this projection, data-driven uncertainties are expected to decrease proportionally to the square root of integrated luminosity. Uncertainties related to normalization cross-sections and theoretical modeling are also expected to halve. Since the data-driven background estimates also rely on the modeling of SM processes in MC simulation, the corresponding uncertainties are halved with respect to the corresponding precision achieved in the Run 2 result. Uncertainties due to detector limitations are anticipated to be consistent with Run 2, including the luminosity measurement and uncertainties associated with analysis methods. Flavor-tagging uncertainties are projected to halve. Table 10.3 summarizes the projection in precision for the production cross-section measurements of W-boson pairs,

[5] Comparisons of the background rejection using $50 \times 50\ \mu\text{m}^2$ and $25 \times 100\ \mu\text{m}^2$ pixel pitches with the currently available flavor tagging algorithms were presented in Ref [520].

[6] This *baseline* scenario has been exploited in e.g. HL-LHC prospects in measurements of Higgs-boson pair production by the ATLAS Collaboration [521], and in the extraction of the longitudinal scattering component in $W^\pm W^\pm jj$ production [379].

Uncertainty source	Run 2 uncertainty [%]	Projection HL-LHC [%]
Top modeling	1.6	0.8
Fake lepton background	1.5	0.8
Flavor tagging	0.7	0.4
Other background	0.9	0.5
Signal modeling	1.0	0.5
Jet calibration	0.6	
Luminosity	0.8	
Other systematic uncertainties	0.9	
Stat. uncertainty	1.1	0.5
Total uncertainty	3.1	2.0

Table 10.3: Projected precision of W^+W^- fiducial production cross-section measurements with the HL-LHC dataset based on the results obtained with the full Run 2 dataset (Table 10.2). The reductions on each uncertainty category are based on the guidelines described in Ref. [379]. While the total uncertainty of the measurement using Run 2 data relies on the profile-likelihood fit, the total uncertainty in the extrapolation to the HL-LHC is computed as the sum in quadrature of all categories.

based on Run 2 data discussed in Section 10.3. This approximation suggests the feasibility of achieving a W^+W^- cross-section precision of approximately $2\,\%$, corresponding to a reduction of $35\,\%$. In HL-LHC projections, achieving a W^+W^- production cross-section precision of $2\,\%$ and halving theoretical uncertainties would improve sensitivity to the W mass to within an uncertainty of $210\,\mathrm{MeV}$. Measurements of W^+W^- production cross-sections are therefore insufficient to help resolving the discrepancies between the CDF measurement and the global average of m_W. To assess this sensitivity more quantitatively, prospective studies should consider signal and background expectations in pp collisions at center-of-mass energies beyond $\sqrt{s} = 13$ TeV, along with full simulation of anticipated detector technologies. Multiple projections should be considered, in both more optimistic and pessimistic scenarios.

Chapter 11

Interpretation of the W^+W^- Cross-Section Measurements in the Context of the Standard Model Effective Field Theory

"...the direct method may be used...but indirect methods will be needed in order to secure victory.... The direct and the indirect lead on to each other in turn. It is like moving in a circle.... Who can exhaust the possibilities of their combination?"

— Sun Tzu, *The Art of War*.

In this chapter, distributions sensitive to the production of W-boson pairs, presented in Chapter 10, are interpreted to constrain a subset of anomalous couplings[1] in the context of the Standard Model Effective Field Theory (SMEFT). Effective Field Theories, and concretely the SMEFT, were discussed in Section 1.7. The SMEFT operators considered in this interpretation, sensitive to the W^+W^- production at the LHC, are introduced in Section 11.1. The anomalous effects arising from the consideration of such operators in the SMEFT model are evaluated using MC simulation to extract confidence intervals on Wilson coefficients. The validation of the simulated SMEFT contributions is outlined in Section 11.2. Section 11.3 discusses the statistical model, designed to interpret the reconstructed data by including the effects of both SM and SMEFT contributions. The limits constructed using Asimov data based on the estimated contributions are shown in Section 11.4. Once the data are unblinded for the SMEFT interpretation, the observed constraints on anomalous couplings are presented in Section 11.5.

11.1 The SMEFT Model

As studied in Section 1.7, the formalism of the SMEFT allows for the description of phenomena resulting from a variety of theories beyond the SM that introduce anomalous effects at a mass scale Λ, which is large in comparison to the electroweak scale. By constructing a Lagrangian with a series of operators $\mathcal{O}_{i,d}$ as given in Eq. (1.16), consisting of gauge invariant combinations of SM fields with an energy dimension $d > 4$, the theory provides predictions for experimental observables in terms of an expansion in E/Λ where E is the typical energy exchanged in the process. Measurements of observables sensitive to the effect of SMEFT operators allow constraining the Wilson coefficients $c_{i,d}/\Lambda^{d-4}$, where $c_{i,d}$ is the dimensionless coupling strength associated to the dimension-d operator $\mathcal{O}_{i,d}$. Odd-dimensional operators introduce lepton and baryon number violation and are not relevant for this measurement. Leading effects of new physics are therefore expected

[1] Physics phenomena that are not described in the SM formalism are referred to as *anomalous*.

Interaction type	Wilson coefficient	Operator
Triple-gauge coupling	c_W	$\mathcal{O}_W = \epsilon^{IJK} W_\mu^{I\nu} W_\nu^{J\rho} W_\rho^{K\mu}$
Quark-boson coupling	$c_{Hq}^{(1)}$	$\mathcal{O}_{Hq}^{(1)} = (H^\dagger i \overleftrightarrow{D}_\mu H)(\bar{q}\gamma^\mu q)$
	$c_{Hq}^{(3)}$	$\mathcal{O}_{Hq}^{(3)} = (H^\dagger i \overleftrightarrow{D}_\mu^I H)(\bar{q}\tau^I\gamma^\mu q)$
	c_{Hu}	$\mathcal{O}_{Hu} = (H^\dagger i \overleftrightarrow{D}_\mu H)(\bar{u}\gamma^\mu u)$
	c_{Hd}	$\mathcal{O}_{Hd} = (H^\dagger i \overleftrightarrow{D}_\mu H)(\bar{d}\gamma^\mu d)$
Four fermion couplings	$c_{\ell q}^{(1)}$	$\mathcal{O}_{\ell q}^{(1)} = (\bar{l}\gamma_\mu l)(\bar{q}\gamma^\mu q)$
	$c_{\ell q}^{(3)}$	$\mathcal{O}_{\ell q}^{(3)} = (\bar{l}\gamma_\mu \tau^I l)(\bar{q}\gamma^\mu \tau^I q)$
	$c_{\ell u}$	$\mathcal{O}_{\ell u} = (\bar{l}\gamma_\mu l)(\bar{u}\gamma^\mu u)$
	$c_{\ell d}$	$\mathcal{O}_{\ell d} = (\bar{l}\gamma_\mu l)(\bar{d}\gamma^\mu d)$
Strength of weak interaction	$c_{H\ell}^{(3)}$	$\mathcal{O}_{H\ell}^{(3)} = (H^\dagger i \overleftrightarrow{D}_\mu^I H)(\bar{l}\tau^I\gamma^\mu l)$
	$c_{\ell\ell}$	$\mathcal{O}_{\ell\ell} = (\bar{l}\gamma_\mu l)(\bar{l}\gamma^\mu l)$

Table 11.1: Field operators and corresponding Wilson coefficients incorporated into the SMEFT model given in Eq. (11.1).

to manifest themselves as dimension-6 operators, as higher-dimensional operators are suppressed by greater powers of Λ^{-1}. Therefore, an SMEFT expansion of the form

$$\mathscr{L}_{\text{SMEFT}} = \mathscr{L}_{\text{SM}} + \sum_i \frac{c_{i,6}}{\Lambda^2}\mathcal{O}_{i,6} + O(\Lambda^{-4})\,, \tag{11.1}$$

is considered in this dissertation. The Warsaw basis [137] provides a complete set of dimension-6 operators allowed by SM gauge symmetries.

For this analysis, a $U(2)_q \times U(2)_u \times U(2)_d \times U(3)_\ell \times U(3)_e$ [471] flavor symmetry is assumed, in which case eleven dimension-6 Wilson coefficients impact the W^+W^- final states significantly. The considered operators are listed in Table 11.1. The Wilson coefficient c_W modifies the triple-gauge coupling, where measurements of diboson production provide the best sensitivity. Boson-to-quark couplings are denoted by $c_{Hq}^{(1)}$, $c_{Hq}^{(3)}$, c_{Hu}, c_{Hd}. For these, the constraints in W^+W^- measurements are expected to be strong, as these effects increase with the center-of-mass energy $\sqrt{s}$. These coefficients perturb the cancellations between triple-gauge and quark couplings in the SM (related to the gauge symmetry), producing effects that diverge at high energies for certain observables. The Wilson coefficients $c_{\ell q}^{(1)}$, $c_{\ell q}^{(3)}$, $c_{\ell u}$, and $c_{\ell d}$ denote operators of four-fermion couplings between two quarks and two fermions. Despite the sensitivity achieved in diboson measurements, these terms can be better constrained in high-mass dilepton observables or lepton+E_T^{miss}. Finally, the coefficients $c_{\ell\ell}$ and $c_{H\ell}^{(3)}$ modify the weak coupling.

BSM contributions from the Lagrangian given in Eq. (11.1) have sizable effects on EW observables [139]. In the case of the decay width of W-bosons (Γ_W) at leading order, these can be parameterized as

$$\Gamma_W = \Gamma_{W,\text{SM}}\left(1 - 0.081c_{H\ell}^{(3)} + 0.081c_{Hq}^{(3)} + 0.061c_{\ell\ell}\right) + O(c_i^2)\,, \tag{11.2}$$

which translates into shifts of the predicted kinematic distributions in the SMEFT model[2].

[2]The differences of this expression with respect to Ref. [139] are caused by different EW input schemes and α_S values used in the simulation.

This effect is considered as a relative linear correction on each bin of the kinematic distributions equal to the negative factor for $c_{H\ell}^{(3)}$, $c_{Hq}^{(3)}$, and $c_{\ell\ell}$ multiplied by two, to consider the presence of two $W^{\pm}$ bosons in the final state.

The expected contributions from each SMEFT operator are evaluated using MC simulation. Details on the production and validation of the simulated sample incorporating the presented model are outlined in the following.

11.2 Simulation of SMEFT Effects

Fits to the measured data distributions are performed to extract confidence intervals of the Wilson coefficients listed in Section 11.1. For these, the expected contributions of each Wilson coefficient are modeled using MC simulations of $q\bar{q} \to WW$ production. Since the dominant backgrounds in both event yields and systematic uncertainties are estimated using data-driven techniques, BSM contributions arising from the background processes are neglected. The contributions from $gg \to WW$ production, highly suppressed in the jet-inclusive region considered (Table 7.2), are also not implemented. Events are generated using the MADGRAPH5_AMC@NLO 2.9.5 generator at leading-order accuracy relying on the SMEFTSIM TOPU3L model[3] [470], matched to the PYTHIA 8.244 parton-shower model. The contributions of each Wilson coefficient are obtained at reconstruction level including detector effects with the ATLAS full-simulation infrastructure, discussed in Section 4.2.8. The MADGRAPH5_AMC@NLO reweight module is used to model the effect of the eleven Wilson coefficients affecting W^+W^- production, listed in Table 11.1, including linear and quadratic contributions. For all relevant operators $\mathcal{O}_i$, the contributions to the W^+W^- production cross section can be predicted via weights in a single MC sample as

$$\frac{|\mathscr{M}_{\mathrm{SM}} + \sum_i c_i \mathscr{M}^i_{\mathrm{dim6}}|^2}{|\mathscr{M}_{\mathrm{original}}|^2}\,, \tag{11.3}$$

where $\mathscr{M}_{\mathrm{original}}$ is the matrix element used for event generation where some of the Wilson coefficients are non-zero for a better coverage of the phase space. The matrix element of the SM-only process is denoted as $\mathscr{M}_{\mathrm{SM}}$, and $\mathscr{M}^i_{\mathrm{dim6}}$ refers to the matrix element corresponding to the dimension-6 operator $\mathcal{O}_i^{(6)}$. In this way, reweighting to an arbitrary parameter point for linear terms, quadratic contributions of the included dimension-6 operators, and interference among dimension-6 operators (referred to as *cross terms*) is possible using this minimal set of weights via

$$\begin{aligned}\frac{|\mathscr{M}_{\mathrm{new}}|^2}{|\mathscr{M}_{\mathrm{original}}|^2} &= \frac{|\mathscr{M}_{\mathrm{SM}} + \sum_i c_i \mathscr{M}^i_{\mathrm{dim6}}|^2}{|\mathscr{M}_{\mathrm{original}}|^2} \\ &= \frac{|\mathscr{M}_{\mathrm{SM}}|^2}{|\mathscr{M}_{\mathrm{original}}|^2} + \sum_i c_i \frac{2\mathrm{Re}|\mathscr{M}^{(i*)}_{\mathrm{dim6}} \mathscr{M}_{\mathrm{original}}|}{|\mathscr{M}_{\mathrm{original}}|^2} + \sum_i c_i^2 \frac{|\mathscr{M}^{(i)}_{\mathrm{dim6}}|^2}{|\mathscr{M}_{\mathrm{original}}|^2} \\ &\quad + \sum_{i\neq j} c_i c_j \frac{2\mathrm{Re}|\mathscr{M}^{(i*)}_{\mathrm{dim6}} \mathscr{M}^{(j*)}_{\mathrm{dim6}}|}{|\mathscr{M}_{\mathrm{original}}|^2}\,,\end{aligned} \tag{11.4}$$

[3] The same model as in previous combined SMEFT interpretations of electroweak processes is used [522]. NLO corrections and effects due to extra jets are not included. These could be potentially relevant for some operators but relatively small in W^+W^- production, as suggested in Refs. [523, 139]. The LO sample is preferred to find results compatible with other global fits presented in, e.g., Ref. [524].

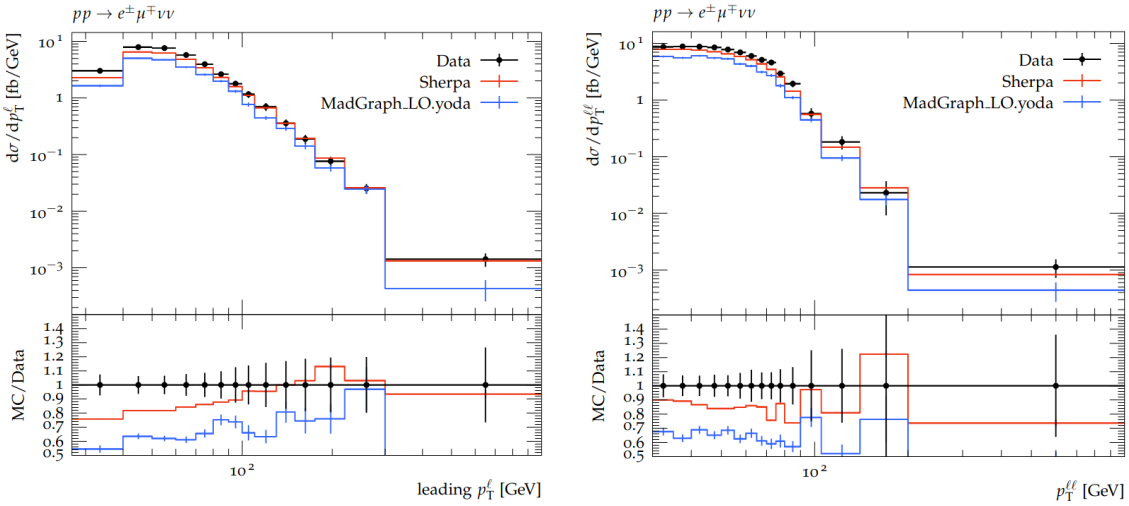

(a) Leading-lepton trasnverse momentum.

(b) Dilepton transverse momentum.

Figure 11.1: Distributions of (a) the leading lepton p_T and (b) transverse momentum of the dilepton system generated for $q\bar{q} \to WW$ production using MC simulation with MADGRAPH 5 +PYTHIA 8 at leading order (blue) and SHERPA 2.2.2 sample at NLO (red). Production via gluon-gluon fusion is not included in these predictions. Only statistical uncertainties from the simulation are show on the theoretical predictions. The SM predictions are compared to measured differential distributions in W^+W^-+0 jets final states determined with the ATLAS experiment [79], including uncertainties from experimental and theoretical sources.

which can be done either event-by-event or at distribution level. The reweighting setup is validated against dedicated samples generated for the SM, as well as the linear term ($2\mathrm{Re}|\mathscr{M}^{(i*)}_{\mathrm{dim6}}\mathscr{M}_{\mathrm{original}}|$), quadratic ($|\mathscr{M}^{(i)}_{\mathrm{dim6}}|^2$) and cross-terms ($2\mathrm{Re}|\mathscr{M}^{(i*)}_{\mathrm{dim6}}\mathscr{M}^{(j*)}_{\mathrm{dim6}}|$) contributions. The result is a single MC sample including about 120 additional weights for the estimation of SMEFT effects on the SM prediction. These weights include the interference terms between SM and SMEFT operators (linear term), pure contributions of the SMEFT coefficients (quadratic term), and cross terms among all combinations of SMEFT operators listed in Section 11.1.

The samples are analyzed with RIVET [525]. Figure 11.1 shows the $p_T^{\text{lead. lep.}}$ and $p_T^{\ell\ell}$ distributions in comparison to the SHERPA 2.2.2 MC simulation employed in previous ATLAS analyses of W^+W^- production [79, 81], compared to the data distributions from W^+W^- measurements from ATLAS using a dataset of 36 fb^{-1} in a jet-vetoed region [79]. As expected, good agreement with the shape of the SHERPA distribution is found. Due to the different accuracy of the SHERPA sample in the matrix-element, calculated at NLO in QCD, the difference in normalization of about 25 % is anticipated from the corresponding K_{QCD} factor. Contributions from $gg \to WW$ production are not included in both distributions, which are needed to describe the data. To avoid inconsistencies due to the use of MADGRAPH instead of the nominal signal prediction POWHEG MINNLO+PYTHIA8, all the kinematic distributions considered in the SMEFT intepretation relying on the MADGRAPH prediction are scaled differentially via the ratio to POWHEG MINNLO+PYTHIA8, both for the SM and BSM effects. The corresponding modeling uncertainties of the SM distribution, estimated as described in Section 9.2, are implemented using the nominal POWHEG MINNLO samples for $q\bar{q} \to WW$ production described in Section 7.4.

The contributions of different anomalous interactions in SMEFT, as predicted by MAD-

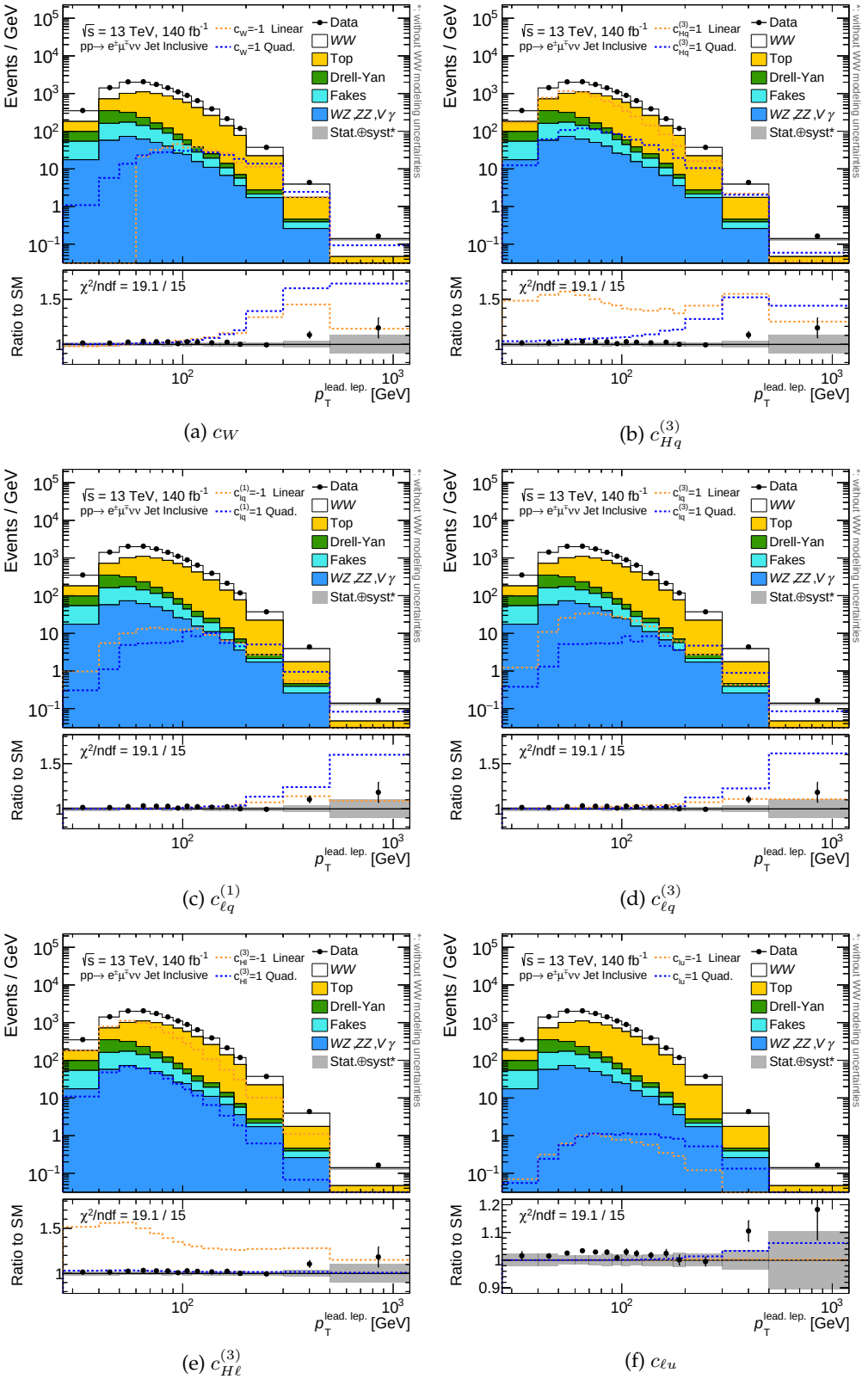

(a) c_W (b) $c_{Hq}^{(3)}$

(c) $c_{\ell q}^{(1)}$ (d) $c_{\ell q}^{(3)}$

(e) $c_{H\ell}^{(3)}$ (f) $c_{\ell u}$

Figure 11.2: Comparison of SM versus SMEFT contributions for the linear (orange) and quadratic (blue) terms of the (a) c_W, (b) $c_{Hq}^{(3)}$, (c) $c_{\ell q}^{(1)}$, (d) $c_{\ell q}^{(3)}$, (e) $c_{H\ell}^{(3)}$, and the (f) $c_{\ell u}$ Wilson coefficients included in the SMEFT model described in Section 11.1 as a function of $p_T^{\text{lead. lep.}}$ in the jet-inclusive signal region. At the bottom, the ratio with respect to the SM prediction is shown. The displayed coupling strengths take values of ± 1, while others are set to zero in the Lagrangian expansion. Uncertainties from the W^+W^- modeling are not included in the total error band. The energy scale of new physics is set to $\Lambda = 1\,\text{TeV}$.

GRAPH, are compared to the data and the expected SM distribution in Figure 11.2 as a function of $p_T^{\text{lead. lep.}}$. Effects from anomalous interactions increase with high diboson invariant mass, especially the quadratic terms of the Wilson coefficients. This results in enhanced contributions at high $p_T^{\text{lead. lep.}}$, especially for effects from anomalous triple-gauge couplings modeled by the coupling strength of the Wilson coefficient c_W, as well as the quark-boson coupling $c_{Hq}^{(3)}$. The terms introduced by c_W, $c_{\ell q}^{(1)}$, $c_{Hq}^{(1)}$, $c_{H\ell}^{(3)}$, c_{Hd}, and $c_{\ell u}$ interfere destructively with the SM Lagrangian. Since $c_{H\ell}^{(3)}$ and $c_{\ell\ell}$ only modify the strength of the weak interaction, the expected effects in the shape of observables correlated to the energy of the parton interaction are small, where only the normalization differs between linear and quadratic effects. The operators related to $c_{\ell q}^{(3)}$, $c_{\ell q}^{(1)}$, $c_{\ell u}$, and c_W provide, in decreasing order, the largest deviations with respect to the shape of the SM distribution.

As discussed in Section 1.7, the differences between confidence intervals obtained via the *linear-only* and a *linear+quadratic* models serve as a qualitative assessment of the uncertainty due to the missing $\mathcal{O}(\Lambda^{-4})$ contributions [140]. Dimension-6 operators have been constrained by independent measurements at LEP and the LHC, as well as global fits of Higgs, top-quark, and electroweak production processes [88, 89]. The current experimental constraints of dimension-6 operators are much more stringent than the available unitarity bounds [131], illustrated in Figure 3.3. In this thesis, the limits reported are no subject to upper energy cutoffs, since no intersection of the experimental constraints with the unitarity bounds is expected.

11.3 Statistical Model

The statistical methods outlined in Sections 6.1 and 6.2 are employed to set limits on the Wilson coefficients corresponding to anomalous couplings introduced in Section 11.1, defined in the context of SMEFT. The likelihood for the observation of $\boldsymbol{N} = (N_1, \ldots, N_{n_{\text{bins}}})$ events in the n_{bins} bins of the reconstructed distributions of interest in the jet-inclusive signal region (e.g., in Figure 10.1) is analyzed. Following Eq. (6.2), the binned likelihood function is defined as

$$\mathrm{L}\left(\boldsymbol{N}|\boldsymbol{c},\boldsymbol{\theta}\right) = \prod_{b}^{n_{\text{bins}}} \text{Poisson}\left(N_b \middle| N_b^{\text{pred}}\left(\boldsymbol{c},\boldsymbol{\theta}\right)\right) \times \prod_{i}^{n_{\text{syst}}} f_i\left(\theta_i\right) \,, \tag{11.5}$$

where $\boldsymbol{c}$ encloses the different Wilson coefficients, $\boldsymbol{\theta}$ are the nuisance parameters modeling the systematic uncertainties from both experimental and theoretical sources constrained with Gaussian profiles f_i, N_b is the number of observed events in bin b, and N_b^{pred} is the number of expected events in that bin. The number of expected events N_b^{pred} in each bin b is modeled as a function of both a set of Wilson coefficients and nuisance parameters,

$$N_b^{\text{pred}}\left(\boldsymbol{c},\boldsymbol{\theta}\right) = N_b^{\text{sig,SM}}\left(\boldsymbol{\theta}\right)\left(1 + \sum_i A_{bi}\frac{c_i}{\Lambda^2} + \sum_i B_{bi}\frac{c_i^2}{\Lambda^4} + \sum_{i<j} C_{bij}\frac{c_i c_j}{\Lambda^4}\right) + N_b^{\text{bkg,SM}}\left(\boldsymbol{\theta}\right) \,, \tag{11.6}$$

where $N_b^{\text{sig,SM}}\left(\boldsymbol{\theta}\right)$ is the number of expected signal events in the SM while $N_b^{\text{bkg,SM}}\left(\boldsymbol{\theta}\right)$ is the number of expected background events, being both of these subject to theoretical and

experimental uncertainties which are modeled with nuisance parameters. The SMEFT parametrization is given by the terms A_{bi}, B_{bi}, and C_{bi}, which are derived at leading order using the SMEFTSIM 3.0 [470, 471] sample introduced in Section 11.1. The A_{bi} term arises due to the interference of dimension-6 new-physics effects with the SM and includes the effect of Wilson coefficients on the W-boson width. Additionally, contributions arising from dimension-6 squared amplitudes (B_{bi}) and from the interference of two amplitudes containing two different dimension-6 operators (C_{bi}), are modeled. Other $O(\Lambda^{-4})$ effects, which include the interference of the SM amplitude with dimension-8 operators or with double insertions of dimension-6 operators are neglected. The full simulation of the ATLAS detector response is performed to determine the effects from limited resolution and selection efficiency on the SMEFT contributions. The implementation of the statistical model relies on the ROOFIT toolkit [492] for the fitting and minimization of the log-likelihood function (11.5).

For the estimation of confidence intervals for a Wilson coefficient c_i, a profile-likelihood ratio test statistic is constructed using Eq. (6.5), where the parameters of interest correspond to the different terms c_i/Λ^2 in the SMEFT expansion. Here, $\hat{\hat{\boldsymbol{\theta}}}$ is the maximum likelihood estimate of the nuisance parameters for a fixed value of c_i while $\hat{c}_i$ and $\hat{\boldsymbol{\theta}}$ are unconditional maximum likelihood estimates of c_i and the nuisance parameters, respectively. Maximum likelihood fits are performed for individual Wilson coefficients by setting other coefficients to zero and maximizing the likelihood with respect to the nuisance parameters. Confidence intervals are derived using Wilks' theorem [418], assuming that $q(c_i)$ follows the χ^2 distribution.

11.4 Expected Limits

Employing the SMEFT and statistical models introduced respectively in Sections 11.1 and 11.3, limits at $68\,\%$ and $95\,\%$ CL are extracted using the SM predictions estimated using the background estimation techniques discussed in Chapter 8 and the nominal prediction of W^+W^- contributions (Sec. 7.4) as Asimov data, including contributions from the dimension-6 operators listed in Table 11.1 rescaled to the nominal $q\bar{q} \to WW$ POWHEG MINNLO +PYTHIA prediction. Results are provided for both a *linear* model, which adds the interference terms between SM and $O(\Lambda^{-2})$ SMEFT contributions to the SM Lagrangian, and a *linear+quadratic* model also accounting for $O(\Lambda^{-4})$ quadratic contributions of the dimension-6 operators. The difference between results obtained using the linear and linear+quadratic models can be used for a qualitative assessment of the effects due to the missing $O(\Lambda^{-4})$ contributions [140, 141] of dimension-8 operators. The constraining power of each SMEFT operator is assessed by fitting each parameter individually, fixing the contributions from other operators to zero. To find the observable most sensitive to effects beyond the SM, the constraints are derived in the jet-inclusive signal region using distributions of $\Delta\phi_{e\mu}$, $p_T^{\text{lead. lep.}}$, $m_{T,e\mu}$, $m_{e\mu}$, $p_T^{\ell\ell}$, $H_T^{\text{lep.+MET}}$, and S_T. The binning of the considered distributions respects the optimization discussed in Section 9.1.1 derived for the fiducial differential cross-section measurements. Experimental and theoretical uncertainties are propagated into the fit results via nuisance parameters as described in Section 11.3. Figure 11.3 compares the expected limits for each individual parameter by fitting different observables considered in the W^+W^- measurement performed in this thesis. As discussed in Section 10.1, a good data-to-SM agreement is

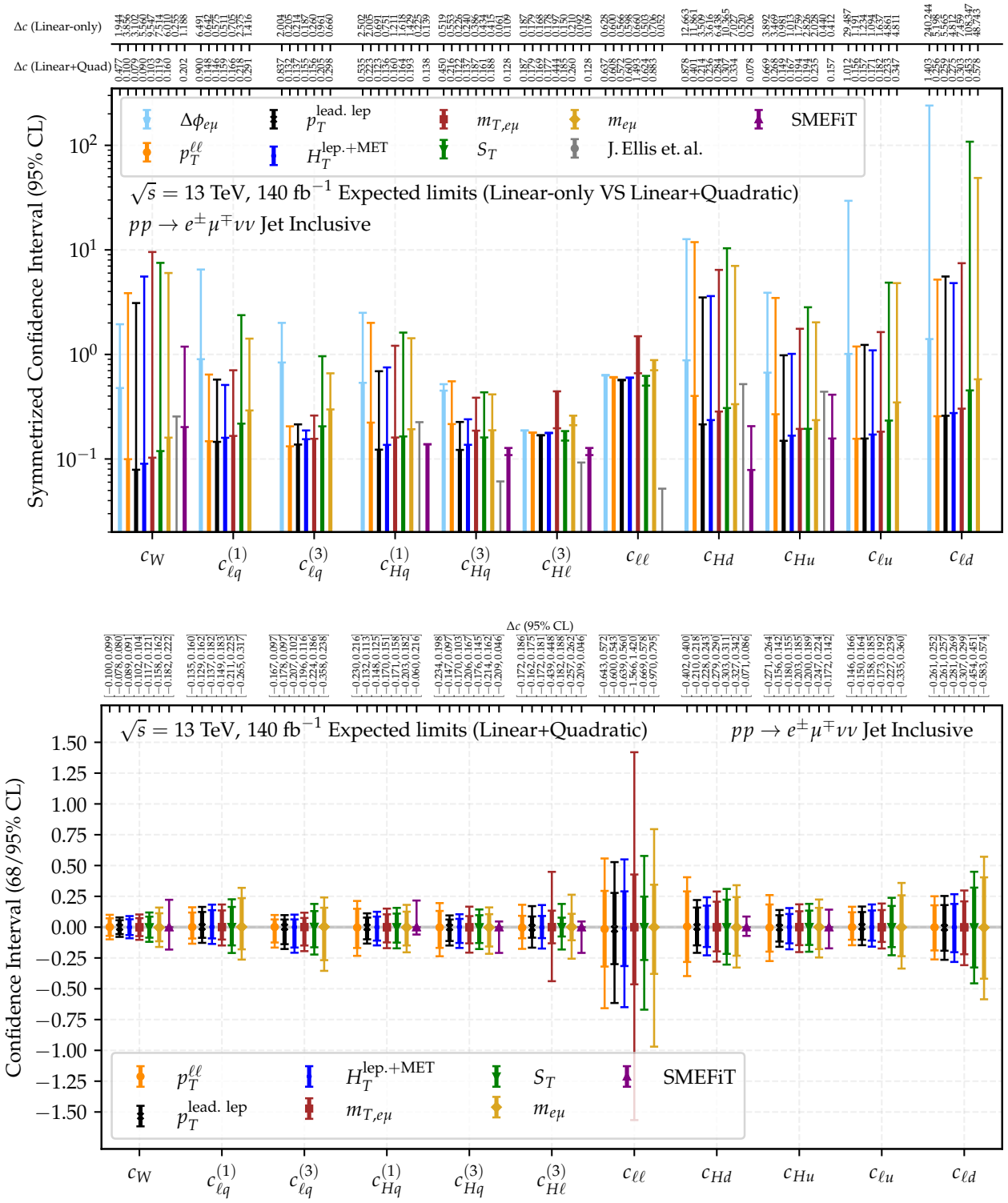

Figure 11.3: Confidence intervals (Δc) obtained from individual binned likelihood fits of Asimov data at reconstructed level in bins of $\Delta\phi_{e\mu}$, $p_T^{\ell\ell}$, $p_T^{\text{lead. lep.}}$, H_T^{lep}, $m_{T,e\mu}$, S_T, and $m_{e\mu}$ of the eleven Wilson coefficients sensitive to W^+W^- production (Table 11.1). In the top plot, both linear-only ($O(\Lambda^{-2}$, inner bar) and linear+quadratic ($O(\Lambda^{-4}$, outer bar) expected limits at 95 % Confidence Level (CL) are symmetrized for a direct comparison using a logarithmic scale. At the bottom, the expected limits at 68 % (wider inner bar) and 95 % (thinner outer bar) CL of the linear+quadratic configuration of the SMEFT expansion are shown without symmetrization. The expected limits are compared to the marginal constraints from global fits performed by J. Ellis et. al. [89] and the SMEFiT collaboration [88]. Only $O(\Lambda^{-2})$ terms are considered by J. Ellis et. al. in the SMEFT Lagrangian. The energy scale of new physics is set to $\Lambda = 1$ TeV.

found across these distributions. For instance, the reduced chi-square value is found to be $\chi^2/\text{d.o.f.} = 19.1/15$ for the $p_T^{\text{lead. lep.}}$ distribution, pulled towards values greater than one by a slight underestimation of the data in bins of intermediate $p_T^{\text{lead. lep.}}$ with no jets in the final state. A similar level of sensitivity is achieved in the linear-only configuration of the fit with respect to the $WW+\geq 1\,\text{jets}$ ATLAS measurement using the full Run 2 dataset [81], which exploited the differential cross-section measurement as a function of $m_{e\mu}$ unfolded to the particle level, when relying on the same distribution at detector level. To reduce the suppression of the interference between the SM and SMEFT contributions, the $WW+\geq 1\,\text{jets}$ analysis restricted the fiducial phase space to $p_T^{\text{lead. jet}} > 200\,\text{GeV}$, improving the sensitivity to the linear term by a factor of 2 and reducing the discrepancies with respect to the limits including quadratic terms in the SMEFT Lagrangian. When including quadratic terms in the Lagrangian expansion, using the $m_{e\mu}$ distribution in the jet-inclusive region, the expected constraints improve previous ATLAS global fits [524] and measurements [79, 81] by a factor of 2.

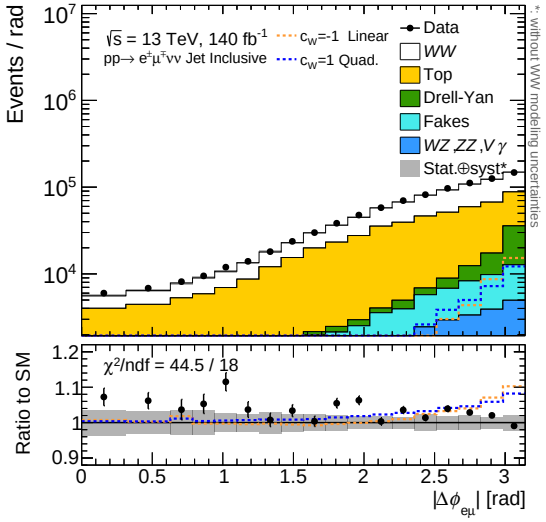

Figure 11.4: Comparison of SM versus SMEFT contributions for the linear (orange) and quadratic (blue) terms of the c_W Wilson coefficient as a function of $\Delta\phi_{e\mu}$ in the jet-inclusive signal region. At the bottom, the ratio with respect to the SM prediction is shown. The displayed coupling strengths take values of ± 1, while others are set to zero in the Lagrangian expansion. Uncertainties from the W^+W^- modeling are not included in the total error band. The energy scale of new physics is set to $\Lambda = 1\,\text{TeV}$.

Even more stringent constraints are expected when fitting the binned likelihood in Eq. (11.5) as a function of other observables such as S_T, $m_{T,e\mu}$, $H_T^{\text{lep.+MET}}$, $\Delta\phi_{e\mu}$, or $p_T^{\ell\ell}$, based on the modeling of the SM and SMEFT contributions[4]. The $\Delta\phi_{e\mu}$ distribution, presented in Figure 11.4, provides the best constraints of the c_W coupling via the linear-only fit, owing to the enhanced sensitivity of the destructive interference with the SM in bins where background contributions are lowest. This distribution is also successful in diminishing the suppression of the interference between $O(\Lambda^{-2})$ contributions from the $\mathcal{O}_W$ operator with the SM. However, the sensitivity of the $\Delta\phi_{e\mu}$ distribution to constrain the quadratic term but also other Wilson coefficients is limited in W^+W^- production. Among all the considered differential observables, the $p_T^{\text{lead. lep.}}$ and $H_T^{\text{lep.+MET}}$ distributions yield the best constraints across most of the considered Wilson coefficients, in both fits of the interference term only but also when including $O(\Lambda^{-4})$ contributions.

The expected limits are compared to the marginal constraints resulting in global fits of Higgs, electroweak, and top-quark processes performed by J. Ellis et. al. [89] (reported only for interference terms between SM and SMEFT operators) and the SMEFiT collaboration [88]. In the fit including only linear terms, the best constraints are achieved by J. Ellis and collaborators [89]. For the c_W Wilson coefficient, these are more strongly con-

[4]Expected constraints relying on observables such as $p_T^{\text{sublead. lep.}}$, $y_{e\mu}$, $\cos\theta^*$, E_T^{miss}, or N_{jets} are not competitive with the ones shown in Figure 11.3 and therefore not further considered.

strained by differential cross-section measurements in vector-boson fusion production of Zjj[5]. J. Ellis et. al. improve the sensitivity to $c_{Hq}^{(1)}$ and $c_{Hq}^{(3)}$ via both inclusive and differential cross-section measurements of single-top production. The anomalous couplings c_{Hu} and c_{Hd} can be strongly constrained taking into account measurements of Electroweak Precision Observables (EWPO) from the LEP combination [59] but also sensitive to measurements of Higgs production, included in the global fits. EW precision measurements at LEP are also very sensitive to anomalous effects from $c_{H\ell}^{(3)}$ and $c_{\ell\ell}$[6]. Although limits for $c_{\ell u}$ and $c_{\ell d}$ are not explicitely reported by J. Ellis et. al. and SMEFiT, final states in Drell-Yan production provide a better sensitivity to the effects introduced by these four-fermion anomalous couplings. However, diboson production leads the sensitivity to anomalous triple-gauge couplings. When considering linear and quadratic terms, the expected sensitivity on c_W exceeds the ones reported in global fits by a factor of 2. Since the global fits incorporate $WW + 0\,\text{jet}$ measurements using a portion of the Run 2 dataset ($36\ \text{fb}^{-1}$), the improvement arises mainly due to the increased set of $q\bar{q} \to WW$ candidates in the event selection, which reduces statistical fluctuations at the high-energy tails of differential distributions where the best sensitivity to SMEFT effects in $q\bar{q} \to WW$ production is achieved. Additionally, the jet-inclusive selection reduces uncertainties related to the modeling of the $q\bar{q} \to WW$ predictions but also from jet-related experimental sources. A similar level of sensitivity of the SMEFT fit at $O(\Lambda^{-4})$ with respect to the global fits is found for the $c_{Hq}^{(1)}$ and $c_{Hq}^{(3)}$ Wilson coefficients. Additionally, the expected sensitivity achieved for the Wilson coefficient $c_{H\ell}^{(3)}$ becomes competitive with global fits, owing to the fully jet-inclusive selection criteria.

The pulls and impacts of the nuisance parameters obtained in likelihood fits of the c_W and $c_{Hq}^{(3)}$ Wilson coefficients to Asimov data in bins of the $p_T^{\text{lead. lep.}}$ distribution are presented in Figure 11.5. Uncertainties on the modeling of the signal $q\bar{q} \to WW$ and top-quark background have the largest impact in the fit to constrain Wilson coefficients in the jet-inclusive region, mainly arising from the theoretical modeling of the $t\bar{t}$ contributions (necessary for the calculation of the correlation factor C_b in the data-driven b-counting method described in Section 8.1.1) and limited statistics in the b-jet regions defined for the data-driven estimation of the $t\bar{t}$ background (Sec. 8.1). Systematic uncertainties from the lepton misidentification background play an important role, relying also on limited statistics in the ID+AntiID control region. For SMEFT operators affecting mainly the total W^+W^- production cross section, such as $c_{H\ell}^{(3)}$ and $c_{\ell\ell}$, the luminosity uncertainty becomes also a limiting factor.

The differential observable providing best sensitivity to the SMEFT operators can be inferred from the presented expected limits. Both $H_T^{\text{lep.+MET}}$ and $p_T^{\text{lead. lep.}}$ observables are strongly correlated to the invariant mass of the W^+W^- system and therefore provide sensitivity to SMEFT effects that increase with the collision energy. Nevertheless, the hadronic radiation in W^+W^- final states of the SMEFT MC prediction is simulated with the parton-shower model, as the matrix-element is calculated at leading-order accuracy. This leads to a potential mismodeling of the E_T^{miss} calculation (Sec. 4.3.6), to which the

[5]The $\Delta\phi_{jj}$ distribution in Zjj production is more sensitive to the interference term of the anomalous triple-gauge coupling.

[6]Limits on the $c_{\ell\ell}$ coefficient, strongly constrained by the LEP EWPO observables [526], are not reported by the SMEFiT collaboration.

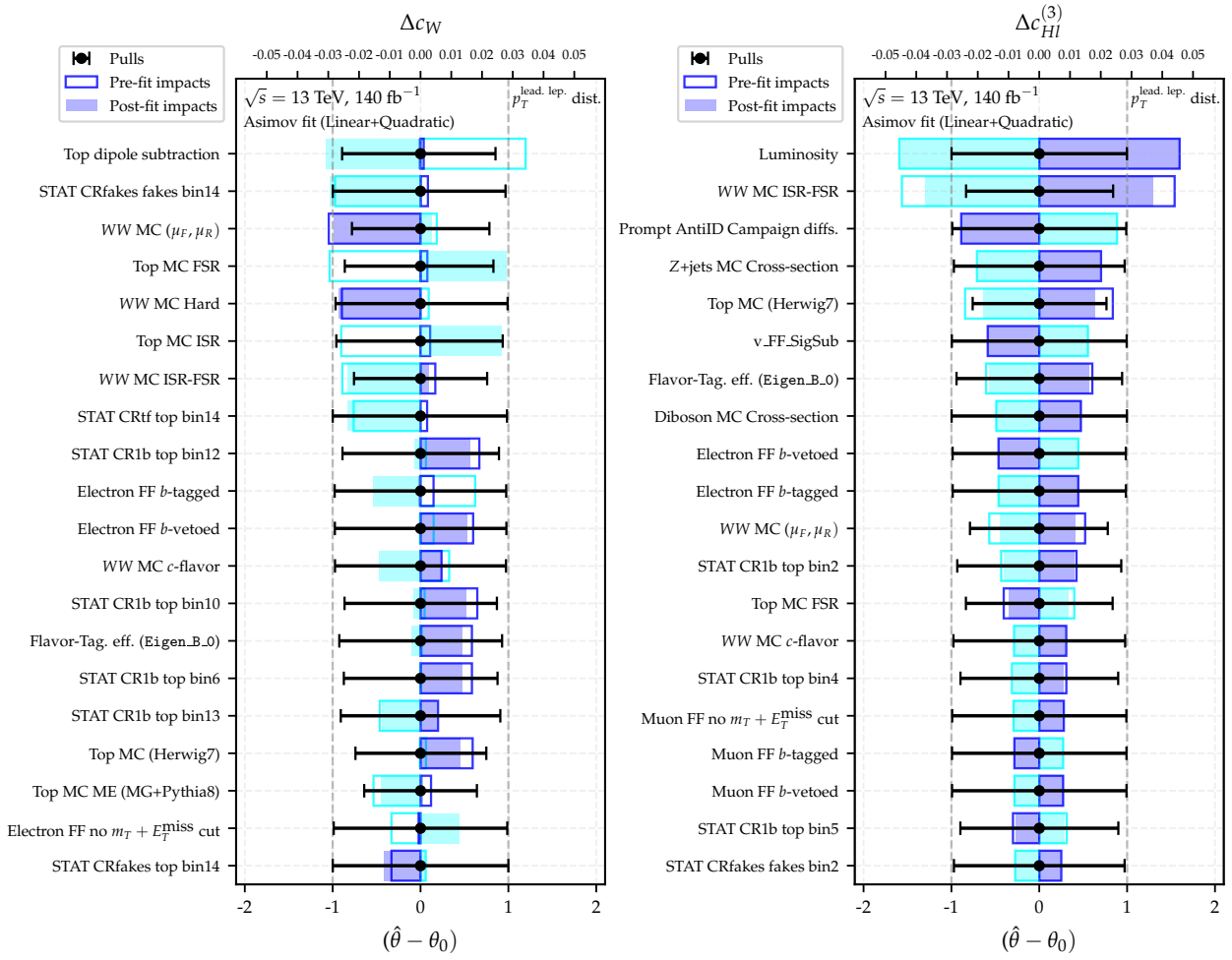

(a) c_W fit. (b) $c_{H\ell}^{(3)}$ fit.

Figure 11.5: Pulls (shown as black dots) and impacts (horizontal bands) for the 20 nuisance parameters of highest post-fit impact in the individual likelihood fit of the (a) c_W and (b) $c_{H\ell}^{(3)}$ Wilson coefficients to Asimov data profiled in bins of $p_T^{\text{lead. lep.}}$ as shown in Figure 11.2. The vertical dashed lines indicate the 1σ thresholds of the pulls at the bottom horizontal axis. The upper axis displays the absolute impact on c_W of each nuisance parameter for both pre-fit (white horizontal bands) and post-fit (filled blue bands).

$H_T^{\text{lep.+MET}}$ observable is susceptible. To be less sensitive to these limitations, the $p_T^{\text{lead. lep.}}$ distribution is chosen to constrain SMEFT operators in this thesis. The observed limits resulting from the binned likelihood fits to data are discussed in the next section.

11.5 Observed Limits

The $p_T^{\text{lead. lep.}}$ distribution is used to fit the SMEFT model introduced in Section 11.1 to the data via the binned likelihood function given in Eq. (11.5), as it provides the best sensitivity to most of the considered anomalous couplings. Curves for the log-likelihood scans of $-2\Delta \ln \mathrm{L} = -2(\ln \mathrm{L} - \ln \mathrm{L}_{\min})$ are shown in Figures 11.6 and 11.7 for all the anomalous couplings listed in Table 11.1 considering both dimension-6 terms only in the SMEFT Lagrangian (11.1), but also including quadratic terms, respectively. The minimization of the log-likelihood function is presented for (i) an Asimov dataset using only statistical uncertainties, (ii) an Asimov dataset including both statistical and systematic uncertainties from theoretical and experimental sources, and (iii) the fit to the experimental data, also including all sources of uncertainties as listed in Section 9.2. The difference between the two Asimov fits illustrates the impact of these two error categories in the expected sensitivity. Using the full Run 2 dataset of pp collisions at center-of-mass energies of $\sqrt{s} = 13$ TeV, systematic and statistical uncertainties have a similar impact on the reported limits for the linear terms of the Wilson coefficients. Exceptions can be found for operators that have mild effects on the shape of the SM distribution, such as $c_{H\ell}^{(3)}$ and $c_{\ell\ell}$. Since these anomalous couplings contribute similarly in regions of low and high statistics, the sensitivity to their effects is driven by systematic uncertainties in regions with abundant statistics. For the linear-only fit, good agreement between expected and observed limits is found within 1σ. The observed constraints agree with the SM prediction at $95\,\%$ confidence level. The addition of the quadratic terms into the individual fits introduces interesting features in the observed likelihood scans, where the SM prediction is excluded at $68\,\%$ confidence level. This exclusion is largely symmetric, since the quadratic term is not sensitive to the sign of the Wilson coefficient under consideration. This tendency can be explained as an artifact of the data-to-MC agreement observed in Figure 11.2, taking place at the intermediate-p_T regime but most importantly for the fit of BSM effects in the region $300 < p_T^{\text{lead. lep.}} < 500\,\text{GeV}$. Since the contributions from quadratic SMEFT terms are large at the high-energy tails of the $p_T^{\text{lead. lep.}}$ distribution, the scope of the binned log-likelihood scans is driven by the dominating statistical uncertainties. This feature is not present for quadratic terms of Wilson coefficients introducing flat contributions to the SM prediction. These Wilson coefficients deviate the largest with respect to the SM, owing to the slight underestimation of the data at the intermediate-p_T regime of the $p_T^{\text{lead. lep.}}$ distribution that is filled with SMEFT contributions by the fitting procedure. Within the $95\,\%$ confidence level, the observed limits for the fits of individual Wilson coefficients are in agreement with the SM prediction also when including quadratic terms in the SMEFT model. As in the Asimov fits, the pulls and impacts of the individual likelihood fits of the c_W and $c_{Hq}^{(3)}$ Wilson coefficients to the experimental data in bins of the $p_T^{\text{lead. lep.}}$ distribution are presented in Figure 11.8. No nuisance parameters are pulled beyond the 1σ bands. No significant constraints of the nuisance parameters are observed. The fits to experimental data are also dominated by modeling uncertainties of the signal $q\bar{q} \to WW$ and the top-quark background, as well as the limited statistics in the control regions defined for the data-driven estimation of the $t\bar{t}$ and lepton misidentification backgrounds. The luminosity uncertainty dominates for SMEFT operators with small effects on the shape of the distributions.

The results are summarized in Figure 11.9, comparing the individual fits to Asimov and experimental data. Confidence intervals are provided for both (i) the linear model, that includes contributions up to $O(\Lambda^{-2})$, and (ii) the linear+quadratic model, containing the square of amplitudes involving pure dimension-6 operators. As not all $O(\Lambda^{-4})$ effects are known and quadratic dimension-6 terms only constitute a subset, the difference between the results obtained using the linear and linear+quadratic models can be used as a qualitative measure of the uncertainty due the missing $O(\Lambda^{-4})$ contributions. For $c_{Hq}^{(3)}$, $c_{\ell q}^{(3)}$, $c_{\ell\ell}$, and $c_{H\ell}^{(3)}$ constraints are similar for both models while $O(\Lambda^{-4})$ contributions are important for the remaining Wilson coefficients. The observed limits largely agree with the expected results from Asimov fits owing to the accurate SM prediction implemented in the jet-inclusive analysis, both in fits of $O(\Lambda^{-2})$ terms but also when including quadratic terms. The most stringent constraints on contributions from anomalous triple-gauge couplings obtained in hadron collisions (summarized in Figure 7.5), modeled by the c_W Wilson coefficients in the context of SMEFT, are reported in this thesis. These improve the constraints from global fits by a factor of 2, owing to the larger dataset and enhanced sensitivity to $q\bar{q} \to WW$ event candidates. Additionally, similar constraining power has been achieved for boson-quark operators such as $c_{Hq}^{(1)}$, $c_{Hq}^{(3)}$, and c_{Hu}. These results highlight the relevance for future global fits of the measurements of W^+W^- production in a jet-inclusive phase space reported in this thesis.

The exclusions observed in individual fits including quadratic effects are discarded when fitting two Wilson coefficients at a time. Figures 11.10 and 11.11 show contours with $68\,\%$ and $95\,\%$ confidence intervals between different combinations of the c_W, $c_{\ell q}^{(1)}$, $c_{\ell q}^{(3)}$, $c_{Hq}^{(1)}$, and $c_{Hq}^{(3)}$ Wilson coefficients. Among these, no significant correlations are found, as expected from the definition of the Warsaw basis and the small contributions of the cross terms. The observed 2σ confidence intervals found in the two-dimensional fits are largely in agreement with the results from the individual fits. When fitting more than one Wilson coefficient simultaneously, no deviations from the SM prediction are observed within the $68\,\%$ intervals.

11.6 Outlook

In this chapter, an interpretation of the W^+W^- measurements has been reported in the context of the SMEFT. The reported $95\,\%$ confidence intervals for anomalous triple-gauge, boson-fermion, and four-fermion couplings are in agreement with the SM. The most stringent constraints on anomalous triple-gauge couplings relying on hadron-collision data are reported in this thesis, improving by a factor of 2 previous results from ATLAS and CMS, but also from global fits of Higgs, top-quark, and electroweak measurements.

The reconstructed distribution of the leading lepton transverse momentum $p_T^{\text{lead. lep.}}$ in a fully jet-inclusive selection (summarized in Table 7.2) sensitive to W^+W^- production is used to fit the SMEFT model introduced in Section 11.1 to the data via the binned likelihood function given in Eq. (11.5), as it provides the best sensitivity to most of the considered anomalous couplings. The sensitivity of differential observables reported in the W^+W^- cross-section measurements has been assessed from fits to Asimov data discussed in Section 11.4. The binning used for the differential observables, optimized in the context of fiducial differential cross-section measurements, is kept as reported in

the fiducial jet-inclusive phase space. Since the resolution of the used binning for the $p_T^{\text{lead. lep.}}$ distribution is particularly better than for other observables in the comparison, this could explain the apparently better sensitivity achieved via this observable. Sensitivity to anomalous effects at the high-energy tails of differential observables can be further enhanced by performing a dedicated optimization of the binning targeting a high significance of SMEFT contributions. Once the binning optimization had been performed for all the observables under the same criteria, the reported constraints on Wilson coefficients could be further improved.

To reduce the suppression of the interference of SMEFT contributions at $O(\Lambda^{-2})$ with the SM, the ATLAS measurement of $WW+\geq 1\,\text{jets}$ final states restricted the leading jet p_T to $p_T^{\text{jet}} > 200\,\text{GeV}$ [81]. Although this approach has not been pursued in this work, the same strategy could be followed in a fully jet-inclusive phase space for events where at least one jet was reconstructed. This would allow to increase the sensitivity to W^+W^- event candidates in the 0-jet bin while reducing the suppression of the interference in events with jets in the final state. However, the interpretation of the data relies on the simulation of SMEFT effects computed at leading-order accuracy. Since the modeling of the additional hadronic activity in $q\bar{q} \to WW$ final states relies solely on the parton shower, these limitations propagate to the recoil of the leptons in the final state. The mismodeling of the recoil becomes particularly important at the high-energy tails of distributions such as $p_T^{\text{lead. lep.}}$ or $p_T^{\ell\ell}$, most sensitive to SMEFT contributions. As discussed in Chapter 3, the scale uncertainties at LO are not sufficient to account for missing higher-order corrections in predictions of $q\bar{q} \to WW$ production. Therefore, the experimental results presented in this thesis should be reinterpreted with a simulation of SMEFT effects with higher accuracy, which are now available at NLO accuracy in QCD in, e.g., the MADGRAPH5_AMC@NLO generator with SMEFTSIM [470] including the package SMEFT@NLO [527].

Furthermore, the absolute value of azimuthal difference between the two leptons in the final state $|\Delta\phi_{e\mu}|$ provides the strongest suppression of the interference term between SM and the $\mathcal{O}_W$ SMEFT operator, sensitive to anomalous triple-gauge couplings, in the jet-inclusive signal region. However, the sensitivity of this observable to both other considered SMEFT operators and their quadratic terms is not competitive with those observables correlated to the invariant mass of the diboson system. In the future, double-differential distributions of $|\Delta\phi_{e\mu}|$ and observables such as $p_T^{\text{lead. lep.}}$, $H_T^{\text{lep.+MET}}$, or $m_{e\mu}$ could be considered to enhance the sensitivity to various dimension-6 SMEFT operators while suppressing the interference of their linear terms in the SMEFT expansion.

As the constraints on anomalous interactions are affected by the limited dataset at the highest energies of the differential distributions, the prospects of the LHC in the incoming years, especially during the operation of the HL-LHC, are exciting for SMEFT interpretations. With a greater center-of-mass energy and a ten-times bigger dataset, the present limits are expected to improve considerably in the near future, once the data are available to be analyzed. Additionally, several strategies are being discussed to further optimize SMEFT interpretations. For instance, combinations of EW measurements following a Simplified Template cross section approach used in measurements of the Higgs boson [528, 529], including ATLAS and CMS data along with state-of-the-art predictions of SMEFT contributions, are being discussed in forums such as the LHC-EW working group [530].

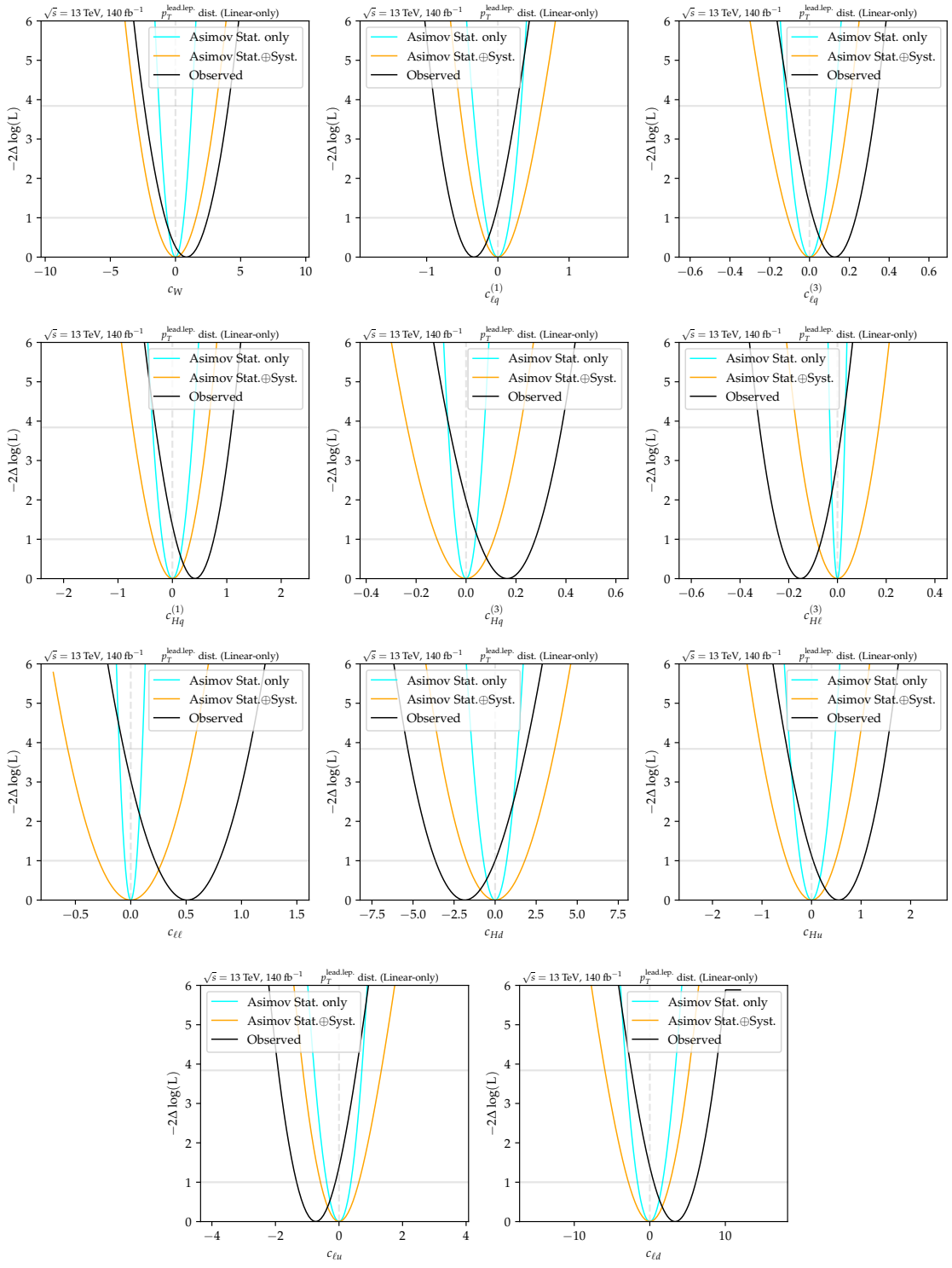

Figure 11.6: Log-likelihood scans of $-2\Delta \ln \mathrm{L} = -2(\ln \mathrm{L} - \ln \mathrm{L}_{\min})$ in bins of $p_T^{\text{lead. lep.}}$ for the Wilson coefficients listed in Table 11.1 , considering only dimesion-six terms in the SMEFT Lagrangian given in Eq. (11.1). Horizontal lines show the limits of the log-likelihood fit at 68 % and 95 % confidence levels. The vertical dashed line shows the SM prediction. The energy scale of new physics is set to $\Lambda = 1\,\mathrm{TeV}$.

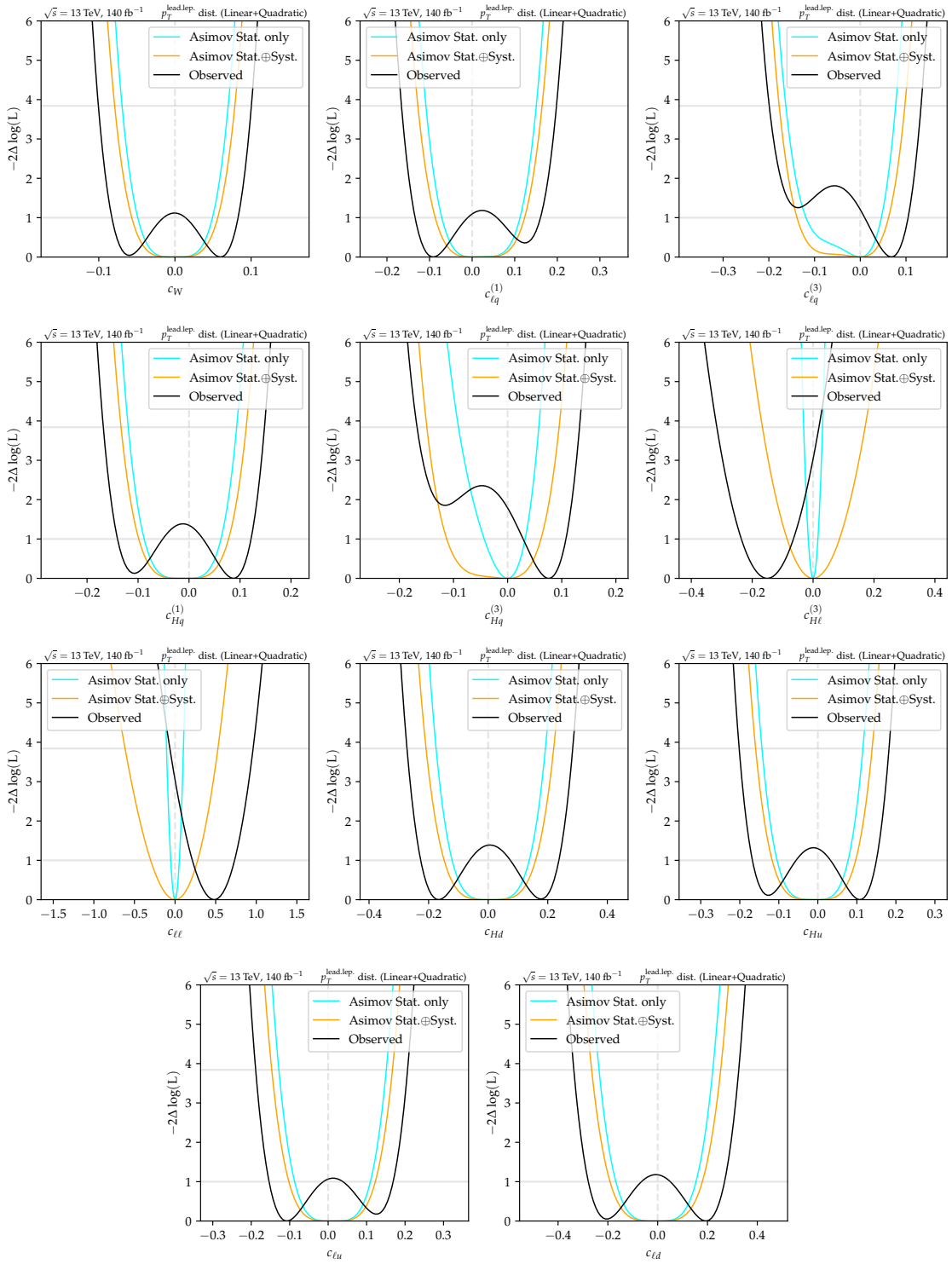

Figure 11.7: Log-likelihood scans of $-2\Delta \ln \mathrm{L} = -2(\ln \mathrm{L} - \ln \mathrm{L}_{\min})$ in bins of $p_T^{\text{lead. lep.}}$ for the Wilson coefficients listed in Table 11.1, considering linear and quadratic terms in the SMEFT Lagrangian given in Eq. (11.1). Horizontal lines show the limits of the log-likelihood fit at 68 % and 95 % confidence levels. The vertical dashed line shows the SM prediction. The energy scale of new physics is set to $\Lambda = 1$ TeV.

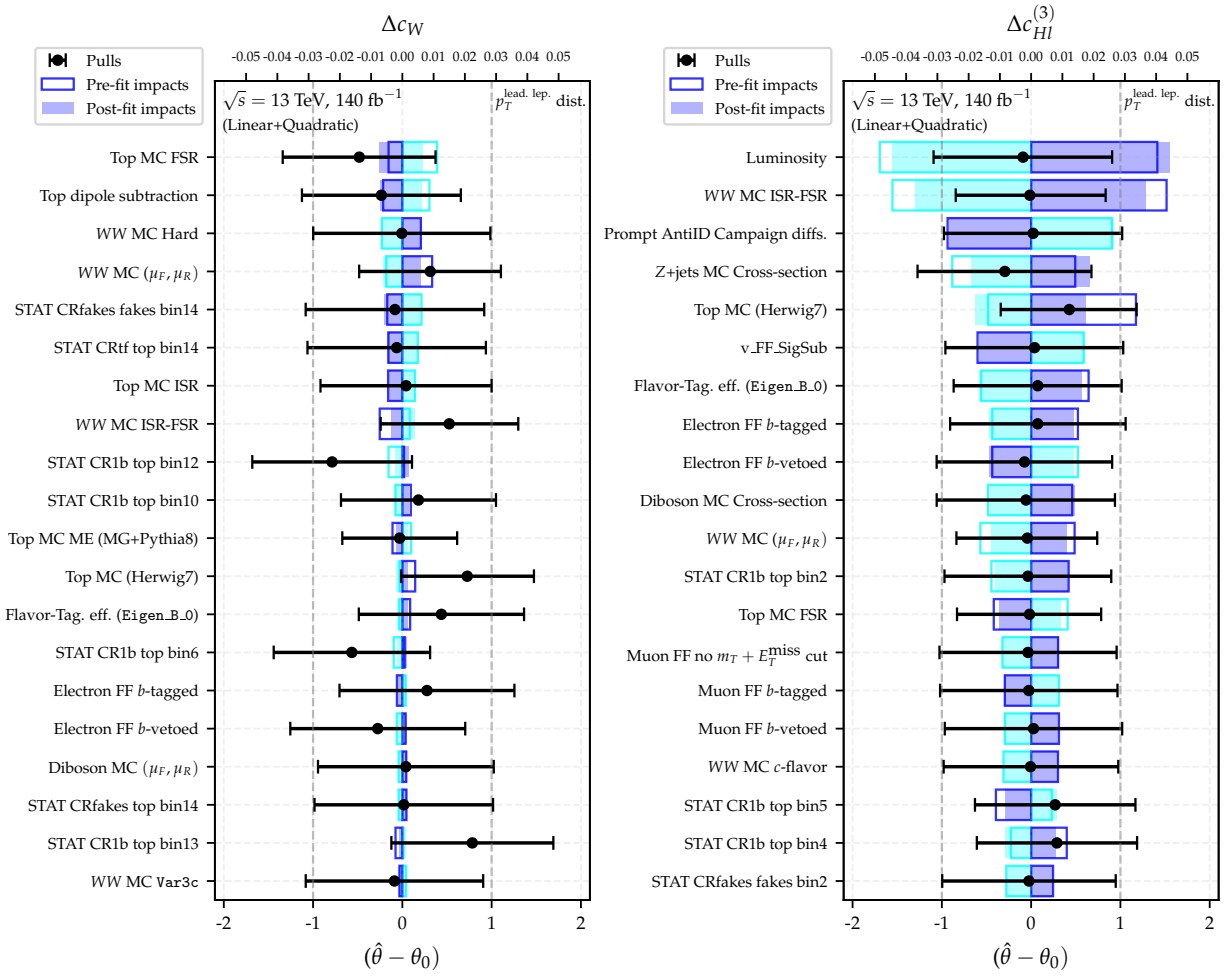

(a) c_W fit.

(b) $c_{H\ell}^{(3)}$ fit.

Figure 11.8: Pulls (shown as black dots) and impacts (horizontal bands) for the 20 nuisance parameters of highest post-fit impact in the individual likelihood fit of the (a) c_W and (b) $c_{H\ell}^{(3)}$ Wilson coefficients to Asimov data profiled in bins of $p_T^{\text{lead. lep.}}$ as shown in Figure 11.2. The vertical dashed lines indicate the 1σ thresholds of the pulls at the bottom horizontal axis. The upper axis displays the absolute impact on c_W of each nuisance parameter for both pre-fit (white horizontal bands) and post-fit (filled blue bands).

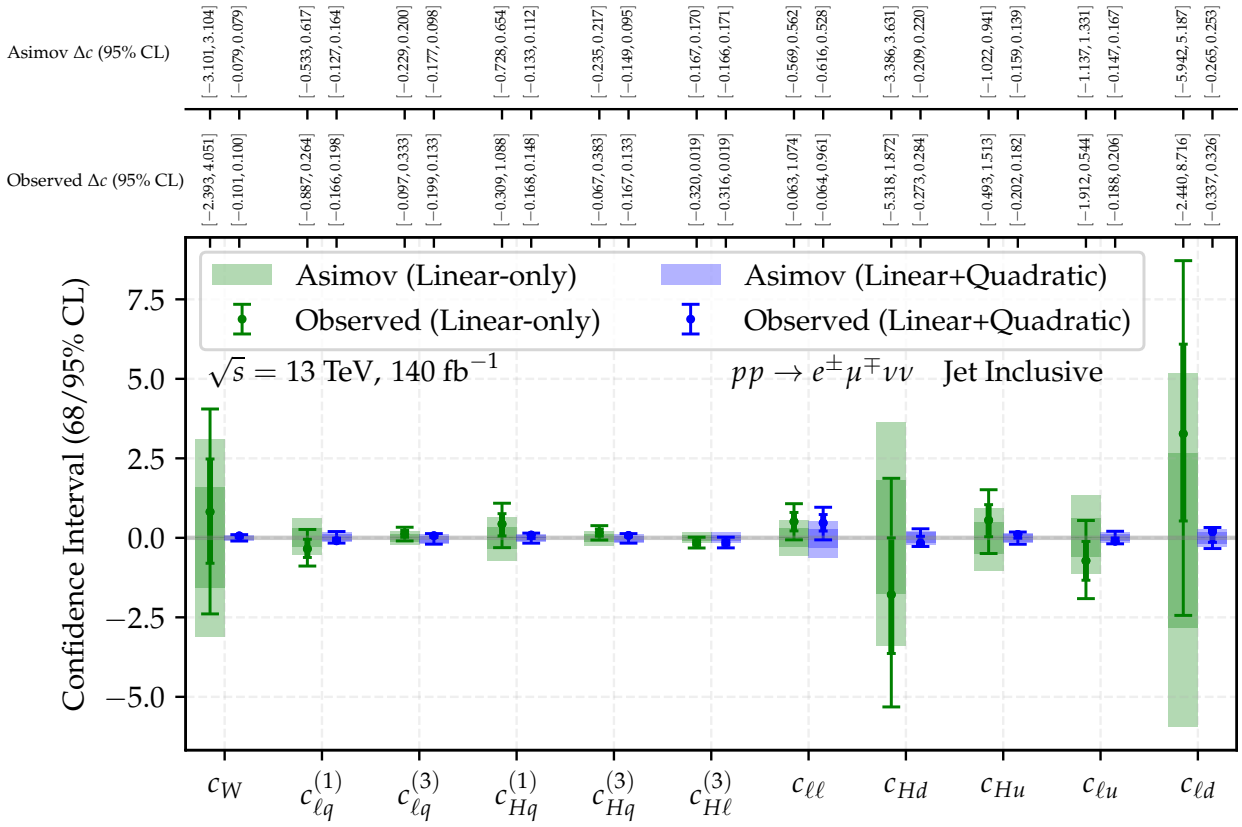

Figure 11.9: Expected and observed confidence intervals obtained from the fit of the $p_T^{\text{lead. lep.}}$ distribution at reconstruction level with the linear-only (green) and the linear+quadratic (blue) configurations of the SMEFT model. For each coefficient, the confidence intervals at 68 % (inner error bar) and 95 % (outer error bar) confidence level, respectively, are shown.

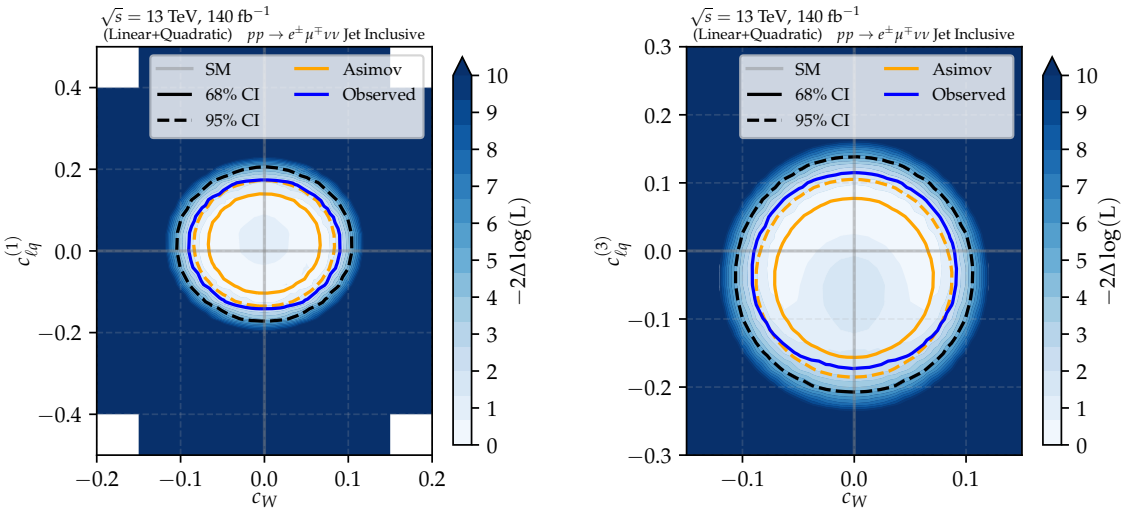

(a) $c_W - c^{(1)}_{\ell q}$ (b) $c_W - c^{(3)}_{\ell q}$

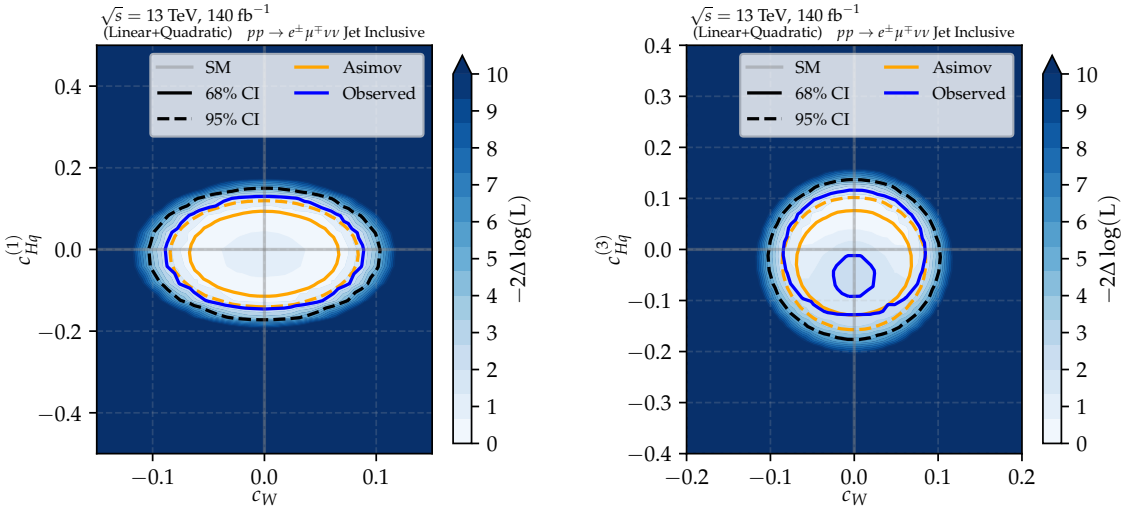

(c) $c_W - c^{(1)}_{Hq}$ (d) $c_W - c^{(3)}_{Hq}$

Figure 11.10: Contours with two-dimensional log-likelihood scans of $-2\Delta \ln \mathrm{L} = -2(\ln \mathrm{L} - \ln \mathrm{L}_{\min})$ resulting from fits to Asimov (orange) and experimental (blue) data binned as a function of $p_T^{\text{lead. lep.}}$ for pairs of Wilson coefficients between c_W and (a) $c^{(1)}_{\ell q}$, (b) $c^{(3)}_{\ell q}$, (c) $c^{(1)}_{Hq}$, and (d) $c^{(3)}_{Hq}$, considering linear and quadratic terms in the SMEFT Lagrangian given in Eq. (11.1). Confidence intervals at 68 % (solid) and 95 % (dashed) confidence level are displayed. The solid gray lines shows the SM prediction. The energy scale of new physics is set to $\Lambda = 1$ TeV.

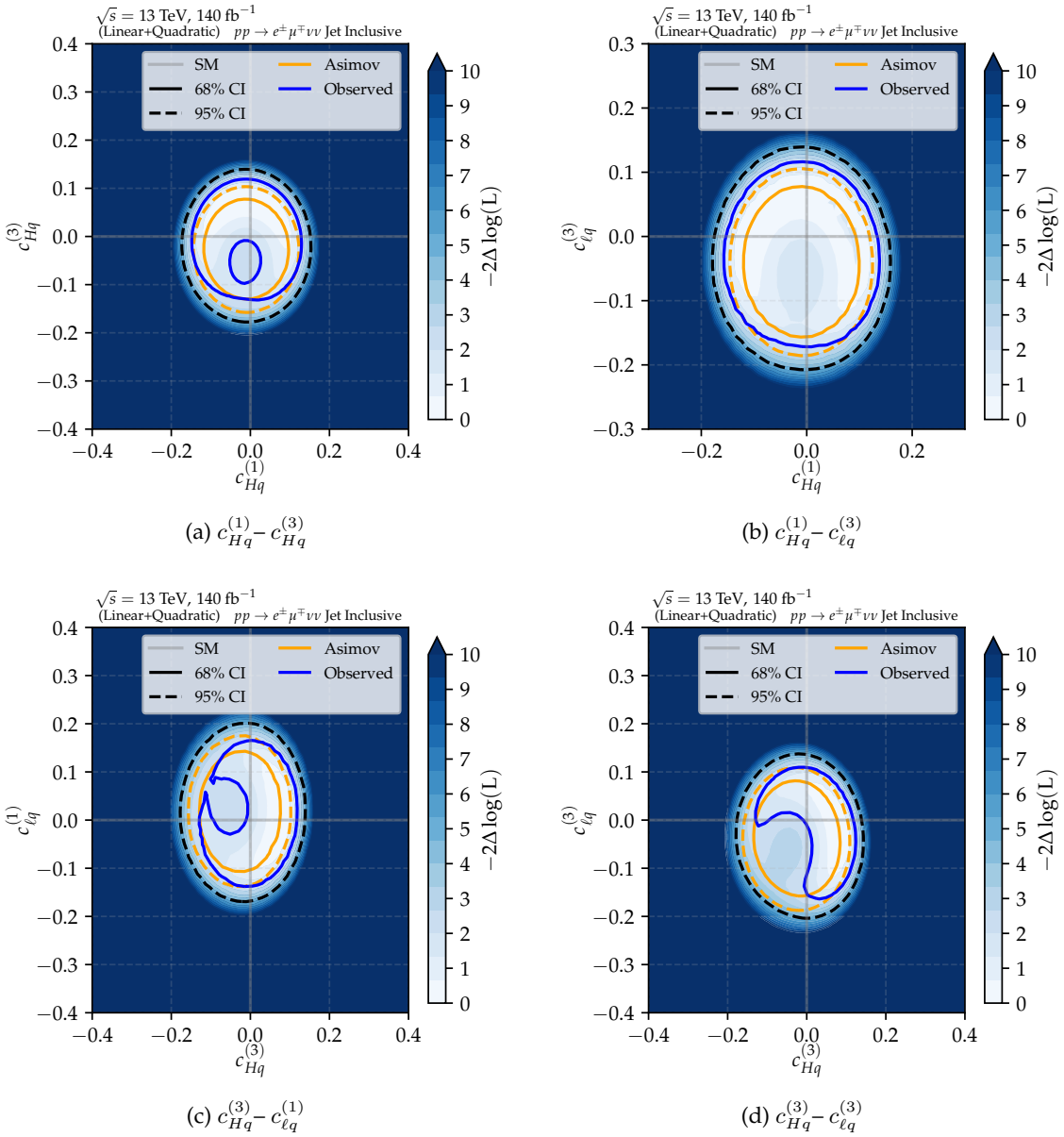

(a) $c_{Hq}^{(1)}$– $c_{Hq}^{(3)}$ (b) $c_{Hq}^{(1)}$– $c_{\ell q}^{(3)}$

(c) $c_{Hq}^{(3)}$– $c_{\ell q}^{(1)}$ (d) $c_{Hq}^{(3)}$– $c_{\ell q}^{(3)}$

Figure 11.11: Contours with two-dimensional log-likelihood scans of $-2\Delta \ln \mathrm{L} = -2(\ln \mathrm{L} - \ln \mathrm{L}_{\min})$ resulting from fits to Asimov (orange) and experimental (blue) data binned as a function of $p_T^{\text{lead. lep.}}$ for the (a) $c_{H\ell}^{(1)}$–$c_{Hq}^{(3)}$, (b) $c_{Hq}^{(1)}$–$c_{\ell q}^{(3)}$, (c) $c_{Hq}^{(3)}$–$c_{\ell q}^{(1)}$, and (d) $c_{Hq}^{(3)}$–$c_{\ell q}^{(3)}$ pairs of Wilson coefficients, considering linear and quadratic terms in the SMEFT Lagrangian given in Eq. (11.1). Confidence intervals at 68 % (solid) and 95 % (dashed) confidence level are displayed. The solid gray lines shows the SM prediction. The energy scale of new physics is set to $\Lambda = 1$ TeV.

Summary

The measurement of W-boson pair production cross sections at hadron colliders is an important test of the Standard Model (SM). It is sensitive to the self-couplings of vector bosons and provides a test of the electroweak (EW) theory as well as perturbative Quantum Chromodynamics (QCD). In this thesis, a dataset of proton-proton (pp) collisions at a center-of-mass energy of $\sqrt{s} = 13$ TeV recorded between 2015 and 2018 with the ATLAS detector at the Large Hadron Collider (LHC), corresponding to an integrated luminosity of $140\ \mathrm{fb}^{-1}$, has been analyzed. The best signal-to-background ratio in W^+W^- production is achieved using fully-leptonic decays. With such a signature, large irreducible backgrounds arise mainly due to the production of top-quarks, dominated by $t\bar{t}$, and Drell-Yan $Z+\mathrm{jets}$. The former were traditionally suppressed by rejecting events with jets in the final state, which lead in increased theoretical and experimental uncertainties. For the first time, measurements of fiducial integrated and differential cross sections of W-boson pair production have been performed in a fully jet-inclusive phase space in this thesis, allowed by an accurate data-driven estimation of the $t\bar{t}$ and lepton misidentification backgrounds. The results have been publicly released in Ref. [87]. Selecting decays into one electron and one muon of opposite electric charge, Drell-Yan contributions are suppressed by requiring a dilepton invariant mass greater than $85\,\mathrm{GeV}$. Top-quark contributions, comprising $48\,\%$ of the overall SM prediction and $80\,\%$ of the total background within the fiducial region, are mitigated by rejecting events featuring jets involving b-hadron decays (b-jets).

Contributions from $t\bar{t}$ events are estimated by an in-situ determination of both the $t\bar{t}$ effective production cross section and the b-jet reconstruction efficiency bin by bin, using two regions with exactly one and two b-jets. Input from Monte Carlo (MC) simulations is required to infer the correlations between reconstructing the first and the second b-jet in the event. Single-top contributions, dominated by Wt production, are estimated using MC simulation. The estimation of background contributions due to lepton misidentification relies on the extrapolation from a control region where one of the leptons in the final state fulfills selection criteria designed to select mostly misidentified leptons. The extrapolation factors are determined in a region dominated by multijet production, where a lepton candidate recoiling against a jet is selected. The jet-flavor composition of the validation region of this background and the signal region is assessed by computing jet-flavor fractions in processes leading to lepton misidentification, dominated by $W+\mathrm{jets}$ and semileptonic $t\bar{t}$. Contributions from events containing prompt AntiID leptons yield $75\,\%$ of the total events in the control region used for the extrapolation. This contamination has to be subtracted from the data, ensuring a good modeling of these contributions by performing a dedicated calibration of the misidentified lepton selection criteria. This

calibration drastically reduces the associated uncertainties, becoming no longer a limiting factor in the precision of W^+W^- cross-section measurements. Events arising from Drell-Yan Z-boson and diboson (VZ and $V\gamma$, with $V = W^{\pm}, Z$) production are estimated using MC simulation. The modeling of each background source is validated in dedicated regions, where the data are well described within uncertainties.

Unfolded distributions across twelve differential observables related to the kinematics of leptons, jets, and E_T^{miss} in the event are reported in a fiducial region defined at particle level close to the signal region. The measurements are compared to state-of-the-art theoretical predictions. A fixed-order calculation at nNNLO QCD [247] using NNPDF3.1@NNLO LUXQED [493, 186] gives a good description of differential cross sections. The multiplicative combination with EW corrections improves the description of some observables while it does not represent an adequate description in other cases, as the combination cannot take into account non-factorizing EW-QCD effects [231]. Predictions matched to parton showers, generated with POWHEG MINNLO +PYTHIA 8 [216, 147] and SHERPA 2.2.12 [148], better describe bins dominated by events with small p_T of the W^+W^- system or high jet activity. Within uncertainties, the predictions are observed to be in excellent agreement with the measurement. The integrated fiducial cross section is obtained by multiplying the unconditional maximum-likelihood estimate of the signal strength modifier times the fiducial cross section prediction of the signal model at particle level, accounting for all theoretical and experimental systematic uncertainties as Gaussian nuisance parameters in the profile likelihood fit. A fiducial cross section of

$$\sigma_{\text{fid}}(pp \to e^{\pm}\nu_e\mu^{\mp}\nu_\mu) = 707 \pm 7\,(\text{stat.}) \pm 20\,(\text{syst.})\,\text{fb}$$

is measured, with a total uncertainty of $3.1\,\%$ dominated by systematic uncertainties of top-quark and lepton misidentification background estimates. The fit strongly reduces the dominating uncertainties from the background estimates, especially from the top-quark background. Based on the acceptance calculated at NNNLO(QCD)⊗NLO(EW) with the MATRIX prediction, a total cross section of W^+W^- production of

$$\sigma\,(pp \to W^+W^-) = 127 \pm 1\,(\text{stat.}) \pm 4\,(\text{syst.})\,\text{pb}\,,$$

is obtained after the extrapolation of the fiducial cross-section measurement to the full phase space. The MATRIX prediction $\sigma_{\text{MATRIX}}\,(pp \to W^+W^-) = 123 \pm 1\,(\text{PDF}) \pm 2\,(\text{scale})\,\text{pb}$ at NNNLO(QCD)⊗NLO(EW) is in excellent agreement with the reported cross-section measurement and previous LHC results at center-of-mass energies of $\sqrt{s} = 13$ TeV.

The distribution of reconstructed number of events as a function of the transverse momentum of the leading lepton provides the best sensitivity to constrain anomalous couplings in the context of an Effective Field Theory using the SM degrees of freedom and local gauge symmetries. No deviations from the SM expectation are observed, and limits to the magnitude of eleven couplings between gauge vector bosons, the Higgs scalar field, and fermions are derived at $95\,\%$ confidence level. The observed constraints improve previous results by a factor of 2, owing to the increased dataset, enhanced precision and sensitivity to $q\bar{q} \to WW$ production in the jet-inclusive region. The results are compared to global fits of top-quark, Higgs, electroweak measurements, finding a similar or even better sensitivity for some Wilson coefficients. This highlights the relevance of the presented W^+W^- cross-section measurements for future iterations of SMEFT global fits.

The instantaneous luminosity delivered by the LHC is rising since 2022, increasing the average number of collisions per bunch crossing by up to a factor of 4 during the operation of the High-Luminosity LHC. This presents numerous challenges to overcome for a successful physics program. Upgrades were carried out between 2019 and 2022 to address these, involving the replacement of the innermost muon chambers in the ATLAS detector's endcaps with the New Small Wheels (NSWs). A new laboratory to test small-strip Thin Gap Chambers, one of the main technologies of the NSW, has been commissioned in Freiburg. The design, installation, and validation of gas and high-voltage systems necessary for operating a sTGC prototype under nominal data-taking conditions are reported in this thesis, including the implementation of monitoring and control systems to ensure secure and effective remote operation.

Appendix A
Additional Results on the Top Background

A.1 Derivation of the b-tag Counting Method

The b-tag counting method is a data-driven technique used to estimate the $t\bar{t}$ background contributions, performed in each individual bin for the differential measurements. Following the procedure used in a measurement of the $t\bar{t}$ production cross-section [477] and in the measurement of $WW+\geq 1\,\text{jets}$ production [81], two regions requiring exactly one and exactly two b-tagged jets are defined on a common selection baseline. The number of $t\bar{t}$ events with exactly two b-jets is given by

$$N_{2b}^{t\bar{t}} = \mathcal{L}\sigma_{t\bar{t}}\varepsilon_{e\mu} \cdot \varepsilon_{bb} \,, \tag{A.1}$$

where $\mathcal{L}$ is the integrated luminosity, $\sigma_{t\bar{t}}$ the $t\bar{t}$ cross-section, $\varepsilon_{e\mu}$ is the selection efficiency, and ε_{bb} is the efficiency to find and tag two b-jets in a $t\bar{t}$ event simultaneously. $\mathcal{L}\sigma_{t\bar{t}}\varepsilon_{e\mu}$ then provides the number of $t\bar{t}$ events in the given region selected with efficiency $\varepsilon_{e\mu}$, denoted to as $N_{\geq 0b}^{t\bar{t}}$, which in this analysis corresponds to the number of $t\bar{t}$ events without requirements on the b-jet multiplicity. The number of events with exactly one b-jet can be written as

$$N_{1b}^{t\bar{t}} = N_{\geq 0b}^{t\bar{t}} \cdot 2\left(\varepsilon_b - \varepsilon_{bb}\right) \,. \tag{A.2}$$

Here, ε_b accounts for the efficiency of the b-tagging algorithm as well as the acceptance of b-jets. This includes events where additionally the second b-jet is tagged, which thus have to be subtracted. The factor two comes from the two available b-jets in $t\bar{t}$ events.

After introducing the b-tagging correlation factor $C_b = \varepsilon_{bb}/\varepsilon_b^2$, which accounts for the fact that tagging one b-jet can in principle affects the efficiency of tagging the second b-jet, the two equations can be written as

$$N_{1b}^{t\bar{t}} = N_{\geq 0b}^{t\bar{t}} \cdot 2\varepsilon_b\left(1 - C_b\varepsilon_b\right) \,, \tag{A.3}$$

$$N_{2b}^{t\bar{t}} = N_{\geq 0b}^{t\bar{t}} \cdot C_b\varepsilon_b^2 \,. \tag{A.4}$$

The number of $t\bar{t}$ events with zero b-jets are then given by all $t\bar{t}$ events that do not have one or two b-jets:

$$N_{0b}^{t\bar{t}} = N_{\geq 0b}^{t\bar{t}} \cdot \left(1 - 2\varepsilon_b\left(1 - C_b\varepsilon_b\right) - C_b\varepsilon_b^2\right) \tag{A.5}$$

$$= N_{\geq 0b}^{t\bar{t}} \cdot \left(1 - 2\varepsilon_b + C_b\varepsilon_b^2\right) \,. \tag{A.6}$$

The number of observed events in data can thus be written as

$$N_{0b} = N_{\geq 0b}^{t\bar{t}} \cdot \left(1 - 2\varepsilon_b + C_b\varepsilon_b^2\right) + N_{0b}^{\text{bkg}} \,, \tag{A.7}$$

$$N_{1b} = N_{\geq 0b}^{t\bar{t}} \cdot 2\varepsilon_b \left(1 - C_b\varepsilon_b\right) + N_{1b}^{\text{bkg}} \,, \tag{A.8}$$

$$N_{2b} = N_{\geq 0b}^{t\bar{t}} \cdot C_b\varepsilon_b^2 + N_{2b}^{\text{bkg}} \,, \tag{A.9}$$

By measuring N_{1b} and N_{2b} in data, the effective b-tagging efficiency as well as the effective $t\bar{t}$ cross-section ($N_{\geq 0b}^{t\bar{t}}$) can be calculated. This also applies in regions of phase space requiring events with less than two jets, since b-tagged jets are selected with a lower p_T threshold (20 GeV) than regular jets (30 GeV). The number of $t\bar{t}$ events with no reconstructed b-jets in the final state can hence be inferred as

$$\varepsilon_b = \frac{2N_{2b}^{t\bar{t}}}{C_b\left(N_{1b}^{t\bar{t}} + 2N_{2b}^{t\bar{t}}\right)} \tag{A.10}$$

$$N_{\geq 0b}^{t\bar{t}} = \frac{C_b}{4}\frac{\left(N_{1b}^{t\bar{t}} + 2N_{2b}^{t\bar{t}}\right)^2}{N_{2b}^{t\bar{t}}} \tag{A.11}$$

$$\implies N_{0b}^{t\bar{t}} = N_{\geq 0b}^{t\bar{t}} \cdot \left(1 - 2\varepsilon_b + C_b\varepsilon_b^2\right) = \frac{C_b}{4}\frac{\left(N_{1b}^{t\bar{t}} + 2N_{2b}^{t\bar{t}}\right)^2}{N_{2b}^{t\bar{t}}} \tag{A.12}$$

where $N_{kb}^{t\bar{t}} = N_{kb} - N_{kb}^{\text{bkg}}$ for $k = 1, 2$. The *b-tagging correlation factor* C_b is estimated from $t\bar{t}$ MC simulation. This constitutes the only input that is susceptible to $t\bar{t}$ modeling uncertainties in the b-tag counting method. The correlation factor C_b is derived as follows,

$$C_b = \frac{4 \cdot N_{\text{MC}}^{t\bar{t}} N_{2b,\text{MC}}^{t\bar{t}}}{\left(N_{1b,\text{MC}}^{t\bar{t}} + 2 \cdot N_{2b,\text{MC}}^{t\bar{t}}\right)^2} \,, \tag{A.13}$$

with $N_{\text{MC}}^{t\bar{t}} = N_{0b,\text{MC}}^{t\bar{t}} + N_{1b,\text{MC}}^{t\bar{t}} + N_{2b,\text{MC}}^{t\bar{t}}$ and $N_{kb,\text{MC}}^{t\bar{t}}$ being the number of $t\bar{t}$ events estimated from MC with $k = 0, 1, 2$ selected b-jets.

A.2 Breakdown of the Systematic Uncertainties

Table A.1 shows the breakdown of systematic uncertainties on the top-quark background in the jet inclusive region, comparing the background estimate relying purely on the MC simulation using POWHEG + PYTHIA 8, the estimation of $t\bar{t}$ contributions via the b-tag counting method, as well as single-top quark production based on the MC simulation.

The transfer factor method is used in bins in which at least one of the $t\bar{t}$ control regions has 100 events or less. As shown in Figure A.1, this approach is found to be optimal. The predictions from both transfer factor and b-tag counting methods are in very good agreement.

Jet-inclusive	Top (MC)	Top (b-tag)	$t\bar{t}$	Single-top Wt
Events	68 273	68 273	53 211	12 828
Total unc.	± 10349 (15.2%)	± 2001 (2.9%)	± 3361 (6.3%)	± 4522 (35.3%)
Data stat.	± 0 (0.0%)	± 0 (0.0%)	± 0 (0.0%)	± 0 (0.0%)
Total syst.	± 10349 (15.2%)	± 2001 (2.9%)	± 3361 (6.3%)	± 4522 (35.3%)
MC stat.	± 63 (0.1%)	± 89 (0.1%)	± 100 (0.2%)	± 42 (0.3%)
STAT_CR1b	± 0 (0.0%)	± 243 (0.4%)	± 240 (0.5%)	± 0 (0.0%)
PRW_DATASF	± 281 (0.4%)	± 6 (0.0%)	± 41 (0.1%)	± 47 (0.4%)
FT_EFF_Eigen_B_0	± 4840 (7.1%)	± 890 (1.3%)	± 264 (0.5%)	± 614 (4.8%)
FT_EFF_Eigen_B_1	± 1093 (1.6%)	± 173 (0.3%)	± 44 (0.1%)	± 127 (1.0%)
FT_EFF_Eigen_B_2	± 734 (1.1%)	± 155 (0.2%)	± 67 (0.1%)	± 85 (0.7%)
FT_EFF_Eigen_Light_0	± 315 (0.5%)	± 1 (0.0%)	± 45 (0.1%)	± 42 (0.3%)
JET_BJES_Response	± 450 (0.7%)	± 59 (0.1%)	± 2 (0.0%)	± 61 (0.5%)
JET_EtaIntercalibration_Modelling	± 421 (0.6%)	± 48 (0.1%)	± 15 (0.0%)	± 63 (0.5%)
JET_EffectiveNP_Modelling1	± 559 (0.8%)	± 64 (0.1%)	± 14 (0.0%)	± 79 (0.6%)
JET_Flavor_Composition	± 49 (0.1%)	± 27 (0.0%)	± 10 (0.0%)	± 120 (0.9%)
JET_Flavor_Response	± 666 (1.0%)	± 60 (0.1%)	± 32 (0.1%)	± 64 (0.5%)
JET_Pileup_OffsetMu	± 218 (0.3%)	± 29 (0.0%)	± 2 (0.0%)	± 32 (0.3%)
JET_Pileup_OffsetNPV	± 517 (0.8%)	± 71 (0.1%)	± 4 (0.0%)	± 75 (0.6%)
JET_Pileup_RhoTopology	± 1587 (2.3%)	± 201 (0.3%)	± 20 (0.0%)	± 220 (1.7%)
JET_JER_EffectiveNP_2	± 264 (0.4%)	± 52 (0.1%)	± 22 (0.0%)	± 30 (0.2%)
FF_EWSUBTR	± 0 (0.0%)	± 0 (0.0%)	± 205 (0.4%)	± 0 (0.0%)
top_gen	± 5159 (7.6%)	± 747 (1.1%)	± 1430 (2.7%)	± 2172 (16.9%)
top_frag	± 4877 (7.1%)	± 1272 (1.9%)	± 1953 (3.7%)	± 3222 (25.1%)
top_isr	± 435 (0.6%)	± 8 (0.0%)	± 103 (0.2%)	± 107 (0.8%)
top_fsr	± 3131 (4.6%)	± 720 (1.1%)	± 292 (0.5%)	± 417 (3.3%)
top_interf	± 2038 (3.0%)	± 31 (0.0%)	± 2076 (3.9%)	± 2038 (15.9%)
ttbar_xs	± 3326 (4.9%)	± 0 (0.0%)	± 0 (0.0%)	± 0 (0.0%)
wt_xs	± 679 (1.0%)	± 14 (0.0%)	± 695 (1.3%)	± 679 (5.3%)
bcount_r32	± 0 (0.0%)	± 552 (0.8%)	± 527 (1.0%)	± 0 (0.0%)
lumi	± 546 (0.8%)	± 19 (0.1%)	± 77 (0.1%)	± 105 (0.8%)

Table A.1: Breakdown of systematic uncertainties on the top-quark background in the jet inclusive region. The first column gives the pure MC estimate for all top events ($t\bar{t}$ + Wt), compared to the b-tag counting estimate in the second column. The third column shows the b-tag counting estimate for $t\bar{t}$, and the last column the uncertainties in the Wt simulation alone. Uncertainties below $0.3\,\%$ are not shown. The data driven estimates are using pseudo-data, based on the nominal simulation.

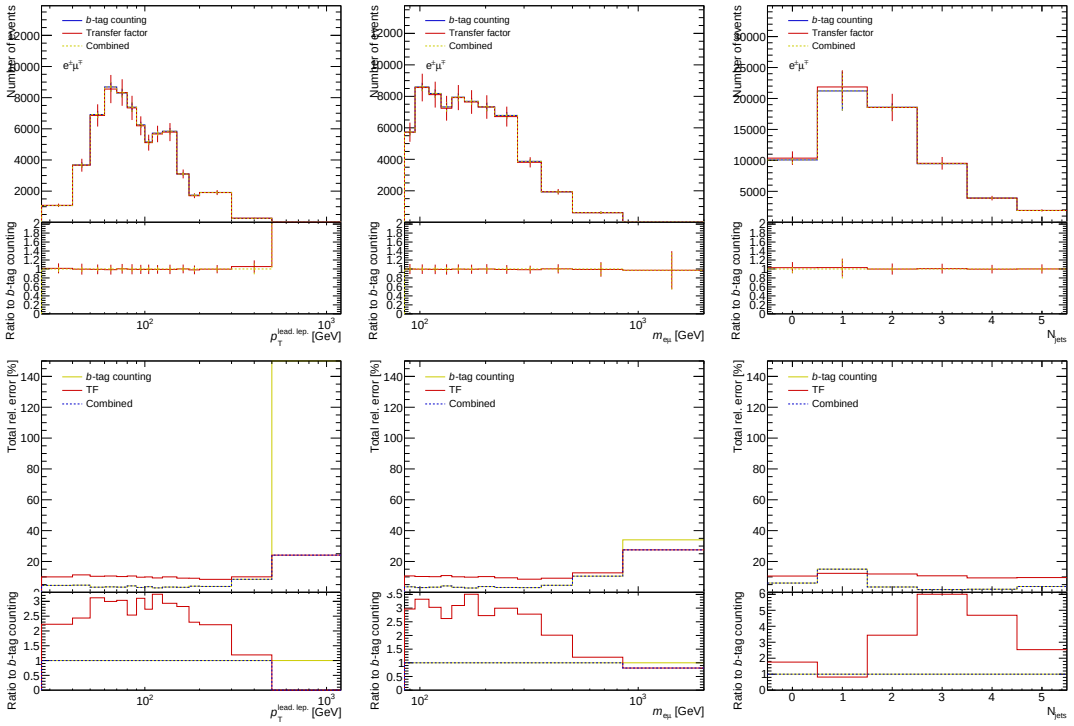

Figure A.1: Comparison of the (top) event yields within total uncertainties and (bottom) the total relative uncertainties of both *b*-tag counting and transfer factor methods for the top-quark background estimate in the jet-inclusive signal region. The chose method for the nominal analysis is labelled as ”Combined”.

Appendix B

Additional Results on the Lepton Misidentification Background

B.1 Fake Lepton Composition Studies Using `MCTruthClassifier`

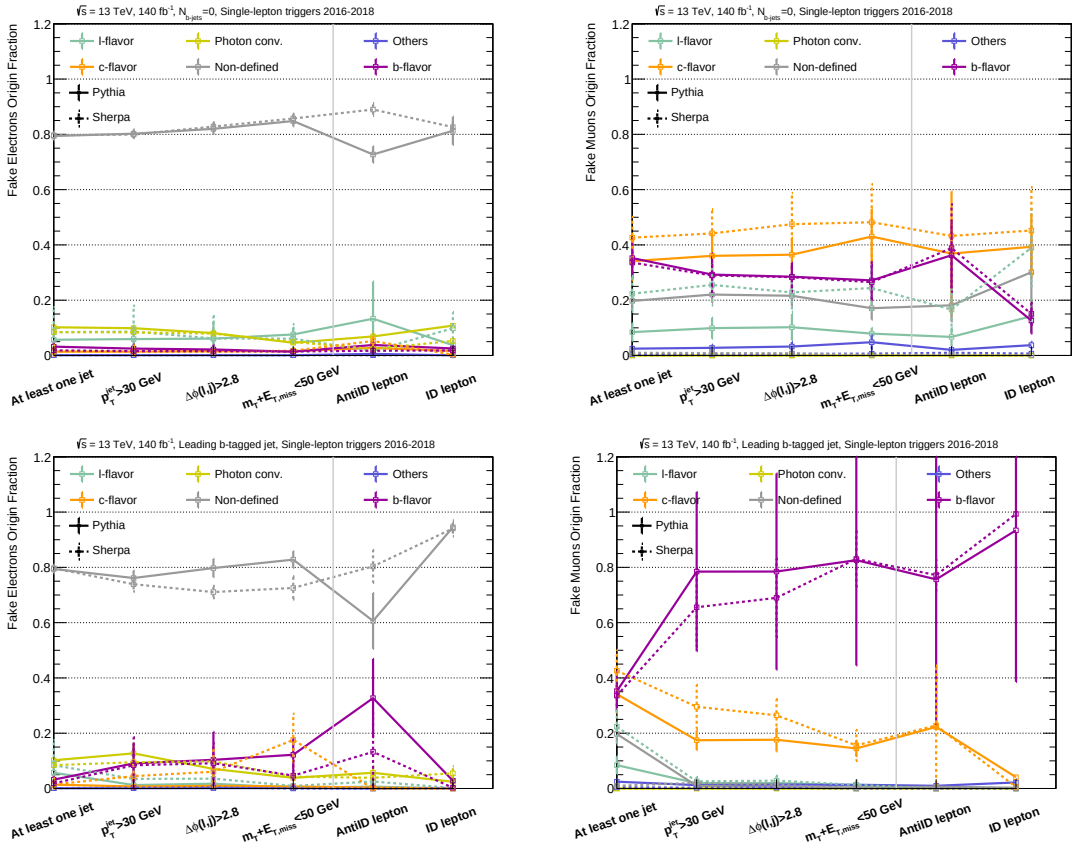

Figure B.1: `MCTruthClassifier` in dijets POWHEG + PYTHIA 8 (solid lines) and SHERPA (dashed lines), with triggers from 2016-2018. Sources with a composition lower than 2 % are not shown. Cuts on the right-hand side of the vertical gray line are not sequential. Only statistical uncertainties are displayed.

The sources of lepton misidentification are studied in the dijet region discussed in Section 8.4.3. The studies are carried out using MC simulation of multijet production, where no leptons are produced at generator level. Using single-lepton triggers between 2016 and 2018 (see Table 4.4), the origin process of the misreconstructed lepton is shown in Figure B.1 across the different stages of the dijet selection criteria presented in Table 8.5. A fraction of $82.6 \pm 0.05\,\%$ ($72.7 \pm 0.03\,\%$) of ID (AntiID) electrons are tagged as *non-*

defined. The fraction of *non-defined* AntiID electrons is larger in SHERPA ($89.0 \pm 0.02\,\%$). The largest disagreements between electron origin fractions from SHERPA and PYTHIA8 arise when applying the AntiID lepton selection. While a considerable fraction of fake ID (AntiID) electrons are produced after photon conversions and light-flavor decays when the leading jet is b-vetoed, light- (l-) and charm-flavored (c-flavor) fake electron production is rejected by the b-tag requirement on the leading jet. With this requirement, the majority of fake ID muons arise from heavy flavor decays. With a b-vetoed leading jet, $30\,\%$ of the fake muons are *non-defined*, fraction that drops to zero when the leading jet is b-tagged. The category *Others* is mainly composed by leptons produced after a decay of a τ lepton. Since a few dijet events events fulfill the lepton+jet selection, large statistical uncertainties limit the conclusions that can be drawn from this study.

B.2 Prompt AntiID lepton calibration factors

Distributions of the calibration factors for prompt AntiID electrons are shown in Figures B.2 and B.3 for regions B and C, respectively, for bins of $|\eta|$ within the inner detector acceptance as a function of the prompt AntiID lepton p_T. Similarly, scale factors for prompt AntiID muons are presented in Figures B.4 and B.5 for regions B and C. Systematic variations from the jet requirement in the selection criteria as well as variations observed across different data-taking campaigns for both prompt AntiID electrons and muons are displayed. Calibration factors derived at the Z-peak, whose selection is summarized in Table 8.6, are derived using either SHERPA or POWHEG + PYTHIA 8 MC simulation of $Z + \text{jets}$ events. The corrections derived at the $Z \to \tau^-\tau^+$ region (Table 8.7) rely on SHERPA 2.2.2 and are used to correct prompt AntiID electrons and muons from $Z \to \tau^-\tau^+$ MC simulation using SHERPA. Significant differences exist between the calibration factors for prompt AntiID leptons obtained from Z-peak (defined in Table 8.6) and $Z \to \tau^-\tau^+$ (Table 8.7) regions, surpassing the bounds of both statistical and systematic uncertainties. The simulation of prompt AntiID muons with $|d_0/\sigma_{d_0}| > 3$ is corrected using scale factors derived in a same-sign $t\bar{t}$ region defined in Table 8.6.

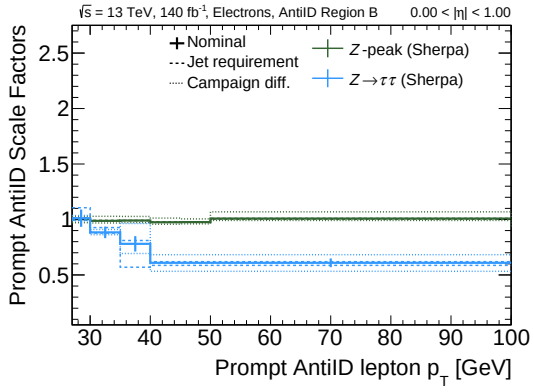

(a) $0.0 < |\eta| < 1.0$.

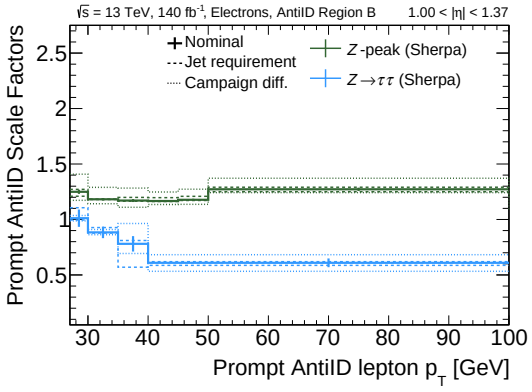

(b) $1.0 < |\eta| < 1.37$

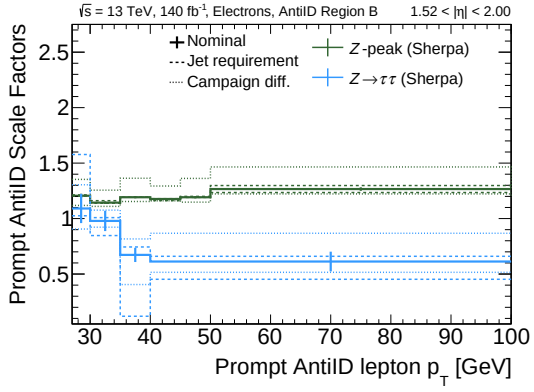

(c) $1.52 < |\eta| < 2.0$

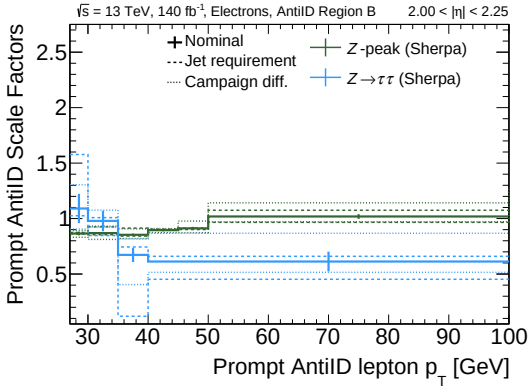

(d) $2.0 < |\eta| < 2.25$

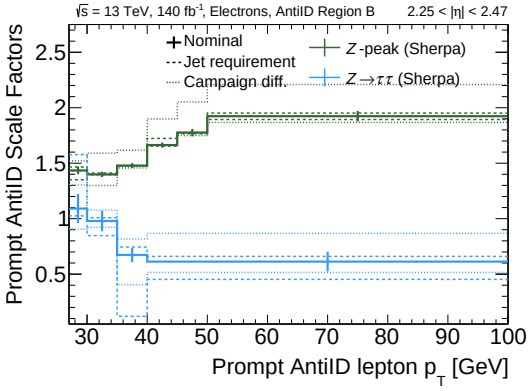

(e) $2.25 < |\eta| < 2.47$

Figure B.2: Prompt AntiID electron calibration factors in the AntiID region B at the Z-peak (Table 8.6, shown in green), and $Z \to \tau^-\tau^+$ regions (Table 8.7, shown in blue) in bins of $|\eta|$ (a) $0.0 < |\eta| < 1.0$, (b) $1.0 < |\eta| < 1.37$, (c) $1.52 < |\eta| < 2.0$, (d) $2.0 < |\eta| < 2.25$, and (e) $2.25 < |\eta| < 2.47$ Statistical uncertainties are displayed on the nominal scale factors. Systematic variations due to the jet-activity requirement (either jet-veto or one-jet-inclusive selection, displayed as dashed lines) and the envelope of differences across data-taking campaigns (dotted lines) are also compared to the nominal calibration factors (solid lines).

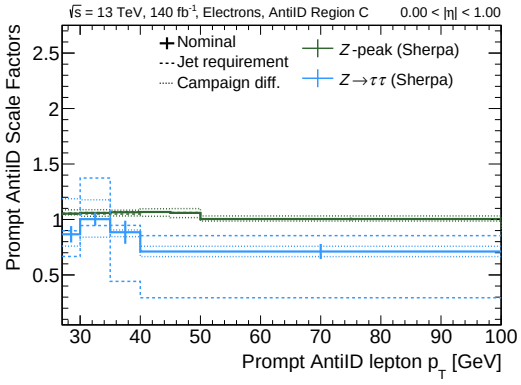

(a) $0.0 < |\eta| < 1.0$.

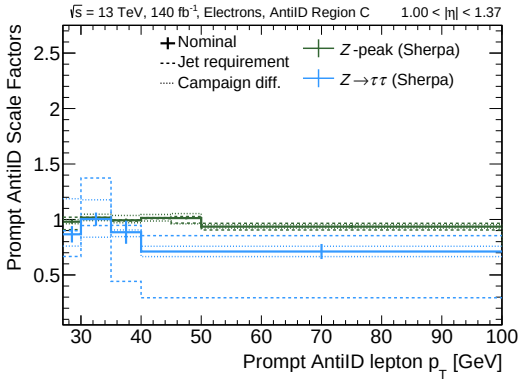

(b) $1.0 < |\eta| < 1.37$

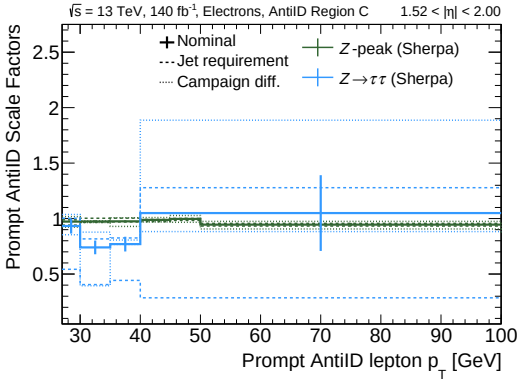

(c) $1.52 < |\eta| < 2.0$

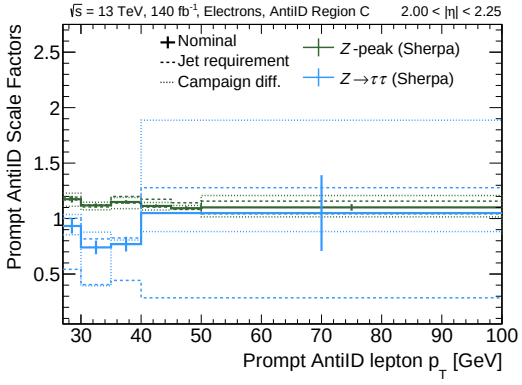

(d) $2.0 < |\eta| < 2.25$

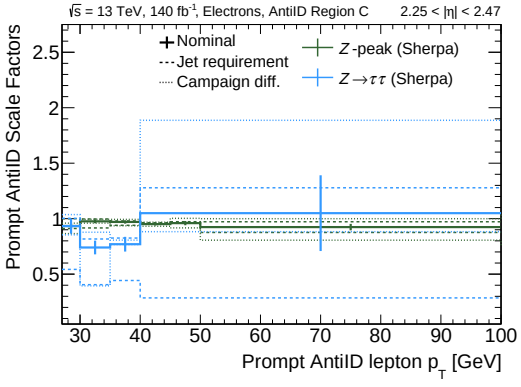

(e) $2.25 < |\eta| < 2.47$

Figure B.3: Prompt AntiID electron calibration factors in the AntiID region C at the Z-peak (Table 8.6, shown in green), and $Z \to \tau^-\tau^+$ regions (Table 8.7, shown in blue) in bins of $|\eta|$ (a) $0.0 < |\eta| < 1.0$, (b) $1.0 < |\eta| < 1.37$, (c) $1.52 < |\eta| < 2.0$, (d) $2.0 < |\eta| < 2.25$, and (e) $2.25 < |\eta| < 2.47$ Statistical uncertainties are displayed on the nominal scale factors. Systematic variations due to the jet-activity requirement (either jet-veto or one-jet-inclusive selection, displayed as dashed lines) and the envelope of differences across data-taking campaigns (dotted lines) are also compared to the nominal calibration factors (solid lines).

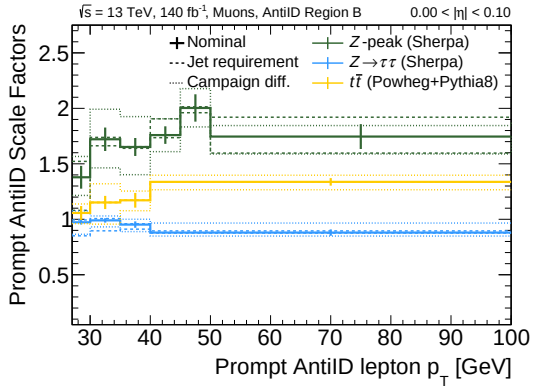

(a) $0.0 < |\eta| < 0.1$ in Region B.

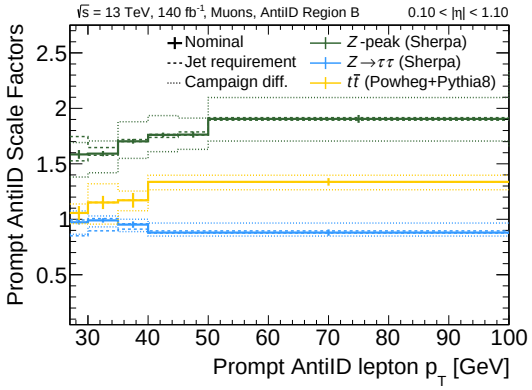

(b) AntiID $\mu^{\pm}$ with $0.1 < |\eta| < 1.1$ in Region B.

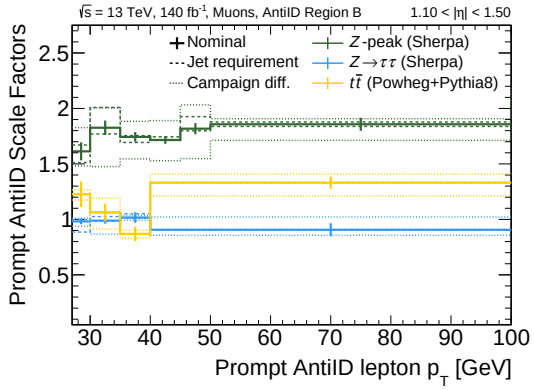

(c) AntiID $\mu^{\pm}$ with $1.1 < |\eta| < 1.7$ in Region B.

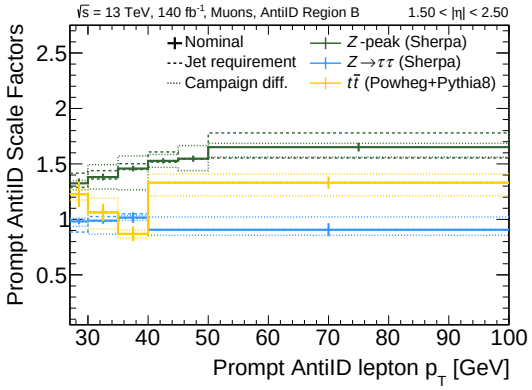

(d) AntiID $\mu^{\pm}$ with $1.7 < |\eta| < 2.5$ in Region B.

Figure B.4: Prompt AntiID muon calibration factors in the AntiID region B at the Z-peak (Table 8.6, shown in green), same-flavor $t\bar{t}$ (Table 8.6, shown in orange), and $Z \to \tau^{-}\tau^{+}$ regions (Table 8.7, shown in blue) in bins of $|\eta|$ (a) $0.0 < |\eta| < 0.1$, (b) $0.1 < |\eta| < 1.1$, (c) $1.1 < |\eta| < 1.7$, and (d) $1.7 < |\eta| < 2.5$. Statistical uncertainties are displayed on the nominal scale factors. Systematic variations due to the jet-activity requirement (either jet-veto or one-jet-inclusive selection, displayed as dashed lines) and the envelope of differences across data-taking campaigns (dotted lines) are also compared to the nominal calibration factors (solid lines). Scale factors in the $t\bar{t}$ region are derived only for muons with $|d_0/\sigma_{d_0}| > 3$ (region B) and are no subject to systematic variations due to the jet activity.

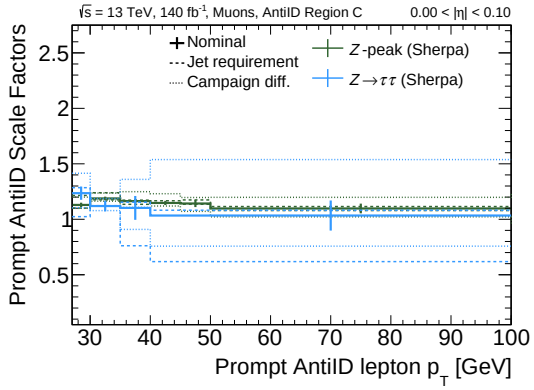

(a) $0.0 < |\eta| < 0.1$ in Region B.

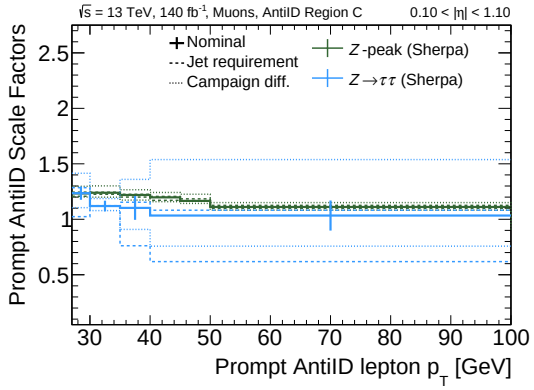

(b) AntiID $\mu^{\pm}$ with $0.1 < |\eta| < 1.1$ in Region B.

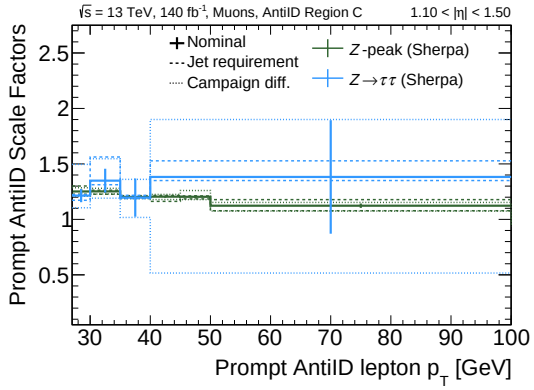

(c) AntiID $\mu^{\pm}$ with $1.1 < |\eta| < 1.7$ in Region B.

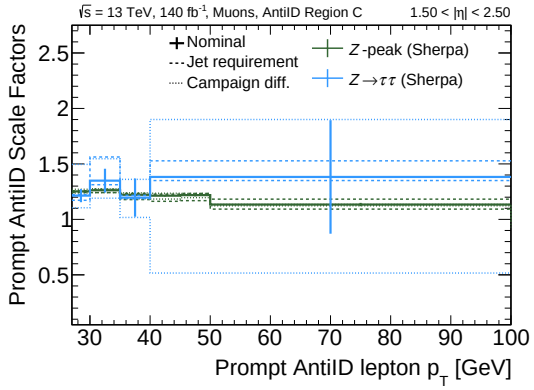

(d) AntiID $\mu^{\pm}$ with $1.7 < |\eta| < 2.5$ in Region B.

Figure B.5: Prompt AntiID muon calibration factors in the AntiID region C at the Z-peak (Table 8.6, shown in green), same-flavor $t\bar{t}$ (Table 8.6, shown in orange), and $Z \to \tau^{-}\tau^{+}$ regions (Table 8.7, shown in blue) in bins of $|\eta|$ (a) $0.0 < |\eta| < 0.1$, (b) $0.1 < |\eta| < 1.1$, (c) $1.1 < |\eta| < 1.7$, and (d) $1.7 < |\eta| < 2.5$. Statistical uncertainties are displayed on the nominal scale factors. Systematic variations due to the jet-activity requirement (either jet-veto or one-jet-inclusive selection, displayed as dashed lines) and the envelope of differences across data-taking campaigns (dotted lines) are also compared to the nominal calibration factors (solid lines). Scale factors in the $t\bar{t}$ region are derived only for muons with $|d_0/\sigma_{d_0}| > 3$ (region B) and are no subject to systematic variations due to the jet activity.

Appendix C
Additional Results

The total number of W^+W^- candidate events selected in the jet-inclusive signal region is presented in Figure C.1 as a function of the dilepton invariant mass $m_{e\mu}$, the subleading lepton transverse momentum $p_T^{\text{sublead. lep.}}$, the trasverse momentum of the dilepton system $p_T^{\ell\ell}$, the transverse mass of the dilepton system $m_{T,e\mu}$ (defined in Section 9.1.1), the sum of transverse momenta from leptons and jets in the final state S_T, and the sum of lepton transverse momenta and missing transverse energy $H_T^{\text{lep.+MET}}$. Similarly, Figure C.2 shows the number of selected events in the jet-inclusive signal region as a function of the absolute azimuthal difference between the two leptons $|\Delta\phi_{e\mu}|$, the magnitude of the transverse missing energy vector in the event E_T^{miss}, the value of the $\cos\theta^*$, and the absolute value of rapidity of the dilepton system $|y_{e\mu}|$. Expected contributions from signal and background predictions and their respective uncertainties, as estimated using the techniques considered in Chapter 8, are also shown as stacked histograms. Section 9.2 provides details on the calculation of the reported uncertainties. Approximately $60\,\%$ of events meeting requirements of the signal region selection are background events, with the top-quark background (either from $t\bar{t}$ or single-top Wt production) being the largest, constituting about $80\,\%$ of the total background in the signal region. The total number of events observed in data slightly exceeds the sum of estimated background and signal yields based on the SM predictions. Figure 10.1 presents a comparison of the observed number of events in data against the expected signal prediction, and the background estimate in bins of leading lepton p_T (Fig. 10.1a) and jet-multiplicity (Fig. 10.1b). A slight underprediction of data occurs at intermediate values of p_T (between 50 and $90\,\text{GeV}$) and low jet activity, attributed to the choice of the PDF set for the W^+W^- prediction as discussed in Section 9.3. Overall, good agreement between the SM prediction and data is observed.

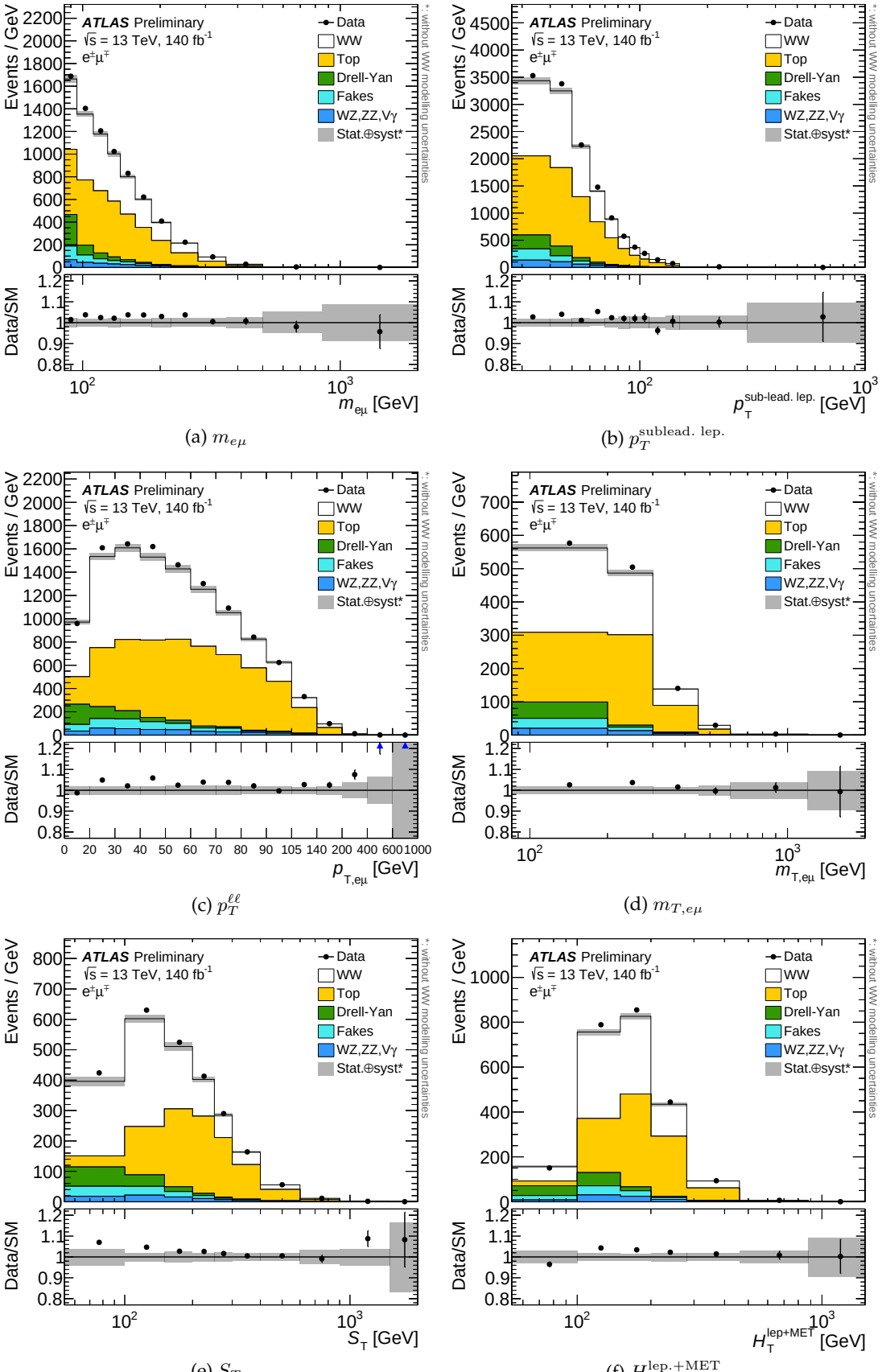

(a) $m_{e\mu}$ (b) $p_T^{\text{sublead. lep.}}$

(c) $p_T^{\ell\ell}$ (d) $m_{T,e\mu}$

(e) S_T (f) $H_T^{\text{lep.+MET}}$

Figure C.1: Detector-level distributions of (a) $m_{e\mu}$, (b) $p_T^{\text{sublead. lep.}}$, (c) $p_T^{\ell\ell}$, (d) $m_{T,e\mu}$, (e) S_T, and (f) $H_T^{\text{lep.+MET}}$ in the jet-inclusive signal region. Data are shown as black markers together with histograms for the predictions of signal and background processes. The rightmost bin contains overflow events. The lower panels show the ratio of the data to the total prediction. Top and fake backgrounds are determined using data-driven methods. The displayed uncertainty bands include statistical and systematic uncertainties, excluding theory uncertainties on the signal, which largely cancel in the measurement of W^+W^- cross-sections. Published in Ref. [87].

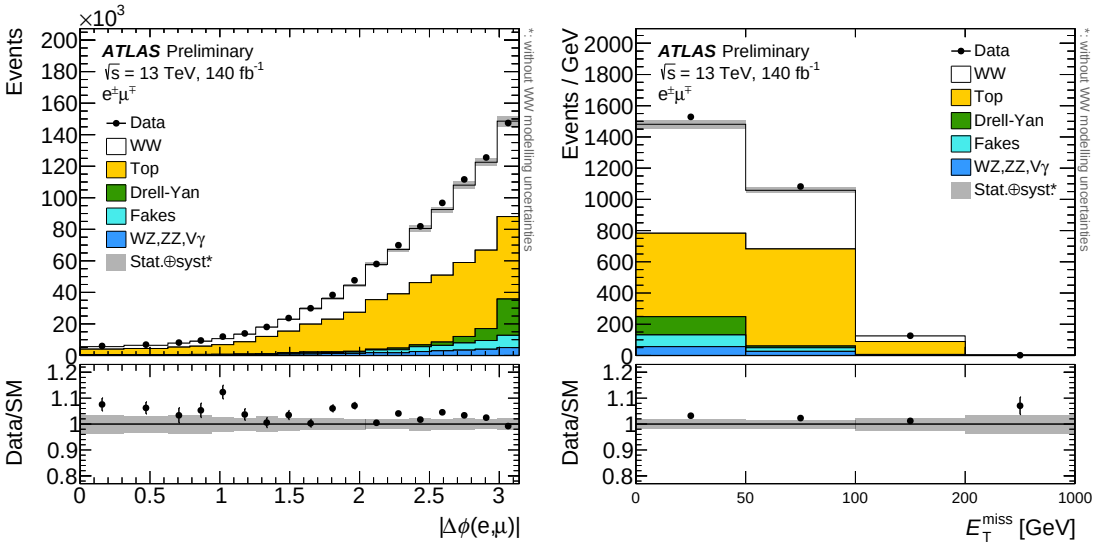

(a) $|\Delta\phi_{e\mu}|$ (b) E_T^{miss}

(c) $\cos\theta^*$ (d) $|y_{e\mu}|$

Figure C.2: Detector-level distributions of (a) $|\Delta\phi_{e\mu}|$, (b) E_T^{miss}, (c) $\cos\theta^*$, and (d) $|y_{e\mu}|$ in the jet-inclusive signal region. Data are shown as black markers together with histograms for the predictions of signal and background processes. The rightmost bin contains overflow events. The lower panels show the ratio of the data to the total prediction. Top and fake backgrounds are determined using data-driven methods. The displayed uncertainty bands include statistical and systematic uncertainties, excluding theory uncertainties on the signal, which largely cancel in the measurement of W^+W^- cross-sections. Published in Ref. [87].

List of Figures

List of Tables

References

[1] J. C. Maxwell, *Treatise on Electricity and Magnetism*, *Dover, New York* **2** (1854) .

[2] J. J. Thomson, *Cathode rays*, *Phil. Mag. Ser. 5* **44** (1897) 293.

[3] J. J. Thomson, *On the structure of the atom: an investigation of the stability and periods of oscillation of a number of corpuscles arranged at equal intervals around the circumference of a circle; with application of the results to the theory of atomic structure*, *Phil. Mag. Ser. 6* **7** (1904) 237.

[4] A. Einstein, *Concerning an heuristic point of view toward the emission and transformation of light*, *Annalen Phys.* **17** (1905) 132.

[5] M. Planck, *On the Law of Distribution of Energy in the Normal Spectrum*, *Annalen Phys.* **4** (1901) 553.

[6] A. H. Compton, *The spectrum of scattered X-rays*, *Phys. Rev.* **22** (1923) 409.

[7] A. H. Compton, *A Quantum Theory of the Scattering of X-rays by Light Elements*, *Phys. Rev.* **21** (1923) 483.

[8] C. D. Anderson, *The Positive Electron*, *Phys. Rev.* **43** (1933) 491.

[9] P. A. M. Dirac, *The quantum theory of the electron*, *Proc. Roy. Soc. Lond. A* **117** (1928) 610.

[10] S. H. Neddermeyer and C. D. Anderson, *Note on the Nature of Cosmic Ray Particles*, *Phys. Rev.* **51** (1937) 884.

[11] F. Reines and C. L. Cowan, *Detection of the free neutrino*, *Phys. Rev.* **92** (1953) 830.

[12] R. Davis, Jr. and D. S. Harmer, *Attempt to observe the $Cl^{37}(\bar{\nu}e^{-})Ar^{37}$ reaction induced by reactor antineutrinos*, *Bull. Am. Phys. Soc.* **4** (1959) 217.

[13] B. Pontecorvo, *Electron and Muon Neutrinos*, *Zh. Eksp. Teor. Fiz.* **37** (1959) 1751.

[14] G. Danby, J. M. Gaillard, K. A. Goulianos, L. M. Lederman, N. B. Mistry, M. Schwartz et al., *Observation of High-Energy Neutrino Reactions and the Existence of Two Kinds of Neutrinos*, *Phys. Rev. Lett.* **9** (1962) 36.

[15] F. Reines and C. L. Cowan, *A Proposed experiment to detect the free neutrino*, *Phys. Rev.* **90** (1953) 492.

[16] C. L. Cowan, F. Reines, F. B. Harrison, E. C. Anderson and F. N. Hayes, *Large liquid scintillation detectors*, *Phys. Rev.* **90** (1953) 493.

[17] E. J. Konopinski and H. M. Mahmoud, *The Universal Fermi interaction*, *Phys. Rev.* **92** (1953) 1045.

[18] M. Gell-Mann and Y. Ne'eman, *The Eightfold way: a review with a collection of reprints*. New York, W.A. Benjamin, 1964.

[19] V. E. Barnes et al., *Confirmation of the existence of the Ω^{-} hyperon*, *Phys. Lett.* **12** (1964) 134.

[20] M. Gell-Mann, *A Schematic Model of Baryons and Mesons*, in *50 years of quarks*, pp. 1–4, (2015), DOI.

[21] G. Zweig, *An SU(3) model for strong interaction symmetry and its breaking*, in *Developments in the quark theory of hadrons*, pp. 22–101, (1964).

[22] A. Petermann, *Propriétés de l'étrangeté et une formule de masse pour les mésons vectoriels*, *Nucl. Phys.* **63** (1965) 349.

[23] O. W. Greenberg, *Spin and Unitary Spin Independence in a Paraquark Model of Baryons and Mesons*, *Phys. Rev. Lett.* **13** (1964) 598.

[24] Y. Nambu, *The Confinement of Quarks*, *Sci. Am.* **235N5** (1976) 48.

[25] JADE collaboration, *Observation of Planar Three Jet Events in $e^{+}e^{-}$ Annihilation and Evidence for Gluon Bremsstrahlung*, *Phys. Lett. B* **91** (1980) 142.

[26] D. J. Gross and F. Wilczek, *Ultraviolet Behavior of Nonabelian Gauge Theories*, *Phys. Rev. Lett.* **30** (1973) 1343.

[27] D. J. Gross and F. Wilczek, *Asymptotically Free Gauge Theories - I*, *Phys. Rev. D* **8** (1973) 3633.

[28] H. D. Politzer, *Reliable Perturbative Results for Strong Interactions?*, *Phys. Rev. Lett.* **30** (1973) 1346.

[29] H. D. Politzer, *Asymptotic Freedom: An Approach to Strong Interactions*, *Phys. Rept.* **14** (1974) 129.

[30] D. d'Enterria et al., *The strong coupling constant: State of the art and the decade ahead*, *Snowmass 2021* (2022) [2203.08271].

[31] E. Fermi, *An attempt of a theory of beta radiation. 1.*, *Z. Phys.* **88** (1934) 161.

[32] C. S. Wu, E. Ambler, R. W. Hayward, D. D. Hoppes and R. P. Hudson, *Experimental Test of Parity Conservation in β Decay*, *Phys. Rev.* **105** (1957) 1413.

[33] S. L. Glashow, *The renormalizability of vector meson interactions*, *Nucl. Phys.* **10** (1959) 107.

[34] A. Salam and J. C. Ward, *Weak and electromagnetic interactions*, *Nuovo Cim.* **11** (1959) 568.

[35] S. Weinberg, *A Model of Leptons*, *Phys. Rev. Lett.* **19** (1967) 1264.

[36] G. 't Hooft, *Renormalizable Lagrangians for Massive Yang-Mills Fields*, *Nucl. Phys. B* **35** (1971) 167.

[37] G. 't Hooft and M. J. G. Veltman, *Regularization and Renormalization of Gauge Fields*, *Nucl. Phys. B* **44** (1972) 189.

[38] GARGAMELLE NEUTRINO collaboration, *Observation of Neutrino Like Interactions Without Muon Or Electron in the Gargamelle Neutrino Experiment*, *Phys. Lett. B* **46** (1973) 138.

[39] UA1 collaboration, *Experimental Observation of Isolated Large Transverse Energy Electrons with Associated Missing Energy at $\sqrt{s} = 540\,\mathrm{GeV}$*, *Phys. Lett. B* **122** (1983) 103.

[40] UA2 collaboration, *Observation of Single Isolated Electrons of High Transverse Momentum in Events with Missing Transverse Energy at the CERN $p\bar{p}$ Collider*, *Phys. Lett. B* **122** (1983) 476.

[41] UA1 collaboration, *Experimental Observation of Lepton Pairs of Invariant Mass Around 95 GeV/c^2 at the CERN SPS Collider*, *Phys. Lett. B* **126** (1983) 398.

[42] UA2 collaboration, *Evidence for $Z^0 \to e^+e^-$ at the CERN $\bar{p}p$ Collider*, *Phys. Lett. B* **129** (1983) 130.

[43] J. Gareyte, *The CERN $p\bar{p}$ Complex*, *Experientia* **40** (1980) 79.

[44] H. Koziol and D. Mohl, *The CERN antiproton collider programme: accelerators and accumulation rings*, *Phys. Rept.* **403-404** (2004) 91.

[45] A. Astbury et al., *A 4π solid angle detector for the SPS used as a proton-antiproton collider at a centre of mass energy of $540\,\mathrm{GeV}$*, *CERN-SPSC-78-06* (1978) .

[46] E598 collaboration, *Experimental Observation of a Heavy Particle J*, *Phys. Rev. Lett.* **33** (1974) 1404.

[47] SLAC-SP-017 collaboration, *Discovery of a Narrow Resonance in e^+e^- Annihilation*, *Phys. Rev. Lett.* **33** (1974) 1406.

[48] KTEV collaboration, *Observation of direct CP violation in $K_{S,L} \to \pi\pi$ decays*, *Phys. Rev. Lett.* **83** (1999) 22 [hep-ex/9905060].

[49] NA48 collaboration, *A New measurement of direct CP violation in two pion decays of the neutral kaon*, *Phys. Lett. B* **465** (1999) 335 [hep-ex/9909022].

[50] M. Kobayashi and T. Maskawa, *CP Violation in the Renormalizable Theory of Weak Interaction*, *Prog. Theor. Phys.* **49** (1973) 652.

[51] E288 collaboration, *Observation of a Dimuon Resonance at $9.5\,\mathrm{GeV}$ in $400\,\mathrm{GeV}$ Proton-Nucleus Collisions*, *Phys. Rev. Lett.* **39** (1977) 252.

[52] M. L. Perl et al., *Evidence for Anomalous Lepton Production in e^+e^- Annihilation*, *Phys. Rev. Lett.* **35** (1975) 1489.

[53] CDF collaboration, *Evidence for top quark production in $\bar{p}p$ collisions at $\sqrt{s} = 1.8\,\mathrm{TeV}$*, *Phys. Rev. Lett.* **73** (1994) 225 [hep-ex/9405005].

[54] ALEPH, DELPHI, L3, OPAL, SLD, LEP ELECTROWEAK WORKING GROUP, SLD ELECTROWEAK GROUP, SLD HEAVY FLAVOUR GROUP collaboration, *Precision electroweak measurements on the Z resonance*, *Phys. Rept.* **427** (2006) 257 [hep-ex/0509008].

[55] *LEP Design Report Vol.1: The LEP Injector Chain*, *CERN-LEP-TH-83-29* (1983) .

[56] *LEP Design Report: Vol.2. The LEP Main Ring*, *CERN-LEP-84-01* (1984) .

[57] *LEP Design Report: Vol.3: LEP2*, *CERN-AC/96-01* (1996) .

[58] DONUT collaboration, *Observation of tau neutrino interactions*, *Phys. Lett. B* **504** (2001) 218 [hep-ex/0012035].

[59] ALEPH, DELPHI, L3, OPAL, LEP ELECTROWEAK collaboration, *Electroweak Measurements in Electron-Positron Collisions at W-Boson-Pair Energies at LEP*, *Phys. Rept.* **532** (2013) 119 [1302.3415].

[60] B. W. Lee, C. Quigg and H. B. Thacker, *Weak Interactions at Very High-Energies: The Role of the Higgs Boson Mass*, *Phys. Rev. D* **16** (1977) 1519.

[61] S. Dittmaier and M. Schumacher, *The Higgs Boson in the Standard Model - From LEP to LHC: Expectations, Searches, and Discovery of a Candidate*, *Prog. Part. Nucl. Phys.* **70** (2013) 1 [1211.4828].

[62] O. S. Brüning, P. Collier, P. Lebrun, S. Myers, R. Ostojic, J. Poole et al., *LHC Design Report*, vol. 1 of *CERN Yellow Reports: Monographs*. CERN, Geneva, 2004, 10.5170/CERN-2004-003-V-1.

[63] O. S. Brüning, P. Collier, P. Lebrun, S. Myers, R. Ostojic, J. Poole et al., *LHC Design Report*, vol. 2 of *CERN Yellow Reports: Monographs*. CERN, Geneva, 2004, 10.5170/CERN-2004-003-V-2.

[64] M. Benedikt, P. Collier, V. Mertens, J. Poole and K. Schindl, *LHC Design Report*, vol. 3 of *CERN Yellow Reports: Monographs*. CERN, Geneva, 2004, 10.5170/CERN-2004-003-V-3.

[65] G. S. Guralnik, C. R. Hagen and T. W. B. Kibble, *Global Conservation Laws and Massless Particles*, *Phys. Rev. Lett.* **13** (1964) 585.

[66] F. Englert and R. Brout, *Broken Symmetry and the Mass of Gauge Vector Mesons*, *Phys. Rev. Lett.* **13** (1964) 321.

[67] P. W. Higgs, *Broken Symmetries and the Masses of Gauge Bosons*, *Phys. Rev. Lett.* **13** (1964) 508.

[68] ATLAS collaboration, *Evidence for the spin-0 nature of the Higgs boson using ATLAS data*, *Phys. Lett.* **B726** (2013) 120 [1307.1432].

[69] CMS collaboration, *Observation of a New Boson at a Mass of* $125\,\mathrm{GeV}$ *with the CMS Experiment at the LHC*, *Phys. Lett.* **B716** (2012) 30 [1207.7235].

[70] ATLAS collaboration, *Improved W boson Mass Measurement using* $7\,\mathrm{TeV}$ *Proton-Proton Collisions with the ATLAS Detector*, *ATLAS-CONF-2023-004* (2023) .

[71] ATLAS collaboration, *A precise determination of the strong-coupling constant from the recoil of Z bosons with the ATLAS experiment at* $\sqrt{s} = 8\,\mathrm{TeV}$, *ATLAS-CONF-2023-015* (2023) .

[72] CMS collaboration, *Measurements of the electroweak diboson production cross sections in proton-proton collisions at* $\sqrt{s} = 5.02\,\mathrm{TeV}$ *using leptonic decays*, *Phys. Rev. Lett.* **127** (2021) 191801 [2107.01137].

[73] ATLAS collaboration, *Measurement of* W^+W^- *production in pp collisions at* $\sqrt{s} = 7\,\mathrm{TeV}$ *with the ATLAS detector and limits on anomalous* WWZ *and* $WW\gamma$ *couplings*, *Phys. Rev. D* **87** (2013) 112001 [1210.2979].

[74] CMS collaboration, *Measurement of the* W^+W^- *Cross Section in pp Collisions at* $\sqrt{s} = 7\ \mathrm{TeV}$ *and Limits on Anomalous* $WW\gamma$ *and* WWZ *Couplings*, *Eur. Phys. J. C* **73** (2013) 2610 [1306.1126].

[75] ATLAS collaboration, *Measurement of total and differential* W^+W^- *production cross sections in proton-proton collisions at* $\sqrt{s} = 8\,\mathrm{TeV}$ *with the ATLAS detector and limits on anomalous triple-gauge-boson couplings*, *JHEP* **09** (2016) 029 [1603.01702].

[76] CMS collaboration, *Measurement of the* W^+W^- *cross section in pp collisions at* $\sqrt{s} = 8\,\mathrm{TeV}$ *and limits on anomalous gauge couplings*, *Eur. Phys. J. C* **76** (2016) 401 [1507.03268].

[77] ATLAS collaboration, *Measurement of* W^+W^- *production in association with one jet in proton–proton collisions at* $\sqrt{s} = 8\,\mathrm{TeV}$ *with the ATLAS detector*, *Phys. Lett. B* **763** (2016) 114 [1608.03086].

[78] ATLAS collaboration, *Measurement of the* W^+W^- *production cross section in pp collisions at a centre-of-mass energy of* $\sqrt{s}$ *= 13* TeV *with the ATLAS experiment*, *Phys. Lett. B* **773** (2017) 354 [1702.04519].

[79] ATLAS collaboration, *Measurement of fiducial and differential* W^+W^- *production cross-sections at* $\sqrt{s} = 13\ \mathrm{TeV}$ *with the ATLAS detector*, *Eur. Phys. J. C* **79** (2019) 884 [1905.04242].

[80] CMS collaboration, W^+W^- *boson pair production in proton-proton collisions at* $\sqrt{s} = 13\,\mathrm{TeV}$, *Phys. Rev. D* **102** (2020) 092001 [2009.00119].

[81] ATLAS collaboration, *Measurements of $W^+W^-+\geq 1$ jet production cross-sections in pp collisions at $\sqrt{s} = 13$ TeV with the ATLAS detector*, *JHEP* **06** (2021) 003 [2103.10319].

[82] ATLAS collaboration, *Measurements of W^+W^- production in decay topologies inspired by searches for electroweak supersymmetry*, *Eur. Phys. J. C* **83** (2023) 718 [2206.15231].

[83] CDF collaboration, *Observation of W^+W^- production in $\bar{p}p$ collisions at $\sqrt{s} = 1.8$ TeV*, *Phys. Rev. Lett.* **78** (1997) 4536.

[84] D0 collaboration, *Search for Higgs boson production in oppositely charged dilepton and missing energy final states in 9.7 fb^{-1} of $p\bar{p}$ collisions at $\sqrt{s} = 1.96$ TeV*, *Phys. Rev. D* **88** (2013) 052006 [1301.1243].

[85] CDF collaboration, *Measurement of the Production and Differential Cross Sections of W^+W^- Bosons in Association with Jets in $p\bar{p}$ Collisions at $\sqrt{s} = 1.96$ TeV*, *Phys. Rev. D* **91** (2015) 111101 [1505.00801].

[86] *Design Report Tevatron 1 project*, *FERMILAB-DESIGN-1984-01* (1984) .

[87] ATLAS collaboration, *Measurements of W^+W^- production cross sections in pp collisions at $\sqrt{s} = 13$ TeV with the ATLAS detector*, *ATLAS-CONF-2023-012* (2023) .

[88] SMEFiT collaboration, *Combined SMEFT interpretation of Higgs, diboson, and top quark data from the LHC*, *JHEP* **11** (2021) 089 [2105.00006].

[89] J. Ellis, M. Madigan, K. Mimasu, V. Sanz and T. You, *Top, Higgs, Diboson and Electroweak Fit to the Standard Model Effective Field Theory*, *JHEP* **04** (2021) 279 [2012.02779].

[90] F. Halzen and A. D. Martin, *Quarks and Leptons: An Introductory Course in Modern Particle Physics*. Wiley, 1984.

[91] M. D. Schwartz, *Quantum Field Theory and the Standard Model*. Cambridge University Press, 2014.

[92] E. Noether, *Invariant variation problems*, *Nachr. d. Koenig. Gesellsch.d. Wiss. zu Goettingen, Math-phys. Klasse* (1918) 235–257.

[93] N. Cabibbo, *Unitary Symmetry and Leptonic Decays*, *Phys. Rev. Lett.* **10** (1963) 531.

[94] L.-L. Chau and W.-Y. Keung, *Comments on the Parametrization of the Kobayashi-Maskawa Matrix*, *Phys. Rev. Lett.* **53** (1984) 1802.

[95] Particle Data Group, *Review of Particle Physics*, *PTEP* **2022** (2022) 083C01.

[96] C. Burgard, *Standard model of physics: Tikz Template*, *[texample.net]* .

[97] ATLAS collaboration, *Measurement of the Higgs boson mass with $H \to \gamma\gamma$ decays in 140 fb^{-1} of $\sqrt{s} = 13$ TeV pp collisions with the ATLAS detector*, *Phys. Lett. B* **847** (2023) 138315 [2308.07216].

[98] ATLAS collaboration, *Combined measurement of the Higgs boson mass from the $H \to \gamma\gamma$ and $H \to ZZ^* \to 4\ell$ decay channels with the ATLAS detector using $\sqrt{s} = 7, 8$ and 13 TeV pp collision data*, *Phys. Rev. Lett.* **131** (2023) 251802 [2308.04775].

[99] CMS collaboration, *Measurement of the Higgs boson width and evidence of its off-shell contributions to ZZ production*, *Nature Phys.* **18** (2022) 1329 [2202.06923].

[100] ATLAS collaboration, *Evidence of off-shell Higgs boson production from ZZ leptonic decay channels and constraints on its total width with the ATLAS detector*, *Phys. Lett. B* **846** (2023) 138223 [2304.01532].

[101] ATLAS collaboration, *A detailed map of Higgs boson interactions by the ATLAS experiment ten years after the discovery*, *Nature* **607** (2022) 52 [2207.00092].

[102] CMS collaboration, *A portrait of the Higgs boson by the CMS experiment ten years after the discovery*, *Nature* **607** (2022) 60 [2207.00043].

[103] T. D. Cohen, *Does chiral perturbation theory rule out QCD-based solutions to the strong CP problem?*, *Phys. Rev. D* **99** (2019) 094007 [1811.04833].

[104] J. Greensite, *An introduction to the confinement problem*, vol. 821. 2011, 10.1007/978-3-642-14382-3.

[105] Y. Nambu, *Quasiparticles and Gauge Invariance in the Theory of Superconductivity*, *Phys. Rev.* **117** (1960) 648.

[106] J. Goldstone, *Field Theories with Superconductor Solutions*, *Nuovo Cim.* **19** (1961) 154.

[107] ATLAS collaboration, *Standard Model Summary Plots October 2023*, *ATL-PHYS-PUB-2023-039* (2023) .

[108] F. Zwicky, *Die Rotverschiebung von extragalaktischen Nebeln*, *Helv. Phys. Acta* **6** (1933) 110.

[109] F. Zwicky, *On the Masses of Nebulae and of Clusters of Nebulae*, *Astrophys. J.* **86** (1937) 217.

[110] V. C. Rubin and W. K. Ford, Jr., *Rotation of the Andromeda Nebula from a Spectroscopic Survey of Emission Regions*, *Astrophys. J.* **159** (1970) 379.

[111] J. Silk et al., *Particle Dark Matter: Observations, Models and Searches*. Cambridge Univ. Press, Cambridge, 2010, 10.1017/CBO9780511770739.

[112] A. H. Guth, *The Inflationary Universe: A Possible Solution to the Horizon and Flatness Problems*, *Phys. Rev. D* **23** (1981) 347.

[113] M. Dine and A. Kusenko, *The Origin of the matter - antimatter asymmetry*, *Rev. Mod. Phys.* **76** (2003) 1 [hep-ph/0303065].

[114] A. D. Sakharov, *Violation of CP Invariance, C asymmetry, and baryon asymmetry of the universe*, *Pisma Zh. Eksp. Teor. Fiz.* **5** (1967) 32.

[115] SUPER-KAMIOKANDE collaboration, *Evidence for oscillation of atmospheric neutrinos*, *Phys. Rev. Lett.* **81** (1998) 1562 [hep-ex/9807003].

[116] E. Akhmedov, *Quantum mechanics aspects and subtleties of neutrino oscillations*, in *International Conference on History of the Neutrino: 1930-2018*, 2019, 1901.05232.

[117] E. Gildener, *Gauge Symmetry Hierarchies*, *Phys. Rev.* **D14** (1976) 1667.

[118] MUON G-2 collaboration, *Measurement of the Positive Muon Anomalous Magnetic Moment to* 0.46 ppm, *Phys. Rev. Lett.* **126** (2021) 141801 [2104.03281].

[119] MUON G-2 collaboration, *Measurement of the Positive Muon Anomalous Magnetic Moment to* 0.20 ppm, 2308.06230.

[120] CDF collaboration, *High-precision measurement of the W boson mass with the CDF II detector*, *Science* **376** (2022) 170.

[121] E. E. Boos, *The SMEFT formalism: the basis for finding deviations from the Standard Model*, *Usp. Fiz. Nauk* **192** (2022) 697.

[122] I. Zurbano Fernandez et al., *High-Luminosity Large Hadron Collider (HL-LHC): Technical design report*, *CERN-2020-010* **10/2020** (2020) .

[123] *Longer term LHC schedule (updated in January 2022)* (*https://lhc-commissioning.web.cern.ch/schedule/LHC-long-term.htm*), .

[124] T. Appelquist and J. Carazzone, *Infrared Singularities and Massive Fields*, *Phys. Rev. D* **11** (1975) 2856.

[125] T. Becher, A. Broggio and A. Ferroglia, *Introduction to Soft-Collinear Effective Theory*, vol. 896. Springer, 2015, 10.1007/978-3-319-14848-9, [1410.1892].

[126] A. Pich, *Chiral perturbation theory*, *Rept. Prog. Phys.* **58** (1995) 563 [hep-ph/9502366].

[127] A. Pich, *Effective Field Theory with Nambu-Goldstone Modes*, *Les Houches Lecture Notes 108* (2018) [1804.05664].

[128] A. V. Manohar and M. B. Wise, *Heavy quark physics*, vol. 10. Cambridge University Press, 2000.

[129] W. Buchmuller and D. Wyler, *Effective Lagrangian Analysis of New Interactions and Flavor Conservation*, *Nucl. Phys. B* **268** (1986) 621.

[130] C. N. Leung, S. T. Love and S. Rao, *Low-Energy Manifestations of a New Interaction Scale: Operator Analysis*, *Z. Phys. C* **31** (1986) 433.

[131] C. Degrande, N. Greiner, W. Kilian, O. Mattelaer, H. Mebane, T. Stelzer et al., *Effective Field Theory: A Modern Approach to Anomalous Couplings*, *Annals Phys.* **335** (2013) 21 [1205.4231].

[132] I. Brivio and M. Trott, *The Standard Model as an Effective Field Theory*, *Phys. Rept.* **793** (2019) 1 [1706.08945].

[133] A. Falkowski, *Lectures on SMEFT*, *Eur. Phys. J. C* **83** (2023) 656.

[134] A. Falkowski and R. Rattazzi, *Which EFT*, *JHEP* **10** (2019) 255 [1902.05936].

[135] T. Cohen, N. Craig, X. Lu and D. Sutherland, *Is SMEFT Enough?*, *JHEP* **03** (2021) 237 [2008.08597].

[136] S. Weinberg, *Baryon and Lepton Nonconserving Processes*, *Phys. Rev. Lett.* **43** (1979) 1566.

[137] B. Grzadkowski, M. Iskrzynski, M. Misiak and J. Rosiek, *Dimension-Six Terms in the Standard Model Lagrangian*, *JHEP* **10** (2010) 085 [1008.4884].

[138] B. Henning, X. Lu, T. Melia and H. Murayama, *2, 84, 30, 993, 560, 15456, 11962, 261485, ...: Higher dimension operators in the SM EFT*, *JHEP* **08** (2017) 016 [1512.03433].

[139] S. Dawson and P. P. Giardino, *Electroweak and QCD corrections to Z and W pole observables in the standard model EFT*, *Phys. Rev. D* **101** (2020) 013001 [1909.02000].

[140] I. Brivio et al., *Truncation, validity, uncertainties*, *CERN-LHCEFTWG-2021-002* (2022) [2201.04974].

[141] D. Barducci et al., *Interpreting top-quark LHC measurements in the standard-model effective field theory*, *CERN-LPCC-2018-01* (2018) [1802.07237].

[142] C. Bierlich et al., *A comprehensive guide to the physics and usage of* PYTHIA 8.3, *SciPost Phys. Codeb.* **2022** (2022) 8 [2203.11601].

[143] G. Corcella, I. G. Knowles, G. Marchesini, S. Moretti, K. Odagiri, P. Richardson et al., *HERWIG 6: An Event generator for hadron emission reactions with interfering gluons (including supersymmetric processes)*, *JHEP* **01** (2001) 010 [hep-ph/0011363].

[144] M. Bahr et al., HERWIG ++ *Physics and Manual*, *Eur. Phys. J. C* **58** (2008) 639 [0803.0883].

[145] J. Bellm et al., HERWIG 7.0/HERWIG ++ *3.0 release note*, *Eur. Phys. J. C* **76** (2016) 196 [1512.01178].

[146] T. Sjöstrand, S. Mrenna and P. Z. Skands, PYTHIA 6.4 *Physics and Manual*, *JHEP* **05** (2006) 026 [hep-ph/0603175].

[147] T. Sjöstrand, S. Ask, J. R. Christiansen, R. Corke, N. Desai, P. Ilten et al., *An Introduction to* PYTHIA 8.2, *Comput. Phys. Commun.* **191** (2015) 159 [1410.3012].

[148] SHERPA collaboration, *Event Generation with* SHERPA 2.2, *SciPost Phys.* **7** (2019) 034 [1905.09127].

[149] P. Nason, *A New method for combining NLO QCD with shower Monte Carlo algorithms*, *JHEP* **11** (2004) 040 [hep-ph/0409146].

[150] S. Alioli, P. Nason, C. Oleari and E. Re, *A general framework for implementing NLO calculations in shower Monte Carlo programs: the* POWHEG BOX, *JHEP* **06** (2010) 043 [1002.2581].

[151] J. Alwall, M. Herquet, F. Maltoni, O. Mattelaer and T. Stelzer, *MadGraph 5: Going Beyond*, *JHEP* **06** (2011) 128 [1106.0522].

[152] A. Buckley et al., *General-purpose event generators for LHC physics*, *Phys. Rept.* **504** (2011) 145 [1101.2599].

[153] R. P. Feynman, *Very high-energy collisions of hadrons*, *Phys. Rev. Lett.* **23** (1969) 1415.

[154] J. C. Collins, D. E. Soper and G. F. Sterman, *Factorization for Short Distance Hadron - Hadron Scattering*, *Nucl. Phys. B* **261** (1985) 104.

[155] J. C. Collins, D. E. Soper and G. F. Sterman, *Soft Gluons and Factorization*, *Nucl. Phys. B* **308** (1988) 833.

[156] J. C. Collins, D. E. Soper and G. F. Sterman, *Factorization of Hard Processes in QCD*, *Adv. Ser. Direct. High Energy Phys.* **5** (1989) 1 [hep-ph/0409313].

[157] G. C. Wick, *The Evaluation of the Collision Matrix*, *Phys. Rev.* **80** (1950) 268.

[158] H. Lehmann, K. Symanzik and W. Zimmermann, *On the formulation of quantized field theories*, *Nuovo Cim.* **1** (1955) 205.

[159] J. M. Campbell and R. K. Ellis, *An Update on vector boson pair production at hadron colliders*, *Phys. Rev. D* **60** (1999) 113006 [hep-ph/9905386].

[160] NNPDF collaboration, *Parton distributions from high-precision collider data*, *Eur. Phys. J. C* **77** (2017) 663 [1706.00428].

[161] Y. L. Dokshitzer, *Calculation of the structure functions for deep inelastic scattering and e^+e^- annihilation by perturbation theory in Quantum Chromodynamics.*, *Sov. Phys. JETP* **46** (1977) 641.

[162] V. N. Gribov and L. N. Lipatov, *Deep inelastic ep scattering in perturbation theory*, *Sov. J. Nucl. Phys.* **15** (1972) 438.

[163] G. Altarelli and G. Parisi, *Asymptotic Freedom in Parton Language*, *Nucl. Phys.* **B126** (1977) 298.

[164] S. Catani and M. H. Seymour, *A General algorithm for calculating jet cross-sections in NLO QCD*, *Nucl. Phys. B* **485** (1997) 291 [hep-ph/9605323].

[165] H1 collaboration, *The H1 detector at HERA*, *Nucl. Instrum. Meth.* **A386** (1997) 310.

[166] ZEUS collaboration, *The ZEUS detector: Status report 1993*, *ZEUS-STATUS-REPT-1993* (1993) .

[167] A. Buckley, J. Ferrando, S. Lloyd, K. Nordström, B. Page, M. Rüfenacht et al., *LHAPDF6: parton density access in the LHC precision era*, *Eur. Phys. J. C* **75** (2015) 132 [1412.7420].

[168] NNPDF collaboration, *The path to proton structure at* $1\,\%$ *accuracy*, *Eur. Phys. J. C* **82** (2022) 428 [2109.02653].

[169] L. A. Harland-Lang, A. D. Martin, P. Motylinski and R. S. Thorne, *Parton distributions in the LHC era: MMHT 2014 PDFs*, *Eur. Phys. J. C* **75** (2015) 204 [1412.3989].

[170] T.-J. Hou et al., *New CTEQ global analysis of quantum chromodynamics with high-precision data from the LHC*, *Phys. Rev. D* **103** (2021) 014013 [1912.10053].

[171] T. Cridge, L. A. Harland-Lang, A. D. Martin and R. S. Thorne, *An investigation of the* α_S *and heavy quark mass dependence in the MSHT20 global PDF analysis*, *Eur. Phys. J. C* **81** (2021) 744 [2106.10289].

[172] A. D. Martin, W. J. Stirling, R. S. Thorne and G. Watt, *Heavy-quark mass dependence in global PDF analyses and 3- and 4-flavour parton distributions*, *Eur. Phys. J. C* **70** (2010) 51 [1007.2624].

[173] H1, ZEUS collaboration, *Combination of measurements of inclusive deep inelastic* $e^{\pm}p$ *scattering cross sections and QCD analysis of HERA data*, *Eur. Phys. J. C* **75** (2015) 580 [1506.06042].

[174] ATLAS collaboration, *Determination of the parton distribution functions of the proton using diverse ATLAS data from pp collisions at* $\sqrt{s} = 7,\ 8$ *and* $13\,\mathrm{TeV}$, *Eur. Phys. J. C* **82** (2022) 438 [2112.11266].

[175] CMS collaboration, *Measurement of the differential cross section and charge asymmetry for inclusive* $pp \to W^{\pm} + X$ *production at* $\sqrt{s} = 8\,\mathrm{TeV}$, *Eur. Phys. J. C* **76** (2016) 469 [1603.01803].

[176] CMS collaboration, *Measurement of double-differential cross sections for top quark pair production in pp collisions at* $\sqrt{s} = 8\,\mathrm{TeV}$ *and impact on parton distribution functions*, *Eur. Phys. J. C* **77** (2017) 459 [1703.01630].

[177] PDF4LHC WORKING GROUP collaboration, *The PDF4LHC21 combination of global PDF fits for the LHC Run III*, *J. Phys. G* **49** (2022) 080501 [2203.05506].

[178] A. De Roeck and R. S. Thorne, *Structure Functions*, *Prog. Part. Nucl. Phys.* **66** (2011) 727 [1103.0555].

[179] J. Gao, L. Harland-Lang and J. Rojo, *The Structure of the Proton in the LHC Precision Era*, *Phys. Rept.* **742** (2018) 1 [1709.04922].

[180] J. J. Ethier and E. R. Nocera, *Parton Distributions in Nucleons and Nuclei*, *Ann. Rev. Nucl. Part. Sci.* **70** (2020) 43 [2001.07722].

[181] G. Falcioni, F. Herzog, S. Moch and A. Vogt, *Four-loop splitting functions in QCD – The gluon-to-quark case*, 2307.04158.

[182] G. Falcioni, F. Herzog, S. Moch and A. Vogt, *Four-loop splitting functions in QCD – The quark-quark case*, *Phys. Lett. B* **842** (2023) 137944 [2302.07593].

[183] J. McGowan, T. Cridge, L. A. Harland-Lang and R. S. Thorne, *Approximate* N^3LO *parton distribution functions with theoretical uncertainties: MSHT20a*N^3LO *PDFs*, *Eur. Phys. J. C* **83** (2023) 185 [2207.04739].

[184] A. Manohar, P. Nason, G. P. Salam and G. Zanderighi, *How bright is the proton? A precise determination of the photon parton distribution function*, *Phys. Rev. Lett.* **117** (2016) 242002 [1607.04266].

[185] A. V. Manohar, P. Nason, G. P. Salam and G. Zanderighi, *The Photon Content of the Proton*, *JHEP* **12** (2017) 046 [1708.01256].

[186] NNPDF collaboration, *Illuminating the photon content of the proton within a global PDF analysis*, *SciPost Phys.* **5** (2018) 008 [1712.07053].

[187] L. A. Harland-Lang, R. Nathvani, R. S. Thorne and A. D. Martin, *MMHT PDFs: updates and outlook*, *Acta Phys. Polon. B* **48** (2017) 1011 [1704.00162].

[188] S. Camarda, L. Cieri and G. Ferrera, *Drell-Yan lepton-pair production:* q_T *resummation at N3LL accuracy and fiducial cross sections at N3LO*, *Phys. Rev. D* **104** (2021) L111503 [2103.04974].

[189] S. Kallweit, E. Re, L. Rottoli and M. Wiesemann, *Accurate single- and double-differential resummation of colour-singlet processes with MATRIX+RADISH:* W^+W^- *production at the LHC*, *JHEP* **12** (2020) 147 [2004.07720].

[190] U. Baur, *Weak Boson Emission in Hadron Collider Processes*, *Phys. Rev. D* **75** (2007) 013005 [hep-ph/0611241].

[191] W. J. Stirling and E. Vryonidou, *Electroweak corrections and Bloch-Nordsieck violations in 2-to-2 processes at the LHC*, *JHEP* **04** (2013) 155 [1212.6537].

[192] A. Denner and S. Dittmaier, *Electroweak Radiative Corrections for Collider Physics*, *Phys. Rept.* **864** (2020) 1 [1912.06823].

[193] R. Frederix, S. Frixione, V. Hirschi, D. Pagani, H. S. Shao and M. Zaro, *The automation of next-to-leading order electroweak calculations*, *JHEP* **07** (2018) 185 [1804.10017].

[194] B. Biedermann, S. Bräuer, A. Denner, M. Pellen, S. Schumann and J. M. Thompson, *Automation of NLO QCD and EW corrections with* SHERPA *and* RECOLA, *Eur. Phys. J. C* **77** (2017) 492 [1704.05783].

[195] T. Sjostrand, *A Model for Initial State Parton Showers*, *Phys. Lett. B* **157** (1985) 321.

[196] G. Marchesini and B. R. Webber, *Simulation of QCD Jets Including Soft Gluon Interference*, *Nucl. Phys. B* **238** (1984) 1.

[197] T. D. Gottschalk, *Backwards evolved initial state parton showers*, *Nucl. Phys. B* **277** (1986) 700.

[198] J. M. Campbell et al., *Event Generators for High-Energy Physics Experiments*, in *Snowmass 2021*, 2022, 2203.11110.

[199] S. Gieseke, P. Stephens and B. Webber, *New formalism for QCD parton showers*, *JHEP* **12** (2003) 045 [hep-ph/0310083].

[200] M. Bengtsson and T. Sjostrand, *A Comparative Study of Coherent and Noncoherent Parton Shower Evolution*, *Nucl. Phys. B* **289** (1987) 810.

[201] G. Gustafson and U. Pettersson, *Dipole Formulation of QCD Cascades*, *Nucl. Phys. B* **306** (1988) 746.

[202] S. Schumann and F. Krauss, *A Parton shower algorithm based on Catani-Seymour dipole factorisation*, *JHEP* **03** (2008) 038 [0709.1027].

[203] A. Buckley, C. White and M. White, *Practical Collider Physics*. IOP, 2021, 10.1088/978-0-7503-2444-1.

[204] S. Alioli, C. W. Bauer, C. Berggren, F. J. Tackmann, J. R. Walsh and S. Zuberi, *Matching Fully Differential NNLO Calculations and Parton Showers*, *JHEP* **06** (2014) 089 [1311.0286].

[205] S. Catani, F. Krauss, R. Kuhn and B. R. Webber, *QCD matrix elements + parton showers*, *JHEP* **11** (2001) 063 [hep-ph/0109231].

[206] H. Brooks and C. T. Preuss, *Efficient multi-jet merging with the Vincia sector shower*, *Comput. Phys. Commun.* **264** (2021) 107985 [2008.09468].

[207] S. Frixione and B. R. Webber, *Matching NLO QCD computations and parton shower simulations*, *JHEP* **06** (2002) 029 [hep-ph/0204244].

[208] J. Alwall, R. Frederix, S. Frixione, V. Hirschi, F. Maltoni, O. Mattelaer et al., *The automated computation of tree-level and next-to-leading order differential cross sections, and their matching to parton shower simulations*, *JHEP* **07** (2014) 079 [1405.0301].

[209] J. Alwall et al., *Comparative study of various algorithms for the merging of parton showers and matrix elements in hadronic collisions*, *Eur. Phys. J.* **C53** (2008) 473 [0706.2569].

[210] S. Hoeche, F. Krauss, M. Schonherr and F. Siegert, *QCD matrix elements + parton showers: The NLO case*, *JHEP* **04** (2013) 027 [1207.5030].

[211] K. Hamilton, P. Nason and G. Zanderighi, *MINLO: Multi-Scale Improved NLO*, *JHEP* **10** (2012) 155 [1206.3572].

[212] P. F. Monni, P. Nason, E. Re, M. Wiesemann and G. Zanderighi, *MiNNLO$_{\rm PS}$: a new method to match NNLO QCD to parton showers*, *JHEP* **05** (2020) 143 [1908.06987].

[213] K. Hamilton, P. Nason, C. Oleari and G. Zanderighi, *Merging H/W/Z + 0 and 1 jet at NLO with no merging scale: a path to parton shower + NNLO matching*, *JHEP* **05** (2013) 082 [1212.4504].

[214] K. Hamilton, T. Melia, P. F. Monni, E. Re and G. Zanderighi, *Merging WW and WW+jet with MINLO*, *JHEP* **09** (2016) 057 [1606.07062].

[215] E. Re, M. Wiesemann and G. Zanderighi, *NNLOPS accurate predictions for W^+W^- production*, *JHEP* **12** (2018) 121 [1805.09857].

[216] D. Lombardi, M. Wiesemann and G. Zanderighi, *W^+W^- production at NNLO+PS with MiNNLO$_{PS}$*, *JHEP* **11** (2021) 230 [2103.12077].

[217] A. Huss, J. Huston, S. Jones and M. Pellen, *Les Houches 2021—physics at* TeV *colliders: report on the standard model precision wishlist*, *J. Phys. G* **50** (2023) 043001 [2207.02122].

[218] H.-U. Bengtsson and T. Sjostrand, *The Lund Monte Carlo for Hadronic Processes:* PYTHIA *Version 4.8*, *Comput. Phys. Commun.* **46** (1987) 43.

[219] B. Andersson, *The Lund model*, vol. 7. Cambridge University Press, 2005, 10.1017/CBO9780511524363.

[220] T. D. Gottschalk, *A Realistic Model for e^+e^- Annihilation Including Parton Bremsstrahlung Effects*, *Nucl. Phys. B* **214** (1983) 201.

[221] T. D. Gottschalk, *An Improved Description of Hadronization in the QCD Cluster Model for e^+e^- Annihilation*, *Nucl. Phys. B* **239** (1984) 349.

[222] B. R. Webber, *A QCD Model for Jet Fragmentation Including Soft Gluon Interference*, *Nucl. Phys. B* **238** (1984) 492.

[223] D. Amati and G. Veneziano, *Preconfinement as a Property of Perturbative QCD*, *Phys. Lett. B* **83** (1979) 87.

[224] G. Marchesini, L. Trentadue and G. Veneziano, *Space-time Description of Color Screening via Jet Calculus Techniques*, *Nucl. Phys. B* **181** (1981) 335.

[225] J.-C. Winter, F. Krauss and G. Soff, *A Modified cluster hadronization model*, *Eur. Phys. J. C* **36** (2004) 381 [hep-ph/0311085].

[226] T. Sjostrand and M. van Zijl, *A Multiple Interaction Model for the Event Structure in Hadron Collisions*, *Phys. Rev. D* **36** (1987) 2019.

[227] S. Gieseke, C. Rohr and A. Siodmok, *Colour reconnections in* HERWIG ++, *Eur. Phys. J. C* **72** (2012) 2225 [1206.0041].

[228] T. Sjostrand and P. Z. Skands, *Multiple interactions and the structure of beam remnants*, *JHEP* **03** (2004) 053 [hep-ph/0402078].

[229] T. Sjostrand and V. A. Khoze, *On Color rearrangement in hadronic W^+W^- events*, *Z. Phys. C* **62** (1994) 281 [hep-ph/9310242].

[230] R. W. Brown and K. O. Mikaelian, *W^+W^- and Z^0Z^0 Pair Production in e^+e^-, pp, $p\bar{p}$ Colliding Beams*, *Phys. Rev. D* **19** (1979) 922.

[231] M. Grazzini, S. Kallweit, J. M. Lindert, S. Pozzorini and M. Wiesemann, *NNLO QCD + NLO EW with Matrix+OpenLoops: precise predictions for vector-boson pair production*, *JHEP* **02** (2020) 087 [1912.00068].

[232] T. Gehrmann, M. Grazzini, S. Kallweit, P. Maierhöfer, A. von Manteuffel, S. Pozzorini et al., *W^+W^- Production at Hadron Colliders in Next to Next to Leading Order QCD*, *Phys. Rev. Lett.* **113** (2014) 212001 [1408.5243].

[233] M. Grazzini, S. Kallweit, S. Pozzorini, D. Rathlev and M. Wiesemann, *W^+W^- production at the LHC: fiducial cross sections and distributions in NNLO QCD*, *JHEP* **08** (2016) 140 [1605.02716].

[234] J. M. Campbell, R. K. Ellis and C. Williams, *Gluon-Gluon Contributions to W^+W^- Production and Higgs Interference Effects*, *JHEP* **10** (2011) 005 [1107.5569].

[235] N. Kauer, *Interference effects for $H \to WW/ZZ \to \ell\bar{\nu}_\ell\bar{\ell}\nu_\ell$ searches in gluon fusion at the LHC*, *JHEP* **12** (2013) 082 [1310.7011].

[236] J. M. Campbell, R. K. Ellis and C. Williams, *Bounding the Higgs Width at the LHC*, *PoS* **LL2014** (2014) 008 [1408.1723].

[237] S. Frixione, *A Next-to-leading order calculation of the cross-section for the production of W^+W^- pairs in hadronic collisions*, *Nucl. Phys. B* **410** (1993) 280.

[238] J. Ohnemus, *Hadronic ZZ, W^-W^+, and $W^\pm Z$ production with QCD corrections and leptonic decays*, *Phys. Rev. D* **50** (1994) 1931 [hep-ph/9403331].

[239] L. J. Dixon, Z. Kunszt and A. Signer, *Helicity amplitudes for $O(\alpha_S)$ production of W^+W^-, $W^\pm Z$, ZZ, $W^\pm\gamma$, or $Z\gamma$ pairs at hadron colliders*, *Nucl. Phys. B* **531** (1998) 3 [hep-ph/9803250].

[240] L. J. Dixon, Z. Kunszt and A. Signer, *Vector boson pair production in hadronic collisions at order α_s: Lepton correlations and anomalous couplings*, *Phys. Rev. D* **60** (1999) 114037 [hep-ph/9907305].

[241] D. A. Dicus, C. Kao and W. W. Repko, *Gluon Production of Gauge Bosons*, *Phys. Rev. D* **36** (1987) 1570.

[242] E. W. N. Glover and J. J. van der Bij, *Vector boson pair production via gluon fusion*, *Phys. Lett. B* **219** (1989) 488.

[243] T. Binoth, M. Ciccolini, N. Kauer and M. Kramer, *Gluon-induced WW background to Higgs boson searches at the LHC*, *JHEP* **03** (2005) 065 [hep-ph/0503094].

[244] T. Binoth, M. Ciccolini, N. Kauer and M. Kramer, *Gluon-induced W-boson pair production at the LHC*, *JHEP* **12** (2006) 046 [hep-ph/0611170].

[245] J. M. Campbell, R. K. Ellis and C. Williams, *Vector boson pair production at the LHC*, *JHEP* **07** (2011) 018 [1105.0020].

[246] F. Caola, K. Melnikov, R. Röntsch and L. Tancredi, *QCD corrections to W^+W^- production through gluon fusion*, *Phys. Lett. B* **754** (2016) 275 [1511.08617].

[247] M. Grazzini, S. Kallweit, M. Wiesemann and J. Y. Yook, *W^+W^- production at the LHC: NLO QCD corrections to the loop-induced gluon fusion channel*, *Phys. Lett. B* **804** (2020) 135399 [2002.01877].

[248] A. Bierweiler, T. Kasprzik, J. H. Kühn and S. Uccirati, *Electroweak corrections to W-boson pair production at the LHC*, *JHEP* **11** (2012) 093 [1208.3147].

[249] J. Baglio, L. D. Ninh and M. M. Weber, *Massive gauge boson pair production at the LHC: a next-to-leading order story*, *Phys. Rev. D* **88** (2013) 113005 [1307.4331].

[250] M. Billoni, S. Dittmaier, B. Jäger and C. Speckner, *Next-to-leading order electroweak corrections to $pp \to W^+W^- \to 4$ leptons at the LHC in double-pole approximation*, *JHEP* **12** (2013) 043 [1310.1564].

[251] B. Biedermann, M. Billoni, A. Denner, S. Dittmaier, L. Hofer, B. Jäger et al., *Next-to-leading-order electroweak corrections to $pp \to W^+W^- \to 4$ leptons at the LHC*, *JHEP* **06** (2016) 065 [1605.03419].

[252] S. Kallweit, J. M. Lindert, S. Pozzorini and M. Schönherr, *NLO QCD+EW predictions for $2\ell 2\nu$ diboson signatures at the LHC*, *JHEP* **11** (2017) 120 [1705.00598].

[253] M. Grazzini, S. Kallweit and M. Wiesemann, *Fully differential NNLO computations with MATRIX*, *Eur. Phys. J. C* **78** (2018) 537 [1711.06631].

[254] W. Bizon, P. F. Monni, E. Re, L. Rottoli and P. Torrielli, *Momentum-space resummation for transverse observables and the Higgs $p_\perp$ at N^3LL+NNLO*, *JHEP* **02** (2018) 108 [1705.09127].

[255] T. Becher, R. Frederix, M. Neubert and L. Rothen, *Automated NNLL + NLO resummation for jet-veto cross sections*, *Eur. Phys. J. C* **75** (2015) 154 [1412.8408].

[256] L. Arpino, A. Banfi, S. Jäger and N. Kauer, *BSM WW production with a jet veto*, *JHEP* **08** (2019) 076 [1905.06646].

[257] T. Melia, P. Nason, R. Rontsch and G. Zanderighi, *W^+W^-, WZ and ZZ production in the* POWHEG BOX, *JHEP* **11** (2011) 078 [1107.5051].

[258] K. Hamilton, *A positive-weight next-to-leading order simulation of weak boson pair production*, *JHEP* **01** (2011) 009 [1009.5391].

[259] F. Cascioli, S. Höche, F. Krauss, P. Maierhöfer, S. Pozzorini and F. Siegert, *Precise Higgs-background predictions: merging NLO QCD and squared quark-loop corrections to four-lepton + 0,1 jet production*, *JHEP* **01** (2014) 046 [1309.0500].

[260] J. M. Campbell, R. K. Ellis, T. Neumann and S. Seth, *Transverse momentum resummation at N^3LL+NNLO for diboson processes*, *JHEP* **03** (2023) 080 [2210.10724].

[261] A. Gavardi, M. A. Lim, S. Alioli and F. Tackmann, *NNLO+PS W^+W^- production using jet veto resummation at NNLL′*, 2308.11577.

[262] M. Chiesa, C. Oleari and E. Re, *NLO QCD+NLO EW corrections to diboson production matched to parton shower*, *Eur. Phys. J. C* **80** (2020) 849 [2005.12146].

[263] S. Bräuer, A. Denner, M. Pellen, M. Schönherr and S. Schumann, *Fixed-order and merged parton-shower predictions for WW and WWj production at the LHC including NLO QCD and EW corrections*, *JHEP* **10** (2020) 159 [2005.12128].

[264] R. Poncelet and A. Popescu, *NNLO QCD study of polarised W^+W^- production at the LHC*, *JHEP* **07** (2021) 023 [2102.13583].

[265] A. Denner, C. Haitz and G. Pelliccioli, *NLO QCD corrections to polarized diboson production in semileptonic final states*, *Phys. Rev. D* **107** (2023) 053004 [2211.09040].

[266] A. Ballestrero, E. Maina and G. Pelliccioli, *W boson polarization in vector boson scattering at the LHC*, *JHEP* **03** (2018) 170 [1710.09339].

[267] T. Kim and A. Martin, *A $W^\pm$ polarization analyzer from Deep Neural Networks*, 2102.05124.

[268] M. Grossi, M. Incudini, M. Pellen and G. Pelliccioli, *Amplitude-assisted tagging of longitudinally polarised bosons using wide neural networks*, *Eur. Phys. J. C* **83** (2023) 759 [2306.07726].

[269] D. Liu and L.-T. Wang, *Prospects for precision measurement of diboson processes in the semileptonic decay channel in future LHC runs*, *Phys. Rev. D* **99** (2019) 055001 [1804.08688].

[270] P. Jaiswal and T. Okui, *Explanation of the WW excess at the LHC by jet-veto resummation*, *Phys. Rev. D* **90** (2014) 073009 [1407.4537].

[271] P. Meade, H. Ramani and M. Zeng, *Transverse momentum resummation effects in W^+W^- measurements*, *Phys. Rev. D* **90** (2014) 114006 [1407.4481].

[272] P. F. Monni and G. Zanderighi, *On the excess in the inclusive $W^+W^- \to l^+l^-\nu\bar{\nu}$ cross section*, *JHEP* **05** (2015) 013 [1410.4745].

[273] M. Grazzini, *Soft-gluon effects in WW production at hadron colliders*, *JHEP* **01** (2006) 095 [hep-ph/0510337].

[274] Y. Wang, C. S. Li, Z. L. Liu, D. Y. Shao and H. T. Li, *Transverse-Momentum Resummation for Gauge Boson Pair Production at the Hadron Collider*, *Phys. Rev. D* **88** (2013) 114017 [1307.7520].

[275] S. Dawson, P. Jaiswal, Y. Li, H. Ramani and M. Zeng, *Resummation of jet veto logarithms at N^3LL_a + NNLO for W^+W^- production at the LHC*, *Phys. Rev. D* **94** (2016) 114014 [1606.01034].

[276] S. Dawson, I. M. Lewis and M. Zeng, *Threshold resummed and approximate next-to-next-to-leading order results for W^+W^- pair production at the LHC*, *Phys. Rev. D* **88** (2013) 054028 [1307.3249].

[277] V. Bertone, S. Carrazza, D. Pagani and M. Zaro, *On the Impact of Lepton PDFs*, *JHEP* **11** (2015) 194 [1508.07002].

[278] K. J. F. Gaemers and G. J. Gounaris, *Polarization Amplitudes for $e^+e^- \to W^+W^-$ and $e^+e^- \to ZZ$*, *Z. Phys. C* **1** (1979) 259.

[279] K. Hagiwara, J. Woodside and D. Zeppenfeld, *Measuring the WWZ Coupling at the Tevatron*, *Phys. Rev. D* **41** (1990) 2113.

[280] D. Zeppenfeld and S. Willenbrock, *Probing the Three Vector - Boson Vertex at Hadron Colliders*, *Phys. Rev. D* **37** (1988) 1775.

[281] U. Baur and D. Zeppenfeld, *Unitarity Constraints on the Electroweak Three Vector Boson Vertices*, *Phys. Lett. B* **201** (1988) 383.

[282] Z. Zhang, *Time to Go Beyond Triple-Gauge-Boson-Coupling Interpretation of W Pair Production*, *Phys. Rev. Lett.* **118** (2017) 011803 [1610.01618].

[283] A. De Rujula, M. B. Gavela, P. Hernandez and E. Masso, *The Selfcouplings of vector bosons: Does LEP-1 obviate LEP-2?*, *Nucl. Phys. B* **384** (1992) 3.

[284] K. Hagiwara, S. Ishihara, R. Szalapski and D. Zeppenfeld, *Low-energy constraints on electroweak three gauge boson couplings*, *Phys. Lett. B* **283** (1992) 353.

[285] K. Hagiwara, S. Ishihara, R. Szalapski and D. Zeppenfeld, *Low-energy effects of new interactions in the electroweak boson sector*, *Phys. Rev. D* **48** (1993) 2182.

[286] J. Wudka, *Electroweak effective Lagrangians*, *Int. J. Mod. Phys. A* **9** (1994) 2301 [hep-ph/9406205].

[287] J. Ellison and J. Wudka, *Study of trilinear gauge boson couplings at the Tevatron collider*, *Ann. Rev. Nucl. Part. Sci.* **48** (1998) 33 [hep-ph/9804322].

[288] F. Wilczek, *Problem of Strong P and T Invariance in the Presence of Instantons*, *Phys. Rev. Lett.* **40** (1978) 279.

[289] S. Weinberg, *A New Light Boson?*, *Phys. Rev. Lett.* **40** (1978) 223.

[290] M. B. Gavela, J. M. No, V. Sanz and J. F. de Trocóniz, *Non-resonant Searches for Axionlike Particles at the LHC*, *Phys. Rev. Lett.* **124** (2020) 051802 [1905.12953].

[291] F. Arias-Aragón, J. Quevillon and C. Smith, *Axion-like ALPs*, *JHEP* **03** (2023) 134 [2211.04489].

[292] S. Carra, V. Goumarre, R. Gupta, S. Heim, B. Heinemann, J. Kuechler et al., *Constraining off-shell production of axion-like particles with $Z\gamma$ and WW differential cross-section measurements*, *Phys. Rev. D* **104** (2021) 092005 [2106.10085].

[293] J. Bonilla, I. Brivio, J. Machado-Rodríguez and J. F. de Trocóniz, *Non-resonant searches for axion-like particles in vector boson scattering processes at the LHC*, *JHEP* **06** (2022) 113 [2202.03450].

[294] A. Biekötter, J. Fuentes-Martín, A. M. Galda and M. Neubert, *A global analysis of axion-like particle interactions using SMEFT fits*, *JHEP* **09** (2023) 120 [2307.10372].

[295] *The ATLAS Collaboration webpage*, https://atlas.cern/discover/collaboration (2024) .

[296] J. Vollaire et al., *Linac4 design report*, vol. 6/2020 of *CERN Yellow Reports: Monographs*. CERN, Geneva, 2020, 10.23731/CYRM-2020-006.

[297] E. Mobs, *The CERN accelerator complex in 2019. Complexe des accélérateurs du CERN en 2019*, *CERN-GRAPHICS-2019-002* (2019) .

[298] Y. Ohnishi et al., *Accelerator design at SuperKEKB*, *PTEP* **2013** (2013) 03A011.

[299] SuperKEKB, *Press release: Superkekb collider achieves the world's highest luminosity*, *[KEK webpage]* (2020) .

[300] W. Herr and B. Muratori, *Concept of luminosity*, *CERN article* (2006) .

[301] C.Møller, *General Properties of the Characteristic Matrix in the Theory of Elementary Particles. I*, *K. Danske Vidensk. Selsk. Mat.-Fys. Medd. 23* **1** (1945) .

[302] J. Wenninger, *Operation and Configuration of the LHC in Run 2*, *CERN-ACC-NOTE-2019-0007* (2019) .

[303] S. van der Meer, *Calibration of the Effective Beam Height in the ISR*, *CERN-ISR-PO-68-31* (1968) .

[304] ATLAS collaboration, *ATLAS Luminosity Public Results*, https://twiki.cern.ch/twiki/bin/view/AtlasPublic/LuminosityPublicResultsRun2 (2024) .

[305] ATLAS collaboration, *The ATLAS Experiment at the CERN Large Hadron Collider*, *JINST* **3** (2008) S08003.

[306] CMS collaboration, *The CMS Experiment at the CERN LHC*, *JINST* **3** (2008) S08004.

[307] ALICE collaboration, *The ALICE experiment at the CERN LHC*, *JINST* **3** (2008) S08002.

[308] LHCb collaboration, *The LHCb Detector at the LHC*, *JINST* **3** (2008) S08005.

[309] TOTEM collaboration, *The TOTEM experiment at the CERN Large Hadron Collider*, *JINST* **3** (2008) S08007.

[310] LHCf collaboration, *Technical design report of the LHCf experiment: Measurement of photons and neutral pions in the very forward region of LHC*, *CERN-LHCC-2006-004* (2006) .

[311] SND@LHC collaboration, *SND@LHC: The Scattering and Neutrino Detector at the LHC*, 2210.02784.

[312] J. L. Feng, I. Galon, F. Kling and S. Trojanowski, *ForwArd Search ExpeRiment at the LHC*, *Phys. Rev. D* **97** (2018) 035001 [1708.09389].

[313] MoEDAL collaboration, *Technical Design Report of the MoEDAL Experiment*, *CERN-LHCC-2009-006* (2009) .

[314] J. Pequenao, *Computer generated image of the whole ATLAS detector*, *CERN-GE-0803012* (2008) .

[315] ATLAS collaboration, *ATLAS detector and physics performance: Technical design report, 1*. CERN, Geneva, 1999.

[316] H. Kolanoski and N. Wermes, *Particle Detectors*. Oxford University Press, 2020.

[317] R. L. Gluckstern, *Uncertainties in track momentum and direction, due to multiple scattering and measurement errors*, *Nucl. Instrum. Meth.* **24** (1963) 381.

[318] ATLAS collaboration, *ATLAS inner detector: Technical Design Report, 1*. CERN, Geneva, 1997.

[319] ATLAS collaboration, *ATLAS inner detector: Technical design report. Vol. 2*, *CERN-LHCC-97-17* (1997) .

[320] *Studies of the ATLAS Inner Detector material using $\sqrt{s} = 13\,\text{TeV}$ pp collision data*, Tech. Rep. ATL-PHYS-PUB-2015-050, CERN, Geneva, 2015.

[321] ATLAS collaboration, *ATLAS Insertable B-Layer Technical Design Report*, Tech. Rep. CERN-LHCC-2010-013, 2010.

[322] ATLAS collaboration, *Track Reconstruction Performance of the ATLAS Inner Detector at $\sqrt{s} = 13\,\text{TeV}$*, Tech. Rep. ATL-PHYS-PUB-2015-018, CERN, Geneva, 2015.

[323] A. Abdesselam and T. Akimoto, *The Barrel Modules of the ATLAS SemiConductor Tracker*, Tech. Rep. ATL-INDET-PUB-2006-005, CERN, Geneva, 2006. 10.1016/j.nima.2006.08.036.

[324] ATLAS collaboration, *Operation and performance of the ATLAS semiconductor tracker in LHC Run 2*, *JINST* **17** (2022) P01013 [2109.02591].

[325] ATLAS collaboration, *Performance of the ATLAS Transition Radiation Tracker in Run 1 of the LHC: tracker properties*, *JINST* **12** (2017) P05002 [1702.06473].

[326] ATLAS collaboration, *Performance of the ATLAS muon triggers in Run 2*, *JINST* **15** (2020) P09015 [2004.13447].

[327] P. Jenni and M. Nessi, *ATLAS Forward Detectors for Luminosity Measurement and Monitoring*, Tech. Rep. CERN-LHCC-2004-010, CERN, Geneva, 2004.

[328] P. Jenni, M. Nordberg, M. Nessi and K. Jon-And, *ATLAS Forward Detectors for Measurement of Elastic Scattering and Luminosity*, Technical design report. CERN, Geneva, 2008, 10.17181/CERN-LHCC-2008-004.

[329] G. Avoni et al., *The new LUCID-2 detector for luminosity measurement and monitoring in ATLAS*, *JINST* **13** (2018) P07017.

[330] P. Grafström and W. Kozanecki, *Luminosity determination at proton colliders*, *Prog. Part. Nucl. Phys.* **81** (2015) 97.

[331] ATLAS collaboration, *Operation of the ATLAS trigger system in Run 2*, *JINST* **15** (2020) P10004 [2007.12539].

[332] ATLAS collaboration, *ATLAS level-1 trigger: Technical Design Report*, *ATLAS-TDR-12* (1998) .

[333] R. Achenbach et al., *The ATLAS level-1 calorimeter trigger*, *JINST* **3** (2008) P03001.

[334] S. Artz et al., *The ATLAS Level-1 Muon Topological Trigger Information for Run 2 of the LHC*, *JINST* **10** (2015) C02027.

[335] S. Ask et al., *The ATLAS central level-1 trigger logic and TTC system*, *JINST* **3** (2008) P08002.

[336] ATLAS collaboration, *ATLAS high-level trigger, data acquisition and controls: Technical design report*, *ATLAS-TRD-016* (2003) .

[337] ATLAS collaboration, *Trigger Menu in 2016*, *ATL-DAQ-PUB-2017-001* (2017) .

[338] ATLAS collaboration, *Trigger Menu in 2017*, *ATL-DAQ-PUB-2018-002* (2018) .

[339] ATLAS collaboration, *Trigger menu in 2018*, *ATL-DAQ-PUB-2019-001* (2019) .

[340] ATLAS collaboration, *Performance of electron and photon triggers in ATLAS during LHC Run 2*, *Eur. Phys. J.* **C80** (2020) 47 [1909.00761].

[341] ATLAS collaboration, *Improved luminosity determination in pp collisions at $\sqrt{s} = 7$ TeV using the ATLAS detector at the LHC*, *Eur. Phys. J. C* **73** (2013) 2518 [1302.4393].

[342] ATLAS collaboration, *Luminosity determination in pp collisions at $\sqrt{s} = 13$ TeV using the ATLAS detector at the LHC*, *Eur. Phys. J. C* **83** (2023) 982 [2212.09379].

[343] ATLAS collaboration, *ATLAS data quality operations and performance for 2015–2018 data-taking*, *JINST* **15** (2020) P04003 [1911.04632].

[344] GEANT4 collaboration, *GEANT4: A Simulation toolkit*, *Nucl. Instrum. Meth.* **A506** (2003) 250.

[345] ATLAS collaboration, *The ATLAS Simulation Infrastructure*, *Eur. Phys. J. C* **70** (2010) 823 [1005.4568].

[346] G. Gaycken and E. Moyse, *Tracking EDM in ATLAS*, *ATLAS Software tutorial* (2020) .

[347] T. Cornelissen, M. Elsing, I. Gavrilenko, W. Liebig, E. Moyse and A. Salzburger, *The new ATLAS track reconstruction (NEWT)*, *J. Phys. Conf. Ser.* **119** (2008) 032014.

[348] R. Fruhwirth, *Application of Kalman filtering to track and vertex fitting*, *Nucl. Instrum. Meth.* **A262** (1987) 444.

[349] R. Fruhwirth, *Track fitting with nonGaussian noise*, *Comput. Phys. Commun.* **100** (1997) 1.

[350] ATLAS collaboration, *Reconstruction of primary vertices at the ATLAS experiment in Run 1 proton–proton collisions at the LHC*, *Eur. Phys. J.* **C77** (2017) 332 [1611.10235].

[351] ATLAS collaboration, *Vertex Reconstruction Performance of the ATLAS Detector at $\sqrt{s} = 13$ TeV*, *ATL-PHYS-PUB-2015-026* (2015) .

[352] ATLAS collaboration, *Performance of the ATLAS Inner Detector Track and Vertex Reconstruction in the High Pile-Up LHC Environment*, *ATLAS-CONF-2012-042* (2012) .

[353] ATLAS collaboration, *Electron reconstruction and identification in the ATLAS experiment using the 2015 and 2016 LHC proton-proton collision data at $\sqrt{s} = 13$ TeV*, *Eur. Phys. J.* **C79** (2019) 639 [1902.04655].

[354] ATLAS collaboration, *Electron and photon performance measurements with the ATLAS detector using the 2015–2017 LHC proton-proton collision data*, *JINST* **14** (2019) P12006 [1908.00005].

[355] W. Lampl, S. Laplace, D. Lelas, P. Loch, H. Ma, S. Menke et al., *Calorimeter clustering algorithms: Description and performance*, *ATL-LARG-PUB-2008-002* (2008) .

[356] ATLAS collaboration, *Electron and photon reconstruction and performance in ATLAS using a dynamical, topological cell clustering-based approach*, *ATL-PHYS-PUB-2017-022* (2017) .

[357] ATLAS collaboration, *Electron and photon energy calibration with the ATLAS detector using 2015–2016 LHC proton-proton collision data*, *JINST* **14** (2019) P03017 [1812.03848].

[358] ATLAS collaboration, *Muon reconstruction and identification efficiency in ATLAS using the full Run 2 pp collision data set at* $\sqrt{s} = 13$ TeV, *Eur. Phys. J. C* **81** (2021) 578 [2012.00578].

[359] M. Cacciari, G. P. Salam and G. Soyez, *The anti-k_t jet clustering algorithm*, *JHEP* **04** (2008) 063 [0802.1189].

[360] ATLAS collaboration, *Topological cell clustering in the ATLAS calorimeters and its performance in LHC Run 1*, *Eur. Phys. J.* **C77** (2017) 490 [1603.02934].

[361] ATLAS collaboration, *Jet energy scale and resolution measured in proton–proton collisions at* $\sqrt{s} = 13$ TeV *with the ATLAS detector*, *Eur. Phys. J. C* **81** (2021) 689 [2007.02645].

[362] ATLAS collaboration, *Jet energy scale measurements and their systematic uncertainties in proton-proton collisions at* $\sqrt{s} = 13$ TeV *with the ATLAS detector*, *Phys. Rev.* **D96** (2017) 072002 [1703.09665].

[363] ATLAS collaboration, *Jet global sequential corrections with the ATLAS detector in proton-proton collisions at* $\sqrt{s} = 8$ TeV, *ATLAS-CONF-2015-002* (2015) .

[364] ATLAS collaboration, *Selection of jets produced in* 13 TeV *proton-proton collisions with the ATLAS detector*, *ATLAS-CONF-2015-029* (2015) .

[365] ATLAS collaboration, *Tagging and suppression of pileup jets with the ATLAS detector*, *ATLAS-CONF-2014-018* (2014) .

[366] ATLAS collaboration, *Identification and rejection of pile-up jets at high pseudorapidity with the ATLAS detector*, *Eur. Phys. J. C* **77** (2017) 580 [1705.02211].

[367] ATLAS collaboration, *Forward Jet Vertex Tagging: A new technique for the identification and rejection of forward pileup jets*, *ATL-PHYS-PUB-2015-034* (2015) .

[368] ATLAS collaboration, *Selection of jets produced in* 13 TeV *proton-proton collisions with the ATLAS detector*, *ATLAS-CONF-2015-029* (2015) .

[369] ATLAS collaboration, *ATLAS flavour-tagging algorithms for the LHC Run 2 pp collision dataset*, *Eur. Phys. J. C* **83** (2023) 681 [2211.16345].

[370] ATLAS collaboration, *Optimisation and performance studies of the ATLAS b-tagging algorithms for the 2017-18 LHC run*, *ATL-PHYS-PUB-2017-013* (2017) .

[371] ATLAS collaboration, *Identification of Jets Containing b-Hadrons with Recurrent Neural Networks at the ATLAS Experiment*, *ATL-PHYS-PUB-2017-003* (2017) .

[372] ATLAS collaboration, *ATLAS b-jet identification performance and efficiency measurement with $t\bar{t}$ events in pp collisions at* $\sqrt{s} = 13$ TeV, *Eur. Phys. J. C* **79** (2019) 970 [1907.05120].

[373] ATLAS collaboration, *Measurement of b-tagging Efficiency of c-jets in $t\bar{t}$ Events Using a Likelihood Approach with the ATLAS Detector*, *ATLAS-CONF-2018-001* (2018) .

[374] ATLAS collaboration, *Measurement of the c-jet mistagging efficiency in $t\bar{t}$ events using pp collision data at* $\sqrt{s} = 13$ TeV *collected with the ATLAS detector*, *Eur. Phys. J. C* **82** (2022) 95 [2109.10627].

[375] ATLAS collaboration, *Calibration of the light-flavour jet mistagging efficiency of the b-tagging algorithms with Z+jets events using* 139 fb^{-1} *of ATLAS proton–proton collision data at* $\sqrt{s} = 13$ TeV, *Eur. Phys. J. C* **83** (2023) 728 [2301.06319].

[376] *Pile-up Suppression in Missing Transverse Momentum Reconstruction in the ATLAS Experiment in Proton-Proton Collisions at* $\sqrt{s} = 8$ TeV, *ATLAS-CONF-2014-019* (2014) .

[377] ATLAS collaboration, *Performance of missing transverse momentum reconstruction with the ATLAS detector using proton-proton collisions at* $\sqrt{s} = 13$ TeV, *Eur. Phys. J.* **C78** (2018) 903 [1802.08168].

[378] D. Adams and e. a. Anastopoulos, *Recommendations of the Physics Objects and Analysis Harmonisation Study Groups 2014*, *ATL-PHYS-INT-2014-018* (2014) .

[379] A. Dainese, M. Mangano, A. B. Meyer, A. Nisati, G. Salam and M. A. Vesterinen, eds., *Report on the Physics at the HL-LHC,and Perspectives for the HE-LHC*, vol. 7/2019 of *CERN Yellow Reports: Monographs*. CERN, Geneva, Switzerland, 2019, 10.23731/CYRM-2019-007.

[380] R. K. Ellis et al., *Physics Briefing Book: Input for the European Strategy for Particle Physics Update*, *CERN-ESU-004* (2019) [1910.11775].

[381] M. Narain et al., *The Future of US Particle Physics - The Snowmass 2021 Energy Frontier Report*, *FERMILAB-FN-1219-PPD-T* (2022) [2211.11084].

[382] ATLAS collaboration, *Letter of Intent for the Phase-I Upgrade of the ATLAS Experiment*, *CERN-LHCC-2011-012* (2011) .

[383] T. Kawamoto et al., *New Small Wheel Technical Design Report*, *ATLAS-TDR-020* (2013) .

[384] ATLAS collaboration, *Technical Design Report for the Phase-I Upgrade of the ATLAS TDAQ System*, *ATLAS-TDR-023* (2013) .

[385] M. Aleksa, W. Cleland, Y. Enari, M. Fincke-Keeler, L. Hervas, F. Lanni et al., *ATLAS Liquid Argon Calorimeter Phase-I Upgrade Technical Design Report*, *ATLAS-TDR-022* (2013) .

[386] ATLAS collaboration, *Letter of Intent for the Phase-II Upgrade of the ATLAS Experiment*, *CERN-LHCC-2012-022* (2012) .

[387] ATLAS collaboration, *Technical Design Report for the ATLAS Inner Tracker Pixel Detector*, *ATLAS-TDR-030* (2017) .

[388] ATLAS collaboration, *Technical Design Report for the ATLAS Inner Tracker Strip Detector*, *ATLAS-TDR-025* (2017) .

[389] ATLAS collaboration, *A High-Granularity Timing Detector for the ATLAS Phase-II Upgrade: Technical Design Report*, *ATLAS-TDR-031* (2022) .

[390] ATLAS collaboration, *Technical Design Report for the Phase-II Upgrade of the ATLAS Muon Spectrometer*, *ATLAS-TDR-026* (2022) .

[391] ATLAS collaboration, *ATLAS Liquid Argon Calorimeter Phase-II Upgrade: Technical Design Report*, *ATLAS-TDR-027* (2022) .

[392] ATLAS collaboration, *Technical Design Report for the Phase-II Upgrade of the ATLAS Tile Calorimeter*, *ATLAS-TDR-028* (2022) .

[393] ATLAS collaboration, *Technical Design Report for the Phase-II Upgrade of the ATLAS TDAQ System*, *ATLAS-TDR-029* (2022) .

[394] ATLAS collaboration, *The ATLAS Experiment at the CERN Large Hadron Collider: A Description of the Detector Configuration for Run 3*, *CERN-EP-2022-259* (2023) [2305.16623].

[395] J. Dubbert, S. Horvat, H. Kroha, F. Legger, O. Kortner, R. Richter et al., *Development of precision drift tube detectors for very high background rates at the super-LHC*, in *2007 IEEE Nuclear Science Symposium and Medical Imaging Conference*, vol. 3, pp. 1822–1825, 2007, DOI.

[396] Y. Giomataris, P. Rebourgeard, J. P. Robert and G. Charpak, *MICROMEGAS: A High granularity position sensitive gaseous detector for high particle flux environments*, *Nucl. Instrum. Meth. A* **376** (1996) 29.

[397] T. Alexopoulos et al., *Performance studies of resistive-strip bulk micromegas detectors in view of the ATLAS New Small Wheel upgrade*, *Nucl. Instrum. Meth. A* **937** (2019) 125.

[398] G. Charpak and F. Sauli, *High-Resolution Electronic Particle Detectors*, *Ann. Rev. Nucl. Part. Sci.* **34** (1984) 285.

[399] G. Charpak, *Electronic imaging of ionizing radiation with limited avalanches in gases*, *Rev. Mod. Phys.* **65** (1993) 591.

[400] S. Majewski, G. Charpak, A. Breskin and G. Mikenberg, *A thin multiwire chamber operating in the high multiplication mode*, *Nucl. Instrum. Meth.* **217** (1983) 265.

[401] A. Abusleme et al., *Performance of a Full-Size Small-Strip Thin Gap Chamber Prototype for the ATLAS New Small Wheel Muon Upgrade*, *Nucl. Instrum. Meth. A* **817** (2016) 85 [1509.06329].

[402] S. Aefsky et al., *The optical alignment system of the ATLAS muon spectrometer endcaps*, *JINST* **3** (2008) P11005.

[403] G. Bella et al., *Development of Calorimeters Using Thin Chambers Operating in a High Gain Mode*, *Nucl. Instrum. Meth. A* **252** (1986) 503.

[404] OPAL ISRAEL collaboration, *A New High Gain Thin Gap Detector for the Opal Hadron Calorimeter*, *Nucl. Instrum. Meth. A* **252** (1986) 511.

[405] K. Nagai, *Thin gap chambers in ATLAS*, *Nucl. Instrum. Meth. A* **384** (1996) 219.

[406] H. Fukui et al., *Studies on ageing effects and rate dependence of Thin Gap Chambers*, *Nucl. Instrum. Meth. A* **419** (1998) 497.

[407] E. Etzion, Y. Benhammou, J. Ginzburg, M. Ishino, L. Levinson, G. Mikenberg et al., *The Certification of ATLAS thin gap chambers produced in Israel and China*, in *2004 IEEE Nuclear Science Symposium and Medical Imaging Conference*, vol. 1, pp. 236–241, 2004, DOI [physics/0411136].

[408] R. Keyes et al., *Development and Characterisation of a Gas System and its Associated Slow-Control System for an ATLAS Small-Strip Thin Gap Chamber Testing Facility*, *JINST* **12** (2017) P04027 [1702.01240].

[409] VDI, ed., *VDI Heat Atlas*. Springer-Verlag Berlin, Heidelberg, 2010, 10.1007/978-3-540-77877-6.

[410] IPCC, *Atmospheric chemistry and greenhouse gases*, in *Climate Change: The Scientific Basis*, (2001), https://www.ipcc.ch/report/ar3/wg1/.

[411] The SCPI Consortium, *SCPI Syntax and Style*. USA, 1999.

[412] P. T. Boggs and J. R. Donaldson, *Orthogonal Distance Regression*, *Contemporary Mathematics, vol. 112, pg. 186, 1990* **112** (1990) 186.

[413] W. Wagner, *New vapour pressure measurements for argon and nitrogen and a new method for establishing rational vapour pressure equations*, *Cryogenics* **13** (1973) 470.

[414] L. A. Forero G. and J. A. Velásquez J., *Wagner liquid–vapour pressure equation constants from a simple methodology*, *The Journal of Chemical Thermodynamics* **43** (2011) 1235.

[415] O. Behnke, K. Kröninger, T. Schörner-Sadenius and G. Schott, eds., *Data analysis in high energy physics: A practical guide to statistical methods*. Wiley-VCH, Weinheim, Germany, 2013.

[416] L. Lyons and L. Demortier, *Everything you always wanted to know about pulls*, *CDF Note 5776* (2002) .

[417] J. Neyman and E. S. Pearson, *On the Problem of the Most Efficient Tests of Statistical Hypotheses*, *Phil. Trans. Roy. Soc. Lond. A* **231** (1933) 289.

[418] S. S. Wilks, *The Large-Sample Distribution of the Likelihood Ratio for Testing Composite Hypotheses*, *Annals Math. Statist.* **9** (1938) 60.

[419] T. Adye, *Unfolding algorithms and tests using RooUnfold*, in *PHYSTAT 2011*, (Geneva), pp. 313–318, CERN, 2011, DOI [1105.1160].

[420] G. D'Agostini, *A Multidimensional unfolding method based on Bayes' theorem*, *Nucl. Instrum. Meth. A* **362** (1995) 487.

[421] G. D'Agostini, *Improved iterative Bayesian unfolding*, *Alliance Workshop on Unfolding and Data Correction* (2010) [1010.0632].

[422] D0 collaboration, *The Upgraded D0 detector*, *Nucl. Instrum. Meth. A* **565** (2006) 463 [physics/0507191].

[423] CDF collaboration, *The CDF Detector: An Overview*, *Nucl. Instrum. Meth. A* **271** (1988) 387.

[424] D0 collaboration, *Measurement of the WW production cross section with dilepton final states in $p\bar{p}$ collisions at $\sqrt{s} = 1.96\,\mathrm{TeV}$ and limits on anomalous trilinear gauge couplings*, *Phys. Rev. Lett.* **103** (2009) 191801 [0904.0673].

[425] CDF collaboration, *Measurement of the W^+W^- Production Cross Section and Search for Anomalous $WW\gamma$ and WWZ Couplings in $p\bar{p}$ Collisions at $\sqrt{s} = 1.96$˜TeV*, *Phys. Rev. Lett.* **104** (2010) 201801 [0912.4500].

[426] ALEPH collaboration, *ALEPH: A detector for electron-positron annnihilations at LEP*, *Nucl. Instrum. Meth. A* **294** (1990) 121.

[427] L3 collaboration, *The Construction of the L3 Experiment*, *Nucl. Instrum. Meth. A* **289** (1990) 35.

[428] OPAL collaboration, *The OPAL detector at LEP*, *Nucl. Instrum. Meth. A* **305** (1991) 275.

[429] DELPHI collaboration, *The DELPHI detector at LEP*, *Nucl. Instrum. Meth. A* **303** (1991) 233.

[430] OPAL collaboration, *Measurement of the $e^+e^- \to W^+W^-$ cross section and W decay branching fractions at LEP*, *Eur. Phys. J. C* **52** (2007) 767 [0708.1311].

[431] ALEPH collaboration, *Measurement of W-pair production in e^+e^- collisions at centre-of-mass energies from $183\,\mathrm{GeV}$ to $209 -$ GeV*, *Eur. Phys. J. C* **38** (2004) 147.

[432] L3 collaboration, *Measurement of the cross section of W-boson pair production at LEP*, *Phys. Lett. B* **600** (2004) 22 [hep-ex/0409016].

[433] DELPHI collaboration, *Measurement of the W pair production cross-section and W branching ratios in e^+e^- collisions at $\sqrt{s} = 161$ GeV to 209 GeV*, *Eur. Phys. J. C* **34** (2004) 127 [hep-ex/0403042].

[434] ATLAS collaboration, *Measurement of the WW cross section in $\sqrt{s} = 7$ TeV pp collisions with ATLAS*, *Phys. Rev. Lett.* **107** (2011) 041802 [1104.5225].

[435] ATLAS collaboration, *Measurement of the WW cross section in $\sqrt{s} = 7$ TeV pp collisions with the ATLAS detector and limits on anomalous gauge couplings*, *Phys. Lett. B* **712** (2012) 289 [1203.6232].

[436] CMS collaboration, *Measurement of W^+W^- production and search for the Higgs boson in pp collisions at $\sqrt{s} = 7$ TeV*, *Phys. Lett. B* **699** (2011) 25 [1102.5429].

[437] A. Azatov, R. Contino, C. S. Machado and F. Riva, *Helicity selection rules and noninterference for BSM amplitudes*, *Phys. Rev. D* **95** (2017) 065014 [1607.05236].

[438] A. Falkowski, M. Gonzalez-Alonso, A. Greljo, D. Marzocca and M. Son, *Anomalous Triple Gauge Couplings in the Effective Field Theory Approach at the LHC*, *JHEP* **02** (2017) 115 [1609.06312].

[439] A. Azatov, J. Elias-Miro, Y. Reyimuaji and E. Venturini, *Novel measurements of anomalous triple gauge couplings for the LHC*, *JHEP* **10** (2017) 027 [1707.08060].

[440] B. Mellado, X. Ruan and Z. Zhang, *Extraction of Top Backgrounds in the Higgs Boson Search with the $H \to WW^\star \to \ell\ell + E_T^{\rm miss}$ Decay with a Full-Jet Veto at the LHC*, *Phys. Rev. D* **84** (2011) 096005 [1101.1383].

[441] M. Grazzini, S. Kallweit, D. Rathlev and M. Wiesemann, *$W^\pm Z$ production at hadron colliders in NNLO QCD*, *Phys. Lett. B* **761** (2016) 179 [1604.08576].

[442] M. Grazzini, S. Kallweit, D. Rathlev and M. Wiesemann, *$W^\pm Z$ production at the LHC: fiducial cross sections and distributions in NNLO QCD*, *JHEP* **05** (2017) 139 [1703.09065].

[443] M. Grazzini, S. Kallweit and D. Rathlev, *ZZ production at the LHC: fiducial cross sections and distributions in NNLO QCD*, *Phys. Lett. B* **750** (2015) 407 [1507.06257].

[444] F. Cascioli, T. Gehrmann, M. Grazzini, S. Kallweit, P. Maierhöfer, A. von Manteuffel et al., *ZZ production at hadron colliders in NNLO QCD*, *Phys. Lett. B* **735** (2014) 311 [1405.2219].

[445] NNPDF collaboration, *Parton distributions for the LHC Run II*, *JHEP* **04** (2015) 040 [1410.8849].

[446] *ATLAS* PYTHIA 8 *tunes to* 7 TeV *data*, tech. rep., CERN, Geneva, 2014.

[447] R. D. Ball et al., *Parton distributions with LHC data*, *Nucl. Phys. B* **867** (2013) 244 [1207.1303].

[448] T. Gleisberg and S. Hoeche, *Comix, a new matrix element generator*, *JHEP* **12** (2008) 039 [0808.3674].

[449] S. Hoeche, F. Krauss, M. Schonherr and F. Siegert, *A critical appraisal of NLO+PS matching methods*, *JHEP* **09** (2012) 049 [1111.1220].

[450] S. Hoeche, F. Krauss, S. Schumann and F. Siegert, *QCD matrix elements and truncated showers*, *JHEP* **05** (2009) 053 [0903.1219].

[451] F. Cascioli, P. Maierhofer and S. Pozzorini, *Scattering Amplitudes with Open Loops*, *Phys. Rev. Lett.* **108** (2012) 111601 [1111.5206].

[452] A. Denner, S. Dittmaier and L. Hofer, *Collier: a fortran-based Complex One-Loop LIbrary in Extended Regularizations*, *Comput. Phys. Commun.* **212** (2017) 220 [1604.06792].

[453] S. Frixione, P. Nason and G. Ridolfi, *A Positive-weight next-to-leading-order Monte Carlo for heavy flavour hadroproduction*, *JHEP* **09** (2007) 126 [0707.3088].

[454] S. Frixione, P. Nason and C. Oleari, *Matching NLO QCD computations with Parton Shower simulations: the* POWHEG *method*, *JHEP* **11** (2007) 070 [0709.2092].

[455] ATLAS collaboration, *Studies on top-quark Monte Carlo modelling for Top2016*, *ATL-PHYS-PUB-2016-020* (2016) .

[456] S. Frixione, E. Laenen, P. Motylinski, B. R. Webber and C. D. White, *Single-top hadroproduction in association with a W boson*, *JHEP* **07** (2008) 029 [0805.3067].

[457] ATLAS Collaboration, *Studies on top-quark Monte Carlo modelling with* SHERPA *and* MG5_AMC@NLO, *ATL-PHYS-PUB-2017-007* (2017) .

[458] M. Beneke, P. Falgari, S. Klein and C. Schwinn, *Hadronic top-quark pair production with NNLL threshold resummation*, *Nucl. Phys. B* **855** (2012) 695 [1109.1536].

[459] M. Cacciari, M. Czakon, M. Mangano, A. Mitov and P. Nason, *Top-pair production at hadron colliders with next-to-next-to-leading logarithmic soft-gluon resummation*, *Phys. Lett. B* **710** (2012) 612 [1111.5869].

[460] P. Bärnreuther, M. Czakon and A. Mitov, *Percent Level Precision Physics at the Tevatron: First Genuine NNLO QCD Corrections to $q\bar{q} \to t\bar{t} + X$*, *Phys. Rev. Lett.* **109** (2012) 132001 [1204.5201].

[461] M. Czakon and A. Mitov, *NNLO corrections to top-pair production at hadron colliders: the all-fermionic scattering channels*, *JHEP* **12** (2012) 054 [1207.0236].

[462] M. Czakon and A. Mitov, *NNLO corrections to top pair production at hadron colliders: the quark-gluon reaction*, *JHEP* **01** (2013) 080 [1210.6832].

[463] M. Czakon, P. Fiedler and A. Mitov, *Total Top-Quark Pair-Production Cross Section at Hadron Colliders Through $O(\alpha_S^4)$*, *Phys. Rev. Lett.* **110** (2013) 252004 [1303.6254].

[464] M. Czakon and A. Mitov, *Top++: A Program for the Calculation of the Top-Pair Cross-Section at Hadron Colliders*, *Comput. Phys. Commun.* **185** (2014) 2930 [1112.5675].

[465] N. Kidonakis, *Two-loop soft anomalous dimensions for single top quark associated production with a W^- or H^-*, *Phys. Rev. D* **82** (2010) 054018 [1005.4451].

[466] N. Kidonakis, *Top Quark Production*, *Helmholtz International Summer School on Physics of Heavy Quarks and Hadrons* (2014) 139 [1311.0283].

[467] C. Anastasiou, L. J. Dixon, K. Melnikov and F. Petriello, *High precision QCD at hadron colliders: Electroweak gauge boson rapidity distributions at NNLO*, *Phys. Rev. D* **69** (2004) 094008 [hep-ph/0312266].

[468] D. J. Lange, *The EvtGen particle decay simulation package*, *Nucl. Instrum. Meth. A* **462** (2001) 152.

[469] ATLAS collaboration, *The* PYTHIA 8 *A3 tune description of ATLAS minimum bias and inelastic measurements incorporating the Donnachie-Landshoff diffractive model*, .

[470] I. Brivio, Y. Jiang and M. Trott, *The SMEFTsim package, theory and tools*, *JHEP* **12** (2017) 070 [1709.06492].

[471] I. Brivio, *SMEFTsim 3.0 — a practical guide*, *JHEP* **04** (2021) 073 [2012.11343].

[472] ATLAS collaboration, *Electron and photon performance measurements with the ATLAS detector using the 2015–2017 LHC proton-proton collision data*, *JINST* **14** (2019) P12006 [1908.00005].

[473] ATLAS collaboration, *Muon reconstruction performance of the ATLAS detector in proton–proton collision data at $\sqrt{s}$ =13 TeV*, *Eur. Phys. J. C* **76** (2016) 292 [1603.05598].

[474] ATLAS collaboration, *Jet reconstruction and performance using particle flow with the ATLAS Detector*, *Eur. Phys. J. C* **77** (2017) 466 [1703.10485].

[475] ATLAS collaboration, *Performance of pile-up mitigation techniques for jets in pp collisions at $\sqrt{s} = 8$ TeV using the ATLAS detector*, *Eur. Phys. J. C* **76** (2016) 581 [1510.03823].

[476] ATLAS collaboration, *Optimisation and performance studies of the ATLAS b-tagging algorithms for the 2017-18 LHC run*, *ATL-PHYS-PUB-2017-013* (2017) .

[477] ATLAS collaboration, *Measurement of the $t\bar{t}$ production cross-section and lepton differential distributions in $e\mu$ dilepton events from pp collisions at $\sqrt{s} = 13$ TeV with the ATLAS detector*, *Eur. Phys. J. C* **80** (2020) 528 [1910.08819].

[478] ATLAS collaboration, *Improvements in $t\bar{t}$ modelling using NLO+PS Monte Carlo generators for Run2*, *ATL-PHYS-PUB-2018-009* (2018) .

[479] ATLAS collaboration, *Measurement of $W^{\pm}$ and Z-boson production cross sections in pp collisions at $\sqrt{s} = 13$ TeV with the ATLAS detector*, *Phys. Lett. B* **759** (2016) 601 [1603.09222].

[480] ATLAS collaboration, *Measurement of $W^{\pm}Z$ production cross sections and gauge boson polarisation in pp collisions at $\sqrt{s} = 13$ TeV with the ATLAS detector*, *Eur. Phys. J. C* **79** (2019) 535 [1902.05759].

[481] ATLAS collaboration, *Multi-Boson Simulation for* 13 TeV *ATLAS Analyses*, *ATL-PHYS-PUB-2016-002* (2016) .

[482] M. Grazzini, S. Kallweit and D. Rathlev, *$W\gamma$ and $Z\gamma$ production at the LHC in NNLO QCD*, *JHEP* **07** (2015) 085 [1504.01330].

[483] K. Lehmann and B. Stelzer, *The Fake Factor Method and its relation to the Matrix Method*, *Nucl. Instrum. Meth. A* **1054** (2023) 168376.

[484] ATLAS collaboration, *Tools for estimating fake/non-prompt lepton backgrounds with the ATLAS detector at the LHC*, *CERN-EP-2022-214* (2022) [2211.16178].

[485] ATLAS collaboration, *Measurements of the production cross-section for a Z boson in association with b-jets in proton-proton collisions at $\sqrt{s} = 13$ TeV with the ATLAS detector*, *JHEP* **07** (2020) 044 [2003.11960].

[486] ATLAS collaboration, *Performance of electron and photon triggers in ATLAS during LHC Run 2*, *Eur. Phys. J. C* **80** (2020) 47 [1909.00761].

[487] ATLAS collaboration, *Measurement of the $Z \to \tau\tau$ Cross Section with the ATLAS Detector*, *Phys. Rev. D* **84** (2011) 112006 [1108.2016].

[488] ATLAS collaboration, *Observation of gauge boson joint-polarisation states in $W^{\pm}Z$ production from pp collisions at $\sqrt{s} = 13\,\text{TeV}$ with the ATLAS detector*, *Phys. Lett. B* **843** (2023) 137895 [2211.09435].

[489] ATLAS collaboration, *Measurement and interpretation of same-sign W boson pair production in association with two jets in pp collisions at $\sqrt{s} = 13\,\text{TeV}$ with the ATLAS detector*, *CERN-EP-2023-221* (2023) [2312.00420].

[490] M. Cacciari and G. P. Salam, *Pileup subtraction using jet areas*, *Phys. Lett. B* **659** (2008) 119 [0707.1378].

[491] A. J. Barr, *Measuring slepton spin at the LHC*, *JHEP* **02** (2006) 042 [hep-ph/0511115].

[492] W. Verkerke and D. P. Kirkby, *The RooFit toolkit for data modeling*, *eConf* **C0303241** (2003) MOLT007 [physics/0306116].

[493] NNPDF collaboration, *Parton distributions from high-precision collider data*, *Eur. Phys. J. C* **77** (2017) 663 [1706.00428].

[494] ATLAS collaboration, *Studies of the muon momentum calibration and performance of the ATLAS detector with pp collisions at $\sqrt{s} = 13\,\text{TeV}$*, *Eur. Phys. J. C* **83** (2023) 686 [2212.07338].

[495] ATLAS COLLABORATION collaboration, *Study of top-quark pair modelling and uncertainties using ATLAS measurements at $\sqrt{s} = 13\,\text{TeV}$*, *ATL-PHYS-PUB-2020-023* (2020) .

[496] ATLAS collaboration, *Measurements of the production cross section of a Z boson in association with jets in pp collisions at $\sqrt{s} = 13$ TeV with the ATLAS detector*, *Eur. Phys. J. C* **77** (2017) 361 [1702.05725].

[497] A. von Manteuffel and L. Tancredi, *The two-loop helicity amplitudes for $gg \to V_1 V_2 \to 4$ leptons*, *JHEP* **06** (2015) 197 [1503.08835].

[498] T. Gehrmann, A. von Manteuffel and L. Tancredi, *The two-loop helicity amplitudes for $q\overline{q}' \to V_1 V_2 \to 4$ leptons*, *JHEP* **09** (2015) 128 [1503.04812].

[499] F. Buccioni, J.-N. Lang, J. M. Lindert, P. Maierhöfer, S. Pozzorini, H. Zhang et al., *OpenLoops 2*, *Eur. Phys. J. C* **79** (2019) 866 [1907.13071].

[500] F. Buccioni, S. Pozzorini and M. Zoller, *On-the-fly reduction of open loops*, *Eur. Phys. J. C* **78** (2018) 70 [1710.11452].

[501] S. Catani, L. Cieri, D. de Florian, G. Ferrera and M. Grazzini, *Vector boson production at hadron colliders: hard-collinear coefficients at the NNLO*, *Eur. Phys. J. C* **72** (2012) 2195 [1209.0158].

[502] S. Catani and M. Grazzini, *An NNLO subtraction formalism in hadron collisions and its application to Higgs boson production at the LHC*, *Phys. Rev. Lett.* **98** (2007) 222002 [hep-ph/0703012].

[503] S. Yang, M. Xie, Y. Fu, Z. Zhao, M. Liu, L. Han et al., *Boost asymmetry of the diboson productions in pp collisions*, *Phys. Rev. D* **106** (2022) L051301 [2207.02072].

[504] C. Degrande and J. Touchèque, *A reduced basis for CP violation in SMEFT at colliders and its application to diboson production*, *JHEP* **04** (2022) 032 [2110.02993].

[505] ATLAS collaboration, *Improved Common $t\bar{t}$ Monte-Carlo Settings for ATLAS and CMS*, *ATL-PHYS-PUB-2023-016* (2023) .

[506] CMS collaboration, *Measurement of $t\bar{t}$ normalised multi-differential cross sections in pp collisions at $\sqrt{s} = 13\,\text{TeV}$, and simultaneous determination of the strong coupling strength, top quark pole mass, and parton distribution functions*, *Eur. Phys. J. C* **80** (2020) 658 [1904.05237].

[507] CMS collaboration, *Measurement of differential $t\bar{t}$ production cross sections in the full kinematic range using lepton+jets events from proton-proton collisions at $\sqrt{s} = 13\ TeV$*, *Phys. Rev. D* **104** (2021) 092013 [2108.02803].

[508] ATLAS collaboration, *Inclusive and differential cross-sections for dilepton $t\bar{t}$ production measured in $\sqrt{s}$ = 13 TeV pp collisions with the ATLAS detector*, *JHEP* **07** (2023) 141 [2303.15340].

[509] K. Agashe et al., *Report of the Topical Group on Top quark physics and heavy flavor production*, *Snowmass 2021* (2022) [2209.11267].

[510] S. Catani, S. Devoto, M. Grazzini, S. Kallweit, J. Mazzitelli and H. Sargsyan, *Top-quark pair hadroproduction at next-to-next-to-leading order in QCD*, *Phys. Rev. D* **99** (2019) 051501 [1901.04005].

[511] S. Catani, S. Devoto, M. Grazzini, S. Kallweit and J. Mazzitelli, *Top-quark pair production at the LHC: Fully differential QCD predictions at NNLO*, *JHEP* **07** (2019) 100 [1906.06535].

[512] J. Mazzitelli, P. F. Monni, P. Nason, E. Re, M. Wiesemann and G. Zanderighi, *Next-to-Next-to-Leading Order Event Generation for Top-Quark Pair Production*, *Phys. Rev. Lett.* **127** (2021) 062001 [2012.14267].

[513] J. Mazzitelli, P. F. Monni, P. Nason, E. Re, M. Wiesemann and G. Zanderighi, *Top-pair production at the LHC with MINNLO$_{PS}$*, *JHEP* **04** (2022) 079 [2112.12135].

[514] A. Denner and M. Pellen, *NLO electroweak corrections to off-shell top-antitop production with leptonic decays at the LHC*, *JHEP* **08** (2016) 155 [1607.05571].

[515] M. Czakon, D. Heymes, A. Mitov, D. Pagani, I. Tsinikos and M. Zaro, *Top-pair production at the LHC through NNLO QCD and NLO EW*, *JHEP* **10** (2017) 186 [1705.04105].

[516] M. L. Czakon et al., *Top quark pair production at complete NLO accuracy with NNLO+NNLL' corrections in QCD*, *Chin. Phys. C* **44** (2020) 083104 [1901.08281].

[517] ATLAS collaboration, *Graph Neural Network Jet Flavour Tagging with the ATLAS Detector*, *ATL-PHYS-PUB-2022-027* (2022) .

[518] ATLAS collaboration, *Graph Neural Network Jet Flavour Tagging with the ATLAS Detector*, *Public Plots: FTAG-2023-01* (2023) .

[519] ATLAS collaboration, *Expected tracking and related performance with the updated ATLAS Inner Tracker layout at the High-Luminosity LHC*, *ATL-PHYS-PUB-2021-024* (2021) .

[520] ATLAS collaboration, *Neural Network Jet Flavour Tagging with the Upgraded ATLAS Inner Tracker Detector at the High-Luminosity LHC*, *ATL-PHYS-PUB-2022-047* (2022) .

[521] ATLAS collaboration, *HL-LHC prospects for the measurement of Higgs boson pair production in the $b\bar{b}b\bar{b}$ final state and combination with the $b\bar{b}\gamma\gamma$ and $b\bar{b}\tau^+\tau^-$ final states at the ATLAS experiment*, *ATL-PHYS-PUB-2022-053* (2022) .

[522] ATLAS collaboration, *Combined effective field theory interpretation of differential cross-sections measurements of WW, WZ, 4ℓ, and Z-plus-two-jets production using ATLAS data*, *ATL-PHYS-PUB-2021-022* (2021) .

[523] J. Baglio, S. Dawson and I. M. Lewis, *NLO effects in EFT fits to W^+W^- production at the LHC*, *Phys. Rev. D* **99** (2019) 035029 [1812.00214].

[524] ATLAS collaboration, *Combined effective field theory interpretation of Higgs boson and weak boson production and decay with ATLAS data and electroweak precision observables*, *ATL-PHYS-PUB-2022-037* (2022) .

[525] RIVET, *The Rivet toolkit (Robust Independent Validation of Experiment and Theory)*, *[https://gitlab.com/hepcedar/rivet]* .

[526] A. Falkowski and F. Riva, *Model-independent precision constraints on dimension-6 operators*, *JHEP* **02** (2015) 039 [1411.0669].

[527] C. Degrande, G. Durieux, F. Maltoni, K. Mimasu, E. Vryonidou and C. Zhang, *Automated one-loop computations in the standard model effective field theory*, *Phys. Rev. D* **103** (2021) 096024 [2008.11743].

[528] LHC Higgs Cross Section Working Group, *Handbook of LHC Higgs Cross Sections: 4. Deciphering the Nature of the Higgs Sector*, *CERN-2017-002* **2/2017** (2016) [1610.07922].

[529] N. Berger et al., *Simplified Template Cross Sections – Stage 1.1*, *LHCHXSWG-2019-003* (2019) [1906.02754].

[530] *Webpage: Electroweak precision measurements at the LHC WG*, *https://lpcc.web.cern.ch/content/electroweak-precision-measurements-lhc-wg* .

Acknowledgements

The journey of writing a Ph.D. thesis has been a challenging but immensely enriching endeavor, which requires the guidance of experienced mentors. I am profoundly grateful to Prof. Dr. Beate Heinemann, whose generosity gave me the privilege of joining her group in Freiburg. Working with you has been an inspiring and transformative experience. Through our conversations, I did not only acquired some knowledge in experimental particle physics, but also experienced a personal and professional growth under your supervision. It has truly been an honor to work with you, and I really hope for the opportunity to cross our paths some time in the future.

I am indebted to Oleg Kuprash for his support and patience throughout these years. Our discussions have been enlightening, and I have learned invaluable lessons from your contagious discipline. I also want to thank Prasham Jain for brightening our office. Your optimism and resilience are a source of inspiration.

My gratitude goes to the W^+W^- analysis team, with special thanks to Hannes Mildner. I am truly fortunate to have had such a dedicated colleague throughout my journey. Words fall short in expressing my appreciation for all I learned from you. Your generosity in dedicating time to answer my questions has been immeasurable, and I am really thankful for your unwavering patience in providing those answers. I would also like to extend my appreciation to Jan Küchler, who left our team and the collaboration shortly after my arrival into the team. Despite the brief time we shared, it was a pleasure working with you and I genuinely wish you had stayed with us longer. The work I am presenting in this thesis would not have had the impact it has without your valuable contributions.

I would like to pay special regards to Philip Sommer for his exceptional support. Your essential assistance and engaging discussions on the technicalities of my analyses and my career journey have been crucial. I am still scratching my head trying to figure out how you manage to always make time for physics chats and patiently tackle all my questions over a coffee. I owe you a couple of them, so I look forward to meeting you to pay them back! I also want to thank Monica Dunford, Javier Montejo Berlingen and Kristin Lohwasser for their valuable advice and support.

My sincere gratitude to Constantin Heidegger, Mathieu Pellen, and Jack MacDonald for generously sharing your time and engaging in the content of this thesis. Your comments and remarks have been of great help, contributing significantly to my learning throughout this process.

The studies presented in this thesis also take advantage of the work carried out by thousands of scientists that directly or indirectly contributed to the results achieved by the ATLAS Collaboration. This mention is well deserved.

I am grateful to the University of Freiburg for giving me the opportunity to study in this extraordinary environment and offering me all its facilities in full. This work was carried out using the Black Forest Grid, the National Analysis Facility at DESY, and the CERN facilities. I want to thank their administrators and technical staff for keeping these in their best performance.

I extend my sincere gratitude to Gregor Herten and Ulrich Landgraf for opening the doors of the muon lab in Freiburg to me. Stephanie Zimmermann gave me the invaluable opportunity to work with detectors and other various hardware components, an experience for which I will be always be thankful for. Special thanks to Ksenia for your patience and collaborative support throughout this period. I must also acknowledge the contributions of Patrick Scholer and our technicians, Jürgen Tobias and Bernhard Pfeifer, without whom our work would not have been possible.

The PhD not only taught me profound lessons in physics and resilience, but also gifted me with one of the best times of my lifetime during the Fall of 2022. I feel blessed to have shared this incredible adventure with Simran Gurdasani during our time in Korea. The country, the people we encountered, and your friendship have truly changed my life. And I am confident this friendship will last.

To all my friends and colleagues at the physics institute and the GRK 2044, with a special mention to Julian Bollig. It was a lot of fun organizing the seminars with you and hunting students to give the talks. Special thanks to Robin, Alex, Ilia, Roman, and Mari for making this journey such a lovely time.

I wish to acknowledge the support and great love of my mother. You are my reference in effort and perseverance, and I would not be writing these words without your unconditional support. Special mention to Juan Fierro. I can not express how much I owe you. Rubén, whom was willing to listen to me when I needed it. I am lucky to have you as a friend.

Sayra, I will eternally be grateful for your unwavering assistance throughout this journey, for believing in me when I could not even believe in myself, for your aid during moments of struggle, your continuous smile, your care, and your immense love. I deeply love you.